

# Flexographic printed nanogranular LBZA derived ZnO gas sensors: Synthesis, printing and processing

Aled Rhodri Lewis MEng

Submitted to Swansea University in fulfilment of the requirements for the  
Degree of Doctor of Philosophy

Swansea University

2021

## Abstract

---

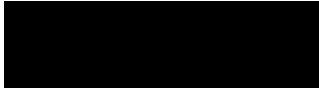
Within this document, investigations of the processes towards the production of a flexographic printed ZnO gas sensor for breath H<sub>2</sub> analysis are presented. Initially, a hexamethylenetetramine (HMTA) based, microwave assisted, synthesis method of layered basic zinc acetate (LBZA) nanomaterials was investigated. Using the synthesised LBZA, a dropcast nanogranular ZnO gas sensor was produced. The testing of the sensor showed high sensitivity towards hydrogen with response ( $\text{Resistance}_{\text{air}}/\text{Resistance}_{\text{gas}}$ ) to 200 ppm H<sub>2</sub> at 328 °C of 7.27. The sensor is highly competitive with non-catalyst surface decorated sensors and sensitive enough to measure current H<sub>2</sub> guideline thresholds for carbohydrate malabsorption (Positive test threshold: 20 ppm H<sub>2</sub>, Predicted response: 1.34). Secondly, a novel LBZA synthesis method was developed, replacing the HMTA by NaOH. This resulted in a large yield improvement, from a [OH<sup>-</sup>] conversion of 4.08 at% to 71.2 at%. The effects of [OH<sup>-</sup>]/[Zn<sup>2+</sup>] ratio, microwave exposure and transport to nucleation rate ratio on purity, length, aspect ratio and polydispersity were investigated in detail. Using classical nucleation theory, analysis of the basal layer charge symmetries, and oriented attachment theory, a dipole-oriented attachment reaction mechanism is presented. The mechanism is the first theory in literature capable of describing all observed morphological features along length scales. The importance of transport to nucleation rate ratio as the defining property that controls purity and polydispersity is then shown. Using the NaOH derived LBZA, a flexographic printing ink was developed, and proof-of-concept sensors printed. Gas sensing results showed a high response to 200 ppm H<sub>2</sub> at 300 °C of 60.2. Through IV measurements and SEM analysis this was shown to be a result of transfer of silver between the electrode and the sensing layer during the printing process. Finally, Investigations into the intense pulsed light treatment of LBZA were conducted. The results show that dehydration at 150 °C prior to exposure is a requirement for successful calcination, producing ZnO quantum dots (QDs) in the process. SEM measurements show mean radii of 1.77-2.02 nm. The QDs show size confinement effects with the exciton blue shifting by 0.105 eV, and exceptionally low defect emission in photoluminescence spectra, indicative of high crystalline quality, and high conductivity. Due to the high crystalline quality and amenity to printing, the IPL ZnO QDs have numerous potential uses ranging from sensing to optoelectronic devices.

# Declaration and Statements

---

## DECLARATION

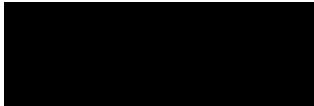
This work has not previously been accepted in substance for any degree and is not being concurrently submitted in candidature for any degree.

Signed :  (candidate)

Date: 23-07-2021

## STATEMENT 1

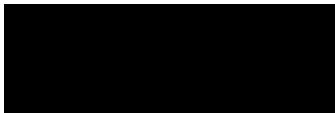
This thesis is the result of my own investigations, except where otherwise stated. Other sources are acknowledged by footnotes giving explicit references. A bibliography is appended.

Signed :  (candidate)

Date: 23-07-2021

## STATEMENT 2

I hereby give consent for my thesis, if accepted, to be available for photocopying and for inter-library loan, and for the title and summary to be made available to outside organisations.

Signed :  (candidate)

Date: 23-07-2021

# Table of Contents

---

Abstract	ii
Declaration and Statements	iii
Table of Contents	iv
Acknowledgments	x
List of Abbreviation	xi
Chapter 1 - Introduction	1
1.1 Printed electronic devices	1
1.2 Gas sensing	4
1.3 Long term project goals	6
1.3.1 Sensing material – Layered basic zinc acetate (LBZA) derived ZnO	6
1.3.2 Deposition technique – Flexographic printing	7
1.4 Thesis Outline	7
1.4.1 Chapter 2 – Literature review and background theory	7
1.4.2 Chapter 3 – Theory of experimental analytical techniques	8
1.4.3 Chapter 4 – HMTA microwave assisted LBZA synthesis, gas sensing and sodium hydroxide-based alternative	9
1.4.4 Chapter 5 - Investigations of sodium hydroxide-based microwave assisted LBZA synthesis	10
1.4.5 Chapter 6 - Flexographic printing of LBZA nanomaterial and proof of concept gas sensors	11
1.4.6 Chapter 7 - Investigation of intense pulsed light (IPL) photonic annealing conditions for the conversion of LBZA to ZnO	12
1.4.7 Chapter 8 and 9, Conclusion and Future work	12
1.4.8 Appendices.	12
Chapter 2 - Literature review and background theory	14
2.1 Zinc oxide	14
2.1.1 General properties	14
2.1.2 Nanoscale zinc oxide synthesis methods	15

2.1.3	LBZA - Layered basic zinc acetate	16
2.1.4	Summary	29
2.2	Chemiresistive gas sensing	30
2.2.1	Chemiresistive sensing working mechanism	30
2.2.2	Factors effecting sensitivity	36
2.2.3	ZnO nanosheet sensors derived from layered zinc hydroxide structures.	38
2.3	Flexographic printing	39
2.3.1	Overview	39
2.3.2	Surface tension – equilibrium and dynamic	40
2.3.3	Surface energy and wetting	42
2.3.4	Ink rheology	45
2.3.5	Flexographic inks and their properties:	46
2.3.6	Print process:	47
2.4	Intense pulse light treatment/ photonic annealing	54
Chapter 3 - Theory of experimental analytical techniques		57
3.1	Introduction	57
3.2	Morphology analytical techniques	58
3.2.1	Scanning electron microscopy (SEM)	58
3.2.2	Atomic force microscopy (AFM)	60
3.3	Chemical, optical and electronic energy level analysis techniques	60
3.3.1	Energy dispersive x-ray spectroscopy (EDS)	60
3.3.2	X-ray photoelectron spectroscopy (XPS)	61
3.3.3	X-ray diffraction analysis (XRD)	64
3.3.4	Photoluminescence (PL) and Ultraviolet-visible spectrophotometry (UV-VIS)	67
3.3.5	Ultraviolet photoelectron spectroscopy (UPS)	68
3.4	Fluid analysis	69
3.4.1	Interfacial/ surface tension (IFT) - Pendant drop method	69
3.4.2	Rotational (dynamic) viscometry	70

3.5	Statistical analysis	71
3.5.1	Mean, standard deviation and number of samples	71
3.5.2	Confidence intervals	71
3.5.3	T-test	72
3.5.4	Regression	73
Chapter 4 - HMTA microwave assisted LBZA synthesis, gas sensing and sodium hydroxide-based alternative		76
4.1	HMTA microwave assisted LBZA, synthesis and gas sensing	76
4.1.1	Methods	77
4.1.2	HMTA based synthesis method – Characterisation	83
4.1.3	HMTA based LBZA synthesis derived ZnO – Gas sensing properties	86
4.2	Sodium hydroxide-based microwave assisted growth method	101
4.2.1	Proposed method rationale	101
4.2.2	Method	102
4.2.3	Results	104
4.3	Conclusion	110
Chapter 5 - Investigations of sodium hydroxide-based microwave assisted LBZA synthesis conditions		112
5.1	Introduction	112
5.2	Methods	113
5.2.1	Effect of microwave time and $[\text{OH}^-]:[\text{Zn}^{2+}]$ ratio on morphology and purity	113
5.2.2	The effect of addition rate and increased shear on purity	117
5.3	Results	120
5.3.1	Purity and morphology as a function of relative concentration and microwave time.	120
5.3.2	The effect of addition rate and increased shear on purity and morphology	155
5.4	Unified discussion	174
5.4.1	Proposed combined LBZA nucleation and growth reaction mechanism for the sodium hydroxide-based microwave assisted growth	174

5.4.2	Relevance and applicability to flexographically printed gas sensors for carbohydrate malabsorption testing and additional uses.	178
5.5	Conclusion	183
Chapter 6	- Flexographic printing of LBZA nanomaterial and proof of concept gas sensors	185
6.1	Introduction	185
6.2	Material selection rationale	186
6.3	Chapter specific equipment overview	189
6.3.1	Flexographic Printers	189
6.3.2	Automated gas sensor testing rig	193
6.4	Methods	197
6.4.1	PFI 722 Ag NP Flexographic print – Interdigitated electrode print optimisation	197
6.4.2	Binderless glycerol based LBZA ink development	202
6.4.3	Binderless ink proof of concept test sensors	206
6.5	Results	209
6.5.1	Silver electrode print optimisation	209
6.5.2	LBZA binderless ink development	224
6.5.3	Proof of concept gas sensor prototype printing and testing	227
6.6	Conclusion	242
Chapter 7	- Investigation of intense pulsed light (IPL) photonic annealing conditions for the conversion of LBZA to ZnO	244
7.1	Introduction	244
7.2	Chapter specific equipment	244
7.2.1	Pulseforge 1200 (Novacentrix)	244
7.3	Methods	245
7.3.1	LBZA synthesis	245
7.3.2	Investigating the optical properties of LBZA	246
7.3.3	Investigation of the effects of dehydration on the intense pulsed light conversion of LBZA to ZnO	247

7.4	Results	250
7.4.1	Investigation of the optical properties of LBZA pre and post dehydration	250
7.4.2	Intense pulsed light calcination of LBZA – the effect of dehydration	253
7.5	Discussion	266
7.6	Conclusion	271
Chapter 8	- Conclusion	272
Chapter 9	- Future Work	281
Chapter 10	– Appendix A1. Additional SEM micrographs for chapter 5	Appendices-1
10.1	SEM Images for the $[\text{OH}^-]/[\text{Zn}^{2+}]$ microwave time growth experiment	Appendices-1
10.1.1	Aggregated 0 s unexposed LBZA	Appendices-1
10.1.2	0 s Microwave exposure i.e. unexposed. (T = 294 K)	Appendices-2
10.1.3	10 s Microwave exposure i.e. unexposed. (T <sub>peak</sub> = 309 K)	Appendices-10
10.1.4	20 s Microwave exposure i.e. unexposed. (T <sub>peak</sub> = 327 K)	Appendices-18
10.1.5	30 s Microwave exposure i.e. unexposed. (T <sub>peak</sub> = 351 K)	Appendices-26
Chapter 11	– Appendix A2. Simplified point charge surface potential calculation and calculation of the electrostatic/ electrochemical contribution to primary particle growth rate.	Appendices-34
11.1	Method and geometry	Appendices-34
11.2	Results and Discussion	Appendices-40
11.2.1	Single layer geometry calculations	Appendices-40
11.2.2	7-layer geometry calculations	Appendices-44
11.2.3	The effect of temperature on the electrostatic factor	Appendices-48
11.3	Conclusion	Appendices-49
Chapter 12	- Appendix B1. Automated gas sensor testing rig	Appendices-50
12.1	Schematic	Appendices-50
12.2	Gas system	Appendices-51
12.3	Electronic systems	Appendices-51
12.4	Measurement System	Appendices-52
12.5	Custom LabVIEW test program	Appendices-53



12.6	Heater track – surface temperature calibration procedure	Appendices-54
Chapter 13	Appendix B2. Flexographic printing of LBZA nanomaterial using binder-based inks	Appendices-56
13.1	Introduction	Appendices-56
13.2	Methods	Appendices-57
13.2.1	PVP Binder based LBZA ink development	Appendices-57
13.3	Results	Appendices-66
13.3.1	LBZA ink development - Ink 1) – PVP binder based	Appendices-66
13.3.2	LBZA ink development - Ink 2 - Polyethylene glycol binder (A brief overview)	Appendices-84
13.4	Conclusion	Appendices-85
Chapter 14	- Appendix B3. Miscellaneous Data	Appendices-87
14.1	Introduction	Appendices-87
14.2	Print plate designs	Appendices-87
14.3	Aqueous hydrolysis of Kapton HN, conversion to polyamic acid	Appendices-87
14.3.1	Methods	Appendices-87
14.3.2	Aqueous hydrolysis of Kapton HN Results	Appendices-90
14.4	0.375 M 75 % ethanol/ 25 % water wet chemical hydrolysis treated Kapton HN survey scans	Appendices-92
14.5	Photo of uncoated 21.8 % weight PVP LBZA ink flexographic test print	Appendices-93
14.6	XPS survey scans of the printed PVP based LBZA ink undergone calcination	Appendices-93
14.7	Measurements of important surface kinetic properties	Appendices-96
Chapter 15	Bibliography	Bibliography-1

# Acknowledgments

---

I dedicate this to my parents. Throughout the trials and tribulations involved you have been steadfast in your support, irrespective of how head strong I have been, provided me with love and support through ups and significant downs. I especially wish to thank my mother who, through thick and thin provided me support, whilst simultaneously acting as my father's carer both prior to and during the pandemic. This thesis simply wouldn't exist without you both. To my long-term friends, who have at time suffered and made great accommodations, I am eternally grateful. Especially within this last year Ian, Phil, Laura and especially Matt and Hannah, thank you.

To my friends in uni, you have all made my time enjoyable, and provided assistance even when you didn't need to whether that was sharing consumables, sacrificing machine time or staying later than necessary to preserve my sanity. Through-out the last year Steve, Emily and especially Jonathan, have provided me with a stable and friendly link to the life that I love but has caused me great stress. Thank you. To James and Dan, you both provided me great help in allowing me to turn my self-taught theoretical knowledge of chemistry and turning it into a practical array of skills. More importantly though, because of your open, friendly and honest personalities you provided me an extended network of friends that a socially awkward individual like myself wouldn't have access to, for which I am incredibly thankful. I'd also like to thank my supervisor Thierry Maffeis who trusted me with the freedom to direct and develop this project, and myself, and when there have been issues has given me stead-fast support. Oh, and grammar corrections, lots of grammar corrections.

To Laura, Sarah and Elizabeth you have no idea how grateful I am for welcoming me into the x-ray lab with open arms. When we first moved campus, SPEC and all the friends I had to come to enjoy the presence of were fractured between two campuses, with practically all of them on Singleton. You may not know it, but you helped with my sanity significantly through that first half year or so. I'd also like to extend my gratitude to the rest of AIM as well. Thank you.

I'd also like to thank Paul and all the other academic and support staff that have provided me significant support over the last year.

This work was funded through the Ser Cymru National Research Network (NRN), project NRN 039. Additional assistance was provided by Swansea University College of Engineering AIM Facility, which was funded in part by the EPSRC (EP/M028267/1), the European Regional Development Fund through the Welsh Government (80708) and the Ser Solar project via Welsh Government. I'd also like to thank SPECIFIC and especially the welsh centre for printing and coating (WCPC) at Swansea University for extensive equipment access and training, without which this thesis would not be possible.

All work in this thesis was performed by the author with the following exceptions:

- DR-UV-VIS experiments were performed by Daniel R. Jones
- Operation of the Pulseforge 1200 was performed by Abdulaziz K. Assaifan
- Automated gas sensor testing rig was designed and implemented with the aid of Josef Náhlík, whose implementation of LABVIEW code, significantly improved its usability

All experimental design and analysis was performed by the author.

## List of Abbreviation

---

Within this document numerous abbreviations are used, below is a non-exhaustive selection of the most commonly used:

- AFM. Atomic force microscopy
- BSE. Back scattered electrons
- BLBZA. Bilayered basic zinc acetate
- Ca. Capillary number
- CB. Conduction band
- CI. Confidence interval
- $E_F$ . Fermi level energy
- IDE. Interdigitated electrode
- IFT. Interfacial tension analysis
- IPA. Isopropyl alcohol a.k.a. 2-propanol
- LBZA. Layered basic zinc acetate
- min. If used as a unit, min represents minutes
- NP. Nanoparticle
- NS. Nanosheets
- OLED. Organic light emitting diode
- PL. Photoluminescence
- SAED. Selected area electron diffraction
- SEM. Scanning electron microscope
- TEM and HRTEM. Transmission electron microscope and high-resolution transmission electron microscope
- UPS. Ultraviolet photoelectron spectroscopy
- UV-VIS. Ultraviolet-visible, usually used in combination with DR-UV-VIS representing diffuse reflectance ultraviolet-visible spectrophotometry
- VB. Valance band
- XPS. X-ray photoelectron spectroscopy
- XRD. X-ray diffraction, usually short for x-ray diffraction crystallography

# Chapter 1 - Introduction

---

## 1.1 Printed electronic devices

Semiconductors are the active material in practically all modern electronic components. Traditional microelectronic device fabrication requires complex multi-step processes. For example, the deposition of a single layer of patterned material requires <sup>[1]</sup>: deposition of a resist layer; photo or electron beam lithographic patterning of the resist layer; removal of un-exposed areas; deposition of an active semiconducting layer by vapour phase deposition techniques; removal of resist and finally annealing of the layer. The procedures often require vacuum and high temperature conditions <sup>[1]</sup>, and toxic materials such as hydrofluoric acid <sup>[1]</sup>; all performed under strict clean room conditions <sup>[1]</sup>. The processes involved makes device development an inherently expensive procedure. In recent years the development of functional (i.e. non-graphic) printing has opened avenues for the cheaper development and manufacturing of devices <sup>[2]</sup>. This has led to the development of printed devices, with market research performed by BCC research <sup>[3]</sup> showing a combined market value of \$14 billion in 2017. Their reported breakdown of primary markets <sup>[3]</sup> split the fields into: 47 % organic light emitting diodes (OLED), 16.2 % electrophoretic displays, 9.0 % photovoltaics, 7.4 % electroluminescent display technology and 6.3 % sensors.

Parameter	Screen	Inkjet	Gravure	Flexographic
Print Resolution ( $\mu\text{m}$ )	$\geq 30$	$\geq 15$	$< 50$	$\geq 30$
Print Thickness ( $\mu\text{m}$ )	3-30	0.01-0.5	0.02-12	0.17-8
Printing Speed ( $\text{m.s}^{-1}$ )	0.01-1.67	$3.3 \cdot 10^{-4} - 0.083$	0.13-1.67	0.08-3
Ink Viscosity (Pa.s)	0.5-5	0.001-0.1	0.01-1.1	$0.02^{[4]} - 0.5$
Articles produced between 2016 and 18/07/21 (according to google scholar*)	26,700	13,900	3,630	3840

Table 1.1: Table of process parameter ranges for the 4 most common electronic device printing methods. \* Google scholar search consisted of the phrase “X printing electronics” where X is the particular method. Unless stated otherwise, values reproduced from a review by Khan, Lorenzelli and Dahiya <sup>[5]</sup>

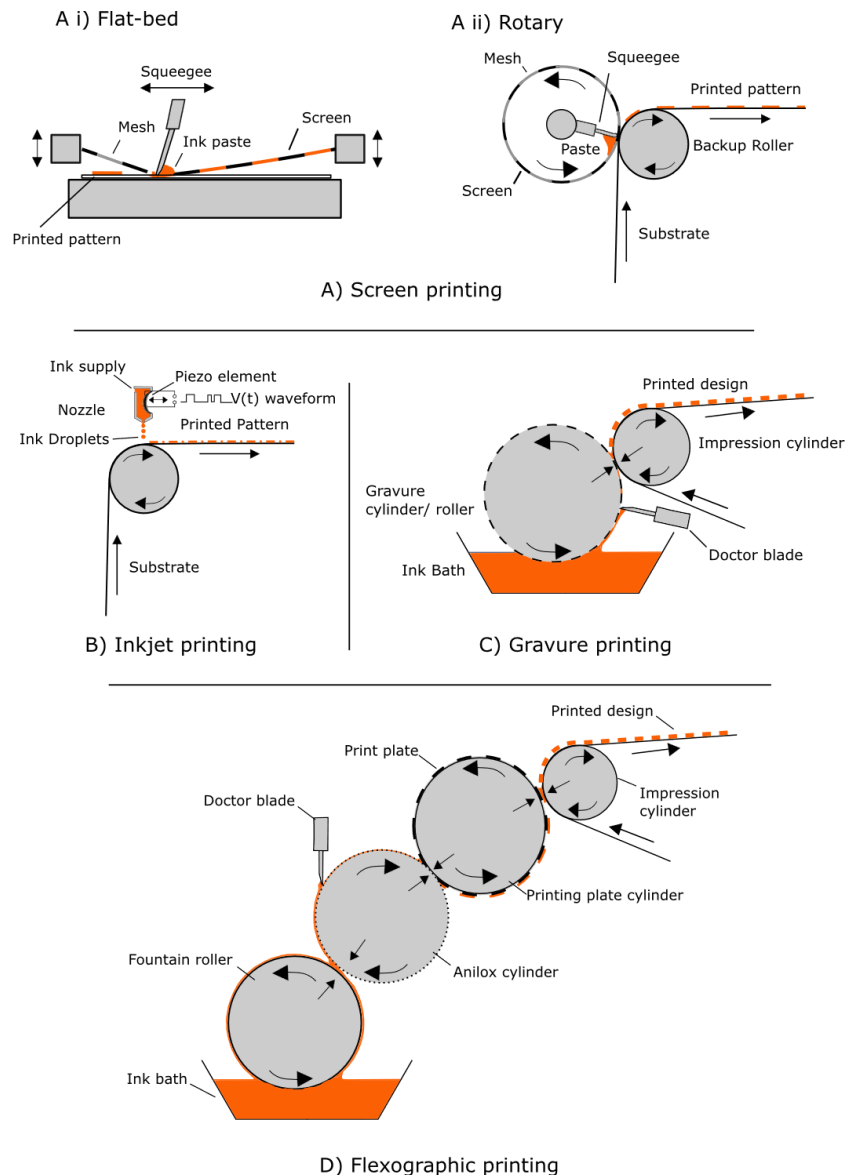


Figure 1.1: Simplified schematic of the 4 most mature functional printing processes derived from traditional graphic industry printing processes. The following brief descriptions are derived from a review by Khan, Lorenzelli and Dahiya [5]. A) Shows the schematic for i) flat-bed and ii) rotary screen-printing techniques. In screen printing a polymer screen is used as image carrier. The screen acts as a stencil, blocking off areas where no ink is to be transferred. Ink transfer volume is controlled by the presence of a mesh of defined size. A squeegee applies an ink paste across the mesh. The paste is then forced through the mesh by the squeegee on to the substrate. The ink paste needs to be shear thinning, with a high ink viscosity at rest to stop it leaking through the mesh prior to printing. B) Shows the schematic of inline inkjet. The ink is fed to a chamber typically containing a heating element or piezo transducer. A voltage is fed to the element, which ejects the ink towards the substrate. The voltage is controlled by a PC, using a digital design file, with the final print design being produced through repeated deposition of individual droplets. The shear forces introduced by the jetting force require inks with low viscosities typically much lower than 0.1 Pa.s. C) Shows the schematic for the roll to roll gravure printing process. In gravure the print design is etched into the gravure cylinder, in the form of multiple individual cells. The cells during printing are filled with ink, with the excess scraped off using a doctor blade. The cylinder is brought into contact with the substrate and the ink is transferred. The shear rate of gravure printing is dependent on the print speed, and as such a relatively broad viscosity ranges are suitable. D) Shows a schematic for the flexographic printing process. In flexographic printing the print design is etched or developed into a soft polymer plate in relief. Ink is initially transferred to the anilox cylinder via a pump or fountain roller. The anilox roller has an array of cells etched into it producing a defined volume per unit area. The doctor blade scrapes off excess ink and the anilox cylinder is brought into contact with printing plate cylinder to which the print plate is mounted, coating the desired print features on the plate in a well-defined ink volume. The print plate is subsequently brought into contact with the substrate, transferring ink and producing the final print.

Of the traditional graphic printing techniques used in literature, the focus of investigations for adoption in the electronic industry has generally been restricted to 4 techniques <sup>[5]</sup>: Silk-screen (a.k.a. screen), inkjet, gravure and flexographic printing. Table 1.1 shows process parameters; and Figure 1.1 shows schematics, and a short description for the listed printed processes. It should be noted that state of the art printing methods such as nano imprint lithography and reverse offset/ gravure offset processes are capable of printing features of 60 nm <sup>[6]</sup>, and below 3  $\mu\text{m}$  respectively <sup>[7]</sup>. The techniques however require the use of the patterning, etching and deposition processes used in the traditional microelectronic semiconductor industries to produce the image carrier <sup>[6][7]</sup>. The techniques are therefore expensive to develop.

Inkjet produces images and printed features by sequentially depositing individual droplets, the direct write nature of the technique limits the print speed attainable to below  $0.083 \text{ m.s}^{-1}$  <sup>[5]</sup>. The nozzles used are also relatively narrow ( $\sim 26 \mu\text{m}$  <sup>[8]</sup>); and can clog if the particles are too large, or the ink not stable enough. As an example, Khan *et al.* <sup>[9]</sup> studied the effects of nozzle size on a 40 % weight copper nanoparticles, with a mean diameter of 20 nm, and found that all nozzles with diameters below 30  $\mu\text{m}$  clogged.

Screen printing is less restricted by particle size, with particle size limited by the mesh size. Typical guidelines suggest that particles be  $<0.3$  times the mesh opening <sup>[10]</sup>. Using the guidelines and a mesh opening of 473  $\mu\text{m}$  <sup>[11]</sup>, particles as large as 141.9  $\mu\text{m}$  can be printed. However, the technique requires a high solid and/or binder contents to stop the ink flowing through the mesh prior to printing <sup>[12]</sup>. High binder content, dependent on the final device structure, can hinder conductivity <sup>[13]</sup> or block active surface sites in sensors <sup>[14]</sup>. This typically requires the binder to be burnt out, which can leave a residue. Ethyl-cellulose for example, which is used in numerous ink pastes, has been shown to leave residue accounting for 15 % of its starting mass, after annealing at 600 °C in air <sup>[15]</sup>.

In comparison flexographic and gravure are both able to print at high speeds <sup>[5]</sup>, with particle sizes typically up to the depth of the anilox/ gravure cells used, and with a significantly reduced viscosity requirements than screen printing as can be seen in Table 1.1. Gravure requires the use of an etched metal cylinder <sup>[5]</sup> for each print design used and development costs to produce a printed device can rapidly grow <sup>[16]</sup>. Flexographic printing in contrast only requires the replacement of the soft polymer print plate to change the print design <sup>[5]</sup>, and is therefore significantly cheaper. Flexographic printing also has additional advantages being capable of printing on practically any substrate; whether it is flexible such as polymer films <sup>[17]</sup>, or brittle such as ceramics and silicon wafers <sup>[17]</sup>. This makes the

technique fundamentally adaptable; able to produce most devices that printing would be used for.

Of the semiconductor materials that can be printed, wet chemical synthesised ZnO, with a wide-band gap of 3.3 eV at room temperature <sup>[18]</sup>, is a promising candidate. The material typically takes the form of an intrinsically n-type material with high conductivity <sup>[18]</sup>, due to the spontaneous formation of defects during its synthesis <sup>[18]</sup>, that act as shallow electron donor species <sup>[18]</sup>. Due to the wide-band gap and fully occupied d-band states; ZnO is chemically stable over a range over a broad range of temperatures <sup>[19]</sup>. Due to its ease of synthesis <sup>[18]</sup>, high conductivity and wide-bandgap, ZnO has been used in a broad range of printed devices such as:

- Thin film <sup>[20]</sup> and nanowire <sup>[21]</sup> transistors, for low power, low frequency integrated circuits
- Memristor devices non-volatile memory <sup>[22][23]</sup>
- Spintronic devices, typically in the form of ferromagnetic doped ZnO <sup>[24]</sup>
- Electron transport layers in photovoltaic cells <sup>[25][26]</sup>
- UV photosensors <sup>[27][28][29]</sup>
- Piezoelectric nanogenerators <sup>[30]</sup>
- Biosensors <sup>[31][32]</sup>
- Gas sensors <sup>[33][34][35][36][37]</sup>

## 1.2 Gas sensing

Gas sensing is the process of the detection and analysis of volatile compounds. The detection and discrimination of gases has a variety of purposes, for example:

- Atmospheric pollution monitoring <sup>[38]</sup>
- Monitoring for food spoilage <sup>[39]</sup>
- Monitoring manufacturing processes <sup>[40]</sup>
- Monitoring for local hazardous environmental conditions e.g. CO concentration testing to prevent CO poisoning <sup>[41]</sup>
- Ethanol breath analysis for the detection of drink drivers <sup>[42]</sup>
- Breath analysis for disease detection and monitoring <sup>[43][44][45][46]</sup>

Breath analysis is a field of research looking at the presence and concentration of specific volatile compounds that can act as biomarkers of underlying diseases <sup>[43]</sup>. The most well-

established breath test used in clinical settings is for the detection of carbohydrate malabsorption <sup>[47][48][49]</sup> e.g. lactose intolerance, and small intestine bacterial overgrowth (SIBO)<sup>[47][50][48][49]</sup>. The breath test measures the concentration of H<sub>2</sub> <sup>[49]</sup>, and in a small proportion of cases, CH<sub>4</sub> <sup>[47]</sup>, in the breath of patients after they have consumed a source of carbohydrate that is being tested for. Current testing procedures can be split into two forms depending on the analysis method used. The first, which is the gold standard, uses mass spectrometry techniques <sup>[43][46]</sup>, such as gas chromatography mass spectrometry (GC-MS)<sup>[46]</sup>. GC-MS is a highly sensitive technique capable of measuring compounds at the single part per billion (ppb) level <sup>[46]</sup> and has exceptionally low interference from other compounds that may be present <sup>[46]</sup>. The technique however requires expensive equipment <sup>[43]</sup> and a skilled operator <sup>[43]</sup> and is therefore not typically used at the point of care, or appropriate for use at home <sup>[46]</sup>. The second method consists of the use of one of several specialised commercial analysis platforms. The platforms typically contain an electrochemical gas sensor for the H<sub>2</sub> sensing element <sup>[51][52][53]</sup>, and an infrared analyser <sup>[51][52]</sup> for the CH<sub>4</sub> sensing element; or metal oxide (MOx) conductometric gas sensors for both gasses <sup>[54][55]</sup>. Electrochemical gas sensors measure the current or voltage produced by reactions at the surface of electrodes immersed in an electrolyte <sup>[56]</sup>; whereas conductometric (a.k.a. chemiresistive) sensors produce a change in resistance due to reactions that occur at the surface of semiconducting materials <sup>[56]</sup>. The devices require significantly less specialised components than GC-MS systems and, as a result, are significantly cheaper <sup>[43][46]</sup>. They also do not require a dedicated, specially trained operator with the testing and interpretation of results performed automatically by the system <sup>[43][46]</sup>.

H<sub>2</sub> electrochemical sensors usually contain an aqueous sodium hydroxide electrolyte <sup>[40]</sup>. Evaporation of aqueous electrolyte can lead to reduced device lifetimes <sup>[40][57][46]</sup> and to counter this, hydrophobic gas permeable membranes are used <sup>[46]</sup>. The presence of a membrane creates a diffusion barrier and as a result electrochemical sensors have long response times <sup>[46]</sup>. In contrast, MOx sensors using wide-band gap semiconductors with fully occupied d-bands such as ZnO and SnO<sub>2</sub> are typically more stable <sup>[58][19]</sup>. Two of the traditional drawbacks of metal oxide conductometric sensing elements are the sensitivity to multiple analytes that maybe present <sup>[19]</sup> and the relatively high temperatures between 250 °C and 500 °C <sup>[19][43]</sup> that limits substrate choice <sup>[59]</sup>, and increases energy consumption <sup>[60][61]</sup>. In recent years, catalysts <sup>[19]</sup> and the use of nanomaterials <sup>[19]</sup> has reduced the operation temperatures, sometimes to as low as room temperature <sup>[60][62][63]</sup>.

The sensitivity to multiple analytes can be addressed through the use of arrays of sensors with different sensing materials, i.e. an electronic nose <sup>[19][64][65]</sup>. Each material has a unique sensitivity to each gas, by analysing the response of the elements in the array, the presence



of specific analytes can be discriminated <sup>[19][66]</sup>. The production of cheap arrays in an easily portable form factor requires patterning techniques such as those produced by the described printing techniques.

### **1.3 Long term project goals**

The long term aims of this project are to produce printed gas sensors for cheap carbohydrate malabsorption sensors. Towards the aims of the project the following sensing material and deposition technique have been identified as promising candidates.

#### **1.3.1 Sensing material – Layered basic zinc acetate (LBZA) derived ZnO**

Layered basic zinc acetate derived nanogranular ZnO has been identified as a promising gas sensing material. The material typical forms sheet <sup>[67][68]</sup> or belt-like structures <sup>[69][70][71]</sup> with lengths up to 250  $\mu\text{m}$  <sup>[69]</sup>, and thicknesses typically between 10 and 50 nm <sup>[69]</sup>. When calcined, LBZA converts to ZnO, producing interconnected grains with minimum reported diameters of 9.25 nm <sup>[69]</sup>. Small grain size in conductometric gas sensors is associated with high sensitivities <sup>[19][72]</sup>, whilst as previously stated, ZnO is known a stable material at the temperatures traditionally required for gas sensing (>300 °C). LBZA can be easily synthesised through a variety of methods <sup>[73][74][71][75]</sup>, these will be described in detail in section 2.1. The initial proposed and presented method in this work is an in-house modification of the hexamethylenetetramine (HMTA) derived microwave assisted synthesis method reported by Tarat *et al.* <sup>[67]</sup> The method consists of microwaving a solution of HMTA and zinc acetate at 800 W for approximately a minute, followed by cooling and centrifuge cleaning.

### **1.3.2 Deposition technique – Flexographic printing**

Flexographic printing has been chosen as the sensing material deposition technique due to its capability of printing:

- Patterned features, therefore allowing for the development of arrays of gas sensors for the uses within an electronic nose
- LBZA particles that would clog inkjet nozzles
- At a rapid rate ( $\leq 3 \text{ m.s}^{-1}$  [5]) reducing the manufacturing costs
- On a variety of substrates, allowing for adaptability in the development process
- Using low-cost flexible polymer print plates as compared to the etched gravure cylinders.

## **1.4 Thesis Outline**

The investigations that follow are presented such that readers from various backgrounds (printing, semiconductor, gas-sensing industries etc.) can understand the experimental results and outcomes. Towards that end, the subsequent chapters are arranged as follows.

### **1.4.1 Chapter 2 – Literature review and background theory**

Chapter 2 presents the theory and a review of literature of the LBZA synthesis methods, gas sensing, flexographic print process and intense pulsed light treatment. The chapter is split into the following sections:

- ZnO properties and synthesis methods (section 2.1 ). With respect to the synthesis methods covered, first a brief overview of methods for producing nanostructured ZnO is presented. Subsequently, the section focusses on LBZA synthesis methods and crystal growth reaction mechanisms
- Conductometric gas sensing (section 2.2 ). First an overview of the theory of conductometric gas sensors is presented. Then a short review of published layered zinc hydroxide derived gas sensors is presented.
- Flexographic printing (section 2.3 ). Initially a cursory overview of devices produced via the flexographic process is presented. Next is a description of

important fluid properties relevant to the process; namely surface/ interfacial tension, contact angle and wetting, and viscosity. The flexographic printing process is then split into its individual steps, starting with inking of the anilox and ending with drying effects on the final print pattern morphology. For each step relevant literature is presented on how process parameters affect the final print quality. Finally, a summary presenting ink and process parameter requirements for optimisation of the print process is presented

- Intense pulsed light treatment (section 2.4 ). The final body of work in the thesis describes the application of intense pulsed light treatment for the conversion of LBZA to ZnO. IPL uses rapid pulses of light to heat the material, and is able to anneal ZnO producing a high quality crystalline material with exposure times  $<7$  ms <sup>[76]</sup>. The final section of chapter 2 is dedicated to a short description of the process and the underlying physics.

## 1.4.2 Chapter 3 – Theory of experimental analytical techniques

Due to the breadth of fields included in the experiments, a brief overview of the theory governing the analysis techniques, and the interpretation of their results is provided. The chapter is split into 3 primary sections:

- Morphological analysis, i.e. techniques that measure the height or width and length of particles and other print features. This section covers scanning electron microscopy (SEM) and atomic force microscopy (AFM)
- Chemical, optical and electronic analysis. This section covers techniques used to analyse the chemistry through elemental concentration and crystallographic analysis; and those that analyse the optical emission related to the crystal band structure and defect states, and the relevant positioning of energy bands relative to vacuum energy. Finally, the section covers theory of the statistical analysis used within the thesis to provide rigour to the conclusions drawn. The techniques described include:
  - o Chemical techniques: Energy dispersive x-ray analysis (EDS) and x-ray photoelectron spectroscopy (XPS) for elemental and functional group quantification; x-ray diffraction analysis (XRD) for crystallographic analysis
  - o Optical techniques: photoluminescence (PL), ultraviolet-visible spectrophotometry
  - o Energy band analysis: Ultraviolet photoelectron spectroscopy (UPS)

- Analysis relating to properties of fluids. The subsection covers interfacial tension analysis, contact angle analysis and viscosity analysis techniques.
- Statistical analysis. The final subsection covers the statistical methods used throughout the thesis to help confirm the results. Specifically, regression, t-tests and the calculation of confidence intervals are described.

Whilst chapter 3 covers the theory behind the experimental techniques; experimental details are provided within each experimental chapter in sections 4.1.1 , 4.2.2 , 5.2 , 6.4 , prior to the presentation of results and discussion.

### **1.4.3 Chapter 4 – HMTA microwave assisted LBZA synthesis, gas sensing and sodium hydroxide-based alternative**

This chapter introduces methods of LBZA production and is split into two sub chapters, each with their own introduction, experimental details, results, discussion and conclusion.

#### ***1.4.3.1 Section 4.1 – HMTA Microwave assisted LBZA, synthesis and gas sensing***

The first sub chapter starts by introducing the inhouse HMTA based microwave assisted LBZA synthesis method. The morphology of the particles is initially analysed, and the mean mass yield of the synthesised LBZA (per synthesis) measured. Subsequently, a dropcast LBZA derived nanogranular ZnO gas sensor using a commercial alumina substrate is manufactured. The gas sensing performance for CO, CH<sub>4</sub> and H<sub>2</sub> for concentrations between 50 and 200 ppm, and temperatures between 234 °C and 328 °C, are measured. The responses are then compared to those from conductometric gas sensors reported in literature, and to guideline malabsorption testing thresholds.

#### ***1.4.3.2 Section 4.2 – Sodium hydroxide-based microwave assisted growth method***

The mass yield measured in the first chapter (mean 32 mg per synthesis) was too low for practical use for the development of printed sensors. The second sub chapter therefore introduces a modified sodium-hydroxide based microwave assisted LBZA synthesis method. A brief trial of the method is presented, with the purity, morphology and mass yield of the

method measured. The technique produced particles with lengths compatible with the flexographic printing process ( $< 24 \mu\text{m}$ ); and a significantly improved yield with mean yield of 1.237 g per synthesis (standard deviation 61 mg), representing an increase base (hydroxide) conversion from 4.08 % to 71.2 %. The high yields showed promise for the synthesis method for the LBZA to be used in the final project aims. However, the method showed reduced purity than compared to the HMTA method, with the presence of trace impurities; with the lengths more polydispersed. As such, the final experiments are split in two directions performed simultaneously: a detailed investigation of the synthesis procedure; and the development of flexographically printed proof of concept gas sensors, and investigations into the processing of LBZA films by intense pulsed light exposure.

#### **1.4.4 Chapter 5 - Investigations of sodium hydroxide-based microwave assisted LBZA synthesis**

In chapter 4 impurities and polydispersity in length were observed. The presence and loss of impurities were theorised to account for the broad standard deviation in the mass yield measurements. To reduce impurities, control length and aspect ratio and reduce polydispersity, two experiments were performed. This chapter presents the most detailed analysis of aqueous synthesis of LBZA in literature, and the first to provide a reaction mechanism capable of describing all observed morphological features.

##### ***1.4.4.1 Section 5.3.1 - Purity and morphology as a function of relative concentration and microwave time***

The first experiment investigates the combination of the  $[\text{OH}^-]/[\text{Zn}^{2+}]$  ratio and the microwave exposure, using diffraction analysis to measure phase purity and derive the conditions where maximum yield exists. SEM is then used to investigate the effects of the synthesis conditions on polydispersity, length and aspect ratio. No reaction mechanism capable of describing the measured data is present in literature at the time of writing. As such the crystalline structure of the LBZA basal layer is analysed for symmetry breaking conditions, and crystal growth theories, classical nucleation theory and oriented attachment theory in particular, applied.

#### ***1.4.4.2 Section 5.3.2- The effect of addition rate and increased shear on purity and morphology***

The inability to remove impurities through controlling microwave exposure times and  $[\text{OH}^-]/[\text{Zn}^{2+}]$  ratio necessitated investigation of the nucleation conditions. The second experiment therefore investigates the combined effect of shear rates and addition rates of the reactants on purity. Two stirring methods are trialled; the first stirring method is the same as used for all previous experiments (a simple stir bar in a beaker), whilst the second uses a higher shear rate method (using a larger area stir bar and a baffle in a beaker). Additionally, three addition rates are trialled. The first, the same as all previous experiments, adds the sodium hydroxide solution to the zinc acetate solution within 1 second. The second introduces the sodium hydroxide solution over a period of 15 seconds. The last method introduces both zinc acetate and sodium hydroxide simultaneously over a period of 20 seconds. Finally, the effect of microwave exposure using the high shear rate and simultaneous addition method is briefly explored.

#### **1.4.5 Chapter 6 - Flexographic printing of LBZA nanomaterial and proof of concept gas sensors**

This chapter focuses on the development of proof of concept flexographic printed LBZA derived gas sensors, and the second ever flexographic printed gas sensor reported in literature. The chapter begins with an overview of material choices for the substrate and conductive ink for the interdigitated electrodes used to connect the sensing layer to test electronics. Based on pricing and thermal requirements needed for both the long term goals and 350 °C LBZA calcination temperature, Kapton HN was chosen as the substrate material; whilst the restricted choices for conductive flexographic inks limited the electrode material to silver produced using silver nanoparticle inks.

Initial printing tests using the commercial nanoparticle ink purchased showed defects due to drying and poor wetting of the substrate. To improve wetting, O<sub>2</sub> plasma, wet chemical hydrolysis, and combined O<sub>2</sub> plasma and wet chemical treatments are trialled. The final combined O<sub>2</sub> plasma and wet chemical treatment led to an improvement in substrate wetting and print quality.

The development of a glycerol-based binderless LBZA flexographic ink is then presented, and print parameters investigated. The optimized print parameters resulted in a uniform

printed film. Using printed silver electrodes with an LBZA overlay a fully flexographic proof of concept gas sensor is presented. Results from 3 sensors are reported and analysed. The sensors showed responses to H<sub>2</sub> 7.8 times greater than that of the HMTA derived sensor, as such the current-voltage characteristics are recorded and energy barriers for conduction approximated. The energy barriers are compared to those measured from a detailed analysis of nanogranular ZnO synthesised from HMTA derived LBZA, presented by Jones <sup>[77]</sup>, and reported literature values of Ag and Ag<sub>2</sub>O.

#### **1.4.6 Chapter 7 - Investigation of intense pulsed light (IPL) photonic annealing conditions for the conversion of LBZA to ZnO**

This chapter details the investigations of intense pulsed light treatment (IPL) as an alternative calcination method to convert LBZA to ZnO. The chapter is split into two sections, the first examines the requirement for dehydration of LBZA prior to IPL treatment, using diffuse reflectance ultraviolet-visible spectrophotometry. The second section investigates the size of crystallites produced, the magnitude of the band-gap and relative energy band positions, and the area ratios of exciton to defect band emission (representative of crystalline quality.) Finally, the values are compared to literature, and the conductivity of the material and its gas sensing properties inferred.

#### **1.4.7 Chapter 8 and 9, Conclusion and Future work**

Highlights and a brief overview of the results presented in previous chapters is initially presented in chapter 8. Finally, chapter 9 presents potential work that needs to be performed next to further develop the project towards the final goals of cheap, flexographically printed, carbohydrate malabsorption sensors. Additionally, potential experiments to further develop and confirm the reaction method for LBZA synthesis present in chapter 5 are proposed.

#### **1.4.8 Appendices.**

Short descriptions of the gas sensor testing equipment; additional data relevant to experiments that would take up excessive space; and the development of a PVP binder based

LBZA flexographic ink that was replaced with the glycerol ink; are presented in the Appendices with references to each piece provided in the main text where relevant.

Appendices with heading A relate to work relevant to chapter 5 and heading B relate to work relevant to chapter 6.



## Chapter 2 - Literature review and background theory

---

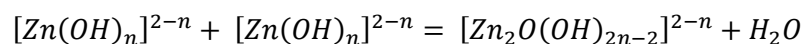
### 2.1 Zinc oxide

#### 2.1.1 General properties

Zinc oxide (ZnO) is a II-VI <sup>[78][79]</sup> wide bandgap amphoteric metal oxide semiconductor, with a direct band gap  $\sim 3.37$  eV at room temperature <sup>[79][80]</sup> and exists generally in one of two crystal types cubic Zincblende and more typically wurtzite with lattice parameters  $a=3.2$  Å and  $c=5.21$  Å <sup>[80][81]</sup>. Under normal conditions zinc oxide is typically an n type semiconductor <sup>[79][80]</sup>, thought to be due to native defects such as oxygen vacancies and hydrogen and zinc interstitials introduced during crystal growth <sup>[80]</sup>, though this is not without controversy <sup>[80]</sup>. Deep level transient spectroscopy (DLTS) and density functional theory (DFT) calculations have shown that oxygen vacancies form deep level donors ( $E_a = 530$  meV via DLTS <sup>[82]</sup>) instead of the required shallow donors to explain the conductivity. In addition, uncomplexed zinc interstitials have been calculated to have high formation energies, and high mobilities and as a result are unstable at room temperature <sup>[80][83]</sup>. Uncomplexed zinc interstitials are therefore unlikely to be present in the concentrations required to be the source of the n type behaviour <sup>[80][83]</sup>. The most likely candidates for the n-type behaviour at present are unintentional hydrogen doping <sup>[80][81]</sup> and zinc interstitial nitrogen complexes (Zni-NO) <sup>[80]</sup>. P type doping has been reported with N <sup>[84][85]</sup>, P <sup>[86][87]</sup>, Sb <sup>[88]</sup>, As <sup>[89][90][91]</sup>, Ag <sup>[92]</sup>, Li <sup>[93][94]</sup>, Na <sup>[95][96][97]</sup> dopants with variety of methods and mechanisms. Reproducibility however, has been a major problem <sup>[83][83]</sup>, with the unintentional n-type dopants both shallow and deep usually act to compensate and counteract any intended doping <sup>[78][80]</sup>. Due to the wide bandgap and full 3d band <sup>[19]</sup> Zinc oxide is typically chemically stable over a large range of temperatures which has allowed for the use in gas sensors <sup>[98][99][100][101][102][102]</sup>, catalysts <sup>[103][104][105][106]</sup> and due to the high exciton binding energy of 60 meV <sup>[79][80]</sup> in optical devices such as UV lasers <sup>[80][107]</sup> and UV photodetector <sup>[108][109]</sup>.

## 2.1.2 Nanoscale zinc oxide synthesis methods

Due to their large surface volume ratio <sup>[19]</sup> and easy processability <sup>[19]</sup> nanomaterials offer an exciting set of properties for a variety of purposes examples of which include various types of sensors <sup>[99][18]</sup>, optoelectronics <sup>[107][18]</sup>, printed photovoltaic materials <sup>[18]</sup> and catalysts <sup>[110]</sup>. Zinc oxide nanoparticles can be grown via a variety of methods <sup>[79][19][18][111]</sup> and dependent on growth conditions in a variety of morphologies <sup>[79][19][18]</sup>. Chemical vapour deposition (CVD) and physical vapour deposition (PVD) <sup>[112]</sup> can produce a large array of highly crystalline Zinc oxide nanoparticles <sup>[79][18]</sup> however it requires high temperatures and requires expensive vacuum-based equipment, where-as solution methods provide cheap and easy processing <sup>[79]</sup>. There are two general methods for producing ZnO in solution: direct synthesis or via synthesis of a precursor particle followed by conversion typically by calcination <sup>[79]</sup>. In the direct synthesis route zinc oxide is produced via dehydration of Zinc hydroxide complexes in a process known as oxolation, as shown in Equation 2.1 <sup>[18][113]</sup>:



Equation 2.1

Where n = 2, 3 or 4.

If a hydroxide bridge ( $\mu$ -OH) is formed instead of an oxo (O) bridge then the process is known as ololation <sup>[113]</sup>. In mildly basic conditions ololation is the main process <sup>[113][113]</sup>, and oxolation in strongly basic conditions <sup>[113]</sup>.

The final morphology is dependent on the degree of supersaturation i.e. the concentration of growth units. Low concentrations of growth units (typically Zinc hydroxide complexes) tends to result in the growth of high aspect nanorods and nanowires <sup>[114][115]</sup>, whereas large concentrations tends to result in microspheres or twinned crystals <sup>[114][116][117]</sup>. The preferential growth in the [001] direction is typically assigned to the higher energy resulting from the  $Zn^{2+}-O^{2-}$  dipole present in the c axis <sup>[118]</sup>. which, when the growth is starved, tends to favour c axis rather than lateral growth. This however has been disputed by Morin *et al.* <sup>[119]</sup> who showed the presence of Eshelby-twist features (a strain induced feature in TEM images <sup>[114]</sup>), running parallel to the c axis. This particular feature is associated with screw defect driven Burton-Carbera-Frank growth (BCF - otherwise known as spiral growth) <sup>[119]</sup>. They then went on to confirm that the kinetics of the reaction conformed to that of BCF growth and not layer by layer growth, which that the dipole model assumes <sup>[119]</sup>.

Irrespective of the reaction mechanism, this effect has been used by many researchers to produce ZnO nanowire/ nanorod arrays typically using ammonia <sup>[120][121]</sup> or hexamethylenetetramine (HMTA) <sup>[122][17][123][124]</sup>, which act as both ligand and base <sup>[120]</sup>. In the HMTA based synthesis, HMTA hydrolyses in water releasing ammonia <sup>[122][17]</sup>. The presence of ammonia in either method, creates soluble ammonia zinc  $[\text{Zn}(\text{NH}_3)_x]^{2+}$  complexes reducing supersaturation <sup>[120][121]</sup>. The reduced supersaturation then results in heterogenous growth when in the presence of a zinc oxide seed layer following the reaction in Equation 2.1 <sup>[120]</sup>. In the HMTA based synthesis, the hydrolysis requirement slows the formation of hydroxide species, further reducing supersaturation.<sup>[125]</sup> Through the introduction of additional ligands such as citrate or ethylenediamine, suppression of growth at the (0001) and (0110) facets respectively allows for a variety of structures such as disks, hexagonal platelets, needles and flowers to be grown <sup>[126]</sup>.

Methods utilising precursor particles synthesized via sol-gel <sup>[127][128]</sup>, hydro/ solvothermal <sup>[129][130]</sup> and microwave methods <sup>[67]</sup> typically rely on co-ordination with organic ligands followed by calcination to convert to zinc oxide. The resultant morphologies produce granular films with grain size dependent on calcination temperature and time <sup>[69][67]</sup>.

## 2.1.3 LBZA - Layered basic zinc acetate

### 2.1.3.1 LBZA crystal structure

A relatively simple route to making quasi 2D zinc oxide is to first make layered basic zinc acetate (LBZA) nanobelt/ nanosheets/ nanoplatelets of general formula  $\text{Zn}_5(\text{OH})_{10-x}(\text{OOCCH}_3)_x \cdot n\text{H}_2\text{O}$  (where x usually is equal to 2 <sup>[131]</sup>) and then thermally decompose the structure resulting in porous nanocrystalline zinc oxide. Layered basic salts (LBS)/ layered metal hydroxides are a form of layered hydroxide clay, a class of materials that also include layered double hydroxides and hydroxyl double salts. LBS consist of stacks of  $[\text{M}(\text{X})_y\text{OH}_{xy-z}]^{+z}$  metal hydroxide basal layers <sup>[132]</sup>. Each basal layer unit cell is under-coordinated, with a net positive charge centred on the under co-ordinated cations <sup>[132]</sup>. To maintain charge neutrality, anions occupy the area between each layer, in an area known as the interlayer gallery, or interbasal space <sup>[132]</sup>. Typically, water and/ or small organic molecules are intercalated alongside the anions <sup>[132]</sup>. LBZA has a hexagonal unit cell, with crystallographic parameters:  $a = 3.183 \text{ \AA}$  and  $c = 14.75 \text{ \AA}$  <sup>[75]</sup>.

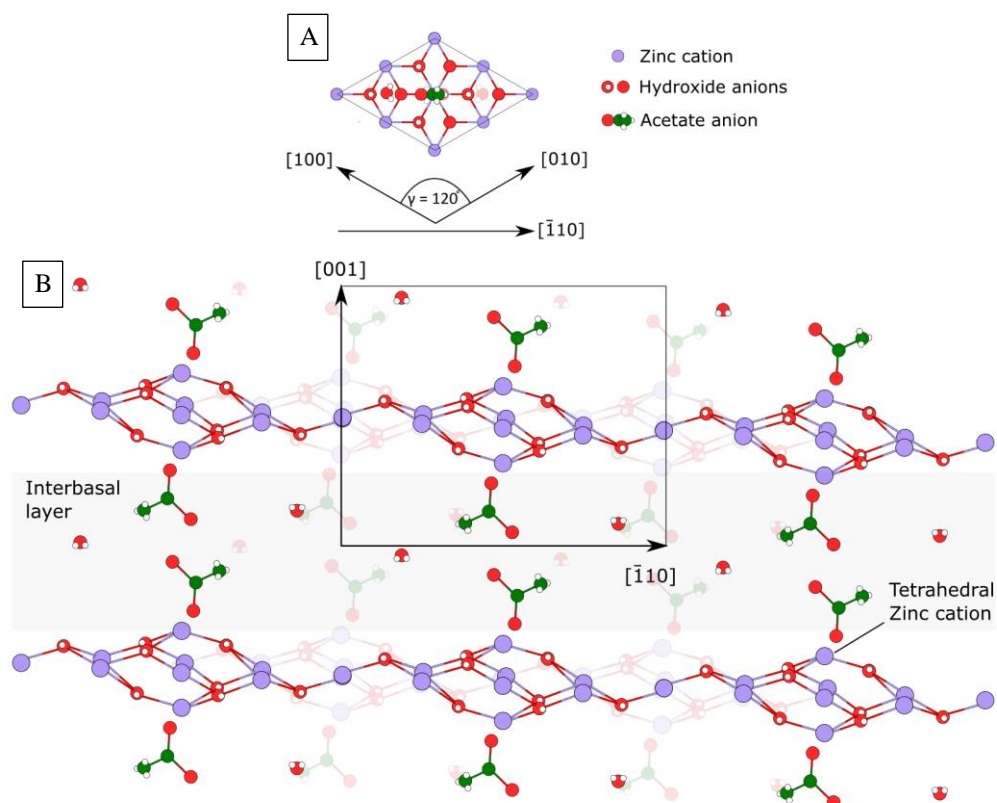


Figure 2.1: A) Top down projection of the LBZA unit cell assuming the crystal structure  $Zn_5(OH)_8Cl_2 \cdot 2H_2O$  <sup>[75]</sup> assumption. Annotations show the  $a$  ([100]) and  $b$  ([010]), unit cell vectors alongside the interplane angle  $\gamma$ . B) Side on projection, showing the  $c$  ([001]) unit cell vector and  $[\bar{1}10]$  direction. The unit cell, centred on a single layer, is enclosed within the box. Annotations show the interbasal layer and position of the tetrahedral zinc cation. Acetate and water are not necessarily accurate of actual conformation and are used to demonstrate co-ordination to the zinc cation.

LBZA normally takes the form of crystallites of sub 100nm thickness with lateral dimensions ranging from sub-micron to hundreds of microns <sup>[132][69]</sup>. Its unit cell is composed of positively charged layers of octahedral and tetrahedral co-ordinated zinc hydroxide with a +2 charge per unit cell <sup>[132]</sup>. To maintain charge neutrality two acetate anions are intercalated within the interbasal spacing <sup>[132]</sup>, along with 2 water molecules per unit cell. The position of the acetate and water within the layer is currently subject to debate, with some authors claiming it is:

- Acetate co-ordinate directly to the tetrahedral zinc, water un-coordinated. Isostructural to  $Zn_5(OH)_8Cl_2 \cdot 2H_2O$  <sup>[75]</sup>
- Acetate un-coordinated, water co-ordinated to the tetrahedral zinc. Isostructural to  $Zn_5(OH)_8(NO_3)_2 \cdot 2H_2O$  <sup>[133]</sup>

Simplified top down (A) and side on (B) projections of the LBZA unit cell, based on the  $Zn_5(OH)_8Cl_2 \cdot 2H_2O$  assumption, are shown in Figure 2.1.

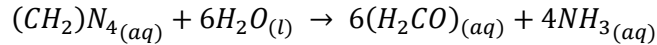
### 2.1.3.2 LBZA synthesis methods

Layered hydroxides are a well-studied class of material and can be synthesized via a variety of methods which can generally be broken down into three main categories. The first two categories are dependent on whether the hydroxide anions are provided by base addition, or hydrolysis of water. The final category relies on the ‘memory effect’. Methods that depend upon addition of base include dropwise addition of sodium hydroxide to zinc acetate at room temperature<sup>[73]</sup>, aqueous mixtures of ammonia and zinc acetate<sup>[74][71]</sup> and microwave irradiation of Zinc salt solutions in the presence of urea or HMTA. Methods based upon hydrolysis of water include hydrolysis of zinc acetate in polyol media under the addition of water<sup>[75][75]</sup>, hydrolysis of zinc acetate dihydrate in methanol at 60 °C<sup>[134]</sup>, sonochemical reaction followed by aging at room temperature of aqueous zinc acetate<sup>[135]</sup>, sonication of zinc acetate in the presence of peroxides in a Fenton like reaction in water ethanol blends<sup>[136]</sup> and directly from hydrolysis of Zinc acetate in water at a variety of temperatures<sup>[68][69]</sup>. The final and arguably most interesting method utilizes the memory effect, where upon addition of zinc oxide to an aqueous solution of zinc acetate the layered hydroxide reforms<sup>[131]</sup>.

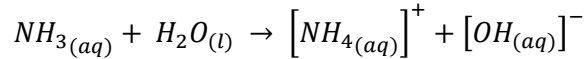
Whilst the main phase of LBZA contains 2 molecules of water and acetate and an interlamellar spacing of 1.34nm, LBZA forms with a variety of hydration states as evident by the  $\pm 0.35\text{nm}$  variation of the (001) reflection recorded by XRD<sup>[131]</sup>. In addition authors report a bilamellar structure based on the presence of 2 sets of basal plane reflections and their subsequent harmonics<sup>[68]</sup>. This is however highly unlikely unless the structure is a heterostructure with distinct sections of the two materials; otherwise a single set of reflections from the periodic bilamellar motif would be present. This will be revisited in Chapter 5 where a separate ultrathin particle is observed both in XRD and SEM. Whilst the authors interpretation of the XRD is incorrect, it is still useful to look at the reactions conditions as to where this so called BLBZA phase exists<sup>[68]</sup>. It is well known that metal cations can act as Brønsted Lowry acids, disassociating the coordinated water in the hydration shell producing metal hydroxide species and liberating protons. In aqueous solutions of zinc acetate, under low concentrations (0.025M) and low temperatures (50 °C) single phase LBZA forms<sup>[68]</sup>. Increasing the concentration increases the acidity and at concentrations between 0.1M and 0.2M the above mentioned ‘BLBZA phase’ forms<sup>[68]</sup>. Zinc oxide starts to form at low concentrations when increasing the temperature to 70 °C and 90 °C<sup>[68]</sup>. At concentrations greater than 0.2 M the pH has dropped to the point where hydrolysis is hindered and formation of the required hydroxide ions for crystallisation and precipitation no longer occurs<sup>[68]</sup>.

TGA analysis of the ‘BLBZA’ phase appears to reveal excess of acetate and a normalised stoichiometry of  $Zn_5(OH)_7(OOCCH_3)_3 \cdot 4H_2O$  [68]. As such ‘BLBZA’ forms when the hydroxide concentration is too low for the pure LBZA phase to form but there is large enough excess that an additional acetate rich phase can form.

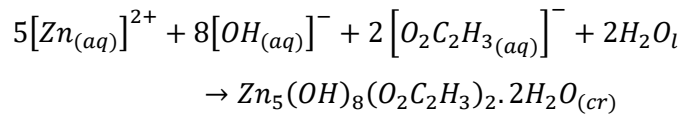
Of the methods proposed microwave assisted growth provides one of the more rapid ways of production of highly crystalline LBZA. In the method produced by Tarat *et al.* [67], which is the first synthesis method trialled in these investigations, 0.02 M hexamethylenetetramine (HMTA) is stirred into an aqueous solution of 0.1 M zinc acetate dihydrate and 0.02M zinc nitrate. The solution is then irradiated for 2 minutes at 800 W. Upon heating in water, HMTA hydrolyses breaking down into ammonia and formaldehyde (Equation 2.2), with ammonia subsequently hydrolysing producing ammonium hydroxide (Equation 2.3). The hydroxide anions being uniformly distributed rapidly co-ordinate to the zinc cations and acetate and start to crystallize (Equation 2.4) and precipitate out of solution resulting in LBZA nanosheets (LBZA NS) with thickness in the range of 20 – 100 nm and lateral dimensions of 1-5  $\mu m$ .



Equation 2.2



Equation 2.3



Equation 2.4

The authors [67] then went on to use the LBZA NS post calcination into ZnO in die sensitized solar cells and gas sensors for which the high surface to volume ratio of the nanogranular zinc oxide is ideal.

### 2.1.3.3 Layered zinc hydroxide growth mechanism

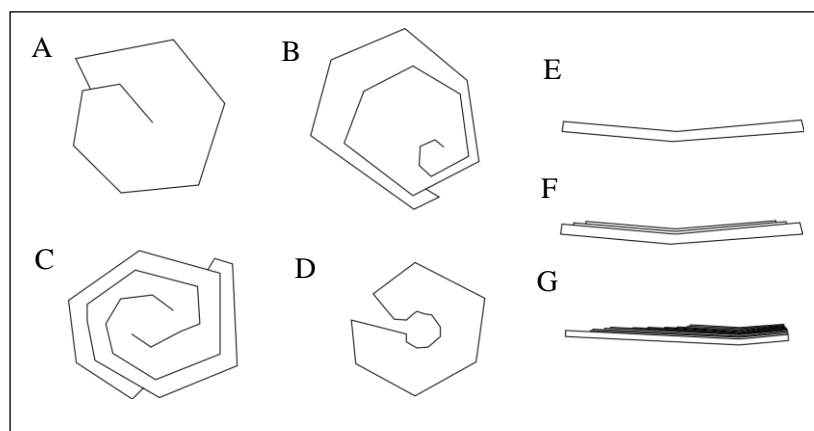


Figure 2.2: Diagram of examples of screw dislocation induced spiral growth features seen in literature of the isostructural chloride analogue of LBZA. A-D) Top down views of A) Single screw defect centred growth with a low Burgers vector (defect displacement vector), B) Off centred single screw defect, C) Twin screw defect spiral growth and D) Hollow core spiral growth with dissolution of the high Burgers vector (high stress) spiral defect centre. E)-G) Side on views of E) Single centered screw defect with growth where each layer's lateral growth is greater than the vertical growth, F) Single centered screw defect with growth where each layer's lateral growth is lower than the vertical growth and G) Single off centered screw defect with growth where each layer's lateral growth is less than the vertical growth resulting in a tapered cross section. Note that the spiral often has very weak contrast in SEM micrographs and the steps at the terminating external surface small and subtle.

Growth of layered metal hydroxides can generally be broken down into 2 main pathways, primary growth, i.e. adsorption/ deposition of mononuclear and polynuclear ionic compounds <sup>[137]</sup> and secondary growth, i.e. aggregation <sup>[138][139]</sup>. For secondary growth, oriented attachment in particular has been directly observed in liquid cell Transmission electron microscopy (TEM) for layered double hydroxides <sup>[137]</sup>. Oriented attachment is a process where multiple particles will align via rotation and translation to lower their free energy and can subsequently either stay aggregated, forming a mesocrystal <sup>[140]</sup> or bond together, undergoing fusion/ coalescence, into a single crystal known as an oriented aggregate <sup>[140][141]</sup>. Primary growth of single crystalline hexagonal layered double hydroxides <sup>[142]</sup> and layered zinc hydroxysulphate <sup>[114]</sup> has been shown to occur via BCF growth. BCF growth, as first described kinetically by Burton, Carbera and Frank in 1951 <sup>[143]</sup>, propagates via kink sites where the energy barrier for growth is lowest. The kink sites within the theory self-propagate and originate at a singular, or multiple, screw dislocation defect/s. BCF growth is generally expected accepted to be one of the major growth modes of anisotropic crystals at relatively low supersaturations <sup>[114]</sup>.

Layered zinc hydroxychloride (simonkolleite), which is assumed to share the same basal layer structure to layered zinc hydroxyacetate (LBZA) <sup>[75]</sup>, has been claimed by multiple authors to occur via a layer by layer (Frank-van der Merwe) growth mechanism. Their claims were based on observation of multiple distinct layers and single crystalline selected area electron diffraction (SAED) patterns <sup>[144][145]</sup>. Close observation of the general morphology of simonkolleite phases reported in the authors' papers <sup>[144][145]</sup> and wider literature <sup>[146][147][148][149][150][150]</sup>, however, shows morphological characteristics of BCF growth <sup>[114][142][151]</sup>, i.e. weakly visible spiral surfaces, centred and off-centred helical hexagonal growth, multiple spiral centres, etc. TEM results <sup>[145][144]</sup> of simonkolleite also show stress induced contrast changes, and hollow cores that occur due to dissolution in highly stressed screw dislocation centres <sup>[114]</sup>. Figure 2.2 provides a schematic overview of observed features.

This was shown to be the case by Song *et al.* <sup>[152]</sup> who synthesised various layered zinc hydroxide crystals with different anions. The varying crystals had differing magnitudes of spiral growth features, created by varying the anion used in a hydrothermal HMTA based method. In their work, systems with:

- Pure zinc acetate resulted in purely LBZA nanobelts
- Zinc chloride resulted in hexagonal simonkolleite with weak but present surface spirals. Furthermore, increased treatment time of the simonkolleite resulted in vertical stacked morphology and more visible and extreme spiral feature formation.
- Zinc acetate with sodium chloride and zinc acetate with sodium chloride both resulted in hexagonal simonkolleite with partial delamination at the ends. The surfaces showed increased roughness such as would be seen through secondary growth via agglomeration with some structures presenting a bowl-like morphology.
- Zinc acetate with Dodecyl trimethylammonium chloride (DTAC) resulted in simonkolleite and more extreme spiral rotation resulting in what could be described as a 'rose like' morphology where the edges partially delaminated and lifted.
- Zinc di-N-ethyl-N,N dimethylammonium acetic chloride (Zn(EDAC)<sub>2</sub>) resulted in simonkolleite with a higher degree of crystallinity and structure than Zinc acetate with DTAC and approaching that of Zinc chloride. Replacing the ethyl hydrocarbon tail with butyl (BDAC) and octyl (ODAC) groups resulted in simonkolleite with higher stress as shown by increased layers, delamination and highly stacked and deformed crystals in the case of ODAC.

Song *et al.* concluded that chloride co-ordinated preferentially with the under co-ordinated positively charged Zn tetrahedra. At the edges however, co-ordination of acetate anions



prevented the basal layers coming within range of the van der Waals contact distance due to their larger molecular size. For cases where the acetate content was larger, delamination occurred. Increasing the molecular size increased stress resulting in more extreme morphologies, however it was assumed by Song *et al.* that the acetate and ammonium groups of the larger molecules co-ordinated to Zinc tetrahedra and underwent electrostatic attraction to the basal plane respectively. The co-ordination of acetate and ammo groups was therefore assumed to help to stabilise against delamination. The arguments provided by Song *et al.* can be expanded and refined further by taking account the crystallographic refinement procedures performed on simonkolleite and their analysis by Hawthorne and Sokolova [153]. Specifically, the Chloride anion must undergo hydrogen bonding with 3 hydrogen atoms on hydroxides within the next layer to satisfy its bond-valency requirements. The larger DTAC and EDAC molecules can both form interlayer hydrogen bonds through the free chloride present in the salts, stabilising the screw dislocation induced stress. Acetate in comparison will have methyl groups facing the next layer which have been predicted by Monte Carlo simulation by Alagona, Ghio and Kollman [154] to not undergo hydrogen bonding in water, even though the methyl group has a partial charge due to induction stemming from the negatively charged oxygen. As a result, it can generally be assumed that the hydrogen bonding between anion and the next layer is required to stabilise the stress induced by the screw dislocation. As the outer facing acetate methyl group is unable to undergo hydrogen bonding and Van der Waals forces are significantly weaker [155], BCF growth is energetically unfavourable. This results in fundamentally different growth mechanisms even though the basal layer structure is equivalent.

BCF growth like features appear to generally exist for LBZA synthesised via hydrolysis of Zinc acetate dihydrate in alcohols/ organic solvents [134][122][127][156][130][75][157]. An often referenced method produced by Hosono *et al.* [134], described the formation of LBZA ‘rose’ like morphology, synthesised via 0.15M Zinc acetate dihydrate in Methanol. Initial heteronucleation on the glass slides due to the very low supersaturation from slow  $[\text{Zn}(\text{MeOH})_6]^{2+}$  hydrolysis is followed by circular growth driven by interfacial tension. Subsequently the formation of the rose morphology was claimed to be due to the nucleated cluster growing into contact with each other. This latter hypothesis is at direct odds with their SEM data where formation of the rose morphology is shown to also be proceeding from isolated particulates. Each individual ‘petal’, for no better term, appears to be hexagonal in form and the general clusters are reminiscent of an amplified version of the most extreme spiral growth formation using DTAC by Song *et al.* [152]. The formation of screw defects can be explained by strain due to mismatched lattice constants, and coefficient of thermal expansions, between substrate and overlayer during epitaxial heteronucleation

and growth <sup>[158][159]</sup>. The observed growth can then be explained by BCF growth theory via the:

- very low supersaturation
- lower permittivity of methanol ( $\epsilon_{r-\text{Methanol}} = 32.6$  <sup>[134]</sup> vs  $\epsilon_{r-\text{Water}} \approx 77.5 - 80$  <sup>[160][161]</sup>)
- reduced solvent hydrogen bonding capacity <sup>[162]</sup> to the outer basal layers that would stabilize against complete delamination.

The mechanism would likely be similar to the epitaxial spiral growth of ZnO NWs nucleated and grown from screw defect in screw defect rich GaN thin films. <sup>[163]</sup> In contrast LBZA growth in water only appears to exist with BCF growth features if the synthesis is performed with:

- the addition of stabilisers such as Pluronic F127 ( $\text{EO}_{106}\text{PO}_{70}\text{EO}_{106}$ ) <sup>[70]</sup>
- significant pressure and reduction of permittivity during hydrothermal synthesis <sup>[164][164]</sup> (for Layered basic zinc nickel acetate where the structure is identical except for the octahedral Zn(II) being directly substituted for Ni(II))
- significantly reduced chemical potential during nucleation (totals far lower than for other anions, no more than a few mM <sup>[68][135]</sup> or via very slow dropwise addition <sup>[165]</sup> <sup>[73]</sup>) and hence growth rates.

Otherwise they always exist in nanobelt or platelet form <sup>[71][131][166][152][133][68][70]</sup>. The belt formation is also seen in ethanol and mixed water solvent blends by Hacıu and Birer <sup>[136]</sup> where supersaturation is rapidly increased via ultrasonication of peroxides increasing chemical potential, whereas zinc oxide was always observed in water. It can generally be assumed then for reactions in water growth proceeds via a different and rapid pathway.

High resolution transmission electron microscopy (HRTEM) of LBZA nanobelts by Li, Zhang and Wang <sup>[70]</sup> show the belts are composed of asymmetric primary nanoparticles, irregular in shape with dimensional anisotropy, and widths on the order of 5 nm and lengths varying between 5 nm to greater than 10 nm. Furthermore, low dose selected area electron diffraction (SAED) patterns of LBZA produced by thermal aqueous hydrolysis of HMTA by van Rijt *et al.* <sup>[166]</sup> produced strong well defined single crystalline  $(\bar{1}20)$  and  $(010)$  reflections showing  $[010]$  preferred growth. Applying Scherrer's equation (Equation 3.3) to the  $(\bar{1}20)$  and  $(010)$  planes from the mature LBZA reflection results in figure 3 of their journal article <sup>[166]</sup> using their 300 keV electron wavelength (70.8 pm) produces values of approximately 13.5 nm for the  $[\bar{1}20]$  direction, and 21.15 nm for the  $[010]$  direction. The values are two to three orders of magnitude smaller than the length of the observed nanobelts

the diffractograms are taken from, and are similar to the HRTEM results of Li, Zhang and Wang. Similar trends in ratio of line width between the two peaks can be seen in XRD diffractograms by Tarat *et al.*<sup>[167][67]</sup>. Furthermore, synthesis of single crystals of alkali-metal rare-earth double carbonates with a general focus on layered  $(\text{NH}_4)_2\text{Y}(\text{CO}_3)_2 \cdot \text{H}_2\text{O}$  produced platelets/ sheets<sup>[168]</sup>. The sheets were shown to be made up of primary particles between 1 and 8 nm under HRTEM, with larger 10 – 60 nm particles using AFM. Their analysis of the kinetics involved showed if primary growth was the expected pathway the timescales involved would require timescales of  $\approx 10^{99}$  days. It was argued that morphological features of the primary particles created differing ion adsorptions and the creation of a dipole resulted in oriented attachment. The belts have remarkably similar structures to the LBZA platelets and nanobelts as those from aqueous synthesised LBZA, whilst similar surface roughness features are seen in AFM scans on LBZA nanobelts performed by Tarat *et al.*<sup>[167]</sup>. The formation of belts with the same multi-length scale features suggests that oriented attachment growth processes likely underlie the growth for aqueous LBZA.

#### **2.1.3.4 Crystal formation - classic nucleation theory**

To fully explain the synthesis of a crystal, the first step is to describe the nucleation conditions from which all other growth stems. According to the LaMer and Dinegar's theory of colloid nucleation and growth<sup>[169][170]</sup> there are 3 stages to colloid growth:

- In the first stage, the phase i.e. the solution, is supersaturated with a molecule. As supersaturation increases nucleation occurs slowly, with the rate increasing with the degree of superstation.
- Once a critical value is reached, the chemical potential of the molecule in the phase exceeds that for the nucleated colloid. As a result, the rate of nucleation rapidly increases with a concurrent drop in supersaturation (stage 2).
- Eventually the degree of supersaturation is lowered to a point where nucleation no longer occurs at a significant rate. Growth of the stable nuclei then proceeds by diffusion limited growth until equilibrium is reached with dissolution of the particle. The degree of dispersal is related to the duration of the first two stages.

When the degree of supersaturation is minimal, as in the case of dilute dropwise reactions the resultant colloid size distribution is polydisperse<sup>[169]</sup>. Alternatively, if the concentration far exceeds the critical threshold for nucleation, then nucleation occurs over a long period of

time and again the resulting size distribution is polydisperse <sup>[169]</sup>. A monodisperse solution is only produced for concentrations moderately above the critical threshold where the stage 2 seeding occurs briefly <sup>[169][171]</sup>.

### 2.1.3.5 Primary growth of ionic crystals

Post nucleation, the crystals undergo primary growth i.e. growth via deposition of growth species on the individual crystals. Crundwell <sup>[172][173]</sup> derived and analysed the effect of surface charge as a result of ion deposition on the growth kinetics of crystal surfaces in liquids, with the aim of understanding how the electrical potential across the Stern layer effects the dehydration and subsequent deposition of the ions. The Stern layer, the region of semi-rigidly adsorbed water and partially or fully dehydrated ions at the interface of the charged surface and the fluid, has an electrical potential usually on the order of 0.1 V <sup>[172][174]</sup> and electric fields on the order of  $10^9 \text{ Vm}^{-1}$  <sup>[172][174]</sup>. As a result, the stern layer potential can have a significant effect on growth kinetics. Crundwell modified Eyring's transition state theory to include a Nernstian electrochemical/ electrostatic static term, based on a Boltzmann distribution, to account for surface potential across the Stern layer. Based on his work on dissolution of ionic crystals (the reverse/ time and energy symmetrical microscopic process) <sup>[175][176]</sup> which successfully modelled crystal growth from literature, he produced the partial deposition rate equations for cations ( $r_+$ ) and anions ( $r_-$ ), shown in Equation 2.5 and Equation 2.6 respectively:

$$r_+ = \overleftarrow{k}_+[M^{Z+}] \exp\left(-\frac{Z_+F\Delta\phi}{2RT}\right) + \overrightarrow{k}_+ \exp\left(\frac{Z_+F\Delta\phi}{2RT}\right)$$

Equation 2.5

$$r_- = \overleftarrow{k}_-[A^{Z-}] \exp\left(\frac{Z_-F\Delta\phi}{2RT}\right) + \overrightarrow{k}_- \exp\left(\frac{Z_-F\Delta\phi}{2RT}\right)$$

Equation 2.6

Where:

$$\overleftarrow{k}_{\pm} = \kappa \frac{k_B T}{h} \exp\left(-\frac{\Delta G_{\pm}^{\# \leftarrow}}{RT}\right)$$

Equation 2.7

$$\overrightarrow{k}_{\pm} = \kappa \frac{k_B T}{h} \exp\left(-\frac{\Delta G_{\pm}^{\# \rightarrow}}{RT}\right)$$

Equation 2.8

Where:

- $\overleftarrow{k}_{\pm}$  is of the form of the typical Eyring reaction rate for the formation of the chemical bond for the cation (+) and anion (-), but with transition state free energy activation barrier purely due to chemical contributions (e.g. species and co-ordination type, bond angles etc)  $\Delta G_{\pm}^{\# \leftarrow}$ .
- $\overrightarrow{k}_{\pm}$  is of the form of the typical Eyring reaction rate for the breaking of the chemical bond for the cation (+) and anion (-), again with transition state free energy activation barrier purely due to chemical contributions  $\Delta G_{\pm}^{\# \rightarrow}$
- $\kappa$  is the transmission coefficient at the barrier
- $k_B$  is Boltzmann's constant
- $T$  is temperature in Kelvin
- $h$  is Planck's constant
- $R$  is the gas constant.
- $Z_{\pm}$  is the charge number on the cation and anion respectively
- $F$  is Faradays constant
- $\Delta\phi$  is the Galvani outer potential between the surface and the outer Helmholtz plane (i.e as measured across the Stern layer) due to surface charge imbalance. The potential is also referred to as the surface potential difference.
- $[M^{Z+}]$  and  $[A^{Z-}]$  are the concentration at the outer Helmholtz plane of cations and anions respectively
- The factor of 2 in the denominator of the exponential of Equation 2.5 and Equation 2.6 represents the fact that the reaction occurs half way through the stern layer.
- The factors  $\exp\left(-\frac{Z_{\pm} F \Delta\phi}{2RT}\right)$  and  $\exp\left(\frac{Z_{\pm} F \Delta\phi}{2RT}\right)$  represent the electrostatic effect on adsorption and desorption for ions in the Stern layer respectively.

It can be seen that while the surface charge is positive, the rate of attraction and deposition of cations/ cation complexes decreases exponentially relative to the typical Eyring reaction

rate (Equation 2.7). However, anions/ anion complexes experience an exponential increase in the reaction rate, with the reverse being true for a net negative surface charge. As a result, the attraction and deposition rate of each ion works to counter each other and reduce the charge imbalance with the surface tending to neutrality. Once an ion deposits in the neutral state, it raises the magnitude of potential across the stern layer. The system then works to restore neutrality by attracting and depositing ions of opposite charge, and repelling ions of like charge. For reactions containing spectating counter-ions, absorption at surface sites will generally be under competition as the same equations apply to them. If the spectator ions have larger ionic radii they would require larger energy to incorporate into the surface due to the increased stress <sup>[177]</sup>. The increased stress would in turn raise the chemical potential of the crystal surface increasing the rate of dissolution in the areas under stress <sup>[178]</sup>.

As deposition proceeds the magnitude of the surface charge and potential increases in the direction of the adsorbed charges, increasing the rate of de-adsorption of ions that have not reacted and formed part of the surface. The factor  $\exp(-Z_{\pm}F\Delta\phi/2RT)$  will be at a minimum when the deposited surface charge is neutral, as such the rate limiting step will most likely be the initial attraction and deposition of an ion under the neutral condition.

### **2.1.3.6 Secondary growth – oriented attachment**

In addition to the primary growth of individual crystals, crystallites can form through the attachment/ aggregation of particles.

As two particles approach each other they feel a variety of forces <sup>[137]</sup>. The strength of the forces acting on both particles will be a function of:

- The inter-particle angle and separation <sup>[141][179]</sup>
- Surface potentials (van-der-Waals, surface charge, dipole etc.) <sup>[141][179]</sup>
- Suspending fluid shear rate <sup>[137]</sup>
- Thermal motion <sup>[141][179]</sup>
- Additional solution properties such as permittivity, and ionic strength <sup>[141][180][179]</sup>

For ionic particles without a dipole and no surface charge the net forces will be generally be attractive van der Waal interactions and, if close enough to the particle, coulombic interactions due to the multipole potential of alternating ionic charges within the crystal lattices <sup>[181]</sup>. The coulombic potential is repulsive if the particles are aligned with similar charges on the closest facets, and attractive if the particles are aligned such that the particles

have opposite charge <sup>[141][181]</sup>. If the repulsive forces are large enough the particle tends to rebound and reorientate until the alignment of opposite charges occur <sup>[141]</sup>. The particles then attract and accelerate towards each other either coagulating (no mass transfer with a layer of intervening solvent) or fusing/ coalescing (mass transfer) <sup>[141]</sup>. For a particle with surface charge, there is an additional dominant coulombic potential that is either repulsive (like charges), or attractive (opposite charges) and can act at a distance <sup>[141]</sup>. If the surface charge of either particle is due to an internal dipole, and if it approaches at an angle, one face feels an attraction and the other repulsion <sup>[141] [179]</sup>. The imbalanced forces cause the particle to rotate to lower its energy <sup>[141] [179]</sup>, once the two particles have orientated so their surfaces have opposite charge facing each other they feel a net attraction. The mechanism as described have been directly viewed and studied in liquid cell TEM for iron oxyhydroxide nanoparticles <sup>[182]</sup>, Pt<sub>3</sub>Fe nanorods <sup>[183]</sup> ZnO nanorods <sup>[179]</sup> and layered double hydroxides <sup>[137]</sup>. By taking advantage of intrinsic dipoles nanorods <sup>[184]</sup>, nanowires <sup>[184]</sup>, nanoprisms <sup>[184]</sup> and other highly anisotropic particles <sup>[185]</sup> have been synthesised via oriented attachment. Oriented attachment does not require surface charge, and can occur on any surface as the final attachment step is driven by van-der-Wall interactions <sup>[141]</sup>.

Liu *et al.* <sup>[179]</sup> performed liquid cell TEM observations; and corresponding classical density functional theory (cDFT), and Langevin dynamics simulation, of oriented attachment of 5 nm ZnO nanoparticles, which contain an internal dipole. They showed that the energy barrier was between  $kT$  and  $3kT$  for all surfaces at room temperature. Liu *et al.* then showed that unlike the non-polar surfaces which entered the attraction process at separations of  $\sim 2$  nm, the process of attraction for the dipole containing surfaces started at  $> \sim 10$  nm, started rotating at  $\sim 5$  nm and are fully aligned by  $\sim 1$  nm. The authors show that effects of the dipole are significant enough to overcome diffusion processes. However, they note that the confined dimensions of the liquid cell, where the presence of a local dielectric interface can change the length scale the electric forces act on and increase viscosity, might produce an anonymously large torque <sup>[179]</sup>. It can be assumed then that depending on the dipole strength, viscosity and temperature <sup>[179]</sup>, that Brownian motion can lower the probability for dipole mediated oriented attachment, which will decrease with increasing temperature and inversely with viscosity. Additionally, permittivity and temperature and ionic strength would also alter the Debye length ( $l_D$ ) i.e. the charge screening distance that the dipole will be felt within, according to Equation 2.9 <sup>[1]</sup>:

$$l_D = \sqrt{\frac{\epsilon_0 \epsilon_r k_B T}{2e^2 \sum C_n Z_n^2}}$$

Equation 2.9

Where  $\epsilon_0$  is the permittivity of free space;  $\epsilon_r$  is the relative permittivity which is inverse proportionality to temperature <sup>[186]</sup>;  $k_B$  is the Boltzmann's constant; T is absolute temperature in Kelvin;  $e$  is the elementary charge; and  $\sum C_n Z_n^2$  represents the sum of the concentration of each ion ( $C_n$ ), multiplied by the square of its charge number ( $Z_n^2$ ) and is equivalent to the ionic strength of solution. The factor 2 is included to account for the reduction in ions of opposite charge to the electric field present.

The strength of the internal dipole is directionally proportional to how many atomic dipoles are present <sup>[187]</sup> and is therefore proportional to the length of the primary particle <sup>[187]</sup>. As such it would be expected that the oriented attachment rate will increase with both primary particle size and the fused particle up to a point where the energy decrease due to attachment has been minimized as seen in CdS nanorods <sup>[188]</sup>.

The temperature dependence of the process is expected to proceed differently for particles with no or alike surface charges. With an increase in the thermal energy, more particles are able to overcome the energy barrier for orientated attachment, whilst simultaneously increasing the probability of collisions <sup>[141]</sup>.

### 2.1.4 Summary

Aqueous LBZA synthesis appears to under follow a different reaction mechanism to either non-aqueous LBZA or  $Zn_5(OH)_8Cl_2 \cdot 2H_2O$  (which shares the same basal layer) synthesis. The inability for the methyl groups of acetate to co-ordinate with the basal layer prevents the BCF growth mechanism. Unlike non-aqueous LBZA synthesis, aqueous LBZA structures appear to be made up of an oriented aggregate of primary particles. No reaction mechanism proposed so far in literature is able to explain the morphology at all length-scales. As a result, making predictions of the effect of altering synthesis conditions is limited. Within chapter 5 through the combination of classical nucleation theory, Crundwells reaction rate, oriented attachment the first reaction mechanism able to describe all length-scale features is presented.



## 2.2 Chemiresistive gas sensing

### 2.2.1 Chemiresistive sensing working mechanism

It is well known since Brattain and Bardeen's <sup>[189]</sup> original paper that the surface potential of a semiconductor varies in the presence of varying atmospheres. Utilising this, Seiyama *et al.* <sup>[190]</sup> created the first chemiresistive semiconductor gas sensor consisting of an evaporated zinc oxide thin film capable of non-selectively detecting the presence of various gasses at the ppm level. It is generally held as true, though with controversial spectroscopic proof <sup>[191]</sup>, that the main sensing mechanism at the typical operating temperatures employed is through the ionosorption model. In the ionosorption model, molecular oxygen ( $O_2$ ) adsorbs to the surface of the semiconductor, and due to the electronegativity of oxygen <sup>[19]</sup>, free electrons in the conduction band are captured and ionize oxygen into the peroxide radical ion ( $O_2^{-*}$ ) <sup>[19]</sup>. The peroxide radical anion then captures another electron into the antibonding orbital splitting the oxygen into atomic oxygen ions ( $O^-$ ) <sup>[19]</sup>.

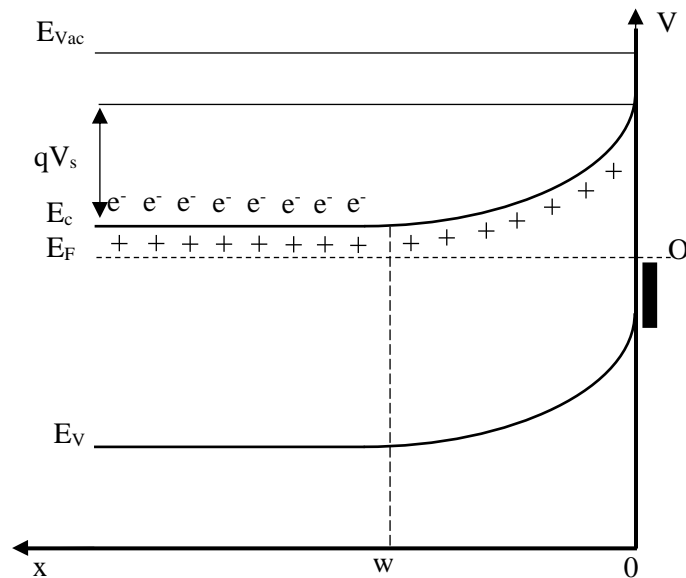


Figure 2.3: Simplified schematic showing band bending at the surface due to oxygen ionosorption. + represents ionized donor sites,  $e^-$  conduction bands,  $O^-$  ionosorbed oxygen and the solid black box representing filled states up to the Fermi level.

Due to the loss of conduction band electrons and the increased concentration of electric charge captured by surface oxygen species, a space charge region is formed inducing upward band bending at the interface (shown graphically in Figure 2.3) as defined by Poisson's equation <sup>[192]</sup>:

$$\frac{d^2V(x)}{dx^2} = -\frac{\rho(x)}{\varepsilon}$$

*Equation 2.10*

Where  $V(x)$  is the voltage at position  $(x)$ , and charge density  $\rho(x)$  is defined as <sup>[192]</sup>:

$$\rho(x) = N_d^+(x) - N_a^-(x) - n(x) + p(x)$$

*Equation 2.11*

Where  $N_d^+$  is the concentration of dopant species,  $N_a^-$  is the concentration of acceptor species,  $n$  is the concentration of electrons in the conduction band and  $p$  is the concentration of holes in the valance band.

For a fully ionized n-type semiconductor with negligible acceptor concentration and assuming the abrupt change model,  $\rho(x)$  is defined at equilibrium as <sup>[192]</sup>:

$$\rho(x) = \begin{cases} qN_d^+ & \text{for } 0 < x < w \\ 0 & \text{for } x \geq w \end{cases}$$

*Equation 2.12*

With the surface charge density due to oxygen adsorption at  $x = 0$  defined by <sup>[192]</sup>:

$$Q_{surf} = qN_d w$$

*Equation 2.13*

Solving Poissons equation with boundary conditions  $V(x) = 0$  and  $dV(x)/dx = 0$  at  $x = w$  and multiplying by the charge of an electron ( $-q$ ) results in the potential at  $x$ :

$$qV(x) = \frac{q^2 N_d^+ (x - w)^2}{2\epsilon}$$

*Equation 2.14*

The surface potential barrier  $qV_s$  is then defined at  $x = 0$  as:

$$qV_s = qV(0) = \frac{q^2 N_d^+ w^2}{2\epsilon}$$

*Equation 2.15*

From which the depletion region  $w$  can be defined <sup>[192]</sup>:

$$w = \sqrt{\frac{2\epsilon V_s}{q N_d^+}}$$

*Equation 2.16*

From the surface potential the surface density of electrons  $[e]$  in the conduction band can then be found using Boltzmann statistics <sup>[192]</sup>:

$$[e] = n = n_b e^{\left(\frac{-qV_s}{k_B T}\right)}$$

*Equation 2.17*

Where  $n_b$  is the bulk electron density,  $k_B$  is Boltzmann's constant and is equal to  $8.617 \times 10^{-5}$  eV.K<sup>-1</sup> and  $T$  is the absolute temperature in Kelvin.

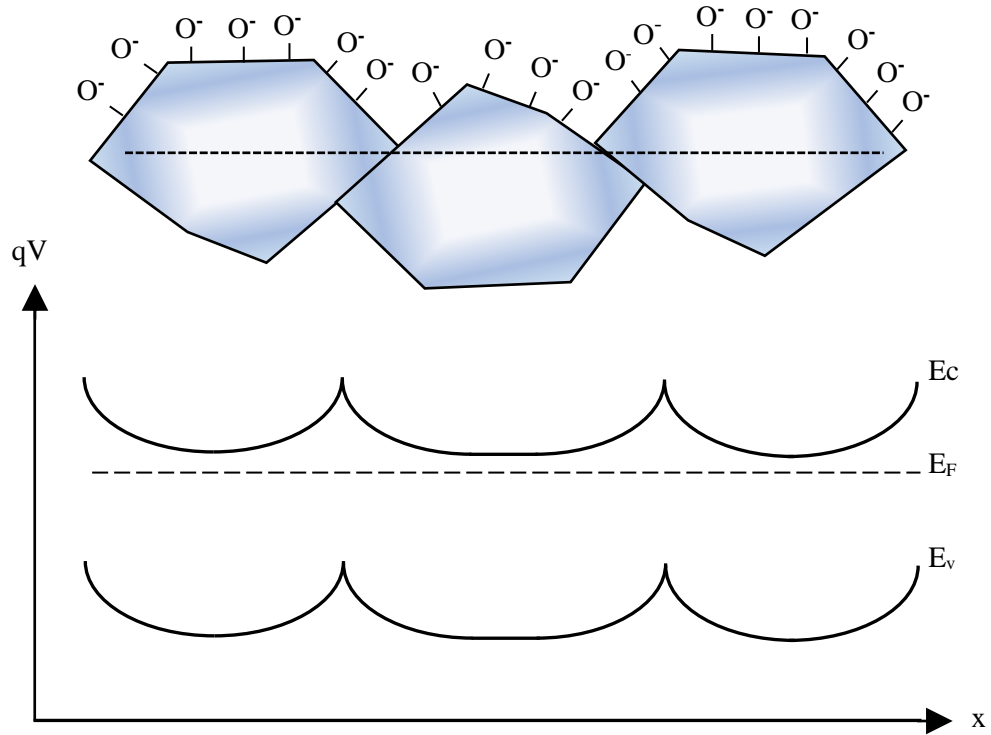


Figure 2.4: Schematic of granular material in the presence of ionosorbed oxygen, with potential energy profile along the dotted line.

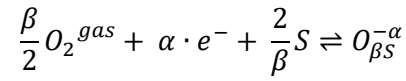
Typically gas sensors are made of polycrystalline granular materials, normally metal oxides, in which an electron travelling through the material will be obstructed by back to back Schottky barriers <sup>[192][19]</sup> as illustrated in Figure 2.4. The resistance of the material is then defined in relation to the bulk resistance without band bending  $R_0$  as:

$$R = R_0 e^{\frac{qV}{k_B T}}$$

Equation 2.18

The surface charge can then be related to the gas phase concentration by considering the surface reaction.

In dry air chemisorption of oxygen at the surface follows the equation <sup>[192]</sup>:



Equation 2.19

Where  $O_2^{gas}$  is the ambient molecular oxygen in the atmosphere, S is a free site required for oxygen adsorption,  $\alpha$  is equal to 1 for singly ionized molecular oxygen and 2 for doubly ionized atomic oxygen and  $\beta$  is 1 for atomic oxygen and 2 for molecular oxygen.

Utilizing the mass action law, the rate of reaction, the energy barriers for adsorption and desorption can be identified and then related to the electron density at the surface at equilibrium using <sup>[192]</sup>:

$$k_{ads} \cdot [S] \cdot n_S^\alpha \cdot p_{O_2}^{\beta/2} = k_{des} \cdot [O_{\beta S}^{-\alpha}]$$

Equation 2.20

Where [S] is the concentration of surface sites;  $p_{O_2}$  is the partial pressure of oxygen; n is the concentration of electrons; and  $k_{ads}$  and  $k_{des}$  are the adsorption and desorption rate reactions respectively, and typically take the form of an Arrhenius like relation <sup>[192]</sup>:

$$k = A e^{(-\frac{E_a}{RT})}$$

Equation 2.21

Where A is a preexponent,  $E_a$  the activation energy, R the gas phase constant and T the absolute temperature in Kelvin.

Rearranging and using  $K_{eq} = K_{ads}/k_{des}$  produces:

$$k_{eq} \cdot [S] \cdot n_S^\alpha \cdot p_{O_2}^{\beta/2} = [O_{\beta S}^{-\alpha}]$$

Equation 2.22

Using the fact that the surface charge  $qN_{aw}$  is equal to  $[O_{ps}^{-\alpha}]$  and must be balanced by the charge in the depletion region allows the partial pressure of oxygen to be linked to the surface potential <sup>[192]</sup>:

$$k_{eq} \cdot [S] \cdot n_s^\alpha \cdot p_{O_2}^{\beta/2} = \frac{2\varepsilon V_s}{w}$$

Equation 2.23

Rearranging for  $V_s$  and inserting into Equation 2.18 links the resistance to the partial pressure in the gas phase <sup>[192]</sup>:

$$R = R_0 e^{\frac{qwK_{eq}[S][n_s^\alpha]p_{O_2}^{\beta/2}}{2\varepsilon K_B T}}$$

Equation 2.24

Reducing gases react with the adsorbed oxygen, reducing the oxygen concentration at the surface and can also directly inject electrons into the semiconductor by adsorbing at other sites on the semiconductor surface therefore reducing the surface charge density <sup>[19][192]</sup>. The lower charge density reduces the barrier height and therefore reduces the resistance <sup>[19][192]</sup>. In the case of oxidizing gasses electrons are captured from the conduction band in the same manner as oxygen and raise the surface potential and resistance <sup>[19][192]</sup>. A more detailed understanding can be produced by considering the transport mechanism across the grain boundary directly, however practically not all the variables are known making it difficult to use directly <sup>[192][77]</sup>. Typically, the concentration of the gas is measured by measuring the response  $R$ , defined for reducing and oxidizing gasses as <sup>[19][192]</sup>:

$$R_{reducing} = \frac{Resistance_{air}}{Resistance_{gas}}$$

Equation 2.25

$$R_{oxidizing} = \frac{Resistance_{gas}}{Resistance_{air}}$$

Equation 2.26

Which is then converted to concentration by using a calibration equation, typically following a power law relation <sup>[193]</sup>. The sensitivity of the sensor under a particular set of conditions then is the response at equilibrium. Alternatively, some authors use a normalised value for the sensitivity, where the sensitivity for reducing or oxidizing gasses is calculated by <sup>[194][195]</sup>:

$$Sensitivity_{\substack{\text{reducing} \\ \text{oxidizing}}} = \frac{Resistance_{\substack{\text{air} \\ \text{gas}}} - Resistance_{\substack{\text{gas} \\ \text{air}}}}{Resistance_{\text{air}}} * 100 \%$$

Equation 2.27

Whilst the normalised % approach can be useful for sensors with low sensitivities, or the test gas concentration is small, for large signals it is easy to see that the sensitivity rapidly saturates. The raw ratio on the other hand does not suffer from the same saturation and is useful over all ranges.

## 2.2.2 Factors effecting sensitivity

In the case of nanomaterials with grain size on the order of twice the depletion width or smaller, the Schottky barriers overlap. As a result the potential at the centre of the grain rises <sup>[19][192]</sup>. As the potential at the centre rises, the potential difference between the surface and the centre decreases until the barrier height is less than  $k_B T/q$  <sup>[19][192]</sup>. Under these conditions the grain becomes fully depleted, the energy bands across the grain flat, and the resistance of the entire grain dependent on the surface interactions <sup>[192]</sup>. In effect, parallel or series resistances that would saturate, or reduce, the response are removed. The lack of a region unresponsive to the surface reactions increases the sensitivity of the grain significantly <sup>[72][196][197][198]</sup>.

The microstructure of the sensing layer also significantly effects the sensitivity of the sensors. For a porous material, gas can diffuse relatively deep into the bulk of the material, as a result a significant proportion of the layer takes part in the reaction <sup>[19][199]</sup>. This allows for large responses in thick layers, with the sensitivity directly dependent on the diffusivity, and diffusion length, of the gas species <sup>[19][200]</sup>. For compact, non-porous, films however, diffusion into the bulk of the layer is hindered <sup>[200]</sup>. This leaves the bulk insensitive to the surface reactions, effectively producing a constant parallel resistance <sup>[19][200]</sup>. The sensitivity

of the layer is then dependent on the resistance of this bulk region, with lower parallel resistances producing smaller responses. As a result, to produce sensitive devices using compact films, the layer need to be a thin film <sup>[19][200]</sup>. Often grain size scales with film thickness <sup>[19]</sup>, as a result there is a trade-off between sensitivity losses due to the increase in grain size for thick films, and the parameters need to be tuned to maximize sensitivity.

In addition to the resistance changes due to the structure of the sensing layer, an additional atmospheric responsive resistance is present at the metal electrode - semiconductor interface <sup>[201]</sup>. Often at a metal-semiconductor, charge is transferred from semi-conductor to metal resulting in a Schottky barrier analogous to that seen for oxygen adsorption <sup>[202]</sup>. The barrier height is dependent on multiple factors inherent to the interface; however, the height is also dependent on the adsorption of surface species <sup>[203]</sup>. Often this effect arises from the metal acting as a catalyst, lowering the adsorption and ionization energy of gas species <sup>[19][204]</sup>. The increase in adsorbed ionized species leads to an increase in the Schottky barriers in the semiconductor <sup>[19][203]</sup>. Additionally, the catalytic action can increase the local reaction rate <sup>[19][203][204]</sup>; with reducing gasses as an example. This leads to an increased reduction in barrier height <sup>[203]</sup>. The large difference in barrier height between increase adsorption and surface reaction allows for large improvements in sensitivity <sup>[19][203]</sup>. This effect is utilized in Schottky diode gas sensors <sup>[205][206][207]</sup> and a modified version in the form of surface decorated catalytically active metallic nanoparticles <sup>[100][208][209][210]</sup>. As the secondary pathway has a reduced activation energy a reduction in operation temperature is often seen <sup>[100][211][212]</sup>. As the effect of the catalyst is inherently localised by diffusion of surface species; the increase in response is dependant on mass loading of the catalyst, and relative distance between catalytic particles <sup>[203]</sup>. At the percolation, limit the improved adsorbed oxygen coverage combined with the metal semiconductor Schottky barrier produces a depletion region that span the entirety of the device <sup>[203]</sup>. Consequently when oxygen reacts with a reducing gas, rapid and large changes in resistance are observed <sup>[213][214][210]</sup>.

Just as surface decorated catalytic nanoparticles can alter sensitivity, so too can dopant species present at the surface. If the test gas of interest has acid-basic characteristics <sup>[19]</sup>, dopants can be introduced into the semiconductor. For instance, to improve sensitivity with ammonia, both a Brønsted-Lowry and Lewis Base <sup>[155]</sup>, then a dopant with Brønsted-Lowry or Lewis acid (i.e. electron accepting <sup>[155]</sup>) properties can be introduced <sup>[215][216]</sup>. If the dopant is present at the surface then it can selectively react with species of the opposite acid-base type, increasing sensitivity and sensor selectivity <sup>[19][215][216]</sup>.



### 2.2.3 ZnO nanosheet sensors derived from layered zinc hydroxide structures.

Due to their high surface to volume ratio, quasi-2D ZnO nanosheets derived from layered zinc hydroxides are ideal for gas sensing and have been investigated by numerous authors [217][218][219][220].

Xu *et al.* [221] investigated the dependence of which crystal facet was exposed using ZnO derived from two sources: LBZA and layered zinc hydroxynitrate calcined at 500 °C. TEM and SAED showed the chloride/ acetate synthesised sheets had exposed (0001) facets where-as the nitrate synthesised sheets were (10 $\bar{1}$ 0) dominant. The (0001) facets were shown more sensitive to C<sub>2</sub>H<sub>5</sub>OH, NH<sub>3</sub>, CH<sub>3</sub>OH, HCHO, CO, H<sub>2</sub> and NO<sub>x</sub>. Measurements for 50 ppm ethanol at 330 °C ( $R_a/R_g$ ), showed the (0001) facet to be significantly more sensitive with a response of 83.6 vs 28.4 for the (10 $\bar{1}$ 0) facet. They then used DFT to investigate the energetic difference for adsorption of O<sub>2</sub> on to zinc cation on the two facets. Their calculations showed the (0001) facet to have a chemisorption energy of -1.0665eV vs the (10 $\bar{1}$ 0) at -0.5233eV. The energy difference would result in a larger absorption of oxygen and a subsequently increasing sensitivity, helping to explain the increased response for LBZA derived ZnO.

Utilizing ZnO derived from Zinc hydroxycarbonate annealed at 400 °C Zhang *et al.* [222] produced ZnO yielding a response of 3.05 at 10 ppb and 399.43 at 200ppm ethanol. The sensors also showed appreciable but much lower responses between 20 and 50 to a range of alkanes, dichloromethane and hydrogen.

Xiao *et al.* [223] produced gas sensors using hydrozincite nanosheets Zn<sub>5</sub>(OH)<sub>8</sub>(CO<sub>3</sub>)<sub>2</sub> synthesized in a modified polyol based synthesis calcined at 400 °C. The sensors showed a response of 37.5 to 100ppm acetone at 420 °C. The response to 100 ppm ethanol at the same temperature was approximately 21, which is much lower than that produced by Zhang *et al.* The authors put the observed sensitivity to the exposed (1000) facet though the references provided by the authors provided no supporting evidence for the claim. The authors also decorated the sensors with palladium nanoparticles (optimum loading 0.5% wt.). This resulted in higher sensitivities for 100 ppm acetone of 70, with the peak operating temperature reducing to 340 °C while maintaining the same selectivity to acetone. Higher responses to acetone than ethanol was also observed by Li *et al.* [138] however selective area electron diffraction (SAED) analysis showed the particulates to be polycrystalline with randomly orientated grains.

Using zinc hydroxycarbonate nanosheets synthesized via hydrothermal synthesis [224] modified with Pt nanoparticles, Gu *et al.* produced gas sensors capable of a response of approximately 4 to 10 ppb chlorobenzene at 300 °C. The sensors were selective with responses (Ra/Rg) less than 15 for 100 ppm of benzene, methylbenzene, ethanol and acetone. Gold nanoparticle, silver nanoparticle and bare zinc oxide were also compared, showing only weak responses to chlorobenzene.

Jing and Zhan [225] created porous polycrystalline zinc oxide nanosheet gas sensors using hydrozincite nanosheets synthesized from a microwave assisted hydrothermal synthesis with zinc acetate and urea as precursors. At 200 °C the sensors showed a peak sensitivity of 6.9 to 100 ppm chlorobenzene with a response to 100 ppm ethanol of around 3 where-as at 380 °C the sensitivities were inverted with a response of 8.9 to ethanol and a sensitivity of approximately 2 to chlorobenzene. No explanation was stated for the decrease in response to chlorobenzene with temperature. However, the authors stated that the reaction was able to proceed at 200 °C by substituting surface oxygen species. Extrapolating it would appear reasonable to suggest the reduction in chlorobenzene, and increase in ethanol responses, are a result of an increase in ionized surface oxygen species at 380 °C.

Using hydrozincite as a precursor Chang *et al.* [226] created gas sensors capable of detecting 10 ppm NO<sub>2</sub> with a responses of 125 at 200 °C.

In addition to the examples listed; an exhaustive literature review of gas sensor responses by Leonardi [217] showed that ZnO derived from layered zinc hydroxide species to be highly competitive, and often superior, to ZnO with other morphologies. The high sensitivity, when combined with the ease of synthesis, shows ZnO derived from LBZA appears to be a promising candidate for large scale sensor production.

## 2.3 Flexographic printing

### 2.3.1 Overview

Flexographic printing is a relief printing process capable of printing relatively low viscosity inks on a variety of substrates, ranging from flexible polymers [17] to brittle semiconductors and ceramics [17], at high speed. While a relatively young field, literature concerning functional flexographic printing is growing, the vast majority of which concerns the printing of silver or conductive polymer electrodes for devices including RFID tags [227], strain gauge

<sup>[228]</sup>, ring oscillators <sup>[229]</sup> and photovoltaics <sup>[230][231][232][233]</sup>. Whilst there are fewer examples, flexographic printing has also been used to produce the active layers in devices.

Examples of devices produced through flexographic printing of the active layer include:

- A cytop fluorinated polymer transistor gate dielectric for a fully printed complementary ring oscillator <sup>[234]</sup>
- An indium zinc oxide amorphous thin film FETs using diaqua-bis[2(methoxyimino)-propanoate] Zinc (II) and tris[2(methoxyimino)-propanoate] Indium (III) complexes <sup>[235]</sup>
- Printed hydrolysed zinc acetate layers, as precursors for ZnO seed layers. The seed layers were then used to grow ZnO nanowire (NW) arrays, that were subsequently used for electrochemical glucose sensors <sup>[32]</sup>. The same ink was also used to produce nanotextured zinc oxide thin film sensors for non-Faradaic detection of the HCMV virus <sup>[31]</sup>. The ink consisted of 0.1 M zinc acetate, mixed in 80% IPA 20% water solution, that subsequently complexed to form basic zinc acetate complexes. (Note basic zinc acetate is a complex consisting of  $[Zn_4O(O_2C_2H_3)_6]$  <sup>[236]</sup> and is separate to the LBZA crystal phases mentioned)

At present there is only one example of gas sensors in literature where flexographic printing was used in the manufacturing process of the active layer. By printing the same printed hydrolysed zinc acetate layers Lloyd *et al.* <sup>[17]</sup> produced a zinc oxide nanowire oxygen sensor. At this point no other flexographic printed sensor has been presented, and there is no example of a fully printed sensor, or a sensor shown to be sensitive to gases other than O<sub>2</sub>.

In the next section literature concerning the printing process is reviewed starting with surface tension, surface energy and wetting with a brief overview of Rheology. Following is a brief description of ink composition, after which aspects of the process is described in detail drawing on literature investigating functional and graphic flexographic printing and relevant literature where appropriate from gravure, offset lithographic and fluid instability investigations.

### 2.3.2 Surface tension – equilibrium and dynamic

In a liquid, the molecules co-ordinate to each other (e.g. hydrogen bonding for H<sub>2</sub>O), lowering the energy of the system in the process <sup>[237]</sup>. At a liquid air interface, this co-

ordination is disrupted, producing a region of high energy <sup>[237]</sup>. To reduce the sudden energy change, the solution will typically alter its conformation to reduce the interfacial area <sup>[237]</sup>. The energy required to make a new surface from liquid in the bulk fluid is equivalent to <sup>[238]</sup>:

$$W = \gamma\Delta A$$

*Equation 2.28*

Where  $W$  is the work done to create a new surface of area  $A$  in a liquid of surface tension  $\gamma$  ( $\text{mN}\cdot\text{m}^{-1}$ ).

Polar hydrophilic liquids with permeant dipoles typically have high surface tensions due to strong internal interactions <sup>[238]</sup>. Water has one of the highest surface tensions at  $72 \text{ Nm}^{-1}$  due to extensive hydrogen bonding <sup>[238]</sup>. In alcohols increasing the number of alcohol groups per molecule increases hydrogen bonding causing a rise in surface tension <sup>[238]</sup> as can be seen in molecules of similar molecular weight such as Propan-1-ol having a surface tension of  $20.9 \text{ mNm}^{-1}$  <sup>[239]</sup>, 1,3 butanediol  $47.1 \text{ mNm}^{-1}$  <sup>[239]</sup>, and 1,2,3, propanetriol (glycerol)  $76.2 \text{ mNm}^{-1}$  <sup>[239]</sup>. In lipophilic hydrocarbon liquids the permanent dipole is for all intents and purposes non-existent and molecular interactions occur primarily via Van-der-Waals interactions in the form of London dispersion forces <sup>[238]</sup>. Surface tension scales with surface area of the molecule and therefore with molecular weight <sup>[238]</sup>. A special set of molecules known as surfactants contain both a polar head group, and a hydrophobic tail <sup>[238]</sup>. As a result, surfactants are able to adsorb at the interface with the polar head group pointing into the liquid, and the tail into the air <sup>[238]</sup>. The presence of the surfactant disrupts the surface coordination, whilst the tail group lowers the energy of the interface, and hence the surface tension <sup>[238]</sup>.

In pure solvents the surface tension is essentially a constant <sup>[238]</sup>. In impure liquids containing surfactants, the surface tension is dependent on the time taking for the component to diffuse to and adsorb at the interface <sup>[240]</sup>. Once the concentration of surfactant at the surface has reached a constant value the surface tension will reach an equilibrium value <sup>[240]</sup>.

### 2.3.3 Surface energy and wetting

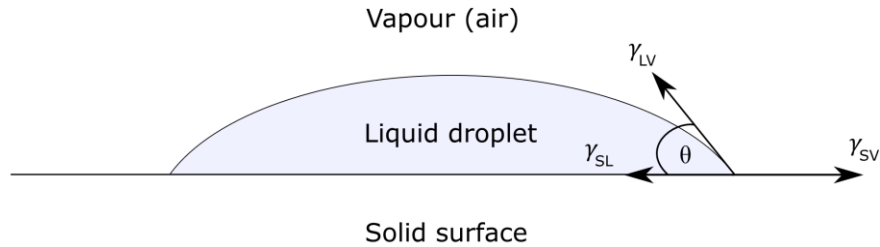


Figure 2.5 : Schematic of sessile droplet. Annotation shows the relevant phases vapour (air), liquid and solid, with the relevant interfacial tensions showing the direction the relevant forces act, and the resulting contact angle of the liquid-surface-air interface.

In a similar manner to liquids the disruption of internal electric fields at a surface creates a region of high energy <sup>[238]</sup>. Once again materials with large cohesive interactions tend to have higher surface energies <sup>[238]</sup> as can be seen by typical surface energy values for the (001) facet of A-TiO<sub>2</sub> of 900 mJ.m<sup>-2</sup> <sup>[241]</sup>, versus polymers such as polypropylene with surface energy of 27 mJ.m<sup>-2</sup> <sup>[242]</sup>.

When a liquid comes into contact with a solid, a new interface is created. If the liquid-surface adhesive forces are greater than the cohesive forces in the liquid; the fluid film will spread until either the solid is fully wetted, or until equilibrium is reached between the interactions <sup>[243]</sup>. The equilibrium values for the contact angle  $\theta$  (for  $\theta > 0^\circ$ ) of a droplet at the liquid, air/ vapour, solid interface (Figure 2.5) are described by the Young equation <sup>[243]</sup>:

$$\gamma_{SV} - \gamma_{SL} - \gamma_{LV} \cos \theta = 0$$

Equation 2.29

Where  $\gamma_{SV}$  is the surface air/vapour interfacial energy,  $\gamma_{SL}$  the surface liquid interfacial energy and  $\gamma_{LV}$  the liquid surface interfacial energy.

Based on the interfacial tensions a spreading parameter  $S$  can be introduced <sup>[243]</sup>:

$$S = \gamma_{SV} - (\gamma_{SL} + \gamma_{LV})$$

Equation 2.30

When  $S > 0$  the fluid spontaneously wets, whereas for  $S < 0$  the fluid will tend to reach an equilibrium.

When liquid spreads on a real surface where surface roughness and chemical inhomogeneity exists, the contact angle tends to exceed the equilibrium angle as predicted by Young's law <sup>[243]</sup>. When liquid is removed from a droplet the contact angle tends to be lower predicted <sup>[243]</sup>.

In the case of a surface with local roughness creating a change in surface angle of  $\varphi$ , then the macroscopic contact angle  $\theta$  at the edge exists in the range:

$$\theta_0 \leq \theta \leq \pi - \varphi + \theta_0$$

Equation 2.31

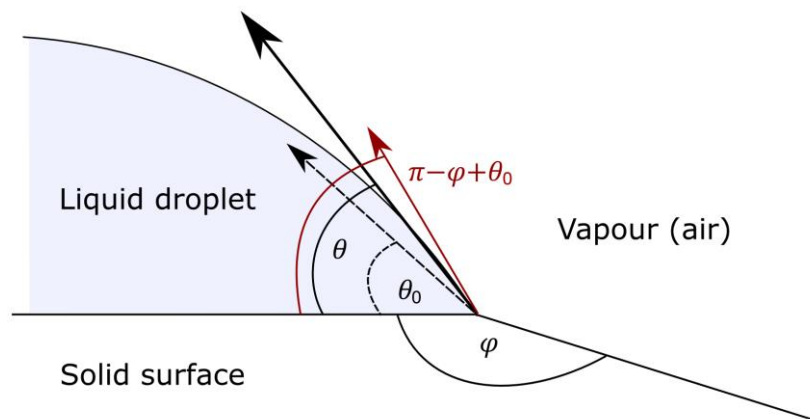


Figure 2.6: Schematic showing range of dynamic angles possible at a defect edge of angle  $\varphi$ , where the minimum angle  $\theta_0$  predicted by Young's equation is shown by the dashed line, and the maximum possible angle  $\pi - \varphi + \theta_0$  is shown in dark red.

A simplified schematic showing this effect at an edge, where the contact angle would normally be predicted to be  $\theta_0$  is shown in Figure 2.6.

The observed contact angle hysteresis has the effect of pinning the contact line of the fluid for small fluctuations <sup>[243]</sup>. While contact line pinning has been observed even on low surface roughness such as that due to step edges on Si wafers it is only macroscopically observed on roughness at the micrometre length scale.

When a fluid with  $S < 0$  is spread into a film with height less than the critical height  $e_c$  the film will tend to break up into small droplets dewetting the substrate in an effort to balance the interfacial tensions <sup>[244]</sup>. Dewetting nucleates around small defects in the fluid film, and if the holes that form are below a critical radius they will self-heal and the film will survive however larger holes above the critical radius will grow and the film will dewet. For  $S > 0$  the film is inherently stable as are films greater than  $e_c$  due to the effect of gravity. This is of obvious importance as if the film produced during printing is unstable and dewets all conductivity and therefore device functionality is lost.

$$e_c = 2\kappa^{-1} \sin \theta/2$$

*Equation 2.32*

Where  $\kappa^{-1}$  is the capillary length and is equal to:

$$\kappa^{-1} = \sqrt{\gamma_{LV}/\rho g}$$

*Equation 2.33*

Where  $\rho$  is the density of the liquid,  $g$  is the gravitational acceleration constant and  $\gamma_{LV}$  the surface tension of the fluid.

### 2.3.4 Ink rheology

Rheology defines how a material flows under an applied stress <sup>[245]</sup> print, as printing relies almost entirely on the flow of ink the rheological properties must be tightly controlled <sup>[242]</sup>. Each stage of the process from ink filling the cells of the anilox and subsequent wiping by the doctor blade, to the ink film splitting in the nip (i.e. the contact point between two cylinders separated by a layer of fluid) and subsequent spreading on the substrate requires its own range of values.

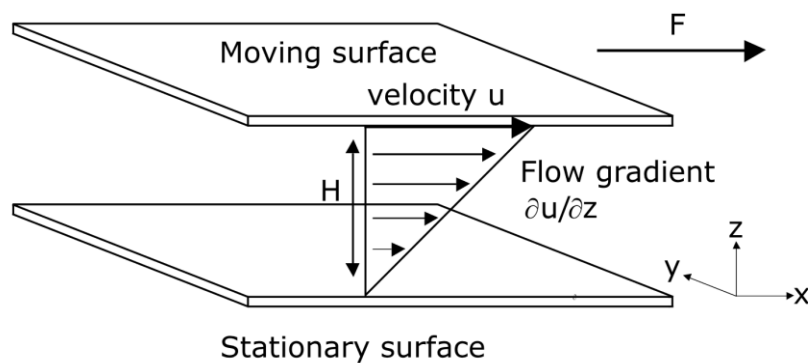


Figure 2.7: Schematic of flow between two parallel surfaces separated by a distance  $H$ , where the bottom surface is stationary. The top surface moving with velocity  $u$  to the right, due to the applied force  $F$ . The flow gradient of the fluid between the two surfaces is directionally proportional to the dynamic viscosity of the fluid.

The simplest case for inks occurs when they only show flowing behaviour under an applied stress. In this case the inks flow properties are described purely by its viscosity <sup>[246]</sup>. Viscosity is defined as the resistance to flow and for the simple case of a fluid between two parallel plates (as shown in Figure 2.7), one of which is moving in the  $x$  direction with velocity  $u$ , and the other is static, the viscosity  $\mu$  is related to the shear strain and stress by <sup>[246]</sup>:

$$\tau = \mu \frac{\partial u}{\partial z}$$

Equation 2.34

Where  $\tau$  is the shear stress and is equal to force applied over area  $A$  and  $\partial u / \partial z$  is the shear rate which defines the rate of change of the velocity of the fluid flow perpendicular to the direction of flow.



In the simple case of a Newtonian fluid, shear stress is directly proportional to shear rate and viscosity is a constant [246]. Typically however, the viscosity of printing inks show non-Newtonian behaviour in that the shear stress is not directly proportional to shear rate and thus the viscosity is shear rate dependant [242][247]. In non-Newtonian inks the particulate and binder content of the ink provide a structure that requires energy to disrupt, inhibiting flow at lower shear rates [242][248]. If under a constant shear rate the viscosity drops, the fluid is said to be thixotropic [249]. In thixotropic inks, once sheared it takes time for the structure in the ink to reform which has consequences of the spreading of the ink on the substrate [249].

In addition to non-Newtonian behaviour inks can show more complicated fluid properties in the form of viscoelastic [242][250] or viscoplastic [251] behaviour. In a viscoelastic ink there is an elastic component that stores energy and provides a restorative force that is dependent on the displacement of the ink [242][250]. In viscoplastic behaviour a minimum amount of stress, the yield stress, is required for the fluid to flow below which the fluid tends to act more as a solid [252]. It is useful at this point to introduce the capillary number,  $C_a$ , which is equal to the ratio of viscous to interfacial-tension forces [253]:

$$C_a = \frac{\mu U}{\gamma_{LV}}$$

*Equation 2.35*

Where  $\mu$  is the dynamic viscosity,  $U$  is the process velocity and  $\gamma_{LV}$  the liquid-vapour interfacial (i.e. surface) tension.

In processes utilising fluids that produce a high  $C_a$  viscous stresses dominate the fluid behaviour, whereas in low  $C_a$  cases interfacial tensions dominate. Through the use of capillary number and a few other unitless numbers such as the Reynolds number  $Re$  (the ratio of inertial to viscous stresses) model systems of different length scales can be compared directly [253].

### **2.3.5 Flexographic inks and their properties:**

Flexographic inks are relatively complex fluids consisting of a variety of components. Typically, a graphic ink would contain [254][255] pigments/ dyes, resin and or binders, slip

additives, wetting agents (surfactants), levelling agents and solvents. Many of the components in graphic inks can disturb or disrupt functional ink, potentially:

- adsorbing to the surface inducing localised interfacial dipoles <sup>[256][257][258][259]</sup> in semiconductors
- in the case of resins/ binders potentially isolating conductive particles from each other and converting the film into an insulator <sup>[13]</sup>.

There are three major types of ink, solvent, water or UV depending on what the carrier fluid is <sup>[260]</sup>. Solvent inks use a variety of solvents to solubilize binder, suspend particles, controllably wet the substrate and control drying and viscosity <sup>[254]</sup>. Whilst solvent inks have a variety of benefits, they are often hazardous and are a major source of greenhouse gases <sup>[260]</sup>, and as such are being replaced with water based and UV cured inks <sup>[255][260]</sup>. Water based inks typically have high surface tensions and require surfactants to wet the substrates <sup>[261]</sup>, control of surfactant levels can be difficult and can create foaming issues that require anti foaming agents to stop defects in the printed layers <sup>[255]</sup>. UV (or e-beam curable) inks on the other hand use low vapour pressure solvents that cross link on exposure to UV thereby removing routes of exposure and emission of green-house gasses <sup>[255]</sup>.

### **2.3.6 Print process:**

In the following section the print process is described starting with ink filling of the anilox. Then the fluid transfer processes are described, followed by the effect of impression on feature size gain, and finally instabilities arising during plate separation and features created during drying.

#### ***2.3.6.1 Anilox ink filling and doctor blade dynamics***

On a full industrial print press ink is applied to the anilox either through:

- a fountain/ metering roll fed via an ink bath that forces ink into the anilox at a defined rate <sup>[262]</sup>
- or from a pressurised ink chamber <sup>[262]</sup>

In contrast lab scale printability testers typically are applied utilizing a pipette or a small bath <sup>[263]</sup>. After the anilox is inked it is typically wiped by a doctor blade leaving a fluid volume defined by the anilox cell geometry <sup>[262][16]</sup>.

Using white light interferometry and non-volatile UV curable ink, Cherry <sup>[262]</sup> investigated anilox ink filling on an F1 IGT flexographic printability tester, and found that the anilox cells contained air after inking. Cell filling was found to improve using a high-speed inking unit which forced ink into the cells. Cherry called into question whether a chambered inking system, as opposed to a fountain roller on a full press, would suffer from partial filling of cells. Previous investigations by Hamblyn <sup>[264]</sup> showed that it takes 3 prints for the printing results to stabilize. Cherry therefore reasoned that the plate would drive trapped air out of the cells during the initial anilox plate engagement, and that after the stabilisation period there would likely be no air trapped in the system.

Cen <sup>[253]</sup> looked at cell filling in a model system of etched cells, it was found that for low capillary numbers (observed  $C_a \leq 0.1$ ) and low fluid material contact angles the cells always completely filled, however at higher values the cells tend to entrap more air until the cell is completely unfilled ( $C_a > 1$ .) This is related to the contact line pinning at the front edge of the cell and the speed that the contact line moves around the edge of the cell, if the front contact line isn't released in time the fluid can not enter the cell at a rapid enough speed for the air to be displaced before the cell is covered and the air is entrapped. In addition, it was also found that as viscosity increased (at  $C_a \leq 0.1$ ) complete filling of the anilox was volume dependant. As such, upper limits on  $C_a$ , and therefore viscosity and process speed, on cell filling provides fundamental limits for successful printing <sup>[253]</sup>. Separation between cells was not investigated, and so a direct comparison with the anilox where the cell wall is narrower than the cell itself, is incomplete. However, it is reasonable to expect that lower capillary numbers would help ink filling in the anilox, and more viscous inks would be more likely to cause air entrapment.

Post ink filling the anilox cells the fluid film is metered by a doctor blade, ideally the film thickness should equal the anilox cell height however interactions with the doctor blade can mean the film is thicker or thinner. In the case of more viscous solutions pressure builds up at the interface and can cause the blade to lift slightly and allows a thicker film to pass. <sup>[265]</sup> It should be pointed out that if the particles in the ink are too large for the anilox cells the anilox may clog resulting in potential damage and a poor print.

### ***2.3.6.2 Ink transfer – Ink splitting in the printing nips***

In contact printing techniques ink is transferred at a minimum between two surfaces, one of which is the substrate, and as such understanding and controlling the transfer of a fluid film is of fundamental importance. When a solid surface comes into contact with a liquid film attached to a second solid surface, a liquid bridge forms <sup>[266]</sup>. Upon separation of the two plates, the liquid bridge extends and narrows until eventually it breaks up. Early systematic investigation by Chadov and Yahkin <sup>[266]</sup>, consisting of a droplet of water between a zinc plate and a variety of polymer plates; revealed at low separation speeds more liquid was transferred to the higher surface energy zinc surface. The amount of fluid transferred increased with the contact angle of the polymer substrate. At higher separation speeds this effect reduced until the fluid was left in equal amounts on both substrates. At intermediate speeds the increase in viscosity due to the addition of glycerol reduced the liquid transfer to the zinc surface as did the reduction in liquid-air interfacial tension through the addition of ethanol.

During his investigations of ink transfer between print plate and substrate, Beynon <sup>[267]</sup> noted that as ink viscosity decreased ink transfer to the print plate from the anilox decreased. As the anilox is traditionally made of a stainless steel with a ceramic coating, and print plates are made from soft photopolymer, the observations line up well with Chadov and Yahkins original investigations.

Cherry <sup>[262]</sup> investigated various anilox cell geometries for multiple tonal coverages (a measure of dot coverage used in the graphics industry to create shaded profiles) on a full scale press. Small dots, where the dot could dip inside of the anilox cell, led to a large percentage release of ink from the anilox (i.e. transferred), alongside large variances in release percentage. The percentage ink release was found to be dependent on anilox line ruling, with the release increasing with a decrease in line ruling. Cherry also investigated ink transfer between the anilox and solid block print plate on an IGT F1. He found that approximately 40% of ink transferred to the plate, showing only a weak variation with velocity, however an increase followed by a decrease in transfer was found with increasing print plate anilox engagement for solid prints using high line count anilox.

### 2.3.6.3 *Printing fine features*

When the printing plate and anilox liquid bridge is forming, ink flows from the anilox to the print plate at the point where contact is made. Surface tension and pressure between the two rollers forces the ink in the nip to spread out. Typically for fine dots as used in the graphics industry it is recommended that an anilox line ruling be 5 times greater than the line ruling of the plate otherwise the dot dips into the cell <sup>[268]</sup>. However, in the cases of fine line meshes investigations by Deganello *et al.* <sup>[268]</sup> have shown that the lines bridge the cells on all but the largest anilox patterns. This led to reproducible printing, even at track widths of 30  $\mu\text{m}$  with a line ruling of 55.1 lines per cm (approximately 181.5  $\mu\text{m}$ .) For larger anilox volumes, larger volumes of ink are transferred, and the mesh line width and cross section correspondingly increased. In the case of fine lines with fine gaps (75  $\mu\text{m}$ / 100  $\mu\text{m}$ ) investigations by Yusof <sup>[16]</sup> have shown that an increase of anilox line ruling, from 350 lines per inch (lpi) to 600 lpi, improves the distribution of ink and results in sharper and more defined lines and gaps.

Deganello *et al.* <sup>[269]</sup> measured line width and height on fine line grids using a silver nanoparticle ink. He found that for a plate nominal line width of 20  $\mu\text{m}$ , 30  $\mu\text{m}$ , 40  $\mu\text{m}$  and 50  $\mu\text{m}$  produced, and a positive substrate plate engagement of 76.2  $\mu\text{m}$ , tracks of mean width 74.6  $\mu\text{m}$ , 85.7  $\mu\text{m}$ , 102.2  $\mu\text{m}$  and 120.2  $\mu\text{m}$  respectively, showing substantial print gains. Based on an investigation by Bould <sup>[270]</sup>, it was reasoned this was primarily due to ink squeezing out of the nip, with a minor contribution from plate deformation. In solid prints this effect was observed by Lloyd *et al.* <sup>[17]</sup> where increasing the print plate impression cylinder force resulted in an almost linear relationship with resultant line width. In the case of excess pressure haloing is produced where the fluid film is driven out of the nip resulting in a thin film surrounded by a thick rim <sup>[271]</sup>.

Beynon <sup>[267]</sup> observed during his investigations that low viscosity inks tended to build up behind the doctor blade and resulted in dot bridging.

Yusof <sup>[16]</sup>, during his investigations of fine line printing, tested two different inks and found that for inks Zahn cup number 5 effluent time of:

- 2 minutes 35 seconds - features with 50  $\mu\text{m}$  line width and spacing printed successfully
- 1 minute 24 seconds had ink bridges between lines.

Ink viscosity was compared with Zahn cups that use time for a set volume to leave a hole in the cup to calculate viscosity. The effluent time is measured under a relatively constant, low shear environment, so is more difficult to interpret actual viscosities under press conditions. In the case of fine parallel lines such as interdigitated electrodes often used in sensors, this could create shorts that would render the device non-operational. Yusof <sup>[16]</sup> also observed that increasing print speed reduces line width and film height, allowing for features with narrower gaps to be printed. However, care is required as the thinness of the film was shown to produce line breakages that would create open circuit.

In cases of extensional flow with non-circular cross section, it has been found that capillary pressure variations along the patterns cross-section work to restore a circular cross-section <sup>[272]</sup>. This can cause the contact line between air, ink and surface to slip, resulting in a loss of feature definition. Increasing liquid viscosity and improving substrate wettability works to counter contact line slip, and therefore improve definition <sup>[272]</sup>.

#### 2.3.6.4 Viscous fingering and fluid levelling

When the print plate and substrate separate, air displaces the more viscous ink, creating a dynamic meniscus where interfacial tensions compete with viscous stresses. The competition of surface tension and viscous forces at the interface create instabilities that create finger like patterns that propagate and separate along the print direction. The wavenumber of the fingers is given by <sup>[273]</sup>:

$$n^* = \sqrt{\frac{2C_a x}{h^3(x, t)}} = \sqrt{\frac{2\mu v_p x}{\gamma_{LV} h^3(x, t)}}$$

Equation 2.36

Where  $\mu$  is the viscosity of the ink,  $\gamma_{LV}$  the surface tension,  $v_p$  the printing velocity,  $x$  the distance of the fluid meniscus at the nip to the point where the print plate touches the substrate, and  $h(x,t)$  is the height distribution of the ink perpendicular to the nip.

Morgan *et al.* <sup>[250]</sup> investigated through the use of Boger fluids (fluids with near constant viscosity but varying elasticities,) the effect of elasticity on finger formation on solid area prints. The authors found that whilst a pure Newtonian fluid ( $\mu = 30$  mPa.s) would produce

near continuous periodic stripes, increasing elasticity heavily increased branching, producing a higher frequency pattern. They then suggested capillary number should be replaced with the elastocapillary number,  $E_c$  (Equation 2.37), as the characteristic number:

$$E_c = \frac{\lambda_E \gamma_{LV}}{\mu x}$$

Equation 2.37

Where  $\lambda_E$  is the extensional relaxation time of the ink,  $\gamma_{LV}$  the ink surface tensions,  $\mu$  the dynamic viscosity, and  $x$  the distance of the fluid meniscus at the nip to the point where the print plate touches the substrate.

The undulations finger pattern increases the radius of curvature, raising the pressure which surface tension works to reduce. The characteristic time scale for levelling is then given for a given wavelength and film thickness <sup>[274]</sup>:

$$\tau_{lev}(\lambda, h) = \frac{3\mu\lambda^4}{16\pi^4\gamma_{LV}\langle h \rangle^3}$$

Equation 2.38

For a given wavelength the levelling time is proportional viscosity, and inversely proportional to surface tension, however it is heavily non-linear with respect to wavelength. Inserting the wavelength for a simple fluid film of constant viscosity without elastic properties, produces a levelling time according to:

$$\tau_{lev}(\lambda, h) = \frac{3\gamma_{LV}h(x, t)^6}{4\eta v_p^2 x^2 \langle h \rangle^3} = \frac{3}{4} \frac{h(x, t)^6}{C_a v_p x^2 \langle h \rangle^3}$$

Equation 2.39

This shows that levelling time is proportional to the fluid surface tension; inversely proportional to viscosity; and related to the square of process velocity, and nip interface distance. However in the case of shear thinning effects; the viscosity in question between

Equation 2.38 and Equation 2.39 can be significantly different, producing larger wavelength features under the high shear conditions in the nip, and effectively freezing out when at rest. In these conditions, increasing elasticity could help reduce the levelling time. If the fluid film dries before the pattern levels out the surface will be rough, potentially hindering conductivity, and in the case of over layers, requiring thicker films to stop pinholing.

### ***2.3.6.5 Drying features – coffee ring effect and Marangoni flow***

When a droplet attached to a substrate with pinned contact line is heated, the evaporation rate at the edges is greater than at the centre<sup>[275]</sup>. This produces a convective flow that drives the liquid outwards leading to the well-known coffee ring effect, where more solute or particles are deposited at the edge of the droplet than at the centre<sup>[275]</sup>. The roughness induced under drying is not ideal and can lead to poor tolerances, and even device failure in the case of gate dielectrics, and as such needs to be reduced wherever possible.

Soltman and Subramanian<sup>[276]</sup> investigated the temperature dependence of the coffee ring effect on inkjet printed droplets. They found that at lower temperatures the effect reduced or even stopped. This however is not realistically useful for on press conditions in a high speed flexographic set up, where printing and rewinding can be on the order of a few seconds. Increasing viscosity under low shear conditions helps to reduce flow rates, and so can limit the effect in high solid inks reducing the displacement before the film dries<sup>[277]</sup>. High solids or binder content may not be preferable in some cases, for instance in printing thin films of large 2D nanoparticles or sol gel inks. In these cases a promising route is through the use of co-solvent systems which utilise Marangoni flow to produce even and more homogenous films<sup>[277][278][279][280]</sup>. In short, two or more solvents are used, one of which has a higher vapour pressure and lower surface tension than the others. The higher rate of evaporation of the higher vapour pressure solvent at the contact line produces a localised region of higher surface tension. The higher surface tension induces a capillary driven flow to the centre which has a lower surface tension.

An example of surface texture induced by drying effects in functional flexographic printing can be seen in the zinc oxide thin film sensors produced by Assaifan *et al.*<sup>[31]</sup>. The partially hydrolysed zinc acetate ink (originally described in section 2.3.1) was printed and dried multiple times, with a ridged texture accumulating with each print. It was suggested by the authors that as drying occurred, localised defects in the underlying layers created pinning points that produced convective flow similar to that produced in the coffee ring effect,



creating larger deposits. With each subsequent print the pinning effect was enhanced and a ridge like pattern was created.

#### **2.3.6.6 Summary**

To summarise, the ink must be of low enough viscosity to fill the cell and stop air entrapment, whilst having a high enough viscosity to improve ink transfer efficiency and to retain feature fidelity. For improved uniformity and conductivity, the viscosity must either be high enough in the nip to produce high wavelength features that relax before drying, or low enough that the wavelength is on the order of, or preferably longer, than the print features.

Solvents require either to be rapid enough drying to limit evaporative flow; viscous enough or set quick enough to freeze out the coffee ring effect; or have solvents blends with compatible surface tensions and vapour pressures to produce a Marangoni flow that counters the convective flow. In addition, the ink must dry in time before being rewound in the case of high-speed roll to roll presses.

On the substrate, wetting must be high enough to pin the pattern to the substrate limiting dewetting, but low enough that continuous ink spreading does not occur or is limited before the ink either sets or dries. Printed films must have the required electronic properties and must not flake off.

When on the press, nip pressures/ engagements need to be high enough to produce a uniform film, but low enough not to produce excess ink squeeze and plate deformation that could short or unfavourably broaden the print features. The anilox used must have a high enough line count to print uniform films, but low enough so that particle fit into the cells to stop clogging whilst allowing for the desired volume/ film thickness. Print speed should be adjusted to allow for the throughput and linewidth required. For slow evaporating solvents and lower wavelength fingering features lower line speeds may be required.

## **2.4 Intense pulse light treatment/ photonic annealing**

In recent years there has been an increase in investigations into alternative calcination and annealing methods that have been published. One of the most promising methods is intense

pulse light treatment (IPL). IPL, a form of photonic annealing, uses flash lamps to produce incredibly intense pulses of light <sup>[281]</sup>. The pulses of light have radiant exposures in the kila-Joules per meters squared range <sup>[281]</sup>, which can heat optically active materials by hundreds of degrees, up to temperatures in excess of 1000 °C in special cases <sup>[281]</sup>, within timescales on the order of milliseconds <sup>[281]</sup>. The incredibly rapid and transient nature of the technique localises the high temperature to the surface. When used in combination with a non-light absorbing substrate, this limits the increase in temperature of the bulk substrate allowing cheaper substrates such as PET to be used <sup>[281]</sup>. IPL has seen a growing trend in functional printing and has been used to:

- Sinter silver nanoparticle films <sup>[282][283][284][285]</sup>
- Thermally disassociate and sinter copper/ copper oxide core/shell nanoparticle <sup>[286][286]</sup> and copper citrate complex precursor <sup>[287]</sup> films
- Anneal methylammonium lead iodide perovskite <sup>[288][289]</sup> and ZnO electron extraction/ hole blocking layers in photovoltaics <sup>[290]</sup>
- Decompose the polymer binder in graphene nanoplatelet printed films <sup>[291][292]</sup>
- Reduce graphene oxide <sup>[293]</sup>.

During the IPL the heat generated  $Q$  at a depth  $y$  over the area of illumination  $A$  is related to the absorption of light via the Beer-Lambert law integrated over all wavelengths that are absorbed <sup>[281]</sup>:

$$Q = A \iint I_0(\lambda) e^{-\alpha y} d\lambda dy$$

Equation 2.40

Where  $I_0(\lambda)$  is the intensity of light at the wavelength  $\lambda$  at the interface, and  $\alpha$  the absorptivity of the material.

For a semiconductor the wavelengths of interest relate to those with energies greater than the bandgap <sup>[281]</sup>. In semiconductors the photons are absorbed, promoting electrons over the bandgap, with an excess energy of energy equivalent to the difference of the photon and bandgap energy <sup>[281]</sup>. The electron rapidly lowers its energy dropping to the conduction band edge transferring energy to phonons in the process heating the system <sup>[281]</sup>. In the case of direct band gap semiconductors the electrons recombine with holes undergoing radiative emission (photoluminescence), reducing the amount of energy inserted into the system <sup>[294]</sup>. As temperature rises and  $k_B T$  becomes of the order or greater than the exciton binding

energy bound excitons are split into separate electron and holes and photoluminescence is quenched <sup>[294]</sup>. In indirect bandgap semiconductors and photoluminescence quenched semiconductors, the electron relaxes across the bandgap recombining with holes by dissipation of excess energy in the form of heat <sup>[294]</sup>. Additional thermal losses occur via black body radiation and can be approximated from Steffan-Boltzmanns law <sup>[295]</sup>.

From the heat inserted into the system the time and spatial temperature response can be calculated using the specific heat of the material  $C_p(y,T)$  in question:

$$\rho(y, T)C_p(y, T)\frac{\partial T(y, t)}{\partial t} = \nabla(k(y, T)\nabla T(y, t)) + Q$$

*Equation 2.41*

Where  $T$  is the absolute temperature in kelvin,  $t$  is time,  $k(y,T)$  is thermal conductivity at position  $y$  and temperature  $T$  and  $\rho(y,T)$  is the density of the material.

The diffusion time in a homogenous material of thickness  $y$  can then be calculated as <sup>[296]</sup>:

$$\tau = \frac{\rho C_p y^2}{4k}$$

*Equation 2.42*

The diffusion time is of the order of microseconds for micron thick films and thus provides near instantaneous and uniform heating of the printed layers.

## Chapter 3 - Theory of experimental analytical techniques

---

### 3.1 Introduction

Due to the breadth of fields covered in this work, the following chapter is dedicated to the theory of the more specialised analytical techniques to aid the reader understand the experiments performed. All experimental details, and material rationale choice where appropriate, is provided at the beginning of each chapter in section 4.1.1 , 4.2.2 , 5.2 , 6.4 .

The techniques are separated into:

- Morphology analysis (section 3.2 ). Techniques that provide information on the size and shape of particles and films. Techniques described include scanning electron microscopy (SEM) and atomic force microscopy (AFM)
- Chemical, optical and electronic energy level analysis (Section 3.3 ). Techniques that provide:
  - o Elemental (Energy dispersive x-ray spectroscopy – EDS) and/or functional group identification (x-ray photoelectron spectroscopy - XPS) and quantification
  - o Crystalline phase analysis (x-ray diffraction analysis – XRD)
  - o Optical bandgap and qualitative optically active defect state analysis (photoluminescence – PL)
  - o Work function and valance band to fermi level energy separation analysis (ultraviolet photoelectron spectroscopy – UPS)
- Fluid analysis (Section 3.4 ). Techniques that measure fluid surface/ interfacial tension (pendant drop) and viscosity of a fluid (dynamic viscometry).
- Statistical analysis (Section 3.5 ). Techniques used to provide an estimation of variance and noise in the data (confidence intervals), hypothesis testing (t-test) and modelling of data (regression analysis).

Each section provides a brief description of the underlying theory and then describes how results are subsequently analysed.

## 3.2 Morphology analytical techniques

### 3.2.1 Scanning electron microscopy (SEM)

Grain structure of polycrystalline metal oxide gas sensors are often in the scale of 10 – 50 nm <sup>[72]</sup>. As such to analyse grain structure techniques capable of measuring below 10 nm are required. Optical microscopy with modern oil immersion lenses is diffraction limited to 171 nm <sup>[1]</sup>, as such specialised techniques are required. One of more useful, routinely used techniques is scanning electron microscopy (SEM). Unlike optical microscopes, state of the art scanning electron microscopes have resolution on the order of 1 nm <sup>[1]</sup>. As electrons can be captured or scattered by gasses, SEM unlike optical microscopy, needs to be performed in a vacuum <sup>[1]</sup>.

Scanning electron microscopes produce images by rastering a highly focussed electron beam across the surface of the sample and measuring the electron flux from the sample. Backscatter electron (BSE) images are produced by measuring the flux of primary electrons from within the beam reflected by the sample <sup>[297]</sup>. Secondary electron (SE) images however are produced by low energy electrons emitted from inelastic collisions in the surface <sup>[297]</sup>. The lower energy of secondary electrons increases allows for the possibility of multiple scattering from a single primary electron <sup>[297]</sup>. As a result, SE images have significantly higher signal to noise ratios than BSE images <sup>[297]</sup>. For both BSE and SE images the increased number of electrons in heavier elements increases the scattering cross sections <sup>[298]</sup>. As such the contrast within both imaging modes is sensitive to elemental composition <sup>[298]</sup>. This can be used to qualitatively examine the distribution of materials, assuming a large difference in atomic number between regions exists. Examples of this can be seen in Figure 3.1 with A) showing LBZA within a polymer film using BSE, and B) Pt electrodes on an Al<sub>2</sub>O<sub>3</sub> substrate with a ZnO sensing layer using SE. In the example images, the higher the average atomic number of the material, the brighter the contrast i.e. LBZA > polymer, Pt > ZnO > Al<sub>2</sub>O<sub>3</sub>.

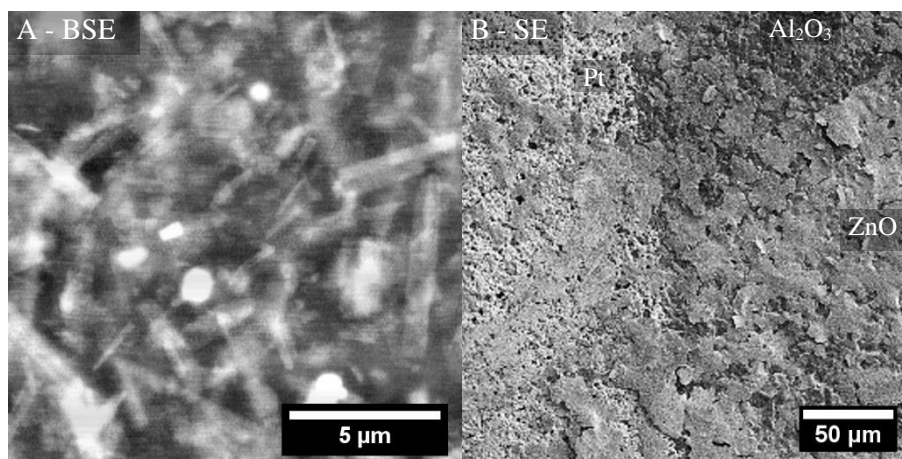


Figure 3.1: Example cropped SEM micrograph images taken within these investigations. A) Backscatter electron images of LBZA (white) buried in a PVP film on a Kapton HN substrate (dark contrast areas). B) Secondary electron image of a calcined dropcast LBZA gas sensor using a commercial substrate. Areas in order of contrast: Brightest – Platinum (Pt) electrode, mid contrast – ZnO, darkest – alumina ( $Al_2O_3$ )

The low energy of SE requires a high voltage applied to the detector to attract them, as a result electron shadows (analogous to light shadows) can be produced dependent on the detector placement <sup>[297]</sup>. This effect produces a level of topological sensitivity that BSE images typically do not display <sup>[297]</sup>. SE, due to their low energy, are emitted only from the absolute surface of a sample with information depths (ID) for metals as short as 1.5-2 nm <sup>[299]</sup>. BSE however retain significant energy and as a result travel further <sup>[297]</sup>. Information depth in BSE images is inversely related to atomic number; with ID in silicon, with primary electron energy of 30 keV of 650 nm <sup>[300]</sup>. This makes bulk BSE images relatively bulk sensitive, being able to provide information of buried heavier element structures inside of lighter atomic number layers (e.g. Figure 3.1A). In contrast optical microscopes have low surface sensitivities for transparent samples.

Image resolution is dependent on:

- Acceleration voltage, with higher voltages producing narrower spot sizes, but at the loss of surface sensitivity <sup>[1][297]</sup>
- Source type. Thermal emission sources such as  $LaB_6$  produce significantly wider spot size than field emission gun (FEG) sources. However thermal emission sources can produce significantly higher electron fluxes. <sup>[1][297]</sup>
- Electron beam current. Higher currents by definition focus more electrons at the sample per second. This results in a broader spot size, but a greater signal to noise ratio. <sup>[1]</sup>
- Aperture size. Narrower apertures help reduce aberration and increase depth of field producing sharper images, with a corresponding loss of signal. <sup>[297]</sup>

### **3.2.2 Atomic force microscopy (AFM)**

Unlike SEM that provides topological information through the yield of electrons from interactions with an electron beam, atomic force microscopy (AFM) uses the deflection of a probe by interactions with the sample surface. Many forms of AFM exist, for the investigations in this document a form known as intermittent contact mode is used. In intermittent contact mode a probe is oscillated at close to its resonant frequency, typically with amplitudes up to 100 nm<sup>[301]</sup>. A tip mounted onto the probe is held at a separation from the surface below the free running amplitude, resulting in the probe briefly being brought into contact with surface with each cycle<sup>[301]</sup>. Changes in the mean tip – surface separation changes the amplitude and/ or frequency and phase changes of the oscillations<sup>[301][302]</sup>. By altering the tip height to keep the amplitude at its set point, and tracking the displacement required, the height of the sample at a position can be measured<sup>[302]</sup>. By rastering the tip along the surface height maps can be recorded.

## **3.3 Chemical, optical and electronic energy level analysis techniques**

### **3.3.1 Energy dispersive x-ray spectroscopy (EDS)**

When a sample is exposed to a high energy electron beam, such as during SEM imaging, electrons are emitted from the sample. If the electrons are emitted from states below the valance band (i.e. core electrons), a vacancy (a core hole) is left leaving the atom in an excited state<sup>[303]</sup>. To lower its energy an electron in a higher energy state can transition to the empty energy state, releasing a photon in the process. For deep core holes the emitted photon is usually the x-ray region of the electromagnetic spectrum<sup>[303]</sup>. The energy of the x-ray photon depends on the difference in energy between the starting and end states that the electron transition between<sup>[303]</sup>, with the energy difference dependent on the element of the emitted atom<sup>[303]</sup>. By measuring the x-ray flux of a sample as a function of x-ray energy, typically below 20 keV, and scaling by various factors<sup>[303]</sup>; the elemental concentration within the electron beam interaction volume can be measured. By rastering the electron beam across the sample, a map displaying how elemental composition is distributed can be created.

### 3.3.2 X-ray photoelectron spectroscopy (XPS)

X-ray photoelectron spectroscopy (XPS), also known as electron spectroscopy for chemical analysis (ESCA), can in some ways be viewed as the reverse process of EDS. In XPS x-rays are focussed onto a sample and the kinetic energy of emitted electrons measured. Unlike EDS however the energy resolution in XPS is significantly better, with the peak energies in EDS having FWHM  $\sim 10$ -250 eV <sup>[304]</sup>, and peak envelopes in XPS typically between 3.2-12 eV (as measured here). As a result, XPS is not limited to just elemental quantification but is also capable of identification and quantification of oxidation states and functional groups. To convert from the kinetic energy recorded by the system to the binding energy of the electrons (i.e. the energy required to escape the surface) the Einstein photoelectron equation is used <sup>[305][204]</sup>:

$$E_{\text{Binding energy}} = h\nu - E_{\text{Kinetic energy}} - \varphi$$

*Equation 3.1*

Where  $h\nu$  is the photon energy defined as the product of Planck's constant  $h$  and photon frequency  $\nu$  and  $\varphi$  the work function of the spectrometer.

Modern spectrometers typically use monochromated x-rays as their excitation source <sup>[305][204]</sup>, with the spectra recorded in this document using aluminium  $K\alpha$  x-rays that have a photon energy of 1486.6 eV <sup>[305]</sup>. At the kinetic energy of emitted photoelectrons ( $\leq 1486.69$  eV) the mean free path of the electron  $\lambda$ , the expected distance where the flux of electrons that have not undergone a collision drops to  $1/e$ , is sub 3 nm <sup>[305]</sup>. Using the standard  $3\lambda$  definition for the sampling depth <sup>[305]</sup>, the sampling depth of XPS is limited to the top 9 nm of the surface. As a result, XPS is one of the most sensitive techniques capable of analysing the chemistry of a solid. This makes it ideal for analysing surface treatments; with the ability to quantitatively measure the elements and their oxidation states provides a powerful tool to analyse the chemistry of a sample in general.



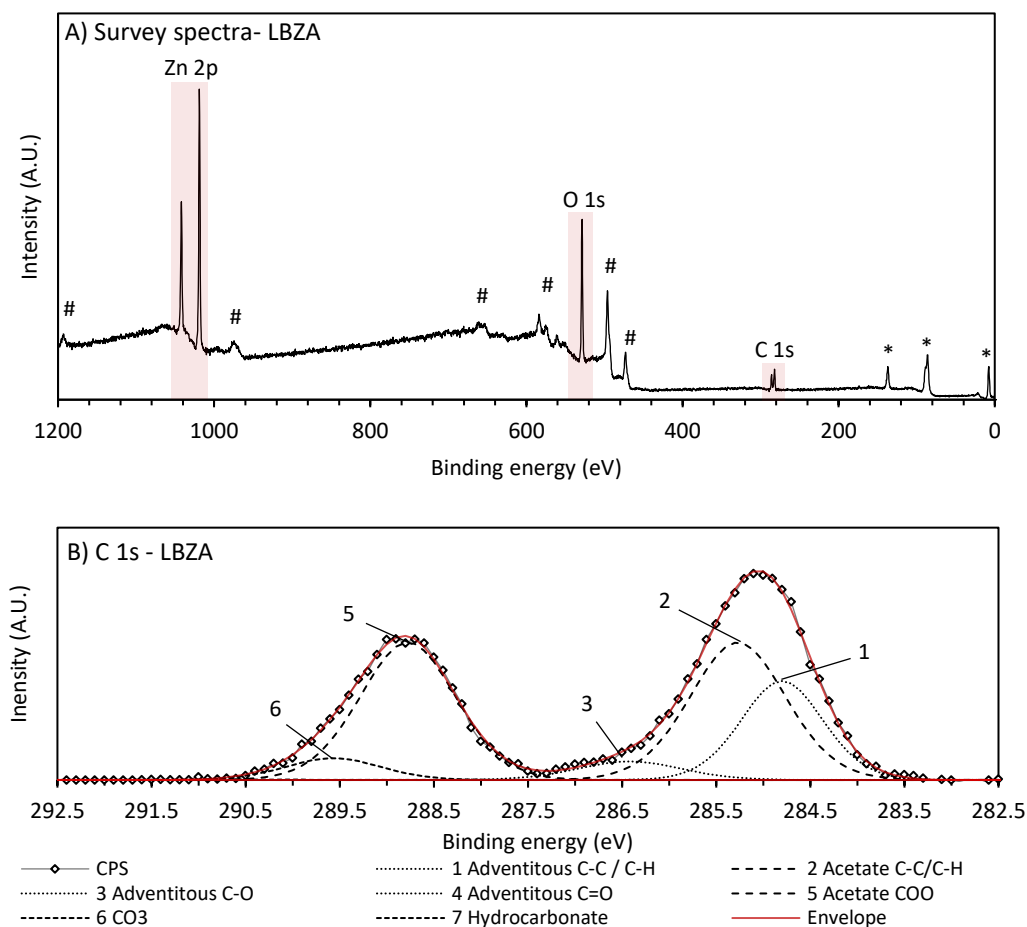


Figure 3.2: Example XPS spectra recorded for a thick film of dropcast LBZA from within chapter 7.4.2, with plots showing intensity as a function of binding energy. A) Survey spectra recorded using a pass energy of 80 eV. Peaks highlighted in red represent typical photoelectron peaks used for analysis for Zn, O, and C. Peaks annotated with # represent Auger electrons, and \* secondary photoelectrons from the same elements but from different orbitals; neither set of peaks are used in quantification. B) C 1s region spectra recorded at a pass energy of 20 eV, with fitted peaks representing individual functional groups. Note that adventitious peak 4 and hydrocarbonate were not present in this sample, however they were in the rest of the data set at binding energies of approximately 287.7 eV and 290.25 eV. Peak energy references are supplied in the relevant sections where the data is presented.

During XPS analysis an electron detector filter and scans through the kinetic energy of the electrons emitted by the sample and captured by the lensing system <sup>[305]</sup>. The intensity and breadth of the signal is dependent on the chemistry of the sample and the energy filter settings of the detector, known as the pass energy <sup>[305]</sup>. During routine analysis, first survey scans are performed at the highest pass energies (80-160 eV here) <sup>[305]</sup>. This produces the broadest peaks and the highest signal to noise ratio. Figure 3.2 A) shows a representative survey scan of a thick film of drop cast LBZA. The peaks highlighted in red represent the photoelectron peaks used to quantify the elemental concentrations of the sample. Peaks with \* notation represent photoelectron lines from the same element but different electron orbitals, and # Auger electrons <sup>[305]</sup>. Neither set of peaks are used for quantification in this

document and the Auger process shall not be discussed further. Figure 3.2 B) shows a carbon 1s (C 1s) scan from the same LBZA sample recorded with a pass energy of 20. The lower pass energy results in reduced signal to noise ratio, requiring longer scan times; however, the reduced peak width allows the oxidation state and functional groups to be ascertained and quantified. To analyse the chemistry present, first the scans need to be fit with a background to remove contributions from scattered electrons <sup>[305][204]</sup>. Then, peaks normally of a hybrid Gaussian-Lorentzian line shape are added and fit using least square methods <sup>[305][204]</sup>. The peak area, when scaled by various factors, and then normalised to the total scaled area, provides the concentration of a particular functional group <sup>[305][204]</sup>. The peak position gives an indication of oxidation state, and by comparing with reference spectra, the functional group <sup>[305][204]</sup>. The more oxidized an atom is, the higher the binding energy; the more reduced the atom, the lower the binding energy <sup>[305][204]</sup>. Different elements produce shifts in binding energy of different magnitude. The C 1s orbital for example can shift by greater than 5.4 eV <sup>[305]</sup>. Others such as zinc produce negligible shifts, with shifts in binding energy between Zn metal and Zn<sup>2+</sup> in ZnO shifting the Zn 2p<sub>3/2</sub> by only 0.3 eV <sup>[306]</sup>. In addition to the magnitude of the binding energy shift, each peak produces relatively characteristic full width at half maxima (FWHM). The C 1s for example has intrinsic FWHM typically between 0.9 and 1.2 eV <sup>[305]</sup>, others such as the O 1s are typically broader with FWHM routinely observed with the spectrometer here > 1.3 eV <sup>[307]</sup>.

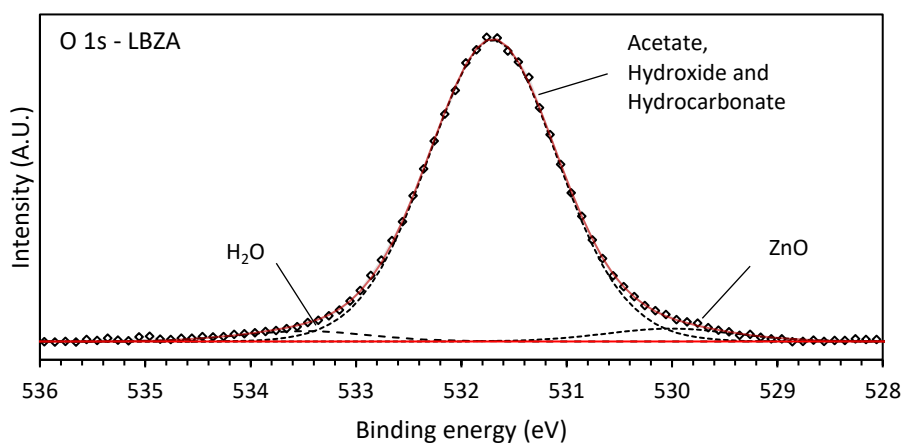


Figure 3.3: Example XPS O 1s region spectrum recorded from the same LBZA sample that the spectra in Figure 3.2 are taken from. Pass energy 20 eV. The ZnO represents minor impurity phases and H<sub>2</sub>O either water within the LBZA structure or adsorbed to the surface. Note that acetate, hydroxide and hydrocarbonate peak separations are too narrow to differentiate.

In these investigations carbon and nitrogen are primarily used for the identification of functional groups. The states in oxygen overlap heavily as can be seen in the O 1s spectra for the LBZA sample in Figure 3.3; where the central peak contains contributions from all

oxygen in hydroxide, acetate, and the potential hydrocarbonates seen in the C 1s spectra. Whilst the O 1s spectra for ZnO shows a sharp peak at  $\sim 530.8$  eV <sup>[308]</sup> the presence of surface hydroxide, carbonate and water surface species lead to a broad second band <sup>[202][308]</sup>; with some authors also attributing components of the broad band to oxygen related defects <sup>[309][310]</sup>. This makes fitting unique solutions to the peak envelope in LBZA/ ZnO mixes impossible. As a result, analysis of oxygen spectra is limited to elemental analysis only.

Due the very small sampling depth XPS is exceptionally prone to surface contamination, with the presence of atmospheric contaminants almost impossible to avoid. This usually results in the presence of adventitious hydrocarbons adsorbed to the surface <sup>[305]</sup>. In Figure 1 A) this is shown by the presence of aliphatic hydrocarbon (C-C/ and C-H) and C-O species. C=O species are often observed as well. While good sample preparation can minimize adventitious carbon, the final concentration is ultimately dependent on the quality of vacuum the spectrometer has <sup>[305]</sup>. In these investigations the adventitious carbon concentration is typically between 7 and 24 atomic %. As XPS ionizes the surface, the charge must be replaced for the sample to stay electrically neutral, with the positively charged surfaces shifting the spectra to higher energies. In conductive samples this is usually performed by grounding the sample, whereas for insulators external electron sources are used <sup>[305]</sup>. The electron sources typically produce a small but stable negative surface charge and corresponding shifts in binding energy <sup>[305]</sup>. By simply shifting the spectra so that the aliphatic hydrocarbon component is at 284.8 eV, the presence of aliphatic hydrocarbon provides a useful way of calibrating the binding energy of the spectra <sup>[305]</sup>.

### 3.3.3 X-ray diffraction analysis (XRD)

Whilst EDS and XPS provide chemical analysis through quantification of at% of the samples constituents, x-ray diffraction analysis (XRD) identifies the phases of crystal structures present. During a typical experiment a sample is illuminated with x-rays with a characteristic wavelength (here Cu K- $\alpha$  = 0.1504 nm <sup>[311]</sup>). When the x-ray passes through the sample, the electric field forces the electrons in the sample to oscillate, which subsequently emit x-rays of the same wavelength <sup>[311]</sup>. As the path length of the x-rays are on the order of the distance between planes in a crystal, the x-rays have significant phase shifts between electrons in sequential planes <sup>[311]</sup>. This consequently produces phase shifts between x-rays emitted. At a distance the x-rays superimpose leading to changes in intensity <sup>[311]</sup>. When the phase shifts are an even multiple of  $\pi$ , they interfere constructively <sup>[311]</sup>; for phases shifts that are odd multiples of  $\pi$ , they interfere destructively <sup>[311]</sup>. The path length, and hence

phase shift, is a function of the interplane distance and angle of incidence <sup>[311]</sup>. When a large number of planes are stacked, such as a crystal, this leads to sharp peaks in intensity at certain angles <sup>[311]</sup>. The angles where reflections exist is given by Bragg's law (Equation 3.2), for integer values of  $n$  <sup>[311][204]</sup>.

$$2d_{[hkl]} \sin(\theta) = n\lambda$$

Equation 3.2

Where  $d_{[hkl]}$  is the interplane distance in the  $[hkl]$  direction in metres,  $\theta$  the angle of incidence in radians and the wavelength of x-rays in metres.

In the experiments used in these investigations the Bragg-Brentano geometry. In the Bragg-Brentano geometry both x-ray source and detector are held at an angle  $\theta$  respective to the horizontal plane of the diffractometer <sup>[312]</sup>. A diffractogram is recorded by measuring the intensity as a function of  $2\theta$ , which is where the secondary name for the geometry i.e. the  $2\theta$  or  $\theta$ - $\theta$  geometry is derived <sup>[312]</sup>.

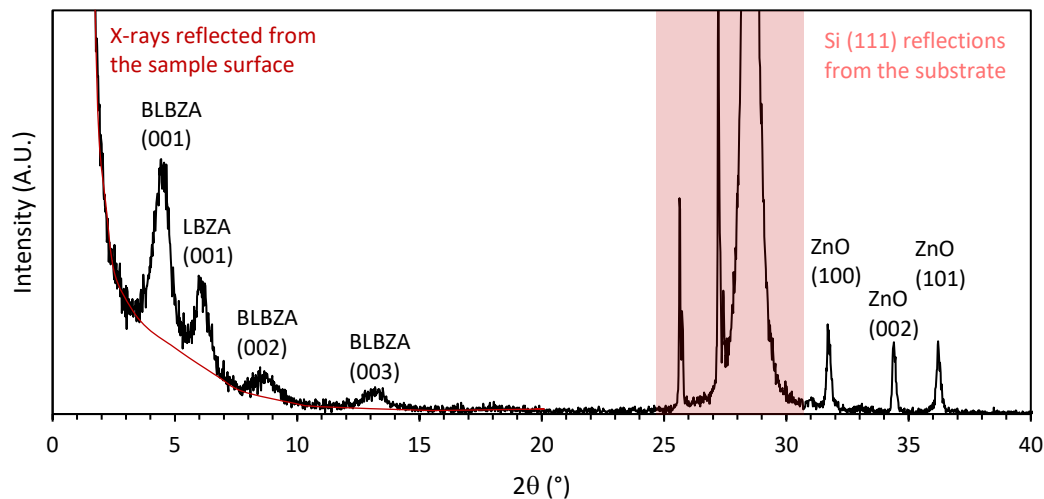


Figure 3.4: Annotated example  $2\theta$  diffractogram of an LBZA synthesis sample extracted from (Figure 5.6). Note that the diffractogram shows the presence of LBZ, ZnO, as well as a so called BLBZA phase. The difference in peak width between BLBZA and LBZA phases, is a result of size broadening (described in main text). The normalised areas for BLBZA (001), LBZA (001) and ZnO ((100)+(002)+(101)), are 0.531, 0.152 and 0.316 respectively. Note that the BLBZA (002) and (003) reflections are higher order harmonics of the (001) axis reflection and are excluded from the area ratio calculations to prevent double counting. As the 3 ZnO reflections are from different planes, they each represent a different set of ZnO particles, each with a different orientation. Therefore, all ZnO reflections are included in the area. Note that both BLBZ and LBZA have sheet-like morphology, as a result they stack in a relatively ordered manner, and all non  $c$  axis reflections have negligible to low intensity <sup>[313]</sup>. The red line represents low angle x-rays that reflect of the surface of the sample <sup>[314]</sup>, as opposed to diffract from the planes of the phases. The shaded red area represents reflections of the underlying silicon substrate <sup>[315]</sup>. Diffractogram extracted from Figure 5.6; for full detailed analysis of the sample, analysis and relevant references, see chapter 5.3

If the particles are narrow in the direction of a particular set of planes (hkl), the corresponding reflections undergo less constructive interference, as a result those reflections broaden <sup>[316]</sup>. Using the FWHM of the peak, the thickness of the crystallite (formally the coherence length of the phase domain) can be measured using the Scherrer equation <sup>[316][311]</sup>:

$$\tau_{[hkl]} = \frac{k\lambda}{\beta \cos \theta}$$

Equation 3.3

Where:

- $\tau_{[hkl]}$  is the size of the coherence length in the [hkl] direction, in single crystal nanoparticles this is typically on the order of the crystal or grain size in the [hkl] direction <sup>[316]</sup>.
- $\lambda$  is the wavelength of the x-ray
- $k$  is the shape factor, taken here as 0.88
- $\beta$  is the FWHM of reflection (hkl)
- $\theta$  is the angle of incidence (the Bragg angle) of the reflection.

It should be noted that  $\beta$  formally is the FWHM after instrumental factors and strain broadening have been subtracted <sup>[316]</sup>. However, in many cases material standards for measuring instrumental width are not available. As such  $\tau_{[hkl]}$  represents the minimum crystallite size in the [hkl] direction.

The effect of size broadening can be seen in Figure 3.4, where the minimum thickness of LBZA in the [001] direction (i.e. in the c axis of the crystal) is 11.6 nm and ZnO in the [002] direction (again in the c axis) is 54.7 nm.

Whilst size and strain broadening reduce the peak maximum intensity, the total area is retained. As such the total area of the peak, ignoring instrumentation dependent factors, is dependent on 4 factors:

- The electron density of the constituent ions or crystals, with increased electron densities producing more intense reflections. <sup>[317][318]</sup>
- The concentration of the phase within the x-ray sample depth. <sup>[318]</sup>
- The distribution of the orientation of the crystallites, respective to the diffractometer normal. If the crystals have a preferred orientation will produce high intensity

reflections for the corresponding planes, and reduced intensity reflections for other planes. <sup>[318]</sup>

- The underlying symmetry of the crystal structure. If multiple planes have the same interplanar distances, then the intensity of the peaks are summed and the total number of reflections (e.g. 2 reflections with the same distance will produce 1 peak with a combined intensity of the individual reflections). <sup>[317][319]</sup>

If the electron density or the intensity of reflections in a powder control are known, the concentration of phases can be measured using the total area intensity of the peaks <sup>[317]</sup>. However, if the materials have similar electron densities and symmetry, then qualitative trends in purity can be measured by using the ratios of reflection areas.

### **3.3.4 Photoluminescence (PL) and Ultraviolet-visible spectrophotometry (UV-VIS)**

If an electron in a material is exposed to light with photon energy equal to the difference in energy between its orbital and an empty state, then it can absorb the photon and transition to the unoccupied state <sup>[320]</sup>. In a crystal the energy difference is equivalent to the optical bandgap of the material. As a crystal typically has a broad empty conduction band, by shining a light source with photon energy greater than the band gap energy, electrons in the valance band can be excited to the conduction band <sup>[320]</sup>. By transitioning to a higher energy state, the electron leaves a vacancy, or hole, that acts as a positively charged mobile quasi particle <sup>[320]</sup>. The electrons and hole rapidly loose energy through phonon interactions i.e. dissipated as heat, until they reach their lowest energies in their respective bands <sup>[320]</sup>. For the electron this corresponds to the conduction band minimum and hole the valance band maximum. If the electron and hole are local to each other then coulombic interactions result in the particles being bound to each other in a new quasi particle known as an exciton <sup>[320]</sup>. The energy of the coulombic interaction is known as the exciton binding energy and represents the difference in energy between the electronic and optical bandgaps. To reduce the energy of the system to the ground state the exciton can, in a direct band gap semiconductor, after a period of time, recombine, emitting a photon <sup>[320]</sup>. Defects in a material can capture (or bind) or scatter excitons and its individual components. As a result, the exciton can no longer directly relax, and a portion of energy is lost as heat. If the defect

is optically active, the exciton can recombine emitting a photon with a characteristic energy in a process known as Shockley-Read-Hall recombination <sup>[320]</sup>.

During a typical photoluminescence experiment a sample is excited by a laser with energy greater than the bandgap of the material and the emission as a function of wavelength recorded. The wavelength can then be converted to photon energy using Equation 3.4, from which the exciton and defect energies can be measured <sup>[1]</sup>.

$$E_{\text{photon}} = \frac{hc}{\lambda} \quad (\text{J}) \quad \text{or} \quad E_{\text{photon}} = \frac{hc}{\lambda q} \quad (\text{eV})$$

Equation 3.4

Where  $h$  is Planck's constant,  $c$  is the speed of light,  $\lambda$  the wavelength. To convert from Joules (J) to electron volts (eV) the energy is divided by the charge of an electron  $q$ .

As the photons with energy below the exciton emission energy are related to the defects in a crystal <sup>[320]</sup>; by measuring the intensity areas of the exciton and defect region (i.e. for  $E_{\text{photon}} < E_{\text{exciton}}$ ) a qualitative measure of defect concentration can be made <sup>[76]</sup>. Comparing the area ratio between samples provides a simple figure of merit for the quality of the crystal material.

Another well-known spectroscopic technique, ultraviolet-visible spectrophotometry (UV-VIS), instead measures the intensity of the light reflected or transmitted as a function of wavelength <sup>[321]</sup>. By comparing the intensity absorbed to a reference beam, changes in the absorbance can be measured <sup>[321]</sup>. UV-VIS can then measure the optical bandgap directly by measuring the wavelength where the intensity in reflected or transmitted light drops <sup>[321]</sup>.

### 3.3.5 Ultraviolet photoelectron spectroscopy (UPS)

Ultraviolet photoelectron spectroscopy (UPS) is a variation of the same photoelectron spectroscopy technique used in XPS. However, instead of an x-ray source an ultraviolet source, such as a He I lamp <sup>[322][323]</sup>, that produces low energy photons is used ( $E_{\text{photon He-I}} = 21.22 \text{ eV}$  <sup>[322]</sup>). The low energy limits the emission of electrons to those originating from valance band states, and also results in an exceptionally short sampling depth  $< 3 \text{ nm}$  <sup>[323]</sup>. Chemical analysis of the valance band is complicated <sup>[324]</sup>; however, the

valance band maxima and work function of the surface of the material can be easily measured <sup>[324][323]</sup>. If the bulk values are known, the valance band maxima and work function measurements allow for surface band bending to be analysed <sup>[323]</sup>. If the grain size of the material is small enough that the grains are in the flat band condition, then the measured values are constant throughout the grains <sup>[323]</sup>. Therefore, by measuring the parameters, and combining them with measured on known bandgap values; important electronic information relating to carrier concentration and conduction barrier energies at the surface can be measured (see chapter 2.2.1 ).

To measure the work function, the kinetic energy of electrons with the highest kinetic energy is measured <sup>[322][324][323]</sup>. The valance band maxima is measured by from the binding energy differences between the lowest binding energy states and the spectrometer fermi level (i.e.  $E_{Binding\ energy} = 0\ eV$ ) <sup>[324][323]</sup>. For each measurement the line of best fit for the steepest slope of the cut off is plotted, with the intersection with the background producing the value of interest <sup>[323]</sup>.

### 3.4 Fluid analysis

#### 3.4.1 Interfacial/ surface tension (IFT) - Pendant drop method

In the pendant drop method of interfacial tension analysis, a droplet (the pendant drop) is formed at the end of a needle within a goniometer, and an image of the droplet captured by a camera <sup>[325]</sup>. The radius of curvature of a droplet is described by Young- Laplace equation <sup>[325]</sup>:

$$\Delta P = \gamma \left( \frac{1}{R_1} + \frac{1}{R_2} \right)$$

*Equation 3.5*

Where:

- $\Delta P$  is the pressure difference within and outside of the droplet, and is related to the pressure exerted by gravity due to difference in the density of the fluid within and external to the droplet.
- $\gamma$  is the interfacial tension
- $R_1$  and  $R_2$  are the radii of curvature of the droplet. Typically, the droplet has axial symmetry so that  $R_1 = R_2 = R$ .



The geometry of the droplet is then analysed by software <sup>[325]</sup>. By using the geometry and numerical solutions to balance the pressures on and within the droplet, the interfacial tension is measured <sup>[325]</sup>. More detail of the geometry and analysis of a pendant drop performed by the software can be found in work by Morita, Carastan and Demarquette <sup>[326]</sup>. If the second fluid is air, then the interfacial tension is equal to the surface tension of the fluid within the droplet <sup>[326]</sup>.

Similar analysis methods are used for sessile drop analysis also known as contact angle analysis <sup>[327]</sup>. In sessile drop analysis, a droplet of the fluid is placed on the sample and the geometry of the droplet recorded and analysed. The droplet placed has a volume small enough that the effects of gravity are negligible, typically  $< 5 \mu\text{L}$  <sup>[327]</sup>, and as a result the shape of the droplet is defined by the balance of solid – vapour, solid-fluid, and fluid-vapour tensions <sup>[327]</sup>. For theory governing the balance of tensions, and the result on the contact angle formed, the reader is directed towards chapter 2.3.3 .

### **3.4.2 Rotational (dynamic) viscometry**

In chapter 2.3.4 a brief theoretical description of dynamic viscosity of fluids was provided. In these investigations rotational viscometry is used to measure the dynamic viscosity of the inks developed and tested. In rotational viscometry a fluid is placed between a plate and a plate or cone attached to a spindle <sup>[328]</sup>. The spindle is then accelerated to a specific shear rate and the resulting torque/ stress on the spindle, imparted by the viscous forces in the fluid, measured <sup>[328][329]</sup>. The viscosity can then be calculated from the applied shear rate and the measured torque <sup>[328]</sup>. To measure the viscosity at the various shear rates, the stepped shear stress (i.e. table of shears) method <sup>[329]</sup> is used here. In the table of shears, stepped shear stress method, a table of pre-set shear rates is populated. The rheometer then accelerates the spindle to the first shear rate; the shear rate is held constant for a period of time until equilibrium is reached <sup>[328][330]</sup> and then the torque integrated over a pre-set time period. Once the torque measurement is complete the spindle is accelerated to the next shear rate and the process repeated <sup>[328]</sup>.

In all cases where viscosity is measured here, the cone and plate geometry is used. In the cone and plate geometry, a cone with small angle  $\sim 4^\circ$  is attached to the spindle <sup>[328]</sup>. The angle of the cone is such that shear rate, which is a function of the differential of flow with respect to separation distance, is approximated as being constant along the cone radius <sup>[328]</sup>.

## 3.5 Statistical analysis

### 3.5.1 Mean, standard deviation and number of samples

Wherever possible 3 or more samples have been analysed for each condition provided in the experiments within these investigations. Whenever multiple measurements have been made the arithmetic mean (i.e. the expected value) has been calculated. To analyse the variance in the measurements, the standard deviation of each sample with more than 1 measurement has been calculated. Whenever values of mean and standard deviation have been presented the number of samples,  $n$ , is reported. For size measurements of particles, unless otherwise stated, the minimum number of particles measured is 100. The number of particles reported was based such that a basic of the underlying population could be ascertained within the time limits of the experiments performed. For experiments where the number of samples per condition is  $\leq 5$ , the standard deviation is used as a measure of error.

### 3.5.2 Confidence intervals

When experimentally measuring the value of any variable, it is important to realise that measurements are of a random variable <sup>[331]</sup>. As a result, the mean and standard deviation of a sample are themselves random variables and represent estimators of the underlying population mean and standard deviations <sup>[331]</sup>. To provide an estimation of how noise, and sampling errors due to variance affect the mean and standard deviation, confidence intervals for each have been calculated. In the frequentist interpretation of statistical analysis, the confidence interval, with confidence level  $\alpha$  or  $100\alpha\%$ , is defined such that if a large number of measurements, each with sample size  $N$ , then in  $100(1-\alpha)\%$  of cases the estimator will fall within the limits of the interval <sup>[331]</sup>. If the confidence intervals between measurements with different dependant variables (i.e. input parameters) overlap, then the samples cannot be classified as statistically different at the confidence level of the interval <sup>[331]</sup>.

To calculate confidence intervals parametrically the population probability density function needs to be known <sup>[331]</sup>. However, the probability density function of a sample may conform to well-known distributions such as gaussian or t distributions. In such cases non-parametric methods are more appropriate <sup>[332]</sup>. In these investigations the bootstrap (resampling) method is implemented by the bootstrap function in MATLAB <sup>[333]</sup>. In the bootstrap method the

originally sampled data is resampled  $n$  times, creating  $n$  data sets. Each data set comprises of samples taken randomly with replacement, i.e. each sample value can be drawn more than once, and the likelihood that any value is taken is constant <sup>[332]</sup>. For each resampled data set the desired estimator (e.g. mean, standard deviation) is calculated and recorded, forming a population of the estimator <sup>[332]</sup>. By measuring the  $100\alpha$  and  $100(1-\alpha/2)$  percentile the confidence interval of the estimator can be obtained <sup>[332]</sup>. The estimators calculated using the bootstrap method follows the law of large numbers <sup>[334]</sup> i.e. as the number of sampled datasets (i.e. the number of iterations) increases, the closer the estimator approaches to its true value. In all cases when the bootstrapped method was used 20,000 iterations were performed.

### 3.5.3 T-test

When different experimental conditions are trialed, it is useful to be able to infer if the treatments produce different outcomes, e.g. whether one surface treatment results in more wetting than another. In such conditions, hypothesis testing is typically used to infer whether the difference between the two datasets is a result of chance. To perform the tests, a hypothesis about multiple population must first be made <sup>[331]</sup>. In the surface treatment example this would be the mean of the two samples is the same, this is typically known as the null hypothesis  $H_0$ . Next the  $p$  (or  $\alpha$ ) value, representing the threshold for significance is decided <sup>[331]</sup>. The  $p$ -value is typically viewed as the probability that the mean of the two sample sets is the same due to chance <sup>[331]</sup>. Note that the threshold must be defined beforehand to prevent shifting the goalposts and corruption of the testing results <sup>[331]</sup>. The test statistic is then measured, for the general case the statistic is calculated by <sup>[331]</sup>:

$$t = \frac{\bar{X}_1 - \bar{X}_2}{\sqrt{\frac{\sigma_1^2}{n_1} + \frac{\sigma_2^2}{n_2}}}$$

*Equation 3.6*

Where  $\bar{X}_a$ ,  $\sigma_a^2$  and  $n_a$  represent the mean, variance and number of sampled values from sample set  $a$ .

Then the combined variance and degrees of freedom (N) are found <sup>[331]</sup>. Using the combined values; the rejection region for the t-distribution is calculated from its cumulative distribution function such that <sup>[331]</sup>:

$$C_{N-1} = \int_{-\infty}^{t_{crit-lower}} P(t|H_0)dt + \int_{t_{crit-upper}}^{\infty} P(t|H_0)dt = \alpha$$

*Equation 3.7*

If  $t_{crit-lower} < t < t_{crit-upper}$  the null hypothesis is accepted at significance level  $\alpha*100$  %, and the samples can not be viewed as statistically different <sup>[331]</sup>. Otherwise the null hypothesis is rejected, i.e. the samples are different at a significance level  $\alpha*100$  % <sup>[331]</sup>.

The t-test assumes that the underlying population follows a gaussian distribution, however it retains a relatively large degree of accuracy, and a remarkable degree for gaussian like functions <sup>[331]</sup>. The test can be viewed as equivalent to calculating the calculation interval for  $\mu_1 - \mu_2$  i.e. for the difference in means for the underlying populations <sup>[331]</sup>. In these studies the t-tests were performed using the inbuilt data analysis toolPak in Microsoft excel <sup>[335]</sup>.

### 3.5.4 Regression

While t-test can be used to differentiate between treatments they cannot be used to predict trends in data or infer results if the dependant variables correlated <sup>[331]</sup>. As an example, whilst t-tests can be performed between different treatments, they would be inappropriate to use for comparing between treatment times. This assumption can be relaxed if different processes occur at different treatment times, i.e. the dependant variable, treatment time, is no longer correlated. In such cases where the values are correlated, regression analysis can be used to predict the underlying relationships in the recorded data sets <sup>[331]</sup>. If the sample statistics were equal to the population statistics, then the relationships between dependant variables (process parameters) and independent variables (the observable or measured parameter) could be calculated exactly. However, as the statistics take the form of random variables, this is not possible <sup>[331]</sup>. As such regression analysis is used to fit a relationship to the underlying dataset.

To do this a least square method of error analysis is used <sup>[331]</sup>, where the test parameters for the assumed function are varied so that the sum of square errors (Equation 3.8 <sup>[331]</sup>) is minimised.

$$\text{Sum of squared error}_{\text{Predicted}} = \sum (Y_{n:\text{Predicted}} - Y_{n:\text{measured}})^2$$

Equation 3.8

Where Y represents the independent variable (i.e. the observable), and the sum is squared over all values of n.

The final goodness of fit statistic,  $R^2$ , for the least square error set of fitting parameters is then defined as <sup>[336]</sup>:

$$R^2 = 1 - \frac{\text{Sum of squared error}_{\text{Predicted}}}{\text{Sum of squared error}_{\text{Mean}}} = 1 - \frac{\sum (Y_{n:\text{Predicted}} - Y_{n:\text{measured}})^2}{\sum (\bar{Y} - Y_{n:\text{measured}})^2}$$

Equation 3.9

Where  $\bar{Y}$  represents the mean of the independent variable dataset.

If  $R^2 \gg 0$  then predicted trendline produced by the fitted relationship is considered to fit the data well; with values approaching 1 indicating that the variance in the data is well described by the relationship as compared to the mean alone <sup>[336]</sup>. If  $R^2 \approx 0$  the predicted trendline is no better at describing the variance in the dataset than the mean, i.e. is equivalent to the mean <sup>[336]</sup>. If  $R^2 < 0$  then the relationship is worse than the mean at describing the variance in the dataset <sup>[336]</sup>.

$R^2$  always increases as the number of test fit parameters (i.e. the predictors), and therefore degrees of freedom, increases <sup>[337]</sup>. In the process the contributions of the noise to the fitted relationship increases, and the ability to produce accurate future predictions diminished <sup>[337]</sup>. To reduce the error of overfitting the data the adjusted  $R^2$  parameter is used instead. The adjusted  $R^2$  (Equation 3.10) reduces if the variance explained by the addition of a predictor is lower than the reduction due to the increase in degrees of freedom <sup>[337]</sup>.

$$\text{adjusted } R^2 = 1 - (1 - R^2) \frac{N - 1}{N - k - 1}$$

*Equation 3.10*

Where N is the number independent samples in the dataset and k the number of predictors. The interpretations of the values of adjusted  $R^2$  is equivalent to that of  $R^2$ .

If the trendline functions are well behaved and easily linearised, simple linear regression or multiple linear regression (i.e. for more than 1 dependent variable) can be used <sup>[336]</sup>. If not, then a brute force method can be performed, where the least square error for each potential combination of dependent variable values within a pre-defined sample space tested <sup>[331]</sup>. The linear methods have the benefit of being orders of magnitude more computationally efficient (i.e. performed here in the space of 1-2 seconds vs minutes.) In addition, Microsoft excel also performs inference hypothesis testing on the predictors for multiple linear regression analysis. This allows the statistical significance of each predictor to be measured. When simple linear, or brute force method have been used, the  $R^2$  or adjusted  $R^2$  value (respectively) is reported. For multiple linear regression, the adjusted  $R$  for the relationship, and the p-value for individual components are reported.

## **Chapter 4 - HMTA microwave assisted LBZA synthesis, gas sensing and sodium hydroxide-based alternative**

---

In Chapter 3 the background theory underpinning the analysis techniques used in this study was presented to aid the readers understanding of the subsequent results and analysis. In this chapter an in-depth investigation of the synthesis of LBZA nanomaterials is presented. Layered basic zinc acetate (LBZA) is a crystal structure with chemical formula  $Zn_5(OH)_8(OOCCH_3) \cdot 2H_2O$  typically taking the form of thin (sub 100 nm) thick sheets that upon calcination breaks down into nanogranular textured zinc oxide ideal for gas sensing. Microwave methods of synthesis have been shown to rapidly produce high quality LBZA nanosheets by Tarat *et al.* <sup>[67]</sup>. The chapter is broken into 2 major sections.

The first comprises of an initial brief investigation into the morphology, purity and yield of LBZA produced via an in-house modified method based on that reported by Tarat *et al.* <sup>[67]</sup>. Following on, the gas sensing properties of drop-cast nanogranular ZnO gas sensors on commercial Alumina substrates using the LBZA synthesized via the investigated method were explored and compared to the requirements for use as part of a carbohydrate malabsorption sensor. Finally, the implications of the low reaction efficiency and mass yield with respect to the use in printed sensors are discussed.

The second section introduces a green alternative microwave assisted method using sodium hydroxide as the base as opposed to HMTA. First, the phase purity with respect to the ZnO by product as a function of Zinc to hydroxide ratio is investigated, then the morphology and yield measured and the implications for printed sensors discussed.

### **4.1 HMTA microwave assisted LBZA, synthesis and gas sensing**

Prior to ink manufacturing and print testing it was important to assess the nanosheets morphology, yield and gas sensing properties to check for compatibility and scalability with the print process and its use as precursor to the hydrogen sensor sensing medium used in a carbohydrate malabsorption breath analyser. In the following section the physical properties are assessed via SEM (morphology) and XRD (crystal structure, phase purity and mean particle height). The mass yield is measured, and the gas sensing behaviour tested at

calcination temperatures (350 °C) compatible with Kapton, the substrate chosen in Chapter 6 as a relatively low-cost substrate for disposable point of care testing.

## **4.1.1 Methods**

### ***4.1.1.1 Microwave synthesis***

Synthesis consisted of dissolving 0.1 M Zinc acetate dihydrate and 0.02 M hexamethylenetetramine (HMTA) into 60 mL of reverse osmosis water and microwaving for 1 minute at 800W using a commercial Sharp R272SLM 20L 2.45 GHz 800 W kitchen microwave with internal cavity measuring W x H x D: 306.6 mm x 208.2 mm x 306.6 mm. The solution was subsequently allowed to cool for an hour and then centrifuged 5 times for 5 minutes at  $\times 3260$  g, replacing the supernatant each time with reverse osmosis water.

### ***4.1.1.2 Morphology characterisation via scanning electron microscopy***

Morphology was assessed using a Hitachi S4800-II FEGSEM (Hitachi High Technologies, Minato-ku, Tokyo, Japan) at  $\times 4k$  magnification and 2.5 kV acceleration voltage. The length of 100 LBZA particles were measured in ImageJ, the mean and standard deviation calculated, and a histogram of the results plotted.

### ***4.1.1.3 Crystal phase purity/ characterisation via XRD***

Phase purity was assessed using a D8 x-ray diffractometer (Bruker, Billerica, MA, USA) in standard coupled  $\theta$ - $2\theta$  mode. 200  $\mu$ L of centrifuge cleaned samples was drop cast on to a silicon wafer and left to air dry. Scans were performed using Cu  $K\alpha$  x-rays ( $\lambda = 0.154$  nm) from an achromatic source set at 40 kV and 40 mA. A Göbel mirror was used to strip the  $K\beta$  lines and convert the beam from dispersive to parallel beam geometry. The diffracted beam was recorded with a linxeye 1D detector over the  $2\theta$  range  $4.8^\circ$  to  $66^\circ$ . Height of the LBZA material was estimated from the (001) reflection using Scherrer's Equation (Equation 3.3).



#### 4.1.1.4 Mass yield measurements

16 LBZA samples were synthesised and cleaned using the method outlined in 4.1.1.1 . Prior to centrifuging the mass of each centrifuge tube was measured. After the final centrifuge step the pelleted samples were dried inside the centrifuge tube under a rough vacuum (estimated pressure between 100 mbar & 300 mbar) with the lid resting (but not screwed) on to prevent loss of mass during any bumping events (flash boiling) under the reduced pressure. The final mass of each centrifuge tube was measured and the difference with respect to the empty centrifuge weight calculated producing the dry mass of LBZA, and the mean and standard deviation recorded.

#### 4.1.1.5 Gas Sensing

##### 4.1.1.5.1 ZnO nanotextured gas sensor manufacturing method.

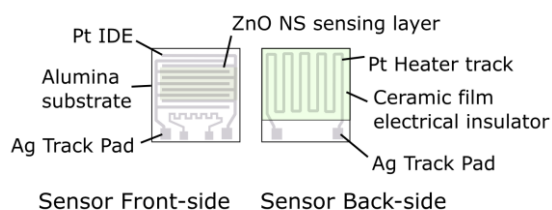


Figure 4.1: Diagram of tested sensor. The substrate consisted of a sintered alumina chip, on the top side was a Pt interdigitated electrode with silver trackpads. The spacing between each electrode 'digit' was 300  $\mu\text{m}$ . The substrates had an additional Pt temperature dependent resistor on the top side that was unused due to limited available feedthrough pins (see 4.1.1.5.2 for more details). A Pt heater track was patterned on the rear side and coated with a non-conductive ceramic film. The ZnO NS sensing layer was produced by dropcasting 100  $\mu\text{L}$  of the cleaned aqueous LBZA NS dispersion and calcined at 350  $^{\circ}\text{C}$  for 30 minutes.

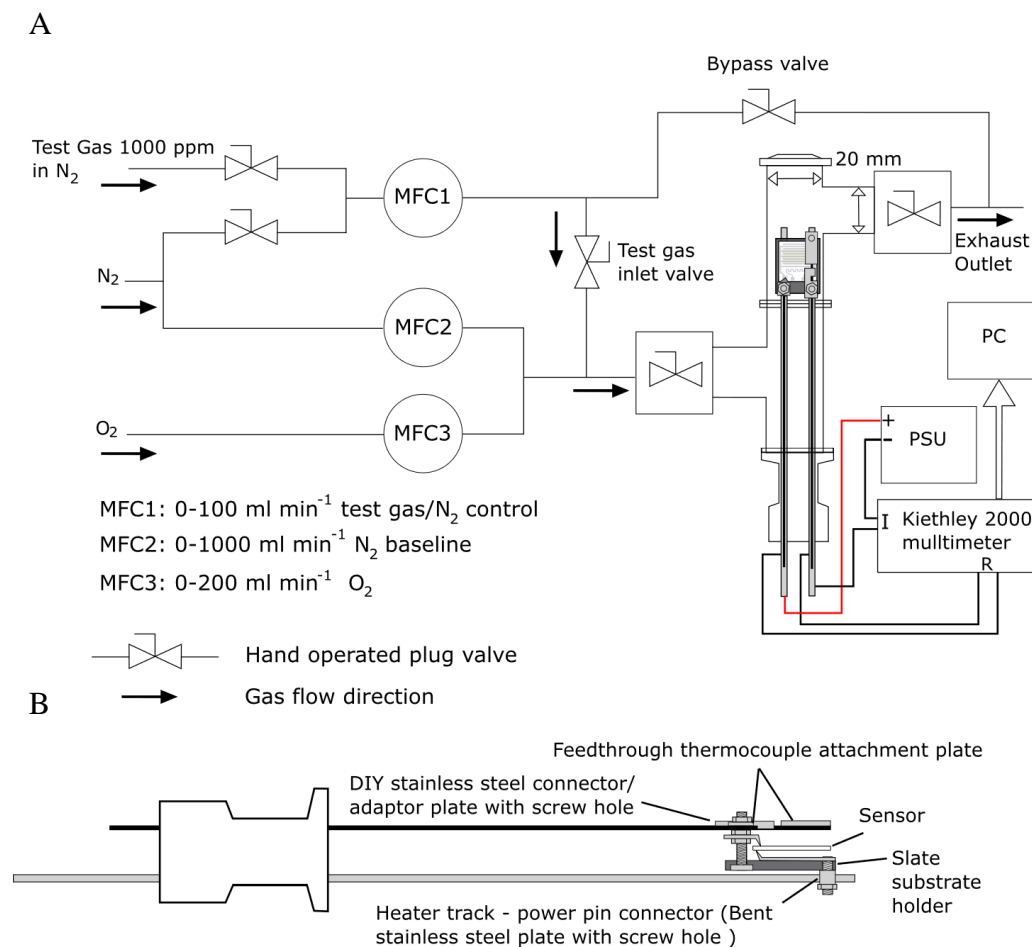
Nanosheets were synthesized and cleaned as outlined in 4.1.1.1 , however only 3 mL of the synthesized sample was centrifuged, as opposed to the entire sample. After the final centrifuge step the sample was topped up to 3 mL, vortexed for 5 minutes and then left in an ultrasonic bath for 2 minutes to allow for complete dispersion of any aggregation. 100  $\mu\text{L}$  of the suspension was drop cost onto an alumina sensing substrate (purchased from The

Electronics Design Centre at Case Western Reserve University, Cleveland, Ohio). The substrates consisted of a sintered alumina chip with patterned platinum interdigitated electrodes (IDE) with 300  $\mu\text{m}$  spacing, silver contact pads and a backside platinum heater track with an insulating ceramic coating (See Figure 4.1 for more details). The substrate with the drop-cast layer was annealed at 350  $^{\circ}\text{C}$  for 30 minutes in a Carbolite tube furnace, removed and allowed to cool.

#### **4.1.1.5.2 Sensing Methodology**

Figure 4.2 shows a representative diagram of the gas sensor testing rig used for testing the LBZA derived ZnO nanosheet gas sensor. The sensor was mounted to a LewVac manufactured 4-pronged (25 mm diameter) stainless steel electrical feedthrough (Figure 4.2(B)) and inserted into a customised manual gas sensing rig created and introduced by Daniel R. Jones<sup>[77]</sup>. In brief the gas sensing rig (Figure 4.2(A)) comprised of a testing chamber made from two flanged stainless-steel T-pieces making up an S bend with tube inner diameter measuring  $\sim 20$  mm (manufactured by LewVac), into which the feedthrough was inserted. Gasses were fed to the chamber via 6 mm diameter stainless steel tubing leading from 3 mass flow controllers (MFC.) The first MFC (MFC1) provided a flow of up to 80  $\text{mL}\cdot\text{min}^{-1}$  of either test gas or 99.998% purity nitrogen (depending on the stage of the test), the third (MFC3) was used to provide a constant 80  $\text{ml}\ \text{min}^{-1}$  flow of 99.999% purity oxygen and the final MFC (MFC2) was used to supply additional 99.998% purity nitrogen (oxygen free nitrogen) to make up a total flow of 400  $\text{mL}\cdot\text{min}^{-1}$ . All gas flows were controlled via manually tuned GFC17 Aalborg manufactured mass flow controllers (Manufacturer calibrated) that had accuracies of  $\pm 1\%$  of the full flow range and test gasses consisted of 1000 ppm  $\text{CH}_4$  in  $\text{N}_2$ , 1000 ppm  $\text{CO}$  in  $\text{N}_2$  and 1000 ppm  $\text{H}_2$  in  $\text{N}_2$ . Oxygen free nitrogen was supplied by BOC industrial and all other gasses by BOC special gasses. By varying the flow between MFC1 and MFC2 (from here on known as the test gas MFC and nitrogen MFC) the test gas concentration could be varied from 0 ppm to 200 ppm (See Table 4.1 for details). Heat was applied to the sensor via application of DC current through the reverse side heater track provided by a standard adjustable 0-32 V, 0-3 A PID controlled laboratory power supply and the sensor temperature estimated by comparing the heater track resistance to a precalibrated surface temperature – heater track resistance calibration curve (Procedure outlined in section 4.1.1.5.3 ). Sensor resistance was measured and logged using a Keithley 2000 multimeter connected to a PC. A ‘by-pass’ or exhaust valve was connected

to the output of the test gas MFC and used to reduce any flow spikes when flow was changed between test gas and nitrogen.



Lewvac DN25KF 20 mm ID - 4 Pin K-type thermocouple/ power electrical

Figure 4.2: (A) Diagram of gas sensor testing rig manufactured from 6 mm OD stainless steel tubing, GFC17 mass flow controllers (manufactured and calibrated by Aalborg) and a test chamber consisting of 2 stainless steel DN25KF T-pieces with internal diameter of approximately 20 mm with 2 DN25KF hand operated valves at the inlet and outlet. Power to heater track was supplied by a 0-32 V PID laboratory PSU. Heater track current (I) and sensor resistance (R) was monitored using a Keithley 2000 multimeter connected to a PC via a GPIB cable. Test gas inlet valve was open for all tests (B) Diagram of feedthrough and holder used for mounting the sensor inside the gas sensor testing Rig. Feedthrough was a stainless steel Lewvac DN25KF 4 pin K-type thermocouple (top 2 pins) and power (bottom 2 pins) feedthrough. Two pieces of thin stainless-steel plate/sheet were bent and drilled such that they would loop over the power pins and when a bolt was inserted into the hole and a nut threaded on and tightened, they would clamp together. Each bolt was mounted through a though-hole drilled into a small approximately 2 cm wide slate chip. The bolt (and hence power pin via the connector) was attached to the heater track through a thin piece of stainless-steel plate/ sheet cut such that it tapered to a point and bent such that the point was in contact with the sensor rear-side platinum heater trackpads. The sensor was connected to the thermocouple pin plates again via custom stainless-steel plate/ sheet that tapered to a point and fastened via a nut and a bolt mounted to the slate chip. Slate chip resistance measured across all measurement pins at 350 °C was in excess of 120 MΩ (Maximum resistance measurable by the Keithley 2000) as such all connections were electrically isolated from each other.

Step	Test gas Valve	N <sub>2</sub> Valve	Bypass valve	Gas mix concentrations	Stage	Stage time period (minutes)	Action
1	Closed	Open	Closed	20% O <sub>2</sub> , 80% N <sub>2</sub>	Baseline measurement	~ 1	Start test
2	Open	Closed	Open	Indeterminate	Baseline to test gas measurement transition	P (typically < 5 seconds)	Close bypass valve when MFC readouts have stabilised.
3	Open	Closed	Closed	20% O <sub>2</sub> , ~ 80% N <sub>2</sub> + Y Test gas	Test gas measurement	15 – P	N/A
4	Closed	Open	Open	Indeterminate	Test gas to recovery measurement	Q (typically < 5 seconds)	Close bypass valve when MFC readouts have stabilised.
5	Closed	Open	Closed	20% O <sub>2</sub> , 80% N <sub>2</sub>	Recovery measurement	44 - Q	End test

*Table 4.1: Table of measurement steps for a test measurement with test gas concentration Y (ppm) with valve states, gas mix concentration and time period for each step. Starting conditions: Gas sensor left at the desired temperature under 'dry air' (320 mL.min<sup>-1</sup> N<sub>2</sub> + 80 mL.min<sup>-1</sup> O<sub>2</sub>) until the sensor has reached a stable baseline/background resistance. MFC1 and MFC2 adjusted such that MFC1 = 80-X mL.min<sup>-1</sup> and MFC2 = 240+X mL.min<sup>-1</sup>, where Flow(MFC1+MFC2) = 320 mL.min<sup>-1</sup>. X is defined such that the desired test gas concentration Y (ppm) = 2.5\*(80-X). Resistance sampling period 4 s. P and Q are the time taken for the MFC's to stabilise during the transition between steps and varies on a case by case basis.*

After insertion into the sensing rig the sensor was ramped to 330 °C and left to stabilize over a weekend in an environment of still dry air, comprised of 20% nitrogen and 80% oxygen. The sensor temperature was ramped down to approximately 240 °C and put under a flow of 320 mL.min<sup>-1</sup> nitrogen and 80 mL.min<sup>-1</sup> oxygen (mix from here on referred to as dry air) and left until the heater track resistance and gas sensor resistance were stable. To characterise the gas sensing response the sensors were put under a continuous flow of 400 mL.min<sup>-1</sup> regardless of gas composition and the resistance across the IDE sampled every 4 seconds. Table 4.1 contains a full list of valve states, time periods and gas concentration for each step undertaken within a test. Each test was conducted over 1 hour, for approximately the first minute the sensors were held in dry air to provide a background reference resistance to which all the data is then normalised (Step 1). After the initial minute the bypass valve was opened to reduce transient spike in mass flow, the Nitrogen supply valve to the test gas MFC closed and a valve to the desired test gas opened (step 2). Once the Mass flow controller read-out had stabilised the by-pass valve was closed. The sensor was left under test gas flow for approximately 15 minutes (step 3) at which point the by-pass line would be reopened, the test gas valve closed, N<sub>2</sub> valve reopened (step 4) and the by-pass line closed once the mass flow controller readout stabilised. The recovery in resistance in dry air was then monitored for 44 minutes (step 5). The data was normalised to the average background resistance measured within the first minute and the sensitivity/ response measured by taking the inverse

of a 5-point average of the normalised resistance (i.e response =  $R_{\text{air}}/R_{\text{gas}}$ ) measured between 900 s and 920 s.

To measure the variation in sensitivity and selectivity with temperature tests for 200 ppm  $\text{CH}_4$ , 200 ppm CO and 200 ppm were measured at 4 different temperatures. The target temperature were 240 °C, 270 °C, 300 °C, 330 °C with the measured and estimated temperatures for the testing based on the recorded heater tracks were 234 °C, 263 °C, 299 °C, 328 °C. Temperature drift due to the lack of room air conditioning was estimated to be sub  $\pm 5$  °C. To measure the sensitivity range for the test gasses at maximum tested temperatures tests were performed for each test gas at concentrations of 50 ppm, 100 ppm, 150 ppm and 200 ppm. Additional scans for each concentration were performed for  $\text{H}_2$  at each temperature.

#### ***4.1.1.5.3 Heater track – surface temperature calibration procedure***

Due to the limited number of pins on the feedthrough temperature could not be sensed in real time via the on-sensor Pt RTD or an external thermocouple. As such temperature was measured and calibrated following the procedure introduced by Daniel R. Jones [77]. Prior to depositing the LBZA nanosheet layer the surface temperature heater track resistance relationship was measured external to the sensing rig. The sensor was mounted to the feedthrough (Figure X(B)) and a defined voltage was applied to the heater track. Heater track current and voltage was monitored using the Kiethley 2000 multimeter and alumina substrate surface temperature using a K-type thermocouple. After applying the voltage, the current, the displayed PSU voltage sense output and surface temperature were monitored until they each reached stability. Once stable the heater track current and voltage was measured every second and the surface temperature every 15 seconds over 15 minutes. The current and temperature was measured between applied heated track PSU sense voltages of 2.5 V and 30 V at 2.5 V intervals. The mean temperature and resistance (estimated from the PSU voltage sense readout and measured current) for each voltage were plotted and a linear trendline fit to plots of temperature as a function of resistance in Excel to produce the temperature resistance calibration relationship used to measure the surface temperatures of the sensing experiments.

### 4.1.2 HMTA based synthesis method – Characterisation

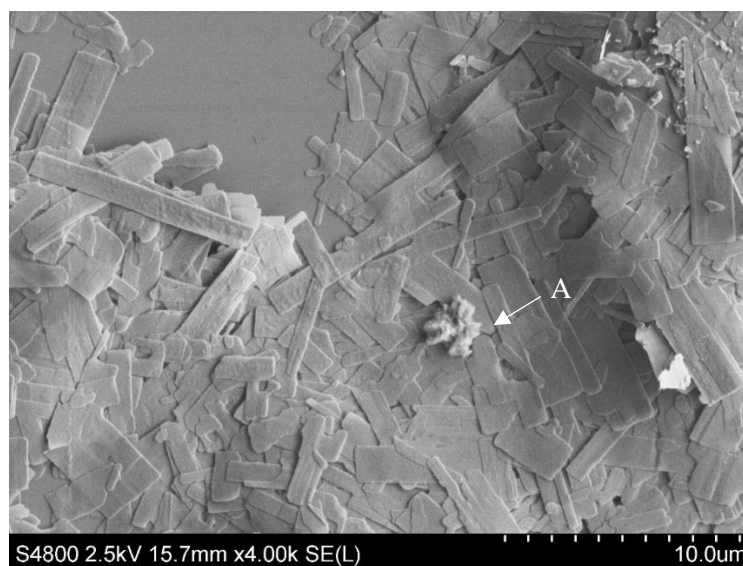


Figure 4.3: SEM image of LBZA nanosheets synthesized via the HMTA microwave assisted synthesis method. The arrow A points to aggregated thin sheet-like material, potentially proto sheets that had not fully formed by the end of the synthesis.

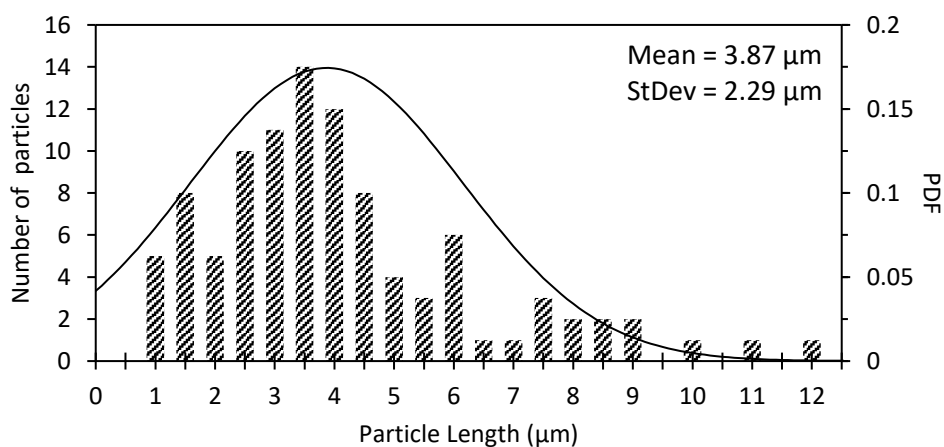


Figure 4.4 Histogram with overlaid normal distribution for the mean and standard deviation measured of LBZA particles. Note that no particles greater than 11.96 µm were observed.

Prior to ink manufacturing and print testing it was important to assess the nanosheets morphology, crystalline purity and mass yield to check for compatibility and scalability with the print process. As the largest anilox available had cells estimated to have a depth of

24  $\mu\text{m}$  based on the quoted ink metering volume (neglecting side wall contribution), any ink particles must be less than 24  $\mu\text{m}$  in length (preferably much less) to reduce impact on ink metering. SEM Images of grown nanosheets (Figure 4.3) show generally well-formed platelet/sheet particulates as would be expected for lamellar crystalline material, though there appears to be some minor aggregation (labelled A) of what appears to be thin layered material, potentially proto sheets of LBZA that had not fully formed within the extent of the synthesis. To check for size compatibility 100 particles were measured (

Figure 4.4), the mean length of the particles measured was 3.87  $\mu\text{m}$  with a standard deviation of 2.29  $\mu\text{m}$ , and no particles observed to be larger than 11.96  $\mu\text{m}$ . As the lateral dimension of the particles were smaller than the estimated depth of the cells of the largest anilox (24  $\mu\text{m}$ ) the morphology was considered compatible.

In addition to the morphology being compatible it was also important that the crystalline phases be pure so that a consistent and predictable print quality and sensing response could be produced. In the original paper published by Tarrat *et al.*<sup>[67]</sup> the presence of small crystalline ZnO was present, this likely formed as the result of the Zinc sources consisting of both 0.1M Zinc acetate and 0.02 M Zinc nitrate. Nitrate is a highly soluble ion and will have a significant proportion of Zinc cations completely co-ordinated to water as compared to acetate. This can be seen from the formation constants (i.e. the equilibrium constant between the complex and separated free species) for the relevant metal ligand species;  $\text{Zn}(\text{NO}_3)^+ = 0.759$  <sup>[338]</sup>,  $\text{Zn}(\text{Ac})^+=19$  <sup>[339]</sup>,  $\text{Zn}(\text{Ac})_2=123$  <sup>[339]</sup>. Due to the more significant formation constant  $\text{Zn}(\text{Ac})_2$  would be expected to be the dominant species in aqueous solutions of Zinc acetate. Zinc nitrate solutions would be expected to have a significant free zinc aqua species (it should be noted that no value for the di-nitrate complex could be found, likely due to an inherently low ability for nitrate to undergo complexation with zinc cations). The resulting free Zinc aqua complexes are capable of forming and precipitating Zinc hydroxide at the pH range the synthesis is conducted at <sup>[120]</sup>, which being thermodynamically unstable would dehydrate into Zinc Oxide. Unlike the original reported method by Tarrat *et al.* no ZnO structures were observed under SEM, and to provide confirmation XRD was performed.

Figure 4.5 shows the XRD results for LBZA synthesized using the in-house modified method, the results show the typical reflections for the LBZA lamellar crystalline structure. It is noticeable that there is a lack of any significant ZnO reflections in the diffractogram even at 100 times magnification indicating a high degree of phase purity, likely a result of

removing Zinc nitrate as precursor. To estimate the mean crystallite height for use in ink loading calculations, the Scherrer equation was applied using the (001) reflection and estimated to be 46.6 nm which corresponds well to the observations of Tarat *et al.* [67] where LBZA crystallites measured via AFM had a range of 20 - 100 nm.

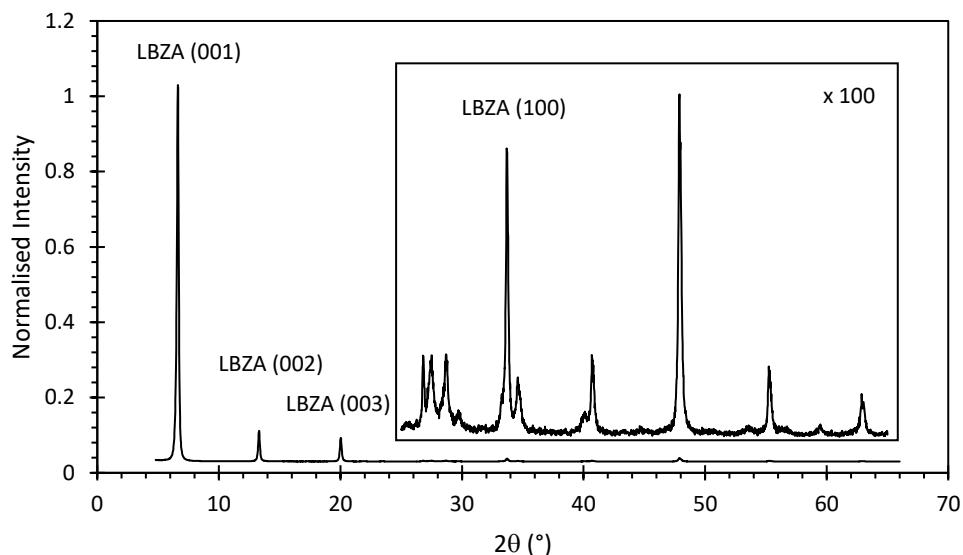


Figure 4.5: XRD diffractogram for the synthesised and centrifuge cleaned LBZA showing the typical lamellar structure. Insert x 100 magnification of the diffractogram between 25° and 65°.

In addition to the structural and purity characteristics; it was important to know the mass yield of the synthesis to be able to create known nanosheet concentration in any inks that would be manufactured, and to confirm that a large enough yield is produced to realistically produce enough material for production runs of cheap, disposable point of care sensors. To measure the yield 16 synthesis runs were produced, cleaned, dried and mass measured. From the 16 measurements a mean mass of 37.2 mg was measured. The results represent a Zinc molar conversion from  $ZnAc_2$  to LBZA of only 5.02% and only a 4.08% conversion of hydroxide to LBZA for the hydroxide produced from ammonia produced via HMTA hydrolysis, showing a poor general conversion efficiency. Whilst a low conversion efficiency is environmentally unfriendly and cost ineffective; if the synthesis produces enough material for printing and the sensing results promising it could potentially still prove to be a useful sensing medium synthesis method, at the very least for proof-of-concept purposes. Ideally for a sensor, at a bare minimum, a continuous and complete layer of nanosheets would be needed to maximise conductivity and sensitivity. Without reports of the density of LBZA in literature and the potential errors due to void spaces in manual measurements, it is difficult to directly calculate accurately the LBZA mass loadings for the



ink. Instead, an estimate can be calculated assuming a continuous layer of printed Zinc Oxide of the same thickness as the sheets by calculating the mass per unit area, and then converting using the relative molar masses of ZnO and LBZA normalised to Zinc concentration in their respective unit cells. The estimate overemphasises the amount of material required as the ZnO unit cell is denser, however it is useful for calculating a first order approximation, which can later be refined through trial and error. Full details of the calculation will be shown and explained in Appendix 13.2.1.2, however using the 24 mL.m<sup>-2</sup> anilox, required for the length of the sheets, and the height estimated via the Scherrer equation of 46.6 nm, a mass concentration of 66.6 mL.m<sup>-2</sup> was calculated. For a simple 2.5 mL volume of ink (the minimum realistically required volume of ink for a single print test of 5 prints for a single testing condition with the 24 mL.m<sup>-2</sup> anilox,) this represents 4.45 individual synthesis and cleaning steps, taking in excess of an hour and a half each. Whilst it may be possible to use the synthesis for lab scale test runs, realistically the required mass loading would be both time and cost prohibitive both for proof of concept work and any potential long-term scale up. Increasing the HMTA concentration would likely result in increased zinc conversion efficiency, however the poor general HMTA conversion efficiency would increase costs and produce larger quantities of formaldehyde by-product which is a carcinogen and green-house gas.

### **4.1.3 HMTA based LBZA synthesis derived ZnO – Gas sensing properties**

Whilst the low yield of the HMTA synthesis is not compatible with the ultimate aim of producing a cheap disposable point of care sensor, the high degree of purity makes it ideal for testing whether the material sensing properties of the derived ZnO show any promise and whether finding an alternative synthesis procedure would be worthwhile. The responses for CH<sub>4</sub>, CO and H<sub>2</sub> were therefore tested. These gasses are reducing agents that may be present in the breath. H<sub>2</sub> is the main gas present in the breath of patients suffering from carbohydrate malabsorption<sup>[44][340][341]</sup> and small intestinal bacterial overgrowth (SIBO) <sup>[49][50][44]</sup>, whilst a small but significant proportion (> 8%) of those afflicted produce CH<sub>4</sub> instead as a result of a significant methanogenic bacterial profile <sup>[44][340][341][47]</sup>. CO may potentially be present in smokers if they have recently inhaled tobacco smoke and is thus a common potential interfering agent <sup>[49][44]</sup>.

### 4.1.3.1 Calcined sensor morphology

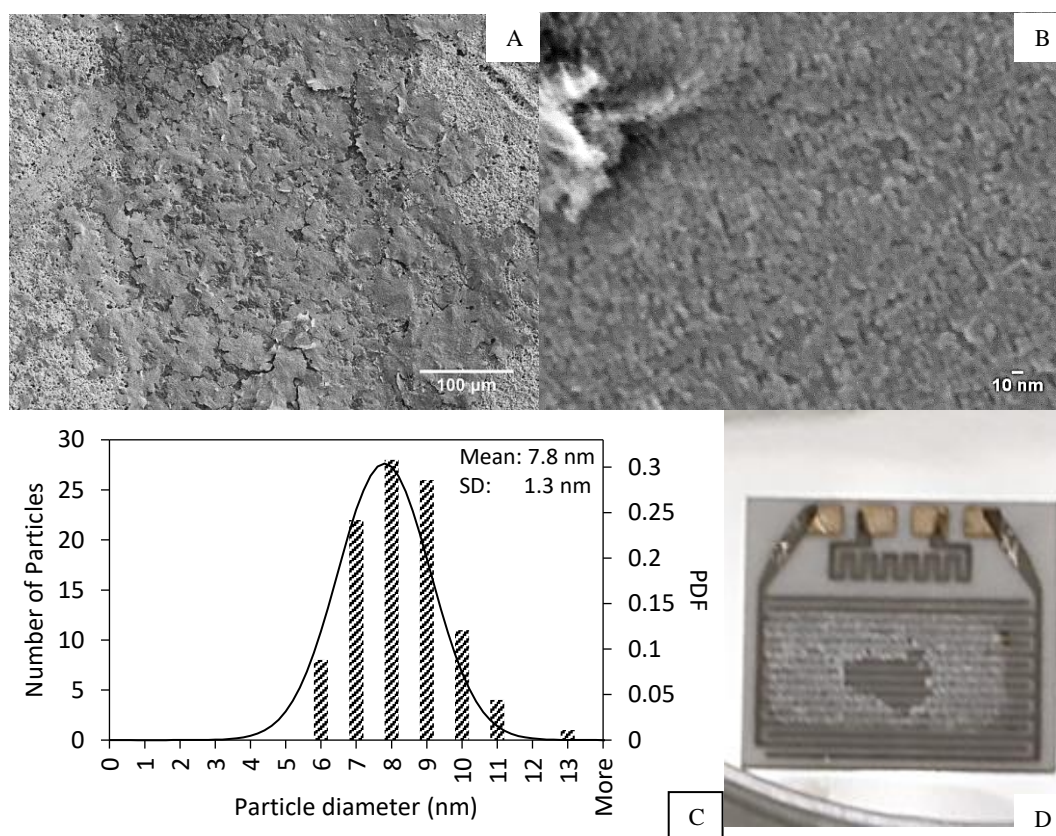


Figure 4.6: A) Low magnification SEM image of the sensor calcined at 350 °C for 30 minutes . The vertical bright stripes are the platinum IDE tracks, the dark stripe in the middle alumina and the mid contrast grey the bridging ZnO sheets. B) High resolution magnification SEM Image of the resulting grain structure. C) Histogram of particle diameter with mean and standard deviation,  $N=100$ . D) Photo of calcined sensor, ZnO nanosheets are the brighter contrast rectangular area over the IDE, the material in the centre of the sensor lost adhesion and lifted during calcination.

To test the sensing properties, 200 μL of nanosheet cleaned solution ( $\approx 124$  μg of LBZA) was drop-cast on a commercial alumina substrate with patterned platinum IDE and rear-side heater and annealed at 350 °C for 30 minutes. Figure 4.6 shows SEM and optical images of the resulting sensor. From Figure 4.6 A) it can be seen that ZnO nanosheet coverage, whilst incomplete, is high enough to bridge the electrodes; it can also be seen that the particles seem to form islands, possibly due to aggregation during cleaning or deposition and partially due to cracking and lifting during the calcination step. The cracking and lifting can be seen on the macroscale in Figure 4.6 D) where a large section in the centre of the sensor lifted off during calcination. No significant breakdown of the sheet macro structure that happens at higher temperature due to sintering<sup>[67]</sup> was observed. From the high resolution SEM images (Figure 4.6 B) it can be seen that surface has taken on a dense nanogranular structure with

mean particle diameters of 7.8 nm and standard deviation 1.3 nm ( $N = 100$ ). The small grain size was attributed to dehydration and breakdown of the organics within the LBZA structure with only limited sintering.

#### ***4.1.3.2 Sensing properties***

Post calcination the sensors were inserted into the gas sensing rig and left to stabilise in dry air at 330 °C over a weekend. Post stabilisation, the sensing response of the sensor was tested at various temperatures. The sensor resistance at room temperature was in excess of the 120 M $\Omega$  limit of the Keithley 2000 used; but despite the cracking and lifting shown in Figure 4.6 the sensors baseline resistance across all tests between 234 °C and 328 °C was between 4 M $\Omega$  and 8 M $\Omega$ , which is easily within the capability of modern measurement electronics and will likely be further reduced if the mentioned cracking problems can be addressed.

Figure 4.7 shows the normalised response to 200 ppm of test gas for the sensor as a function of time for A) H<sub>2</sub>, B) CH<sub>4</sub> and C) CO. At 234 °C the response of the sensor is weak for all gasses with a normalised response of 1.43 for H<sub>2</sub> and 1.02 for CO. As the temperature increases, so does the response as expected, with responses of 2.55 for H<sub>2</sub> and 1.04 for CO at 263 °C and 3.18 for H<sub>2</sub> and 1.07 for CO at 299 °C. Unlike the other test gasses, the CH<sub>4</sub> response seemed to stay constant with responses of 1.034, 1.040 and 1.038 at 234 °C, 263 °C and 299 °C respectively. Retesting produced similar results, and from inspection of the resistance plots likely indicated a small response hidden by drifting background resistance due to room temperature variations, and artefacts due to temperature and pressure change during the switch over from nitrogen to test gas and back again. The maximum response for all gasses within the temperatures tested was reached at 328 °C with responses of 7.27 for H<sub>2</sub>, 1.25 for CO and 1.13 for CH<sub>4</sub> representing a significant gain in response and reduction in cross sensitivity (1.402 vs 5.816 for  $\text{Response}_{\text{H}_2}/\text{Response}_{\text{CO}}$  at 238 °C and 328 °C respectively). In addition to the magnitude of the response, the response rate also increased with temperature. The time taken for 85% of the response for H<sub>2</sub> was reached in 36 seconds at 328 °C compared to 66 seconds at 234 °C. For CO, it took 43 seconds at 328 °C as compared to 212 seconds at 234 °C, and 30 s for CH<sub>4</sub> at 328 °C. The tail end of the hydrogen response appears slower than that for CO and CH<sub>4</sub> with the 90% response times at 328 °C of 144 s for H<sub>2</sub>, 31 s for CH<sub>4</sub> and 47 seconds for CO possibly hinting at a secondary response. There are at least two potential reasons known that may create such an effect.

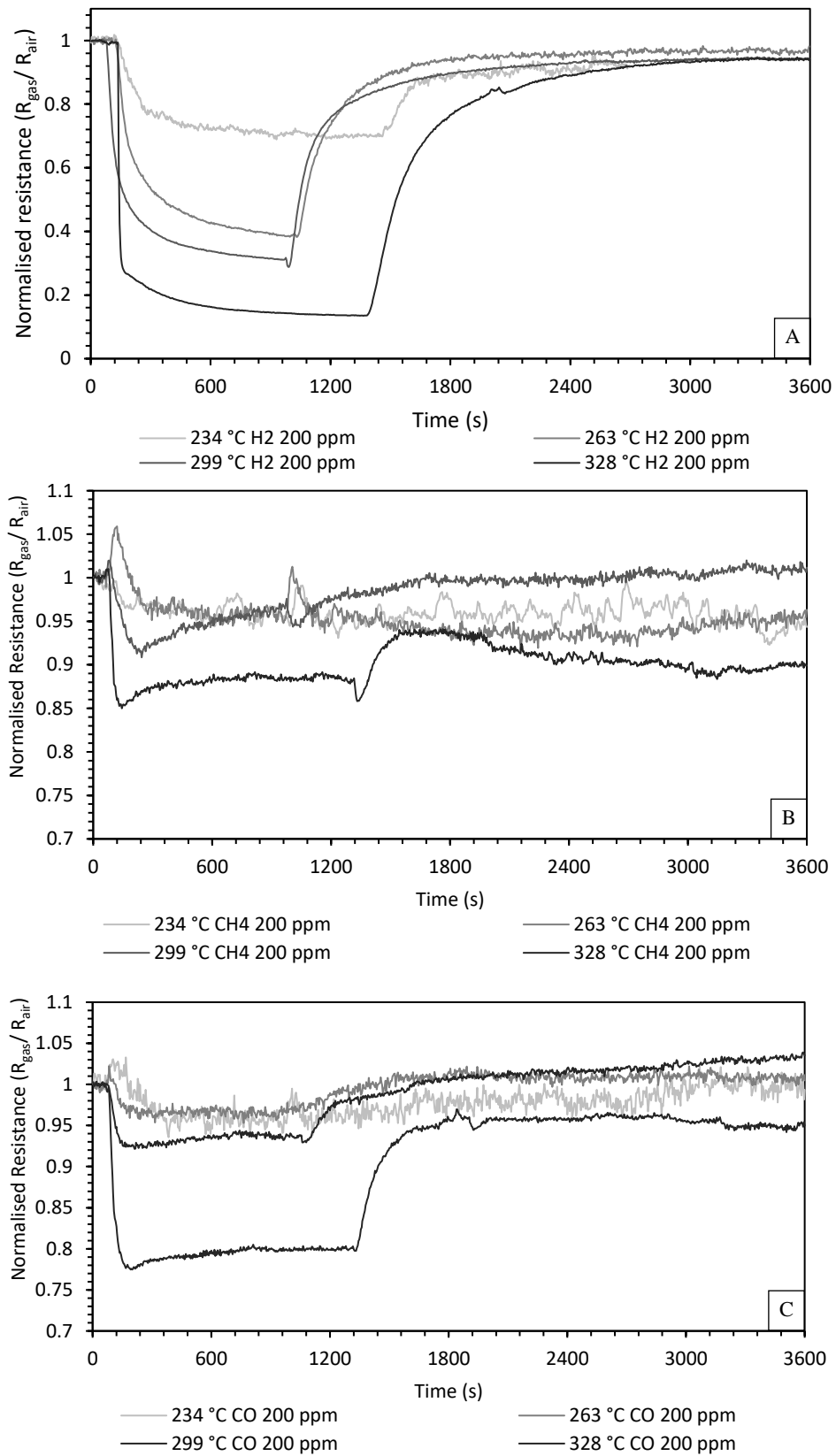


Figure 4.7: Normalised resistance plots as a function of time for the calcined gas sensor tests at 234 °C, 263 °C, 299 °C and 328 °C for test gasses A) H<sub>2</sub>, B) CH<sub>4</sub> and C) CO. Testing conducted in dry air, 200 ppm of test gas is introduced into the system after approximately 60 s and removed at approximately 960 s for 234 °C, 263 °C and 299 °C and at 1260 s for 328 °C. Note H<sub>2</sub> at 234 °C is an exception where it was removed at approx. 1440 s.

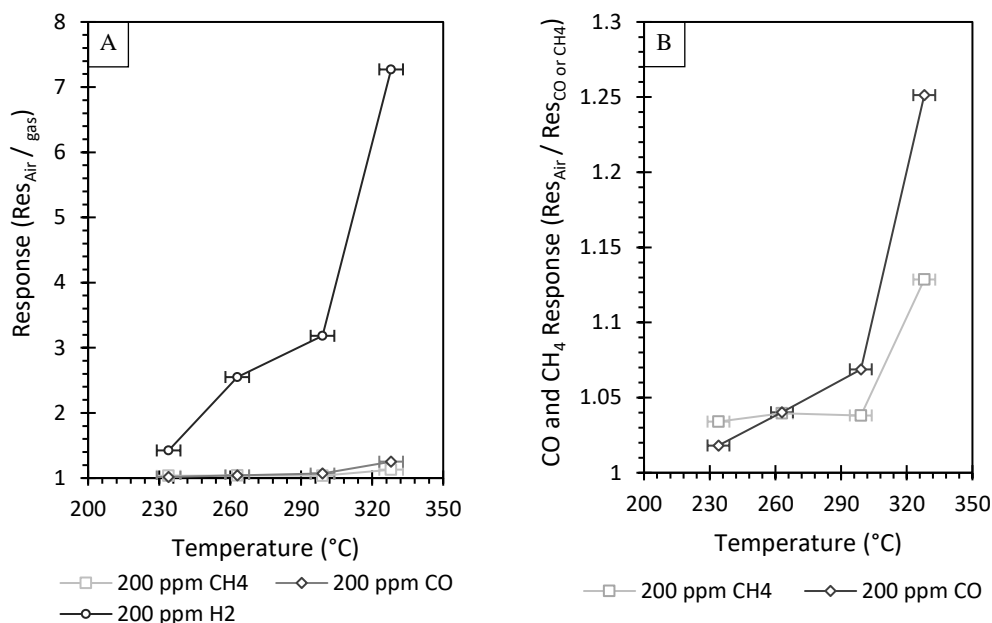


Figure 4.8: A) Gas sensing responses (defined as the background resistance in dry air divided by the resistance of the test gas) as a function of temperature for all gasses. B) CH<sub>4</sub> and CO responses as a function of temperature. Error bars represent the generally observed maximum drift in sensor temperature

It is well known that hydrogen adsorbs and forms shallow donor complexes on certain ZnO facets <sup>[342][343][344]</sup> that allows ZnO sensors to respond to hydrogen even in the absence of oxygen (e.g. in nitrogen or argon) and at room temperature <sup>[345]</sup>, albeit often with responses in minutes as opposed to seconds <sup>[62]</sup> and with poor recovery characteristics <sup>[346]</sup>. Assuming the rapid initial response is due to the consumption of the majority of surface oxygen species the slower tail of the response may correspond to the adsorption of hydrogen. As the adsorbed hydrogen has a high desorption energy (4.77 eV for the O-H bond on the ZnO-O polar face<sup>[342]</sup>) this may also explain the relatively slow recovery to hydrogen that can be seen in the concentration responses at 328 °C (Figure 4.7 A and Figure 4.9 C.) The second potential mechanism for the slower secondary response and recovery is the time dependent diffusion of hydrogen into and out of the bulk of the layer as observed in WO<sub>3</sub> nanowire sensors <sup>[347]</sup> and more importantly in ZnO microrods <sup>[348]</sup>. In the case of the ZnO microrods at low temperature and concentrations, the permeability to hydrogen due to the small size of the hydrogen molecule primarily occurs at the (0001) facet <sup>[348]</sup>. The diffusion gradient of surface adsorbed hydrogen drives adsorbed hydrogen into the bulk of the material once the surface approaches saturation which would slow the accumulation and time to equilibrium. <sup>[348]</sup> Additionally, at concentrations higher than those tested here, this resulted in an overshoot and subsequent recovery to equilibrium in the response under hydrogen flow <sup>[348]</sup>.

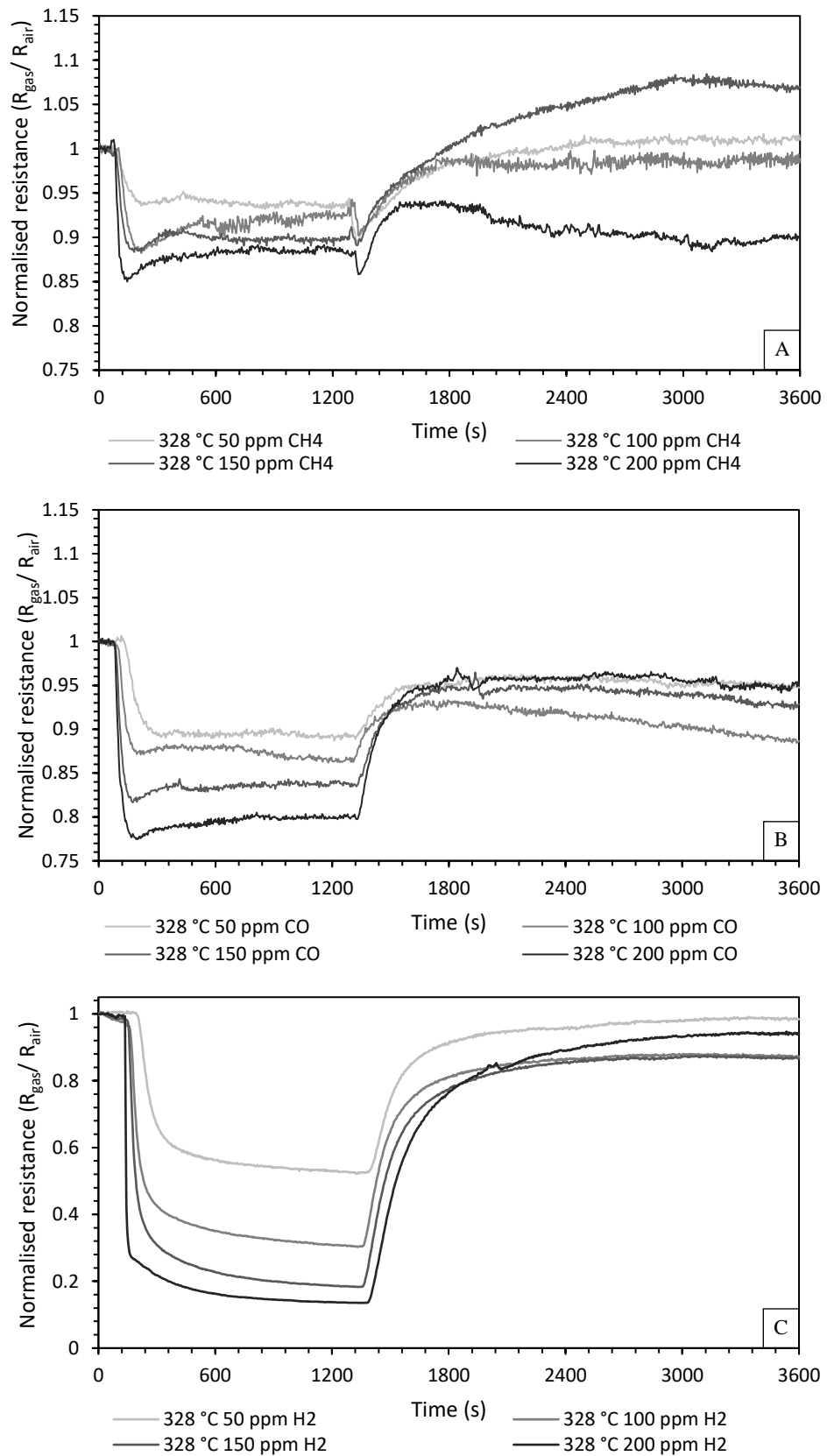


Figure 4.9: Normalised resistance plots as a function of time for the calcined gas sensor tests at 234 °C, 263 °C, 299 °C and 328 °C for test gasses A) H<sub>2</sub>, B) CH<sub>4</sub> and C) CO. Testing conducted in dry air, 200 ppm of test gas is introduced into the system after approximately 60 s and removed at approximately 960 s for 234 °C, 263 °C and 299 °C and at 1260 s for 328 °C.

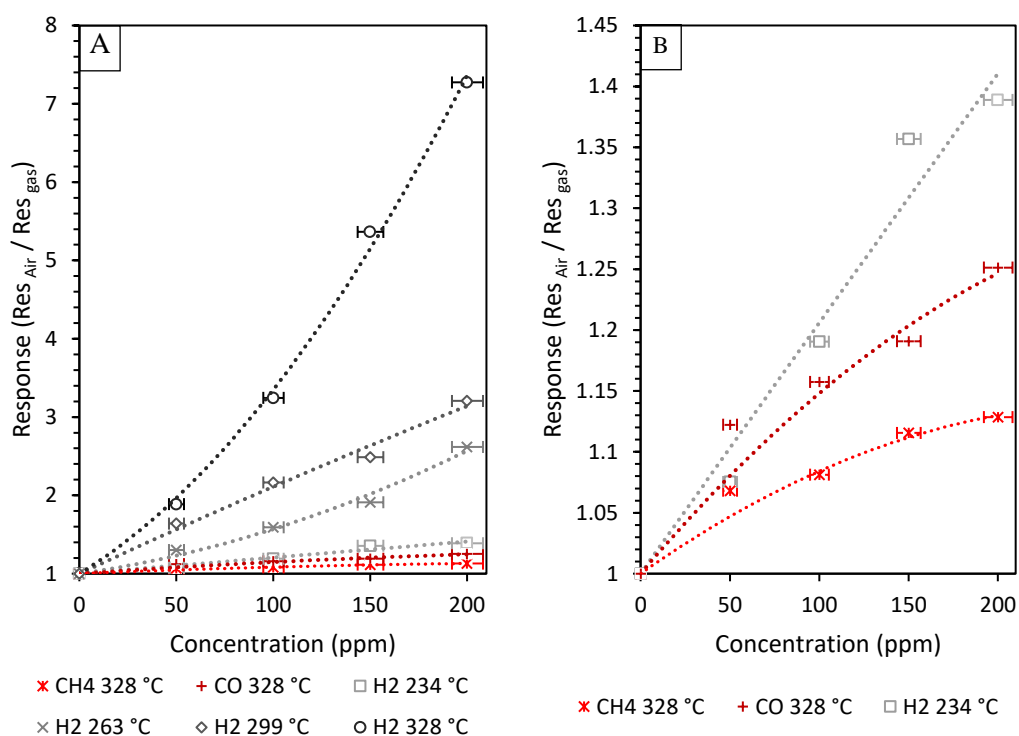


Figure 4.10: Response as a function of concentration for 50, 100, 150 and 200 ppm of each test gas at 328 °C and hydrogen at each temperature and B) for the CH4 and CO at 328 °C and H2 at 234 °C. Error bars are equal to the maximum and minimum concentration using the manufacturer quoted accuracy of 1% of the total flow and defined as maximum concentration = Maximum mass flow (test Gas)/(1000\*(minimum mass flows (N<sub>2</sub>+O<sub>2</sub>)). Minimum concentration = minimum mass flow (test gas)/ (1000\*(maximum mass flow (N<sub>2</sub>+O<sub>2</sub>)). Trend lines (where x = concentration in ppm) and R<sup>2</sup> values for: H<sub>2</sub> at 234 °C:  $y = -7 \cdot 10^{-08}x^2 + 0.0021x + 1$ , R<sup>2</sup> = 0.967, 263 °C:  $y = 2 \cdot 10^{-05}x^2 + 0.0035x + 1$ , R<sup>2</sup> = 0.988, 299 °C:  $y = -4 \cdot 10^{-06}x^2 + 0.0115x + 1$ , R<sup>2</sup> = 0.988, 328 °C:  $y = 8 \cdot 10^{-05}x^2 + 0.0152x + 1$ , R<sup>2</sup> = 0.997. CH<sub>4</sub> at 328 °C:  $y = -2 \cdot 10^{-06}x^2 + 0.001x + 1$ , R<sup>2</sup> = 0.950 and CO at 328 °C:  $y = -2 \cdot 10^{-06}x^2 + 0.0017x + 1$ , R<sup>2</sup> = 0.931. Divergence at 50 ppm expected to be primarily due to pressure spike and/or drop induced artefacts such as cooling and heating during test gas/ Nitrogen transitions.

To find out the response at lower concentrations that are more relevant to carbohydrate malabsorption breath testing, the response of the sensor was tested for each gas at 50, 100, 150 and 200 ppm at 328 °C and the results extrapolated. The gas sensing results for each concentration and gas is shown in Figure 4.9 . The sensor shows a relatively broad range of sensitivities, with responses at 50 ppm concentrations of test gas of 1.89 for H<sub>2</sub>, 1.07 for CH<sub>4</sub> and 1.12 for CO. The sensor appears to show an acceptable degree of recovery repeatability with all CH<sub>4</sub> and CO tests returning to within 6% of their baseline value within the time tested, and the H<sub>2</sub> response at 50 ppm returning to within 2% and 7% at 200 ppm. Due to thermal drift and pressure spikes during the gas change over-steps (which can be seen in the H<sub>2</sub> baseline at 100 and 150 ppm and in the CH<sub>4</sub> response respectively) it is difficult to tell whether the sensors would reach the original value within the testing window.

According to a set of published guidelines on the implementation and interpretation of hydrogen breath tests by A. Eisenmann *et al.*<sup>[49]</sup> based on the analysis of 3374 patients, the general basal rate of hydrogen should be less than 10 ppm (preferably < 5ppm) with a variability of less than 3ppm. A positive case is interpreted as anything greater than 20 ppm, potentially reaching 50 ppm, and borderline cases between 10 ppm and 20 ppm. Figure 4.10 shows the plotted and extrapolated results where it can be seen that the sensor is predicted to still show a significant response at 20 ppm with an estimated response on the order of 1.336 (33.6% increase in current) and an approximate change in response  $\geq 1.5\%$  ppm<sup>-1</sup>.

A lack of general guidelines for methane<sup>[50][349]</sup> has resulted in a variety of threshold values in literature with values of 10 ppm<sup>[350][340]</sup>, 15 ppm<sup>[341][351]</sup> and 20 ppm<sup>[349][352]</sup> for which the sensor is estimated to produce a response ranging between 1.01 (10 ppm) and 1.02 (20 ppm). While the ability to detect the response at the threshold for methane is, depending on the noise floor, within the measurement range of portable signal processing electronics it is likely that the result will be masked by the sensor response due to the natural 3 ppm variation of hydrogen (estimated change in response  $\geq 0.046$  (4.6%) for concentrations less than 10 ppm) in patients presenting with non-hydrogenic bacteria. Therefore, methane detection would require catalysts, either in the form of doping or surface decorating with nanoparticles, or alternatively through the addition of secondary sensors with different sensing material used in an electronic nose like configuration.

According to a study by A. Sandberg *et al.*<sup>[45]</sup> exhaled CO concentrations reached a mean peak of approximately 20 ppm with a 95% confidence interval upper bound of 54.6 ppm directly after smoking a cigarette (the mean value is also equivalent to the HSE 8-hour work exposure limit<sup>[353]</sup>) for which a response on the order of 1.03 and 1.09 respectively are predicted here.

Max CO breath concentration directly after smoking	H <sub>2</sub> concentration (ppm) at threshold for false positive	
	Borderline case threshold	Positive case threshold
Upper 95% value - 54.6 ppm	4.7	15.2
Mean value/ Max resting baseline – 20 ppm	8	18.2
Mean baseline – 8.9 ppm	9.1	19.1
Non-smokers - $\leq 3$ ppm	9.7	19.7

Table 4.2: Breath hydrogen concentrations that produce false positives at the borderline (total response = 1.16 for approximately 10 ppm H<sub>2</sub> threshold) and positive cases (total response = 1.336 for approximately 20 ppm H<sub>2</sub> threshold) for smokers directly after smoking a cigarette and in the morning without smoking overnight<sup>[45]</sup>. Values assume non-interaction reactions on the surface and an additive relationship with adsorbed concentrations below the concentration of surface sites as an approximation.



Table 4.2 shows approximate H<sub>2</sub> concentrations at which false positive for borderline case (breath H<sub>2</sub> concentration threshold 10 ppm) and positive cases (breath H<sub>2</sub> threshold concentration 20 ppm) assuming the gasses don't interact, surface sites aren't saturated, and the resulting current is additive. Whilst such approximate conditions and linear combinations to the response have been assumed in an ad-hoc manner the linear combination of responses using principal component analysis has been used with relative success in the analysis of gas mixtures, experimental determination would still however be a requirement. The approximation predicts a false positive for patients with mean/ upper 95% confidence interval post smoking concentrations of CO at H<sub>2</sub> concentrations 80%/ 47% in borderline case and 90.9 %/ 76 % in positive cases respectively. For smokers who've retained from smoking over night the max concentration observed was  $\approx$  20 ppm with a mean value of 8.99 ppm for false positive concentrations occur at H<sub>2</sub> threshold concentrations of 80 %/ 91 % in borderline case and 90.9 %/ 95.5 % in positive case. The authors reported a coefficient of variance of 8.8 %, corresponding to a standard deviation of 0.79112 ppm. Calculating the upper 99 % prediction interval produced a concentration of 11.031 ppm for which the H<sub>2</sub> concentration at the threshold for false positives for the borderline case is 8.89 ppm/ 88.9% and 18.99 ppm/ 94.95% for positive cases. Testing would not be expected to be practically affected by indoor environmental CO (<2 ppm<sup>[354]</sup>) or background exhaled levels from non-smokers ( $\leq$ 3 ppm producing a response of 1.005, false positive at H<sub>2</sub> threshold concentrations for borderline cases 97 % and positive cases 98.5 %.<sup>[51]</sup>) Comparing predicted CO and H<sub>2</sub> responses at both 20 ppm and 50 ppm produces cross sensitivities of approximately 9.9% and 8.3% respectively which is approximately twice that reported for a commercial electrochemical H<sub>2</sub> breath analysis system (GastroCH4ECK® Gastrolyzer®, cross sensitivity: <4%.) Inclusion of a filter/ sorption column as is typically used in breath analysers<sup>[43][355][356]</sup> would likely remove any practical cross-sensitivity issues for even the highest smoker exhaled CO concentrations.

In addition to the hydrogen response being compatible for use as a hydrogen breath sensor it is also competitive with or exceeds the response of other simple undoped/ decorated sensors, as can be seen by the following comparison:

- Films of drop-cast SnO<sub>2</sub> nanowire grown from evaporated Sn at 900 °C produced maximum responses to 1000 ppm H<sub>2</sub> of 6.5, albeit at 150 °C<sup>[357]</sup> (i.e. 550%)
- Sol gel synthesised SnO<sub>2</sub> and a sol gel synthesised SnO<sub>2</sub> SWCNT composite integrated with micromachined Pt thin film microheaters produced responses of 1.56 (i.e 56%) for 1500 ppm at 300 °C for the pure SnO<sub>2</sub> and 2.47 (i.e. 147%) for 1500

ppm at 250 °C for the composite, though the response was faster for the composite at 2-3 seconds <sup>[358]</sup>

- An ITO based sensor produced for hydrogen safety purposes which produced only a 5% response for 200 ppm at 460 °C. <sup>[359]</sup>

- A ZnO p-n homojunctions produced a maximum response of approximately 1.8 (80%) to 500 ppm at 400 °C <sup>[360]</sup>

- An extrapolated value for 600 ppm of 1.5 (50%) at 400 °C for 1D ZnO nano-assemblies produced via plasma-CVD <sup>[361]</sup>

- A response of 1.29 (29%) to 200 ppm at 400 °C for 250 nm thick RF sputtered ZnO thin films <sup>[362]</sup>

- A response of 2.3 and 3.6 to 100 ppm at 200 °C and 400 °C respectively using hollow polycrystalline ZnO produced by RF sputtering and calcination of aligned electrospun PVP nanofibers <sup>[363]</sup>.

- A response less than 1.95 to 1500 ppm at 250 °C using ZnO nanowires produced from Zinc evaporated using a custom Silicon carbide microwave susceptor in a 1250 W 2.45 GHz domestic microwave <sup>[364]</sup>.

The relatively high sensitivity of the LBZA derived sensor at relatively low temperatures compared to published results can generally be attributed:

- to the small grain size ( $7.8 \text{ nm} \pm 1.3 \text{ nm}$ ) <sup>[72]</sup>
- a crystal orientation that according to the XRD recorded in previous work by Tarat *et al.* <sup>[67]</sup> matches the recorded pattern of ZnO dominated by highly reactive (0001) exposed surface facets derived from LBZA <sup>[221]</sup>
- the thin nature of the compact film that both reduces the volume of the unreactive bulk of the layer <sup>[365]</sup> and the requirement of any time dependent diffusion of gas into the bulk of the layer <sup>[365]</sup>.

The grain size is on the order of the Debye- Length for ZnO at 573 K (299.85 °C).

Li *et al.* [366] calculated it to be approximately 7.5 nm for a charge carrier concentration  $n_c = 4 \times 10^{17} \text{ cm}^{-3}$  and static dielectric constant  $\epsilon = 7.9$ . While the particular Debye-length will vary with the explicit materials properties and sensing temperature, the value suggests that the space charge, and therefore the sensing mechanism, occurs throughout the bulk of each grain at the surface of the layer [367][197]. The small grain size also provides additional advantages, such as high surface area to volume ratio [367][197] and exposure of higher reactivity and responsive surface facets [365] and defective/ under coordinated 2-fold co-ordinated Zinc atom surface sites which are known to be able to adsorb more oxygen and increase sensor response [221]. At no point was a reduction in sensitivity observed with an increase in temperature suggesting that reactant desorption is not favoured over completion of the surface reaction [368][347], nor is there a significant change in space charge layer that alters the reaction transduction and sensing mechanism [367][197]. It is likely any inversion point in sensitivity would be above the annealing temperature that would result in an increase in grain size [67] and a potential decrease in sensitivity.

Whilst competitive with simple sensors, sensors with more complicated structures or more complicated/ expensive and slower methods of production have shown greater responses at lower temperatures, such as:

- A response of approximately 5.3 to 100 ppm H<sub>2</sub> at 200 °C for a multiple ZnO nanowire drop cast gas sensor. However, the growth required 30 minutes at 900 °C with heating and cooling time and produced only small amounts of material (100 mg) [369]
- A Pd nanoparticle coated SWCNT sensor capable of detecting 100 ppm H<sub>2</sub> in air at room temperature. The sensor was created using standard silicon microfabrication techniques, upon which a -COOH functionalised solution of SWCNT was dropcast and Pd electrodeposited subsequently. Whilst the device was sensitive at room temperature the low concentration response was slow at 18 minutes. [370]
- A Pt nanoparticle decorated PdO nanowire room temperature operating hydrogen sensor capable of producing a 14% response to 10 ppm H<sub>2</sub> with response time of approximately 330 s [371]. In addition to the slow response the nanowires were fabricated using photolithography, evaporation and electrodeposition which combined with the materials is an expensive and slow process.

- A Palladium nanoparticle coated  $\text{WO}_3$  sputtered thin film produced a response of 34.1 to 5 ppm  $\text{H}_2$  and 3933 to 50 ppm at 175 °C [372]. The measured speed of response for 5 ppm was slow, though the response at 50 ppm was comparative to that of LBZA derived ZnO sensor in this work. Problematically the resistance at 5ppm was measured in the Gigaohms and only reaching Megaohms at 50 ppm making its use in devices more complicated in comparison and potentially impractical.
- A Pd Nanoparticle/ Pd Film/ GaOx/ GaN-Based Metal–Oxide–Semiconductor Diode grown on a silicon substrate produced a room temperature response of 6.2 for 1 ppm  $\text{H}_2$  (150 pA), 1300 for 100 ppm  $\text{H}_2$  (26 nA) [373]. The response time was 800 s for 50 ppm at RT and whilst the response time dropped to 10 s at 273 °C the response dropped 2 orders of magnitude. The very small currents, epitaxial GaN- $\text{Al}_{0.2}\text{Ga}_{0.8}\text{N}$  - GaN layer and multiple processing steps would make devices difficult to use and unnecessarily expensive in comparison to the simple LBZA derived sensor.
- A Palladium nanoparticle coated tubular  $\text{TiO}_2$  layer manufactured via evaporation and subsequent anodization of tin with sputtered Pd produced a response of 3.4 at 10 ppm and 7.2 for 20 ppm  $\text{H}_2$  at 180 °C with a response time below 30 seconds [374]. The sensor additionally had high selectivity with a response of 92 and 2.2 for 100 ppm  $\text{H}_2$  and ethanol respectively. The high response at low temperature was primarily attributed to a combination of internal Schottky barriers at the metal oxide interface and catalytic disassociation and adsorption of  $\text{H}_2$  on the surface of the Pd nanoparticles. A significantly higher response was observed in  $\text{N}_2$  as opposed to dry air due to the partial oxidation of the palladium nanoparticles in air.
- A 1 mol% Co doped  $\text{SnO}_2$  thin film produced a response of 3.75 to 50 ppm  $\text{H}_2$  at 225 °C with a response time of 101 seconds [375]. The sensor was produced from 10 spin coated layers of a  $\text{CoCl}_2$  and  $\text{SnCl}_2$  solution and subsequent annealing for 2 hours at 500 °C.
- A highly sensitive mesoporous  $\text{In}_2\text{O}_3$  sensor had a response to 10 ppm  $\text{H}_2$  at 260 °C of 1.83 with a very fast response below 2 second and a response of 1.2 to 10 ppb  $\text{H}_2$ . [376] The sensors were produced via a simple hydrothermal synthesis of indium hydroxide over 10 hours at 150 °C, annealed at 500 °C in air for 2 hours, mixed into

solution and then an alumina ceramic tube with integrated heater dip coated and annealed for another 2 hours. The sensor used simple fabrications however Indium is an expensive metal making sensor cost comparatively high.

- A 1 mol% Pd-doped  $\text{In}_2\text{O}_3$  nanoflower, the sensor produced in a very similar manner to the undoped mesoporous  $\text{In}_2\text{O}_3$  sensor produced a response of 3.6 to 100 ppm  $\text{H}_2$  at a reduced operating temperature of 210 °C with a 4 second reaction time <sup>[377]</sup>. The same cost issues are present as for the other  $\text{In}_2\text{O}_3$  sensor.
- A  $\text{Au@In}_2\text{O}_3$  core shell hetero-nanostructure produced a response of 35 for 100 ppm  $\text{H}_2$  at 300 °C and a response time of 31 seconds and a response of 4.58 at 20 ppm<sup>[378]</sup>. The 90 nm hetero-nanostructures consisted of a 15 nm Au nanoparticle core surrounded by a spherical  $\text{In}_2\text{O}_3$  ‘nanoflower.’ The increased response of the core shell hetero-nanostructure compared to an  $\text{In}_2\text{O}_3$  control was assigned to the band bending caused by charge transfer at the core shell interface and a catalytic effect of increased hydrogen disassociation at reduced temperatures at exposed areas of the Au nanoparticle.
- Additional sensors using noble metal catalysts produced responses of 7.5 to 100 ppm (recorded prior to reaching equilibrium) at room temperature for an Au nanoparticle decorated single ZnO nanowire sensor <sup>[379]</sup>, 6.6 to 50 ppm  $\text{H}_2$  at 290 °C for Au nanoparticle decorated  $\text{WO}_3$  nanotubes <sup>[380]</sup>, 26 to 100 ppm at 250 °C for Pt nanoparticle decorated  $\text{WO}_3$  nanoneedle arrays <sup>[381]</sup>, 26 for 200 ppm  $\text{H}_2$  at 95 °C for a Pt nanoparticle  $\text{WO}_3$  thin film <sup>[382]</sup> and 2.8 at 25 ppm at 300 °C for Pd microisland decorated  $\text{SnO}_2$  thin films <sup>[383]</sup>.

Perhaps the most impressive state of the art sensor using ZnO was a Pt-Au bimetallic nanoparticle decorated ZnO nanorod sensor by Fan *et al.* <sup>[384]</sup> capable of producing a room temperature response to 250 ppm of hydrogen of 25. They also compared the response of various nanoparticle decorated ZnO nanorods to 250 ppm  $\text{H}_2$  at 130 °C, the maximum response operating temperature recorded for the bimetallic Pt-Au nanoparticle decorated ZnO nanorods. The tested nanorods consisted of Pt + Au, Pt and Au decorated and an undecorated ZnO control which produced responses of 157.4, 59.1, 3.4, 16.3, and 1 respectively. The bimetallic nanoparticles were also selective when the response was compared to CO,  $\text{CH}_4$  and  $\text{C}_2\text{H}_2$  and had a rapid response rate, reaching its maximum

response within 3 seconds at 130 °C, though due to overshoot response equilibrium took 115 s to reach. The comparison easily highlighted the catalytic (and additional electronic) effect of the particles on the sensor responses and in most of the various sensors reviewed above, the improved response was produced via the addition of catalytic nanoparticles or doping.

Catalytic nanoparticles can easily be loaded onto the LBZA material prior to processing and in a short study <sup>[385]</sup> performed by the author a Au NP decorated sensor was produced and tested. The nanoparticles with mean diameter of 5 nm, produced via a standard and simple sodium borohydride reduction of hydrogen tetrachloroaurate in the presence of PVP, were added to the HMTA derived LBZA by simply adding the as reacted nanoparticle suspension to freshly centrifuged LBZA and being left overnight. After being left overnight practically all the particles coat the LBZA and after centrifuge cleaning in reverse osmosis water a sensor was produced in the same manner as the sensor presented above.

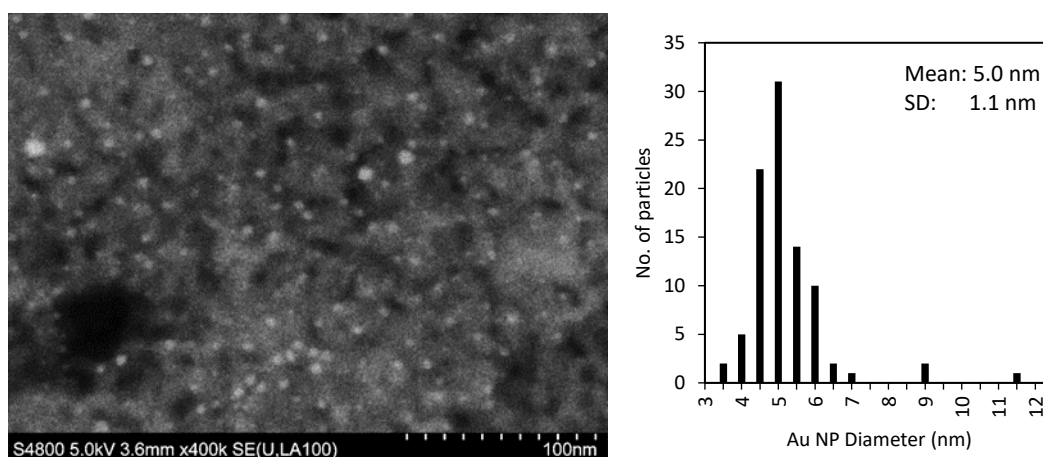


Figure 4.11: Left) High magnification field emission – low angle backscatter electron image of Au NP decorated LBZA derived ZnO sensor. Au NP - bright/ high contrast features, ZnO grain structure - mid contrast grey features. Right) Histogram of measured nanoparticle diameters, mean = 5 nm, standard deviation = 1.1 nm, n= 100. Au NP produced via the simple borohydride reduction in the presence of PVP.

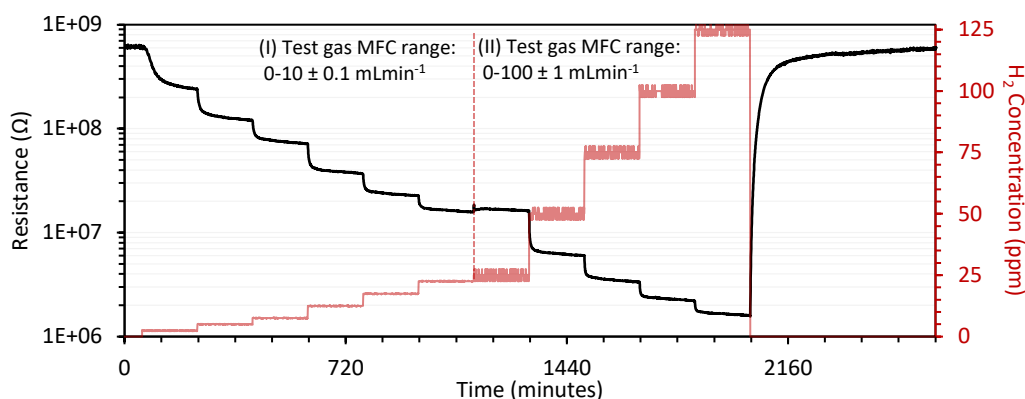


Figure 4.12: Plot of resistance (left hand axis) and  $H_2$  concentration (right hand concentration) as a function of time measured in minutes; for the  $100 \mu\text{L Au } 5 \text{ nm NP}$  decorated LBZA derived ZnO gas sensor (annealing temperature  $350 \text{ }^\circ\text{C}$ ), measured at  $\sim 200 \text{ }^\circ\text{C}$ . Automated switch over between test gas MFC (full details in Appendix Chapter 12) between  $22.5 \text{ ppm}$  (region I) and  $25 \text{ ppm}$  (region II.) Increase in resistance at  $25 \text{ ppm}$  has been generally attributed to the difference in accuracies between mass flow controllers which have a manufacturer stated accuracy of 1% of full range. The Au NP decorated LBZA derived ZnO gas sensor was tested using the gas sensor testing rig that will be outlined in detail in Appendix Chapter 12.

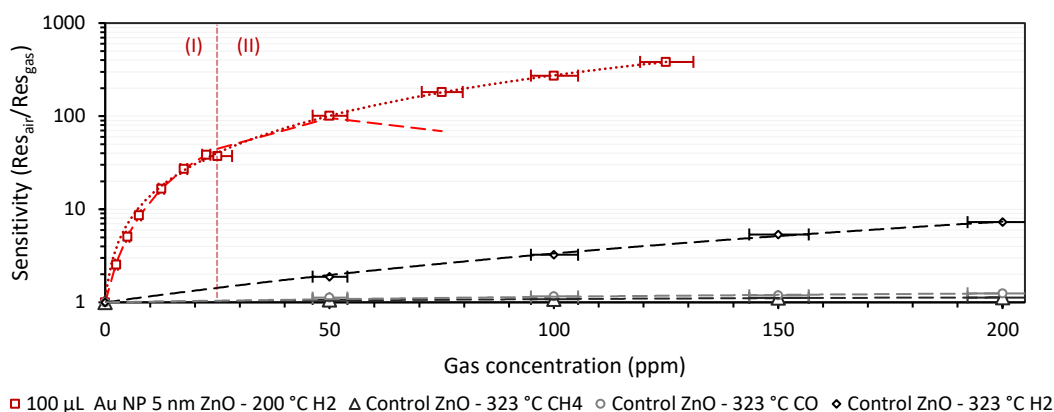


Figure 4.13: Plot of gas sensor sensitivity (defined as sensor resistance in air/ resistance in test gas mixture) as a function of gas concentration in ppm for the  $100 \mu\text{L Au } 5 \text{ nm NP}$  decorated LBZA derived ZnO gas sensor (annealing temperature  $350 \text{ }^\circ\text{C}$ ) measured at  $\sim 200 \text{ }^\circ\text{C}$  and  $H_2$ , CO and  $CH_4$  sensitivities for the bare LBZA derived gas sensor (all ready presented and discussed in this work) measured at  $328 \text{ }^\circ\text{C}$ . Error bars represent maximum and minimum concentration calculated from the manufacturer defined accuracies of 1% of the full range. Region 1 test gas MFC range:  $0-10 \pm 0.1 \text{ mL}\cdot\text{min}^{-1}$ , Region 2 test gas MFC range:  $0-100 \pm 1 \text{ mL}\cdot\text{min}^{-1}$ ,  $O_2$  MFC range:  $0-200 \pm 2 \text{ mL}\cdot\text{min}^{-1}$ ,  $N_2$  MFC range:  $0-1000 \pm 10 \text{ mL}\cdot\text{min}^{-1}$ . Trendline (where  $x$  = gas concentration in ppm and  $y$  = sensitivity) equations with  $R^2$  values: Au NP decorated sensor  $H_2$  trendlines full range (dotted line):  $y = -30.52 \cdot 10^{-6} x^3 + 0.0194 x^2 + 1.103 x + 1$ ,  $R^2 = 0.9998$ . Au NP decorated sensor  $H_2$  trendlines 0-50 ppm range (dashed line):  $-0.0009 x^3 + 0.0731 x^2 + 0.4875 x + 1$ ,  $R^2$  (range 0-50 ppm), trendline diverges after 50 ppm.  $H_2$   $328 \text{ }^\circ\text{C}$ :  $y = 8 \cdot 10^{-05} x^2 + 0.0152 x + 1$ ,  $R^2 = 0.997$ .  $CH_4$  at  $328 \text{ }^\circ\text{C}$ :  $y = -2 \cdot 10^{-06} x^2 + 0.001 x + 1$ ,  $R^2 = 0.950$  and CO at  $328 \text{ }^\circ\text{C}$ :  $y = -2 \cdot 10^{-06} x^2 + 0.0017 x + 1$ ,  $R^2 = 0.931$

Figure 4.12 shows a ramped concentration vs resistance plot and Figure 4.13 the corresponding concentration curve from the study measured at a surface temperature of approximately  $200 \text{ }^\circ\text{C}$ . The sensor response to hydrogen vastly increases in magnitude whilst simultaneously lowering the operating temperature producing responses at  $200 \text{ }^\circ\text{C}$  of 2.54 to

2.5 ppm and 382 to 125 ppm with a measured current on the order of 6  $\mu\text{A}$  (at 10 V applied.) The response however was very slow with the full response time on the order of 2 hours. Further investigation would be required into improving the speed of response and increasing current to use the Au nanoparticles used in the study however it more importantly shows the ease at which the response can be modified and the resultant versatility the LBZA particles have as a sensing material precursor. In addition, the potential for doping via anion exchange [75][73] and addition of other metal acetate precursors during synthesis [117][386][387][164] would allow for adaption in sensitivity and selectivity makes the nanosheets a promising material to potentially build printed sensors for other purposes.

To summarise, whilst only 3 test gasses have been tested at this point, the sensor shows high selectivity and an easily detectable response to hydrogen competitive to other simple sensors in literature and while the methane sensitivity needs to be separately addressed for a complete carbohydrate malabsorption breath tester, LBZA derived ZnO has been shown to be a viable potential sensing material for hydrogen breath analysis required as part of a printed general carbohydrate malabsorption tester if the low mass yield can be addressed. In the following section an introductory study into a novel sodium hydroxide-based microwave assisted growth with high yield is presented as a potential solution.

## **4.2 Sodium hydroxide-based microwave assisted growth method**

### **4.2.1 Proposed method rationale**

One of the traditional methods of production of layered metal hydroxides uses sodium hydroxide as the base where the waste product, sodium acetate, is generally considered a safe and green by product. Whilst sodium hydroxide is potentially dangerous due to its corrosive nature, the risk can be easily managed at varying manufacturing scales [388]. Of the methods that use sodium hydroxide in the synthesis of layered metal hydroxides most appear to use dropwise addition of sodium hydroxide to an aqueous solution containing dissolved metal salt precursor [389][390][391]. It is well known that when particles are seeded over a significant proportion of the reaction time, the resulting morphologies will have a high spread/ standard deviations [392][171][169]. Due to the low solubility of zinc hydroxide complexes [393] this will result in particles seeding within each droplet added, resulting in a large spread in particle length. The high spread would be undesirable for use in a



flexographic printed application where particle size control is an important factor for both printability and controlling ink rheology as outlined in Chapter 2.3.6 . To reduce the spread an alternative approach was attempted here where the sodium hydroxide solution was added ‘instantaneously’ (within a second) to the zinc acetate solution forcing the particles to be seeded simultaneously. According to the classical nucleation theory (CNT) <sup>[169]</sup> described in Chapter 2.1.3.4 ; concentrations producing supersaturation far in excess of the critical threshold for nucleation also results in nucleation occurring over a long period of time, and a polydisperse size distribution. In line with CNT, here after LBZA seeding occurs and the solution stirred to produce a uniform distribution of reactants and seed crystals; the samples are exposed to microwaves. The application of microwave energy rapidly heating the solution and dropping the degree of supersaturation <sup>[394]</sup>, whilst also rapidly increasing the growth kinetics and further reducing the degree of supersaturation <sup>[394]</sup>.

As was stated earlier in section 4.1.2 , zinc acetate aqueous complexes have a higher formation constant than that of the nitrate equivalent and as such, in principle any method of production for layered zinc hydroxy nitrate should work for the acetate equivalent. The initial molar ratio of reactants used in the proposed method was based on those of the sodium hydroxide dropwise growth of the zinc nitrate equivalent by Newmann and Jones <sup>[390]</sup> with concentrations scaled down to within the solubility limit of zinc acetate (i.e. from 3.5 M:0.75 M Zinc nitrate: Sodium hydroxide to 1 M: 0.214 M Zinc acetate: Sodium hydroxide.) After confirmation that LBZA was successfully produced using the drop wise methodology the instantaneous seeding with microwave heating described below was trialled.

## 4.2.2 Method

To find the effect of instantaneous addition and microwaving on the purity and yield of LBZA a series of reactions were performed for defined molar ratios of  $[\text{OH}^-]$  anions to  $[\text{Zn}^{2+}]$  cations of 0.5, 0.7, 0.9, 1.1, 1.3, 1.5, 1.55, 1.60, 1.65, 1.7, 1.8 and 2.0. The ratios were chosen such that more focus was put on concentrations approaching the stoichiometry of LBZA (i.e. 1.6:1  $[\text{OH}^-]$ :  $[\text{Zn}^{2+}]$ .) After synthesis and cleaning XRD was performed to find the phase purity, after which SEM, AFM and mass yield measurements were performed on the highest yield with the lowest measured ZnO (101): LBZA (001) reflection intensity area ratio.

#### **4.2.2.1 Synthesis**

For each reaction two solutions were produced, the first comprising of 11.4 mL of 1 M of Zinc Acetate dihydrate dissolved in reverse osmosis water and the second an aqueous solution of sodium hydroxide with volume equal to 28.6 mL and molarity defined to produce a Zinc: Hydroxide ratio of either 0.5, 0.7, 0.9, 1.1, 1.3, 1.5, 1.55, 1.60, 1.65, 1.7, 1.8 and 2.0. The zinc acetate solution was added to a 100 mL beaker with a PTFE magnetic stir bar and set to stir at 625 RPM on a magnetic stirrer. The sodium hydroxide solution was added and left to stir for one minute. Upon addition precipitation occurs immediately creating a viscous, grey, turbid solution containing aggregated material with a maximum size estimated visually to be on the order 1 mm. After approximately 15 seconds of stirring the solution became more fluid with the vortex reforming. It then slowly turned more viscous as time progressed. After the minute had passed the stir bar was removed and rinsed with reverse osmosis water to make certain any residue was recovered from the stir bar, after which the suspension was topped up to 50 mL manually, swirled for 3 seconds and placed in the microwave. As the solutions started to boil after 25 s of irradiation at 800 W the samples were then irradiated at full power (800W continuous) for 20 s. Upon removal of the beaker from the microwave the suspension transformed from a turbid grey to a solid white colour. The beaker was immediately swirled again after microwaving for 5 seconds to homogenise the temperature of the solution and then left to air cool for 1 hour. Post cooling the samples were centrifuged 3 times for 3 minutes at x3260g with the supernatant replaced with reverse osmosis water each time.

#### **4.2.2.2 XRD**

XRD was performed on each sample using the method outlined in 4.1.1.3 . To assess the phase purity, the ZnO (101) and LBZA (001) reflection peak areas were measured for each sample, and their ratio plotted as a function of  $[\text{OH}^-]:[\text{Zn}^{2+}]$  ratio. According to measurements of zinc hydroxide solutions by Reichle, McCurdy and Helper the total solubility of dissolved zinc containing species (regardless of co-ordination) is approximately 1.78 mM <sup>[393]</sup>. The point of maximum yield at highest purity was therefore taken as the concentration where the ZnO (101) reflection area became measurable above the noise floor (i.e. the onset of ZnO formation.)

#### **4.2.2.3 SEM**

Morphology was assessed using a Hitachi S4800-II FEGSEM (Hitachi High Technologies, Minato-ku, Tokyo, Japan) at x600 magnification in deceleration mode with 1 kV landing voltage to increase surface sensitivity. To characterise the length at the point of maximum yield, as defined by a  $[\text{OH}^-]:[\text{Zn}^{2+}]$  ratio of 1.5:1, the length of 100 particles were measured in ImageJ, the mean and standard deviation calculated and a histogram of the results plotted.

#### **4.2.2.4 AFM**

To assess the average height of the synthesised particles, 100  $\mu\text{L}$  of as cleaned nanosheets produced with a  $[\text{OH}^-]:[\text{Zn}^{2+}]$  ratio of 1.5:1 was diluted with reverse osmosis water to a ratio of 1: 100 after which 5  $\mu\text{L}$  was dropcast onto precleaned Silicon and left to air dry. AFM was performed using a NanoWizard® II NanoScience (JPK Instruments, Bruker, Berlin, Germany) in intermittent contact mode.

#### **4.2.2.5 Mass Yield Measurements**

To assess the mass yield of the reaction with a  $[\text{OH}^-]:[\text{Zn}^{2+}]$  ratio of 1.5:1 the mass of 10 samples was measured using the same methodology for the HMTA sheets as outlined in section 4.1.1.4 .

### **4.2.3 Results**

#### **4.2.3.1 Purity - XRD**

Figure 4.14 shows the diffractograms for the series of cleaned synthesised products for the varying hydroxide to zinc ratios. It can be seen that LBZA was successfully made for all reactions below a ratio of 1.8, by the presence of the (001), (002) and (003) reflections at  $6.6^\circ$ ,  $13.26^\circ$  and  $19.99^\circ$  corresponding to an interlamellar distance of 1.34 nm <sup>[67], [69], [71], [134]</sup> . For ratios equal to or greater than 1.55 that the figure shows that ZnO starts to form by

the presence of the (100), (002), (101) at 31.8 °, 34.4 ° and 36.3 ° respectively (matching JCPDS # 01-079-2205) <sup>[69][127]</sup> and that as the ratio increases the relative amount of ZnO compared to LBZA increases. In the reactions with ratios of 0.7, 0.9 and 1.1 a secondary set of reflections were present at approximately 5.98 ° corresponding to an interplanar distance of 1.48 nm similar to the value of 1.47 nm for LBZA with turbostratic disorder and normalised stoichiometry of  $\text{Zn}(\text{OH})_{1.58}(\text{Ac})_{0.42}(\text{H}_2\text{O})_{0.31}$  as synthesised by Poul, Jouini and Fievet <sup>[75]</sup>. For the ratio of 1.8, no LBZA was observed however, a second set of peaks (indicated as \*I, \*II and \*III) was observed with 2θ of 8.92°, 13.3° and 17.7 ° likely indicating the (002), (003) and (004) reflections for a structure with a (001) 2θ value of approximately 4.46° and d spacing of 1.98 nm typically attributed to BLBZA, a comparatively acetate rich layered hydroxide phase <sup>[68][74]</sup>. The set of BLBZA reflections occurred throughout all the reactions below 1.5 with \*I/ LBZA (001) and \*I/ LBZA (001) area ratios no greater than 0.011 and 0.138 respectively.

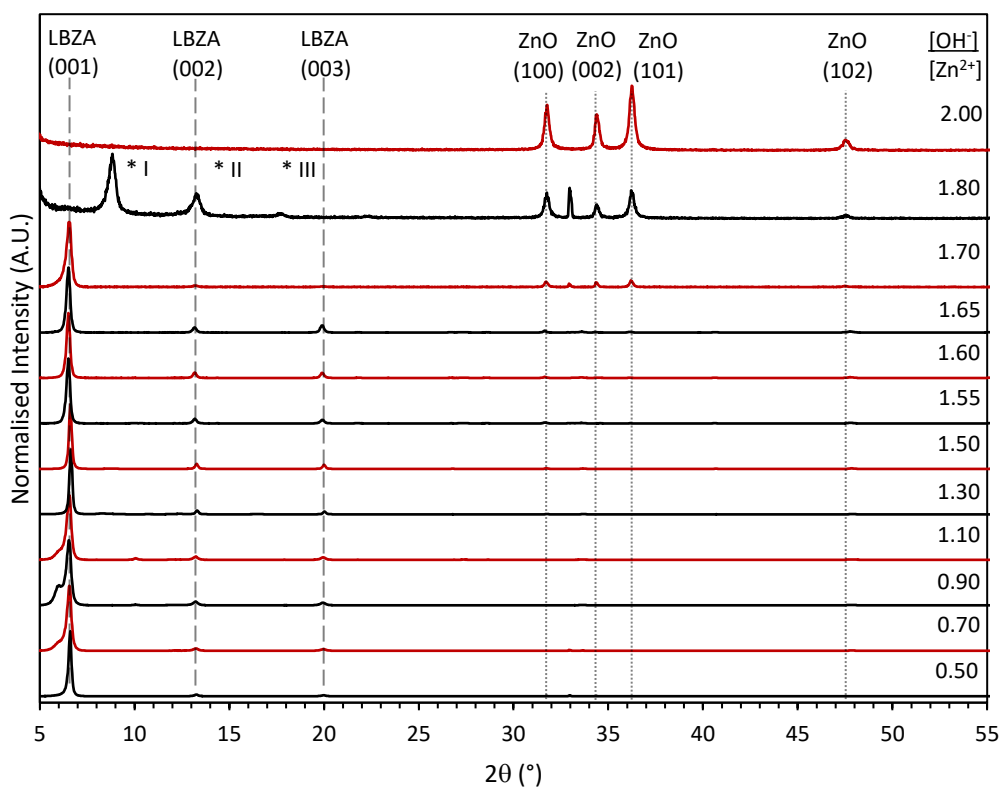


Figure 4.14: XRD diffractograms for the centrifuge cleaned reaction products for the various [OH]:[Zn<sup>2+</sup>] (values listed on the right.) The reflections for ZnO and LBZA have been overlaid and labelled. For the ratio of 1.8 no LBZA reflections were observed and the appearance of another set of reflections \*I, \*II and \*III, potentially another layered hydroxide, were present.

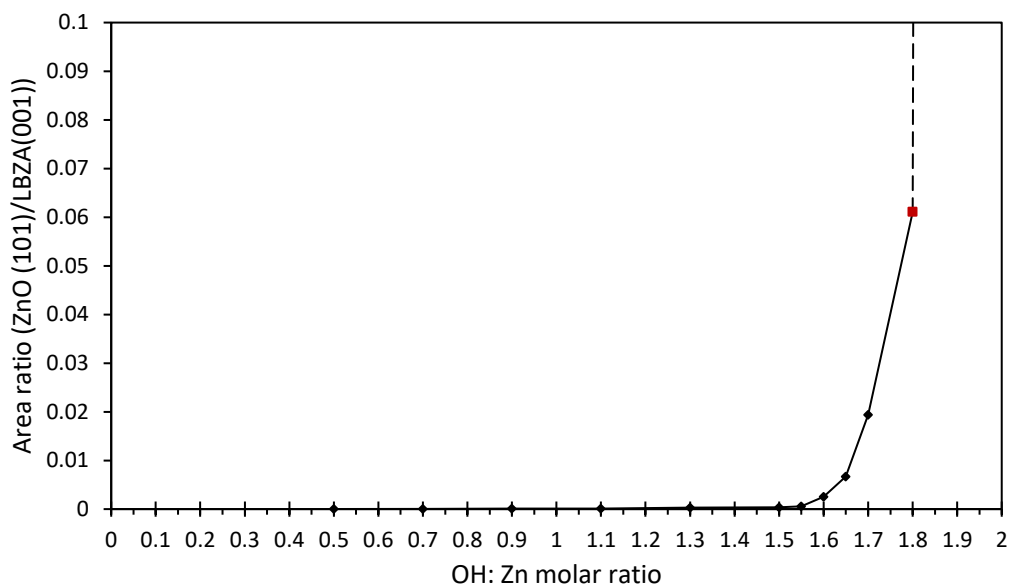


Figure 4.15: Recorded XRD area ratios for the ZnO (101) vs LBZA (001) reflections as a function of  $[\text{OH}^-]:[\text{Zn}^{2+}]$  ratio. Note that 1.8 (red square) represents the area of the first present reflection \*I, and is likely a secondary layered hydroxide. Note that due to preferential stacking the LBZA reflection has a much higher signal for the same amount of material and so the molar ratio of ZnO to LBZA is higher than the area ratio. At a  $[\text{OH}^-]:[\text{Zn}^{2+}]$  ratio of 2 no LBZA was observed hence the area ratio tends to infinity (dashed line).

It is worth noting that TGA of both LBZA and BLBZA have very similar thermal transients with only the magnitude and not the onset of mass loss at each mass loss event altering [68]. Figure 4.15 shows the plotted area ratios of ZnO(101) / LBZA (001) as a function of  $[\text{OH}^-]:[\text{Zn}^{2+}]$  ratio, it can be seen that for hydroxide ratios up to 1.5 the ZnO/ LBZA ratio is negligible with values less than  $0.36 \times 10^{-3}$  after which the ZnO content starts to exponentially rise. Note that due to preferential C axis stacking/ orientation for LBZA, a result of its high aspect ratio, the relative quantity of ZnO is higher than the area would suggest. Riechle, McCurdy and Hepler [393] measured the total solubility of dissolved zinc containing species (regardless of co-ordination) in Zinc hydroxide solutions at 25 °C to be approximately 0.178 mM, significantly lower than the 11.4 mMol of Zinc present here. Considering the solubility and complex formation (i.e., equilibrium) constants for  $\text{Zn}(\text{OH})_2$  of  $1.51 \times 10^{11}$  ( $\beta_{12}$ ) [393] and  $\text{Zn}(\text{OH})^+$  of  $1.46 \times 10^6$  ( $\beta_1$ ) [393] which are both far greater than that of the  $\text{Zn}(\text{Ac})_2$  aquo complex ( $\beta_{12} = 123$ ) [338], it is assumed that virtually all the hydroxide was complexed and precipitated. Based on the assumption that all hydroxide was complexed, the maximum yield of 'pure' LZBA was taken to occur at the highest ratio before ZnO formation began, measured as a  $[\text{OH}^-]:[\text{Zn}^{2+}]$  ratio of 1.5.

#### 4.2.3.2 Morphology – SEM and AFM

After confirmation of the production and measurement of the highest yield at maximum purity it was important to characterise the morphology to check that the synthesised material was compatible with printing. Figure 4.16 (A) shows the SEM images of the cleaned and synthesised LBZA and their measured size distribution. All particles measured had lengths below 15  $\mu\text{m}$  (Figure 1.2), a mean length of 6.95  $\mu\text{m}$  and a standard deviation of 2.42  $\mu\text{m}$ . The distribution seems to follow a relatively normal distribution suggesting the synthesis followed a single process. Also, no particles are lower than 2  $\mu\text{m}$  which suggests, according to CNT [169], limited to no nucleation towards the end of the synthesis. The broad standard deviation (34.8 % of the mean) potentially indicates a single long initial nucleation time prior to the microwave step. The lack of observed particles greater than 15  $\mu\text{m}$  is consistent with the requirement for flexographic printing, i.e. that particle length be below the depth of anilox cells, in this case 24  $\mu\text{m}$ .

The AFM results (Figure 4.17) show a similar profile as the SEM, a relatively normal distribution with broad standard deviation (50.9% of the mean), with a maximum observed size of 37.6 nm and no particles observed below 3 nm. The distribution seems to be slightly skewed towards higher values with more particles expected above 32 nm and less below the mean, which when considering the lack of any observed lengths below 2  $\mu\text{m}$  in the SEM, possibly indicates that the final stage growth occurs at least in part by Ostwald ripening [392][171][170], i.e. growth of larger particles via the consumption of smaller particles. It is also possible the skew is related to the secondary layered hydroxide particles observed in the XRD results, as the particles at the lower end of the measured height distribution wouldn't readily show up under SEM imaging on a silicon substrate.

The smaller mean particle of the sodium hydroxide based growth, as compared to the HMTA based growth, combined with the dense (non-porous) granular layer of particles produced during calcination at 350 °C, could potentially produce a larger gas sensing response due to a combination of smaller grain sizes (with LBZA thickness less than that of the mean measured grain size in the HMTA growth) and a reduction in the proportion of material not exposed to gas. It should be mentioned that the relative polydispersity in thickness could potentially produce a degree of variation in the sensitivity of devices depending on how the particles are deposited on the substrate.

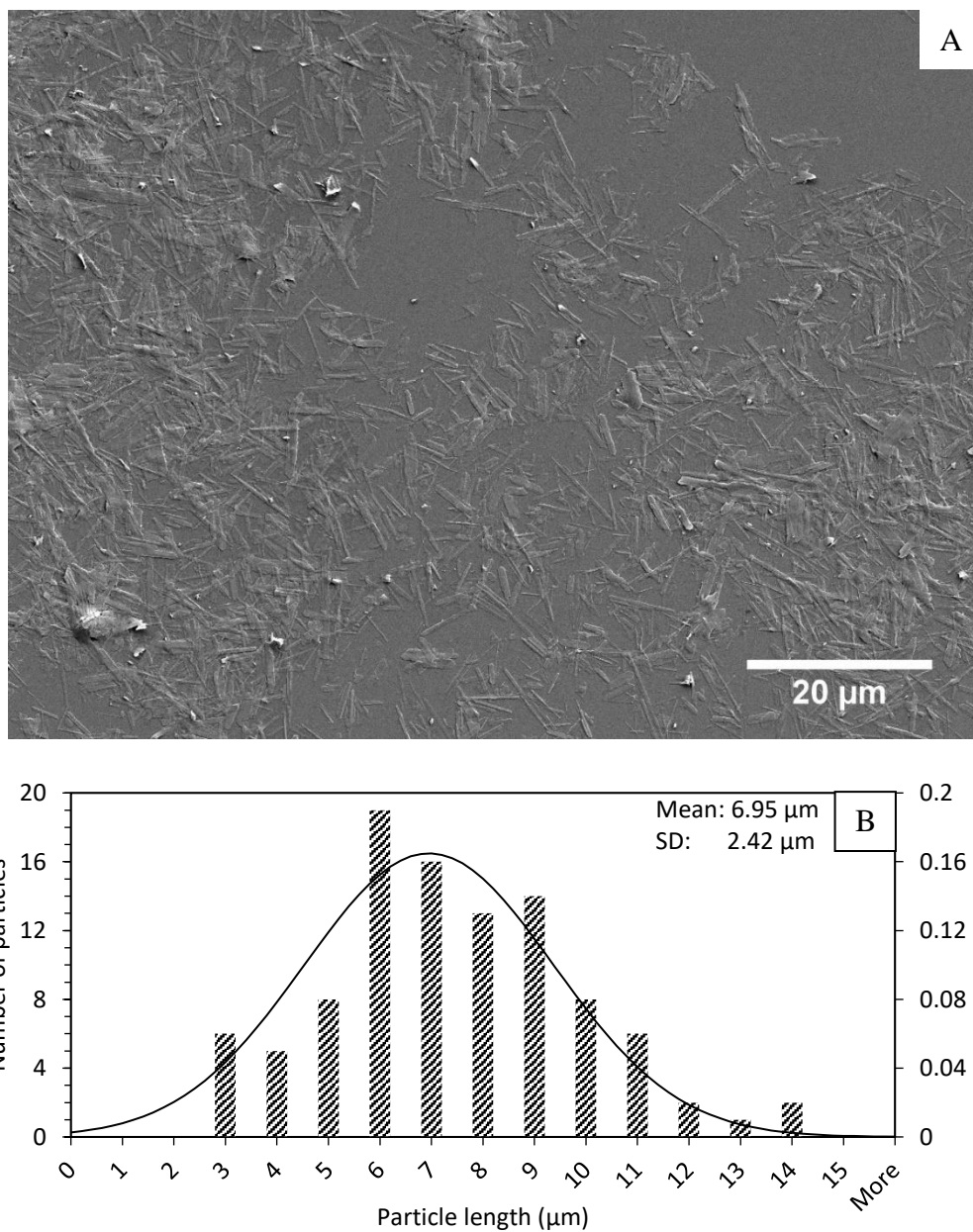


Figure 4.16 :A) SEM images of LBZA synthesised for a  $[OH^-]:[Zn^{2+}]$  ratio of 1.5 irradiated for 20 second at 800 W. B) Histogram of particle length for the same sample with overlaid normal distribution, mean and standard deviation.  $N= 100$ .

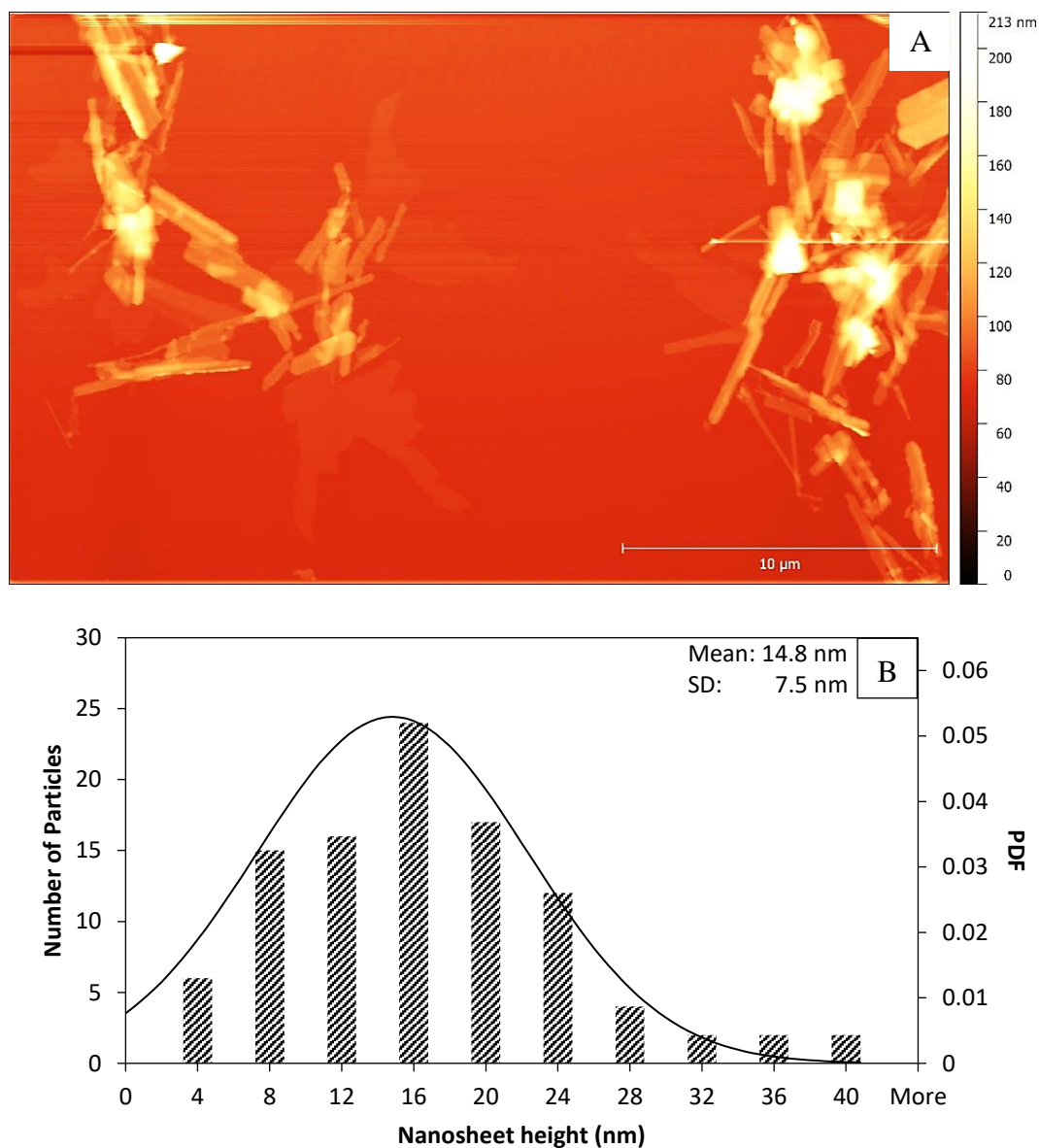


Figure 4.17: A) AFM scan of structures synthesised for a  $[OH^-]:[Zn^{2+}]$  ratio of 1.5 irradiated for 20 second at 800 W. B) Histogram of particle length for the same sample with overlaid normal distribution, mean and standard deviation.  $N= 100$ .

#### 4.2.3.3 Mass yield measurements

Based on the assumption that maximum yield at highest purity occurred at a  $[OH^-]:[Zn^{2+}]$  ratio of 1.5, the mass yield measurements for 10 samples was measured resulting in a mean mass of 1237 mg and a standard deviation of 61 mg (4.9 % of the mean) for a 2.508 g mass of zinc acetate dihydrate. Assuming the measured solids were all LBZA, produces an



approximate molar zinc conversion of 87.3% and 71.2% molar conversion for sodium hydroxide, representing a substantial improvement both in yielded mass per synthesis and molar efficiency of the reactants as compared to the yield for the HMTA synthesis (37.2 mg yield, 5.02% efficiency<sub>zinc</sub> and 4.08% efficiency<sub>base</sub>). It should be stated that the approximation has a degree of error due to the presence of the secondary layered hydroxide with an unknown but acetate rich stoichiometry. During the centrifuge cleaning steps, not all material is compacted into the pellet and a semi-transparent film forms at the liquid air interface, and considering that nanoparticles are known to diffuse to the surface [395] it is likely this is the cause of the relatively high standard deviation. The high yield when considered with the measured morphology and lack of ZnO impurities suggest the sodium hydroxide based method holds promise for use in creating LBZA derived flexographic printed hydrogen breath sensors.

### 4.3 Conclusion

For a synthesised material to be used for the goals of cheap flexographic printed hydrogen gas sensors it is important that its properties are both compatible with the flexographic printing process and provide good sensing characteristics. Starting with an in-house HMTA based microwave growth method, LBZA was grown, characterised and the gas sensing properties of the derived ZnO tested. Whilst the synthesised material had high purity and morphology consistent with the requirements for flexographic printing (i.e. the particles must fit within the anilox regardless of orientation) the mass yield was low at 37.2 mg and had a low conversion efficiency of the reactants. Gas sensor testing of ZnO derived from the material annealed at 350 °C showed promise, with responses and cross sensitivity not only competitive with other simple non catalysed materials in the literature but also sufficient for the use in hydrogen breath tests with an estimated increase in current of 33.6% at the threshold of a positive test (20 ppm H<sub>2</sub>). Considering the response showed promise for LBZA derived ZnO for use as part of a hydrogen breath analyser, a secondary microwave synthesis method was devised using sodium hydroxide as the base. The point of maximum yield at highest purity was predicted at a [OH<sup>-</sup>]:[Zn<sup>2+</sup>] ratio of 1.5:1 and showed a substantial improvement in yield producing 1237 mg in a single synthesis and conversion efficiency of the reactants. Most importantly for the flexographic printing process, SEM results revealed lengths compatible with a 24 mL.m<sup>-2</sup> anilox. The high yield, compatibility with the flexographic print process, and sensitivity of LBZA derived ZnO of similar or greater

thickness suggest that sodium hydroxide based microwave grown LBZA shows promise for use in flexographically printed hydrogen breath sensors.

The experiments in the following 2 chapters were performed simultaneously. Chapter 5 is dedicated to further investigations into the sodium hydroxide-based microwave assisted LBZA synthesis, focussing on the effect of microwave time and how the rate of addition affects the morphology and purity of LBZA relative to synthesized BLBZA. Chapter 6 focuses on the development of flexographic ink using LBZA synthesised from a  $[\text{OH}^-]:[\text{Zn}^{2+}]$  ratio of 1.5:1 presented in this chapter and the production and testing of proof of concept flexographic printed gas sensors using the developed inks.

## Chapter 5 - Investigations of sodium hydroxide-based microwave assisted LBZA synthesis conditions

---

### 5.1 Introduction

In chapter 4.2 a sodium hydroxide-based microwave assisted synthesis method was introduced. The method rapidly produced LBZA structures with lengths short enough to be compatible with the requirements for flexographic printing, with a high enough purity and a yield large enough for practical purposes. The experiments presented within this chapter aim to understand the growth processes and as a result control morphology and further improve purity via removal of the BLBZA phase. The experiments look at four main factors in the reaction: microwave time, hydroxide to acetate ratio, shear rate of stirring and the sodium hydroxide addition rate.

The first experiment (section 1.4.4.1 ) investigated the combined effect of microwave exposure time and hydroxide to zinc ratio on purity and morphology. As highlighted in chapter 4.2 the polydispersity and morphology are controlled by how the particles nucleate, or seed, and how they then grow. As temperature affects supersaturation and the reaction rate of growth, altering the microwave time was expected to alter the length of the synthesised particles. Considering an inverse temperature dependency for the aspect ratio of LBZA produced via aqueous hydrolysis of zinc acetate solutions was observed by Wang *et al.* [68], it was expected that temperature would also affect the aspect ratio. As temperature also controls the chemical potential of the growth monomers [396], it was posited that temperature would also affect the type of the nucleated species, potentially reducing BLBZA concentration. The increased temperature would also increase hydrolysis [68][69] of coordinated water in zinc aquo complexes, and therefore could lower the concentration ratio at which the onset of phase transition to  $\text{Zn}(\text{OH})_2$ , and hence  $\text{ZnO}$ , occurs.

Due to a lack of reaction mechanisms in the literature capable of explaining the size distribution and morphological data, the crystalline structure of the interbasal  $[\text{Zn}_5\text{OH}_8]^{2-}$  layers was examined here, revealing a dipole. Based on an in-depth comparison with the literature (chapter 2.1.3 ), a comprehensive reaction mechanism drawing on concepts of classical nucleation theory, growth kinetics of crystals with charged surfaces in solution, [172] and oriented attachment, the various length scale features of LBZA in the literature and in

this work (primary particle shape, diffraction line shapes, secondary particulate structure/morphology and size distribution) can be mechanistically explained.

The temperature and  $[\text{OH}^-]/[\text{Zn}^{2+}]$  ratio variables investigated within section 1.4.4.1 did not lead to an inhibition of BLBZA and ZnO formation, therefore phase purity was implied to be primarily controlled by the nucleation processes that occurred pre-microwave exposure. The second experiment therefore investigated how mixing efficiency and the rate of sodium hydroxide addition affected the initial nucleation processes within the slurry formed upon hydroxide solution addition. Three rates of addition of sodium hydroxide were investigated: instantaneous (addition time  $< 1$  s), continuous flow (addition time  $\approx 15$  s) and a simultaneous flow addition of  $\text{ZnAc}_2$  and NaOH (addition times  $\approx 20$  s.) Two methods of stirring were also investigated, the low shear method as presented in chapter 4.2 and a higher shear rate method. The higher shear rate was produced via addition of a baffle and increased stirrer area. The effects were monitored by recording the XRD phase areas sampled as a function of stir time. The highest mass transport/ mixing rate set-up was able to successfully halt BLBZA and ZnO formation whilst still retaining high degrees of particulate size monodispersity.

The results and interpretation of the experiments are initially presented in section 5.3 . Subsequently in section 5.4 5.4 , a unified formation and growth mechanism based on the total combined results is presented and its relevance to the gas sensing behaviour and printing process as used in the investigations within this document and the field of layered zinc hydroxide growth discussed.

## 5.2 Methods

### 5.2.1 Effect of microwave time and $[\text{OH}^-]:[\text{Zn}^{2+}]$ ratio on morphology and purity

#### 5.2.1.1 Microwave synthesis

Microwave synthesis of LBZA and subsequent cleaning steps used the method as introduced in chapter 4.2.2.1 . The Zinc acetate molarity and volumes were kept constant and the range of sodium hydroxide concentrations tested was expanded to produce  $[\text{OH}^-]:[\text{Zn}^{2+}]$  ratios of 0.4, 0.8, 1.2, 1.4, 1.44, 1.48, 1.52, 1.6, 1.64, 1.68, 1.72, 1.76, 1.8 and 2 to investigate how

temperature affected the onset of ZnO formation. Microwave times investigated consisted of 0, 10, 20 and 30 seconds which produced temperatures of approximately 294 K, 309 K, 327 K and 351 K respectively as measured with a thermometer directly after exposure. The synthesised material was remixed directly before sampling to provide a reliable representation of particles within the volume.

### ***5.2.1.2 Phase purity assessment via XRD***

Phase purity was assessed qualitatively using a D8 x-ray diffractometer (Bruker, Billerica, MA, USA) in standard coupled  $\theta$ - $2\theta$  mode. 20  $\mu\text{L}$  of centrifuge cleaned samples for each reaction condition was drop cast on to a cleaned silicon wafer and left to air dry. The silicon wafer was cleaned via ultrasonic bath treatments in acetone, IPA, reverse osmosis water and then blown dry with 99.998% pure  $\text{N}_2$ . Scans were performed using  $\text{Cu K}\alpha$  x-rays ( $\lambda = 0.154 \text{ nm}$ ) from an achromatic source set at 40 kV and 40 mA. A Göbel mirror was used to strip the  $\text{K}\beta$  lines and convert the beam from dispersive to parallel beam geometry. Beam area was reduced with a 0.3 mm diameter collimator. Diffractograms were recorded over the  $2\theta$  range of  $1^\circ$  to  $65^\circ$  in  $0.019627^\circ$  increments. The diffracted beam was recorded with a linxeye 1D detector and left to run overnight. Purity was semi-quantitatively assessed by measuring the peak areas of the (001) reflections for the LBZA and BLBZA phases and the sum of the (100), (101) and (002) reflections of the ZnO side product. The ratio of each phase area to the sum of the phase areas was then plotted as a function of  $[\text{OH}^-]:[\text{Zn}^{2+}]$  ratio. Raw phase areas were plotted to measure qualitative trends in absolute reaction product. Due to minor errors in diffractometer focal sample point and the small radius of the deposited droplets, the raw areas contained a large variance in absolute intensity between areas both within and between each sample. To approximate the change in area as a function of the  $[\text{OH}^-]/[\text{Zn}^{2+}]$  ratio, the raw peak areas for  $[\text{OH}^-]/[\text{Zn}^{2+}]$  ratios of 1.4 to 1.6 were each divided by the raw peak area at  $[\text{OH}^-]/[\text{Zn}^{2+}] = 0.4$  (normalisation to initial ratio) and the mean and standard deviation measured and compared. At all points prior, during and after centrifuging particulates could be seen located at the air/ water interface, part of which was lost during exchange of the supernatant. In addition to the visual particulates a transparent film with differing refractive index could be seen forming at the interface. In order to investigate the nature of this film and particulates lost during centrifuge cleaning, a sample was extracted from the interface of the 1.8  $[\text{OH}^-]/[\text{Zn}^{2+}]$  ratio sample and the diffraction pattern recorded using the technique as just described.

### 5.2.1.3 Morphology characterisation via scanning electron microscopy

Morphology was assessed using a Hitachi S4800-II FEGSEM (Hitachi High Technologies, Minato-ku, Tokyo, Japan) at  $\times 1k$  magnification and 1 kV acceleration voltage using the lower secondary electron detector. BLBZA side products were imaged using an in-lens low angle backscatter detector at  $\times 10k$  magnification, with 2.5 kV acceleration voltage and a landing voltage of 1 kV. The length and width of 100 LBZA particles for each condition were measured in ImageJ, the mean and standard deviation of length and aspect ratio calculated, and a histogram of the results plotted. As the underlying distribution was unknown, error was approximated for each sample by calculating the 95% confidence intervals in the mean and standard deviation for the length and aspect ratio using the bootstrap (non-parametric resampling) method <sup>[140][332]</sup> via the bootstrap function in MATLAB <sup>[333]</sup> with 20,000 resampled data sets for each reaction condition. The mean and standard deviations (with 95% confidence level error bars) for the length and aspect ratio were each plotted as a function of  $[\text{OH}^-]:[\text{Zn}^{2+}]$  ratio for each microwave exposure time. The results were then compared to classical nucleation theory <sup>[169][170][171]</sup>, Crundwells' reaction kinetics theory of the surface growth of crystals in the presence of surface charge <sup>[172]</sup> and oriented attachment <sup>[397][141][179][137]</sup>. To approximate the difference in energy barriers between growth in the  $[110]$  and  $[1\bar{1}0]$  directions, regression analysis was performed using the inbuilt regression analyser in Microsoft Excel based on a simplified Arrhenius effective reaction rate model <sup>[155]</sup>. The analysis was performed on the entire data set for aspect ratio with  $[\text{OH}^-]:[\text{Zn}^{2+}]$  ratios of 0.8 and 1.2 with coefficient, relevant p-values and adjusted  $R^2$  reported. Statistical significance was defined as  $p < 0.05$ . To assess Crundwells' modification to reaction rate and qualitatively predict the effect on oriented attachment, a simplified point charge model of the  $(110)$  and  $(1\bar{1}0)$  planar neutral surfaces was performed. Full details of the simplified model and calculation can be found in appendix Chapter 11 with the highlights of the resulted presented within this chapter. The model has been separated from the main text for the sake of brevity.

### 5.2.1.4 Microwave transmission coefficient calculation

To compare the effect of the electric field strength of the microwaves versus the effect of the dipole strength, the transmission coefficient of EM waves at 2.45 GHz for waves passing through the air – borosilicate glass and borosilicate glass – electrolyte interface was calculated. The electric field strength of an electromagnetic wave transmitted through an

interface is dependent on the impedances of each medium and the angle of incidence and can be calculated using Equation 5.1 [161]. Transmission will be at its maximum when the wave travels perpendicular to the interface and its transmission coefficient is given by Equation 5.2 [161]:

$$Transmission = \tau = 1 + reflection = 1 + \rho = 1 + \frac{Z_2 \cos \theta_i - Z_1 \cos \theta_t}{Z_2 \cos \theta_i + Z_1 \cos \theta_t}$$

Equation 5.1

$$\tau_{\perp} = \frac{2Z_2}{Z_1 + Z_2}$$

Equation 5.2

Where  $Z_2$  is the impedance of the medium the electromagnetic wave is entering and  $Z_1$  is the impedance of the medium the electromagnetic wave is exiting. The impedances used were as follows:

- The impedance of air  $\approx$  impedance of free space:  $Z_0 = 376.63 \Omega$  [161]
- The impedance of borosilicate glass:  $Z_{bsg} = 183.77 \Omega$ , ( $\epsilon_{r_{bsg}} = 4.2$  [398])
- As  $\sigma (\leq 50 \times 10^{-5} \text{ Sm}^{-1}$  measurement presented in section 5.3.2.3)  $\ll \omega \epsilon$  (8.69  $\text{radFm}^{-1}\text{s}^{-1}$ ) water can be modelled as a dielectric using the low loss approximation [161]. The impedance of water was then given by:

$$Z_{water} \approx \frac{Z_0}{\sqrt{\epsilon_{r_{water}}'^2 + \epsilon_{r_{water}}''^2}}$$

Equation 5.3

At approximately 295 K (21.8 °C),  $\epsilon_{r_{water}}' = 77.5$  and  $\epsilon_{r_{water}}'' = 9.8$  [160], so  $Z_{water} = 42.61 \Omega$  and at approximately 343.1 K (70 °C),  $\epsilon_{r_{water}}' = 63.7$  and  $\epsilon_{r_{water}}'' = 3.15$  [160], leading to  $Z_{water} = 47.16 \Omega$

### 5.2.1.5 Microwave penetration depth at half power calculation

To check for uniformity of heating, the distance at where the electromagnetic wave had reached half its initial power was calculated. using Equation 5.4 <sup>[160]</sup>. :

$$D = \frac{c}{\omega \sqrt{\epsilon'} \frac{\epsilon''}{\epsilon'}}$$

Equation 5.4

Where:

- $c = 299792458 \text{ ms}^{-1}$  is the speed of light
- $\omega = 2\pi f = 2\pi \times 2.45 \times 10^9 \text{ rad / s}$  is the angular frequency of the electromagnetic wave
- $\epsilon'$  is the relative permittivity (values presented for water in section 5.2.1.4 )
- $\epsilon''$  is the dielectric loss (values presented for water in section 5.2.1.4 )

## 5.2.2 The effect of addition rate and increased shear on purity

### 5.2.2.1 Synthesis

For each method of sodium hydroxide addition, the effect of stir times on purity was tested by sampling 100  $\mu\text{L}$  of the growth solution at set times up to 1200 seconds. For stir times of 30-300 seconds samples were taken in 30 second increments, 300 to 600 seconds in 60 seconds increments and 600 to 1200 seconds in 120 second increments. Each sample was taken from a pre-set height approximately 2 cm deep into the solution at the edge of the beaker to provide consistency. Samples were drop-cast without cleaning directly onto precleaned glass microscope slides. Post drop casting the films were air dried at room temperature ( $21 \text{ }^\circ\text{C} \approx 294 \text{ K}$ ) in a fume cupboard and stored under a rough vacuum (estimated pressure between 100 mbar & 300 mbar.) Samples were compressed between a second glass slide to produce consistent particle orientation and XRD diffractograms subsequently recorded. Each experiment was performed in triplicate. For all experiments,



20 mL of 1 M Zinc acetate solution and a 20 mL 1.58 M sodium hydroxide solution was used producing a  $[\text{OH}^-]:[\text{Zn}^{2+}]$  ratio of 1.58.

Three different rates of additions (simplified schematics shown in Figure 5.1) were tested:

- Instantaneous addition: Reaction was performed as previously described by adding the sodium hydroxide solution to the zinc acetate solution within a second.
- Continuous flow addition: Sodium hydroxide solution was added to a 50 mL polypropylene centrifuge tube with a hole in the bottom such that the solution was added to the zinc acetate solution with a feed rate of  $1.9 \text{ mL}\cdot\text{s}^{-1}$  ( $3.002 \text{ mM}\cdot\text{s}^{-1}$ )
- Simultaneous (dual flow) addition: Both solutions had a volume of 20 mL and were simultaneously added to 50 mL polypropylene centrifuge tubes with holes in the bottom such that each produced a feed rate of approximately  $1 \text{ mL}\cdot\text{s}^{-1}$  ( $1 \text{ mM}\cdot\text{s}^{-1}$  zinc acetate and  $1.58 \text{ mM}\cdot\text{s}^{-1}$  sodium hydroxide)

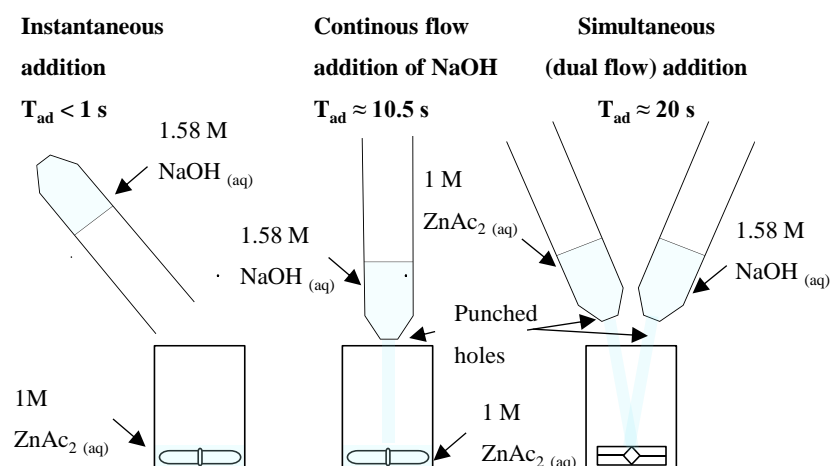


Figure 5.1: To scale simplified diagrams representing the different addition methods and their addition times ( $T_{ad}$ ). Note for the streaming and simultaneous dual stream addition methods clamp stands are used to hold the 50 mL polypropylene centrifuge tubes. All solution volumes are 20 mL. Beaker external dimensions: 50 mm diameter, 70 mm height. For the simultaneous (dual flow) addition the high shear rate was the only stir method used.

As the reaction produced a slurry with shear thinning behaviour, the degree of mixing varied greatly throughout the reaction volume. The effect of mixing was investigated through the introduction of a baffle and a stir bar with increased area (45 mm x 8 mm cylinder to 38 mm x 38 mm x 11 mm cross shaped bar). The baffle consisted of a stainless-steel plate with cross-section of 20 mm x 1 mm held in place by a clamp approximately 2 mm above the stir bar at an  $\sim 65^\circ$  tangent to the beaker wall. The different stirring methods were designated low shear and high shear respectively, simplified schematics are shown in Figure 5.2.

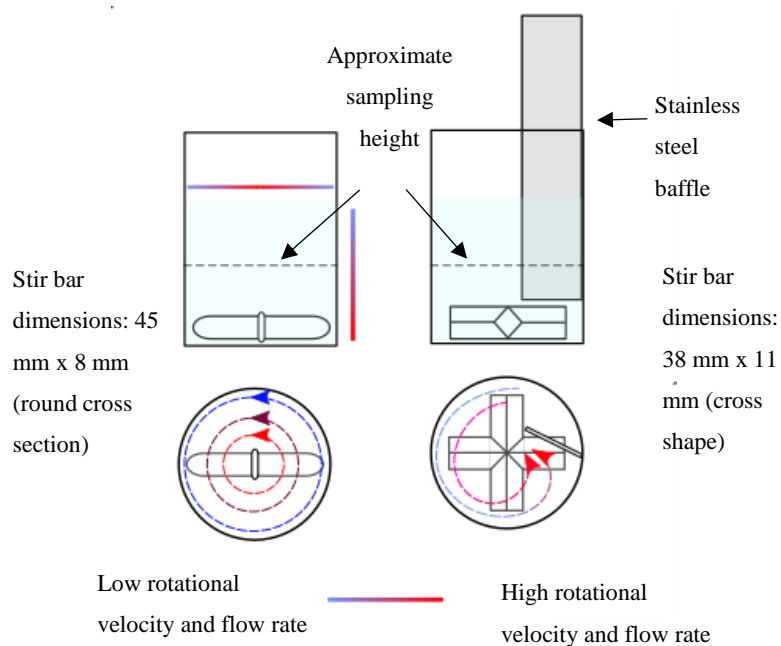


Figure 5.2: To scale diagram of the different stirring set ups with vertical and cross sectional views. Beaker external dimensions: 50 mm diameter, 70 mm height. Flow rate scale bar and arrows added to aid understanding of the baffle effect on the observed flow and mixing and are not set to a scale. Liquid volume represents approximate vortex height. Baffle was clamped in place by a clamp stand (not shown).

Both set ups were tested for the instantaneous addition and streaming addition whilst only the high shear method was tested for the simultaneous dual stream.

### 5.2.2.2 Phase analysis

The same x-ray diffractometer and experimental set up was used as in 5.2.1.2 but without the 0.3 mm collimator. Each individual scan was recorded over 5 minutes with the samples removed from vacuum and the first scan initiated within 5 minutes. Phase areas and their ratios were measured, and the mean and standard deviation calculated and plotted as a function of stir time for each condition.

### ***5.2.2.3 SEM morphological analysis of LBZA synthesised by simultaneous dual flow high shear stirring method***

LBZA was synthesised using the dual flow high shear stirring method as described above. Synthesis experiments were performed for stir time for 5 minutes and 60 minutes. Each sample were subsequently exposed to 800 W of 2.45 GHz microwave exposure for 30 seconds and left to cool for an hour. 100  $\mu\text{L}$  volumes for each stir time were sampled directly prior to microwave exposure, directly after microwave exposure and after cooling for 1 hour. The samples were cleaned via microcentrifugation at 12000 g for 10 seconds, replacing the supernatant with reverse osmosis water 5 times. The samples were dropcast onto highly doped silicon wafers and left to dry. Morphology of the cleaned and deposited LBZA particles was characterised using SEM analyses using a Zeiss EVO LS25 SEM (Carl Zeiss Microscopy GmbH, Jena, Germany) with a  $\text{LaB}_6$  emitter. Secondary electron micrographs were recorded at  $\times 2.5$  k magnification, 3 kV acceleration and 50 pA probe current.

## **5.3 Results**

### **5.3.1 Purity and morphology as a function of relative concentration and microwave time.**

#### ***5.3.1.1 Phase purity***

Figure 5.3 - Figure 5.6 show the series of normalised XRD diffractograms recorded for each tested sodium hydroxide concentration for 0, 10, 20 and 30 seconds of microwave exposure which corresponded to approximate peak temperatures of 294 K, 309 K, 327 K and 351 K respectively. Excluding the reflections from the Si substrate for  $2\theta$  values between  $25^\circ$  and  $30^\circ$  three major set of reflections can be seen that can be attributed to LBZA ( $(001) \approx 6.65^\circ$ ,  $(002) \approx 13.3^\circ$  and  $(003) \approx 19.95^\circ$ )<sup>[67], [71], [122], [127]</sup>, BLBZA ( $(001) \approx 4.4^\circ$ ,  $(002) \approx 8.8^\circ$ ,  $(003) \approx 13.2^\circ$  and  $(004) \approx 17.6^\circ$ )<sup>[1][3]</sup> and ZnO ( $(100) \approx 31.8^\circ$ ,  $(002) \approx 34.4^\circ$ ,  $(101) \approx 36.2^\circ$  matching JCPDS # 01-079-2205)<sup>[69][127]</sup>.

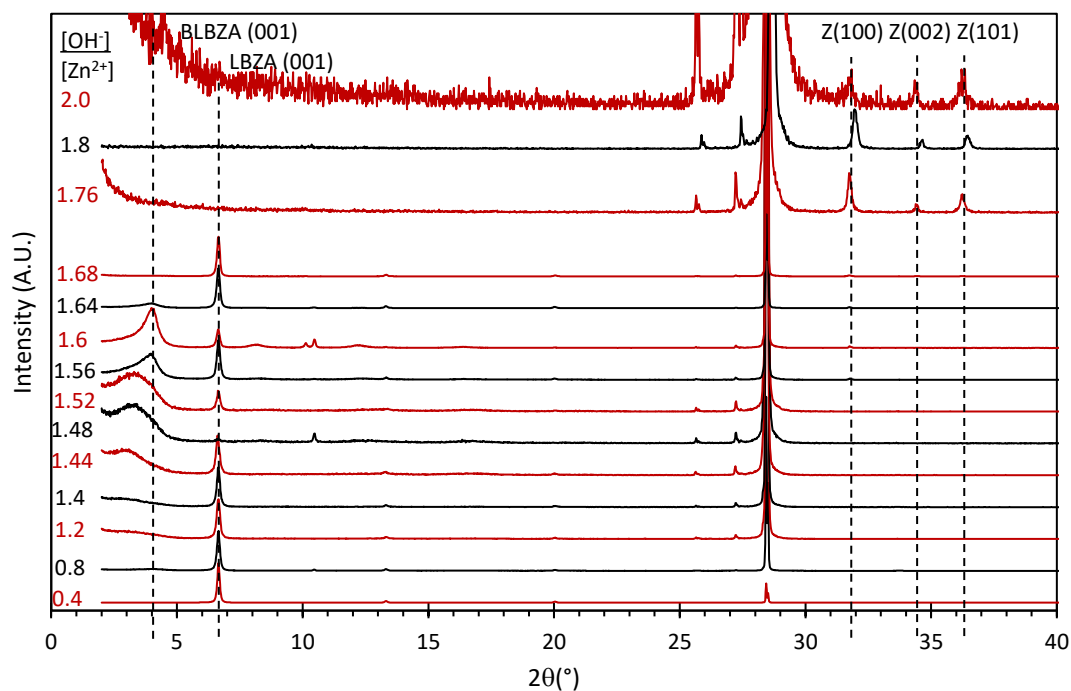


Figure 5.3: Series of XRD diffractograms for LBZA synthesised with 0s of 800W microwave exposure ( $\sim 294$  K) with various  $[\text{OH}^-]/[\text{Zn}^{2+}]$  ratios. Overlaid peak labels for the BLBZA (001), LBZA (001) and ZnO (100), (002) and (101) (labelled Z(100), Z(002), Z(101) respectively) reflections from which the relative peak areas are measured.

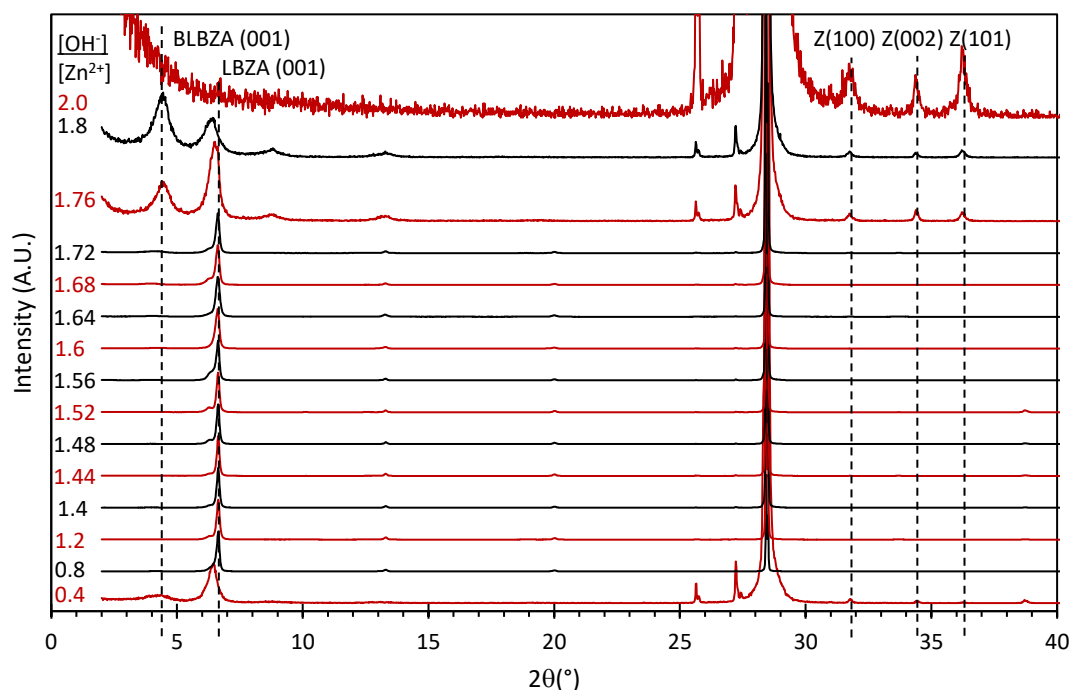


Figure 5.4: Series of XRD diffractograms for LBZA synthesised with 10s of 800W microwave exposure ( $\sim 309$  K) with various  $[\text{OH}^-]/[\text{Zn}^{2+}]$  ratios. Overlaid peak labels for the BLBZA (001), LBZA (001) and ZnO (100), (002) and (101) (labelled Z(100), Z(002), Z(101) respectively) reflections from which the relative peak areas are measured.

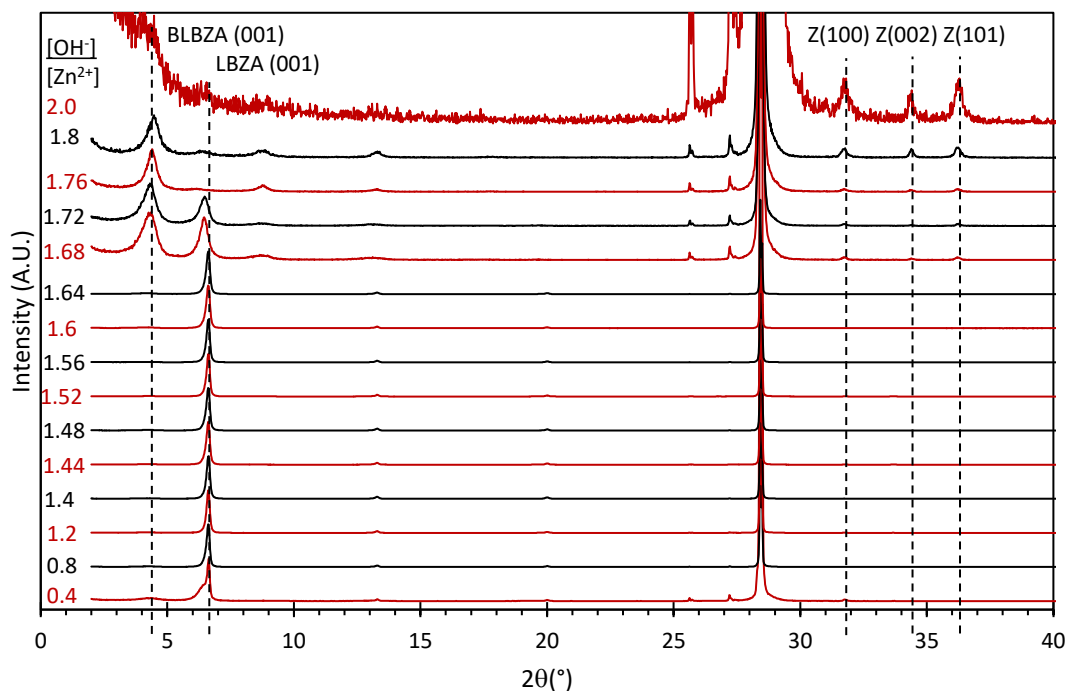


Figure 5.5: Series of XRD diffractograms for LBZA synthesised with 20s of 800W microwave exposure ( $\sim 327$  K) with various  $[\text{OH}^-]/[\text{Zn}^{2+}]$  ratios. Overlaid peak labels for the BLBZA (001), LBZA (001) and ZnO (100), (002) and (101) (labelled Z(100), Z(002), Z(101) respectively) reflections from which the relative peak areas are measured.

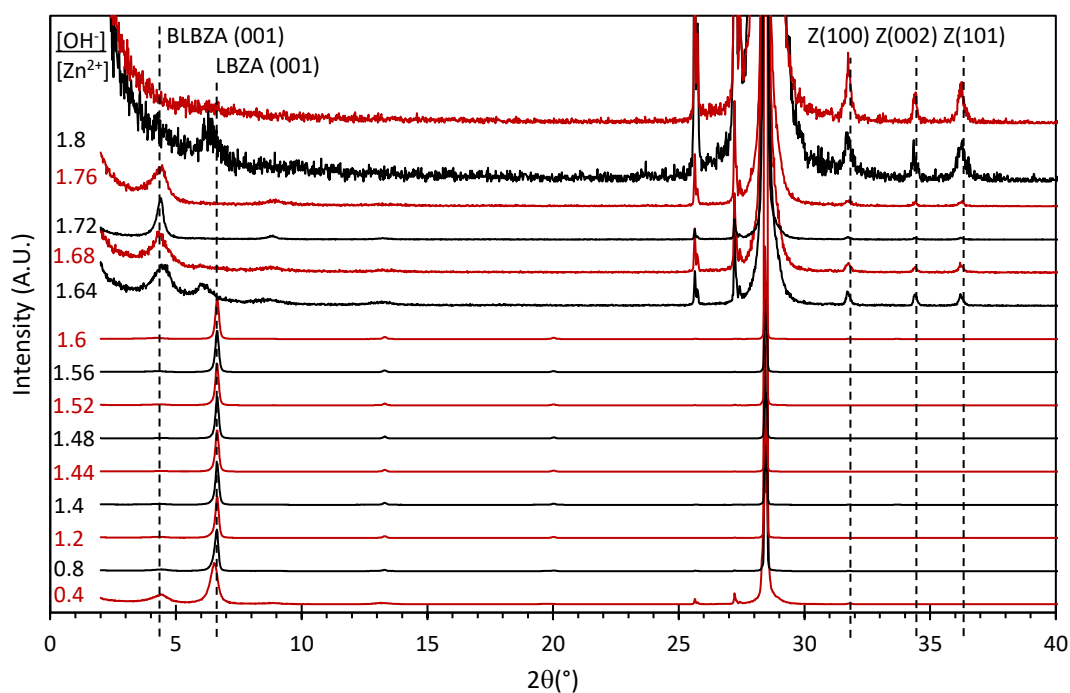


Figure 5.6: Series of XRD diffractograms for LBZA synthesised with 30s of 800W microwave exposure ( $\sim 351$  K) with various  $[\text{OH}^-]/[\text{Zn}^{2+}]$  ratios. Overlaid peak labels for the BLBZA (001), LBZA (001) and ZnO (100), (002) and (101) (labelled Z(100), Z(002), Z(101) respectively) reflections from which the relative peak areas are measured.

The measured relative phase areas for the XRD diffractograms as a function of  $[\text{OH}^-]/[\text{Zn}^{2+}]$  are shown in Figure 5.7. It can be seen that the reactions appear to follow a similar trend with 3 distinct regions for all microwave conditions except for the 0 s unexposed sample (Figure 5.7 a). This sample had a high inter sample variance which was assigned to a high degree of particle entanglement and agglomeration as seen in SEM micrographs (Appendix Chapter 10) and as a result an inhomogeneous reaction medium. The first region consists of  $[\text{OH}^-]/[\text{Zn}^{2+}]$  ratios  $\leq 1.6$  has LBZA as the dominant phase, with BLBZA as second and ZnO as the least dominant phase, the second region consists of ratios in the range  $1.6 < [\text{OH}^-]/[\text{Zn}^{2+}] < 2.0$  where the concentration of LBZA tends to zero, BLBZA initially increases and subsequently tends to zero and ZnO is increasing. The final region consists of  $[\text{OH}^-]/[\text{Zn}^{2+}] = 2.0$  with pure/ nearly pure ZnO and no observed LBZA or BLBZA.

In the first region ( $[\text{OH}^-]/[\text{Zn}^{2+}]$  ratios  $\leq 1.6$ ) the  $[\text{OH}^-]/[\text{Zn}^{2+}]$  ratios of 0.4 had the lowest relative areas of LBZA and highest areas of BLBZA and ZnO within the region irrespective of microwave exposure time (see Table 5.1 for extracted values). Increasing the  $[\text{OH}^-]/[\text{Zn}^{2+}]$  ratio to 0.8 produced a large increase in relative LBZA area and reduction in relative BLBZA and ZnO area. Increasing  $[\text{OH}^-]/[\text{Zn}^{2+}]$  ratio further up to a ratio of 1.6 produced near constant values of relative area with any variations in area over the entire range  $< 0.04$ . Varying microwave time results in a weak change in the mean phase areas with phase areas for 10, 20 and 30 seconds of exposure for LBZA: 0.971, 0.955 and 0.930, BLBZA: 0.016, 0.035 and 0.062 and ZnO: 0.013, 0.009 and 0.008 respectively. The variation with microwave time likely indicates a lower formation energy barrier for LBZA as opposed to BLBZA<sup>[170]</sup>. From TGA experiments of mixed BLBZA/ LBZA systems by Wang *et al.*<sup>[68]</sup> it is known the BLBZA is a layered acetate rich phase and as such the high BLBZA ratio at  $[\text{OH}^-]/[\text{Zn}^{2+}] = 0.4$  is likely due to the high excess of acetate anions in comparison to hydroxide anions. Unlike statements made by Wang and Zhang<sup>[70]</sup>, who reported that the octahedral co-ordination within the unit cell does not exist above a ratio of 1, the results clearly show that the unit cell of LBZA and its octahedral constituents are stable up to an  $[\text{OH}^-]/[\text{Zn}^{2+}]$  ratio of 1.6.

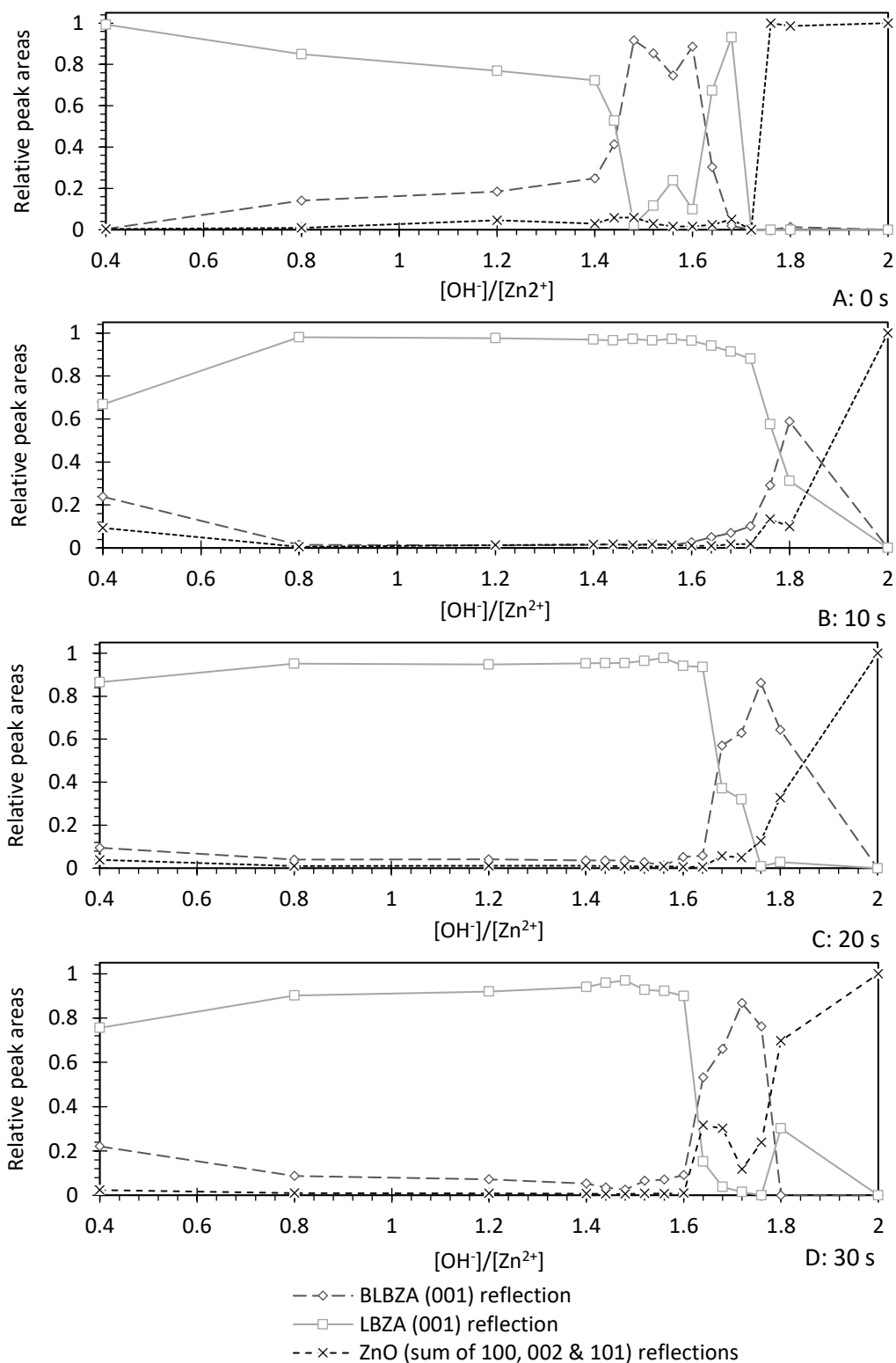


Figure 5.7: Relative peak areas for LBZA (001), ZnO (sum of (100), (002) and (101)) and the (001) peak of a third phase normally attributed to 'BLBZA' as a function of the hydroxide to zinc cation ratio for samples A) without and with B) 10, C) 20 and D) 30 seconds of microwave irradiation at 800 W. The high degree of variability in A is attributed to entanglement of larger particles producing an inhomogeneous distribution of phases. Areas derived from Figure 5.3, Figure 5.4, Figure 5.5 and Figure 5.6.

Phase area	Relative phase areas		
	10 s exposure	20 s exposure	30 s exposure
Region 1: $[\text{OH}^-]/[\text{Zn}^{2+}]$ ratio = 0.4			
LBZA	0.668	0.886	0.756
BLBZA	0.239	0.095	0.221
ZnO	0.093	0.039	0.023
Region 1: Mean and standard deviation of the values of $[\text{OH}^-]/[\text{Zn}^{2+}]$ ratio between 0.8 and 1.6 (Mean $\pm$ 1 S.D.)			
LBZA	$0.971 \pm 0.006$	$0.955 \pm 0.011$	$0.930 \pm 0.025$
BLBZA	$0.016 \pm 0.004$	$0.035 \pm 0.011$	$0.062 \pm 0.023$
ZnO	$0.013 \pm 0.004$	$0.009 \pm 0.002$	$0.008 \pm 0.002$
Region 2: $1.6 < [\text{OH}^-]/[\text{Zn}^{2+}]$ ratio $< 2.0$ Values at peak BLBZA ( $[\text{OH}^-]/[\text{Zn}^{2+}]$ ratio in brackets)			
LBZA	0.574 (1.76)	0.028 (1.8)	0.015 (1.72)
BLBZA	0.291 (1.76)	0.644 (1.8)	0.867 (1.72)
ZnO	0.134 (1.76)	0.328 (1.8)	0.118 (1.72)
Region 3: $[\text{OH}^-]/[\text{Zn}^{2+}] = 2.0$			
LBZA	0	0	0
BLBZA	0	0	0
ZnO	1	1	1

Table 5.1: Representative relative phase areas of LBZA, BLBZA and ZnO in the synthesised and cleaned products for the three regions ( $[\text{OH}^-]/[\text{Zn}^{2+}] \leq 1.6$ ,  $1.6 < [\text{OH}^-]/[\text{Zn}^{2+}] < 2.0$  and  $[\text{OH}^-]/[\text{Zn}^{2+}] = 2.0$ ) for 10, 20 and 30 seconds of microwave exposure. Data extracted from Figure 5.7.

Increasing the  $[\text{OH}^-]/[\text{Zn}^{2+}]$  ratio beyond 1.6 (the second region) results in a decrease in relative LBZA area and an increase in relative BLBZA and ZnO areas suggesting that the chemical potential for hydroxide anions has reached a value favourable for the nucleation and subsequent growth of  $\text{Zn}(\text{OH})_2$ . As  $\text{Zn}(\text{OH})_2$  contains 1.25 times the amount of hydroxide to each zinc cation than LBZA, a higher concentration of hydroxide is consumed per growth unit which results in a rapid drop in hydroxide concentration. As the  $[\text{OH}^-]/[\text{Zn}^{2+}]$  ratio increases, more  $\text{Zn}(\text{OH})_2$  species and nuclei are formed reducing the hydroxide available for LBZA growth and a reduction in measured relative LBZA phase area. In addition to the drop in relative LBZA concentration the consumption of hydroxide leads to an excess in acetate favourable for the formation of BLBZA species. The formation of BLBZA is favoured further by the increase in energy with microwave exposure time as can be seen by comparing the 10 second exposure series to the 20 and 30 s series in Figure 5.7 and the peak measured BLBZA values of 0.291, 0.644 and 0.867 for 10, 20 and 30 seconds respectively (see Table 5.1). Eventually, at  $[\text{OH}^-]/[\text{Zn}^{2+}]$  ratios between 1.72 and 1.8, the increasing zinc hydroxide concentration leaves less zinc cations available to form BLBZA and an inversion point is formed with the relative BLBZA areas reducing and tending to zero as a result. The rate of relative LBZA decrease with  $[\text{OH}^-]/[\text{Zn}^{2+}]$  increases as a function of



microwave time for  $[\text{OH}^-]/[\text{Zn}^{2+}] > 1.6$  and is likely due to a combination of more particles able to cross the activation energy barrier <sup>[170]</sup> and increased hydrolysis of  $[\text{Zn}^{2+}_{(\text{aq})}]$  complexes <sup>[1][9]</sup>. Eventually the  $[\text{OH}^-]/[\text{Zn}^{2+}]$  reaches 2.0 and the area values for LBZA and BLBZA are too low to distinguish from background noise in each scan suggesting near complete conversion to ZnO. This indicates that  $\text{Zn}(\text{OH})_2$  (and subsequently ZnO post hydrolysis) is the most favoured reaction product.

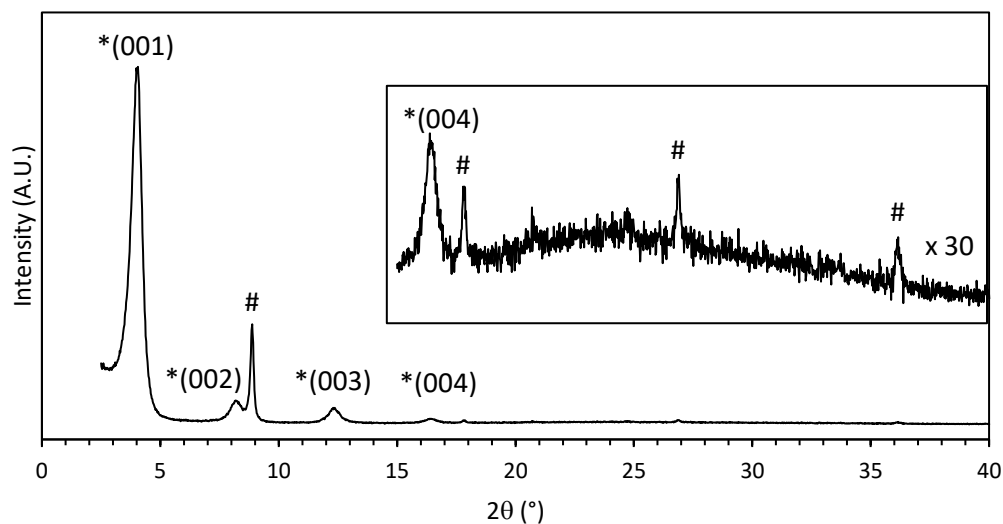


Figure 5.8: XRD diffractogram of particulates sampled from the film present at the liquid air interface of the reaction products for the synthesis using an  $[\text{OH}^-]/[\text{Zn}^{2+}]$  ratio of 1.8 and 20 s of microwave exposure. \* Phase assigned to a hydrated BLBZA <sup>[131]</sup> while # was assigned to a precursor phase <sup>[399]</sup>.

The results follow a similar phase progression for layered hydroxide species produced by Wang *et al.* <sup>[68]</sup> due to hydrolysis of aqueous Zinc acetate species; i.e. at low  $\text{ZnAc}_2$  concentrations, a high acetate to hydroxide ratio results in the formation of mixed BLBZA and LBZA species. Increasing  $\text{Zn}(\text{Ac})_2$  further increases the magnitude of hydrolysis, resulting initially in LBZA, then combined LBZA and ZnO and eventually pure ZnO after which no species were formed. The authors attributed the BLBZA and LBZA to a single ‘BLBZA’ phase, though their arguments in favour of a single phase with double c-axis spacing is not compatible with the Bragg theory of x-ray diffraction as discussed in chapter 3.3.3 where the reflections only exist at spacings equivalent to the unit cell. Their analysis is further called into doubt when considering the measured phase areas of LBZA and BLBZA in Figure 5.7 and Table 5.1, which tended to vary inversely to each other. Figure 5.8 shows a diffractogram of particulates sampled from the film at the liquid air interface of the 20 second irradiated sample with a  $[\text{OH}^-]/[\text{Zn}^{2+}]$  ratio of 1.8 (chosen due to its high BLBZA relative phase area and only minor LBZA phase area). The XRD diffractogram shows a set of peaks relating to the interlayer spacing of a layered structure and its higher order

harmonics. The assigned (001) reflection had a Bragg angle of  $4.07^\circ$  and  $d_{(001)}$  spacing of 2.17 nm which is similar to the lowest reported value of BLBZA Bragg angles of approximately  $4.2^\circ$  and  $d_{(001)} = 2.1$  nm [68]. The difference in value suggests the particles either have internal strain [311] or a different hydration state which has previously been shown to produce shifts of up to 0.5 nm in layered hydroxyacetates [131]. The presence of the BLBZA reflections without LBZA reflections proves that the reflections come from different crystalline phases. Whilst the results show they are separate phases, at present it is not known what the so called BLBZA phase is, as such for the rest of the text the secondary  $d_{(001)}=2.17$  nm phase will still be referred to as BLBZA for simplicity.

Interestingly an additional set of reflections at a Bragg angle of  $8.86^\circ$  and  $d = 0.997$  nm was present which was very similar to a synthesised phase observed by Moezzi *et al.* (distance = 0.94 nm [131]), Biswick *et al.* (Bragg angle =  $8.39^\circ$ ,  $d = 9.337$  nm [400]) and Poul, Jouini and Fievet ( $d = 0.939$  nm [75]), whilst another similar phase was observed by Jingwei *et al.* with  $d = 1.04$  nm [399]. Jingwei *et al.* synthesised the phase in a polyol based hydrolysis reaction whereas the other authors observed the phase during thermal conversion of LBZA to ZnO in TGA and XRD analysis. The phase/s was/ were observed to be extremely moisture sensitive by both Jingwei *et al.* and Biswick *et al.*, transforming to LBZA at room temperature at ambient humidity. This phase is seen heavily during the time progression XRD diffractograms of the stir-rate and addition experiments in section 5.3.2. The phase appears to represent an initial metastable zinc hydroxy acetate precursor phase that is acetate rich in comparison to LBZA, and it appears to undergo a secondary reaction and transformation to form LBZA and will be discussed in detail there. The presence of the phase of the interface suggests an incomplete transformation into LBZA, potentially due to the consumption of hydroxide anions to form zinc hydroxide (and subsequently zinc oxide.) In addition to the relative phase areas, the raw intensities (as plotted as a function of  $[\text{OH}^-]/[\text{Zn}^{2+}]$  ratio in Figure 5.9) were recorded as a qualitative trend in concentration. Whilst there is a high degree of variation with  $[\text{OH}^-]/[\text{Zn}^{2+}]$ , likely a result of minor sample position-diffractometer focal point errors and the small droplet radii, it can be seen for  $[\text{OH}^-]/[\text{Zn}^{2+}] \leq 1.6$  that the magnitude of all phases increases with increasing hydroxide concentration, with the exception of the 0 s sample with a ratio of 0.4, suggesting increased formation and precipitation of all reaction products.

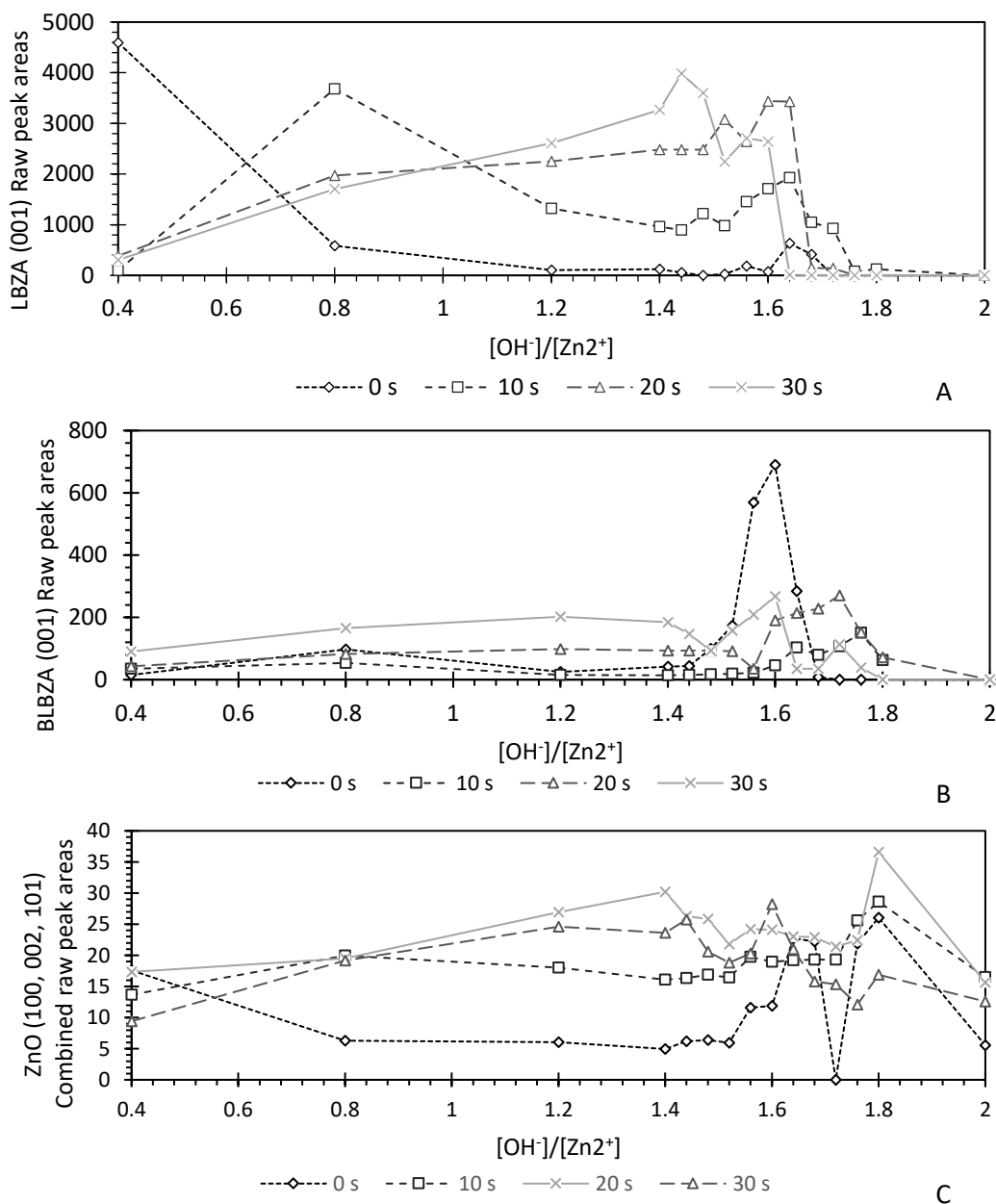


Figure 5.9: Raw recorded area intensities for the A) LBZA (001), B) BLBZA (001) and C) ZnO (combined (100), (002), (101)) as a function of the hydroxide to zinc cation ratio for the sampled volumes microwaved at 800 W for 0, 10, 20 and 30 seconds from the diffractograms shown in Figure 5.3, Figure 5.4, Figure 5.5 and Figure 5.6. All drop-cast samples had a constant 20  $\mu$ L sample volume. Note: Caution should be taken when drawing conclusions on the observed variations of raw intensity as small variations of the sample to focal position and angle can result in large values of error and only broad trends should be considered significant.

An increase in magnitude can also be seen with increasing microwave time suggesting a reaction rate increase. The similarity of the 20 and 30 second intensities suggest either:

- The reaction rate is fast enough for the reaction to complete before being halted by the removal of reactants in the centrifuge step.

- The temperature dependence on the rate of reaction has plateaued, *i.e.*  $e^{-\frac{\Delta G}{RT}}$  (where  $\Delta G$  is the free energy of the transition state) has approached 1 and the reaction rate is diffusion limited [155].

For all microwave times, the raw area shows that LBZA formation increases at a rate at least 3.06 times faster than either BLBZA or Zn(OH)<sub>2</sub>, suggesting a significantly higher reaction rate. Whilst the magnitude of recorded signal and hence products increases with microwave time, the increase in mean absolute area divided by the area at [OH<sup>-</sup>]/[Zn<sup>2+</sup>] = 0.4 for LBZA decreases with microwave time whilst BLBZA and ZnO increase as shown in Table 5.2.

Microwave time (s)	Mean area of intensity for [OH <sup>-</sup> ]/[Zn <sup>2+</sup> ] ratios of X / Intensity area for [OH <sup>-</sup> ]/[Zn <sup>2+</sup> ] ratio = 0.4 (1.4 ≤ X ≤ 1.6)					
	LBZA		BLBZA		ZnO	
	Mean	Std Dev	Mean	Std Dev	Mean	Std Dev
10	12.21	3.28	0.63	0.34	1.27	0.11
20	7.19	1.05	2.35	1.19	1.46	0.16
30	8.40	1.74	1.96	0.66	2.43	0.38

Table 5.2: Table of Mean and St Dev of raw XRD intensity area ratios for ([OH<sup>-</sup>]/[Zn<sup>2+</sup>] = X) divided by the area ratio for ([OH<sup>-</sup>]/[Zn<sup>2+</sup>] = 0.4 for values of 1.4 ≤ X ≤ 1.6 for LBZA, BLBZA and ZnO for each microwave exposure time. Derived from the values in Figure 5.9.

Combining the absolute and relative phase area results suggest that for [OH<sup>-</sup>]/[Zn<sup>2+</sup>] ratios ≤ 1.6 the reaction rate of all products increases with both microwave time (at least up to exposure times of 20 seconds) and [OH<sup>-</sup>]/[Zn<sup>2+</sup>] ratio (increasing the [OH<sup>-</sup>]/[Zn<sup>2+</sup>] by a factor of 4 results in at least a factor of 8 increase in raw recorded area for LBZA.) From the relative results, increasing the [OH<sup>-</sup>]/[Zn<sup>2+</sup>] ratio above 0.4 increases phase purity because of the increased LBZA reaction rate compared to the BLBZA and ZnO side products, as shown by the absolute phase areas. In comparison to the purity increase with the [OH<sup>-</sup>]/[Zn<sup>2+</sup>] ratio, increasing microwave time results in a decrease in relative purity as a result of the higher relative increase in reaction rate of BLBZA and ZnO, suggesting the phases may be thermodynamically more stable [155].

### 5.3.1.2 Morphological analysis

#### 5.3.1.2.1 Results

Figure 5.10 to Figure 5.13 show representative SEM micrographs with measured length histograms ( $n = 100$ ) for the reaction products at  $[\text{OH}^-]/[\text{Zn}^{2+}]$  ratios of 0.4, 0.8, 1.2, 1.4, 1.6, 1.8 and 2.0 for microwave exposures of 0, 10, 20 and 30 s (peak temperatures of 294 K, 309 K, 327 K and 351 K) respectively.

In the secondary electron images two main phases can be generally seen, for  $[\text{OH}^-]/[\text{Zn}^{2+}]$  ratios  $\leq 1.6$  the particles are predominantly long nanobelts or nanosheet/ nanoplatelets typical of LBZA whilst for  $[\text{OH}^-]/[\text{Zn}^{2+}]$  ratio  $> 1.6$  increasing amounts of nanocrystalline ZnO forms. Low angle backscatter images (labelled 1.6:1 IL i.e. in lens detector) reveal an additional nanocrystalline phase much shorter, narrower and thinner than that of the LBZA phase present in all samples imaged ( $[\text{OH}^-]/[\text{Zn}^{2+}]$  ratios  $\leq 1.6$ ; all images are available in Appendix Chapter 10). Low angle backscatter images (Figure 5.15) of the particles sampled from the 1.8  $[\text{OH}^-]/[\text{Zn}^{2+}]$  ratio, 20 seconds irradiated liquid air interface reveal the same particles which from the XRD data of Figure 5.8 can be assigned to the so called BLBZA phase.

It can be seen that length and lateral aspect ratio of the precipitated LBZA is heavily dependent on both the  $[\text{OH}^-]/[\text{Zn}^{2+}]$  ratio and microwave time forming nanobelts at low microwave times and  $[\text{OH}^-]/[\text{Zn}^{2+}]$  ratios with a maximum observed length of 162.6  $\mu\text{m}$  and aspect ratio of 263 ( $[\text{OH}^-]/[\text{Zn}^{2+}]$  ratio = 1.4, microwave exposure time = 0 s) and platelets or sheets at an  $[\text{OH}^-]/[\text{Zn}^{2+}]$  ratio = 1.6 and microwave time of 30 s.

Figure 5.14 shows plots for the mean and standard deviations of both length and aspect ratio as a function of  $[\text{OH}^-]/[\text{Zn}^{2+}]$  ratio for each microwave time, representing the magnitude and polydispersity of values. For all microwave times a similar trend can be seen in length and aspect ratio where the LBZA particles initially get longer and more polydisperse in aspect ratio with an increase with  $[\text{OH}^-]/[\text{Zn}^{2+}]$  ratio, as shown by an increase in both mean and standard deviation initially, before reaching a maximum length at an  $[\text{OH}^-]/[\text{Zn}^{2+}]$  ratio of 1.2 - 1.4, after which a reduction is observed.

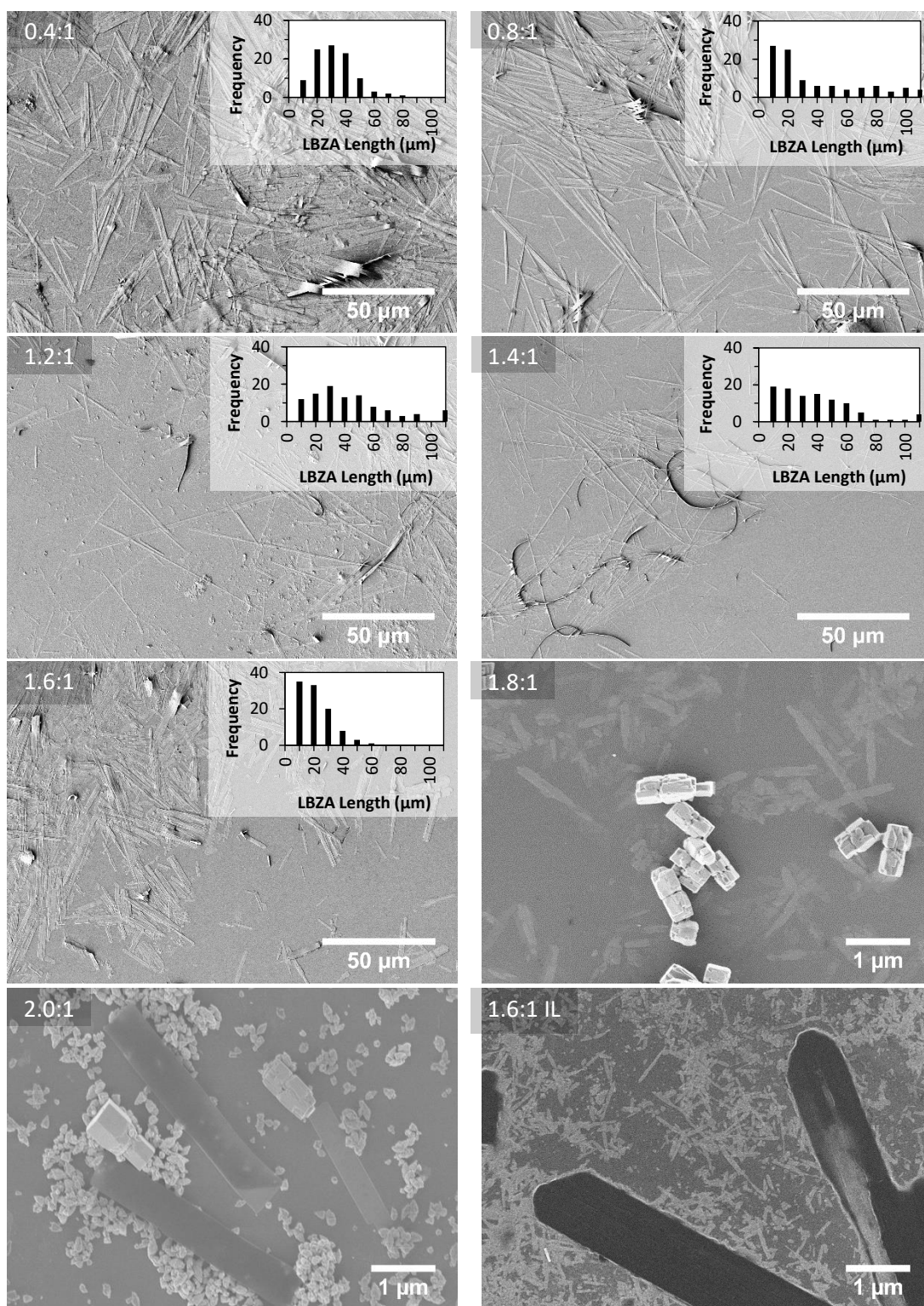


Figure 5.10: SEM micrographs of LBZA synthesised without microwave exposure ( $\sim 294$  K) using  $[\text{OH}^-]/[\text{Zn}^{2+}]$  ratios (ratio in top left corner) of 0.4:1, 0.8:1, 1.2:1, 1.4:1, 1.6:1, 1.8:1, 2.0. For the ratios of 1.8 and 2.0 the light product is ZnO nanocrystals whilst the darker structures are LBZA. 1.6:1 IL shows a higher magnification low angle backscatter micrograph containing LBZA (Large dark crystal) and BLBZA (smaller light colour structures.) Inserts: LBZA length measurement histograms showing degree of polydispersity,  $n = 100$ .

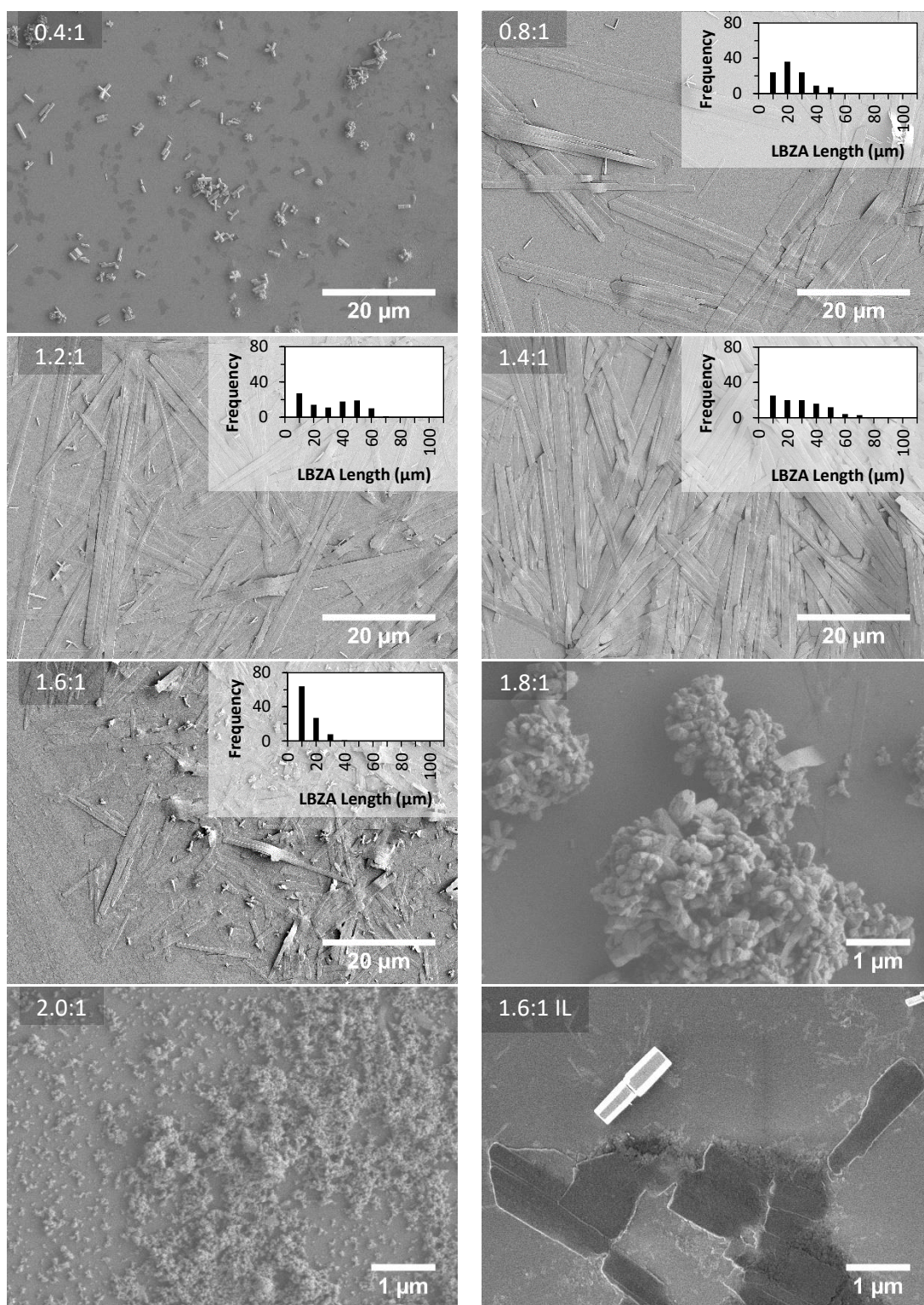


Figure 5.11: SEM micrographs of LBZA synthesised with 10 seconds of microwave exposure ( $\sim 309$  K) using  $[OH^-]/[Zn^{2+}]$  ratios (ratio in top left corner) of 0.4:1, 0.8:1, 1.2:1, 1.4:1, 1.6:1, 1.8:1, 2.0. For the ratios of 0.4, 1.8 and 2.0 the light product is ZnO nanocrystals whilst the darker structures are LBZA. 1.6:1 IL shows a higher magnification low angle backscatter micrograph containing dumbbell ZnO (bright white), LBZA (Large dark crystal) and BLBZA (smaller light colour structures). Inserts: LBZA length measurement histograms showing degree of polydispersity,  $N = 100$ .

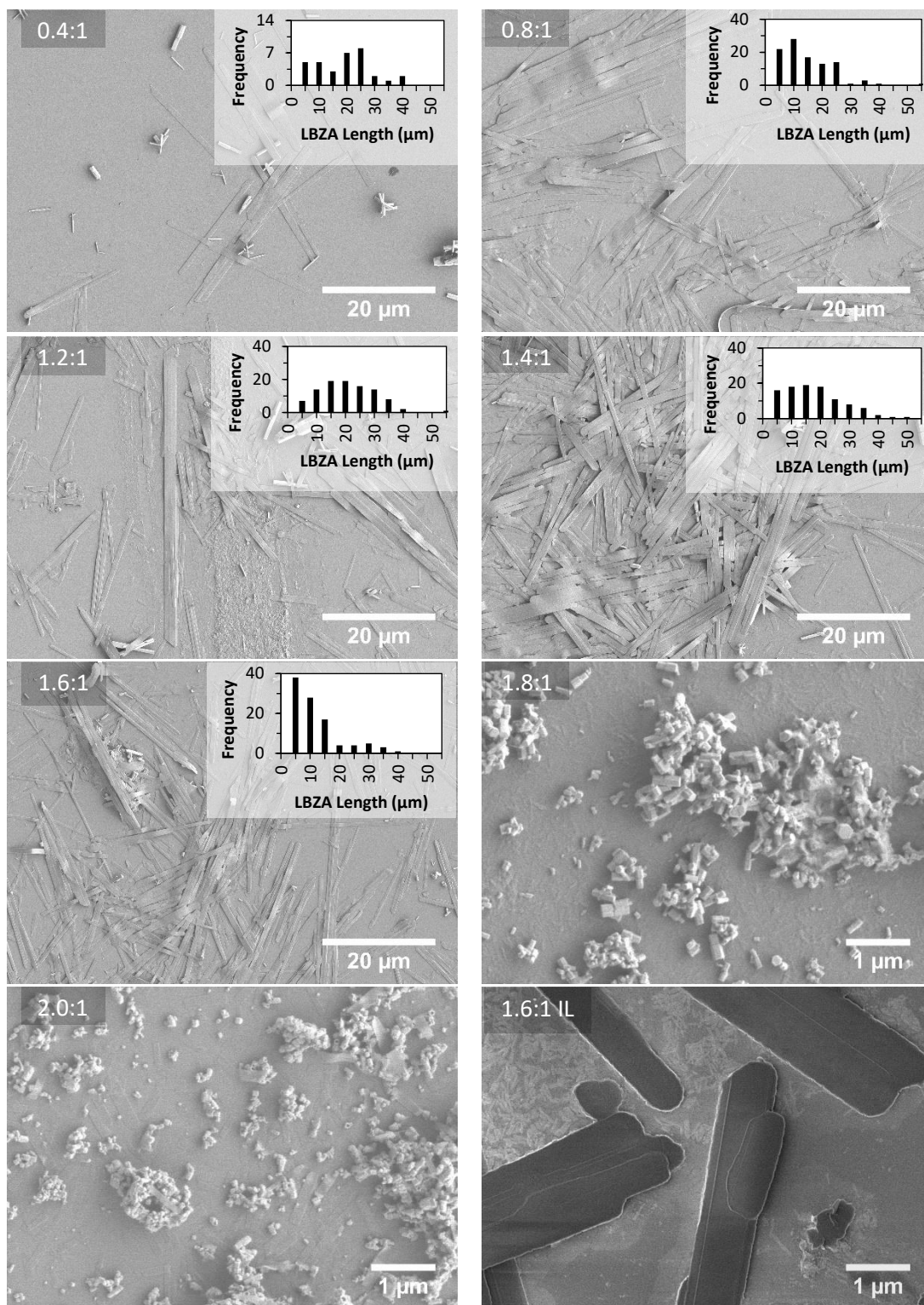


Figure 5.12: SEM micrographs of LBZA synthesised with 20 seconds of microwave exposure ( $\sim 327$  K) using  $[\text{OH}^-]/[\text{Zn}^{2+}]$  ratios (ratio in top left corner) of 0.4:1, 0.8:1, 1.2:1, 1.4:1, 1.6:1, 1.8:1, 2.0. For the ratios of 0.4, 1.8 and 2.0 the light product is ZnO nanocrystals whilst the darker structures are LBZA. 1.6:1 IL shows a higher magnification low angle backscatter micrograph containing dumbbell ZnO (bright white), LBZA (Large dark crystal) and BLBZA (smaller light colour structures). Vertical strip through the centre of 1.2 appears to be made from smaller crystallites. Inserts: LBZA length measurement histograms showing degree of polydispersity,  $N = 100$ .



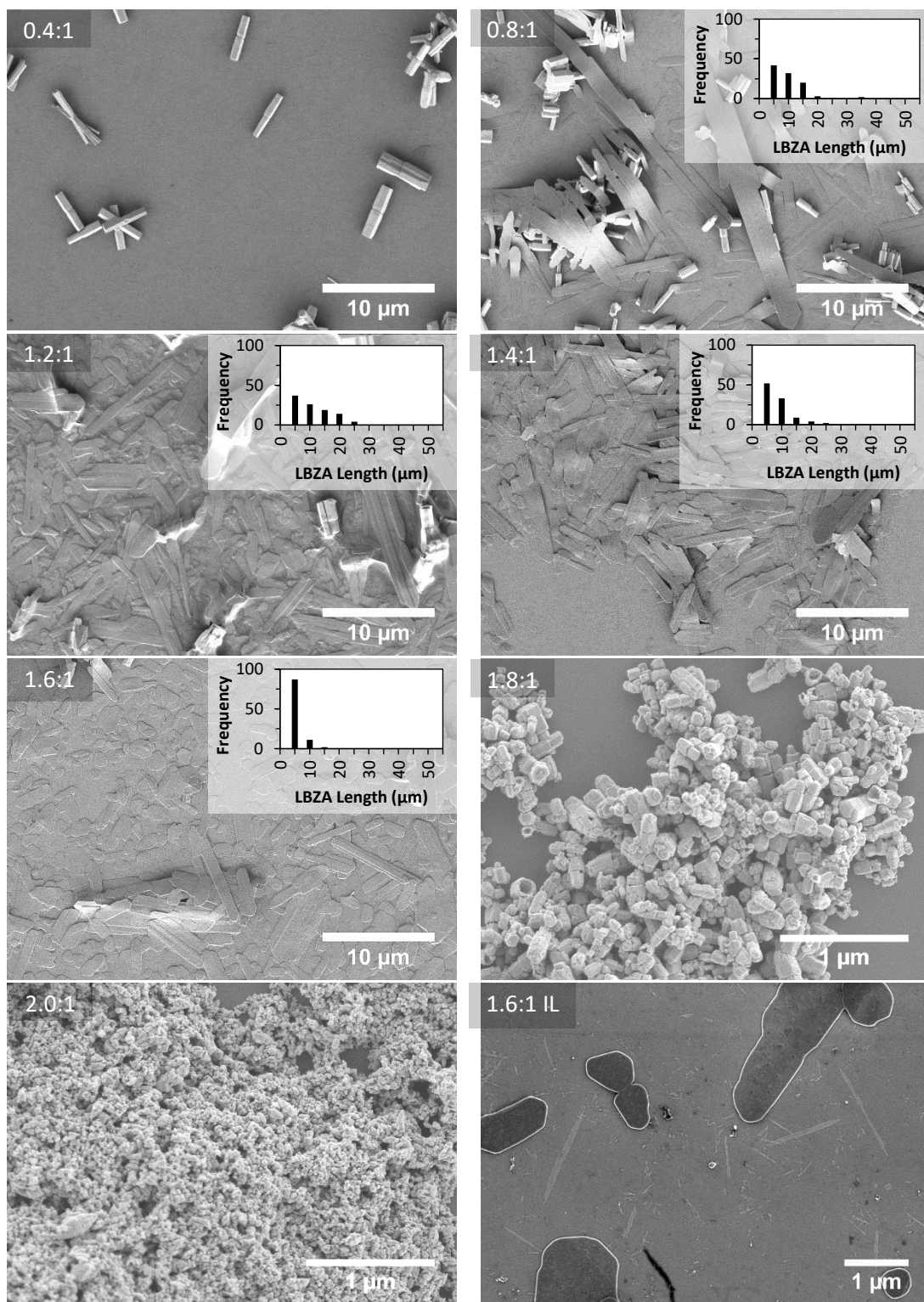


Figure 5.13: SEM micrographs of LBZA synthesised with 30 seconds of microwave exposure ( $\sim 351$  K) using  $[\text{OH}]:[\text{Zn}^{2+}]$  ratios (ratio in top left corner) of 0.4:1, 0.8:1, 1.2:1, 1.4:1, 1.6:1, 1.8:1, 2.0. For all ratios the light product is ZnO nanocrystals whilst the darker structures are LBZA. 1.6:1 shows a higher magnification low angle backscatter micrograph LBZA (Large dark crystal) and BLBZA (smaller light colour structures). Inserts: LBZA length measurement histograms showing degree of polydispersity,  $N = 100$ .

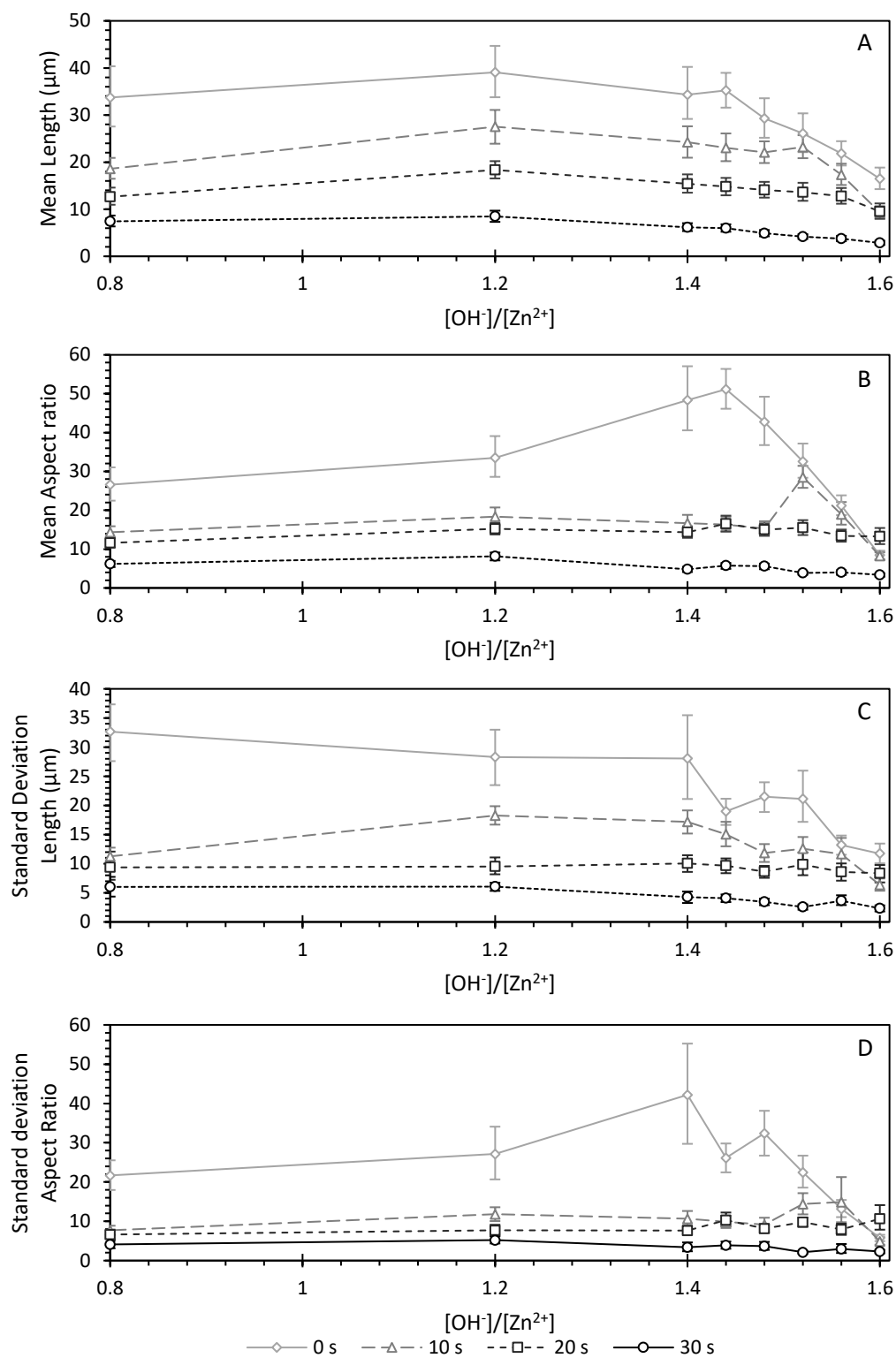


Figure 5.14: Plots of the measured and calculated A) Mean particle length B) Mean particle aspect ratio, C) Standard deviation of particle length and D) Standard Deviation of particle aspect ratio as a function of hydroxide to zinc cation ratio for 0, 10, 20 and 30 seconds 2.45 GHz microwave irradiation at 800 W measured from SEM micrographs. Samples measured = 100, error bars represent the 95% confidence intervals calculated by the bootstrapping method in MATLAB. Standard deviation values represent polydispersity in particle size distribution.

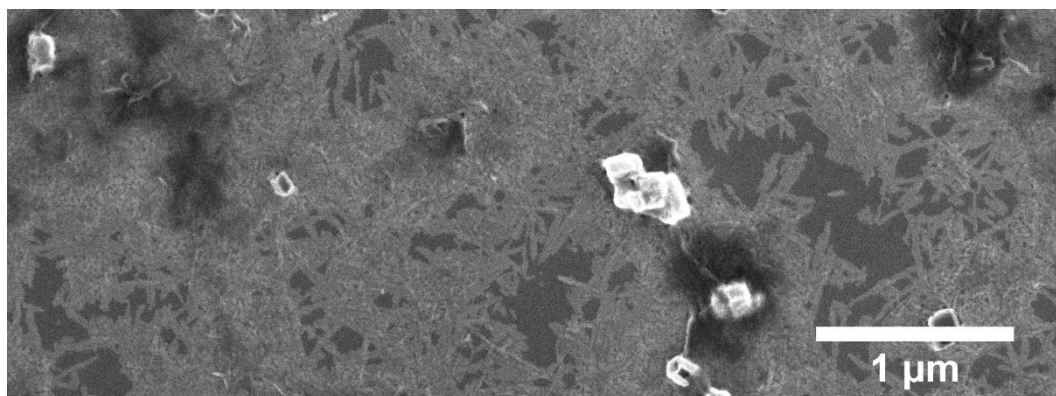


Figure 5.15: Low angle backscatter SEM micrograph of the particles sampled from the 20 s irradiated 1.8 [OH<sup>-</sup>]/[Zn<sup>2+</sup>] ratio liquid air interface film. From the XRD analysis of Figure 5.8, the majority of observed particles (light grey, rectangular structures) are assigned to be 'BLBZA'.

Using simplified assumptions that growth in length and width are proportional to reaction rate and the effective rates follow a simple Arrhenius relation <sup>[155]</sup> of the form seen in Equation 5.5:

$$\text{Growth rate} \approx A[\text{reactant}]^n e^{-\frac{E_a}{RT}}$$

Equation 5.5

Where  $A$  represents the collision frequency of reactants in the correct configuration required to react,  $[\text{reactant}]$  is the concentration of growth unit,  $n$  the order of reaction (dependent on the number of reactant molecules used in the reaction),  $E_a$  is the energy barrier of activation in  $\text{Jmol}^{-1}$ ,  $R$  is the gas constant  $8.314 \text{ JK}^{-1}\text{mol}^{-1}$  and  $T$  is temperature in K.

The aspect ratio can then be calculated according to:

$$\begin{aligned} \text{Aspect ratio} &\propto \frac{\text{Growth rate}_{\text{length}}}{\text{Growth rate}_{\text{width}}} \approx \frac{A_l[\text{reactant}]^n e^{-\frac{E_{a-\text{length}}}{RT}}}{A_w[\text{reactant}]^n e^{-\frac{E_{a-\text{width}}}{RT}}} \\ &\approx A_{l/w} e^{-\frac{(E_{a-\text{length}} - E_{a-\text{width}})}{RT}} = A_{l/w} e^{\frac{E_{a-\text{width}} - E_{a-\text{length}}}{RT}} \end{aligned}$$

Equation 5.6

Where  $A_{l/w}$  represents the ratio of  $A_l$  and  $A_w$ , and reactants are approximated to cancel on the basis that the crystal must be homogenous in each direction based on the definition of a crystal (i.e. the requirement of long range translation symmetry).

Performing regression analysis on the entire data sets of aspect ratio for all microwave times and  $[\text{OH}^-]/[\text{Zn}^{2+}]$  ratios of 0.8 and 1.2 ( $n_{\text{total}}=800$ ), on  $\ln(\text{Aspect ratio})$ ,  $1/T_{\text{peak}}$  and  $\ln([\text{OH}^-]/[\text{Zn}^{2+}])$  produces the following relation:

$$\ln(\text{Aspect ratio}) = \frac{792.74}{T_{\text{peak}}} + 0.588 \ln\left(\frac{[\text{OH}^-]}{[\text{Zn}^{2+}]}\right)$$

Equation 5.7

Where the  $\frac{1}{T_{\text{peak}}}$  coefficient has a p-value of 0 (rounding error due to the finite memory size in Excel), the  $\ln\left(\frac{[\text{OH}^-]}{[\text{Zn}^{2+}]}\right)$  coefficient has a p-value of  $2.29 \times 10^{-5}$  and the adjusted  $R^2$  value of the regression relation is 0.9066. The adjusted  $R^2$  and p-values suggest a good fit to the data, accounting for the vast majority of the variance within the data and that the coefficients are statistically significant. Scaling the  $\frac{1}{T_{\text{peak}}}$  coefficient by  $R$  to get the energy barrier difference and taking the exponential of Equation 5.7 results in the relation:

$$\text{Aspect ratio} = 1.8 \left(\frac{[\text{OH}^-]}{[\text{Zn}^{2+}]}\right) e^{\frac{6590.84}{RT_{\text{peak}}}}$$

Equation 5.8

Where the energy barrier difference  $E_{a \text{ width}} - E_{a \text{ length}} = 6590.8 \text{ Jmol}^{-1} = 6.59 \text{ kJmol}^{-1}$  or  $E_{a \text{ width}} - E_{a \text{ length}} = 0.0683 \text{ eV per growth unit} = 2.697 k_B T$  at 294 K. The small difference in apparent rate energy barriers compared to the thermal energy per growth unit  $k_B T$  can describe the dramatic difference in morphology with relatively small changes in temperature. The  $\frac{[\text{OH}^-]}{[\text{Zn}^{2+}]}$  dependency likely arises due to a non-linear effect of concentration in the pre-exponent factor and the chemical potential factor which would appear in the exponent and is therefore a result of the simplification in the approximation. For higher ratios a secondary process can be seen and would reduce the accuracy of the energy barrier difference.

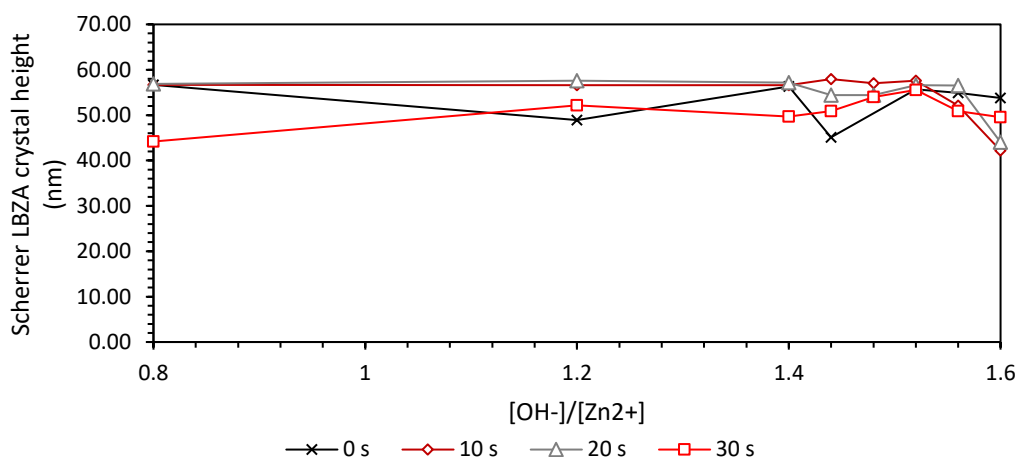


Figure 5.16: Thicknesses for LBZA as a function of  $[OH^-]/[Zn^{2+}]$  ratio for 0 s, 10 s, 20 s and 30 s microwave exposure. Heights calculated via Scherrer equation on the LBZA (001) from the diffractograms in Figure 5.3 - Figure 5.6

Figure 5.16 shows Scherrer equation analysis of the synthesised LBZA, which shows little to no change in LBZA thickness with microwave exposure or  $[OH^-]/[Zn^{2+}]$  ratio, with means (standard deviation) of 53.1 nm (4.4 nm), 54.6 nm (5.33 nm), 54.7 nm (4.5 nm) and 50.8 nm (3.4 nm) for 0, 10, 20, and 30 seconds of microwave exposure respectively. It should be noted that in section 5.3.2.1 that two peaks, likely from two separate LBZA phases with different hydration number were present in non-microwave exposed samples with reflections at  $6.00^\circ$  and  $6.25^\circ$ . The variance in here likely results from a change in the envelope FWHM due to a relative change in area between the LBZA peak at approximately  $6.6-6.65^\circ$  and that at  $6.25^\circ$ . Consequently, the Scherrer derived crystalline thickness should be taken as a minimum value. The lack of any significant change in mean height, however, suggests that the energy barriers for growth in the [001] direction are significantly greater than that for both lengthwise and width-wise growth.

### 5.3.1.2.2 Discussion

#### 5.3.1.2.2.1 Polydispersity and total magnitude of dimensions

Based on the observed instantaneous precipitation in all systems it is likely that burst nucleation (as described by continuous nucleation theory (CNT) covered in chapter 2.1.3.4) occurs to an extent under all concentrations. As stated earlier, it will be shown in section 5.3.2 that LBZA formation proceeds via complexation and precipitation of a zinc hydroxy

acetate precursor phase (that was first observed in the supernatant diffractogram in section 5.3.1.1) . It will be shown there that an inefficiency in mass transport/ mixing rate at the point of addition results in slurry formation and consequently that the hydroxide is not fully mixed until stir times  $\geq 75$  seconds. As such, the observed increase and subsequent decrease in length and aspect ratio polydispersity with increasing  $[\text{OH}^-]/[\text{Zn}^{2+}]$  ratio can be interpreted by the following factors:

- The initial increase in polydispersity results from a reduction in mass transport due to increased slurry formation in combination with incomplete formation of the precursor phase. The increased slurry formation results from an increase in particle density that undergoes agglomeration due to the high ionic strength of the solution<sup>[401]</sup>. In light of CNT this region can be considered to have a Zinc hydroxy acetate and Zinc hydroxide complex chemical potentials large enough to undergo burst potential at the point of addition (indicated by formation of the slurry). The formation of the slurry reduces the mixing and the ability to homogenise the reactants. Nucleation therefore occurs over the period of the reaction resulting in high polydispersity. The increased length with concentration is simply due to more material being available for growth to occur.
- The subsequent decrease in polydispersity, that was observed to coincide with a reduction in viscosity, can be viewed as a decrease in the nucleation time period due to greater diffusion gradients, and a lowering of the ionic strength due to more particulates.. The reduced ionic strength would limit aggregation<sup>[401]</sup> and thus reduce viscosity, improving mixing and reducing the nucleation time period. This can be viewed as being analogous to the presence of reducing amounts of initial continuous nucleation, and an increase in burst nucleation, on the effects of nucleation time on polydispersity in CNT. As more particles are produced over a shorter time period there is a larger total nucleated particle surface area and so the amount of growth per particle, and hence length, decreases.

As nucleation is spontaneous, diffusion barriers control the reaction rate for nucleation. Increasing temperature increases diffusion rates<sup>[1]</sup>;reducing the time period that nucleation occurs over.. As the diffusion rate increases, due to an increase in temperature, the effect of formation and viscosity of the slurry on the nucleation rate is reduced. The magnitude of the aforementioned trend in polydispersity with  $[\text{OH}^-]/[\text{Zn}^{2+}]$  ratio reduces, as observed by the reduction in the rate of change of the standard deviation at  $[\text{OH}^-]/[\text{Zn}^{2+}]$  ratios between 1.4 and 1.6 as temperature increases.

### 5.3.1.2.2.2 *Lateral and vertical aspect Ratio*

The high aspect ratio of the synthesised particles and decreasing aspect ratio with microwave time suggests that the anisotropy has a kinetic rather than thermodynamic origin <sup>[170]</sup>. For the resulting anisotropy to occur there must be a breaking of symmetry, with a difference in the rate of reaction between the different axis, leading to a more significant reaction rate and growth along the length as compared to the width <sup>[170]</sup>. At room temperature the difference in reaction rates produces the high aspect ratio nanobelts as seen in Figure 5.10, as temperature increases, the aspect ratio reduces resulting in the more typical platelet like morphology with more irregular shapes.



Figure 5.17: (Cropped and enlarged image of Figure 5.11 1.6 IL) Low angle backscatter micrograph of aggregation of small LBZA nanoparticles and larger LBZA particles suggesting growth of oriented attachment in the  $[\bar{1}10][1\bar{1}0]$  direction (directions of attachment shown by arrows). Growth conditions  $[OH^-]/[Zn^{2+}]$  ratio of 1.6, microwave exposure 10 seconds at 800 W. The size of individual small nanoparticles (with size large enough to measure) had a mean of 58 nm ( $n=35$ ).

The appearance of what appears to be oriented attachment can be seen in the enlarged in lens backscatter images (Figure 5.17) extracted from the 10s exposure 1.6 ratio synthesis, where particles appear to either be undergoing fusion or dissolution/ breakup at their ends (white arrows). Close observation of the surface texture reveals patterns like those seen forming at the ends suggesting that a significant portion of growth is due to undergo end to end oriented attachment of smaller sub 90 nm particles in accordance with the HRTEM results presented by Li, Zhang and Wang <sup>[70]</sup>. The presence of aggregation of nanoparticles and the high aspect ratio is therefore expected to proceed via the same process for all the reactions in water which produce similar results, evolving from both primary growth (deposition) and oriented attachments on multiple scales.

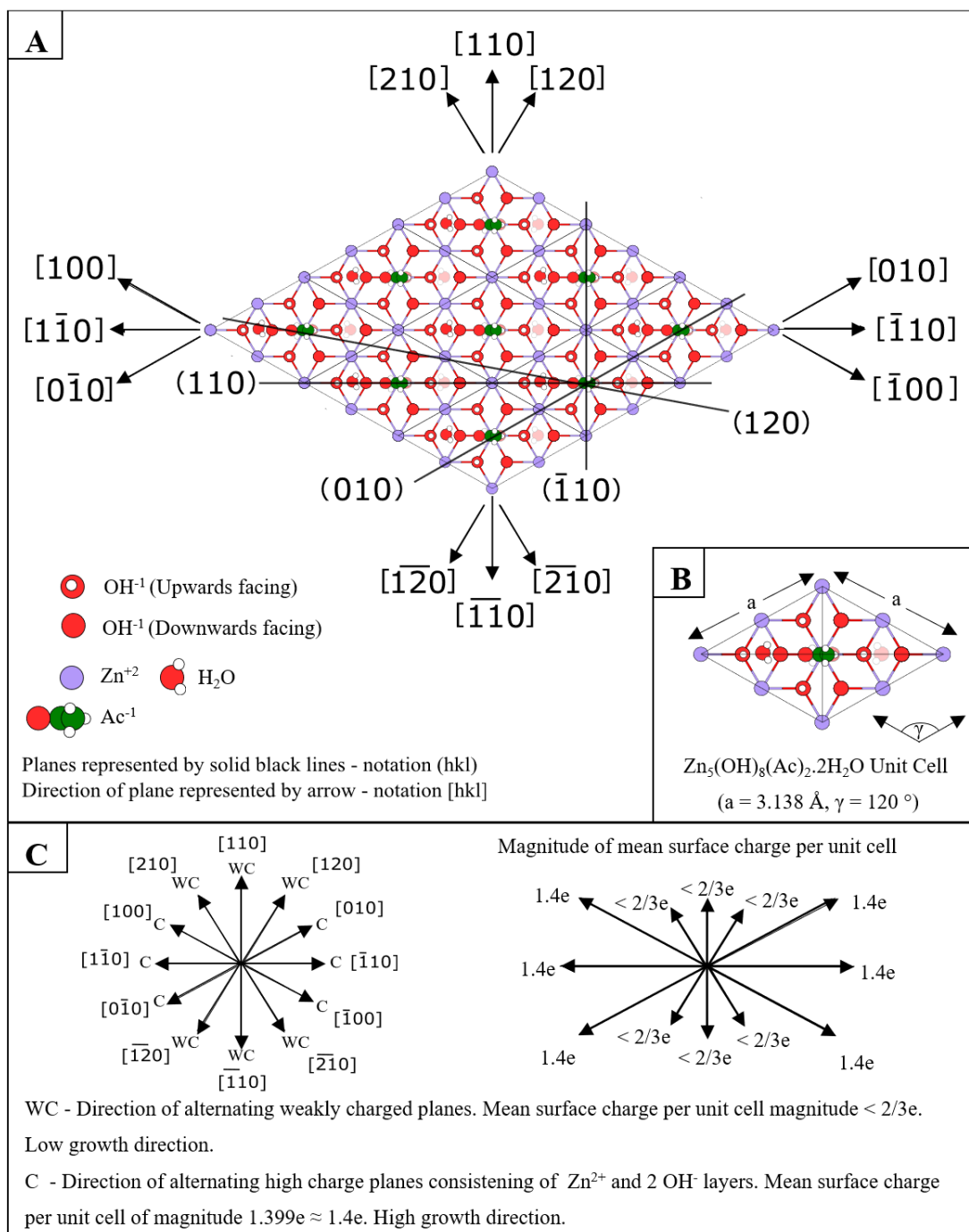


Figure 5.18: (A) Representative LBZA super cell structure (for  $c = 0$ ) with annotated plane directions and example planes. The planes represent surfaces with the 4 main lines of symmetry produced using the  $120^\circ$  rotation symmetry operation of the space group on the hexagonal basis unit vectors. Note that it reproduces the cubic/ cartesian basis unit vectors i.e.  $[\bar{1}\bar{1}0]$  representing the x axis and  $[110]$  the y axis. (B) Top down view of the LBZA unit cell. LBZA unit cell structure based on the structure of  $Zn_5(OH)_8Cl_2 \cdot H_2O$ <sup>[132]</sup> which is an isostructural chloride analogue<sup>[75]</sup> of the hydrozincite. Both tetrahedral zinc and acetate ions are directly below the visible acetate. Each tetrahedral zinc is co-ordinated to 3 hydroxide and 1 acetate anion. Values for the LBZA lattice constants from measurements by Poul, Jouini and Fievet<sup>[75]</sup>, crystal belongs to the  $R\bar{3}M$  space group. (C) Diagrams represent the surface charge density for the planes in each  $[hkl]$  direction. C notation - planes consisting of alternating layers of all  $[Zn^{2+}]$  or  $2[OH^-]$ , surfaces consist of planes with a mean charge of magnitude 1.39e per unit cell. WC notation - planes have a mixed species with a slight imbalance in co-ordination number and with a mean charge magnitude  $< 0.667e$  per unit cell. Plotting the mean observed surface charge density per unit cell produces the observed anisotropy.



To understand how primary growth and orientated attachment affect the growth mechanism and the aspect ratio and morphology produced here, and for water based LBZA growth in general, it is important to analyse the unit cell for any breaks in symmetry that would result in the observed anisotropy and to account for any effects of the microwave exposure that may alter the reaction pathway. LBZA and simonkolleite (zinc hydroxychloride) belong to the hydrozincite family of layered hydroxides sharing a common basal layer <sup>[400]</sup>, and are part of the  $R\bar{3}M$  space group <sup>[75]</sup> (unit cell shown in Figure 5.18 (b)) and as a result is symmetrical upon rotating  $120^\circ$  and inverting.

LBZA has unit cell parameters (abc) within the hexagonal basis of  $a = b = 3.138 \text{ \AA}$  (lateral or basal layer basis vectors),  $c = 14.75 \text{ \AA}$  <sup>[75]</sup> (vertical or interbasal/ gallery layer unit vector)  $\alpha = \beta = 90^\circ$  (basal to interbasal angle) and  $\gamma = 120^\circ$  (basal angle) and has lattice spacing  $d_{(hkl)}$  for the plane (hkl) with unit cell basis vectors (abc) described by Equation 5.9 <sup>[402]</sup>:

$$\frac{1}{d^2} = \frac{4}{3} \left( \frac{h^2 + hk + k^2}{a^2} \right) + \frac{l^2}{c^2}$$

Equation 5.9

It should be noted that the unit cell of the LBZA grown in an organic medium by Poul *et.al.* <sup>[75]</sup> showed significant turbostratic (misaligned layer) lattice distortion, they are to the authors knowledge the only authors to measure the lattice cell constants for each dimension.

This is a general property of LBZA grown in organic solvents <sup>[403]</sup>, the values for LBZA synthesised in water would be expected to differ via a small degree due to the reduced distortion. In addition, analysis by Biswick *et al.* suggested that the position of acetate and water were inverted in comparison to simonkoellite as in the case of Zinc hydroxynitrate <sup>[400]</sup>.

Figure 5.18 (a) shows a 2D slab made up of a single basal layer of 3x3 unit cell of LBZA in the hexagonal basis with annotated plane directions and example planes. Analysing the slab reveals 3 sets of planes, (100), (010) and (1 $\bar{1}$ 0), each with a repeating pattern of alternating  $n[\text{Zn}^{2+}]$  and  $2n[\text{OH}^-]$  layers, where n is dependent on the width of the layer. The layers have inversion symmetry, with the symmetry point located between the tetrahedrally co-ordinated zinc cations. Applying the symmetry operations to the planes with net charge produces the (110), (210) and (120) and their inversion symmetric planes. The (110), (210) and (120) planes are made up of mixed  $[\text{Zn}^{2+}]$  and  $[\text{OH}^-]$  layers with minor charge imbalance. Creating a surface by plotting an example plane for each and then counting the number of dangling

bonds per ion, multiplying each by the ion charge and summing over a unit cell produce the net charge of the surface per unit cell as a result of symmetry disruption. Taking the mean of the net charge of the surface per unit cell then allows for calculating the mean charge per unit cell direction. Figure 5.18(c) shows the plane directions vectors with the relative magnitude of the mean net charge and can be seen to exhibit the observed symmetry breaking required to reproduce the observed aspect ratio. The fact that:

- a stronger charge is present in the  $[1\bar{1}0]$  direction which has the same interplane distance as in the  $[010]$  direction,
- a weaker charge is present in the the perpendicular  $[110]$  direction, that has the same interplane distance as in the  $[\bar{1}20]$  direction

correlates well with the SAED results of van Rijt *et al.* <sup>[166]</sup> where a preferential  $[010]$  growth was observed. It should be noted that due to the large number of potential surfaces that each spanned 2 or more unit cells in the  $[120]$  and  $[210]$ , only the largest observed net charges for the weakly charged surfaces were counted. This resulted in a mean of  $(2/3)e$  per unit cell which can be assumed to be an upper bound.

To describe growth completely, both primary and secondary growth need to be accounted for. Initially, to assess if the internal dipole was significant enough to account for the majority of aspect ratio differences observed, simplified point charge models for neutral edges of the basal layer were created. Calculations were performed on 10 nm, 50 nm and 500 nm wide surfaces for:

- A neutral  $(110)$  surface, with no dipole present
- A  $[Zn^{2+}]$  terminated  $(1\bar{1}0)$  surfaces with an overlayer of  $[OH^-]$  anions. The anions filled 50 % of the  $[OH^-]$  vacancies for the next layer producing a neutral surface.
- A  $[OH^-]$  terminated  $(1\bar{1}0)$  surfaces with an overlayer of  $[Zn^{2+}]$  cations. The cations filled 50 % of the  $[Zn^{2+}]$  vacancies for the next layer producing a neutral surface.

A simplified ball and stick graphical representation of each surface is shown in Figure 5.19. The surfaces were arranged such that all surfaces were neutral, representing the lowest surface potential case, whilst still producing the dipole for the  $(1\bar{1}0)$  surfaces. The arrangement is approximately equivalent to the definition of the Stern layer, where a rigidly bound layer of ions (the overlayer here) is attached to the (terminated) surface to counter any potential arising from the surface charge. For each of the surfaces the stern layer potential  $\Delta\phi$  was calculated for ions approaching the surface along its width, for a single basal layer (thickness =  $c = 1.475$  nm), and 7 stacked basal layers (thickness =  $7c = 10.325$  nm). Then,

the electrostatic factor  $\exp(-Z_{\pm}F\Delta\phi/2RT)$  from Crundwells modification for the reaction kinetics of a charged surface (described in Chapter 2.1.3.5) was calculated. For the factor  $Z$  is the charge number of the ion approaching the surface,  $F$  Faradays constant,  $R$  the gas constant and  $T$  the absolute temperature. The factor was calculated at 294 K and 351 K to check for the magnitude of the change with respect to temperature. The full details (including geometry and effective charges), results and discussion can be found in appendix Chapter 11, with the highlights presented here and compared with the microwave electric field to assess if the microwave is likely to produce a direct (i.e. non thermal) effect on growth. For the calculation Stern layer thickness has been approximated as the radius of the hydrated ion <sup>[404]</sup>.

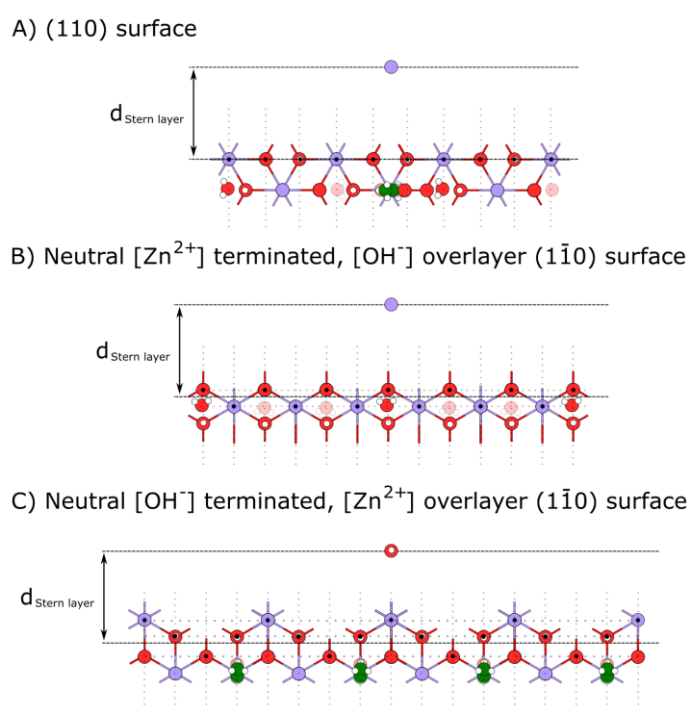


Figure 5.19: Graphical ball and stick representation of a section of the A) Neutral (110), B) Neutral  $[Zn^{2+}]$  terminated  $[OH^-]$  overlayer ( $1\bar{1}0$ ), and C) Neutral  $[OH^-]$  terminated,  $[Zn^{2+}]$  overlayer ( $1\bar{1}0$ ) surfaces used to calculate the Stern layer potential. Note: Red circles (with and without a central white circle) represent  $[OH^-]$  anions, purple  $[Zn^{2+}]$  cations, green circles represent carbon within the acetate molecule. The Black dots represent the placement of the modelled equivalent point charges in the surface calculations, whilst the dashed black line within the surface layer represents the position of the surface i.e. the 0 point from which the 0.25 nm Stern layer is calculated from. A full description of the geometry is provided in appendix Chapter 11.

Table 5.3 shows calculated electrical parameters for a stern layer of thickness  $\sim 0.25$  nm taken in between that of the hydration radius of zinc <sup>[405]</sup> and hydroxide <sup>[406]</sup> aquo complexes. The mean stern layer potential calculated along the single layer ( $1\bar{1}0$ ) surfaces are

approximately 12.4 and 3.32 times the magnitude of the (110) surface for the  $[Zn^{2+}]$  and  $[OH^-]$  overlayer surfaces respectively.

$d_{Stern\ layer} = 0.25\ nm$		( $\bar{1}\bar{1}0$ ) $[OH^-]$ terminated $[Zn^{2+}]$ overlayer	( $\bar{1}\bar{1}0$ ) $[Zn^{2+}]$ terminated $[OH^-]$ overlayer	(110)
1 Layer, thickness = 1.475 nm				
$\phi_{Mean}$ (mV)		104.7	-28.0	8.44
Standard deviation: $\phi$ (mV)		12.2	3.4	6.1
Electric Field <sub>Mean</sub> (V/m)		$4.19 \times 10^8$	$-1.12 \times 10^8$	$3.37 \times 10^7$
294 K	$exp(-Z_+F\Delta\phi/2RT)_{Zn^{2+}}$	0.02	3.02	0.72
	$exp(-Z_+F\Delta\phi/2RT)_{OH^-}$	7.89	0.58	1.18
	Maximum ratio $(\bar{1}\bar{1}0)_{Mean}/(110)_{Mean}$	5.75		
354 K	$exp(-Z_+F\Delta\phi/2RT)_{Zn^{2+}}$	0.03	2.52	0.76
	$exp(-Z_+F\Delta\phi/2RT)_{OH^-}$	5.56	0.633	1.15
	Maximum ratio $(\bar{1}\bar{1}0)_{Mean}/(110)_{Mean}$	4.28		
7 Layers, thickness = 10.325 nm				
$\phi_{Mean}$ (mV)		104.9	-29.9	7.72
Standard deviation: $\phi$ (mV)		24.4	7.8	14.9
Electric Field <sub>Mean</sub> (V/m)		$4.19 \times 10^8$	$-1.20 \times 10^8$	$3.09 \times 10^7$
294 K	$exp(-Z_+F\Delta\phi/2RT)_{Zn^{2+}}$	0.02	3.26	0.74
	$exp(-Z_+F\Delta\phi/2RT)_{OH^-}$	5.66	0.55	1.14
	Maximum ratio $(\bar{1}\bar{1}0)_{Mean}/(110)_{Mean}$	5.88		
354 K	$exp(-Z_+F\Delta\phi/2RT)_{Zn^{2+}}$	0.03	2.693	0.77
	$exp(-Z_+F\Delta\phi/2RT)_{OH^-}$	5.66	0.61	1.14
	Maximum ratio $(\bar{1}\bar{1}0)_{Mean}/(110)_{Mean}$	4.37		

Table 5.3: Table of calculated electrical parameters from the 50 nm wide point charge modelled:  $[Zn^{2+}]$  terminated ( $\bar{1}\bar{1}0$ ) surfaces with an overlayer of  $[OH^-]$  anions,  $[OH^-]$  terminated ( $\bar{1}\bar{1}0$ ) surfaces with an overlayer of  $[Zn^{2+}]$  cations, and the neutral (110) surface. Listed parameters include: mean Stern potential ( $\phi_{Mean}$ ), standard deviation of the Stern potential  $\phi$ , mean electric field, the electrostatic factor  $exp(-Z_+F\Delta\phi/2RT)$  for  $[Zn^{2+}]$  and  $[OH^-]$  ions taken from Crundwells reaction kinetics at a charged surface. The values have been calculated for surfaces containing a single layer (thickness 1.475 nm) and 7 layers (thickness 10.325 nm). Maximum ratio  $(\bar{1}\bar{1}0)_{Mean}/(110)_{Mean}$  is the mean value of the maximum electrostatic factors for the two ( $\bar{1}\bar{1}0$ ) surfaces, and the mean of the two electrostatic factors for the (110) surface. The relative permittivity was taken as 39.2 and the stern layer thickness taken as the intermediate value between the hydration radius of  $Zn(H_2O)_6^{2+} = 0.219\ nm$  <sup>[405]</sup> and  $OH(H_2O)_3^- = 0.3\ nm$  <sup>[406]</sup>.

The difference in magnitude between the two ( $\bar{1}\bar{1}0$ ) surfaces is due to the distribution and relative distance between ions of opposite charges, with the relative distances significantly shorter for the  $[OH^-]$  overlayer surface. The increase in the magnitude of the potential for the ( $\bar{1}\bar{1}0$ ) surfaces is in line with what would be expected for the dipole from analysis of the unit cell. The limited increase in potential when the number of layers increases is likely due to

the relative length scales of the Stern layer and the LBZA layer separation (0.3183 nm vs 1.475 nm.) As a result, the relative increase in potential upon addition of layers is likely greater at increased distances. Using the calculated electric field strengths in Table 5.3 allows the effect of microwave exposure on growth and on aspect ratio to be predicted. The mean electric fields calculated across the stern layer are expected to be on the order of, or greater, than  $33.7 \text{ MVm}^{-1}$ , far in excess of the maximum electrical fields produced by typical domestic microwaves that produce electric fields between  $20 \text{ kVm}^{-1}$  and  $60 \text{ kVm}^{-1}$  [161][407].

Furthermore calculating the transmission coefficient using Equation 5.2 and values of  $\epsilon_{r_{bsg}} = 4.2$  [398],  $\epsilon_{r_{water}}' = 77.5$  and  $\epsilon_{r_{water}}'' = 9.8$  [160] at 295 K (21.8 °C) produces transmission coefficients of 0.656 at the air-beaker interface and 0.377 at the beaker-solution interface, resulting in only 24.5 % of the initial electric field strength i.e. approximately 5 – 15  $\text{kVm}^{-1}$  being expected to be transmitted into the reaction media. As such the microwaves will be expected to have no direct effect on ions depositing as a result of the electric field at the stern layer.

The effect of increased collision frequencies due to ionic drift and power absorption gradients can also be accounted for by calculating the displacement of ions and the penetration depth of the electric field at half power. Typical hydrated ion and both Layered double hydroxide and clay drift velocities are on the order of  $10 \text{ mm.s}^{-1}$  [408] and  $4 \text{ mm.s}^{-1}$  [409] [410] at field strengths of  $10^5 \text{ Vm}^{-1}$  respectively. The oscillation period for microwaves at 2.45 GHz is equal to 0.408 ns resulting in an oscillatory ion and clay displacements on the order of  $\pm 2 \text{ pm}$  and  $\pm 0.8 \text{ pm}$ . Calculating the volume of solution each ion occupies from the molar values and assuming the volume to be a sphere for simplicity, produces radial distances between individual hydroxide and zinc ions of  $\sim 0.795 \text{ nm}$  and  $\sim 0.897 \text{ nm}$ , respectively. These are far greater than the oscillatory ion displacement. Microwave electric field induced enhancements to the collision rate can thus be ruled out as taking part in the growth.

The penetration depth at half power, representing the energy adsorbed as heat due to dielectric and conductive losses, was calculated using Equation 5.4 with the values of permittivity for water at 295 K and 343 K (70 °C) (presented in section 5.2.1.4 ), producing values of 17.5 mm and 197.3 mm respectively. The low temperature values calculated is a significantly short distance compared to the 25 mm radius of the beaker whilst the values at higher temperature exceeds it. At short exposure times, depending on the timescale of the reaction compared to the internal convective heat transfer timescale, the power drop might result in temperature gradients that increase the polydispersity of particle lengths and aspect ratios. Whilst the effect of temperature gradients might increase the complexity of analysis,

microwave exposure can generally be ruled out as a contributor to the growth mechanism in any capacity other than through the production of heat.

As non-thermal electric field effects of microwave exposure can be ignored the effects of the internal dipole would be expected to be the dominant effect on the aspect ratio. To account for the effect of the surface potential on the reaction rate of primary particles and their aspect ratios, two parameters need to be assessed:

- The attraction of ions to the surface and their subsequent dehydration, which is predicted by the electrostatic Nernstian factor  $\exp(-Z_{\pm}F\Delta\phi/2RT)$
- The concentration of free  $[\text{Zn}^{2+}]$  and  $[\text{OH}^-]$  ions in the solution that can be affected by the potential.

Assuming that all variables for the reaction rate, excluding those due to the presence of a surface potential, are constant; then the ratio of the mean electrostatic factors for the  $(1\bar{1}0)$  surfaces divided by  $(110)$  surface represents the maximum effect of the dipole on the aspect ratio due to primary growth. Extracted values of the  $\exp(-Z_{\pm}F\Delta\phi/2RT)$  factor at  $d_{\text{Stern layer}} = 0.25$  nm are shown in Table 5.3. From the magnitudes calculated the  $(1\bar{1}0)$  surfaces will experience greater growth enhancement than the  $(110)$  surfaces. Ions with like charges to the outmost surface ion will be unlikely to significantly participate in reactions at the  $[\text{OH}^-]$  terminated  $(1\bar{1}0)$  surface with the  $[\text{Zn}^{2+}]$  overlayer and can be ignored. Based on the assumptions stated; taking the mean value of the maximum electrostatic factor for each  $(1\bar{1}0)$  surfaces, and dividing by the mean value of the factors for the  $(110)$  surfaces, allows for an approximation of the effect the surface potential has on aspect ratio for primary growth. The ratios suggest a modest aspect ratio at room temperature (294 K) of 5.75 and 5.88 depending on whether 1 layer or 7 was modelled. The values reduce to 4.28-4.37 at 351 K, the reduction is significantly lower than that reduction in aspect ratio seen experimentally here of 51.1 to 5.7 for  $[\text{OH}^-]/[\text{Zn}^{2+}]$  ratios of 1.44. The reduced value of the calculated mean ratios compared to the aspect ratio, and the relative difference between the reduction with temperature for the two values can likely be partially attributed to the assumptions made. Whilst a more detailed analysis of the reaction rate would need to be performed to refine the effect of the calculated potential due to the dipole on aspect ratio would be needed, the refined model would also need to account for the free ion concentration.

To account for the free ion concentration it is useful to first calculate the concentration of uncharged, complexed Zinc acetate ( $[\text{ZnAc}_2(\text{H}_2\text{O})_n]_{n=2 \text{ or } 4}$ ) species. By inserting the measured stability constants of zinc acetate in the literature (equilibrium constant ( $\beta_{12}$ ) for

$[\text{ZnAc}_2(\text{H}_2\text{O})_n]_{n=2 \text{ or } 4}$  vs  $[\text{Zn}(\text{H}_2\text{O})_6]^{2+} + 2[\text{Ac}]^-$ ;  $\beta_{12} = 123$  <sup>[122]</sup>) into Equation 5.10 <sup>[155]</sup> and Equation 5.11 <sup>[155]</sup>, approximately 88% of zinc cations in the reactions in this work are  $[\text{ZnAc}_2(\text{H}_2\text{O})_n]_{n=2 \text{ or } 4}$  prior to hydroxide addition.

$$\text{Stability constant } \beta_{12} = 123 = \frac{[\text{ZnAc}_2]}{[\text{Zn}^{2+}][\text{Ac}]^2}$$

Equation 5.10

$$[\beta_{12}] = \frac{[x]}{[c-x][2c-2x]^2}$$

Equation 5.11

$$\text{For } c = 1 \text{ M, } [\text{ZnAc}_2] = [x] \approx 88\%$$

Where  $c$  is the total concentration of zinc ions,  $2c$  is the total concentration of acetate ions,  $x$  is the final concentration of  $\text{ZnAc}_2$ ,  $c-x$  is the final concentration of free zinc cations and  $2c-2x$  is the final concentration of free acetate at equilibrium .

The combination of the relatively small ratio between calculated electrostatic factors, and the concentration of complexed uncharged zinc acetate at the time of addition of sodium hydroxide into account, suggests that the effect of dipole on primary growth is limited. This is further supported by the HRTEM observations of belt like LBZA containing asymmetric 5-10 nm primary particles in by Li, Zhang and Wang <sup>[70]</sup>, and the previously stated observation of what appears to be oriented attachment in Figure 5.17. As such the the large aspect ratios produced and the large temperature variance observed here likely relates to the temperature dependence of the secondary growth processes. It is worth noting though that the ratios between electrostatic factors calculated are sufficient to produce aspect ratios (AR) as seen in the primary particles viewed under HRTEM (AR=1-2) by Li, Zhang and Wang <sup>[70]</sup> and those predicted by applying Scherrer analysis to van Rijt *et al.* SAED data <sup>[166]</sup> (AR=1.55) (as described in Chapter 2).

In the literature reviewed in chapter 2.1.3.6 it was shown that the alternating layers of  $\text{Zn}^{2+}$  and  $\text{O}^{2-}$  in the  $c$  axis of zinc oxide produced a  $c$  axis oriented dipole in primary particles <sup>[179]</sup>. The dipole forces between two zinc oxide primary particles created a spontaneous acceleration that results in the polar faces preferentially rotating and adsorbing to each other over the non polar faces i.e. oriented attachment, resulting in high aspect ratio

nanowires<sup>[179]</sup>. It would be expected then that similarity in dipole structures, with the  $\text{Zn}^{2+}$ - $2[\text{OH}^-]$  induced dipole in LBZA oriented in the  $[1\bar{1}0]$ , and  $\text{Zn}^{2+}$ - $\text{O}^{2-}$  induced dipole in the  $[001]$  direction in ZnO, would also result in a preferential acceleration towards, and oriented attachment of, the polar facets. The effective length and shape of the primary particles will in part determine the dipole strength.

Figure 5.20, Figure 5.21 and Figure 5.22 show a graphical representation of how the proposed oriented attachment process relates the affect of the dipole to the observed LBZA morphologies. At very short lengths the two opposing charged faces are close enough that the electric field measured external to a certain face will be lower in magnitude than that produced by the charge at that face alone. As a result the potential due to the dipole is proportional to the length of the particle<sup>[141]</sup> in the nucleated primary particles. At longer particle lengths where the two faces are at a significant enough distance the surfaces no longer interact and the potential saturates<sup>[161]</sup>. The effect of nucleation conditions, and the effect of the dipole enhanced growth of the primary particles, would therefore be expected to influence the oriented attachment process.

The greater the growth rate of primary particles, the longer the particle and greater the dipole strength. With increased dipole strength the greater the acceleration and degree of oriented attachment, and hence secondary particle growth in the  $[1\bar{1}0]$  direction, would be expected to occur<sup>[411]</sup>. The partial reaction rates for primary growth related to anions is described by Equation 2.6 and can be simplified to  $r_- = \bar{k}_- [A^{Z-}] \exp\left(\frac{Z_- F \Delta \phi}{2RT}\right)$  assuming desorption is negligible. Considering that the  $[\text{Zn}^{2+}]$  concentration has been constant throughout the experiments, an increase in  $[\text{OH}^-]$  concentration will lead to an increase in enhancement in primary particle growth in the  $[1\bar{1}0]$  direction as compared to the  $[110]$  direction. As a result secondary particle (nanobelt/ nanoplate/ nanosheet) aspect ratio and length would be expected to increase with  $[\text{OH}^-]/[\text{Zn}^{2+}]$  ratio which has been observed here (as shown in Figure 5.14) for:

- all temperatures at  $[\text{OH}^-]/[\text{Zn}^{2+}]$  ratios of 0.8 and 1.2
- for 294 K (0 s exposure) up to a ratio of 1.4 – 1.44 (where the confidence intervals overlap).

For  $[\text{OH}^-]/[\text{Zn}^{2+}]$  ratio exceeding 1.4 – 1.44 for 294 K and 1.2 for all other temperatures, length starts to decrease. As previously discussed in section 5.3.1.2.2.1, the nucleation time period in this region is expected to decrease leading to an increase in the concentration of particles nucleated. The increase in particle concentration leads to a reduction in particle size. The reduction in length will decrease the dipole strength, decreasing the rate of



attachment in the  $[1\bar{1}0]$  direction. With a reduction in dipole strength and increase in particle concentration is a greater chance of collisions and aggregation occurring at the (110) surface resulting in a decrease in aspect ratio.

Aspect ratio and length decrease significantly with increasing temperature, as would be expected for the system if Brownian motion was able to partially overcome the dipole induced torque at the reorientation stage (previously described in the theory section Chapter 2.1.3.6 ). In addition to an increase in Brownian motion the increase in temperature would produce a strong reduction in permittivity <sup>[160]</sup>. This would reduce the charge screening distance (Equation 2.9) and reduce the effect of the dipole. Similar trends in aspect ratio with temperature have been observed in the aging of ferrihydrite/ goethite system by Burleson *et al.* <sup>[397]</sup> however, polydispersity showed the opposite trend. Considering Burleson *et al.* started with a relatively monodisperse dispersion of nanoparticles and here the primary particles are generally expected to be polydisperse due to the nucleation conditions (as described in section 5.3.1.2.2.1 ), the trends in polydispersity likely have separate origins.

From the calculations of the (110) surface stern layer, the potential in the  $[110]$  direction is very weak. If the interaction energy for the  $[1\bar{1}0]$  direction is attractive and the barrier for attachment negligible; then the difference in energy barriers, calculated from the measured aspect ratios in 5.3.1.2.1 , would suggest an energy barrier for attachment in the  $[110]$  direction to be approximately  $2.697 k_B T$  eV at 294 K. These value are in line with those seen for oriented attachment of ZnO <sup>[179]</sup>; where attachment in the  $[001]$  direction (the direction of the dipole) had no energy barrier, and the maximum observed barrier for attachment was  $\sim 3 k_B T$ . The similarity in energies, combined with the presence of primary particles with a preferred orientation in the direction of the predicted dipole <sup>[70][166]</sup> strongly suggests the aspect ratio of LBZA to be a product of oriented attachment.

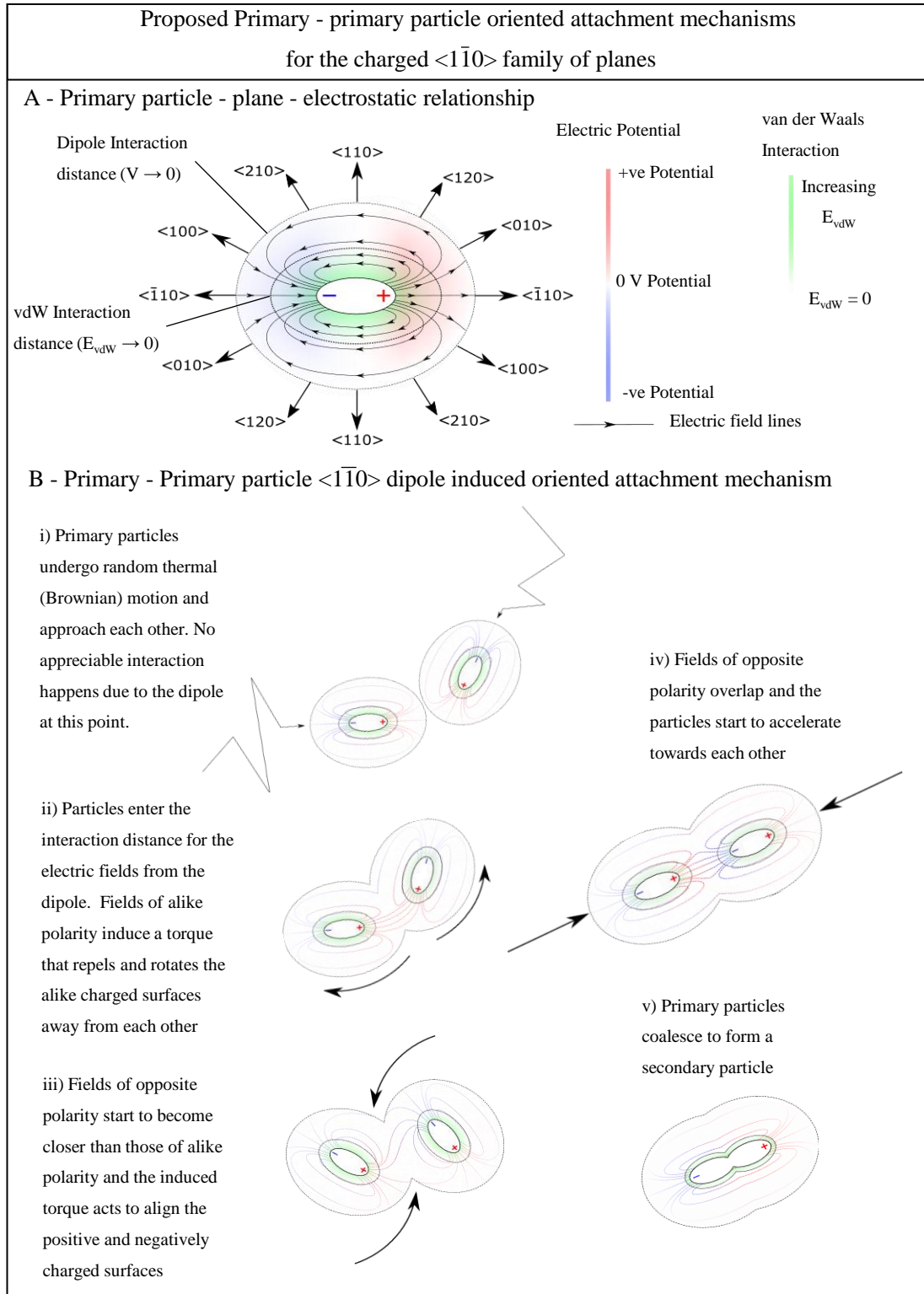


Figure 5.20: A) Schematic of LBZA primary particle showing the relation of the dipole potential and vdW forces with respect to the plane directions. Note that the notation  $\langle hkl \rangle$  indicates the family of equivalent planes e.g.  $\langle 1\bar{1}0 \rangle$  includes  $(1\bar{1}0)$  and  $(\bar{1}10)$ , and  $\langle 110 \rangle$  includes  $(110)$  and  $(\bar{1}\bar{1}0)$  planes. The interaction distance is a function of primary particle length, and is proportional to  $\exp(-r/l_D)$  and that the Debye Length =  $l_D = \sqrt{\epsilon k_B T / (2 * N_A * \sum C_i Z_i^2 q^2)}$  [1] where  $r$  is the distance from the particle surface,  $\epsilon$  is the permittivity,  $k_B$  is the Boltzmann constant,  $T$  is absolute temperature in Kelvin,  $N_A$  is Avogadro's constant,  $C_i$  is the concentration of ion  $i$  with charge number  $Z_i$  and  $q$  is the elementary charge. B) Annotated schematic of dipole driven primary-primary particle oriented attachment in the  $[1\bar{1}0]$  direction.

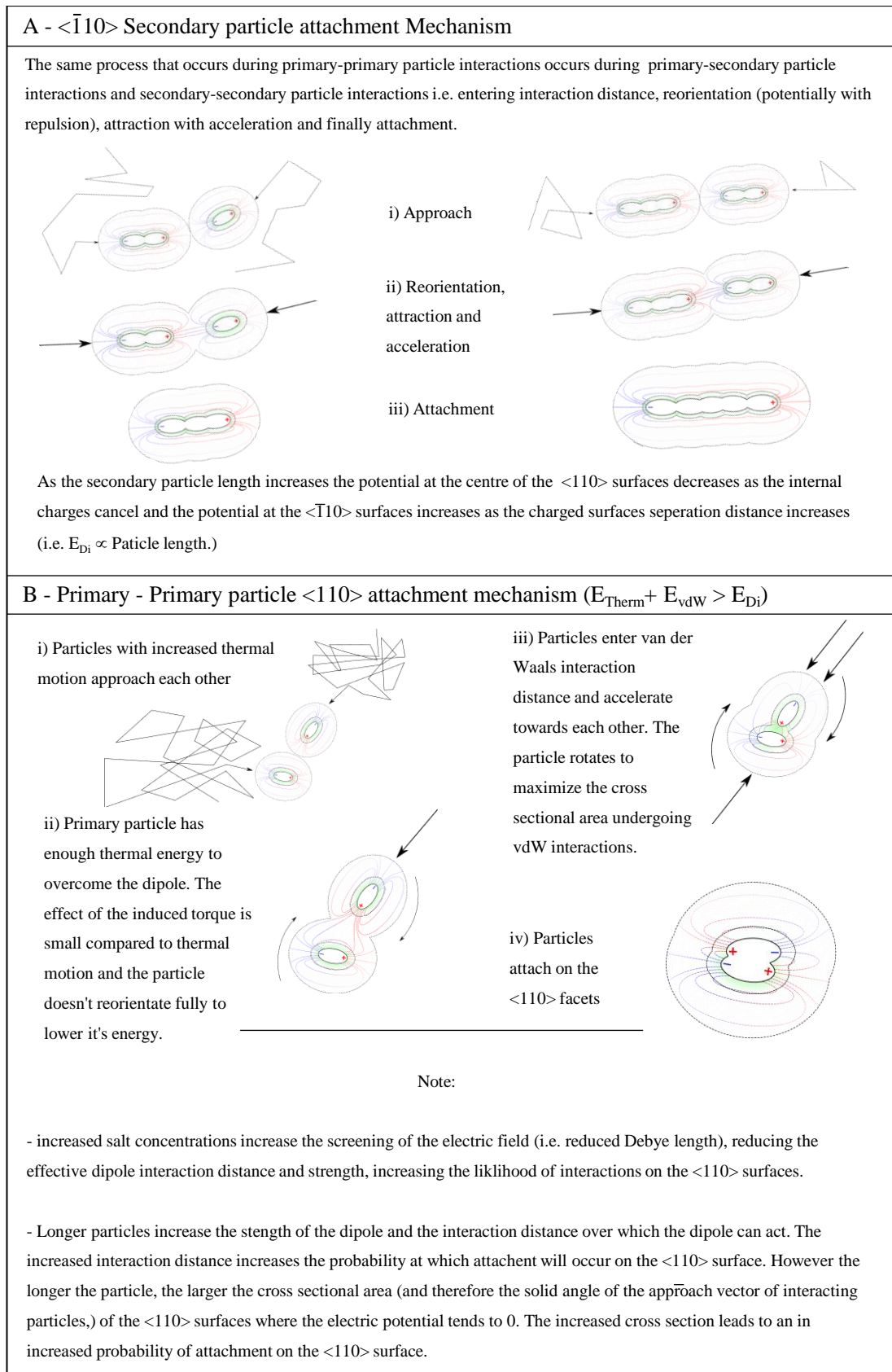


Figure 5.21: Schematic of secondary particle oriented attachment in the  $\langle \bar{1}10 \rangle$  direction. B) Schematic of Primary particle interaction in the  $\langle 110 \rangle$  direction due to increased thermal energy and or decreased dipole interaction energy.

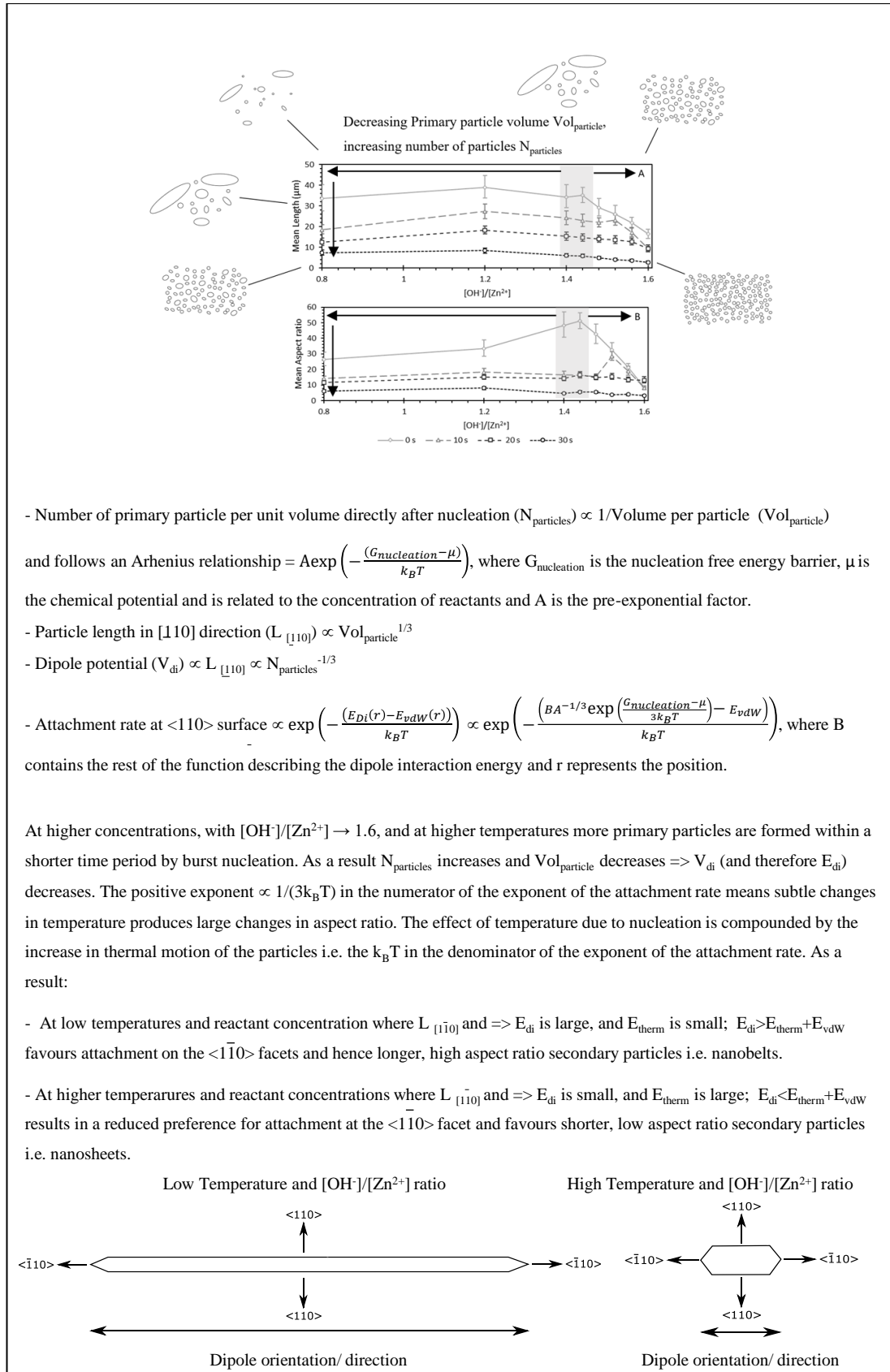


Figure 5.22: Top - Schematic showing how reactant concentration ( $[OH^-]/[Zn^{2+}]$ ) and reaction temperature effect primary particle size, and secondary particle morphology extracted from Figure 5.14. Middle and bottom – Relation between primary particle nucleation conditions [412], dipole strength [141], attachment rate on the unchanged (110) surfaces and as a result secondary particle morphology.

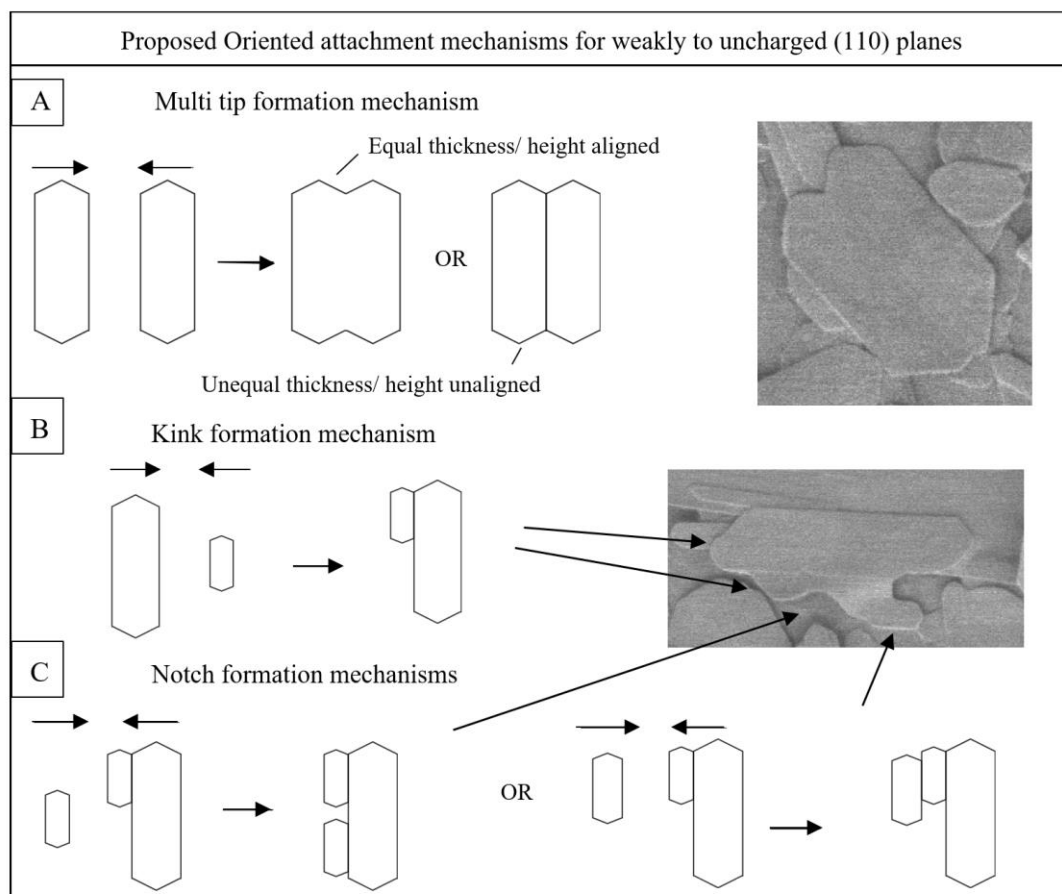


Figure 5.23: A) Multi-tip, B) kink and c) notch formation mechanisms and examples due to oriented attachment along the (110) planes of LBZA after the alignment phase. The more rounded than faceted interfaces are likely a result of field enhanced heterogenous nucleation and mass transfer upon fusion. The particles show a reduction in aspect ratio with value for the particles in A) half the individual particle aspect ratios.

In addition to growth via attachment of primary particles to primary or secondary particles, secondary particles can undergo OA which can help explain irregular morphological features such as kinks/ notches and multiple tips. For the higher aspect ratio secondary particles, the increased cross section of the (110) surface planes and the mirror symmetry in charge compared to the asymmetrically charged ( $1\bar{1}0$ ) surfaces increases the probability of a collision that can orient to minimise its energy and undergo attachment. From Figure 5.10 it can be seen that at room temperatures ( $T_{\text{peak}} \sim 294$  K) the particles show well defined regular morphology. In comparison, the particles produced at higher microwave times in Figure 5.12 ( $T_{\text{peak}} \sim 327$  K) and Figure 5.13 ( $T_{\text{peak}} \sim 351$  K) are less well defined and more varied. The trend in definition is also seen in  $[\text{OH}^-]/[\text{Zn}^{2+}]$  ratio within Figure 5.13 where an increase in ratio corresponds to an increase in irregular features. The increasing trend with temperature would result from increased collisions and reduction in permittivity<sup>[186]</sup> whilst

an increase in  $[\text{OH}^-]/[\text{Zn}^{2+}]$  ratio would increase the number of particles increasing the chance of a collision with the (110) surface <sup>[141]</sup>.

Figure 5.23 shows the (simplified) proposed oriented attachment mechanisms for multiple tip (A), kink (B) and notch (C) formation after alignment has occurred. Particles with multiple end tips would emerge from more than one particle, each with defined tips, aligning, attaching and fusing. Kinks and notches would emerge from attachment and fusion of single and multiple particles separated by a gap, onto the single edge of a particle. Growth from primary particles enhanced by the field at the tip, along with mass transfer at the interface <sup>[141]</sup>, coarsening <sup>[397][411]</sup> and recrystallisation<sup>[411]</sup> would fill in the gap between the tip and the edge of the other particle creating the observed smoother interface.

Molecular dynamic simulations of the oriented attachment process by Sathiyarayanan *et al.* <sup>[413]</sup> predicted that attachment was expected at edges and vertices and much rarer on faces of particles. The edges and vertices had reduced solvent barriers in part due to their reduced areas. The increased energy barriers due to the rigidly attached solvent layer can provide an explanation for the largest aspect ratio between the c axis and the basal layer axes (i.e. aspect ratio of thickness vs length and width).

As the effect of microwave exposure are expected to be purely thermal in nature, the reaction mechanism is expected to be intrinsic to the LBZA crystalline structure and its interaction with the medium. As such the reaction mechanism would be applicable to all water-based synthesis without the addition of steric hinderance reagents. The ability for dipole driven oriented attachment process to explain all the observed features provides the first reaction mechanism in literature to fully describe the observed morphologies. Further literature review and refinement of the arguments presented could potentially lead to a general mechanistic understanding, from which practical predictions and semi-empirical models could eventually be made for other layered zinc hydroxides that share the same basal structure.

### **5.3.2 The effect of addition rate and increased shear on purity and morphology**

Whilst oriented attachment with classical nucleation theory can describe the morphologies presented in section 5.2.1.3, it is unable to explain the presence of ZnO and the so called

BLBZA impurities. The fact that BLBZA and ZnO was observed in all reaction conditions with respect to  $[\text{OH}^-]/[\text{Zn}^{2+}]$  ratio and temperature implied phase formation occurred either during the stirring step or at the point of addition. Therefore, it was important to investigate how these steps affected phase purity. Figure 5.24 - Figure 5.28 show representative diffractograms as a function of stir time for particles synthesised using:

- The low shear stirring method used in the preceding investigations with an addition time of sodium hydroxide  $< 1$  s (instantaneous addition - Figure 5.24) and 15 s (continuous flow addition - Figure 5.25)
- A high shear rate stirring method using a higher surface area stir bar and baffle (known to increase mixing in high viscosity liquids <sup>[414][415]</sup>), to increase shear rate and increase efficiency of mixing. Tested additions times of sodium hydroxide  $< 1$  s (instantaneous addition - Figure 5.26) and 15 s (continuous flow addition - Figure 5.27)
- The high shear rate stirring method and simultaneous continuous zinc acetate and sodium hydroxide addition with addition time 20 s (Figure 5.28)

The continuous flow additions were trialled to test whether slowing the sodium hydroxide rate improved mixing at the formation of the slurry, while the high shear stirring methods were investigated to see whether improving the shear rate and altering the path of fluid to increase the cross flow would improve mixing. All the testing was performed at room temperature to isolate the effects of nucleation and mixing conditions.

### 5.3.2.1 Results

Figure 5.24 - Figure 5.28 show waterfall diffractogram plots of the low and high shear methods with instantaneous and continuous NaOH addition, as a function of stir time for an  $[\text{OH}^-]/[\text{Zn}^{2+}]$  ratio of 1.58. The diffractograms show the presence of the BLBZA (001) reflection between  $2\theta$  values of  $4.2^\circ$  and  $4.4^\circ$  and 'LBZA' (001) at approximately  $6 - 6.6^\circ$ . An additional reflection approximately at  $8.879^\circ$  with  $d_{(001)} = 0.995$  nm (Precursor peak A \*1) was assigned to a 1<sup>st</sup> order (001) reflection in the zinc hydroxyacetate 'precursor' phase, previously observed in the phases sampled from the liquid-air interface in Figure 5.8 and similar to the zinc hydroxyacetate phases measured by Jingwei *et al.* <sup>[399]</sup>, Brunswick *et al.* <sup>[400]</sup>, Moezzi *et al.* <sup>[131]</sup>, and Poul, Jouini and Fievet <sup>[75]</sup>.

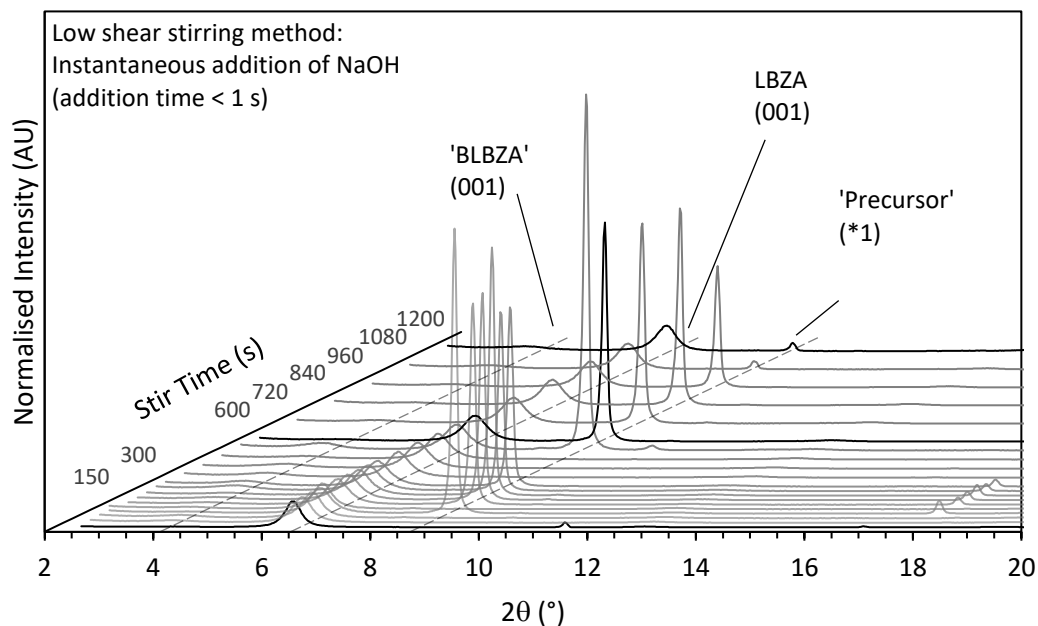


Figure 5.24: XRD diffractogram waterfall plots for uncleaned particles synthesised using the original low shear stirring method with a sodium hydroxide addition time < 1 s and  $[OH^-]/[Zn^{2+}]$  ratio = 1.58. Waterfall plot of LBZA normalised intensity as a function of  $2\theta$  and stir time for a single synthesis run.

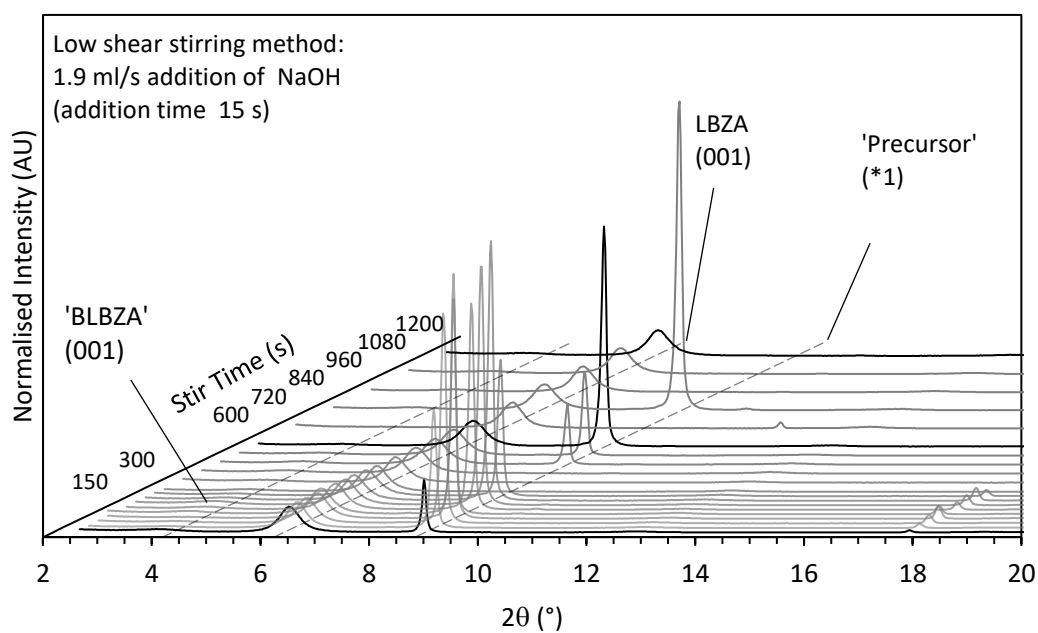


Figure 5.25: XRD diffractogram waterfall plots for uncleaned particles synthesised using the original low shear stirring method with a continuous  $1.9 \text{ mL}\cdot\text{s}^{-1}$  sodium hydroxide addition rate, addition time  $\approx 15 \text{ s}$  and  $[OH^-]/[Zn^{2+}]$  ratio = 1.58. Waterfall plot of LBZA normalised intensity as a function of  $2\theta$  and stir time for a single synthesis run.



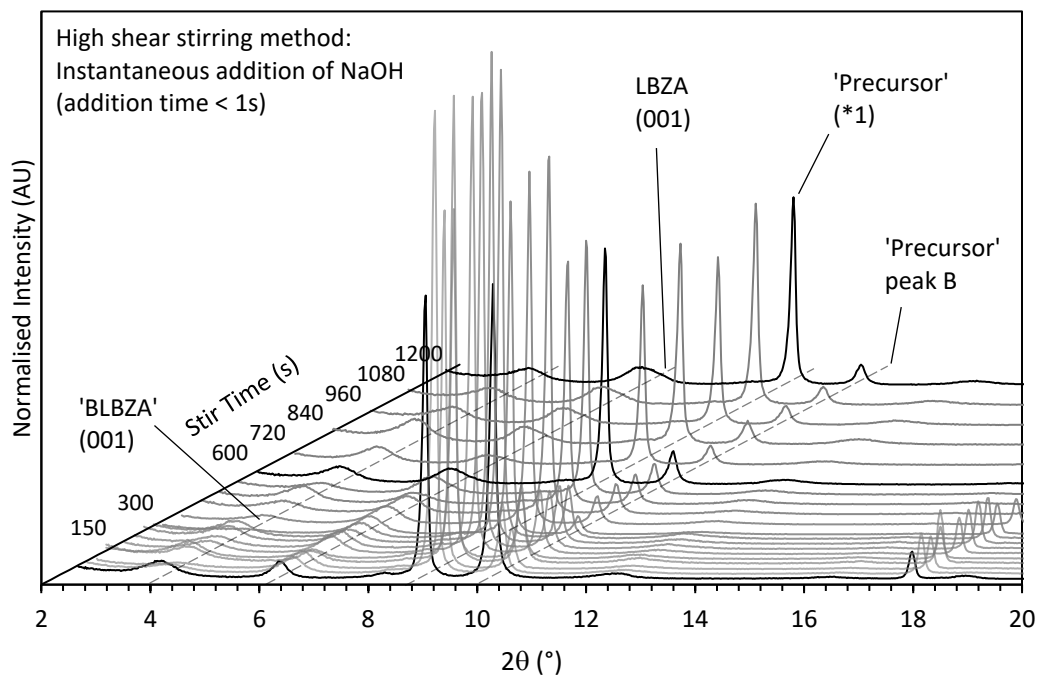


Figure 5.26: XRD diffractogram waterfall plots for uncleaned particles synthesised using the high shear stirring method with a sodium hydroxide addition time < 1s and  $[OH^-]/[Zn^{2+}]$  ratio = 1.58. Waterfall plot of LBZA normalised intensity as a function of  $2\theta$  and stir time for a single synthesis run.

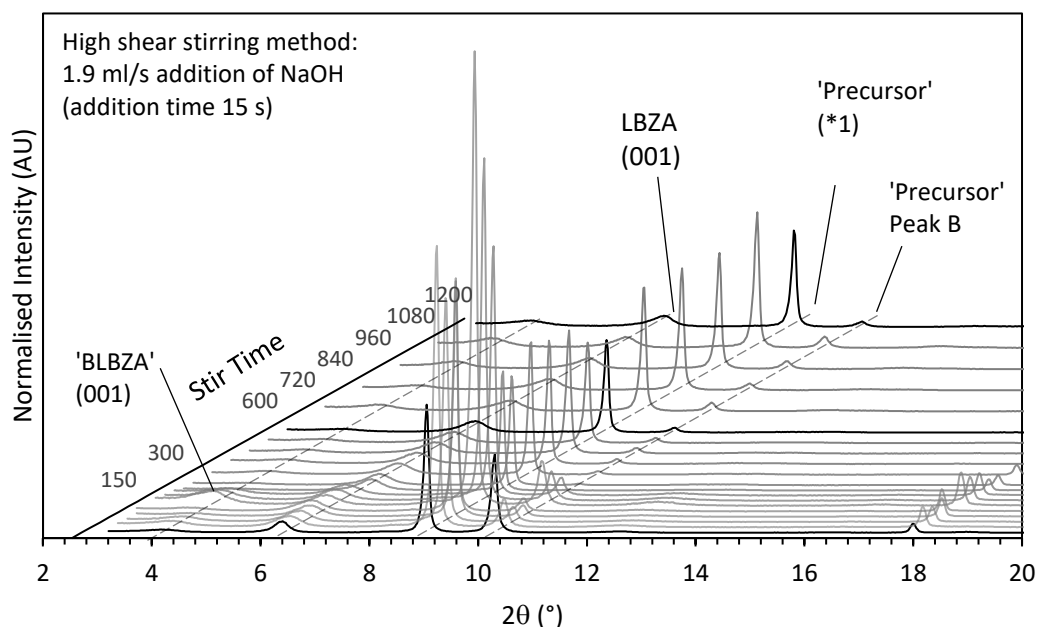


Figure 5.27: XRD diffractogram waterfall plots for uncleaned particles synthesised using the high shear stirring method with a continuous  $1.9 \text{ mL}\cdot\text{s}^{-1}$  sodium hydroxide addition rate, addition time  $\approx 15 \text{ s}$  and  $[OH^-]/[Zn^{2+}]$  ratio = 1.58. Waterfall plot of LBZA normalised intensity as a function of  $2\theta$  and stir time for a single synthesis run.

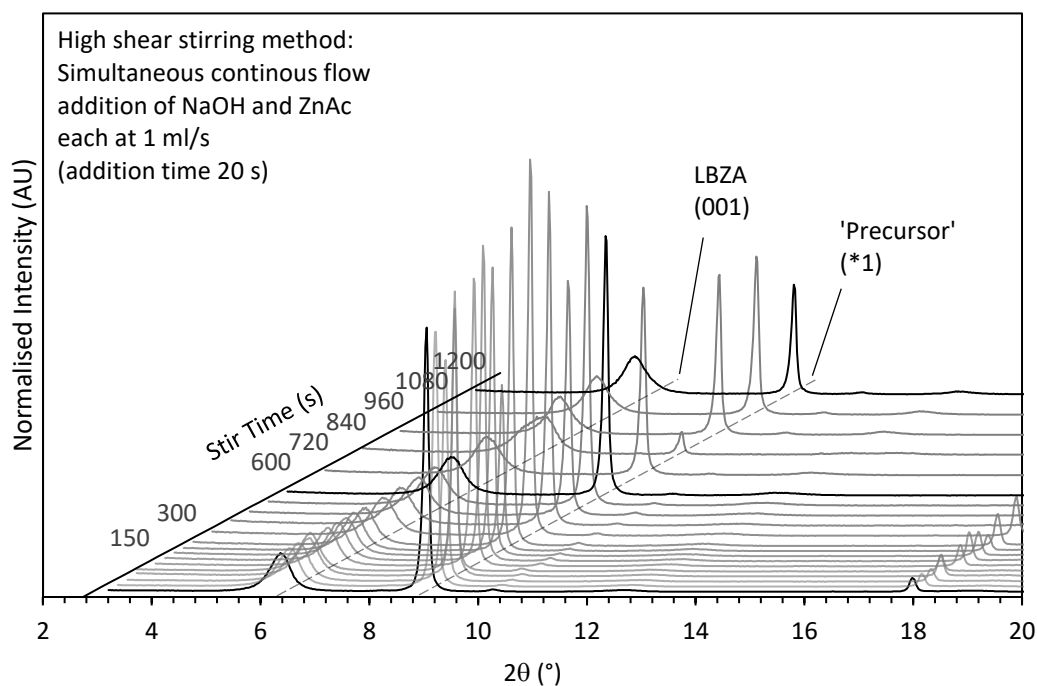


Figure 5.28: XRD diffractogram waterfall plots for particles synthesised using the high shear stirring method with continuous  $1 \text{ mL}\cdot\text{s}^{-1}$  sodium hydroxide addition rate, continuous  $1 \text{ mL}\cdot\text{s}^{-1}$  zinc acetate addition rate, addition time  $\approx 20 \text{ s}$  and  $[\text{OH}^-]/[\text{Zn}^{2+}]$  ratio = 1.58. Waterfall plot of LBZA normalised intensity as a function of  $2\theta$  and stir time for a single synthesis run.

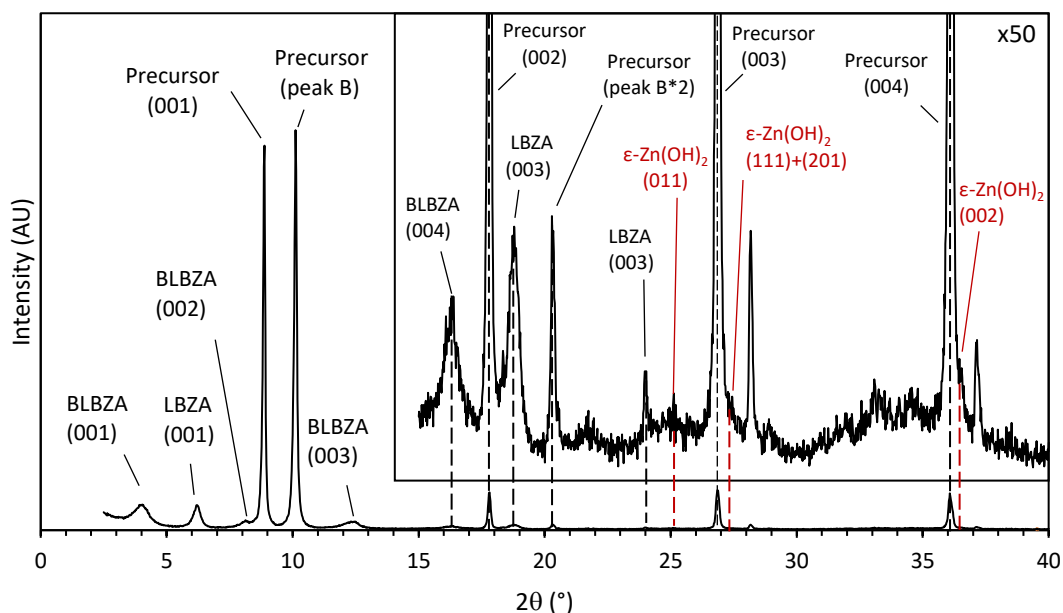


Figure 5.29: XRD diffractogram of intensity as a function of  $2\theta$  for the uncleaned particles sampled at 30 s from the high shear rate stirring method with a time of addition  $< 1 \text{ s}$  and  $[\text{OH}^-]/[\text{Zn}^{2+}]$  ratio = 1.58, insert shows an  $\times 50$  magnification of the values of  $2\theta$  between  $15^\circ$  and  $40^\circ$ . Labelled reflections assigned to BLBZA, 'LBZA', precursor,  $\epsilon$  phase  $\text{Zn}(\text{OH})_2$  and a second observed reflection (precursor (peak B)) present in diffractograms recorded during thermal degradation studies of LBZA<sup>[400][131]</sup>. The presence of  $\epsilon$ - $\text{Zn}(\text{OH})_2$  at  $t = 30 \text{ s}$  suggests the phase forms at or close to the point of addition. The reflections noted as precursor peak B is most likely  $\text{ZnAc}_2$ , as previously assigned by Biswick et al.<sup>[400]</sup> based on combined XRD and TGA-mass spectrometry investigations of the thermal decomposition of LBZA.

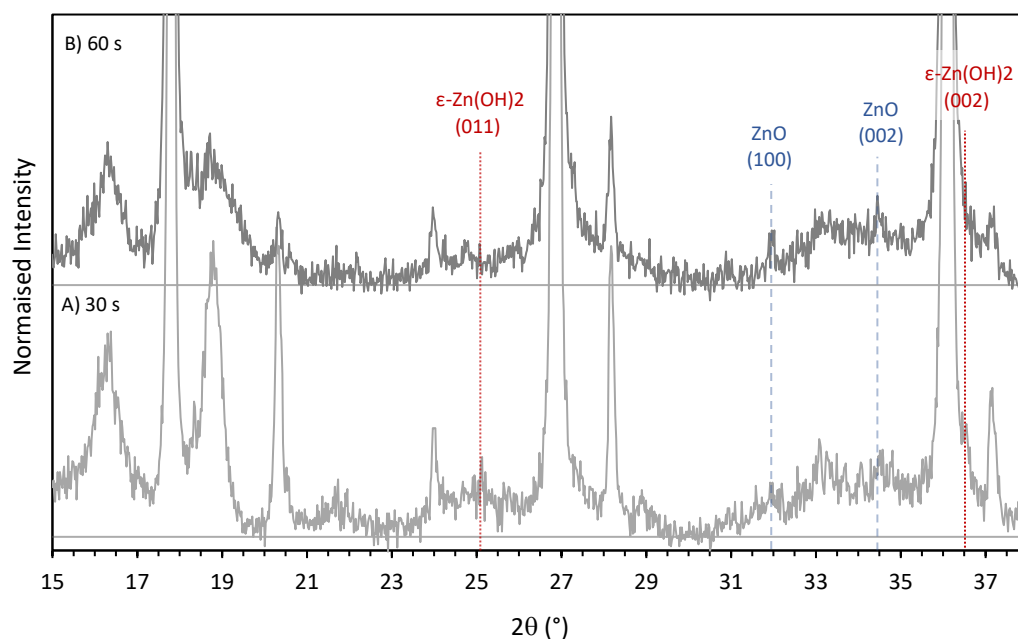


Figure 5.30: Plots of magnified diffractograms for the uncleaned particles sampled at 30 s from the high shear rate stirring method with a time of addition < 1 s and  $[OH^-]/[Zn^{2+}]$  ratio = 1.58, with stir times of: A) 30 seconds (the diffractogram is the same as in Figure 5.29) and B) 60 seconds. Note that B is from the same synthesis run as A) with the diffractogram recorded immediately after (i.e. on the same sample substrate.) Dark horizontal lines represent the background intensity. Annotation shows peaks for  $\epsilon$  phase  $Zn(OH)_2$  and ZnO. The increased presence of ZnO and reduction in  $Zn(OH)_2$  at 60 seconds is likely in part due to the effect of exposure to atmospheric moisture during the scan time of sample A. The ZnO (101) reflection at  $36.2^\circ$  overlaps with the precursor (004) and is unobservable, as is the  $Zn(OH)_2$  (111) at  $27.2^\circ$  that overlaps the precursor (003).

The high shear stirring methods (Figure 5.26 and Figure 5.27) show an additional peak at approximately  $10.1^\circ$  ( $d_{(001)} = 0.875$  nm). A similar phase was seen by Jingwei *et al.* [399], Moezzi *et al.* [27] [110] and Biswick *et al.* [400] but with slightly lower d values of  $d_{(001)} = 0.73 - 0.76$  nm that Biswick *et al.* and Moezzi *et al.* attributed to anhydrous zinc acetate on the basis of mass loss and measurement of the evolved volatile species in TG-mass spectroscopy analysis. The variation in d values between here and in their investigations could be indicative of a separate phase, internal strain [417] and/ or a differing hydration number (i.e. hydrated zinc acetate) [131]. The latter case in particular would appear reasonable as the phase/s was/were produced via a polyol synthesis by Jinwei *et al.*, by thermal treatment in nitrogen by Moezzi *et al.* [131] and Biswick *et al.* [400] and in aqueous conditions here. As such the phase has been cautiously assigned to a partially hydrated zinc acetate phase. Figure 5.28 (high shear stirring method – simultaneous continuous flow addition) notably contains only the ‘LBZA’ (001), Precursor peak A \*1 reflections and a very weak reflection from  $ZnAc_2$  reflection. Figure 5.29 shows the full diffractogram for the reaction products from the synthesis using the high shear stirring method with sodium hydroxide addition time < 1 s sampled at 30 seconds of stir time. In addition to the already mentioned phases there are also broad weak reflections at approximately  $25^\circ$ , between

27.2 ° and 27.8 ° and at 36.5 ° indicative of the (011), (111), (201) and (002) reflections (25.02 °, 27.20 °, 27.78 ° and 36.58 ° respectively) from nanoparticulate  $\epsilon$  phase  $\text{Zn}(\text{OH})_2$  [418] suggesting that the ZnO precursor forms within the first 30 seconds. This is supported by the observations in the diffractogram of the sample taken at 60 seconds that shows a reduction in intensity for  $\epsilon$ - $\text{Zn}(\text{OH})_2$ , and the presence of peaks at 31.94 ° and 34.47 ° corresponding to the (110) and (002) of nanocrystalline ZnO [419].

Figure 5.31 and Figure 5.32 show the normalised relative phase areas as a function of stir time for the 'BLBZA' (001), 'LBZA' (001), Precursor peak A (\*1) and  $\text{ZnAc}_2$ . For the low shear stirring methods for sodium hydroxide with addition times < 1s (Figure 5.31- A) and 15 s (Figure 5.31- B), there are two significant observations that can be drawn:

- The presence of all three phases appearing in the first 30 seconds suggesting that nucleation starts/ happens within the 30 seconds suggesting rapid burst nucleation.
- A very high degree of variability in the intensities of the samples as shown by the high variability in mean with respect to stir time and high standard deviation for all samples. The high variability in intensities between stirring times and between samples at each stir time suggests an inhomogenous distribution of phases within the reaction media due to low mixing efficiency. The lack of reaction media homogeneity is known to produce a high polydispersity in the final morphology of synthesised particles [420].

In comparison to the low shear stirring method, the higher shear stirring method shown in Figure 5.31 - C and Figure 5.31 – D for addition times < 1 s and 15 s show a much lower variance in the relative phase areas. The difference in variation is highlighted in Table 5.4 which shows the mean coefficient of variation (CoV) for each reaction condition. For the higher shear rate stirring method the CoV in the precursor phase (the most significant peak area) is only 23.4 % and 13.0% of the low shear rate equivalents for < 1s and  $\approx$ 15 s addition time respectively. The low variance suggests a homogenous reaction medium as a result of improved mixing efficiency as required for the creation of monodisperse particles [420]. As a result of the lower variance it can be observed that the precursor, BLBZA, LBZA and  $\epsilon$ - $\text{Zn}(\text{OH})_2$  form within the first thirty seconds with the precursor and  $\text{ZnAc}_2$  area decreasing whilst BLBZA and LBZA areas increase as a function of stir time.

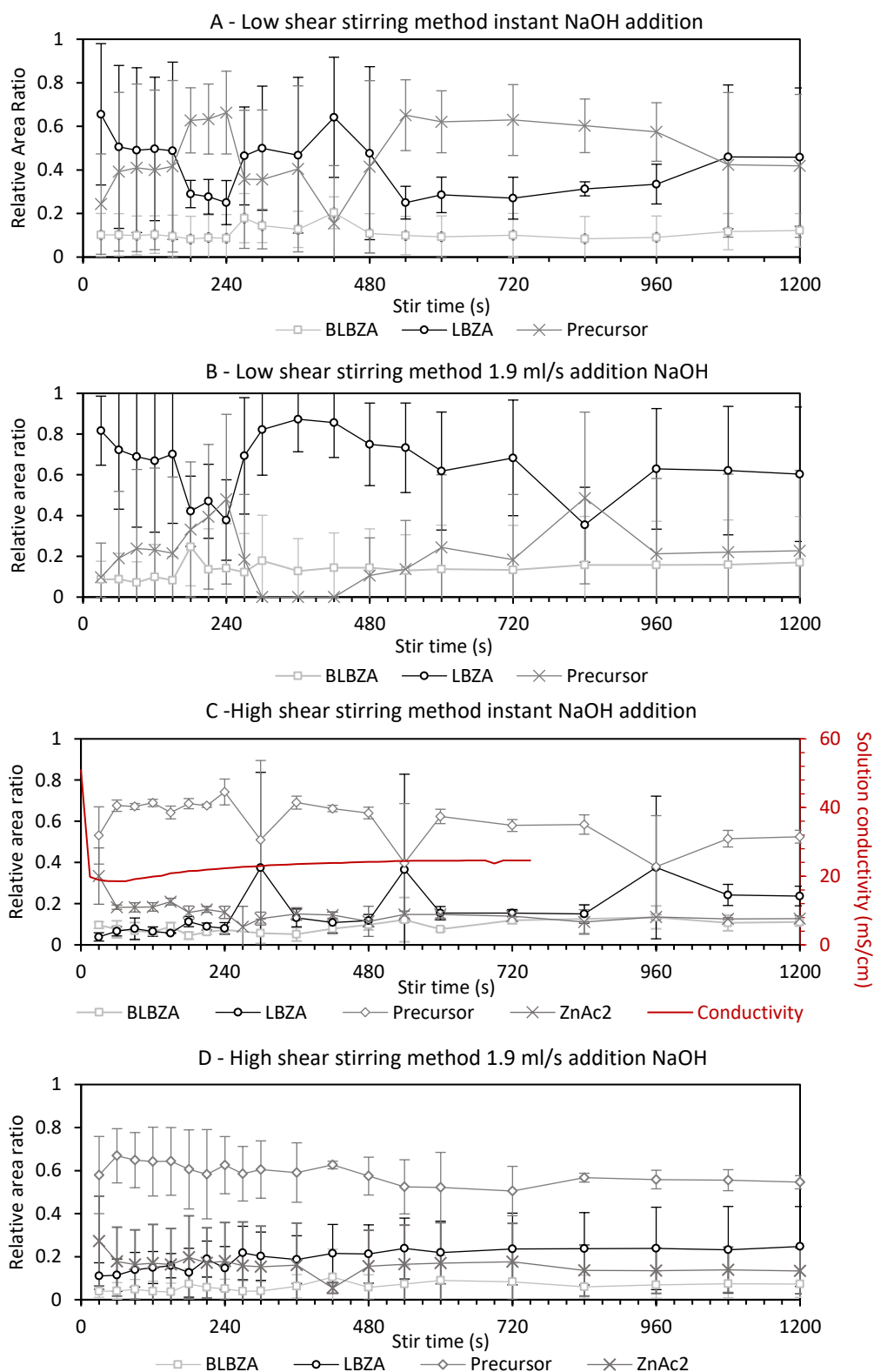


Figure 5.31: Relative area ratios of uncleaned BLBZA, LBZA, ZnAc<sub>2</sub> (Precursor peak B) and precursor phases as a function of stir time for the high shear stirring method with addition time for NaOH < 1 s (top) and 15 s (bottom). [OH<sup>-</sup>]/[Zn<sup>2+</sup>] ratio = 1.58. Top contains a representative set of solution conductivity for the reaction as a function of stir time. Error bars equal to 1 standard deviation of each stir time sample mean. The relative areas produced from measuring the sum if each peak area and taking the ratio of each peak relative to the sum.

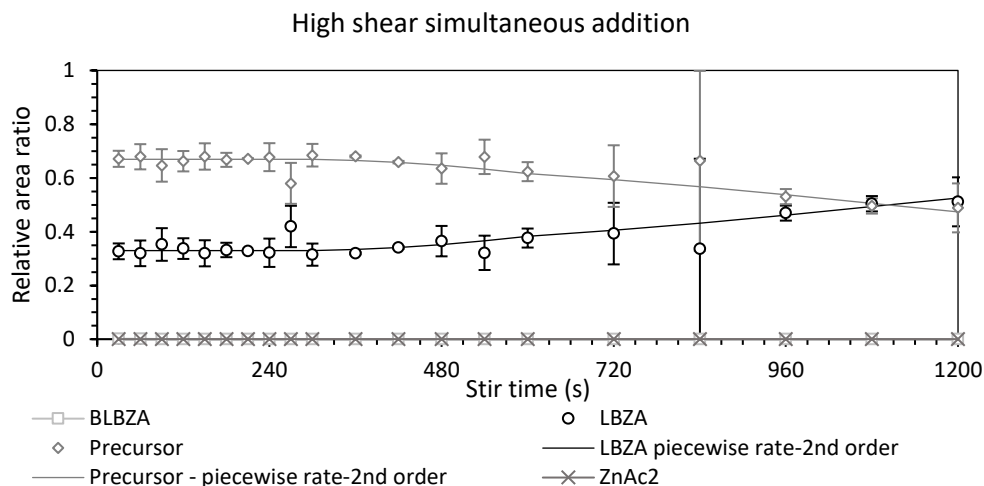


Figure 5.32: Relative area ratios of uncleaned BLBZA, LBZA and precursor phase as a function of stir time for the high shear stirring method with continuous rates of addition of  $1 \text{ mL}\cdot\text{s}^{-1}$  for both Zinc acetate and Sodium hydroxide, addition time 20 s.  $[\text{OH}^-]/[\text{Zn}^{2+}]$  ratio = 1.58. Error bars equal to 1 standard deviation of each stir time sample Note: the Std Dev. at  $t = 360\text{s}$  and  $420 \text{ s}$  are 10% of the other values and therefore not visible. The relative areas produced from measuring the sum of each peak area and taking the ratio of each peak relative to the sum. Fitted piecewise trendlines based on 2<sup>nd</sup> order process i.e.  $d[\text{product}]/dt = k[\text{precursor}]^2$  where  $k$  is the rate constant of the reaction: LBZA: 0 – 300 s:  $\text{LBZA}_t = 0.3297$ , 300 – 1200 s:  $\text{LBZA}_t = 0.00014 * [\text{Precursor}_{t-1}]^2 * \Delta t + \text{LBZA}_{t-1}$ ,  $R^2=0.992$ . Precursor: 0 – 300 s:  $\text{Precursor}_t = 0.66946$ , 300 – 1200 s:  $\text{Precursor}_t = -0.00014 * [\text{Precursor}_{t-1}]^2 * \Delta t + \text{Precursor}_{t-1}$ ,  $R^2=0.997$ . Trendline fitted by fitting a linear trendline in excel using  $1/(\text{relative area})$  vs time plots for  $t \geq 300\text{s}$  (i.e. fitting the integrated rate equation for a 2<sup>nd</sup> order reaction <sup>[155]</sup>).

Phase	Mean coefficient of variation in relative areas ( $\sigma/\mu * 100\%$ )				
	Old stirring method		New stirring method		
	Addition time				
	<1 s	$\approx 15 \text{ s}$	<1 s	$\approx 15 \text{ s}$	simultaneous
BLBZA	89.5	137.0	37.1	100.9	
LBZA	51.1	40.0	41.2	63.9	16.5
Precursor	67.9	151.6	15.9	19.7	9.5
ZnAc <sub>2</sub>			23.9	97.1	141.4

Table 5.4: Table of coefficients in relative areas showing the mean coefficient of variation of the two comparable stir rate (low and high shear rate) methods and sodium hydroxide addition times (< 1 s,  $\approx 15 \text{ s}$  and simultaneous addition). Mean values were calculated from the coefficient of variation calculated at each sampling time from the normalised phase areas shown in Figure 5.31. Note: Grey boxes indicate an absence of any reflections from that phase peak. The high value of CoV for ZnAc<sub>2</sub> in the simultaneous method should be taken in context of the peak area which comprises of a mean of 0.37 % of the total peak areas and therefore more prone to experimental noise. The CoV at each stir time is calculated for  $n=3$ , where each sample is taken from a separate synthesis run.

The relative areas for the precursor, ZnAc<sub>2</sub> (precursor peak B), LBZA and BLBZA phases at a stirring time of 30s for the <1 s addition rate are 0.531, 0.334, 0.039 and 0.096, respectively; whilst for the 15 s addition rate the areas are 0.579, 0.272, 0.110 and 0.038,

respectively. This shows that both ZnAc<sub>2</sub> and BLBZA phase areas reduce with the slower rate of addition, likely a result of the increased mixing efficiency due to the slower viscosity increase upon precipitation as observed by the visual change in fluid velocity. The slower addition rates however have increased CoVs, potentially a result of the lower [OH<sup>-</sup>]/[Zn<sup>2+</sup>] ratio during the first 15 seconds and subsequent variation in the concentration in the various complexes formed.

Figure 5.32 shows the relative phase areas of the high shear stirring method setup with simultaneous addition and addition time of 20 s. Compared to the other addition rates for the high shear method, LBZA had an increased area of 0.327, whilst no measurable BLBZA was observed. The reflection of ZnAc<sub>2</sub> had a mean value of 0.0037 therefore significantly lower than the other addition methods. Assuming that Biswick *et al.* assignment of zinc acetate to the reflection is accurate, the minor presence of ZnAc<sub>2</sub> is unlikely to be a result of the stirring or addition conditions, and more likely to be due to either:

- the sub ideal stoichiometry of hydroxide to zinc acetate ratio used in the experiment (i.e. [OH<sup>-</sup>]/[Zn<sup>2+</sup>]= 1.58 vs the ideal ratio of 1.6)
- a low volume of residual hydroxide solution (~ 74 μL based on relative phase areas and the 20 mL volume of solution) left in the feed centrifuge tube.

The observed phase areas show a significantly increased precursor and LBZA phase purity compared to the other stirring and addition conditions. Considering the low solubility and high stability constant for Zinc hydroxide compounds <sup>[421][422]</sup> that would be present in the diffractograms, suggests an increased LBZA phase content. The solution was visually observed to have a much higher fluid flow rate and therefore lower viscosity than any of the other methods. This generally suggests the presence of ZnAc<sub>2</sub> and/ or BLBZA precipitation is an important part of slurry/ gel formation. The lack of BLBZA or ε-Zn(OH)<sub>2</sub> (110) suggests no regions of excess hydroxide or acetate <sup>[68]</sup> are formed at the point of addition. The homogeneity is also seen in the significant reduction in the CoV. The precursor phase area at t = 60 s was approximately 0.67 for all addition rates, suggesting that a similar reaction was occurring in all methods using high shear stirring and that the impurities formed were forming simultaneously via a separate process.

Like all the high shear stirring method samples, the precursor phase area decreases with increasing stir times whilst the LBZA area increases. The fact that the LBZA content increases with increased exposure to water is in line with the precursor phase instability with respect to moisture and conversion to LBZA observed by Jingwei *et al.* <sup>[399]</sup> and Biswick *et al.* <sup>[400]</sup>. This suggests that precursor phase formation and conversion is a major

component of the reaction mechanism. The fitted trendlines show a 2<sup>nd</sup> order reaction process ( $d[\text{product}]/dt = k[A][B]$ , where A and B can be the same or different reactants) as would be expected for two component reaction processes such as oriented attachment [140][411][179] and are in excellent agreement with data with  $R^2$  values for LBZA = 0.992 and Precursor = 0.997. The primary error in the mean values of the high shear stir rate simultaneous addition phase areas, especially within the first 300 s, is expected to arise from the humidity sensitivity of the precursor phase during diffractogram acquisition. Each sample plate tested consisted of 4 samples that were stored under a rough vacuum immediately after the drop cast layer dried. The samples on each plate was scanned sequentially, and each subsequent sample scanned would absorb increased amounts of atmospheric water and show higher conversion to LBZA.

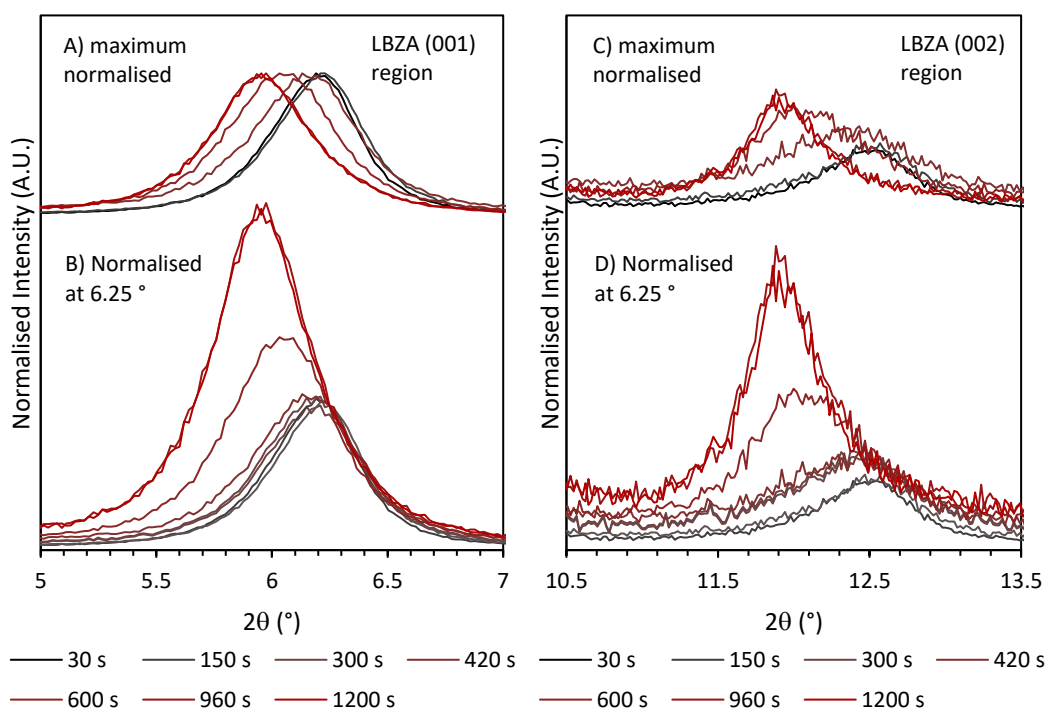


Figure 5.33: Normalised intensity high shear rate simultaneous addition diffractograms of the LBZA (001) (A and B) and (002) (C and D) regions, as a function of stir time. A and C show the diffractograms normalised to the LBZA region maxima (as was performed for the waterfall plots in Figure 5.24 - Figure 5.28). B and D show the diffractograms to 6.25°. By altering the normalisation method the LBZA region is revealed to contain reflections from two separate phases. The first phase has  $2\theta$  values for the (001) of 6° and (002) of 12°, the second phase has values for the (001) of 6.25° and (002) of 12.5°.

Figure 5.33 shows diffractograms of the (001) (A and B) and (002) (C and D) LBZA regions of the high shear rate stirring method with simultaneous addition reaction as a function of time. In the (001) region a broad asymmetric peak indicative of thin



nanoparticles is seen to be shifting to larger d spacing (smaller  $2\theta$  values) when normalised to the maxima of the LBZA (001) region. From the (002) region it can be seen that the peak envelope is made up of multiple separate phases. Normalising to the intensity at  $6.25^\circ$  reveals the region to comprise of reflections from two separate phases. Peak fitting the envelopes in casaXPS using sum-gaussian lorentzian line shaping produces two peaks with d spacings of  $\sim 1.476$  nm ((001)  $\approx 6.0^\circ$  and (002)  $\approx 12.0^\circ$ ) and  $\sim 1.420$  nm ((001)  $\approx 6.25^\circ$  and (002)  $\approx 12.5^\circ$ ). Both d spacing are broader than that of LBZA, likely representing an intermediate stage, potentially a LBZA phase with additional intercalated water, with the phase with the d  $\sim 1.476$  nm phase increasing with stir time.

### 5.3.2.2 Discussion

#### 5.3.2.2.1 Precursor phase assignment and phase transformation to LBZA

The precursor phase has been observed in previous studies, with each author noting its humidity sensitivity and tendency to convert into LBZA. As it stands there has been no agreement on what the precursor phase is with Poul, Jouini and Fievet suggesting the phase to be basic zinc acetate/ zinc oxoacetate ( $\text{Zn}_4\text{O}(\text{Ac})_6$ )<sup>[75]</sup>, Biswick *et al.* suggesting anhydrous layered  $\text{Zn}_3(\text{OH})_4(\text{Ac})_2$ <sup>[400]</sup> and Jingwei *et al.* an ethylene glycol containing zinc compound based on FTIR analysis<sup>[399]</sup>. Considering the lack of ethylene glycol in all other processes and a relatively large difference in the number of other diffractogram peak positions, the phase observed by Jingwei *et al.* is likely a similar but separate phase and can be discarded.  $\text{Zn}_4\text{O}(\text{Ac})_6$ , which has a cubic unit cell with  $a = 1.6402$  nm<sup>[423]</sup> shows a similar diffraction pattern to the observed precursor. However, there is a disagreement in the the peak spacing between  $15^\circ$  and  $20^\circ$  with a noticeable systematic absence at  $17.056^\circ$  ((301)) that is difficult to explain in a cubic unit cell with high symmetry. It should be noted these were peak patterns synthesised using the crystallographic data from the literature as no diffractograms of the phase with  $2\theta$  values in the range of interest were accessible by the author. Considering the mismatch in d spacing between the peak present in this work (0.995 nm measured vs 0.94-0.945 nm from literature) and the aqueous reaction conditions it is probable there is a difference in hydration state. The crystallised complex here would then more likely be  $\text{Zn}_4(\text{OH})_2(\text{Ac})_6$  which might reduce the cubic symmetry such that only a single high intensity peak with significantly weaker reflections from the other planes, and subtle shifts in d spacing would be observed. Furthermore, whilst highly sensitive to humidity,  $\text{Zn}_4\text{O}(\text{Ac})_6$  typically decays by hydrolysis and release of acetic acid producing

ZnO [236]. Considering the aqueous nature of the reaction, the  $Zn_4O(Ac)_6$  should be exceptionally unstable and the observation of the precursor phase in question decaying into LBZA suggests that:

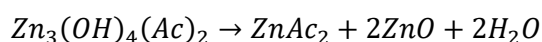
- either the local species can stabilise the compound, and the compound decays here via hydroxide acetate exchange
- or the observed precursor and  $Zn_4O(Ac)_6$  phases are different.

Biswicks *et al.* assumption of a layered  $Zn_3(OH)_4(Ac)_2$  structure stemmed from a shoulder in the dehydroxylation mass loss event observed during TGA. Their conclusion was influenced by stoichiometric equivalent phases being present in thermally decomposed copper and nickel LBZA analogues, where the acetate analogues had similar d spacings (0.934 nm and 0.908 nm respectively vs 0.945 nm [400].) Comparison was drawn with respect to nitrate versions (i.e.  $M^{2+}_3(OH)_4(NO_3)_2$  where M = Zn, Cu or Ni) derived from nitrate LBZA equivalents for each metal, that were thought to be observed in their previous studies [424], to infer the equivalency. The mass loss event was thought to evolve according to:



Equation 5.12

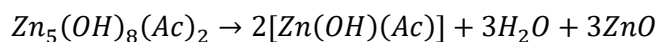
Followed by dehydration of the  $Zn_3(OH)_4(Ac)_2$  phase into anhydrous zinc acetate, zinc oxide and water.



Equation 5.13

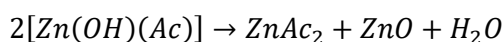
The final mass was in good agreement with complete dehydration of LBZA into zinc acetate, zinc oxide and water (error between prediction and observation less than 0.1 % of the starting mass). However, no evidence of fitting any of the profiles at the mass loss shoulder or evolved gasses in the mass spectroscopy was provided to presume the proposed intermediary process was anymore than a hypothesis.

The mass loss event observed could also be explained by dehydration producing anhydrous Zn(OH)(Ac), water and zinc oxide:



*Equation 5.14*

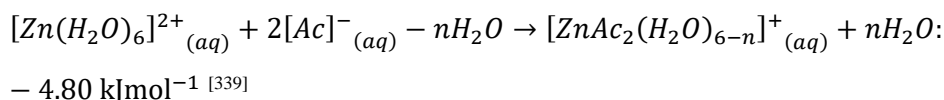
Followed by further dehydration of the Zn(OH)(Ac) phase in anhydrous zinc acetate, zinc oxide and water:



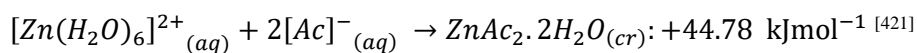
*Equation 5.15*

For each case reversability would be possible then by hydrolysis of ZnO by atmospheric water reforming  $2\text{Zn}(\text{OH})_2$ . The  $\text{Zn}(\text{OH})_2$  which could then react with either  $\text{Zn}_3(\text{OH})_4(\text{Ac})_2$  or Zn(OH)(Ac) to reproduce LBZA.

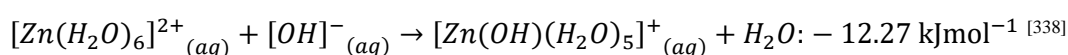
To compare the two possibilities it is useful to account for the concentration of fully complexed of  $\text{Zn}(\text{Ac})_2$ , that was calculated in section 5.3.1.2.2.2 to be  $\approx 88\%$  of all zinc species. Upon addition of sodium hydroxide, hydroxide anions form complexes with  $[\text{ZnAc}_2(\text{H}_2\text{O})_n]$ ,  $[\text{ZnAc}(\text{H}_2\text{O})_5]^+$  and  $[\text{Zn}(\text{H}_2\text{O})_6]^{2+}$  via replacement of acetate and attachment of (respectively) at least 1 hydroxide forming a mixture of  $[\text{ZnAc}_2(\text{H}_2\text{O})_n]$ ,  $[\text{Zn}(\text{Ac})(\text{OH})(\text{H}_2\text{O})_n]$ ,  $[\text{Zn}(\text{OH})(\text{H}_2\text{O})_5]^+$  and  $[\text{Zn}(\text{OH})_2(\text{H}_2\text{O})_n]$ . Nucleation of the precursor phase instead of LBZA could then be explained kinetically by the need to replace only a mean value of 1 – 1.33 Acetate anions per  $\text{Zn}(\text{Ac})_2$  as opposed to 1.6 Acetate anions for LBZA before nucleation could occur, forming either Zn(OH)(Ac) or  $\text{Zn}_3(\text{OH})_4(\text{Ac})_2$ . Thermodynamically the initial formation of the precursor phase is in general accordance with the Oswald step rule <sup>[425][426]</sup>, where reactions tend to proceed via the closest thermodynamically metastable phase instead of directly to the most thermodynamically stable state. Increasing hydroxide concentration in the unit cell via acetate replacement is expected to increase thermodynamical stability, as can be inferred from the formation energies for Zinc acetate and Zinc hydroxide complex and crystals (Equation 5.16 - Equation 5.19).



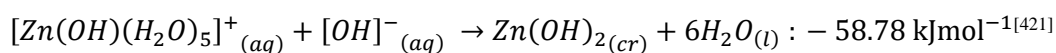
Equation 5.16



Equation 5.17



Equation 5.18



Equation 5.19

Where (aq) represents aqueous species, (cr) crystalline species and (l) liquid.

The energetics show that formation of both zinc acetate complexes and zinc hydroxide complexes are exothermic with zinc hydroxide being more stable. Unlike complexation, crystallisation of zinc acetate is endothermic and energetically unfavourable. In contrast to Zinc acetate, zinc hydroxide is strongly exothermic, as such it would be expected that greater quantities of hydroxide within the lattice would be more thermodynamically stable. The first metastable state, in accordance with Ostwalds rule, would therefore be the first metastable crystal that can form with the minimum number of hydroxides possible. As such the reduced hydroxide content in Zn(Ac)(OH) would make it the more likely candidate than the Zn<sub>3</sub>(OH)<sub>4</sub>(Ac)<sub>2</sub> proposed by Biswick *et al.*

From the 2<sup>nd</sup> order trendline for the simultaneous addition method phase areas (Figure 5.32), the reaction is a two component <sup>[155]</sup> or pseudo-two component reaction (i.e.  $A + B \leftrightarrow P$  or  $2[A] \leftrightarrow P$ ) where the rate limiting step is a two component reaction <sup>[155]</sup>. Phase transformation from precursor to LBZA could result from surface nucleation or interfacial nucleation processes <sup>[427]</sup>. If the precursor structure also contains a dipole this would mean that the transformation could potentially occur preceding oriented attachment or

initiated by oriented attachment respectively <sup>[427]</sup> As both can be diffusion limited second order diffusion processes <sup>[140][411][179]</sup> it is not clear with the available data what the underlying process is. Further work would be required to elucidate the mechanism.

### 5.3.2.2.2 Nucleation and phase purity

In all non-simultaneous addition methods the mass transport rate is lower than the complexation and nucleation rates as indicated by the significant presence of Zinc acetate, and its decreasing phase area with time; and increasing precursor phase content for the first 60 seconds. This is further demonstrated by the conductivity of the high shear rate stirring method with <1 s sodium hydroxide addition time (Figure 5.31 C) that decreases continuously over the first 75 s indicating a consumption of free ionic charge carriers <sup>[428]</sup>. The low mass transport rate results in a region of excess sodium hydroxide with  $[\text{OH}^-]/[\text{Zn}^{2+}]$  in excess of 1.6 at the point of addition, forcing  $\text{Zn}(\text{OH})_2$  complexation and precipitation as can be seen by the presence of:

- (110) and (201) reflections of  $\epsilon\text{-Zn}(\text{OH})_2$  <sup>[421][418]</sup> within the stir time of 30 seconds for the high shear rate stirring method with sodium hydroxide addition time less than 1 second (Figure 5.29).
- The presence of (100) and (002) reflections of ZnO at a stir time of 60 s for the same conditions (Figure 5.30)

Either simultaneously or directly after, the precursor and LBZA phases start to form from  $[\text{Zn}(\text{Ac})(\text{OH})(\text{H}_2\text{O})_n]$  and  $[\text{Zn}(\text{OH})_2(\text{H}_2\text{O})_n]$ . Due to the localised consumption of excess hydroxide in  $\epsilon\text{-Zn}(\text{OH})_2$  nucleation and growth some of the Zinc species remain unattached to hydroxide anions. It has been observed that the so called BLBZA phase forms in conditions with high  $[\text{Ac}^-]/[\text{OH}^-]$  ratios <sup>[68]</sup> and based on TGA and FTIR analysis of mixed phases containing 'BLBZA' that the phase likely contains excess acetate to hydroxide as compared to LBZA <sup>[68]</sup>. As a result it can be cautiously assumed that the so called BLBZA phase nucleates due to interactions between the free  $[\text{ZnAc}_2(\text{H}_2\text{O})_n]$  species and a mixture of  $[\text{Zn}(\text{Ac})(\text{OH})(\text{H}_2\text{O})_n]$  and  $[\text{Zn}(\text{OH})_2(\text{H}_2\text{O})_n]$  species. As stirring proceeds the freshly nucleated particles are mixed into unreacted regions with high ionic strength. The increase in ionic strength causes the Debye layer of the particles to shrink<sup>[1]</sup> and the particles agglomerate <sup>[401]</sup>. The agglomeration results in the instantaneous formation of a slurry <sup>[429]</sup> and visible aggregates (estimated visually to be on the order of ~ 0.1 - 1 mm in diameter) forming within the first second after hydroxide addition. As the ions are consumed the ionic

strength drops and hydrodynamic forces at the stir bar start to disperse the aggregates, resulting in a lower observed slurry viscosity (i.e increased fluid velocity at a constant stir rate) <sup>[430]</sup>. In contrast, the simultaneous addition rate has a mass transport rate on the order of, or greater than the complexation and nucleation rate required for uniform mixing <sup>[431]</sup> and inhibition of  $\epsilon$ -Zn(OH)<sub>2</sub> nucleation. Due to the increased transport and uniformity resulting from:

- the high shear rates within the first few seconds of reactant addition, partially due to the low volume of reactant media
- adding the reactants together with a feed rate with an equivalent molar ratio of 1:1.58, approximately equal to the molar ratio in LBZA of 1:1.6

no localised inhomogeneity in concentration ratios would be expected inhibiting the formation of  $\epsilon$ -Zn(OH)<sub>2</sub> and the so called BLBZA phase. The increased mixing results in complexation and nucleation completing within the first 30 seconds, and the low ionic strength and high shear forces inhibit aggregation <sup>[401]</sup> and slurry formation, <sup>[429]</sup> resulting in the lower visually observed viscosity (i.e. higher flow rate). The slurry formation and lengthened reaction time at low shear rates help to explain the polydispersity observed in section 5.3.1.2.2.1 where the rapid observed kinetics of formation should produce homogenous particle distributions according to CNT <sup>[170][169][171]</sup>. As the particles are nucleated over extended times due to the reduced mixing, the nucleated particles at the point of addition grow more than those that nucleate at a delayed time due to the high viscosity of the slurry.

### ***5.3.2.3 Effect of high shear simultaneous continuous flow addition and stir time on morphology of synthesised LBZA***

Figure 5.34, Figure 5.35 and Figure 5.36 show LBZA synthesised using the high shear simultaneous addition method, pre microwave exposure (A), freshly exposed for 30 s at 800 W (B) and after 1 hour of cooling (C) for stir times of 30 seconds, 5 minutes and 60 minutes, respectively.

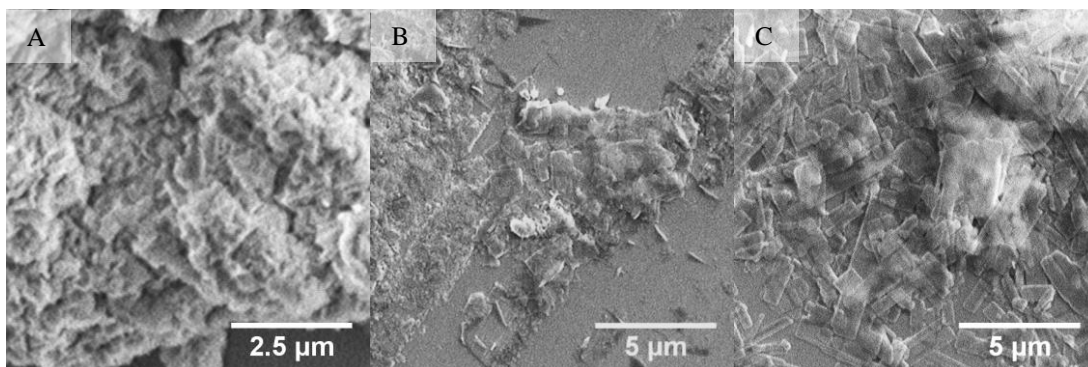


Figure 5.34: SEM micrographs of LBZA synthesised using the high shear simultaneous addition method with 1 M Zinc Acetate and 1.58 M NaOH, stirred for 30 seconds and sampled A) prior to microwaving, B) directly after 30s of 2.45 GHz microwave exposure at 800 W and C) being left to cool for 1 hour post microwave exposure. Scale bar for A – 2.5 μm, B and C scale bars - 5 μm.

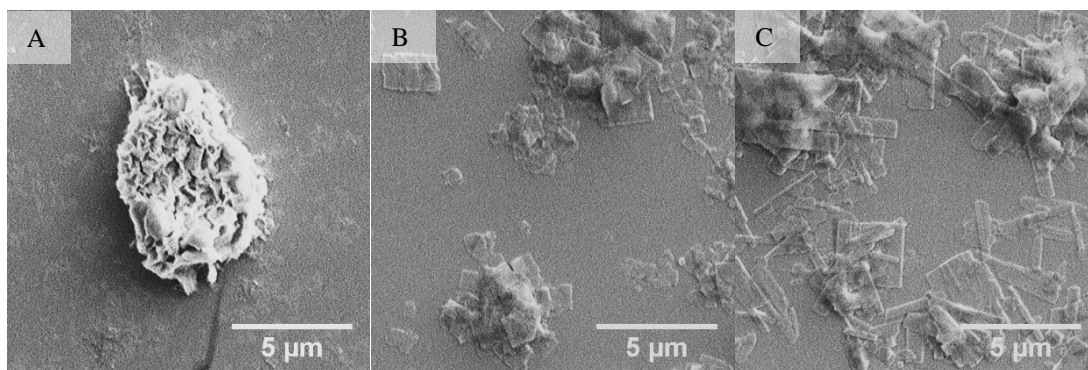


Figure 5.35: SEM micrographs of LBZA synthesised using the high shear simultaneous addition method with 1 M Zinc Acetate and 1.58 M NaOH, stirred for 5 minutes and sampled A) prior to microwaving, B) directly after 30s of 2.45 GHz microwave exposure at 800 W and C) being left to cool for 1 hour post microwave exposure. All scale bars 5 μm.

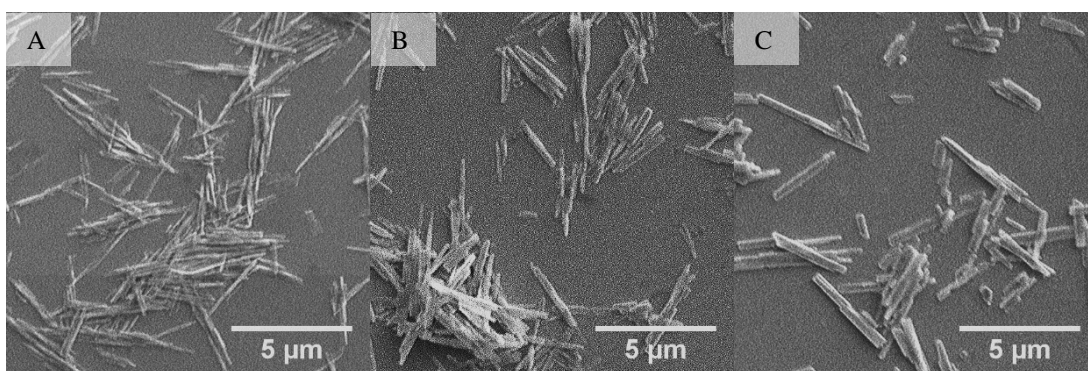


Figure 5.36: SEM micrographs of LBZA synthesised using the high shear simultaneous addition method with 1 M Zinc Acetate and 1.58 M NaOH, stirred for 60 minutes and sampled A) prior to microwaving, B) directly after 30s of 2.45 GHz microwave exposure at 800 W and C) being left to cool for 1 hour post microwave exposure. All scale bars 5 μm.

After 30 seconds of stirring (Figure 5.34 A) an aggregate of sub 1  $\mu\text{m}$  nanoparticles with widths less than 200 nm can be seen. Considering the phase areas at 30 s (Figure 5.32) it is likely the aggregate is either formed from the precursor phase or LBZA produced during the centrifuge cleaning and upon exposure to atmospheric humidity. Directly after 30 seconds of microwave exposure (Figure 5.34 B) a mixture of fully formed secondary particulate sheets and dispersed smaller particulates and particles at various length scales and stages of oriented attachment are visible. After being left to cool over an hour (Figure 5.34 C) none of the smaller particles observed directly after microwave exposure are present, and all LBZA appear fully formed with both regular and irregular morphologies (kinks, notches etc.)

After 5 minutes of stirring (Figure 5.35 A) an aggregated collection of particulates can again be seen. Directly after 30 seconds of microwave exposure (Figure 5.35 B) only secondary particulates similar in form to LBZA nanosheets are observed and have undergone significant growth. No smaller particles like that observed for the 30 seconds stirred samples, directly after 30 seconds of microwave exposure, are observed. This suggests that the smaller particles have undergone increased attachment during the stirring phase, likely due to the applied shear forces as has been observed in layered double hydroxides <sup>[137]</sup>. The low aspect ratio rectangular morphology agrees with the theorised temperature dependent suppression of the dipole induced oriented attachment growth mechanism as described in section 5.3.1.2 . Presence of what appears to be secondary particle – secondary particle oriented attachment can be seen in the top left corner where a particle with three steps, each with a small change in length, suggests fusion of three almost equivalent length particles. After cooling (Figure 5.35 C) particles with increased aspect ratio, general dimensions and polydispersity are seen. As the samples cool the effect of the internal dipole on growth rate increases resulting in the higher aspect ratio. Considering the presence of large amounts of smaller secondary and/ or primary particulates in the freshly 30 second exposed sample; increases in polydispersity is likely due to changes in secondary particle formation times during the cooling period, temperature gradients or increased secondary-secondary particle attachment. In all cases, longer stirring prior to microwave exposure would likely help to reduce the polydispersity. Additionally, the following steps might reduce polydispersity:

- If due to secondary particle formation time or thermal gradients, maintaining the temperature post microwave exposure by transferring the reaction media to a water bath until the reaction is finished and additional stirring.
- Alternatively, if due to thermal gradients only, quenching the reaction by rapidly dropping the temperature in an ice bath or solvent exchanging the electrolyte with water would reduce the effect of thermal gradients on secondary particle oriented attachment and should result in reduced sizes.



In comparison to the samples stirred for 5 minutes the particles stirred for 60 minutes (Figure 5.36) show high aspect ratio as would be expected for low temperature oriented attachment growth with lengths on the order of 5  $\mu\text{m}$ . Notably the particles appear to have a high degree of monodispersity and reduced length compared to the unexposed samples with  $[\text{OH}^-]/[\text{Zn}^{2+}]$  ratio of 1.6 in Figure 5.10, most likely due to the reduced nucleation time period as a result of the improvement in mixing. Prior to microwave exposure (Figure 5.36 A) the particles show regular, defined and dispersed secondary particles suggesting growth via attachment of primary and smaller secondary particulates is completed. After 30 seconds of exposure (Figure 5.36 B) the particles have increased width that further increases as the sample cools (Figure 5.36 C.) The sample shows little if any growth in length and have a reduced aspect ratio suggesting that the particle growth is generally due to lateral secondary particle attachment of the particulates present due to a reduction in dipole force driven longitudinal attachment.

It is clear that due to the rapid reaction kinetics, control of mass transport rates with respect to complexation and nucleation rates is one of the most important factors for the control of the phase purity and morphological monodispersity for  $[\text{OH}^-]/[\text{Zn}^{2+}]$  ratios  $\leq 1.58$  and likely up to 1.6.

## 5.4 Unified discussion

### 5.4.1 Proposed combined LBZA nucleation and growth reaction mechanism for the sodium hydroxide-based microwave assisted growth

Figure 5.37 and Figure 5.38 show flow diagrams of the processes that make up the growth mechanism of the LBZA produced via the sodium hydroxide-based microwave assisted growth, based on the observations in this work. Upon addition of sodium hydroxide to zinc acetate, hydroxide anions rapidly co-ordinates to  $[\text{ZnAc}_y(\text{H}_2\text{O})_{6-y}]^{2-y}_{y=0,1,2}$  species, forming  $[\text{Zn}(\text{Ac})_x(\text{OH})_y(\text{H}_2\text{O})_{6-x-y}]^{2-x-y}_{x=0,1,2, y=0,1,2 \text{ and } x+y \leq 2}$  complexes. The high chemical potential of the hydroxide containing species causes the particles to undergo burst nucleation <sup>[170][169][171]</sup>. In the case of the non-simultaneous flow addition methods the ability to uniformly mix the reactants is lower than the rate of addition of hydroxide and nucleation of the precursor phase.

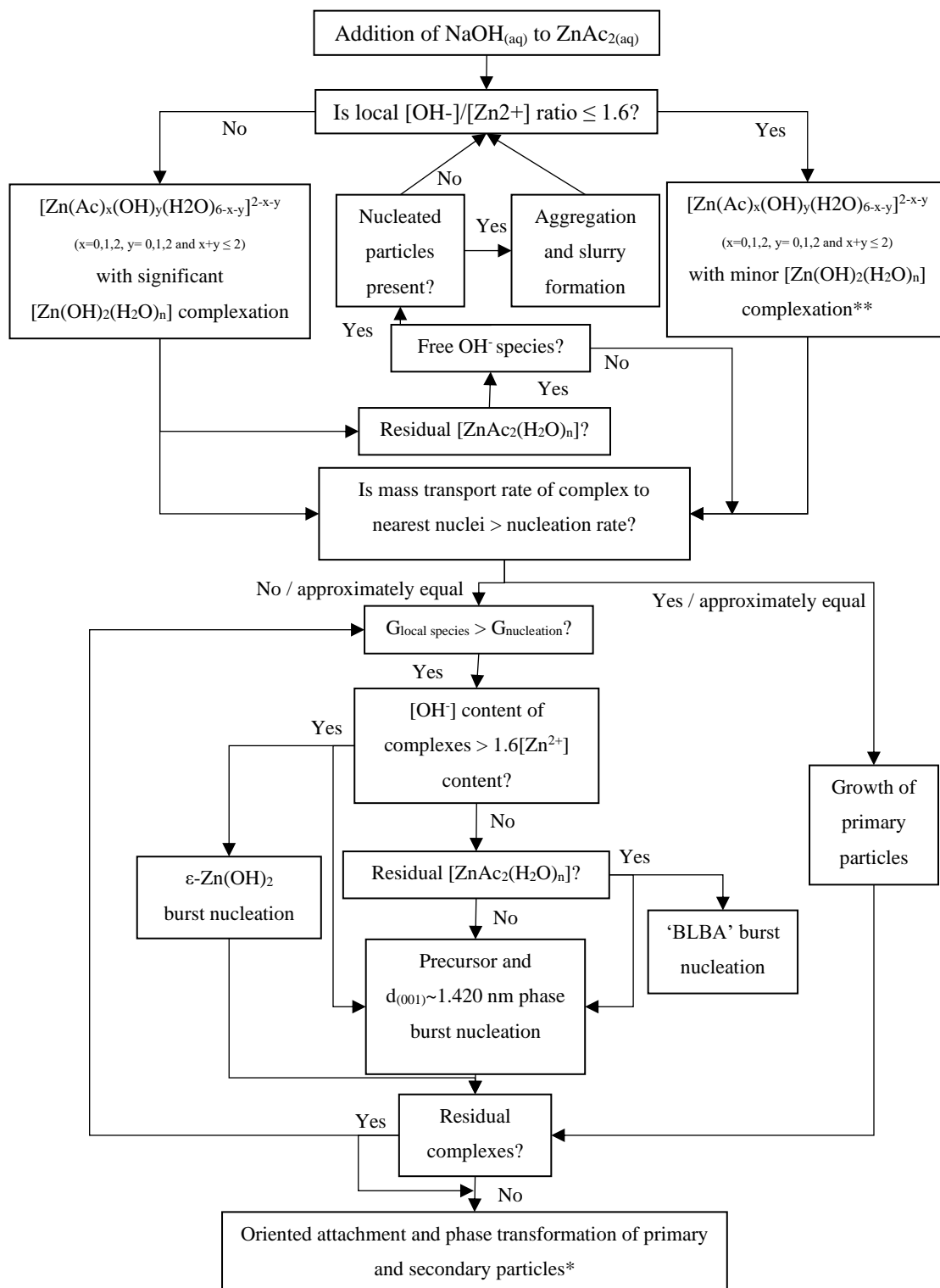


Figure 5.37: Flow diagram of the initial events that occur at the point of addition. Local  $[OH^-]/[Zn^{2+}]$  ratio is dependent on both total molar ratios as well as the addition and stir/ mass transport rate of species. Due to the rapidity of the reaction non burst nucleation has been removed for simplicity and is unlikely to occur as a major contributor to the reaction. Growth/ morphology of primary particles is governed primarily by electrostatic/ electrochemical modified transition state theories such as that produced by Crundwell<sup>[173]</sup>. Nucleation theory is well described and governed by classical nucleation theory<sup>[170][169][171]</sup>. \*\* Minor  $[Zn(OH)_2(H_2O)_n]$  complexation is expected to occur from free  $[Zn(H_2O)_6]^{2+}$  and likely account for the presence of the LBZA region peak 2 -  $d \sim 1.420$  nm phase. Note:  $G_{local\ species}$  represents the free energy of the local species and  $G_{nucleation}$  the free energy barrier for nucleation

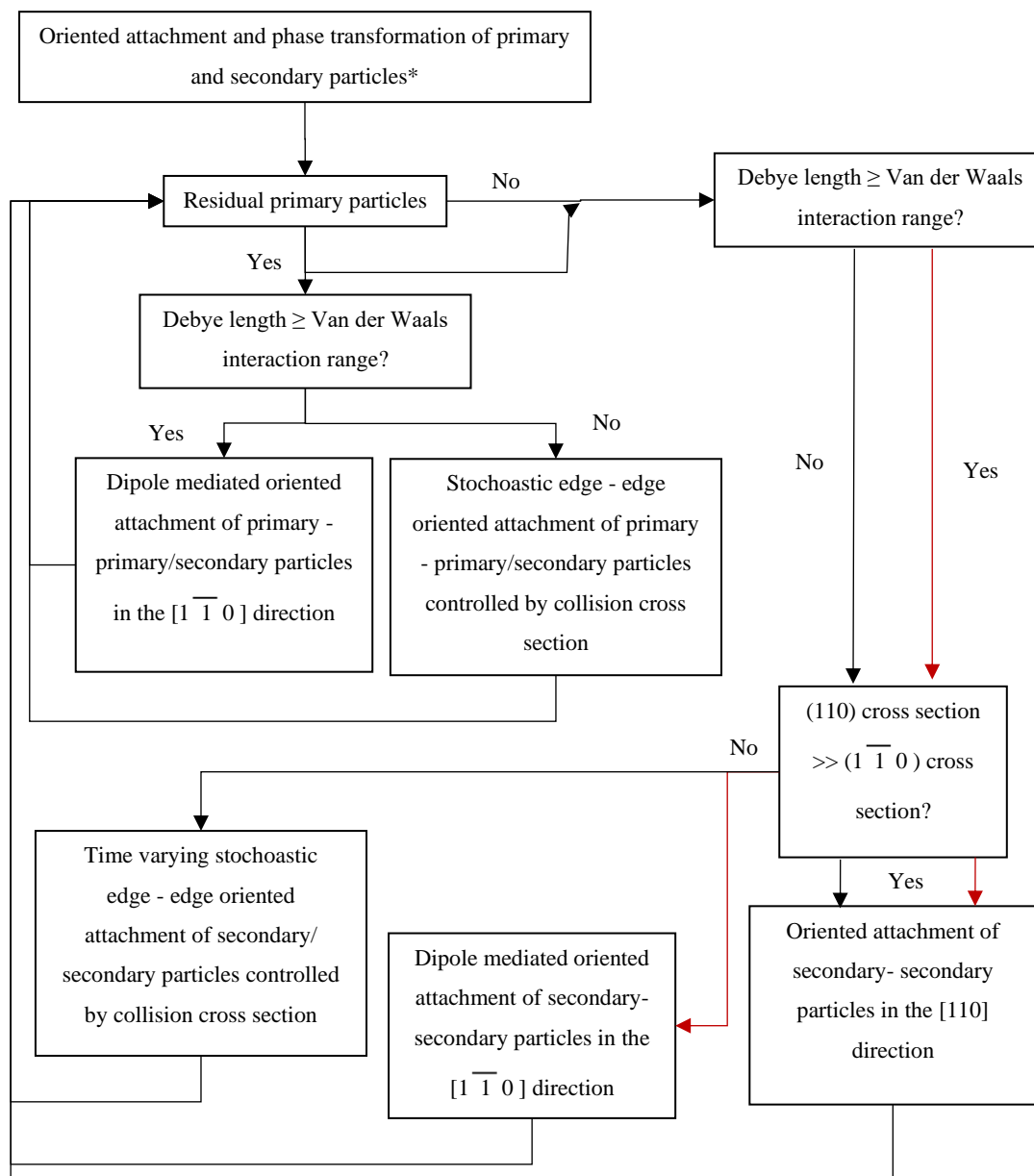


Figure 5.38: Flow diagram of the dipole mediated oriented attachment process that drive the growth mechanism of the LBZA formed within this work. The processes are expected to occur both simultaneously and after the nucleation and primary particle growth phases.

A surface layer with excess hydroxide concentration forms, rapidly nucleating and precipitating out  $\text{Zn(OH)}_2$ ,  $d \sim 1.420$  nm (LBZA region peak 2,  $2\theta = 6.25^\circ$ ) and precursor phases. As the suspension is stirred into unreacted regions the high ionic strength causes the particles to aggregate and form a slurry<sup>[429][401]</sup> further reducing the mass transport/ mixing rate. The high relative consumption of hydroxide in  $\epsilon\text{-Zn(OH)}_2$  leaves residual  $[\text{ZnAc}_2(\text{H}_2\text{O})_n]$  which complexes with other residual species and nucleating the so called

BLBZA phase. In the case of the simultaneous continuous flow addition, the rate of addition is lower than the rate of mixing, producing a homogenous reaction phase and precipitation of only the precursor zinc hydroxyacetate phase, and phases contained within the LBZA region. The phase appears to then undergo a transformation via exchange of acetate by hydroxide, resulting in the formation of the expanded  $d \sim 1.476$  nm (LBZA region peak 1) phase.

Due to the dipole present in the basal layer structure of LBZA, the primary particles undergo dipole mediated oriented attachment in the  $[1\bar{1}0]$  direction, forming small high aspect ratio secondary particles. As the secondary particles grow the dipole strength of the system grows<sup>[141]</sup> and the oriented attachment rate between primary-secondary and secondary-secondary particles increases. If the Debye length of the particle-electrolyte interface is lower than the van-der Waal interaction distance the dipole is effectively screened, and oriented attachment proceeds purely via van-der Waals interaction. As there is limited long range interaction and the energy barrier for attachment is expected to be between  $k_B T$  and  $3k_B T$ ,<sup>[179]</sup> the relative attachment direction and angle is driven by Brownian motion and the collision cross section of the edges, where the solvation barrier is lower, and is therefore stochastic in nature. In addition, if the temperature is raised, thermal energy approaches the order of the dipole driving force energy and oriented attachment again becomes generally stochastic in nature leading to a reduction in aspect ratio of the formed secondary particulates. As a result, particles that undergo microwave exposure rapidly heat and produce low aspect ratio secondary particulates.

No other effect of microwave exposure is generally expected to occur based on comparisons of field strength on both primary nanoparticle growth models of the stern layer and ion and particle electrophoretic mobilities, except for thermal gradients that may be present at short microwave times.

Whilst microwave time affects growth rate via altering temperature, altering the  $[\text{OH}^-]/[\text{Zn}^{2+}]$  ratio changes the Gibbs free energy of the starting solution and thus the magnitude of the activation barrier height. As hydroxide concentration increases the chemical potential, and as a result the Gibbs free energy increases. Based on the rapidity of reactions observed, the particulates are generally expected to undergo burst nucleation at all the tested ratios in accordance with classical nucleation theory<sup>[169][171][170]</sup>. As the particles in all but the simultaneous addition high shear stirring method samples undergo slurry formation, the early stages of the reaction become diffusion limited. The diffusion limitation results in a delayed time period over which nucleation can occur and as a result a high standard deviation/ polydispersity in length and aspect ratio. The initial increase in polydispersity

with  $[\text{OH}^-]/[\text{Zn}^{2+}]$  ratio between 0.4 and 1.2-1.4 results from both an increasing concentration of growth units and larger primary particles with greater dipole strength producing more growth at all stages and greater aggregation due to an increased ionic strength. For  $[\text{OH}^-]/[\text{Zn}^{2+}]$  ratio greater than 1.4 the increased diffusion gradient and the reduction in slurry viscosity due to smaller particulate size and increased zinc complex consumption leads to a reduction in the time period that nucleation occurs in, leading to a reduction in polydispersity. Increasing the temperature through microwave exposure decreases slurry viscosity and the diffusion rates of the reactants. This causes an increase in the nucleation rate, resulting in a further reduced nucleation time period and reduction in polydispersity. For reaction conditions with low temperatures and mass transport/ mixing rates relative to the nucleation and complexation speeds, nanobelts are produced with high polydispersity and low purity. Increasing the mass transport rate produces high purity, highly monodisperse  $\sim 5 \mu\text{m}$  high aspect ratio nanobelt without microwave exposure, and low aspect ratio nanosheets with microwave exposure.

## **5.4.2 Relevance and applicability to flexographically printed gas sensors for carbohydrate malabsorption testing and additional uses.**

### ***5.4.2.1 Relating to flexographically printed gas sensors for carbohydrate malabsorption testing***

Control and consistency of variables is an important factor for the development of reproducible and predictable industrial processes. For gas sensing and printing of inks containing particulates, the purity, structure and polydispersity of the particles are important factors. For gas sensing the primary size and size distribution effects would manifest by influencing film thickness <sup>[203][432]</sup>, grain size <sup>[203][433]</sup> and porosity <sup>[203][199][433]</sup>. Considering the particulate thickness is generally consistent to within the step resolution of the diffractograms (45 – 50 nm) and approximately equal to that of the HMTA sensor in Chapter 4.1.3 it is expected that the grain size and sensitivity/ selectivity and resistivity will generally be intrinsically similar to that of the HMTA sensor under the same annealing conditions. The main effects of size and distributions will therefore arise as a result of the printed film microstructure.

While there has been to the author's knowledge no direct systematic study on the impact of size polydispersity on flexographic printing, the effect on viscosity has been studied.

Increasing size polydispersity in suspensions leads to a lowering in viscosity at constant volume fractions <sup>[434][435][252][429]</sup>. As discussed in the Literature Review (section 2.3.6 ) lower viscosities can lead to:

- thinner films (weaker print colour) <sup>[436][267][262]</sup>
- uneven coverages (i.e. mottling) <sup>[436]</sup>
- an increase in the expansion of print features (i.e. dot gain) <sup>[437]</sup>,
- frequency of dot bridging <sup>[267]</sup> (i.e. the merging of nearest neighbour dots in tonal coverages used in the graphics industry)
- and bridging and shorting of conductive lines <sup>[16]</sup>.

Whilst Bohlin, Lestelius and Johansson <sup>[438]</sup> did not include any rheological measurements beyond stating that all inks had 1000 mPa.s at 100 rpm (spindle 4, Brookfield Viscosity), their printing study on 95% Calcium carbonate/ Kaolin pigment showed that the highest particle size distribution had the lowest print density, highest dot gain and highest mottling within lateral ranges of 0.13 – 0.25 mm. The inks tested contained particle size distributions described as:

- ‘Broad’ – 90 wt% of particles with sizes < 2 µm, 64 wt% < 1 µm and 17 wt% < 0.2 µm, total solid content 67%. Ink had the lowest print density and greatest dot gain.
- ‘Narrow’ – 95 wt% of particles with sizes < 2 µm, 75 wt% <1 µm, and 12 wt% < 0.2 µm, total solid content 63 %. Ink had the highest print density and lowest dot gain.
- ‘Small particles with broad PSD’ – 98 wt% of particles with sizes < 2 µm, 90 wt% < 1 µm and 30 wt% < 0.2 µm, total solid content of 67 %. Print density was similar to the ‘Narrow’ ink whilst dot gain was similar to the ‘Broad’ distribution ink.

Reducing polydispersity in particle length and aspect ratio is therefore of great importance. From the investigations presented it can be shown that the magnitude of polydispersity for the sodium hydroxide-based microwave assisted method at high reaction concentrations is a result of four factors: the concentration of reactants, the mixing efficiency as a function of addition rate, the stirring time and the thermal gradients during the growth period. The effect of mixing efficiency is simply a result of an inhomogeneous reaction medium and slurry formation, so improving shear rate and reducing addition rate results in improvements in polydispersity. The high shear method of stirring with a reduced addition rate (yet rapid in comparison to dropwise,) as presented is ideal for tightening particle distributions at low cost and can be improved by replacing the centrifuge tubes used to control the rate of

addition with 30 – 60+ mL.min<sup>-1</sup> syringe pumps. Further significant improvements could be made however using:

- two phase annular mixer microreactors (shear rates of 10<sup>5</sup> s<sup>-1</sup>) as used for layered double hydroxides <sup>[137]</sup>
- static t-mixer sol gel reactors with a traditional reactor post-static mixer as used for TiO<sub>2</sub> nanoparticle growth <sup>[439]</sup>
- glass fibre membrane microreactor used for metal organic frameworks <sup>[440]</sup>
- other microreactors with millisecond order mixing

Moving to a more rapid, consistent, and controllable microreactor should produce increased reproducibility, size dispersity and purity ideal for any mid to high scale project.

Microreactors also have two additional ideal properties:

- rapid heat transfer due to their high surface area/ volume ratios <sup>[441]</sup>
- scale up from lab to any other scale proceeds simply via additional parallel microreactor tubes and therefore no further optimisation is needed beyond the lab-scale <sup>[442]</sup>.

The highest concentration ratio of [OH<sup>-</sup>]/[Zn<sup>2+</sup>] = 1.6 was shown to produce both smallest, least polydisperse particles whilst simultaneously producing the highest yield and should be used with an improved experimental set-up. With the current experimental set-up, and in light of the rapidity of reaction and sensitivity of the reaction to subtle changes at a ratio of [OH<sup>-</sup>]/[Zn<sup>2+</sup>] = 1.6, an [OH<sup>-</sup>]/[Zn<sup>2+</sup>] ratio of 1.58 or 1.59 is recommended to increase reproducibility. Stirring times should be used such that any primary particles and the smallest secondary particles have already undergone oriented attachment. Thermal gradients during growth as a result of differential cooling post microwave exposure, coupled with the presence of primary and or smaller secondary particles result in higher polydispersity due to varying oriented attachment rates. Stir times greater than 5 minutes will therefore be required.

Final recommendations on the microwave exposure time is currently not possible, as while the results at low shear and rapid addition rates show a clear reduction in polydispersity with increasing microwave exposure, the opposite was seen under high mass transport rate conditions. At the present time it is recommended in general that the reaction should not be microwaved due to the increased polydispersity observed in the simultaneous addition high shear stir rate method.

The effect of morphology is more complicated and will depend on the specific printing process and gas sensing architecture. In the present situation all observed high shear

methods should result in morphologies that should easily fit within the 24  $\mu\text{m}$  anilox used for the majority of the work in this thesis. It is also highly likely, based on qualitative observations of the SEM images for the simultaneous addition stir times of 5 and 60 minutes that a smaller anilox, such as an 8  $\mu\text{m}$  anilox, with higher line count could be used without issue, providing higher fidelity features at smaller sizes <sup>[268]</sup>. The effect of length-width aspect ratios will alter on the coverage degree of the printed films. For 3D films with binder and planar 2D films with coverage far below a single layer of particulates, higher aspect ratio will increase the number of particles overlapping and increase conductivity through a lowering of the percolation threshold (the threshold at which particles overlap and form a conductive path) <sup>[443][444][445]</sup>. At layers approaching a monolayer of particulates or greater, particles tending towards 1D high aspect ratio structures (nanowires, nanotubes, high aspect ratio nanobelts) produce increased porosity under wet chemical casting methods <sup>[446]</sup> whereas 2D platelet structures tend to form denser stacked structures <sup>[446]</sup>. Increased porosity is linked with increased gas sensing sensitivity through greater exposed surface to volume ratios but conductivity decreases due to a reduction in particle-particle contact area <sup>[447]</sup>. A reduction in adhesion is also seen with an increase in porosity which would reduce device stability <sup>[448]</sup>. Considering the sensitivity of the HMTA derived LBZA device presented in section 4.1.3, which has practically the same thicknesses and observed crystal quality, and therefore expected to produce the same granular structure under the same annealing conditions, improvements in sensitivity whilst preferable are not likely to be necessary for the hydrogen sensing element in a carbohydrate malabsorption sensor. Improvements in conductivity will however lead to improved signal to noise ratio and a reduction in electronic measurement circuit costs. Increasing aspect ratio will lead to an increase in the shear thinning behaviour of the ink at higher loadings <sup>[248][449]</sup> with the internal structure under low/ no shear having the same percolation dependencies as conductivity. Although not a necessity, Newtonian behaviour will produce more consistent behaviour under different printing conditions and would help to reduce viscous fingering levelling times (as discussed in literature review section 2.3.6.4). As such, lower aspect ratio particles such as those produced under microwave exposure are preferable if the improvements in polydispersity can be produced through the previously mentioned strategies; otherwise the un-microwaved simultaneous addition 60-minute stir times samples would be preferable.



#### 5.4.2.2 *Relating to growth of layered zinc hydroxide salts*

The studies as performed within this chapter naturally arose as an attempt of applying basic growth science theories such as classical nucleation theory to the growth of LBZA to increase the control of purity and morphology, and increase yield. To the authors knowledge, based on an extensive literature review, this work represents one of the only systematic studies on the effect of  $[\text{OH}^-]/[\text{Zn}^{2+}]$  ratio, temperature and effect of mass transport on layered zinc hydroxide salts crystal growth and nucleation for any counter-ion. The only other systematic study found was performed on Simonkoellite <sup>[146]</sup> for which the chemistry was discussed in great detail but no mechanism of growth effects on morphology was provided. Based on the calculations presented, the crystal structure induced electric field is expected to be approximately 4 orders of magnitude greater than the microwave electric field strength for the uncharged (110) surface. Combined with the short microwave induced ion drift distances vs ion spacing in the reaction volume, the results presented here are expected to be fundamental to the underlying reaction instead of microwave exposure and therefore directly comparable to other LBZA reactions.

The two other studies that attempt to categorise the effects both use HMTA <sup>[166][152]</sup>, where the hydroxide concentration is not known a priori but inferred from parallel experiments on pH due to thermal hydrolysis without zinc salts which can alter the buffer system dynamics <sup>[155]</sup>. This, combined with assumptions made by authors within the literature, has led to erroneous conclusions, such as stating that the maximum  $[\text{OH}^-]/[\text{Zn}^{2+}]$  ratio before forming ZnO was 1 <sup>[70]</sup>, yet the studies presented here clearly show that not only is LBZA stable at  $[\text{OH}^-]/[\text{Zn}^{2+}]$  ratios up to 1.6 but also that the presence of ZnO derives from inhomogeneities in the reaction mixture due to poor mass transport to complexation and nucleation rate ratios. Again, fundamental misunderstanding of the analytic techniques used in the literature and a lack of rigor have resulted in erroneous conclusions that BLBZA is a single bilayered structure <sup>[68][74][450][71]</sup> and not two separate crystallographic phases, i.e. LBZA and a secondary phase (which has been called BLBZA/ so called BLBZA within this work for simplicity), with very few authors arguing for separate phases based on the fundamental theory of the techniques used <sup>[135][131]</sup>.

Very few models for aqueous LBZA growth exist. At best they describe growth as aggregation <sup>[70]</sup> or self-assembly of primary particles with no underlying reason or structure to the mechanism or simply describe the complexation that occurs <sup>[68]</sup>. As such, no understanding in literature is presented for the resulting morphology and size distributions seen in LBZA growth. Analysis of basal layer crystal structure revealed a dipole not

described in the literature. Applying simple calculation of the effect of the dipole to the electrostatic/ electrochemical modifier in Crundwells modified chemical kinetic theories, [172][173] the underlying anisotropy of primary particles shown in HRTEM [70] and measured from XRD [167][67] and SAED [166] in the literature can be explained. More importantly the presence of dipole driven oriented attachment can explain the preferential [110] attachment direction of primary particles. It also describes both the temperature and, when combined with the effect of diffusion time on nucleation time period, concentration dependence on secondary particle morphology. Furthermore, this is the first time where the presence of a metastable precursor phase with  $d_{(011)} \approx 0.995$  nm, an apparent transition to a second LBZA region phase with a d spacing  $\sim 1.476$  nm ( $2\theta = 6^\circ$ ), or the presence of the LBZA region phase at the point of nucleation with d spacing  $\sim 1.420$  nm ( $2\theta = 6.25^\circ$ ) during synthesis has been reported. Based on thermodynamic data for Zinc acetate, zinc hydroxide and the ratio of fully complexed Zinc acetate to total zinc species prior to hydroxide addition, a candidate phase of Zn(OH)Ac is suggested for the precursor phase.

## 5.5 Conclusion

Combining electrostatic/ electrochemical modified kinetics and oriented attachment theory, a mechanistic process capable of successfully describing features of aqueous LBZA growth, ranging from morphology and size distribution of the primary particle to that of the secondary particles, has been produced based on the internal dipole structure of LBZA. Clearly the results of the studies present a large and fundamental step forward in the understanding of LBZA growth within aqueous media and show the ability to separate nucleation and growth periods, a requirement for control of crystal growth purity, morphology and particle size distribution [169] [451][452][453][454]. Considering the increasing frequency of studies using layered zinc hydroxides for purposes such as gas sensing [145][138][129][130], supercapacitors [144][147][152] photocatalysts [148][455][456][135], quantum dot sensitized solar cells [457], dye sensitized solar cells [458][70], galvanic protection [150], drug delivery system [459] and expressed interests in use as part of bacteriocidal coatings [389], understanding and controlling the morphology and purity of structures is becoming increasingly important. It is hoped that prior to the publication of results that further literature review and comparison of separate counter ions in the layered zinc hydroxide crystal family will produce a consistent and uniform theory or a clear distinction of where particular theories should be applied. As an example, layered zinc carbonate has been shown to produce hierarchical flower structures that are made up of nanobelts expanding radially

from a central point <sup>[130][138]</sup>. HRTEM and SAED results showed the belts to be made up of primary nanoparticles with an oriented/ preferential direction. The common secondary and primary particle structures follow the same expected results as presented here, yet the common origin and hierarchical tertiary structure suggest a differing nucleation mechanism. Further review and application of the current theories may result in a simple explanation arising from basic anion chemical properties and its ability to undergo complexation with zinc cations.

At the current state of experimental understanding, the high shear stir rate method with simultaneous steady flow addition method is recommended with  $[\text{OH}^-]/[\text{Zn}^{2+}]$  ratios between 1.58 – 1.6 and stir times of 60 minutes without microwave exposure, for use in carbohydrate malabsorption printed gas sensors. Recommendations to both experimental set up (microreactor and/ or syringe pumps) and reaction conditions have further been suggested based on the results of the experimental observations. Microwave exposure of 30 s at 800 W at the current reaction volume and reactor vessel cross section is recommended if a stir time between 5 and 60 minutes and cooling rates can be found that reduce the polydispersity resulting from application of microwave exposure. Based on calculations of the depth at half power at low temperatures (17.5 mm at 295 K/ 21.8 °C) the reaction vessel diameter should not be increased as this would produce increased temperature gradients and an increased size distribution.

## Chapter 6 - Flexographic printing of LBZA nanomaterial and proof of concept gas sensors

---

### 6.1 Introduction

In this chapter, flexographically printed nanogranular ZnO gas sensors using the particles synthesised in Chapter 4 are designed, created and discussed. As mentioned previously, flexographic printing is a roll to roll printing technique capable of reproducing printed design at (up to ~4) meters per second line speeds <sup>[245]</sup>. Through the development of a layered basic sheet ink, printed gas sensors are designed and discussed.

For the printed sensors Kapton HN was chosen as the substrate material for its capability of continuous operation at 350 °C, and brief operation above 400 °C and for its flexibility, which is required to unlock the high throughput potential of roll-to-roll printing. Initial tests utilising a commercial water-based silver nanoparticle ink for the interdigitated electrodes showed poor wetting and printability on the Kapton substrate and therefore led to a need for surface treatments. To improve wettability, oxygen plasma, wet chemical treatment, and a combination of both were investigated and optimized.

For the sensing layer, initially a solvent based LBZA NS ink was created and optimized utilising polyvinylpyrrolidone as a binder/ resin to increase viscosity. However, characterisation of the thermal treatments required to remove the binder to expose the surface showed binder removal occurred at temperatures ( $\geq 450$  °C) that created instabilities in the substrates and lead to catastrophic failure of a tested sensor. During the experiments an empirical  $\ln(\text{viscosity}/\text{nominal width relation})$  was observed for nominal line width/ anilox cell width ratios greater than 0.492. The observations appear to be the first reported within ratio ranges of 0.496-7.2. The results, including the LBZA mass loadings used as guidance for the work within this chapter, are presented in Appendix Chapter 13 for reference.

During the investigations within Appendix Chapter 13 glycerol was observed to successfully suspend LBZA particulates. The observation allowed for the creation of a binderless ink, removing the 450+ °C binder burn out step that led to the substrate failure for the PVP based proof of concept sensors. Within this chapter a binder-less glycerol-based ink is created and used to make and test 3 proof of concept gas sensors. The proof of concept sensors, the first

in the literature to sense more than oxygen, showed problems with transfer of the underlying Ag electrode material to the sensing layer, altering the sensor response. Potential solutions to the problem are then discussed for future development.

## 6.2 Material selection rationale

### 6.2.1.1 Substrate selection – Kapton HN

The elevated temperature requirement that are generally necessary for gas sensing (approximately 235 °C to 325 °C for H<sub>2</sub> and higher for other gasses for LBZA derived ZnO – see chapter 4.1.3 for details) restrict substrate material to a select few material types. Furthermore, to not influence the sensing response, the electrical resistance of the substrate must be at least 3 to 4 orders of magnitude greater than the sensing layer such that current flow within the substrate can be neglected. Substrate materials in literature for deposited synthesised nanomaterial typically take the form of ceramics (most notably alumina [460][461][69][462][356][463][464],) and high temperature polymers (most notably polyimides [465][466][467][38][59].)

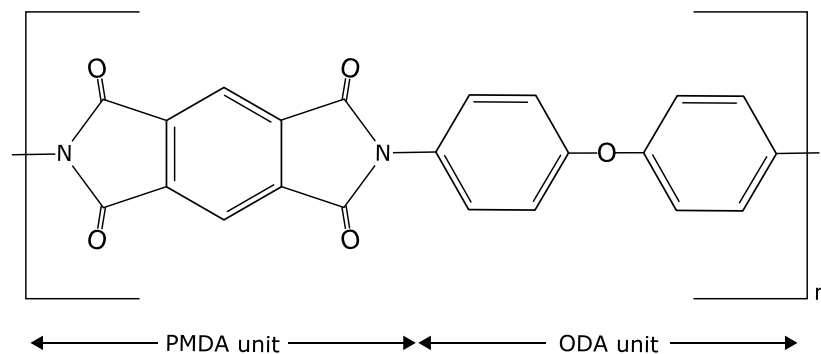


Figure 6.1: Skeleton diagram of Kapton (poly(4,4'-oxydiphenylene-pyromellitimide)) high temperature stable polyimide chosen as substrate material for the proof of concept flexographic printed gas sensors.

Both alumina and polyimides have high volume resistivities of  $10^{14} \Omega \cdot \text{cm}$  [468] and  $2.3 \cdot 10^{17} \Omega \cdot \text{cm}$  at 25 °C [469] respectively, with alumina dropping to  $5 \cdot 10^{10} \Omega \cdot \text{cm}$  [468] at 300 °C and polyimides to approximately  $10^{13} \Omega \cdot \text{cm}$  at 205 °C (value for Kapton - i.e. poly(4,4'-oxydiphenylene-pyromellitimide, skeleton diagram shown in Figure 6.1)) [469]. Alumina is both chemically and mechanically stable at high temperatures and has been used

to make gas sensors with process temperatures of up to 950 °C [462]. In comparison polyimides are generally restricted to gas sensor calcination processes and operation temperatures below 350 °C [59] - 500 °C [59] depending on the particular polymer. Metal oxide gas sensors using polyimide substrates, annealed at 400 °C, have however been shown to produce stable and reproducible gas sensing responses over a 2 months period at 300 °C in ambient air [38]. As the long-term aim of the project was to produce low cost sensors, not only for breath analysis but to potentially expand into other application markets, price per unit surface area was an important factor when deciding between the two substrates. Alumina is significantly more expensive than polyimides per square metre with prices of £1242.60 per m<sup>2</sup> (0.5 mm thick) for 96% alumina [470] versus £129.08 per m<sup>2</sup> (25 µm thick) [471] to £249.28 per m<sup>2</sup> (75 µm thick) [472] for Kapton HN polyimide (manufactured by DuPont, Wilmington, Delaware, US.)

TGA experiments conducted in dry air on Kapton HN polyimide (PMDA-ODA, poly(4,4'-oxydiphenylene-pyromellitimide)), performed by DuPont and reported within the product data sheet [469], show the onset of mass loss to be 450 °C. The temperature exceeds the calcination temperature that the HMTA derived LBZA was converted into ZnO in chapter 4.1.3 by 100 °C. Isothermal weight loss measurements performed at 400 °C in air [469] also show no mass loss within the 1000 minutes data range shown. Combining the TGA data with the glass temperature of the material which was reported at between 360 °C and 410 °C [469] suggests Kapton HN films should be stable over the needed processing and operating temperatures ( $\leq 350$  °C). Based on the reasoning and properties as listed above Kapton HN was chosen as the substrate material to use.

### **6.2.1.2 Conductive electrode – PFI-722 Ag NP flexographic ink**

Typical gas sensors use platinum [463][433][214][65][473] or gold [474][475][476][345] as electrode/contact material due to their high temperature and chemical stability. Recently examples of silver electrode/ contacts have been reported [477][65][17][478]. The aim of producing low cost gas sensors guided the choice of electrode deposition material to flexographic printing in line with the gas sensing layer deposition.

At the time of these investigation no commercial flexographic platinum or gold ink was available to purchase, as such both materials were removed as a material choice. Electrode material was therefore limited to the choice of silver or carbon commercial flexographic inks. Design and development of a custom platinum or gold ink was ruled out due to the

high cost of the materials that would be incurred during development. The ability to make an informed rational decision on electrode ink was limited to the information available and provided by ink manufacturers. Most manufacturers only list cure temperature and not operational or thermal stability range, as a result electrode ink choice was justified by comparing inks manufactured by Creative materials (Maryland, US) which had the data provided. Carbon based inks had useful operation ranges of 175 °C<sup>[479]</sup> – 200 °C<sup>[480][481]</sup> with thermal stability ranges up to 325 °C<sup>[479]</sup>. In comparison silver inks had operation ranges between 200 °C<sup>[482]</sup> and 275 °C<sup>[483]</sup> with thermal stability up to 325 °C<sup>[482][483]</sup>. Thermal stability of both materials is below that of the required temperatures for the LBZA derived gas sensor and is likely limited by the binder material. Binder burn out can introduce adhesion issues between the conductive film and substrate in printed carbon based conductive ink films<sup>[254]</sup>. Furthermore in a technical report by DuPont (U.K.) Ltd.<sup>[484]</sup> low binder content in conductive carbon films were reported to undergo cohesive failure. In contrast to carbon inks, silver nanoparticles ink sinter at temperature improving cohesiveness of the film. Unlike carbon, silver can undergo oxidation at low temperatures, however the oxides are thermodynamically unstable. XRD of isothermally annealed Ag(I)Ag(III)O<sub>2</sub><sup>[485]</sup> in dry air for 1 hour showed that Ag(I)Ag(III)O<sub>2</sub> decomposed to Ag<sub>2</sub>O at 119.85 °C, whilst Ag<sub>2</sub>O started to decompose to Ag metal between 199.85 °C - 349.85 °C<sup>[485]</sup>. Measurements of the equilibrium pressure for Ag<sub>2</sub>O meanwhile show that the temperature where the dissociation pressure exceeds 1 atmosphere is 190 °C<sup>[486]</sup>, above 190 °C Ag<sub>2</sub>O decomposes into Ag and O<sub>2</sub>. The combination of Polyimide and silver nanoparticle ink has also been used successfully in the only report in literature of flexographic printed gas sensor<sup>[17]</sup>, where both silver electrodes and a Zinc acetate seed layer for hydrothermally growth of ZnO nanowires were printed and calcined at 350 °C. Based on thermal stability silver nanoparticle ink was chosen over carbon-based inks. The particular ink chosen was PFI-722 conductive flexographic ink manufactured by Novacentrix (Austin, Texas, US)<sup>[487]</sup>. The ink was chosen for its advertised high silver content (60 %), low volume resistivity (5 – 7 μΩ.cm), listed compatibility with polyimide substrates and its capability of printing sub 25 μm features. Sensor resistance using an IDE is geometrically defined by the area of electrode-sensing layer interface and the distance between electrodes. Therefore, maximizing the number of electrodes within a defined area via the reduction of line width can reduce sensor resistance without impacting sensitivity. Reduced resistance can lead to improved signal to noise ratio and the price of test electronics in the final product. The ability to print fine lines without shorting was therefore considered a critically important factor.

## 6.3 Chapter specific equipment overview

### 6.3.1 Flexographic Printers

Two separate flexographic lab scale ‘proof’ printers are used within the investigations within this chapter, namely the F1 flexographic printability tester (IGT testing systems, Amsterdam, Netherlands) and the FlexiProof 100 (RK PrintCoat Instruments Ltd., Hertfordshire, UK.) All test prints reported within this document were performed at room temperature,  $\sim 20$  °C.

#### 6.3.1.1 F1 Flexographic printability tester (IGT testing systems)

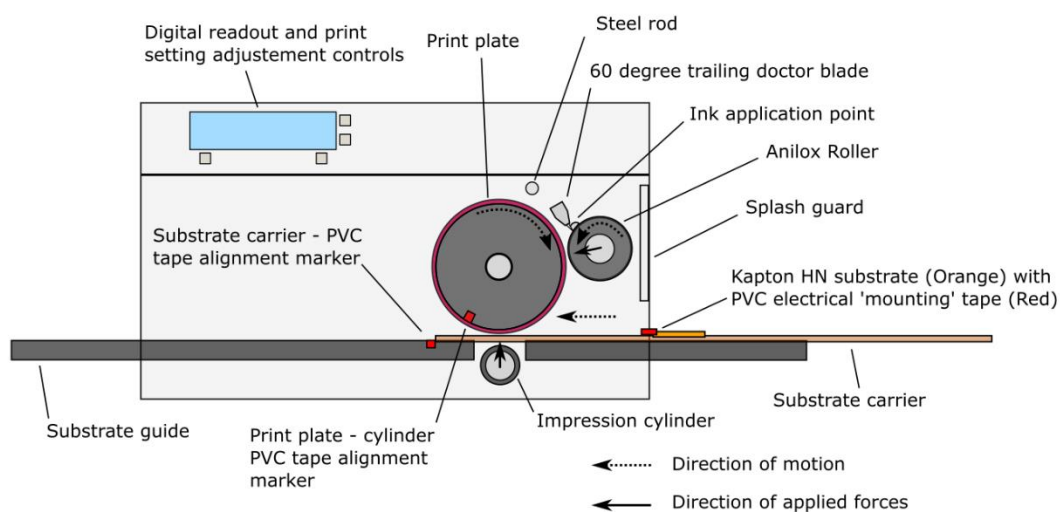


Figure 6.2: Annotated schematic of F1 flexographic printability tester (IGT Testing systems) used for printing the LBZA inks within these investigations. Dotted lines represent the direction of motion for the anilox cylinder/roller, print plate roller and substrate carrier. Solid arrows show direction of forces controllable by the printer i.e. anilox roller-print plate roller force and print plate roller-impression cylinder roller. PVC tape alignment markers were initially placed such that the desired print feature would be printed approximately halfway through each print. Permanent marker was used to mark on the side of the substrate carrier where the print pattern would be printed. For all prints the substrate, substrate carrier, and when removed and remounted, print plate were referenced consistently to the alignment markers for repeatable alignment. Print plate total length  $\sim 500$  mm long x 50 mm wide. Substrates ‘mounted’ on substrate carrier using PVC tape such that under normal conditions the tape was greater than 10 mm away from print feature location.

The F1 has been used successfully by Yusof <sup>[16]</sup> to print fine lines of 75  $\mu\text{m}$  with 75  $\mu\text{m}$  gaps using graphical inks, whilst Lloyd *et al.* <sup>[17]</sup> successfully printed basic zinc acetate ( $\text{Zn}_4\text{OAc}_6$ )



ink lines with widths down to 60  $\mu\text{m}$ . The F1 is a lab scale roll to plate printer that, unlike traditional industrial flexographic printers, uses pre-set forces to control the applied pressure within the print nips <sup>[488]</sup>. The roll to plate configuration as shown in the annotated schematic in Figure 6.2 allows the printer to print on a wide variety of substrates and not just flexible foils. The print parameters that can be varied on the F1 are:

- Print speed which can be varied between 0.1  $\text{m}\cdot\text{s}^{-1}$  and 1.5  $\text{m}\cdot\text{s}^{-1}$ .
- Engagement force between print-plate cylinder and impression cylinder which can be varied between 10 N and 300 N. <sup>[488]</sup>
- Engagement forces between print plate cylinder and anilox cylinder can be varied between 10 N and 300 N. <sup>[488]</sup>
- Anilox volume, line count and material. For these studies' ceramic anilox with volumes of 24  $\text{mL}\cdot\text{m}^{-2}$  (line count - 80 lines per cm) and 2.7  $\text{mL}\cdot\text{m}^{-2}$  (line count 180 lines per cm) were available. A larger selection can be purchased directly from the manufacturer.
- The number of preprint inking steps. During the inking steps, the print plate cylinder and anilox are brought into contact and rotated a pre-set number of times (up to 20) during which ink is transferred to the print plate.

Ink is applied to the anilox roller with a disposable pipette <sup>[488]</sup>, the ink volume applied is dependent on the roller volume and how much ink has already been applied. Typical initial volumes applied are on the order of 300  $\mu\text{L}$  and are topped up when the applied ink is running low. When ink is reapplied however is left to operator intuition and due to a lack of side-dams, application of too much ink can cause the ink to overflow onto the substrate carrier and substrate. The doctor blade assembly comprises of a plastic doctor blade held within a steel holder at a trailing 60 ° angle with respect to the anilox roller. During printing the typical applied force between the doctor blade and is approximately 6-7 N <sup>[488]</sup>.

The technical specifications list substrate and print plate sizes of up to approximately 500 mm by 40 mm <sup>[488]</sup>. Substrates are mounted to the substrate carrier typically with adhesive tape. A generic brand PVC electrical tape is used within these investigations for its low cost and ready availability. To produce reproducible alignments, PVC tape was applied to the side of the print roller as a reference marker for print plate mounting. An additional piece of PVC tape was applied to the substrate guide to allow for the alignment of the substrate holder rapidly by touch. Lengthwise substrate holder alignments on the order of 1 mm are possible within no more than 2 seconds, an important factor considering the volatility of the solvent ink components. Practical lateral alignment is generally limited to between 1 and 2 mm. To align the substrate to the desired features on the print plate a test print is performed,

either on a substrate or directly onto the holder. The desired print features can then be marked out on the side of the holder with permanent marker to which the substrate can be aligned to. Within these investigations IPA was used as the testing fluid for the alignment test prints. Substrates are generally cut oversize for the desired print design/ feature to allow for room for the print to restabilize after the adhesive tape and to allow room for alignment error. A minimum of 10 mm was left between PVC tape and the desired print feature print location. Discontinuity in the printed features at the transition between adhesive tape and substrate is usually no more than ~2 mm.

During a typical print test, first a substrate is mounted to the substrate holder at the desired location and the print buttons are pressed during which the printer resets the print roller to an initial location. Ink is manually applied to the anilox via a pipette after which the ink is applied to the anilox during the inking step. Post inking step, the impression cylinder forces the substrate carrier into contact with the print plate accelerating the carrier and substrate and printing the desired pattern. Post printing, the substrate is removed, the next substrate mounted, and the substrate holder is aligned to the PVC tape. Printing steps are repeated until the desired number of steps are reached.

*Note that from here in, anilox-print roller forces are referred to as anilox force whilst print-impression roller forces are referred to as print force.*

### **6.3.1.2 FlexiProof 100 (RK PrintCoat Instruments Ltd.)**

In comparison to the IGT F1 the RK FlexiProof 100 as shown in Figure 6.3, is a lab scale roll to roll printer that uses the industrial standard of positive engagement (a measure of relative displacement) to control the printing pressures <sup>[263]</sup>. The use of engagement creates more even pressure between varying scale features than the force-based approach of the F1. In addition ink application is controlled via an open air reservoir formed between the doctor blade assembly, anilox cylinder and PTFE side dams <sup>[263]</sup>. The doctor blade used is made from hardened steel and the pressure applied to the anilox is controlled manually via a threaded screw mechanism <sup>[263]</sup>. Substrate with dimensions of 105 mm width and up to 297 mm in length are mounted directly to a self-adhesive strip and tabs embedded within the steel impression roller. Alignment of substrate is therefore defined by how accurate the operator can manually mount the substrate. The print plate is aligned to radially engraved lines on the print cylinder.

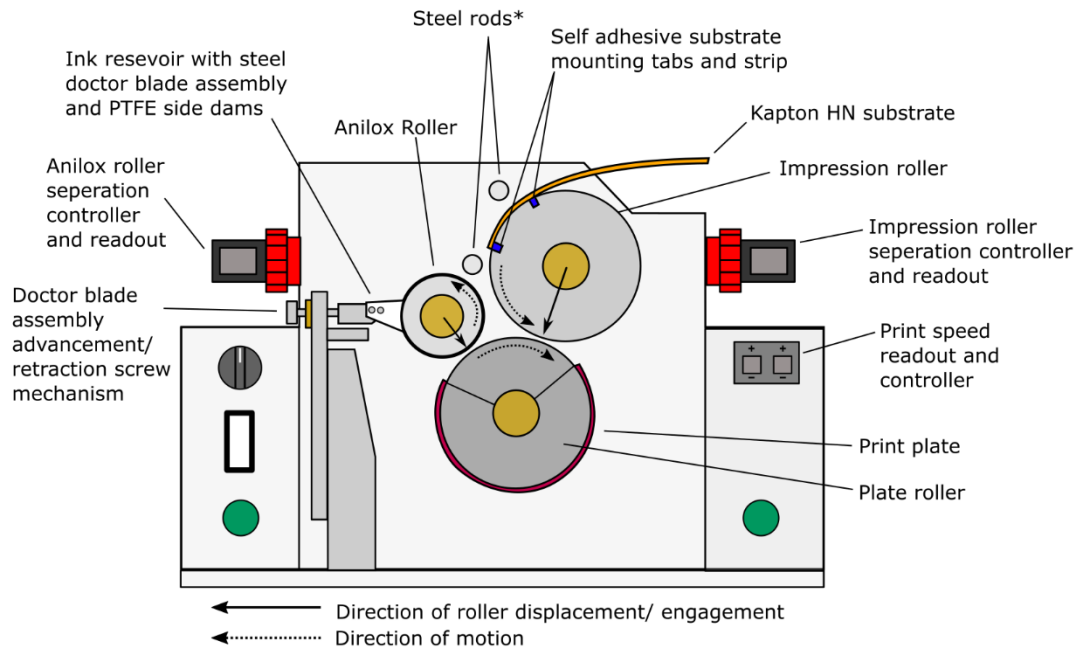


Figure 6.3: Annotated schematic of FlexiProof 100 (RK PrintCoat Instruments LTD.) used for printing the conductive silver electrodes used within these investigations. Dotted line arrows represent the direction of rotational motion for each printing cylinder, solid line arrows represent the direction of the controllable displacement/ engagement of the cylinder. Ink is applied to an open-air reservoir comprised of the stainless-steel doctor blade assembly with PTFE side dams. Doctor blade contact pressure is controlled by advancing or retracting the screw mechanism. Anilox and impression roller displacements are controlled via the twist mechanism controllers in 4  $\mu\text{m}$  steps. Print plate is aligned to the radial lines of the print cylinder. Substrate is mounted to the self-adhesive strip and pads. Substrate dimensions 297 mm x 105 mm (Half an A4 sheet), \* Steel rods prevent the substrate from making contact with the anilox roller and ink reservoir.

The print parameters that can be varied on the FlexiProof 100 are:

- Print speed which can be varied between  $0.333 \text{ m.s}^{-1}$  and  $1.65 \text{ m.s}^{-1}$ . [263]
- The displacement of the impression cylinder towards the plate cylinder which can be incremented in 4  $\mu\text{m}$  steps. [263]
- The displacement of the anilox cylinder towards the plate cylinder which can be incremented in 4  $\mu\text{m}$  steps. [263]
- Anilox volume, line count and material. For these studies, ceramic anilox with volumes of  $24 \text{ mL.m}^{-2}$  and  $3.5 \text{ mL.m}^{-2}$  were available. A larger selection can be purchased directly from the manufacturer.

Print tests follow the same general format as for the IGT F1 except that ink is applied to the reservoir and the substrate mounted to the predetermined self-adhesive mounting position.

### **6.3.1.3 Specific printer usage rationale**

For the LBZA ink development the IGT F1 flexographic printability tester was chosen for its ability to print on smaller substrates reducing ink development costs. For the conductive electrode printing the RK FlexiProof 100 was chosen both for its open-air ink reservoir to alleviate the rapid drying of the PFI-722 ink on the press observed in section 6.5.1.2 , and for its theoretical ability to print finer and multiscale features more uniformly. All print plates used for the printing experiments were custom designs, plates were manufactured by SGS Packaging Europe Ltd. (East Yorkshire, UK) using 1.7 mm Digital Rave flexographic plates with the HD Lux process (MacDermid Graphics Solutions, Georgia, US.)

## **6.3.2 Automated gas sensor testing rig**

In Chapter 4.1.3 , gas sensor tests suffered from artefacts due to pressure variations and temperature variations that limited the ability to discern the underlying response to methane. Furthermore, the manual nature of the test procedures naturally led to increased timing variations. To increase repeatability, accuracy and process capability a new gas sensor testing rig was designed and produced.

### **6.3.2.1 System Overview**

Figure 6.4 shows a simplified schematic of the automated gas sensor testing rig for which a comprehensive diagram and description is provided in Appendix Chapter 13. In brief the gas sensing chamber consisted of the 20 mm internal diameter DN25KF T-pieces (LewVac components Ltd, Sussex, UK) used in Chapter 4.1.2 . SCG256A404VMS normally closed solenoid valves (ASCO Numatics, Emerson. United States) were used to control the test gas entering the system and to control the chamber exhaust. After the solenoid valves the gasses are fed into GFC-17 mass flow controllers (Aalborg) and then into the sensing chamber where the sensor is mounted on a DN25KF 4 pin K-type thermocouple feedthrough (LewVac components Ltd, Sussex, UK.) All gas flow components were connected with ¼ inch outer diameter, unpassivated 304 stainless steel tubing (Swagelok, Bristol, England, UK,) and ¼ inch 304 stainless steel t-piece and elbow connectors with Swagelok compression fittings (Swagelok, Bristol, England, UK.). Tests were performed using the

same 1000 ppm H<sub>2</sub>, CO and CH<sub>4</sub> in N<sub>2</sub> test gasses and N5 O<sub>2</sub> provided by BOC special gasses division, and OFN from BOC industrial division as used in chapter 4. All gas bottles were connected via two stage regulators.

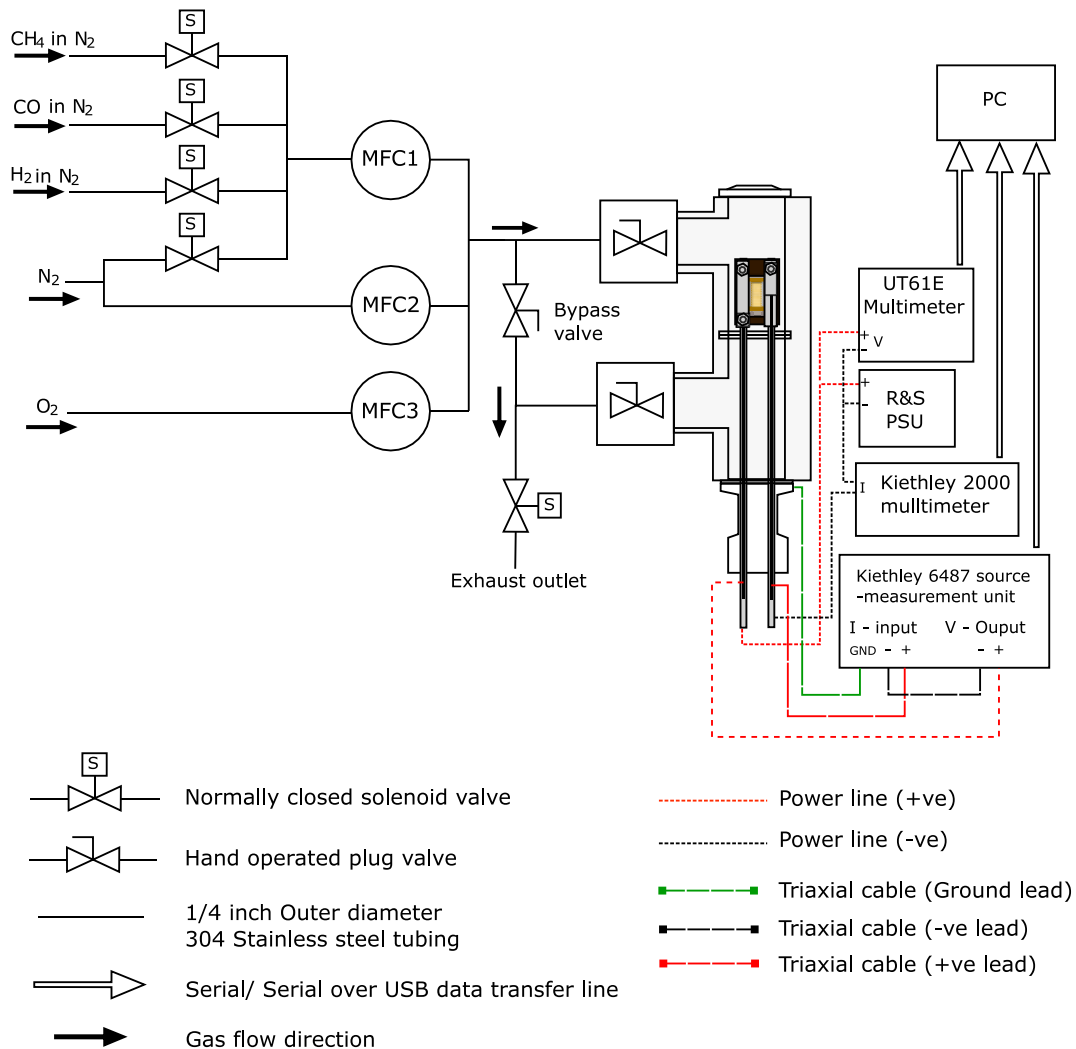


Figure 6.4: Simplified annotated schematic of the automated gas sensor testing rig used within these investigations. The GFC 17 (Aalborg) mass flow controllers and DN25KF T-pieces (Lewvac) with internal diameter of approximately 20 mm used for the manual gas sensor testing rig presented in Chapter 4.1.1.5 . were reused for the automated rig. Mass flow controller flow ranges: MFC1 (Test gas line): 0–100 mL.min<sup>-1</sup>, MFC2 (N<sub>2</sub> balance line): 0-1000 mL.min<sup>-1</sup> and MFC3 (O<sub>2</sub> line): 0-200 mL.min<sup>-1</sup>. GFC 17 MFC accuracy 1% of total flow range<sup>[489]</sup>.

Gas sensor current and resistance was measured by a Keithley 6487 source measurement unit (Keithley Instruments LLC, Ohio, US.) Power to the heater track was provided by a HMC8042 PSU (Rohde & Schwarz, Munich, Germany), with the voltage across the feedthrough electrodes measured by an UT61E Multimeter (UNI-T, Unit trend Co. Ltd. China) and the current by a Keithley 2000 multimeter (Keithley Instruments LLC, Ohio,

US.) Room temperature and external chamber temperature were monitored using DHT22 temperature sensors (Aosong Electronics co. Ltd. China.) A custom in house LabVIEW program (LabVIEW - National Instruments, Austin, Texas, US) was used to control the testing rig. The LabView program was able to control and record the solenoid valves, MFCs, Keithley 6487 SMU, UT61E Multimeter and Keithley 2000 multimeter. Sensor temperature was estimated using a pre-determined calibration curve. All parameters, including acquisition time, multimeter measurement ranges, sensor resistance, heater track current, voltage and estimated temperature, mass flow rates and individual solenoid states were monitored and provided in real time and recorded in csv. format. Individual measurement conditions can be pre-set prior to the start of a test and updated at any point during.

### 6.3.2.1.1 Printed sensor substrate holder and test set-up

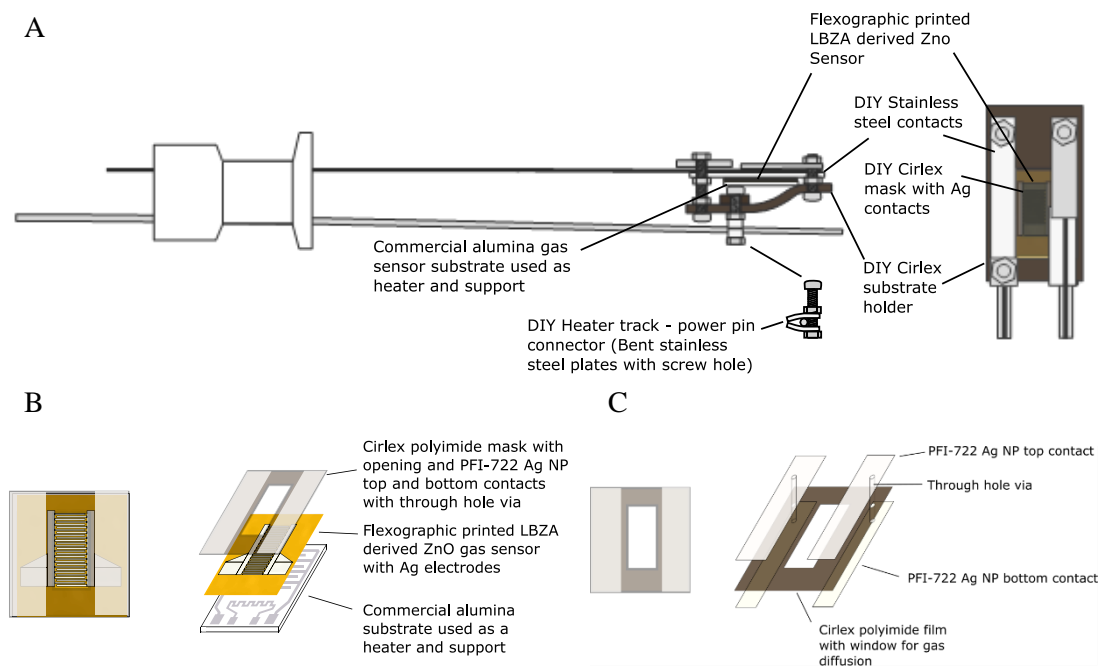


Figure 6.5: Annotated schematics of the substrate holder used in this chapter. A) shows the Cirlex polyimide substrate holder, Cirlex polyimide mask, printed LBZA derived ZnO sensor and commercial substrate used as a heater. 316 stainless steel bolts are used to attach the sensor and heater contacts to the 4-pin thermocouple feedthrough used originally in Chapter 4.1.3. B) shows how the mask, printed sensor and commercial substrate are assembled prior to mounting in the substrate holder. C) Shows a schematic of the Cirlex polyimide mask. A window was cut into the mask to allow gas diffusion to the sensing layer. A through hole via was created by piercing an approximately 1 mm diameter hole in the Cirlex after which silver electrically connected top and rear side contacts were created by painting, curing and sintering PFI-722 Ag NP ink. The width of the electrodes was such that the sensing area, and hence IDE's, of the electrodes would not short. Low outgassing Kapton vacuum tape was used to isolate the rear side fasteners from contact with the sensing chamber.

The sensors were mounted on a custom substrate holder as shown in Figure 6.5. The substrate holder was mounted to the same LewVac thermocouple/ power 4 pin electrical feedthrough as used in chapter 4.1.3 . The substrate holder was made up of 6 sheets of 0.3 mm Cirlex polyimide (Katco Ltd., Hertfordshire, UK) into which 5 holes were punched and 316 stainless steel nuts and bolts were used as fasteners and connectors. Cirlex was chosen for the following reasons:

- It is made of the same polymer as Kapton (PMDA-ODA) providing high temperature electrical insulation <sup>[490]</sup>. In addition, it should possess the same thermal stability as the sensor substrate at the temperatures used for sensor testing.
- its ease of machinability
- and its ready availability.

Mounted onto the substrate holder was an assembly of commercial alumina substrate, the printed LBZA derived ZnO sensor and a Cirlex polyimide mask. The alumina substrate was of the same type as used for the LBZA derived ZnO sensor presented in chapter 4.1.3 . The Cirlex mask was used to provide even pressure to the printed sensor and contained a 10 mm long window cut into it to provide access for the gasses to reach the sensing layer. To provide electrical connectivity between the sensor and the feedthrough, top side and rear side contacts connected by a through hole via were created. To create the via two approximately 1 mm diameter holes were pierced into the substrate with an awl. Top side and rear side electrodes were then sequentially painted on using PFI-722 Ag NP ink and cured, following curing of the contacts on both sides, the mask was annealed at 350 °C on a hotplate to sinter the silver. Stainless steel strip contacts were used to connect the mask to the feedthrough and provide structural rigidity to the assembly. The contacts were fastened via drilled holes through which the substrate holder stainless steel fasteners were attached. The commercial substrate was mounted to the substrate holder such that the rear side heater contacts of the commercial substrate was connected to the head of two stainless steel bolts which were filed flat. Application of pressure using the fasteners bent the Cirlex such that it provided a pinching point for the commercial substrate holder providing further rigidity to the assembly. Each bolt connecting the heater track was then electrically connected to the feedthrough using two stainless steel plates drilled and bent in such a way that when pressure from the fastener nut was applied the power pins were pinched and trapped.

## 6.4 Methods

### 6.4.1 PFI 722 Ag NP Flexographic print – Interdigitated electrode print optimisation

#### 6.4.1.1 Surface energy optimisation – O<sub>2</sub> plasma treatment

Initial print tests of PFI-722 showed 2 main problems, low ink spreading and problems relating to ink drying on the print press during operation. To improve wetting, solvent exposed washed Kapton HN films were exposed to low pressure O<sub>2</sub> plasma (99.999 % purity) in an HPT-100 barrel reactor RF plasma generator (Henniker plasma, Runcorn, UK). First the substrate was cleaned in an ultrasonic bath for 15 minutes in acetone, 15 minutes in IPA and then 15 minutes in reverse osmosis water. Post cleaning, the substrates were exposed to 0, 1, 5, 10, 20, 30, 40, 50 and 60 seconds of O<sub>2</sub> plasma at a flow rate of 20 mLmin<sup>-1</sup>, producing an equivalent chamber pressure of 1-1.03 mbar. Post treatment contact angle and surface chemistry (via XPS) measurements were performed.

##### 6.4.1.1.1 Contact angle measurements

As the PFI-722 Ag NP ink is aqueous based, changes in surface energy were qualitatively monitored by measuring the contact angle of water as a function of plasma time. Contact angle measurements were performed using an FTÅ-1000B goniometer (First Ten Ångstroms, California, US) and analysed using the as packaged FTÅ-32 software (First Ten Ångstroms, California, US.) The goniometer used the manual touch off method to form the sessile drop measured. For each test a droplet of water, typically 3- 4 µL in volume, was first formed at the end of a 1 mL syringe with a 22 gauge, 0.7mm external diameter flat tip needle (Becton, Dickinson and Company, New Jersey, US) mounted within the goniometer. The droplet was placed onto the substrate and syringe and the needle rapidly withdrawn. The droplet was recorded during the placement and for 20 seconds after using the CCD camera within the goniometer. The equilibrium water contact angle was then measured from the recorded video using the FTÅ-32 software. For each plasma condition 5 equilibrium contact angles were recorded with mean and standard deviation calculated. T-tests were performed to test whether the control and 1 s plasma exposed sample, and between samples exposed to



30 and 60 seconds of plasma were statistically significant. A p-value of 0.05 was used as the threshold for significance. Finally, PFI-722 Ag NP ink contact angle measurements were performed on 10 s O<sub>2</sub> plasma treated substrates. 5 measurements were performed with the mean and standard deviation recorded.

#### ***6.4.1.1.2 XPS surface chemistry analysis***

The change and progression of the surface reactions with plasma treatment time was monitored using an Axis Supra XPS (Kratos Analytics Ltd. Manchester, UK.) Scans were recorded using a monochromated Al K $\alpha$  x-ray source (photon energy - 1486.6 eV) with charge compensation provided by the Supra's proprietary magnetic confinement charge compensation system. Scans were recorded using a 300  $\mu$ m x 700  $\mu$ m slot aperture with hybrid electromagnetic/ electrostatic lens. Region scan pass energy was set to 40 eV with a step size of 0.2 eV, x-ray source electron gun was set to 15 mA current. Typical analysis chamber pressures ranged between 5 \*10<sup>-9</sup> Torr and 5 \*10<sup>-8</sup> Torr. The spectrometer was calibrated by the manufacturer using recorded spectra of in-situ monoatomic argon etched copper, silver and gold samples. Initial survey scans were recorded to tune the charge compensator parameters following which O 1s, C 1s and N 1s regions were recorded for the 0, 1, 5, 10 and 60 seconds plasma exposed samples. Due to heavy differential charging no region spectra for the 20, 30, 40 and 50 seconds samples were recorded. For each exposure time 3 samples were measured. Data fitting was performed in CasaXPS (Casa software Ltd., Devon, UK), for each region linear or Shirley backgrounds were applied and GL(30) gaussian (70%)/ Lorentzian (30%) multiplicative pseudo Voight functions were used. FWHM was generally restricted between 1 and 1.3 eV. Kapton envelope peaks were based on a simplified version of that presented by Briggs<sup>[305]</sup>. C 1s peak energies were referenced to functional groups using a reference list compiled by Briggs<sup>[305]</sup>. T-tests were performed to test whether differences observed in functional group concentration between control and 1 s of plasma exposed samples were statistically significant, a p-value of 0.05 was used as the threshold for significance.

#### **6.4.1.2 Surface energy optimisation – wet chemical hydrolysis and conversion of polyimide to polyamic acid**

Solvent washed Kapton was converted into polyamic acid using a slightly modified method from that presented by Lee *et al.* [491]. Originally the tests were performed under aqueous conditions which led to partial dissolution of the substrate material. The results for the aqueous solution are reported in appendix Chapter 13 for transparency. To inhibit dissolution the aqueous solvent was replaced with a blend of 75% ethanol/ 25 % water. The treatment as reported in the main text was performed as follows:

- Prior to treatment the substrates were cleaned in an ultrasonic bath in acetone, then IPA and finally water. Each step was performed for 15 minutes.
- Substrates were submerged into either a 0.375 M or 1.5 M NaOH solution, using a solvent blend of 75% Ethanol/ 25% water, for 10, 20, 30, 40, 50 or 60 seconds. During this step the imide bonds are broken open and converted into sodium carboxylate and amide functional groups [491]. The amide bonds the ODA ring structure to the PMDA residual. (See Figure 6.1 for a skeleton diagram of the PMDA-ODA, *i.e.* Kapton, structure).
- Substrates were rinsed by submerging into an initial volume of deionized water for 10 seconds, it was then submerged again into a second volume of deionized water for a further 10 seconds.
- Substrates were then submerged into an 0.1 M aqueous HCl solution for 20 seconds. During this step the sodium carboxylate group is protonated into a carboxylic acid group [491].
- Substrates were rinsed by submerging into an initial volume of deionized water for 10 seconds. Finally, it was then submerged again into a second volume of deionized water for a further 10 seconds before being left to air dry.

For all steps a volume of 30 mL was used, all solutions and tests were contained and performed inside propylene centrifuge tubes due to its inertness with acidic and basic conditions. The treated substrates deionized water contact angles and XPS surface chemistries were then measured and data processed as presented in sections 6.4.1.1.1 and 6.4.1.1.2 For the XPS measurements the survey and region pass energies were set to 160 eV and 20 eV respectively, step size was set to 0.5 eV and 0.1 eV respectively. Finally, PFI-722 Ag NP ink contact angle measurements were performed on 10 s 0.375 M NaOH 75% Ethanol/ 25% water polyamic conversion treated substrates, 5 measurements were

performed with the mean and standard deviation recorded. T-tests were performed to test whether differences observed in functional group concentration between the control and 10 s hydrolysis treated sample were statistically significant. A p-value of 0.05 was used as the threshold for significance.

#### ***6.4.1.3 Combined 75% Ethanol/ 25% Water polyamic conversion and plasma treatments***

Substrates were washed and subsequently treated in 0.375 M NaOH solutions in a 75% ethanol/ 25% water solvent blend as described in section 6.4.1.2 . Post conversion of the surface polyimide groups to polyamic acid the substrate was exposed to 10 seconds of oxygen plasma as described in section 6.4.1.1 . Water contact angle and XPS surface chemistry measurements were measured as described in 6.4.1.1.1 and 6.4.1.1.2 respectively. Finally, PFI-722 Ag NP ink contact angle measurements were performed on the combined treatment substrates, 5 measurements were performed with the mean and standard deviation recorded. T-tests with a cut off for significance of 0.05 was used to test whether the effects of the various treatments were significant compared to the control. From here on in the combined conversion and plasma treatments are simply referred to as the combined wet chemical and plasma surface treatments for simplicity.

#### ***6.4.1.4 Silver interdigitated electrode (IDE) prints***

##### ***6.4.1.4.1 Initial test prints***

Silver electrode test prints were performed on 50  $\mu\text{m}$  Kapton HN film treated using the wet chemical and plasma surface treated substrates described in section 6.4.1.3 . Test prints were performed on the FlexiProof 100 (RK PrintCoat Instruments Ltd.) using PFI-722 Ag NP ink (Novacentrix, Austin, Texas, US). Substrate and ink choice rationale can be found in section 6.2 , printer detail and substrate alignment description were outlined in section 6.3.1.2 . The RK FlexiProof 100 was chosen over the IGT F1 to combat the drying issues observed in the initial test print. The anilox used had a volume of 3.5 mL.m<sup>-2</sup>. Print speed was set to 1.5 m.s<sup>-1</sup> based on observations by Yusof, that higher print speeds led to reduced printed line width <sup>[16]</sup>. Prior to printing the ink reservoir was filled with PFI-722 until it was

approximately half full (between 1 and 2 mL of ink). Print tests were performed keeping the impression roller at a constant position and advancing the anilox roller until a uniform coating of ink was transferred to the print plate. The impression roller was then advanced until the substrate was brought into contact with all features just printing (i.e. a kiss print.) From this position an additional dummy print was done followed by:

- 2 prints at 0 distance (i.e. at the kiss press distance)
- 2 prints at 40  $\mu\text{m}$  positive engagement between impression and plate rollers (i.e. 40  $\mu\text{m}$  reduction in roller centre to centre distance.)
- 2 prints at 80  $\mu\text{m}$  positive engagement between impression and plate rollers
- 2 prints at 120  $\mu\text{m}$  positive engagement between impression and plate rollers
- 2 prints at 160  $\mu\text{m}$  positive engagement between impression and plate rollers.

The digital print plate design can be seen in appendix Chapter 13.

#### ***6.4.1.4.2 Electrode test prints for the binder-based gas sensor tests***

Variation in impression pressure over the print surface seen in section 6.5.1.2 , with over impression of features centred at the right-hand side adhesive mounting pad led to high degree of shorts forming. To combat the presence of shorting for the binder-based gas sensors, silver electrode prints were performed on 50  $\mu\text{m}$  thick Kapton HN foils treated using the wet chemical and plasma surface treatment (Section 6.4.1.3 ). Printer set up was performed as described as in section 6.4.1.4.1 however engagement was kept at the kiss print distance.

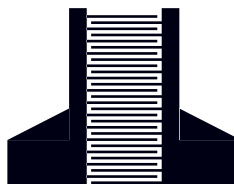


*Figure 6.6: Interdigitated electrode design at 300 % scale of the digital file. IDE geometry of the design shown corresponds to the 150  $\mu\text{m}$  wide electrode with 200  $\mu\text{m}$  spacing*

The print plate design contained only IDE with digital design geometries of:

- 150  $\mu\text{m}$  electrode width and 200  $\mu\text{m}$  spacing as shown in Figure 6.6
- 175  $\mu\text{m}$  electrode width and 175  $\mu\text{m}$  spacing

The design of the plate was split into 2 halves length wise, each half contained 3 rows of 14 IDE of one of the as described geometries. Each IDE had a total width of 13.25 mm x 10 mm in the digital file. 5 prints were performed in total.

## **6.4.2 Binderless glycerol based LBZA ink development**

### ***6.4.2.1 LBZA nanomaterial synthesis***

All LBZA nanomaterial was synthesised and centrifuge cleaned using the method outlined in chapter 4.2.2.1 using  $[\text{OH}^-]/[\text{Zn}^{2+}]$  ratios of 1.5 and microwave time of 20 seconds. To produce inks, 4 synthesis and cleaning runs were performed. After the final centrifuge cleaning step, all samples were topped up with 99.5 % purity IPA (Fisher Scientific UK Ltd., Leicestershire, UK) and centrifuged at x3260 g for 5 minutes. Post centrifuging the supernatant was discarded and each pellet was dispersed in approximately 20 mL IPA and added to a 100 mL measuring cylinder. The LBZA dispersion was stirred manually with a glass stirring rod for approximately 30 minutes, alternating between mixing within the measuring cylinder and pouring the mixture back into the centrifuge tubes, mixing and pouring back into the measuring cylinder. After the final transfer back into the measuring cylinder the centrifuge tubes were washed with IPA, the IPA residual sheet mix was poured into the measuring cylinder and topped up with IPA to produce a total volume of 100 mL, after which the mixture was finally stirred for 5 minutes. Based on the mean sample mass yield of 1237 mg for the synthesis procedure presented in chapter 4.2.3.3, the concentration of the blend was estimated as  $49.48 \text{ mg}\cdot\text{mL}^{-1}$ . All inks were produced using the IPA LBZA blend, and LBZA mass was measured out volumetrically using the estimated concentration and micropipettes.

### ***6.4.2.2 Solvent blend rationale and mixing***

The solvent blend contained glycerol (1, 2,3 – propanetriol, surface tension:  $45.6 \text{ mN/m}$  <sup>[492]</sup>, dynamic viscosity:  $1.5 \text{ Pa}\cdot\text{s}$  <sup>[492]</sup>, and boiling point:  $290 \text{ }^\circ\text{C}$  <sup>[492]</sup>), propylene glycol (surface tension:  $45.6 \text{ mN/m}$  <sup>[493]</sup>, dynamic viscosity:  $40.4 \text{ mPa}\cdot\text{s}$  <sup>[493]</sup>, and boiling point:  $188.2 \text{ }^\circ\text{C}$  <sup>[494]</sup>) and n-butanol (surface tension:  $25.0 \text{ mN/m}$  <sup>[493]</sup>, dynamic viscosity:  $2.54 \text{ mPa}\cdot\text{s}$  <sup>[493]</sup>, and boiling point:  $117.6 \text{ }^\circ\text{C}$  <sup>[495]</sup>), all solvents were  $\geq 99\%$  purity, Glycerol

and n-butanol were manufactured by Acros-organics and Propylene glycol by Sigma-Aldrich. All short-chain alcohols were chosen due to their miscibility and compatibility with the MacDermid Digital Rave photopolymer plate used <sup>[496]</sup>. N-butanol was chosen over IPA (boiling point 82 °C <sup>[497]</sup>) to reduce surface tension and help prevent dewetting during drying. Propylene glycol was chosen as an intermediate solvent as to:

- Reduce viscosity loss due to the dilution of glycerol
- Reduce ink surface tension during drying when n-butanol has fully, or mostly evaporated, leaving a film of glycerol.

The values of the blend used for all experiments within this chapter was first developed using a simple pass-fail trial and error testing approach. For each test, 3 µL of the solvent test blend was drop cast onto Kapton HN wet chemical and plasma surface treated substrates. The solvent blend was considered to fail if:

- The sessile droplet dewetted during drying on a hotplate at 150 °C.
- The blend viscosity was lower than ~ 20 mPa.s, the minimum required for printing <sup>[4]</sup>. Due to the large number of solvent blends this was qualitatively measured by comparing the vortex height of a set volume of the ink to that of ethylene glycol (16 mPa.s). The vortex height test was justified by the fact that all of the blends are simple Newtonian fluids and so the height of the vortex, which is related to the shear forces, should produce vortexes of equivalent height if both tested solvents have the same viscosity. If the test blend had a lower viscosity a higher vortex would be formed and a lower vortex for a higher viscosity. Vortex heights higher than that produced by ethylene glycol was considered a failure. Vortex height close to that of ethylene glycol were considered unfavourable (partial failure).

For the tests, solvent blends with values of X % glycerol, Y % propylene glycol and Z % n-butanol were produced. Values of X trialled were 10, 20, 30 and 40, for each value of X values of Y up to X+Y=100 in increments of 10 were trialled. To maximize viscosity the blend which passed with the highest glycerol and propylene glycol concentration (prioritizing glycerol) was used for all further binderless ink tests. The blend consisted of 30% glycerol, 30% propylene glycol and 40% n-butanol and had a vortex height approximately equivalent to that of propylene glycol (~40 mPa.s.) LBZA mass loading for the inks was set to 46.6 mg.mL<sup>-1</sup> based on the concentration that produced the highest coverage in the PVP ink LBZA mass loading experiment (appendix Chapter 13) with the expectation of refining the mass loading based on the gas sensing and electrical properties of the printed films. To mix the ink first, the desired volume of ink was extracted from the IPA/LBZA blend and centrifuged, the solvent was first exchanged with the solvent blend,

redispersed and centrifuged again to remove any excess IPA. Post centrifuging, solvent blend was added up to a volume that created the desired  $46.6 \text{ mg.mL}^{-1}$  LBZA concentration. The LBZA nanomaterial was then redispersed and mixed using a combination of a stirring rod and treatment in an ultrasonic bath until complete dispersion was achieved.

### **6.4.2.3 Ink Characterisation**

#### **6.4.2.3.1 Interfacial tension (IFT) measurements**

Surface tension measurements of the inks was measured using the pendant drop method. Tests were performed using a FTÅ-1000B goniometer (First Ten Ångstrom, California, US) and analysed using the as packaged FTÅ-32 software (First Ten Ångstrom, California, US.) For each test a droplet of ink, typically 3- 4  $\mu\text{L}$  in volume, was formed at the end of a 22 gauge, 0.7mm external diameter flat tip needle attached to a 1 mL syringe (Becton, Dickinson and Company, New Jersey, US.) mounted within the goniometer. For each ink 5 measurements were performed, and the mean and standard deviation calculated. To assess the density of the ink for the mass calculations performed by the analysis program, 5 sets of 1 mL ink were extracted, the mass recorded using a 4 decimal point analytical mass balance with accuracy of  $\pm 0.5 \text{ mg}$ , and a mean of  $0.992 \text{ mg.mL}^{-1}$  and standard deviation of  $0.016 \text{ mg.mL}^{-1}$  calculated.

#### **6.4.2.3.2 Dynamic viscosity measurements**

To assess the dynamic viscosity of all inks, viscosity was recorded using a Bohlin Gemini HR nano rheometer (Malvern Panalytical, Worchester, UK). Measurements were performed in the cone and plate geometry using a 20 mm diameter cone with  $2^\circ$  radius. All tests were performed at  $20^\circ\text{C}$  with a solvent trap to reduce the loss of volatile ink components. The table of shears method was used to measure the steady state dynamic viscosity. Two tests, each with measurements of increasing and decreasing shear performed sequentially after each over the full shear range, were performed directly after each other to test for thixotropy. The shear range tested was  $0.1 - 4621 \text{ s}^{-1}$  with 29 data points with a  $\log_{10}$  separation of 0.1667.

#### **6.4.2.4 Ink print tests**

##### **6.4.2.4.1 Force optimisation experiments**

Print tests were performed using the F1 flexographic printability tester (IGT testing systems, Amsterdam, Netherlands,) using a 24 mL/m<sup>2</sup> anilox at approximately 20 °C. In line with the silver electrode print speeds, all print tests were performed at 1.5 m.s<sup>-1</sup> to simulate on-press conditions for sequential silver/ LBZA print. For each print a single revolution pre-coat was used for the inking step. General alignment and printing procedures are described in the printer overview in section 6.3.1.1 . Anilox and print roller were adjusted together with both having forces 80 N, 100 N, 125 N and 150 N.

Tests were performed on 25 µm thick Kapton HN wet chemical and plasma surface treated substrates with a cross sectional area of 50 mm x 50 mm. Thinner substrates than for the silver print were used with the F1 for the LBZA ink test prints. The change was performed to save on costs and was justified by the F1 using forces rather than engagement distances to control impression pressure; as such the change in thickness was not expected to affect the print quality in a significant manner. For each force setting 5 prints were performed, the first two prints of each test were used to allow for the printer to stabilise and were not used for analysis. Directly after each print the substrate was immediately transferred from the substrate to a hotplate set at 150 °C to remove residual solvent. Due to the limitations in alignment capability of the F1 (up to ~2 mm, approximately 20 % of the length of the IDE) a solid block print plate was used for all LBZA test prints. The decision was made such that the optimized values could be used to print initial test sensors with no variation in coverage due to misalignment.

Print film morphology was recorded using the Keyence VHX-1000 optical microscope. From the recorded micrographs pin hole density was compared qualitatively by visual inspection.



### 6.4.3 Binderless ink proof of concept test sensors

#### 6.4.3.1 Test sensor printing

##### 6.4.3.1.1 Silver electrode print

Silver IDE were printed using the general method outlined in 6.4.1.4.2 ; however, to lower the on press drying rate, printing was performed within a fume cupboard, with flow off, at a relative humidity of 90 % at ~20 °C. To reduce drying on the print plate between prints and to increase electrode mechanical stability, the 3.5 mL/m<sup>2</sup> anilox was replaced with a 24 mL/m<sup>2</sup> anilox. The printed electrodes were then cured and dried at 150 °C.

##### 6.4.3.1.2 Binderless ink sensing layer

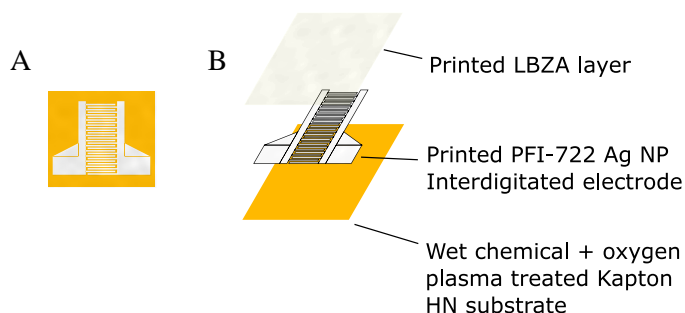


Figure 6.7: A) Top down diagram of the as printed binderless ink sensor B) annotated diagram of the individual comprising layers.

Post drying, the substrates with printed silver electrodes were cut into 50 mm wide strips and LBZA films printed using the F1 flexographic printability tester (IGT). For the layer, the binderless ink was printed with a print and anilox force of 150 N and print speed of 1.5 m.s<sup>-1</sup> using a solid block print plate design. Post printing the ink films were dried at 150 °C. A simple annotated schematic of the final as printed and dried sensor, showing both silver and printed LBZA films, is presented in Figure 6.7.

#### **6.4.3.2 Sensor calcination**

Prior to calcination a Carbolite tube furnace (Carbolite, Derbyshire, UK) was calibrated by measuring the steady state temperature using the RS PRO k type thermocouple at 20 °C intervals of the furnace controller.

To calcine the sensors and check if the thermal ramp rate was part of the silver failure mechanism, 50 IDE with overprinted LBZA films were cut out. 25 electrodes were inserted directly into the tube furnace at 400 °C and annealed for 5 minutes, the other 25 electrodes were inserted into the tube furnace and set to ramp to 400 °C over 11 minutes, and then held for 5 minutes. During the ramping phase the temperature overshoot to 420 °C, the overshoot was attributed in part to the effect of the large temperature separation between room temperature and the set point value on the tube furnace PID temperature controller. All 50 electrodes were then aged in air at ~250 °C for 48 hours.

#### **6.4.3.3 Sensor characterisation**

The distribution of the printed Ag electrode and calcined LBZA derived ZnO material was analysed using energy dispersive x-ray spectroscopy (EDS) mapping. The maps were recorded using EVO LS25 SEM with LaB<sub>6</sub> source (Zeiss, Oberkochen, Germany) equipped with a 50 mm<sup>2</sup> X-Max<sup>N</sup> EDS silicon drift detector (Oxford Instruments NanoAnalysis & Asylum Research, High Wycombe, UK). The ZnO grain structure was recorded using a S4800 Type II FEG-SEM (Hitachi High Technologies, Minato-ku, Tokyo, Japan) using the in-lens secondary electron detector, 3 kV acceleration voltage and x 50k magnification. To characterise the grain structure size population the diameter of 185 nanoparticles were measured in ImageJ (National Institute of Health, US.), the mean, standard deviation and 95% bootstrapped confidence interval (20,000 iterations) recorded and histogram plotted.

#### **6.4.3.4 Gas sensor testing**

During testing procedures to optimize the test methodology and equipment set up, the heater track on the commercial sensor used to heat the sensor failed. Due to technical reasons (the combination of insufficient funds, internal 20 mm chamber size and limited number of feedthrough pins) a replacement heater was unattainable. As such the data reported,

originally for internal use only, and methods that follow this statement are provided primarily for proof of concept purposes.

#### **6.4.3.4.1 Testing procedure**

The response to 200 ppm CH<sub>4</sub>, CO and H<sub>2</sub> were recorded for temperatures between 166 °C and 300 °C for 3 sensors. Heater track resistance-sensor surface temperature calibration was performed using the method as described in the detailed overview of the testing rig in appendix Chapter 13. For the first two sensors the heater track/sensing layer resistance/surface temperature calibration was performed external to the testing rig. For the third sensor the calibration was reperformed within the testing rig under 400 mLmin<sup>-1</sup> flow of nitrogen to improve the accuracy of the calibration factor. The estimated temperatures for the first two sensors were recalculated from the improved calibration relationship. Gas sensor tests at each temperature were recorded using the following steps:

- Resistance was recorded for 10 minutes in dry air to gather the baseline resistance
- The resistance under 200 ppm CH<sub>4</sub> was recorded for 10 minutes
- The resistance under dry air was recorded for 10 minutes to monitor the recovery of response
- The resistance under 200 ppm CO was recorded for 10 minutes
- The resistance under dry air was recorded for 10 minutes to monitor the recovery of response
- The resistance under 200 ppm H<sub>2</sub> was recorded for 10 minutes
- The resistance under dry air was recorded for 10 minutes to monitor the recovery of response

The response was calculated by measuring the baseline resistance prior to the introduction of CH<sub>4</sub> and dividing by the resistance under gas flow for each test gas, prior to dry air being reintroduced to the sensor.

To try and ascertain the contribution of electrode and grain structure to the conductivity, steady state current voltage measurements were performed using the automated rig in dry air, 200 ppm CH<sub>4</sub>, 200 ppm CO and then 200 ppm H<sub>2</sub>. Prior to testing the sensor was left in the test gas until the resistance reached equilibrium. Current measurements were performed at 0.1 V intervals between 0 and ±10 V and 1 V between ±10 V and ±50 V. Measurements at each point were integrated over 3 seconds with 8 measurements performed sequentially and the mean and 99% confidence interval calculated for each voltage.

## 6.5 Results

### 6.5.1 Silver electrode print optimisation

#### 6.5.1.1 Surface energy optimisation

##### 6.5.1.1.1 Description of the problem

Initial test prints of the PFI-722 Ag NP ink on solvent washed Kapton HN substrates showed a high degree of pinholing indicative of poor wetting. Contact angle measurements of the PFI-722 ink revealed a mean contact angle of  $45.9^\circ$  with standard deviation of  $3.9^\circ$  showing incomplete wetting. Based on the aqueous nature of the ink, two well-known surface treatments for Kapton, oxygen plasma<sup>[498]</sup> and wet hydrolysis and conversion of the imide groups to amide and carboxylic acid groups were performed. The conversion to polyamic acid as originally presented by Lee, Kowalczyk and Shaw<sup>[491]</sup> is reversible and upon recurring at temperatures exceeding  $230^\circ\text{C}$  reforms polyimide. In the following sections the results of both treatments and a combination of the two treatments on water contact angle are shown. Following the results, a discussion comparing the treatments and their effects on PFI-722 Ag NP ink wetting is presented.

##### 6.5.1.1.2 Oxygen plasma treatment

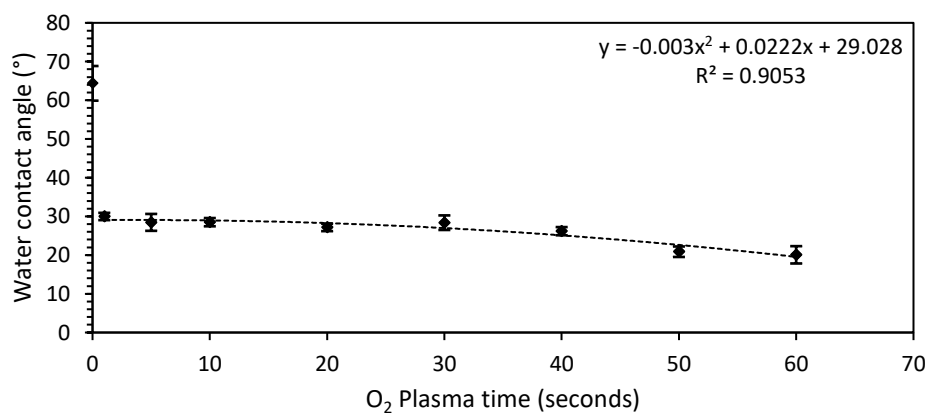


Figure 6.8: Plot of mean deionized water contact angle on Kapton HN films as a function of O<sub>2</sub> plasma treatment time, error bars  $\pm 1$  standard deviation,  $N=5$ . Polynomial trendline excludes the control 0 second exposure sample.

Figure 6.8 shows the mean water contact angle of plasma treated Kapton HN films as a function of plasma exposure time. As is observed in literature <sup>[498]</sup>, an initial significant rapid drop in contact angle from 64.4 ° to 30.0 ° (0 s -> 1 s, T-test  $P_{\text{two tail}} = 3.96 \times 10^{-5}$ ) followed by a slower second reduction to 20.1 ° (30 s -> 60 s, T-test  $P_{\text{two tail}} = 0.0034$ ) can be seen. In addition to the reduction in mean contact angle a reduction in standard deviation can be seen with the standard deviation without treatment being 4.5 °, versus a maximum standard deviation of 2.2 ° and mean standard deviation of 1.5 ° seen with plasma treatment. Figure 6.9 A) show elemental concentration of surface nitrogen, carbon and oxygen as a function of O<sub>2</sub> plasma exposure time.

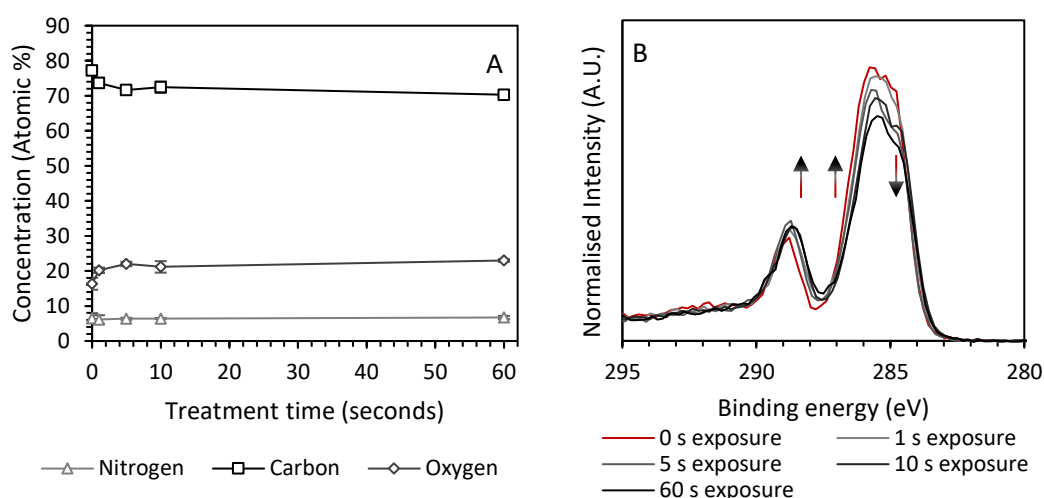


Figure 6.9: A) Relative atomic concentrations of nitrogen, oxygen and carbon as measured from their respective region scans as a function of O<sub>2</sub> plasma treatment time. Error bars  $\pm 3$  standard deviation. B) Background normalised intensity carbon 1s XPS spectra for plasma exposure times of 0, 1, 5, 10 and 60 seconds showing a progressive reduction in lower binding energy components typical of aliphatic hydrocarbons and an increase in higher energy components typical of polar oxygen containing functional groups.

During the first second of plasma exposure a simultaneous reduction in carbon and increase in oxygen can be seen. From high resolution measurements derived from scans of the carbon 1s region as shown in Figure 6.10, it can be seen that reduction in carbon is due to a reduction in ODA/aliphatic hydrocarbon ( $\Delta = -4.6$  at.%, T-test  $P_{\text{one sided tail}} = 0.0013$ ), PMDA hydrocarbon ( $\Delta = -1.21$  at.%, T-test  $P_{\text{one sided tail}} = 0.011$ ) and C-N/C-O ( $\Delta = -1.51$  at.%, T-test  $P_{\text{one sided tail}} = 0.032$ ) groups. Aliphatic hydrocarbons are known to have low surface energy and high water contact angles as exemplified by that of polyethylene and polypropylene <sup>[499]</sup>. The presence of aliphatic hydrocarbon was attributed to surface contamination from environmental carbon i.e. adventitious carbon <sup>[305]</sup> and manufacturing and packaging sources.

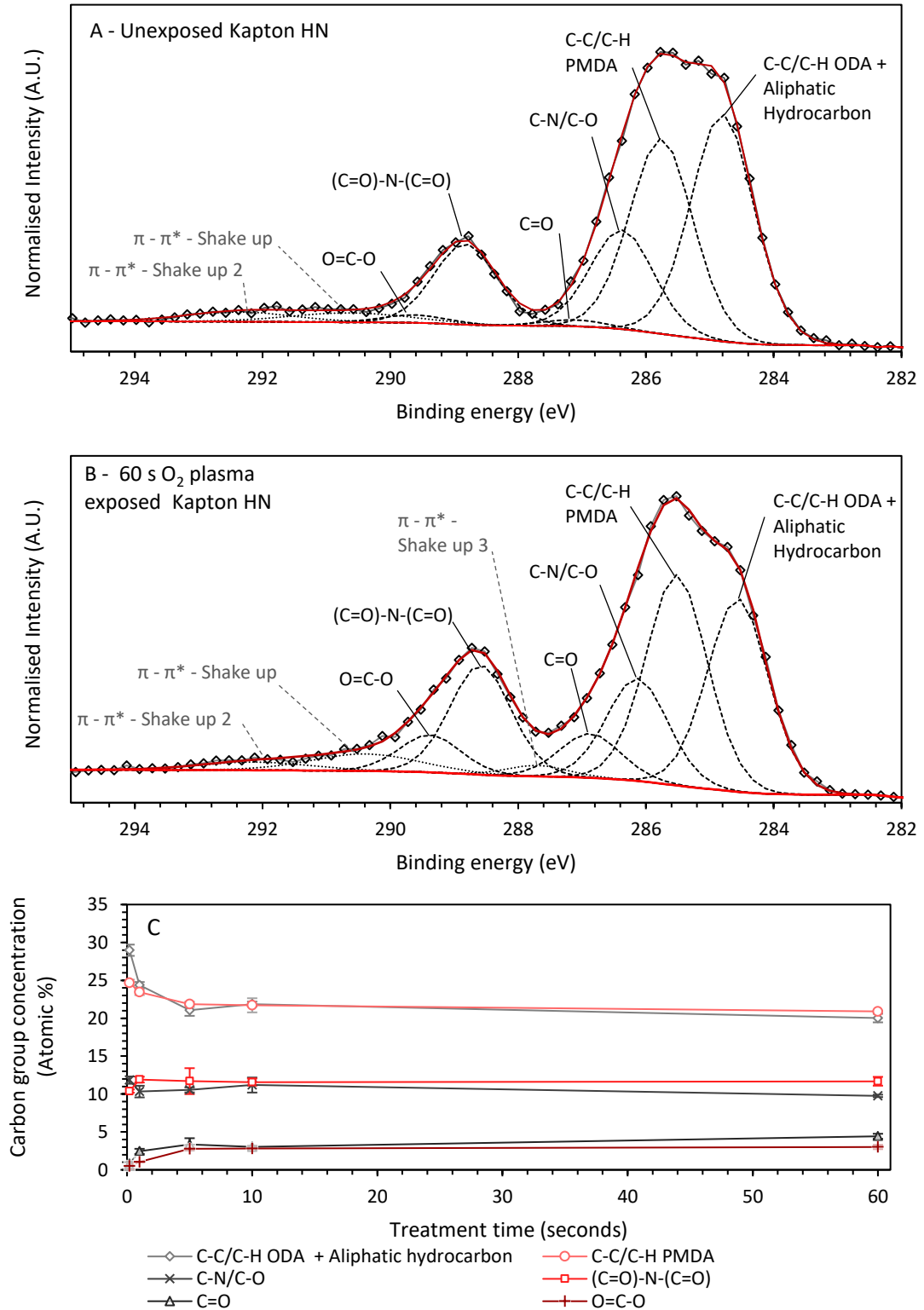


Figure 6.10: A) High resolution carbon 1s spectra as a function of binding energy with corresponding fitted functional groups (dashes) for solvent washed unexposed Kapton HN.  $\pi - \pi^*$  - Shake ups (fine dots) represent photoelectrons that have lost energy exciting molecular orbital states typically present in conjugated molecules and carry little chemical information. B) High resolution carbon 1s spectra as a function of binding energy with corresponding fitted functional groups (dashes) for solvent washed 60 s O<sub>2</sub> plasma exposed Kapton HN. Of note is the reduction in ODA (4,4'-oxydianiline) and aliphatic component and increase in carbonyl and carboxylic acid groups. C) Plot of atomic concentration of fitted carbon components in functional groups as a function of O<sub>2</sub> plasma exposure time. Error bars  $\pm 1$  standard deviation.

It should be noted that from low resolution survey scans presented within appendix Chapter 13 that silicon was present with concentrations varying between 3.31 at.% and 3.85 at.%. Silicon contamination is often seen in studies of Kapton HN sheets <sup>[500][501][502]</sup> and potentially originates from the low adhesion separator sheets the Kapton HN are often packaged with.

Between 0 and 60 s the imide bond increases from 10.4 at.% to 11.7 at.%. The increase in concentration suggests the bond does not undergo bond scissoring that would result in a decrease in imide concentration, and production of carboxylic acid and amide bonds, as seen previously by Inagaki, Tasaki and Hibi <sup>[503]</sup>. The initial reduction in water contact angle within the first second of exposure corresponds well to the reduction in low surface energy aliphatic carbon content (29 at.% to 24.4 at.% after 1 s exposure.)

The reduction in standard deviation in contact angle was attributed to a reduction in localised areas of non-homogenous surface contamination. With a further increase in plasma exposure time a small decrease in both PMDA and ODA aromatic carbon content can be seen. Simultaneously an increase in carboxylic acid and carbonyl groups can be seen, with the majority of chemical changes appearing to be complete within 10 seconds. The slower reduction in low energy aromatic groups and increase in high energy polar groups corresponds well to the slow decrease in water contact angle between 1 and 60 seconds.

### 6.5.1.1.3 Wet hydrolysis and conversion of imide groups to amide and carboxylic acid groups

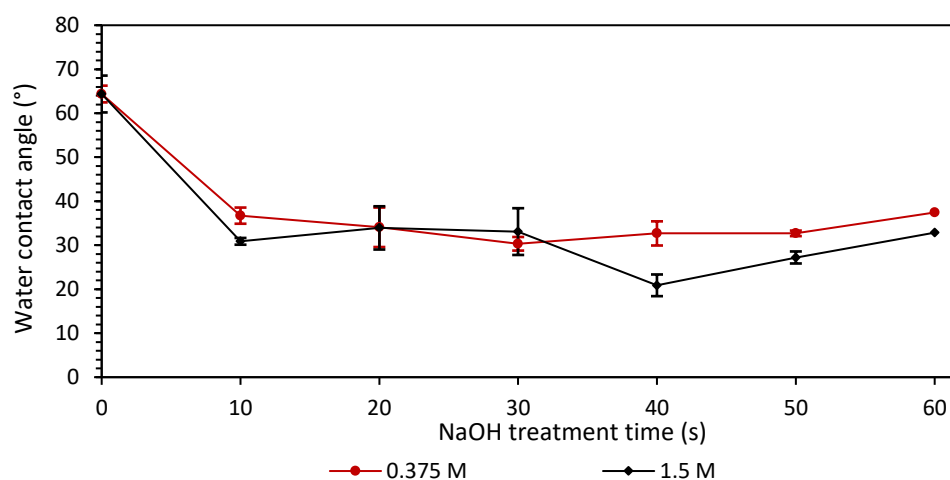


Figure 6.11: Mean deionized water contact angle on treated Kapton HN substrates as a function of NaOH step treatment time for 0.375 M and 1.5 M NaOH in a 75% ethanol/ 25% water solvent blend. Error bars  $\pm 1$  standard deviation.

Figure 6.11 shows the mean contact angle of solvent washed and wet chemical imide conversion treated Kapton HN as a function of the NaOH hydrolysis step treatment time. A large contact angle reduction for both concentrations occurs within the first 10 seconds of treatment, reducing from  $64.4^\circ$  (Standard deviation =  $4.5^\circ$ ) to mean values of  $34^\circ$  (Standard deviation =  $2.2^\circ$ ) for 0.375 M NaOH and  $29.8^\circ$  (standard deviation =  $5^\circ$ ) for 1.5 M NaOH. The relative reduction in contact angle for the 1.5 M treated sample at 40 and 50 seconds was attributed to a partial dissolution/ etching of the surface resulting in increased surface roughness [504].

The increased roughness has been observed by Huang *et al.* [505] using aqueous 1 M KOH and in experiments here using a water-based hydrolysis step ( $R_{RMS} = 64.2$  nm as shown in appendix Chapter 13), and produced pale visual areas on the substrate surface that were also seen on the 40 and 50 s samples. Unlike the aqueous treatment presented in appendix Chapter 13 which had standard deviations of up to  $12.2^\circ$ , the 75% ethanol/25% water solvent blend shows a significant improvement in repeatability. Performing regression analysis on all measured contact angles of 0.375 M treated substrates produced relations for the intercept of  $33.826^\circ$ , P value =  $2.6 \times 10^{-20}$  and for treatment time  $0.0054 \times \text{Hydrolysis step time}$ , P value = 0.881. The P values of the regression analysis suggests that after the initial 10 seconds of treatment the contact angle is well described by the mean value and not with treatment time i.e. further treatment has no clear effect on contact angle.

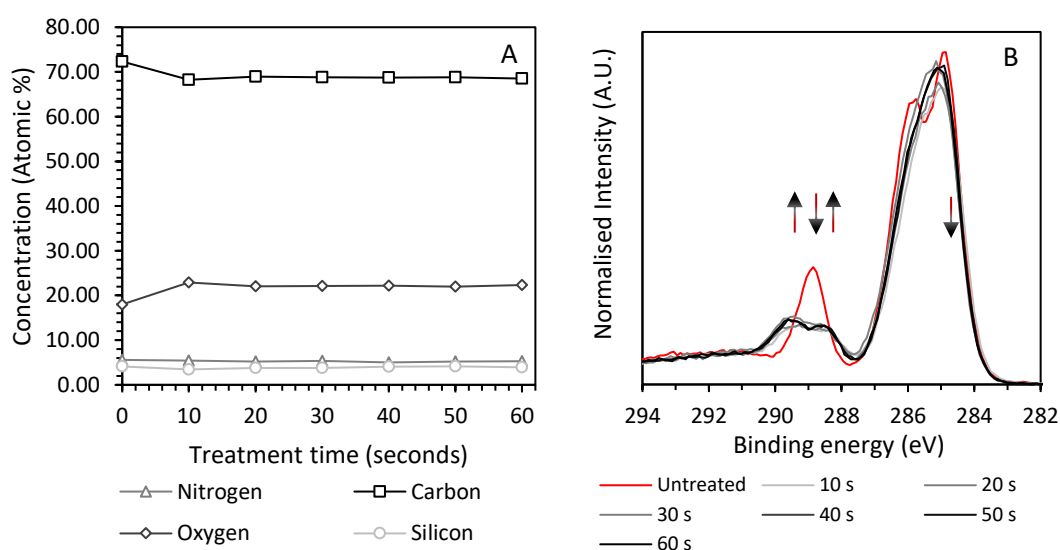


Figure 6.12: A) Relative atomic concentrations of nitrogen, oxygen, carbon and silicon as measured from their respective region scans as a function of NaOH hydrolysis step treatment time. B) Background normalised intensity carbon 1s XPS spectra for NaOH hydrolysis step treatment times of 0, 10, 20, 30, 40, 50 and 60 seconds showing the imide bond hydrolysis into amide and carboxylic acid groups happens within the first 10 seconds of treatment.



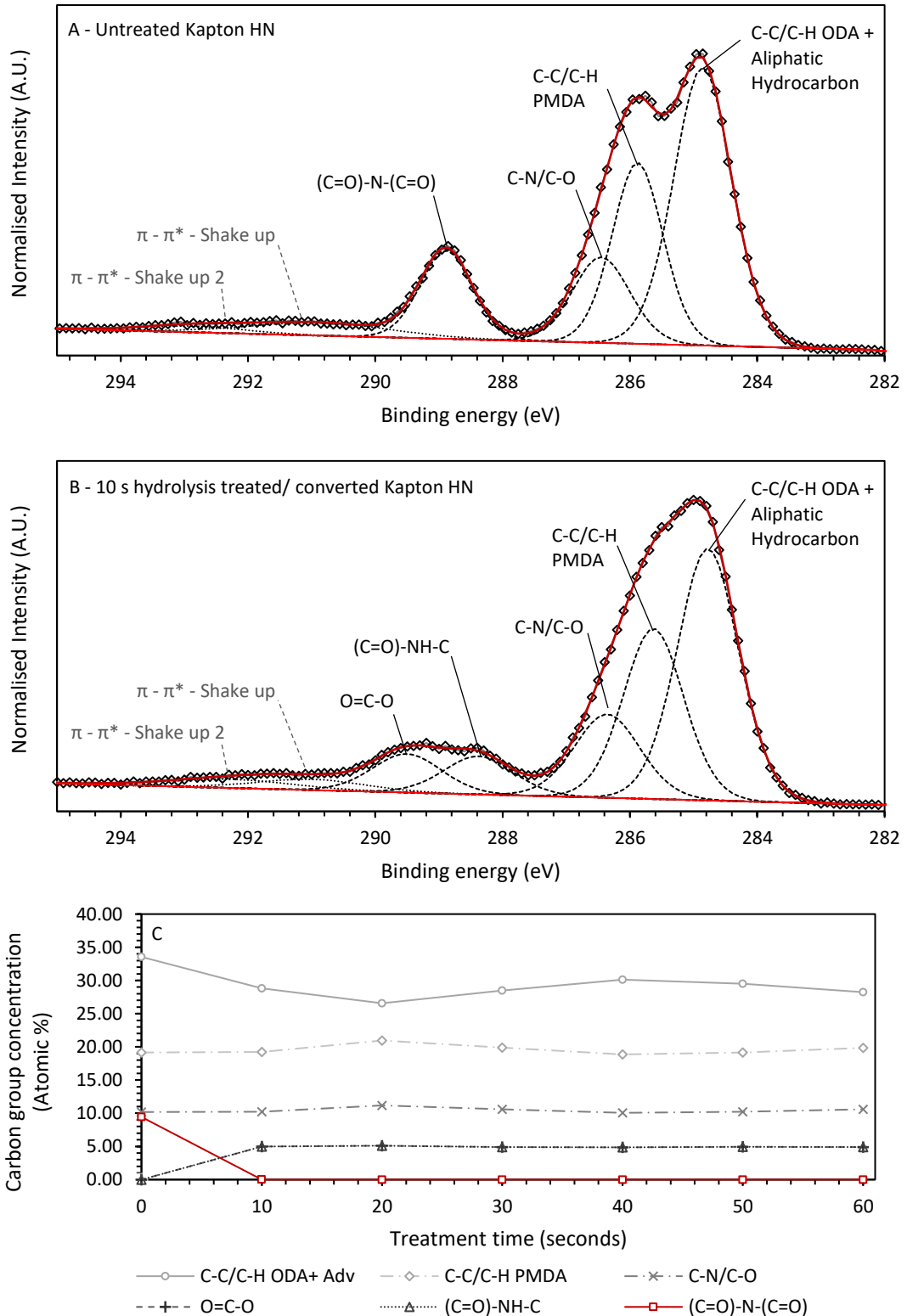


Figure 6.13: A) & B) High resolution carbon 1s XPS spectra of solvent washed Kapton HN and 10 s hydrolysis and conversion treated Kapton HN with annotated functional group components. The lack of imide ((C=O)-N-(C=O)) groups post treatment shows conversion of the surface is completed within 10 seconds. C) Plot of concentration of carbon versus hydrolysis step treatment time for aliphatic and aromatic hydrocarbons within the ODA ring structure, aromatic hydrocarbons within the PMDA ring structure, aromatic carbon linked to oxygen or nitrogen via a single bond, carboxylic acid, amide and imide functional groups. Note that carboxylic acid and amide groups have the same concentrations and overlap.

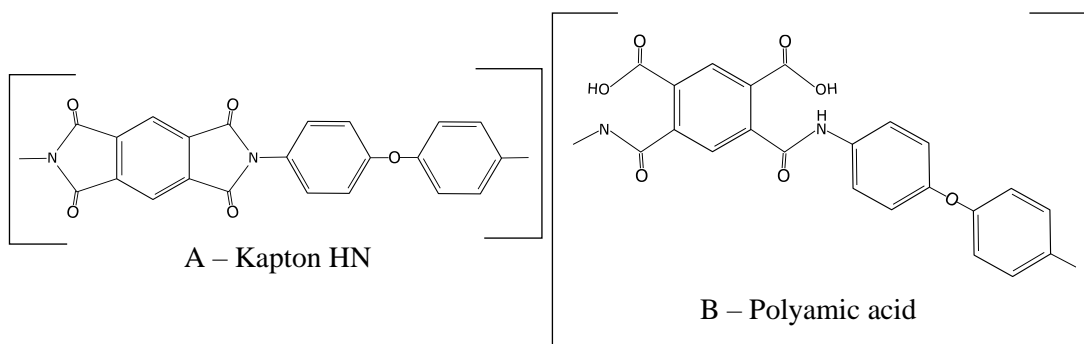


Figure 6.14: Skeletal formula of A) Kapton HN control and B) Polyamic acid produced by the hydrolysis of the imide bond followed by reprotonation as performed by the NaOH and HCl steps respectively during the wet chemical conversion treatment.

Figure 6.12 (A) shows elemental concentrations of the treated Kapton HN surfaces as measured by XPS, showing the presence of carbon, oxygen, nitrogen and silicon. After the first 10 seconds of treatment the carbon concentration drops from 72.3 at.% for the untreated control to a mean value of 68.7 at.%, oxygen simultaneously shows an increase from 18.0 at.% to mean value of 22.3 at.%. Nitrogen and silicon values vary by less than 0.6 at.%.

High resolution spectra of the carbon 1s as shown in Figure 6.13 show that within the first 10 seconds of treatment hydrolysis of the imide bond is complete, converting to amide and carboxylic acid groups (skeleton diagrams of the modifications represented in Figure 6.14), in line with the regression analysis of the contact angle. Figure 6.13 (C) shows measured concentrations of the individual functional groups as plotted out as a function of hydrolysis step treatment time. The measurements show PMDA aromatic hydrocarbon and aromatic carbon-nitrogen and carbon-oxygen single bonds appear to be unaffected by the treatment, with the untreated substrate within 0.58 standard deviations of the combined mean values of the treated groups. Aliphatic hydrocarbon and aromatic hydrocarbon contained within the ODA ring structure show a drop of 4.92 at.% (T-test  $P_{\text{two tail}} = 0.014$ ), potentially indicating an enhanced cleaning of the substrate. It should be noted that organic silicon (C-Si) is separated from C=C groups, contained in the ODA ring structure, by  $< -0.4$  eV<sup>[305]</sup> and could be masked by the ODA peak which would be significantly more intense. As organic silicones are susceptible to hydrolysis, if weakly, under both strong acidic and basic conditions<sup>[506]</sup> the reduction could also potentially be attributed to a partial removal and/or modification of organic silicones. In comparison with the other functional groups, the ODA+ hydrocarbon envelope had a higher standard deviation of 1.22 at.% vs. 0.75 at.% for PMDA and 0.40 % for aromatic carbon-nitrogen and carbon-oxygen single bonds. The increased variation was attributed to localised aliphatic/ silicon containing hydrocarbon contamination

and likely the source of the variation in mean contact angle for the 0.375 M NaOH treated samples.

Both XPS C 1s region envelope and mean contact angle are in close agreement with values provided by Lee, Kowalczyk and Shaw <sup>[491]</sup> in the original method, for which angles of 59.6 ° and 32.0° for untreated and treated Kapton respectively were reported (calculated from their advancing and receding contact angles using equation 16 in the work presented by Tadmor <sup>[507]</sup>). The results however show that treatment times of only 10 s in 0.375 M NaOH in the solvent blend are required as opposed to the 60 s treatment in aqueous 1 M NaOH reported by Lee, Kowalczyk and Shaw <sup>[491]</sup>. Contact angle measurements by Lee et al. <sup>[500]</sup> showed slower hydrolysis in water up to 3 M NaOH, with contact angles reaching the same values within 10 seconds at 5M NaOH. As the hydrolysis reaction is a nucleophilic addition reaction the increased hydrolysis here suggests either the activity of nucleophile within the reaction is greater in the ethanol/water blend, or that dissolution has a greater effect at lower concentrations in water. Karásková and Mollin measured the equilibrium concentrations of sodium ethoxide/ sodium hydroxide equilibrium concentrations in solutions of sodium hydroxide ethanol/ water mixtures <sup>[508]</sup>. Their results revealed that at 80 % ethanol by weight (~76 % by volume), the equilibrium constant for the ethoxide anion was 7.75 times that of the hydroxide anion and its activity was 2.16 times greater. As the ethoxide anion is a stronger nucleophile than the hydroxide anion <sup>[155]</sup>, it would appear reasonable that the apparent increased rate of reaction is potentially due to the presence of ethoxide anions. The lack of increase in aliphatic hydrocarbon and C-O bonds representative of ethyl ester formation would however generally suggest a reduction in dissolution. Though it is possible that ethyl ester is unstable in the treatment solution and that the reaction proceeds via:

- formation of amide and intermediary ethyl-ester groups
- reaction of the ethyl-ester groups with hydroxide to form the final carboxylate anions and ethanol (i.e. saponification) <sup>[155]</sup>.

#### **6.5.1.1.4 Combined treatments**

Based on the variance in aliphatic carbon concentration and mean contact angle observed during the 0.375 M NaOH wet chemical conversion treatment, additional plasma treatment was trialled post conversion.

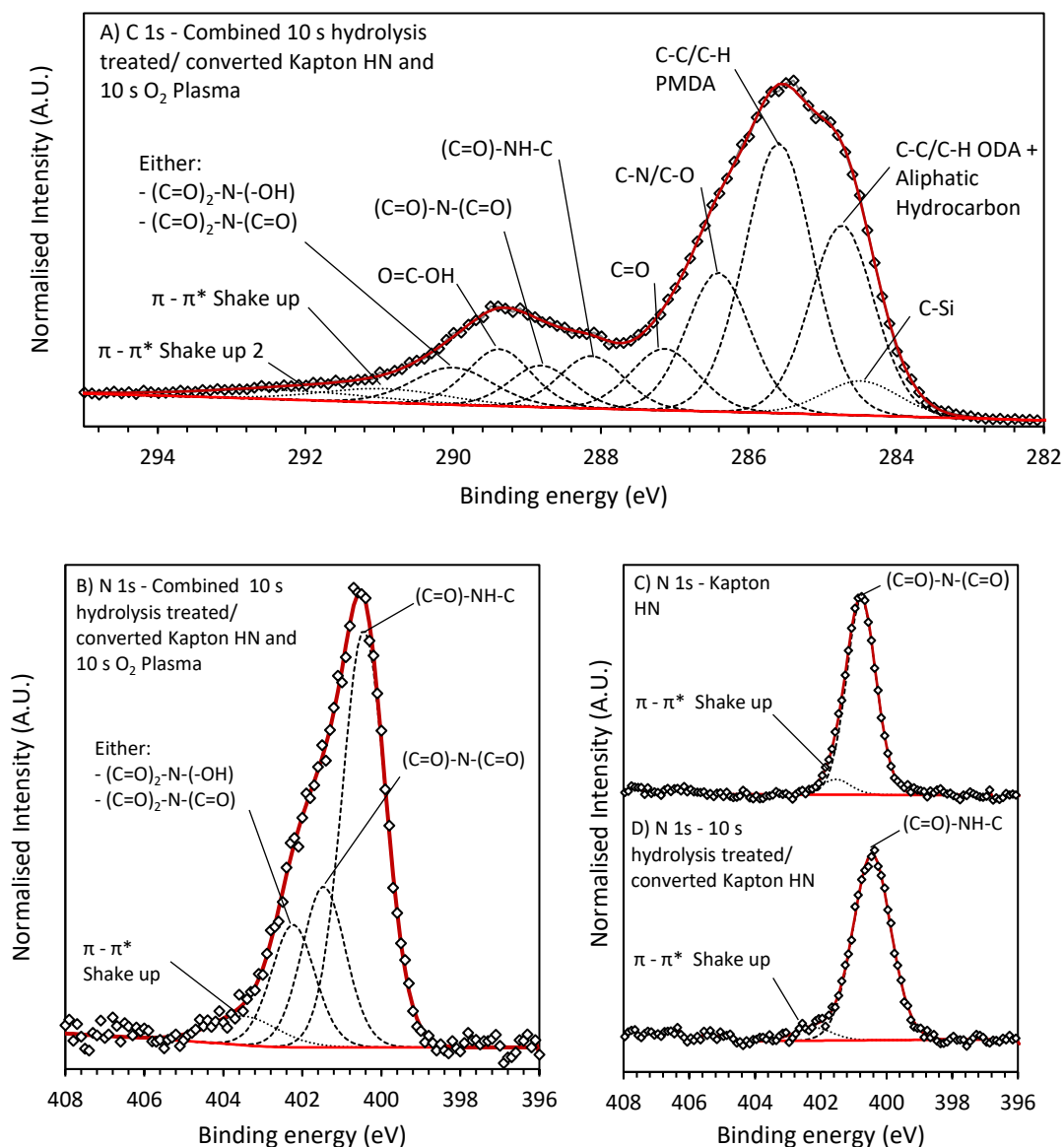


Figure 6.15: Annotated normalized high resolution XPS spectra as a function of binding energy for A) C 1s and B) N 1s regions of the combined 10 s 0.375 M wet hydrolysis and conversion treatment followed by 10 s O<sub>2</sub> plasma treated Kapton HN sample and C) N 1s region of Kapton HN and D) N 1s region of 10 s 0.375 M wet hydrolysis and conversion treated Kapton HN for comparison. The introduction of plasma post wet chemical treatment reforms polyimide bonds and creates an oxidized imide, most likely a tricarbonyl nitrogen equivalent of a polyimide (dicarbonyl) bond i.e. (C=O)<sub>2</sub>-N-(C=O).

As the wet chemical conversion was shown to be complete with a 10 s hydrolysis step in 0.375 M NaOH solutions and that plasma cleaning reached completion within 10 s (primarily within the 1<sup>st</sup> second,) 10 second treatments of wet chemical conversion followed by a 10 second plasma treatment was chosen. Combining both treatments produced mean water contact angles of 9.0° (Std. Dev. 1.3°), a significant improvement in wetting on the original 64.4° (Std. Dev. 4.5°) and an improvement compared to the conversion treatment 34.0° (Std. Dev. 2.2°) and plasma treatment of 28.5° (Std. Dev. 1.1°).

Region and component	Concentration (at.%) - Region	Concentration (at.%) - Component	Binding energy (eV)
Na 1s	0.08		
O 1s	28.33		
Si 2p	3.16		
Si Organic 3/2		1.23	101.64
Si Inorganic 3/2		0.61	102.27
Si Organic 1/2		0.88	103.17
Si inorganic 1/2		0.44	103.80
N	5.87		
Amide		3.49	400.45
Imide		1.35	401.46
Tricarbonyl imide		1.03	402.23
C	62.57		
C-Si		2.75	284.48
Unoxidized ODA		12.93	284.73
PMDA		19.57	285.59
Amine + Ether & hydroxyl		9.42	286.41
Carbonyl		4.41	287.14
Amide		3.62	288.13
Imide		2.80	288.81
Carboxylic acid		3.87	289.38
Tricarbonyl imide		3.20	290.04

Table 6.1: Table of concentration of elements and individual components of the combined 10 s 0.375 M wet hydrolysis and conversion treatment followed by 10 s O<sub>2</sub> plasma treated Kapton HN sample as measured by XPS, with binding energy components as reference for the individual components as shown in Figure 6.15.

Table 6.1 shows the atomic concentration of the of the combined 10 s 0.375 M wet hydrolysis and conversion treatment followed by 10 s O<sub>2</sub> plasma treated Kapton HN sample as measured from high resolution XPS spectra. The combined treatment produces an increased oxygen content of 28.3 at.% as compared to either treatment on its own, with either treatment producing ~22 at.% and the unmodified Kapton HN ~18 at.%. Figure 6.15 shows the fitted spectra for the C 1s (A) and N 1s region (B), with N 1s regions for the untreated (C) and 10 s wet chemical treated Kapton HN (D) for comparison. Compared to the C 1s of the other treatments there are 2 main features of note:

- A reduction in the lowest binding energy components with the combined ODA + aliphatic hydrocarbon (12.93 at.%) and C-Si (2.75 at.%) making up a total of only 15.57 % versus a minimum of 20 % for the plasma treatment and 28.8 % for the wet chemical treatment
- The formation of imide and a higher binding energy component centred at approximately 290.18 eV whilst retaining both amide and carboxylic acid groups.

From the N 1s region, 3 peaks can be seen; the lowest amide at 400.45 eV and two high components at 401.46 eV and 402.23 eV. The central peak is approximately 0.6 eV higher than the imide in the control substrate, suggestive of an imide attached to a more oxidized system and/or disruption of the aromatic system. The third peak represents a significantly more oxidized nitrogen than the other 2 components. The binding energy shift is similar to the shift between amide and imide groups (1 eV vs 0.8 eV) and likely indicates a nitrogen attached to 3 carbonyl groups.

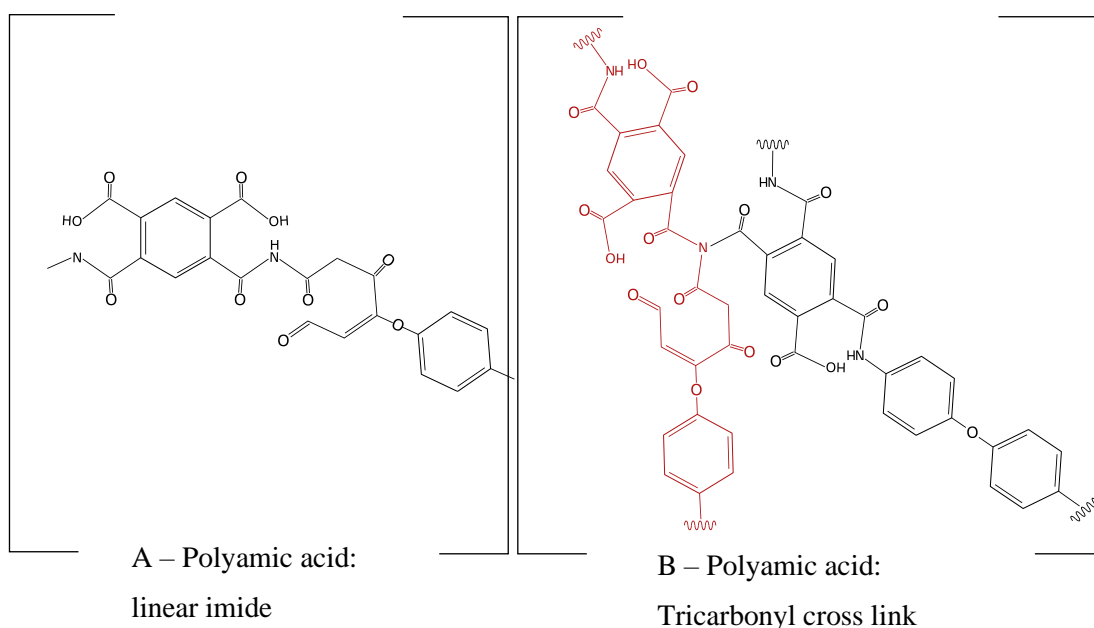


Figure 6.16: Skeletal formula for the proposed A) linear imide ( $N\ 1s = 401.46\ eV$ ) and B) tricarboxyl ( $N\ 1s = 402.23\ eV$ ) groups based on the C 1s and N 1s XPS fittings. B is produced via a condensation reaction (i.e. removal of  $H_2O$ ) between an unmodified polyamic acid (black) and a linear imide (dark red) as shown in A). Note that for the carbon atoms attached to the nitrogen containing groups in the C 1s spectra the sum of amide (3.20 at.%), half the imide (2.57 at.%/2) and a third of tricarboxyl groups (2.94 at.%/3) is approximately equal to the carboxylic acid (5.43 at.% vs sum of 5.47 at.%). Note that the curly lines in B) are used to indicate attachment/ bonding points for the next monomer.

Considering the combination of:

- Reduction in ODA (12.8 at% vs 28.8 at%) and amide concentrations (3.62 at.% vs 5 at.% for the wet chemical treatment)
- The sum of the C 1s groups assigned to amide (3.62 at.%) and half the imide (1.40 at.%) is approximately equal to the sum of the carboxylic acid (3.87 at%) and a third of the highest binding energy component assigned to tricarboxyl imide (1.07 at%) (5.02 at.% versus a sum of 4.94 at.%).

- Each N 1s components match their C 1s equivalent within 0.13 at% with the ratios of 1 C: 1 N for the amide, 2 C: 1 N for the imide and 3 C: 1 N for the tricarbonyl imide equivalent.

The above suggests a surface with reduced hydrocarbon contamination than the wet chemical treated substrate consisting of a mixture of:

- pure polyamic acid (skeletal formula shown in Figure 6.14)
- oxidized polyamic acid where some of the aromatic hydrogen is converted to carbonyl groups
- a linear imide (skeletal formula shown in Figure 6.16 A) formed by oxidation and ring opening of one of the ODA rings attached to an amide group. The most likely terminal group of the open ring would be a carbonyl group.
- A combined polyamic acid and linear imide cross linked by condensation between the hydrogen of the linear imide and the hydroxyl group of the carboxylic acid of the unmodified polyamic acid. A skeletal formula of the proposed structure is shown in Figure 6.16 B with the linear imide in dark red and polyamic acid in black.

The reduction in low polarity ODA and increase in higher polarity carbonyl, imide and tricarbonyl imide equivalent groups, as compared to either individual treatment, is the most likely cause for the further decrease in water contact angle.

#### ***6.5.1.1.5 Comparison of treatments and the effects on PFI-722 Ag NP ink (Novacentrix) wetting.***

Based on the water contact angle for each treatment PFI-722 contact angle analysis was performed on 10 s O<sub>2</sub> plasma treated Kapton HN, 10 s 0.375 M NaOH wet chemical hydrolysis conversion treated Kapton HN and the combined 10 s wet chemical and 10 s O<sub>2</sub> plasma treated Kapton HN.

Measuring the PFI-722 contact angle for each treatment produced contact angles ( $n=5$ , T-test significance cut-off  $p = 0.05$ ) of:

- Unmodified (control) Kapton HN:  $\mu = 45.9^\circ$ ,  $\sigma = 3.9^\circ$
- 10 s O<sub>2</sub> plasma treated Kapton HN:  $\mu = 43.6^\circ$ ,  $\sigma = 0.7$ , T-test  $P_{\text{two tail}} = 0.23$
- 10 s wet chemical hydrolysis and conversion treated Kapton HN:  $\mu = 27.5^\circ$ ,  $\sigma = 2.7^\circ$ , T-test  $P_{\text{two tail}} = 2 \times 10^{-5}$
- Combined 10 s wet chemical and 10 s O<sub>2</sub> plasma treated Kapton HN:  $\mu = 25.7^\circ$ ,  $\sigma = 1.4^\circ$ , T-test  $P_{\text{two tail}} = 4 \times 10^{-6}$

Compared to the unmodified Kapton HN the change in contact angle following 10 s O<sub>2</sub> plasma treatment was insignificant. A reduction in standard deviation was however observed, similar to that seen with the water contact angle, suggesting an improvement in surface cleanliness and reproducibility. In comparison both treatments containing the wet chemical step produced a statistically significant drop versus the control, the 1.8 ° reduction in contact angle upon adding the plasma step was however insignificant with a p-value of 0.22.

In general, the reduction in contact angle was lower than that seen for water contact angles, with the exception for the wet chemical hydrolysis treatment. This suggests that contact angle for the PFI-722 is generally controlled by the non-solvent ink constituents and not the solvent-substrate surface interactions. A low dependence of surface energy on contact angle has been predicted from thermodynamic modelling on chemically heterogeneous (mixed surface energy) surfaces at significant adsorbed surfactant concentrations <sup>[509]</sup>, with large surface energy changes required to have a noticeable change in contact angle. This suggests the most likely cause for the similar contact angle for the control and plasma treated substrates is the interaction of surfactant at the liquid-solid interfaces. It is known from the datasheets that the PFI-722 ink consistency is controlled by amine concentration <sup>[487]</sup>, undergoing coagulation when the amine and pH content is too low. This, along with the pH of the ink, typically 5.85 freshly opened, suggests the ink is a buffer system and is reactive to Brønsted-Lowry (proton based) acid-base interactions. The statistically insignificant change in contact angle after plasma exposure, which produces approximately 2.8 at.% carboxylic acid groups, versus the significant change in contact angle for the wet chemical treatment, that produces approximately 5 at.% of both carboxylic acid and amide groups, most likely suggests that the amide groups are undergoing protonation upon exposure to the ink. The presence of surface charge at the solid- liquid interface is known to increase surface energy and significantly decrease contact angle <sup>[510][511]</sup>. This produces the lower contact



angle for the wet chemical treated surfaces relative to both the unmodified control and to the O<sub>2</sub> plasma treated substrates. Based on the improved wetting of the wet chemical treatment, and the improved cleanliness produced via plasma exposure as demonstrated by the XPS data, the combined wet chemical and plasma treatment was chosen for all substrates in further experiments.

### 6.5.1.2 PFI-722 Ag NP ink electrode prints on the Combined wet chemical and plasma treated substrates trial

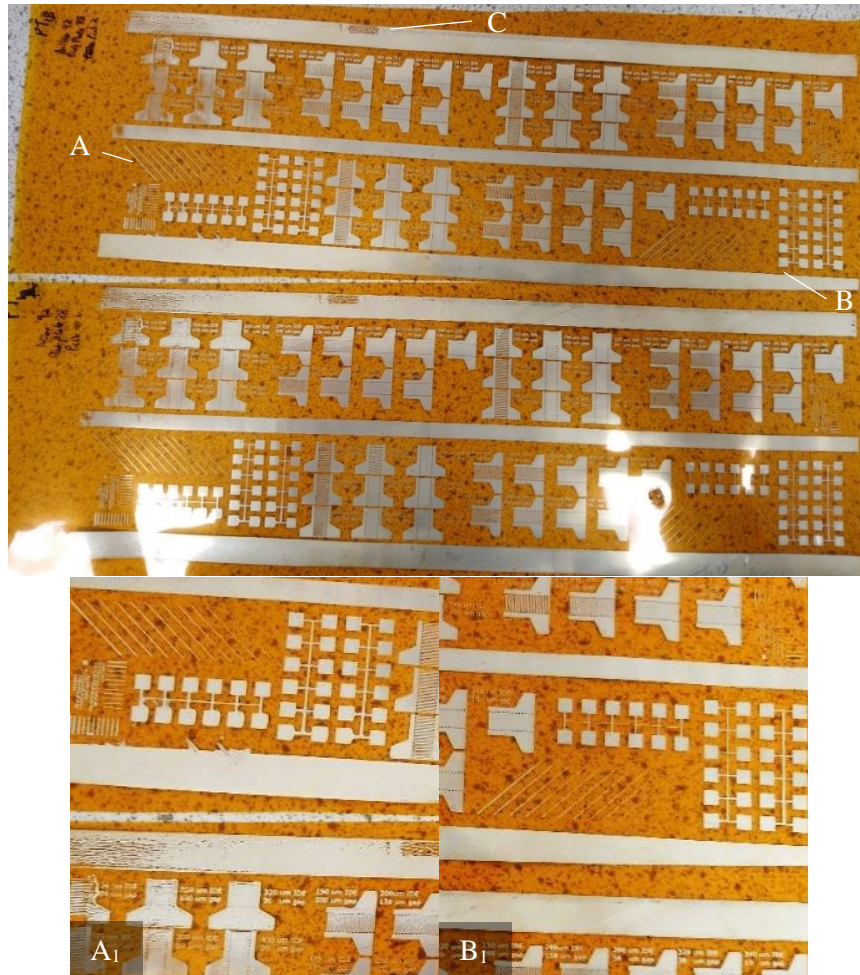


Figure 6.17: Photograph of PFI-722 test prints performed on the combined wet chemical and plasma treated Kapton HN substrates using the flexiproof f100 (RK Printcoat Instruments Ltd.) with a 3.5 mL.m<sup>-2</sup> anilox, print speed of 1.5 m.s<sup>-1</sup> and the lowest non-kiss print - impression cylinder engagement - 40 μm. A - shows areas overimpressed while B - shows area underimpressed with low ink transfer, C - shows an overimpressed feature located at the self-adhesive tabs used for mounting the substrates. A<sub>1</sub> and B<sub>1</sub> show features A) and B) magnified and contrast and brightness adjusted to match each other for visual comparison. Note the difference in ink density for the multi-dimensional fine line arrays (top left A<sub>1</sub> and middle and top right B<sub>1</sub>.)

Initial electrode test prints were performed of the PFI-722 Ag NP ink on the combined wet chemical and plasma treated substrates. Figure 6.17 shows the initial prints performed on the flexiproof 100 (RK Printcoat Instruments) at a print speed of  $1.5 \text{ m}\cdot\text{s}^{-1}$ , anilox volume  $3.5 \text{ mL}\cdot\text{m}^{-2}$  and the lowest plate-impression cylinder engagement trialled of  $40 \text{ }\mu\text{m}$ . Two general features can be seen:

- Features A) and C) corresponding to over impression are present (heavy ink coverage surrounding an area of low ink coverage and expansion and merging of print features such as IDE)
- Feature B) areas of low ink coverage suggestive of under impressed features.

The lowest positive engagement used here was lower than the  $76.2 \text{ }\mu\text{m}$  engagement successfully used by Deganello *et al.* for printing fine lines and grids using nano particle silver ink and a larger  $18 \text{ mL}\cdot\text{m}^{-2}$  anilox without over impression features [269]. The over impression features A and C appear to also suffer from features of ink drying on the print plate. Solvent evaporation and loss of amines on the print plate during the time taken to exchange substrates between prints will increase ink viscosity and cohesiveness and likely exacerbates, and potentially causes, the over impression seen. Unlike Deganello *et al.* that used an industrial scale continuous roll to roll print setup with enclosed and pumped ink storage, the ink drying is a consequence of the discontinuous and open ink storage used by the lab scale proof presses coupled with the sensitive solvent-pH balance of the ink designed for full press systems. Due to the high price of silver ink it was not possible to purchase a conductive ink less sensitive to the drying conditions in use.

To reduce the impact of the observed over-impression a subsequent set of prints was performed at  $0 \text{ }\mu\text{m}$  positive engagement (i.e. just in contact, known as a kiss print). Figure 6.18 shows a micrograph of the print performed with the same settings and a print-impression cylinder engagement of  $0 \text{ }\mu\text{m}$ . From the micrograph no over impression features can be seen, however the low pressure in the print nip appears to stop the ink forming a continuous film, with ink transfer to the substrate only from the edge of the anilox cylinder resulting in the fine regular diamond pattern that can be seen. Measuring the conductivity along the length of the left electrode of 5 IDE printed and dried at  $150 \text{ }^\circ\text{C}$  for 10 minutes produced a resistance of  $\mu = 11.7 \text{ }\Omega$  and  $\sigma = 4.24 \text{ }\Omega$ . While the resistance is much higher than would be expected for a printed silver film with  $60 \text{ m}\Omega$  sheet resistance at  $1 \text{ }\mu\text{m}$

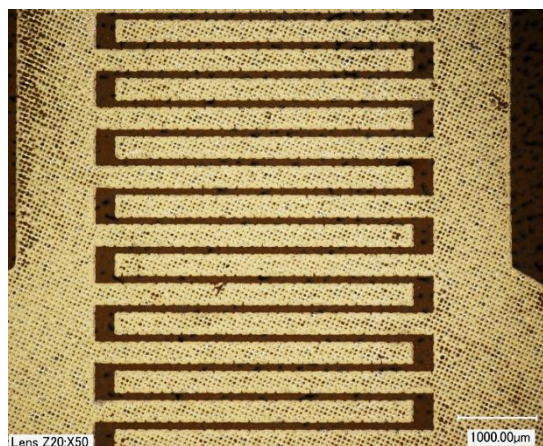


Figure 6.18: Micrograph of an IDE PFI-722 test print performed on the combined wet chemical and plasma treated Kapton HN substrates using the flexiproof f100 (RK Printcoat Instruments Ltd.) with a  $3.5 \text{ mL.m}^{-2}$  anilox, print speed of  $1.5 \text{ m.s}^{-1}$  and 0 positive engagement (i.e. a kiss print). Note the regular pattern produced corresponds to the anilox cell pattern suggesting ink transfer only at the edges of the cell. The pattern is a consequence of the lack of positive engagement forcing the film into a continuous film.

thickness, it is significantly lower than the resistance of the HMTA LBZA derived ZnO sensor presented in chapter 4.1.3 which was on the order of  $4 \text{ M}\Omega - 8 \text{ M}\Omega$ . Based on the significantly lower resistance than the test material, the kiss print IDE was considered acceptable for use in proof of concept trial sensors, with the caveat that future development and optimization would be required.

## 6.5.2 LBZA binderless ink development

### 6.5.2.1 Binderless ink - fluid properties: IFT and viscosity profile

From the tests used to develop the ink it was already known that the ink wet the combined wet chemical and plasma treated substrate. Testing the IFT produced a mean value of  $26.1 \text{ mN/m}$  with a standard deviation of  $0.2 \text{ mN/m}$  ( $n=5$ .) The value was similar to the  $23 - 24 \text{ mN/m}$  observed for the PVP inks, and as such would generally be expected to show similar wetting behaviour within each stage of the print process.

Figure 6.19 shows two representative viscosity profiles for the binder-less ink performed on the same sample immediately after each other. Although the ink had the same  $44.6 \text{ mg.mL}^{-1}$  nanosheet loading as that used for the binder-based ink, the binder-less ink shows a significant increase in shear thinning behaviour. At a shear rate of  $4621 \text{ s}^{-1}$  a viscosity of  $67.7 \text{ mPa.s}$  was observed. The viscosity is lower than ideal for solid block prints, being

similar in value to that of PVP ink C (12.9 % mass PVP, viscosity = 63.4 mPa.s at 1000 s<sup>-1</sup>) that produced pin holing at low print forces.

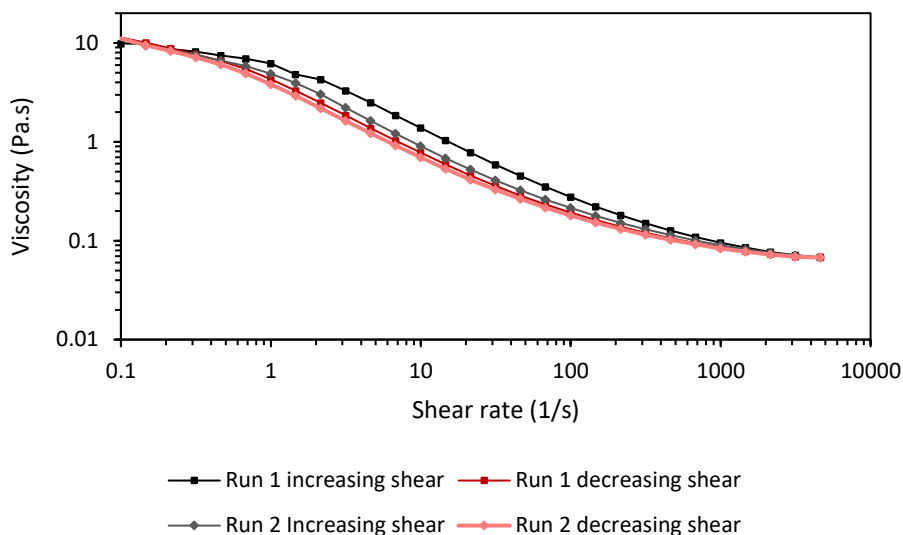


Figure 6.19: Viscosity profile as a function of shear rate for the binder-less ink. The profile shows two consecutive tests performed on the same sample immediately after each other. Each run consisted of an increasing and then decreasing sweep over the shear range used. The hysteresis present is indicative of thixotropic behaviour. Profiles produced using the table of shears methodology.

The ink should however, assuming it follows the log(viscosity) dependency on print gain, be able to produce narrower print features than PVP ink E (21.8 % mass PVP, viscosity = 308.7 mPa.s) and could potentially be used for higher density sensor arrays.

It should also be noted that prior to testing the viscosity, the ink had formed a sol-gel within the centrifuge tube used for storage, suggesting the ink has a yield point before fluid behaviour is observed. The ink also shows a minor amount of thixotropic behaviour as can be seen by the reduction in viscosity after the initial increasing shear portion of the first run, the partial recovery in viscosity between the decreasing shear portion of the first run, and the increasing shear portion of the second run.

The presence of shear thinning and thixotropy behaviour is well known in nanoclay (of which layered metal hydroxides are a subset) suspensions where strong particle-solvent interactions are present <sup>[248]</sup>. The particles can form multiple sol-gel structures at rest and low shear, with the particular microstructure dependent generally on the relative charge density and polarity at the respective particles edge and faces <sup>[180][512]</sup>.

### 6.5.2.2 *Binderless ink – Print force optimization*

Figure 6.20 shows representative micrographs of prints using the binder-less ink at print force equal to anilox force at forces of 80 N, 100 N, 125 N and 150 N. As expected, due to the ink's lower viscosity, the print at 80 N has more pin holing than the 21.8 % mass PVP ink at equivalent print conditions.

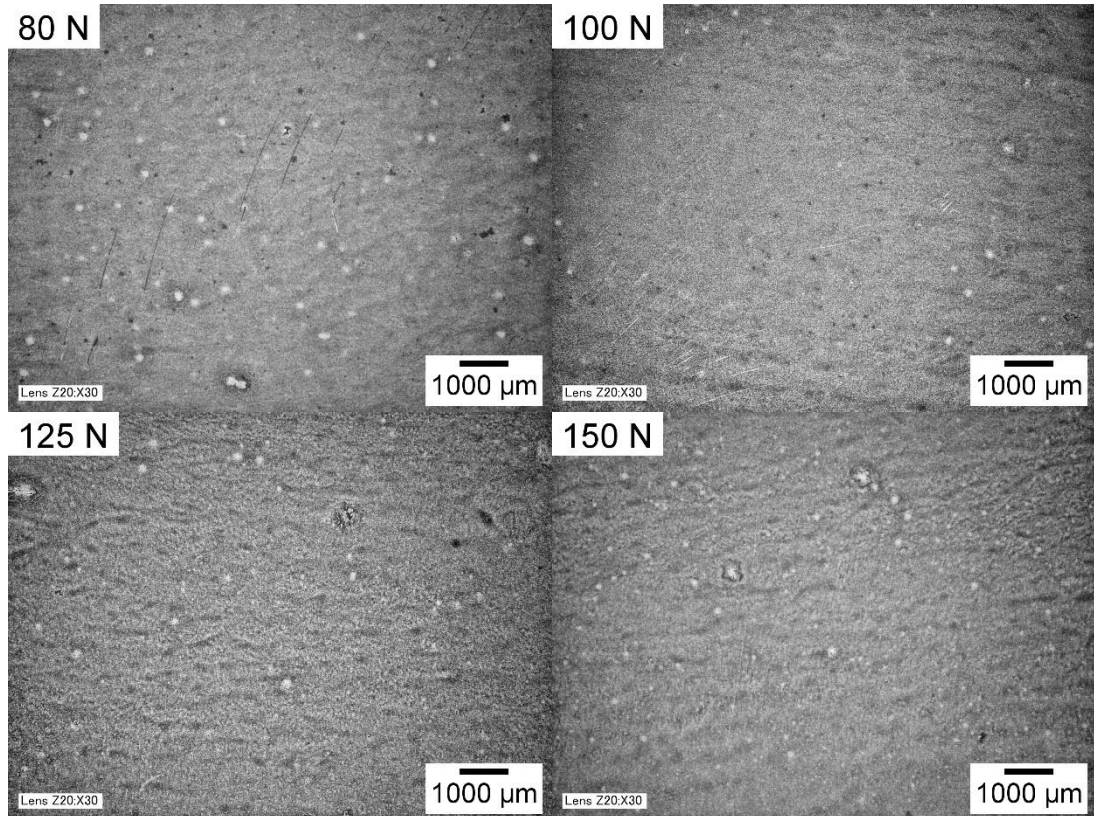


Figure 6.20: Representative micrographs of binder-less ink prints. Prints were performed using the IGT F1 at  $1.5 \text{ m.s}^{-1}$ , anilox force = print force at forces of 80 N, 100 N, 125 N and 150 N.

As the forces increase the pin holing decreases until at 150 N practically all pin holing is removed and the majority of inhomogeneity a result of viscous fingering. Based on the observations anilox and print forces of 150 N were used for all further prints using the binder-less ink.

### 6.5.3 Proof of concept gas sensor prototype printing and testing

#### 6.5.3.1 Sensor Characterisation

In appendix Chapter 13 the electrodes presented in section 6.5.1.2 were used in proof of concept PVP based LBZA ink sensors. The sensor substrate was shown to ultimately fail due to the (460 °C) thermal treatments used, likely due to a reduction in ultimate elongation. Observations taken at each step within the thermal treatment however showed the formation of breaks within the Ag electrodes, with complete loss of conductivity in 60 % of the sensors. This was assigned generally to a lack of ink transfer (as evidenced by the diamond pattern in Figure 6.18) creating a fragile Ag film.

To overcome these issues for the binderless ink prototype sensors, Ag IDE prints were performed using the RK Flexiproof 100 with an anilox volume of 24 mL.m<sup>-2</sup>, kiss print impression at 90 % humidity, dried at 150 °C followed by LBZA overprints using the binderless based LBZA ink. Printing the Ag ink within the high humidity environment significantly arrested on-press drying and resulted in a vast improvement in printability. Post calcination and aging at 246 °C for 2 days, 4 out of a batch of 50 sensors failed (25 ramped to and held at 420 °C for 5 minutes in a tube furnace, and 25 inserted into the tube furnace and calcined at 400 °C for 5 minutes). The 8 % failure rate is a significant improvement over the 60 % failure rate for the PVP based sensors.

Figure 6.21 shows wide area energy dispersive x-ray spectroscopy (EDS) elemental maps of a representative printed and calcined sensor using a ramping thermal profile. Figure 6.21 B) shows the isolated Zn image which shows generally complete coverage, with minor pinholing and inhomogeneities over the 4.36 mm x 3.26 mm area. The high coverage is ideal for maximizing conductivity for the printed area and hence increasing sensor signal to noise ratios. Figure 6.21 C) shows the isolated Ag image, from which incomplete coverage of the interdigitated electrode area can be seen. As a kiss print was used it is likely that the print pressure was too low for complete film formation. Further work would be required to confirm, however as the external walls of the track are continuous no conduction issues would be expected to arise from the internal print defects.

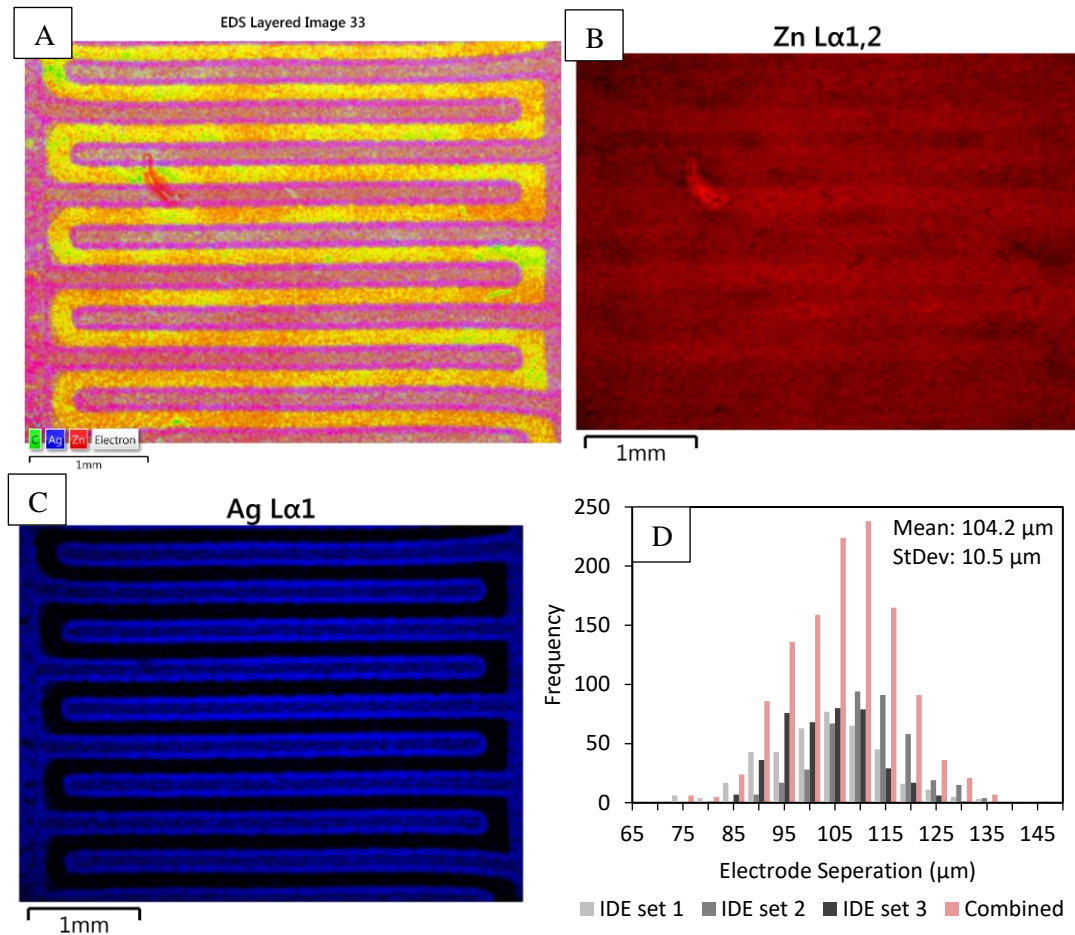


Figure 6.21: Energy dispersive x-ray spectroscopy elemental map of a typical non-shorting printed and calcined sensor. A) overlaid silver (blue), carbon (green), zinc (red) and secondary electron map (white). Due to ZnO layer overlap, areas of the silver electrode show up as pink/purple and the underlying substrate green/ yellow. B) isolated Zn map from (A). C) Isolated Ag Map from (A). (D) Histogram of electrode separation, for each sensor  $n=400$  with 3 sensors measured. Mean  $104.2 \mu\text{m}$  (95% confidence interval  $103.6 \mu\text{m} - 104.8 \mu\text{m}$ ) and standard deviation  $10.5 \mu\text{m}$  (95% confidence interval  $10.0 \mu\text{m} - 10.9 \mu\text{m}$ ) calculated from the entire  $n=1200$  sample. Confidence interval calculated using the bootstrap method in Matlab with 20,000 iterations. IDE Silver electrodes – PFI – 722 Ag NP ink (Novacentrix) printed using the RK flexiproof 100 at  $1.5 \text{ m}\cdot\text{s}^{-1}$  at a kiss print setting (i.e. flexographic plate just in contact with the substrate and anilox). ZnO layer – LBZA binder-less ink printed using the IGT F1 at  $1.5 \text{ m}\cdot\text{s}^{-1}$  with print and anilox forces set at 125 N. After each print the ink was cured/ dried at  $150 \text{ }^\circ\text{C}$  for 10 minutes. Post drying sensor ramped to  $420 \text{ }^\circ\text{C}$  annealed for 5 minutes at  $420 \text{ }^\circ\text{C}$ , and then aged for 2 days at  $246 \text{ }^\circ\text{C}$ . Substrate combined wet chemical and plasma treated Kapton HN. Map area:  $4.36 \text{ mm} \times 3.26 \text{ mm}$ .

Figure 6.21 D) shows a histogram of electrode separation measurements measured from EDS maps from 3 sensors (3 sets of  $n=400$ ). The electrodes had:

- Sensor 1: a mean separation of  $109.8 \mu\text{m}$  (95 % CI:  $108.9 \mu\text{m} - 110.6 \mu\text{m}$ ) and standard deviation of  $8.7 \mu\text{m}$  (95 % CI:  $8.1 \mu\text{m} - 9.3 \mu\text{m}$ .)
- Sensor 2: a mean separation of  $101.6 \mu\text{m}$  (95 % CI:  $100.5 \mu\text{m} - 102.7 \mu\text{m}$ ) and standard deviation of  $11.3 \mu\text{m}$  (95 % CI:  $10.4 \mu\text{m} - 12.2 \mu\text{m}$ .)

- Sensor 3: a mean separation of 101.3  $\mu\text{m}$  (95 % CI: 100.4  $\mu\text{m}$  – 102.1  $\mu\text{m}$ ) and standard deviation of 8.9  $\mu\text{m}$  (95 % CI: 8.3  $\mu\text{m}$  – 9.5  $\mu\text{m}$ .)
- A combined mean separation of 104.2  $\mu\text{m}$  (95 % CI: 103.6  $\mu\text{m}$  – 104.8  $\mu\text{m}$ ) and standard deviation of 10.5  $\mu\text{m}$  (95 % CI: 10.0  $\mu\text{m}$  – 10.9  $\mu\text{m}$ .) (n=1200)

The mean separation is lower than that of the HMTA derived ZnO sensor in Chapter 4, being approximately a third of the 300  $\mu\text{m}$  width of the Pt electrode separation. The reduced separation should allow for lower layer resistances without compromising sensitivity or response time.

The electrode separations show a generally broad distribution with a standard deviation  $\sim 10.1\%$  of the combined mean. The major factor of the underlying distribution likely arises due to the variation in nominal print plate width, which spans  $\sim 39 \mu\text{m}$ , which accounts for  $\sim 93.8\%$  of the combined cumulative distribution function here assuming a normal distribution. The three sensors have similar mean separations, with sensor 1 being statistically different to sensors 2 and 3, though within a single standard deviation. This suggests the process is relatively reproducible which would be a requirement for use as part of healthcare or industrial gas monitoring sensors, though a larger batch size would be required for a complete characterisation of the statistical distribution.

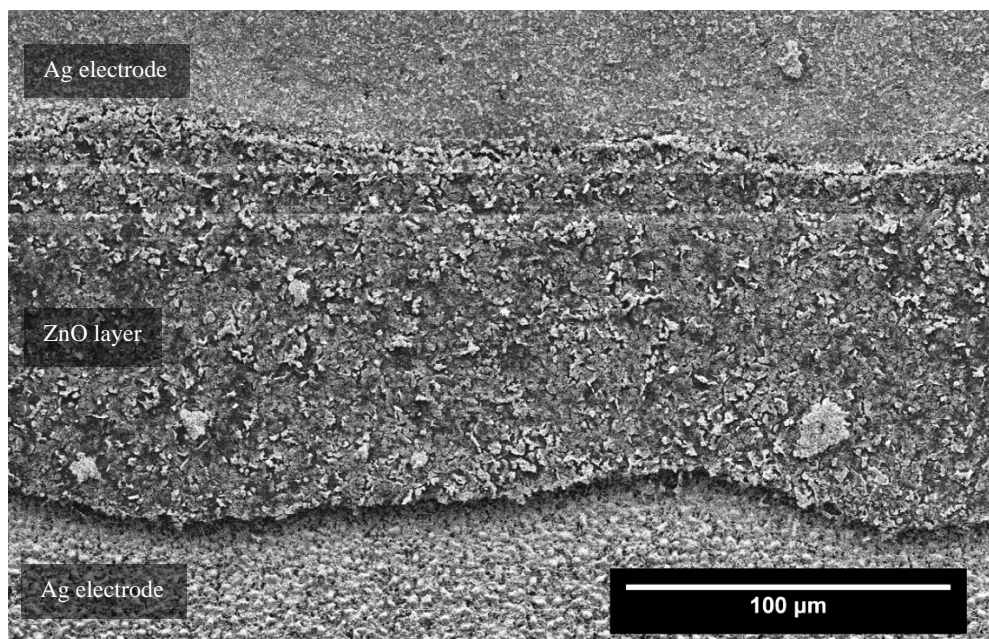


Figure 6.22: SEM micrograph showing the calcined flexographically printed LBZA derived ZnO particles (light overlapping particles) covering two Ag interdigitated electrodes (top and bottom white area) and the Kapton substrate with ZnO overlayer (central dark area) i.e. the sensing region. Note the two parallel light contrast horizontal lines in the top half of the image are charging imaging artifacts.



Figure 6.22 shows a SEM micrograph of a typical gap between Ag interdigitated electrodes for the calcined LBZA derived flexographically printed sensor. At the microscale ZnO coverage of the printed area is near complete and shows a high degree of overlap. At the interface between electrode and sensing layer (i.e. the Kapton area) an intermittent black strip can be seen potentially indicating breaks due to a mismatch in Ag electrode height and ZnO height on the Kapton layer. Cross-sectional SEM or AFM analysis would be required to determine if there is a lack of connection at the interface or if the contrast is a topological imaging artifact.

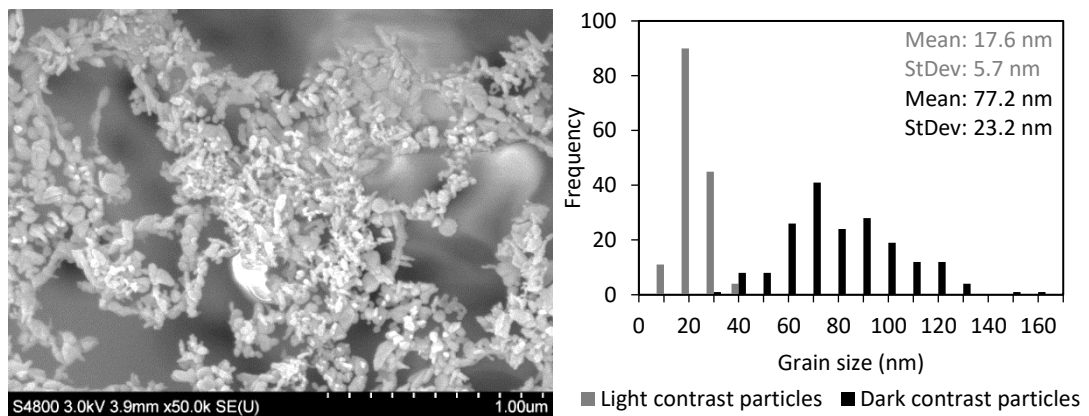


Figure 6.23: A) SEM micrograph of the printed 420 °C calcined LBZA derived ZnO grain structure of the sensor shown in Figure 6.21. B) Histogram of grains measured from A) separated by contrast. Dark contrast particles have a mean grain size of  $77.2 \pm 3.3$  nm and standard deviation of  $23.2 \pm 2.5$  nm (95% CI,  $n=185$ .) Light contrast particles have a mean grain size of  $17.6 \pm 0.9$  nm and standard deviation of  $5.7 \pm 0.7$  nm (95% CI,  $n=185$ ).

Figure 6.23 A) shows an SEM micrograph of the grain structure of a typical flexographically printed LBZA derived ZnO sensor calcined by ramping up to 420 °C, holding for 10 minutes, cooling to 246 °C and aging for 2 days. Two sets of particles with differing contrast can be seen. Figure 6.23 B) shows a histogram of grain size measurements taken from Figure 6.23 A) for each set of contrasts, where the:

- light contrast set had a mean of 17.6 nm (Bootstrap 95% CI: 16.7 nm – 18.5 nm) with standard deviation of 5.7 nm (Bootstrap 95% CI – 4.9 nm – 6.5 nm),  $n=150$ .
- dark contrast set had a mean 77.2 nm (Bootstrap 95% CI: 73.9 nm – 80.5 nm) whilst the standard deviation was 23.2 nm (Bootstrap 95% CI – 20.7 nm – 25.7 nm),  $n=185$ .

The lack of any significant skew to the sample sets and the non-overlapping mean confidence intervals clearly show that the particles arise from separate populations. The lighter contrast suggests the smaller particles have a higher average atomic number <sup>[298]</sup> and are likely Ag, this will be shown and explained further in section 6.5.3.2 .

In each case the mean grain size is greater than the 7.8 nm of the HMTA derived ZnO sensor presented in chapter 4. The increase is most likely a result of increased sintering due to the higher anneal temperature (420 °C compared to 350 °C.)

### **6.5.3.2 Sensor testing results**

Figure 6.24 shows proof of concept test responses for three flexographic printed ZnO sensors on Kapton for 200 ppm H<sub>2</sub>, CO and CH<sub>4</sub> as a function of time and temperature. Like the HMTA derived sensor presented in chapter 4.1.3 , the sensors produce significantly larger H<sub>2</sub> responses than for CO and CH<sub>4</sub>.

Figure 6.25 shows plots of the measured responses for each sensor and test gas as a function of predicted surface temperature. All sensors show similar trends in their response-temperature profiles but with differing magnitudes in response. For H<sub>2</sub> the response increases continuously with increasing temperature for all sensors with sensor 3 reaching a maximum response at 300 °C of 60.24. The response to H<sub>2</sub> is significantly higher than the value of 3.18 measured at 299 °C for the HMTA derived sensor. In comparison, the peak response values of 1.11-1.15 for CO and 1.03-1.06 for CH<sub>4</sub>, whilst larger than the peak responses of 1.07 and 1.04 respectively for the HMTA derived sensor, are of the same magnitude. Unlike the response to hydrogen, both CO and CH<sub>4</sub> responses appear to peak between 240 °C and 250 °C and 240 °C and 285 °C respectively. The presence of a peak response suggests a tipping point between the forward reaction and desorption of the products, and the back reaction and desorption of the reactants. Considering no tipping point was seen in the HMTA derived ZnO sensor response for CO, it is unlikely the response stems purely from the ZnO surface.

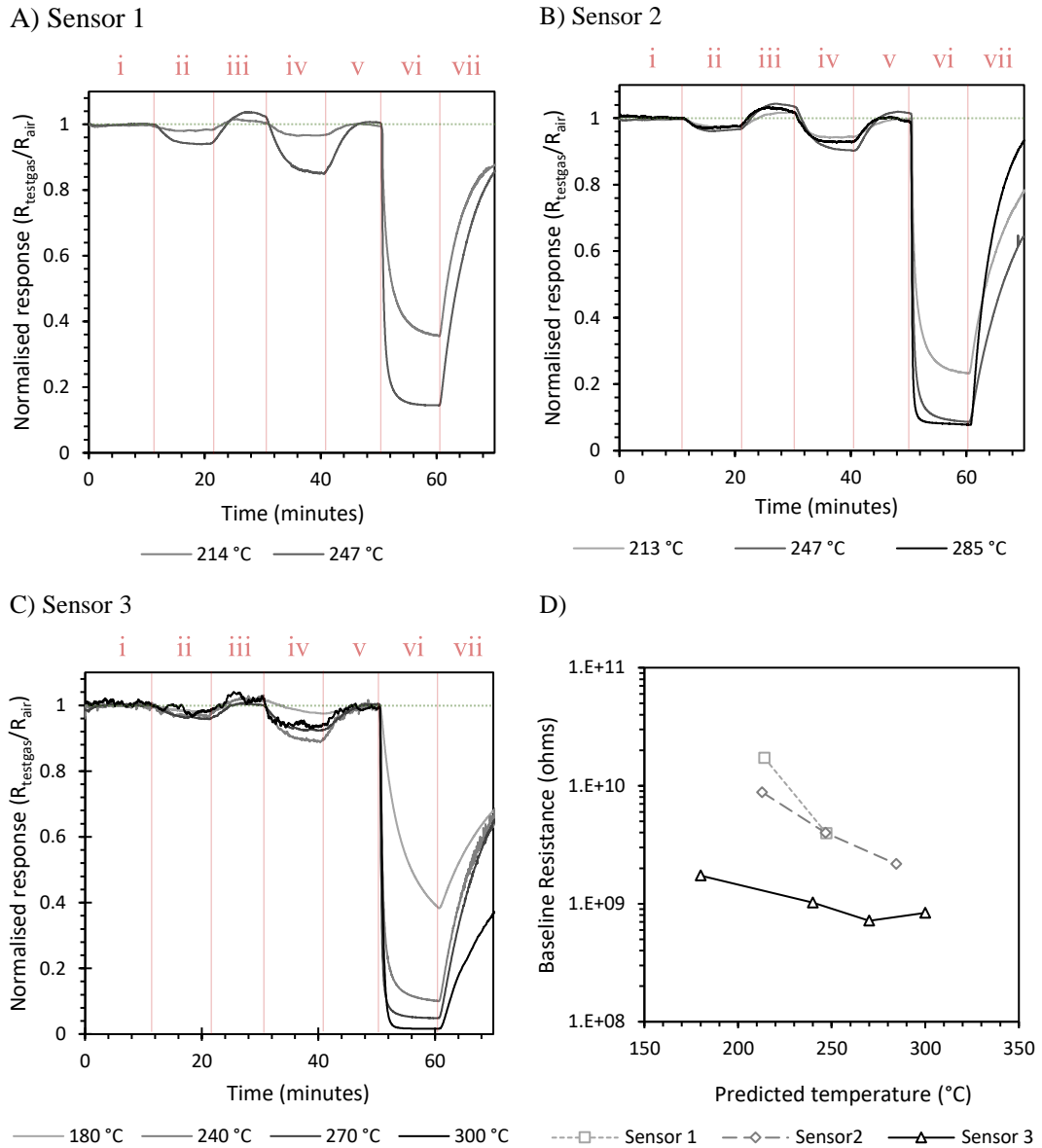


Figure 6.24: A), B) and C) - Proof of concept flexographic printed ZnO gas sensor response profiles as a function of time and predicted surface temperature for 3 test sensors. The test sequence consists of stabilisation/recovery steps: i, iii, v) and vii) – dry air (80 % N<sub>2</sub>, 20 % O<sub>2</sub>); and testing steps in dry air with 200 ppm ii) CH<sub>4</sub>, iv) CO and vi) H<sub>2</sub>. Total flow 400 mLm<sup>-1</sup>. Normalised response defined as resistance (test gas)/ resistance (air). The scans as presented were exploratory and intended for optimising the test set-up. Sensors 1 and 2 were performed without the Cirlex mask shown in the schematic in Figure 6.5 (section 6.3.2.1.1) and sensor 3 with. Sensors 1 and 2 were also calibrated external to the sensor testing rig, with sensor 3 tested within the rig under 400 mLm<sup>-1</sup> flow of N<sub>2</sub>. Sensor 1 and 2 temperatures were re-estimated from the internal calibration using the recorded heater track power. The noise at 300 °C appeared and disappeared consistently with a threshold temperature ~ 290 °C. The noise was primarily attributed to a variation of mechanical properties in the polyimide substrate holder and mask at the threshold temperature. It should be noted there is a possibility the noise was an instability within the commercial heater track that subsequently failed. D) Plot of sensor baseline resistance recorded in stage i as a function of predicted surface temperature.

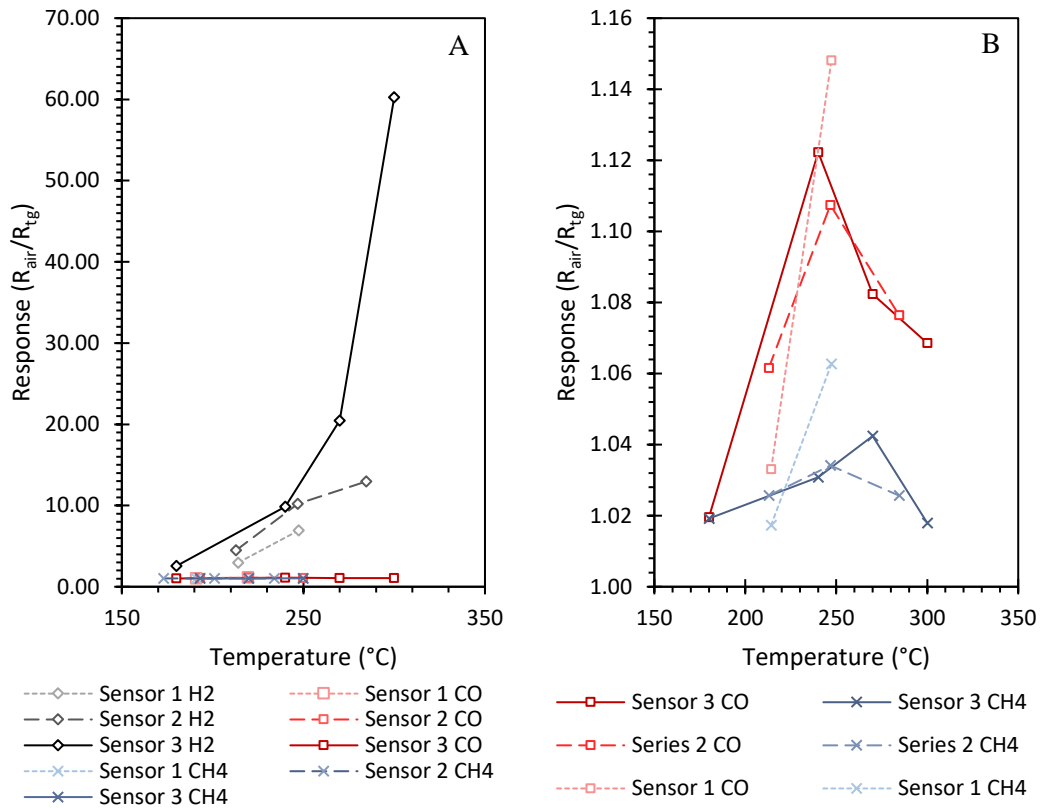


Figure 6.25: A) Plot of measured response as a function of predicted operating surface temperature for the proof of concept flexographic printed ZnO sensors for 200 ppm H<sub>2</sub>, CO and CH<sub>4</sub> in dry air. B) Magnified plots for CO and CH<sub>4</sub> from A).

To try and ascertain whether the electron transport behaviour was dominated by interfacial or grain boundary energy barriers I-V measurements were performed. Figure 6.26 A) shows I-V curves for sensor 3 measured at 302  $^{\circ}C$  in dry air and 200 ppm CH<sub>4</sub>, CO and H<sub>2</sub>. The curves, notably asymmetric, have only minor non-linearities compared to double back-to-back metal-semiconductor-metal Schottky contact junctions <sup>[513][514]</sup>.

In a typical polycrystalline semiconductor where the depletion region is smaller than half the grain size, the grain boundary electron barriers take the form of back to back double Schottky barriers <sup>[203]</sup>. The IV curves can therefore be modelled using thermionic emission theory <sup>[515]</sup> by fitting Equation 6.1 using a least squares method.

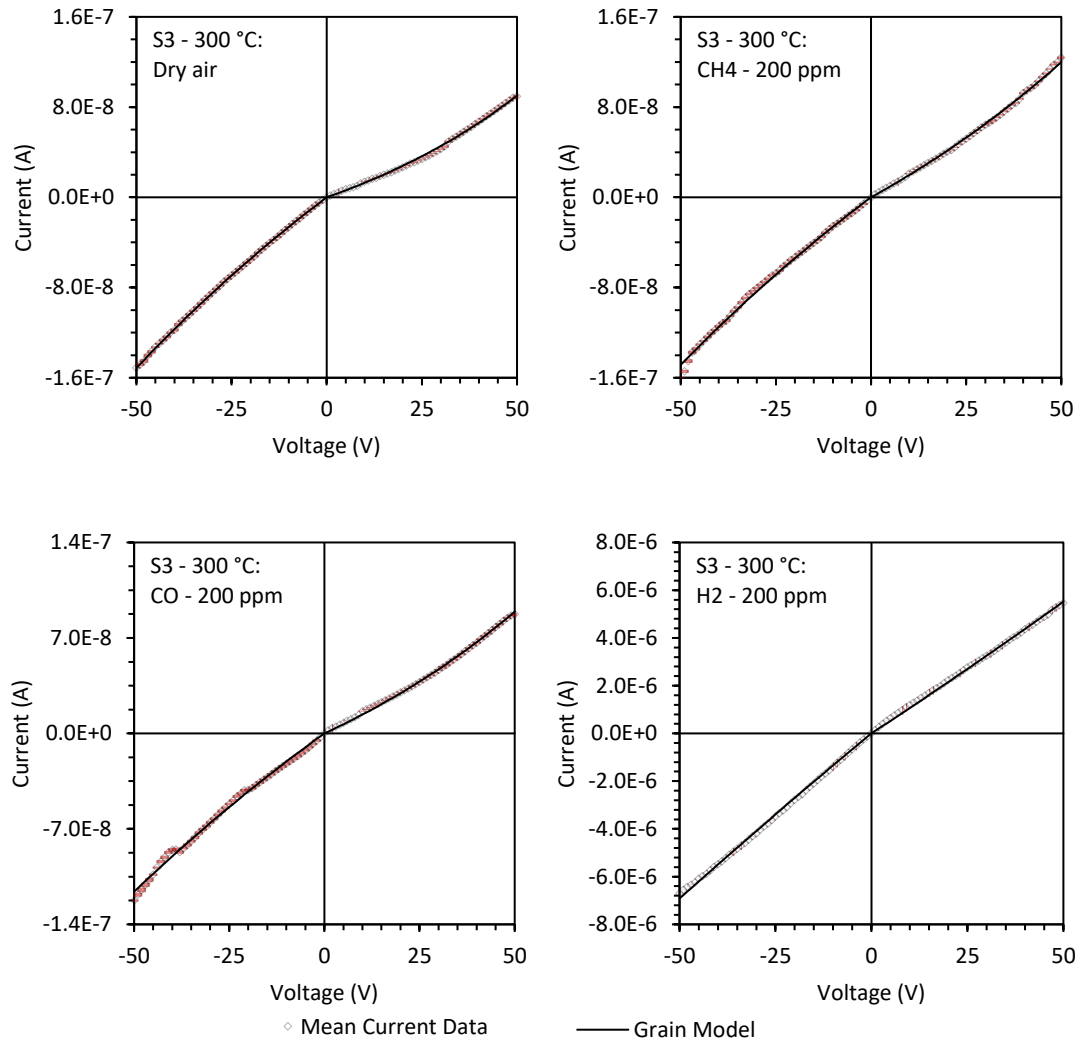


Figure 6.26: A) I-V curves for sensor 3 measured at 302 °C in dry air and 200 ppm CH<sub>4</sub>, CO and H<sub>2</sub> environments. Each data set curve shows the mean measured current, back to back electrode junction (black line) and symmetrical grain (black line) thermionic emission model trend lines. Each measure data point is the mean of 8 measurements with each point integrated over 3 seconds, the 99% confidence interval error margin for each measurement (red) is 3 orders of magnitude lower than the data value.

$$I = \text{sgn}(V_{\text{applied}}) I_s \left( e^{\frac{q|V_{\text{applied}}|}{c \cdot k_B T}} - 1 \right)$$

Equation 6.1

Where T is the temperature in Kelvin, q is the electron charge, k<sub>B</sub> is the Boltzmann constant (8.617 \* 10<sup>-5</sup> eV.K<sup>-1</sup>). c is equal to the product of the ideality factor n and the number of grains N<sub>g</sub>, such that V/N<sub>g</sub> is the voltage applied to each grain barrier.

The saturation current  $I_s$  is given by:

$$I_s = AA^*T^2 e^{\left(-\frac{\phi_{SB} + \varepsilon_\xi}{k_B T}\right)}$$

Equation 6.2

Where  $A$  is the cross-sectional area of the interface in  $\text{cm}^2$ ,  $A^*$  is the Richardson constant equal to between 19.54 and 32  $\text{A}\cdot\text{cm}^{-2}\cdot\text{K}^{-2}$ , and  $\phi_{SB}$  is the energy barrier for electron transport and  $\varepsilon_\xi$  is the difference in energies in the conduction band bulk and the fermi level  $\varepsilon_\xi = E_{CB_B} - E_F$ .

Table 6.2 shows the fitting parameters for the trend lines in Figure 6.26. The  $c$  values are significantly higher than the values of  $n$  in literature (1-25) and are on the order of the mean number of grains per electrode spacing (dark contrast:  $104.2 \mu\text{m}/77.2 \text{ nm} \approx 1353$  grains, light contrast:  $104.2 \mu\text{m}/17.6 \text{ nm} \approx 5920$  grains.) This suggests that the current transport is generally dominated by distributed barriers as opposed to a singular set of large interfacial barriers. The asymmetry in  $I_s$ ,  $c$  and  $\phi_{SB} + \varepsilon_\xi$  would not generally be expected when the barriers arise from purely the grain boundaries suggesting a minor contribution from each electrode-sensing layer interface.

Gas	$I_{S\text{Forward}}$ (* $10^{-6}$ )	$I_{S\text{Reverse}}$ (* $10^{-6}$ )	Forward $c$	Reverse $c$	$R^2$	Estimated Forward $\phi_{SB} + \varepsilon_\xi$ range (eV)	Estimated Reverse $\phi_{SB} + \varepsilon_\xi$ range (eV)
Dry air	0.07608	0.38004	1291	3009	0.9998	0.900- 1.207	0.806- 1.113
CH <sub>4</sub>	0.19995	0.40956	2149	3260	0.9992	0.852- 1.159	0.817- 1.124
CO	0.10882	0.36526	1685	3657	0.9990	0.882- 1.189	0.822- 1.129
H <sub>2</sub>	60.0531	92.484	11465	13999	0.9995	0.569- 0.877	0.548- 0.855

Table 6.2: Table of thermionic emission fitting parameters in Equation 6.1 for the  $I/V$  curves presented in Figure 6.26. Estimated  $\phi_{SB} + \varepsilon_\xi$  derived from  $I_{S\text{Forward}}$  and  $I_{S\text{Reverse}}$  assuming the current measured is purely from the modelled thermionic sources. The estimated barrier range is calculated for a temperature of 302 °C, and 14 pairs of 0.840 cm electrodes (estimated from a combined measurement of 27 electrode outlines measured from EDS maps) for a total width 11.76 cm. The minimum barrier was calculated with the lowest found measured Richardson constant for polycrystalline nanogranular ZnO  $19.54 \text{ A cm}^{-2} \text{ K}^{-2}$  [516], a layer thickness of one mean grain  $\sim 77.2 \text{ nm}$  and 1% interfacial area to account for up to 99% breakage at the interface. The maximum barrier was calculated with the theoretical Richardson constant for ZnO [516]  $32 \text{ A cm}^{-2} \text{ K}^{-2}$ , and a height of 3 mean grains to allow for sheet overlap.

Using the  $I_s$  values,  $\phi_{SB} + \varepsilon_\xi$  was estimated using a temperature of 575.15 K (302 °C) and total electrode length of 11.76 mm (14 sets of electrodes per sensor x 8.40 mm per electrode, based on a combined measurement of 27 printed electrodes from EDS maps). For the maximum value the layer thickness was estimated as three mean grains thick (231.6 nm) to allow for particulate overlap, and the Richardson constant was taken as the theoretical Richardson constant for ZnO of  $32 \text{ A cm}^{-2} \text{ K}^{-2}$  [516]. For the minimum value the layer thickness was estimated as 1 grain thick (77.2 nm), and the Richardson constant was taken as the smallest value found for nanocrystalline ZnO  $19.54 \text{ A cm}^{-2} \text{ K}^{-2}$  [516]. To account for potential breaks at the interface that appear to be present in Figure 6.22, the minimum value was divided by 100 to allow for up to 99 % of the interfacial area being broken.

Jones [77] performed an in depth investigation of the kinetics and energetics of surface reactions in HMTA synthesised LBZA derived ZnO gas sensors. Jones measured an estimated range of values of  $\phi_{SB} + \varepsilon_\xi$  to be  $0.59 \pm 0.09 \text{ eV} + \alpha \theta_{O^2} k_B T \text{ eV}$  where the second term represents the surface potential to occupation of surface sites by  $[\text{O}_2]^-$ ,  $[\text{O}]^-$  and  $[\text{CO}_2]^-$ . Further details can be found in appendix Chapter 13 where values of  $\alpha$  and  $\theta_{O^2}$  by Jones have been measured in imageJ, trendlines produced and extrapolated to 302 °C, resulting in values for  $\alpha \sim 5.55$  and  $\theta_{O^2} \sim 0.056$ . Combining the result produces  $\alpha \theta_{O^2} k_B T \sim 0.016 \text{ eV}$  and an estimated range for  $\phi_{SB} + \varepsilon_\xi$  of 0.606-0.696 eV. The values estimated by Jones are 0.204-0.608 eV and 0.110-0.507 eV lower than the estimated range of barriers for the forward and reverse bias values in Table 6.2. Furthermore, from plots by Jones [77]  $\varepsilon_\xi$  was predicted to change by less than 0.08 eV between 400 °C and 300 °C. The difference in values of  $\phi_{SB} + \varepsilon_\xi$  suggests one of two possibilities:

- A shift in the intrinsic value of  $\phi_{SB} + \varepsilon_\xi$  from the ZnO particulates. This could be a result of the different LBZA synthesis conditions. One candidate would be potential  $\text{Na}^+$  doping which forms acceptor states in ZnO with an ionization energy of 0.17–0.27 eV [517]. Wu *et al.* [518] measured the variation in Fermi level position in ZnO with Na doping and found shifts of 0.33 eV and 0.74 eV for 0.2 at% and 0.7 at.% respectively.
- The second possibility results from factors introduced during the printing process. The most likely candidate would be the transfer/ redistribution of printed Ag nanoparticles to the sensing layer, likely during the LBZA print. Brillson and Lu [514] performed a review of Schottky contacts on ZnO from which a range of total barrier heights of 0.68-1.11 eV with a mean value of 0.88 eV (n=14) can be found. Allen, Durbin and Metson [519] investigated the barrier heights associated with  $\text{Ag}_2\text{O}$ -n-type ZnO contacts and found a total barrier height of  $\sim 1.2 \text{ eV}$ . The transfer and

redistribution of Ag/Ag<sub>2</sub>O nanoparticles would therefore result in an increased depletion region width and energy barrier as compared to just the grain barriers themselves.

Whilst both possibilities are consistent with the estimated energy barrier ranges, a peak response to CH<sub>4</sub> at 285 °C has also been observed by Wang *et al.* [520] in Ag<sub>2</sub>O decorated ZnO nanowire gas sensors. The peak response temperature is similar to the peak in CH<sub>4</sub> response temperature of 240-280 °C observed here and suggests the increased resistance is likely a result of the transfer of Ag nanoparticles. Karami Horastani *et al.* [521] studied the effects of Ag/AgO<sub>x</sub> nanoparticles decorated SnO<sub>2</sub> porous thick films and although peak sensitivities occurred at a different temperature, plots of resistance in air show a peak resistance between 250 °C and 280 °C. The peak in resistance was attributed to the oxidation of the Ag nanoparticles and formation of an AgO<sub>x</sub> shell. The oxide shell increased the depletion region energy barriers for electron transport, at 150 °C calculated as 0.14 eV for pure SnO<sub>2</sub> films and up to 0.99 eV for the Ag/AgO<sub>x</sub> decorated samples. Above 280 °C, AgO and Ag<sub>2</sub>O were stated to be unstable, slowly dissociating into metallic Ag and decreasing barrier height and resistance. For the SnO<sub>2</sub> devices an increase in resistance of 3-4 orders of magnitude was seen upon decoration with Ag, in line with the increase in resistance here from 1-5 MΩ for the HMTA derived sensors to 0.7-8 GΩ for the printed sensors. Furthermore, the observation of two distinct populations in the grain size measurements, where the light contrast mean (17.6 nm) is of the order of the 25 nm Ag NP produced by Novacentrix [522], makes the transferred Ag NP explanation the most likely reason for the increase in device resistance.

The upper limit value of  $\varphi_{SB} + \varepsilon_{\xi}$  in dry air of 1.2 eV and 200 ppm H<sub>2</sub> of 0.877 eV aligns almost exactly with the literature values for  $\varphi_{SB} + \varepsilon_{\xi}$  for n-type ZnO junction with Ag<sub>2</sub>O (~1.2 eV) and the mean reported value for Ag (~0.88 eV.) The significantly increased response to H<sub>2</sub> can therefore likely be explained as a complete reduction of the transferred nanoparticles from Ag<sub>2</sub>O to Ag.



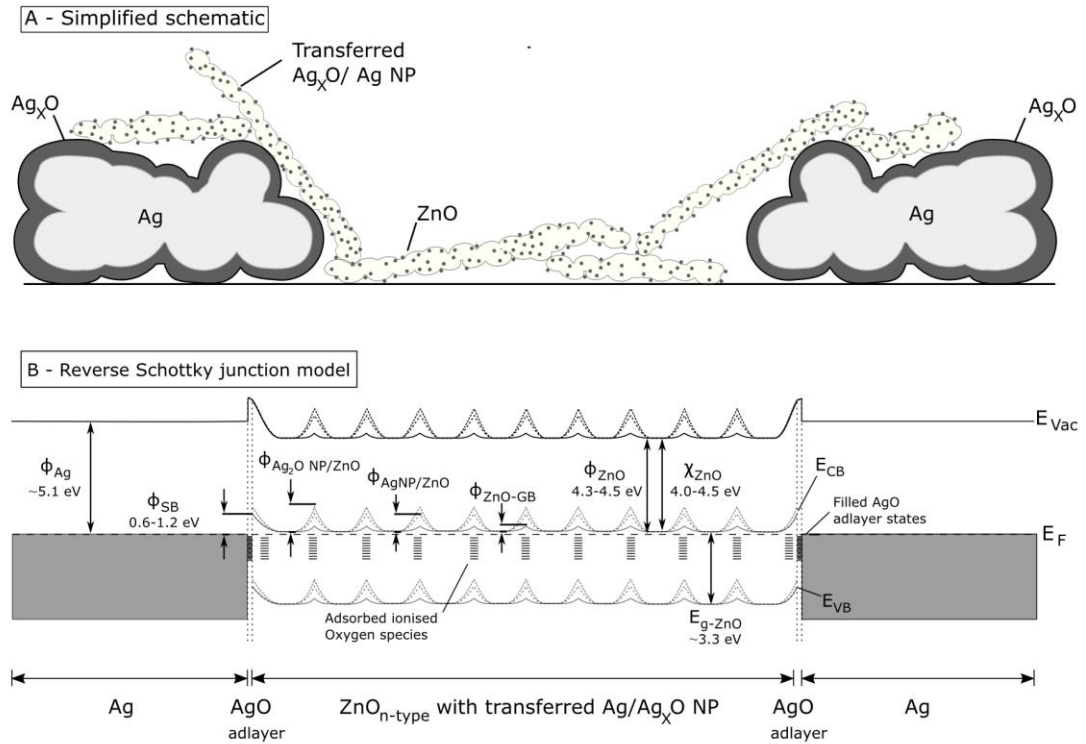


Figure 6.27: A) Simplified schematic of a cross section between two electrodes showing the Ag electrodes with an oxide overlayer, LBZA derived ZnO with a coating of Ag/Ag<sub>x</sub>O nanoparticles transferred during the printing process. B) Shows a simplified band diagram for the reverse Schottky barrier junction model of schematic A. Annotation shows the work function of silver ( $\phi_{\text{Ag}}$ ) and ZnO ( $\phi_{\text{ZnO}}$ ), ZnO electron affinity ( $\chi_{\text{ZnO}} = \phi_{\text{ZnO}} - (E_{\text{CB}} - E_{\text{F}})$ ) and Bandgap ( $E_{\text{g-ZnO}} = E_{\text{CB}} - E_{\text{VB}}$ ), the electrode-ZnO interface Schottky barrier ( $\phi_{\text{SB}}$ ). Also shown are the barriers created due to oxygen adsorbates at the ZnO grain edges ( $\phi_{\text{ZnO-GB}}$ ), as well as the barriers induced by the transferred Ag NP, where ( $\phi_{\text{Ag NP/ZnO}}$ ) corresponds to the barrier due to reduced metallic Ag and ( $\phi_{\text{Ag}_2\text{O NP/ZnO}}$ ) corresponds to the barrier due to oxidized Ag<sub>2</sub>O. Note that the barriers correspond to the barrier heights given by Equation 6.2.

The responses to CH<sub>4</sub> and CO are much lower and suggest that the Ag<sub>2</sub>O nanoparticles are not reduced and the response, which is on the same order as that seen for the HMTA derived sensor, is likely a result of the reaction of surface species. Sensor 1 shows an increase in resistance and CO and CH<sub>4</sub> response versus sensors 2 and 3. Based on the aforementioned reaction model, it is possible that the increases are a result of increased transfer/redistribution of Ag NP during the LBZA overprint resulting in increased band bending distributed over the material. Further work would be required to confirm.

For all sensors, a temporary increase in resistance above the baseline can be seen in the recovery step post CH<sub>4</sub> exposure. In Chapter 4, the HMTA derived sensor response was on the order of experimental artifacts and so a reliable comparison in response and recovery profiles cannot be made. As a result, there are two potential mechanisms depending on whether the response during the recovery step arises from the ZnO layer or from the interfaces introduced by the transferred nanoparticles.

The gas sensing response to methane is generally expected to proceed by stepwise dissociation into  $\text{CH}_X(\text{ads-O}) + \text{XH}(\text{ads})$  species <sup>[207]</sup>, where (ads-O) indicates adsorption at a lattice oxide surface site. Oxygen is expected to react with adsorbed dissociated  $\text{CH}_X(\text{ads})$ ,  $\text{C}(\text{ads})$  and  $\text{H}(\text{ads})$ , either fully oxidising and desorbing as  $\text{CO}_2$  and  $\text{H}_2\text{O}$ , or partially oxidising and desorbing as other small organic molecules such as  $\text{CH}_3\text{OH}$  or  $\text{CH}_2\text{O}$  <sup>[207]</sup>. The results could potentially be explained by the formation of an electron trapping intermediate reaction occurring in competition with the expected reaction pathway. Without spectroscopic evidence it is difficult to precisely define the species being formed. A possible route could be the reaction of  $\text{CH}(\text{ads-O})$  with  $\text{O}_2^-(\text{ads-Zn})$  or  $\text{O}^-(\text{ads-Zn})$ , which are to be the primary chemisorbed oxygen species within the tested temperature range <sup>[19]</sup>, forming  $\text{CHO}_2^-(\text{ads})$  and  $\text{CHO}^-(\text{ads})$  respectively. If the reactions proceed centred on the  $\text{CH}(\text{ads-O})$  species, then it would leave a free Zn cation surface site for additional oxygen chemisorption <sup>[19]</sup>. The presence of two electron trapping sites would increase the depletion region width and barrier height by increasing  $\theta_0^2$ , and therefore the layer resistance, beyond the dry air baseline. For the adsorbed species to desorb,  $\text{CHO}_2^-/\text{CHO}^-$  would need to dissociate back in to  $\text{CH}(\text{ads-O})$  and  $\text{O}_2^-(\text{ads-Zn})/\text{O}^-(\text{ads-Zn})$ , subsequently oxidising into  $\text{CO}_2$  and  $\text{H}_2\text{O}$  or adsorbed OH species. The dissociation reaction would be in competition with  $\text{O}_2$  adsorption, reducing the rate of the reverse reaction and producing the slow kinetics and recovery of resistance to the dry air baseline observed.

For the second mechanism it is important to note that  $\text{Ag}_2\text{O}$  generally forms a p-type semiconductor <sup>[523][524][525]</sup>. The negative response observed during the recovery steps post  $\text{CH}_4$  exposure could potentially be accounted for if the desorption rate of the reaction products on  $\text{Ag}_2\text{O}$  is slower than that on ZnO. In p-type materials resistance increases upon exposure to reducing gasses <sup>[19]</sup>. The slower desorption would lead to an increased resistance within the  $\text{Ag}_2\text{O}$  particles for a short period after the ZnO layer has returned to baseline resistance.

In addition to the catalytic response of the redistributed electrode material there is also the possibility of Ag atom diffusion into the ZnO lattice <sup>[526][527]</sup>, altering the sensing properties of the ZnO layer directly. Ahn *et al.* <sup>[527]</sup> showed from XRD and DTA of a 2%  $\text{Ag}_2\text{O}$  98 % ZnO powder mix that for temperatures below 275 °C,  $\text{Ag}^+$  tended to occupy  $\text{Zn}^{2+}$  substitutional sites, whereas above 275 °C the  $\text{Ag}^+$  ions out diffused with the majority of species forming occupied interstitial sites. They then showed that for pulse laser deposited thin films formed from the powder mixes under a variety of temperatures that below 275 °C the film acted as a p-type material and above 275 °C as a high conductivity n-type material. Postica *et al.* <sup>[528]</sup> showed that Ag (1.3 % total) doped ZnO nanocolumns that underwent

rapid thermal annealing at temperatures exceeding 475 °C produced no appreciable H<sub>2</sub> response at temperatures up to 350 °C, even at 1000 ppm H<sub>2</sub>. The annealing temperature used by Postica *et al.* generally suggests the silver formed interstitial sites as would be the case here. Their lack of response to H<sub>2</sub> generally suggests that Ag doping is unlikely to be a major factor for the improvement in H<sub>2</sub> response here.

### **6.5.3.3 Obstacles that require further development**

The results as presented represent the second published flexographically printed gas sensor of any type, and the first to be both fully printed and shown to respond to more than just oxygen. However, whilst the technique shows potential for producing cheap hydrogen sensors, there currently appear to be four main issues that need to be addressed:

- Print feature edge roughness. In both the PVP based LBZA ink in appendix Chapter 13 and the PFI electrodes in section 6.5.3.2 a consistent edge roughness with span approaching that of the print plate was seen. As the mean electrode separation tends to 0, the ratio of variance/ mean separation increases. As a result, the variation of resistance, which is proportional to length, across the sensor increases. Furthermore, decreasing electrode separation also decreases the number of grains, increasing the non-linear voltage dependence of the resistance. The edge roughness therefore puts a limit on the electrode separation and device resistance obtainable. The problem appears to stem from the inherent roughness of the manufacturing method of the McDermid Digital Rave plates used <sup>[496]</sup>. Altering plate supplier or manufacturing custom plates from a laser engraving company should be able to overcome the issue, allowing for narrower electrode spacing, decreased device resistance, reduced sensor footprint and ultimately cheaper sensors.
- Substrate material choice and reduced availability of high temperature stable commercial conductive flexographic inks at present. Whilst technically two separate issues, the effect of each heavily impacts on the other. Uncatalysed inorganic gas sensors by their very nature require high temperatures to operate. As outlined in section 6.2.1.2, traditionally ceramics such as alumina are used along with gold or platinum electrodes. At present commercial conductive flexographic inks are effectively limited to carbon and silver, with the binder in carbon potentially unstable at sensing temperatures ( $\geq 300$  °C.) Furthermore, the thermal behaviour of silver appears to be variable, with experimental evidence supporting both that the

oxides are unstable above 190 °C <sup>[485][486][529][530]</sup> and stable up to 297 °C <sup>[531][532]</sup> -350 °C <sup>[485]</sup>. In all cases Ag electrodes are expected to be stable at temperatures above 350 °C. At this temperature practically all organic substrates are unstable for long term operation, with the possible exception of Upilex polyimide (UBE Industries, Ltd.) <sup>[533]</sup> which reaches 50 % tensile strength after ~ 40 days at 350 °C and ~ 2 ¼ years at 290 °C. As such, either development of a specialised ink, modification of a commercial screen or inkjet ink, introduction of a more mature patterning and deposition process, or converting to an inorganic substrate that can handle the temperature required to prevent Ag oxidation is needed.

- On press ink drying. Ink drying on press is a well-known problem in the flexographic printing industry, with a range of commercial enclosed anilox inking chambers and automated ink adjustment equipment available to address it <sup>[534]</sup>. The lab scale proof presses available do not contain such equipment, and furthermore the timescale between printing and the print plate being reinked prior to the next print is order of magnitudes different between the two scales (ms vs s.) The combination of factors makes commercial inks, like the PFI-722 Ag NP ink (Novacentrix), which are designed for the industrial scale, relatively unpredictable prior to purchase. This unpredictability led to problems where the Ag electrode ink required the RK Flexiproof 100 to print, preventing the ability to test brittle, inflexible ceramic substrates. The unpredictability can be lessened by using commercial inks with higher boiling point solvents or saturating the local atmosphere in the ink solvent. For flammable inks, saturating the atmosphere poses a fire and health risk and should therefore be restricted to water-based inks.
- Transfer of material between print layers. As gas sensors are inherently surface sensitive devices any transfer of material can alter the sensor response. If the material is chemically/ electrically active, as the transferred Ag here is, then the sensor response can alter dramatically. To prevent material transfer, the cohesion and adhesion of the initial printed film needs to be large enough to withstand the forces induced by the second print. The initial dried printed film also needs to be insoluble in the solvents of the second ink. A potential strategy for limiting the effects of redispersion would be to print the sensing layer and then the electrode material. As the electrode material is significantly more conductive than any dispersed sensing material the effects of any redistribution within the electrode should be minimal to negligible. As the majority of the sensing layer will not be

exposed to the second print, the bulk of the layer should be unaffected. As such the only effects should be limited to within the electrode-sensing layer boundary. By printing the electrode second, any effects of height mismatch between layers should also be reduced. The combined effects should result in an improvement in reliability, consistency and reproducibility. An additional benefit arises if the printed ZnO layer is thicker than the Debye length as the interface should be buried. Assuming that Ag<sub>2</sub>O only forms a shell then the buried interface should be an Ag-ZnO and not Ag<sub>2</sub>O-ZnO junction, which should significantly reduce the interface resistance.

## 6.6 Conclusion

Initial print test of the PFI-722 Ag NP ink used for the interdigitated electrode material showed poor wetting and rapid on press drying. To increase wetting a combined surface tension and XPS investigations of a hydrolysis based wet chemical treatment, O<sub>2</sub> plasma treatment and a combined wet chemical followed by O<sub>2</sub> plasma treatment was performed. All treatments showed a reduced water contact angle with drops from the control ( $\mu=64.4^\circ$ ,  $\sigma=4.5^\circ$ ) for O<sub>2</sub> plasma ( $\mu=28.5^\circ$ ,  $\sigma=1.1^\circ$ ), hydrolysis treatment ( $\mu=34^\circ$ ,  $\sigma=2.2^\circ$ ) and a significant drop for the combined treatment ( $\mu=9.0^\circ$ ,  $\sigma=1.3^\circ$ .) Tests using the PFI-722 ( $\mu=45.9^\circ$ ,  $\sigma=3.9^\circ$ ) however showed statistically significant drops ( $p<0.05$ ) for the hydrolysis treatment ( $\mu=27.5^\circ$ ,  $\sigma=2.7^\circ$ ,  $p=2*10^{-5}$ ) and combined treatment ( $\mu=25.7^\circ$ ,  $\sigma=1.4^\circ$ ,  $p=4*10^{-6}$ .) XPS results showed a significant increase in amine groups for the combined treatment that were not present in the plasma exposed sample. The increase in wetting for the PFI-722 ink was attributed to protonation of the amines by the acidic groups in the ink leading to a significant increase in surface charge. To counteract on press drying for volatile inks it was shown that printing within a solvent saturated environment using a printer with an ink reservoir was a requirement.

LBZA glycerol-based alcohol inks have been shown to produce uniform layers. As the ZnO derived from LBZA was shown to be an ideal candidate for hydrogen sensing in Chapter 4, flexographic printed LBZA shows promise for use in producing cheap commercial hydrogen sensors. Problems arising from transfer of Ag electrode material to the sensing layer were observed, and methods to counteract the issue suggested. The significantly increased hydrogen sensitivity due to the presence of Ag NP should however be noted as a potential method for improving sensitivity for future studies. The current lack of conductive, high temperature (300+ °C) stable, commercial flexographic inks appears to be a major impediment for fully printed sensors and will need further research and development. As

such, flexographic printing of LBZA particulates shows a promising and cheap route for rapidly producing uniform, nanoscale thickness, ZnO semiconducting layers and patterned features. Unlike screen printing, with the correct choice of carrier solvents layers produced without the need for resins or binders that would hinder the conductivity or surface activity of the layer have been produced. As such the technique is ideal for printing layers that require uncontaminated surfaces with higher throughput than inkjet. Furthermore the particles as used here are within the range that would typically clog inkjet nozzles [535].

For the broader flexographic printed device field, an empirical  $\ln(\text{viscosity/nominal width relation})$  has been observed in appendix Chapter 13 for nominal line width/ anilox cell width ratios greater than 0.492. The observations appear to be the first reported within ratio ranges of 0.496-7.2 providing a useful predictive tool for future electronic device development.

The main limitation for further testing was caused by heater track failure which was attributed to a poor-quality batch of commercial alumina substrates. Based on these observations for short term testing a different supplier (or an in-house custom-made heater track and support,) is recommended for further work relating to the development of the sensor. For long term development it would be expected that an integrated rear side heater will be printed directly onto the substrate. Replacing the sensing chamber with a wider diameter chamber would allow for increased options and is recommended. Replacing the feedthrough with a higher pin number feedthrough would allow for further improvements in reliability and capability, allowing for:

- Direct in-situ measurement of surface temperature, either through a Pt temperature dependent resistor or a thermocouple.
- An increase in the number of sensors that can be tested simultaneously, such as in a printed array as would be expected in the end use of the project aims (i.e. in the final breath sensors).

# **Chapter 7 - Investigation of intense pulsed light (IPL) photonic annealing conditions for the conversion of LBZA to ZnO**

---

## **7.1 Introduction**

In Chapter 6 uniform layers of LBZA, with properties ideal for ZnO thin film hydrogen gas sensors as shown in Chapter 4, were produced by flexographic printing. The layers also have additional potential uses such as in the compact hole blocking layers of perovskite photovoltaics <sup>[536]</sup>. As the major forms of scale up being researched for perovskite PV cells are printing and coating techniques <sup>[536]</sup>, the flexographic printing of an n-type thin film semiconductor such as ZnO has great promise. Whilst the ability to rapidly print uniform layers provides great benefits, the 350 °C annealing temperature puts limitations on the substrates that are compatible. Photonic annealing circumvents the problem by focusing the energy on the layer to be annealed, minimising the energy transferred to the bulk of the substrate. This chapter focuses on the optical properties and thermal dehydration pre-treatment required to successfully calcine LBZA via IPL. As IPL uses exposure to light as the energy source for calcination, understanding and controlling the absorptivity of the material is of fundamental importance. Subsequently the chemical, structural, and optical properties of the exposed sample was characterised to check what conditions were necessary for calcination. Finally, the electronic and optical properties of the Zinc oxide quantum dots produced using the technique are investigated and the effects on any sensing material produced using the technique inferred.

## **7.2 Chapter specific equipment**

### **7.2.1 Pulseforge 1200 (Novacentrix)**

The photonic annealing investigated within this chapter was performed using a Pulseforge 1200 photonic curing system (Novacentrix, Austin, Texas, US.) The system consists of a

proprietary reflector optics, flash lamp and electronic system. The system has listed specification <sup>[537]</sup> of:

- Peak radiant power delivered: 4.9 kW/cm<sup>2</sup>
- Max radiant energy delivered: 46 J/cm<sup>2</sup>
- Output spectrum: 200-1500 nm
- Pulse length range: 25-100,000  $\mu$ s (increments of 1  $\mu$ s)
- Curing dimensions per pulse: 75 mm x 150 mm
- Max area cured per sample: 300 mm x 150 mm
- Uniformity of exposure (point to point):  $\pm$  2 % or better
- Max pulse rate: >kHz [*sic*]
- Max linear processing speed: 30 m/s (dependent on pulse conditions)
- Lens sample distance: 0-60 mm

A bolometer is used to calibrate the sample exposure energy from the lamp settings and pulse shape, and table distances. The bolometer is a black body with well-defined thermal and optical absorption properties and an inbuilt temperature sensor, allowing for the delivered electromagnetic energy per unit area to be calculated from the rise in bolometer temperature during exposure. During a typical experiment the system is set to the desired settings and the sample exposure energy calculated. Then a sample is loaded onto the table and the sample exposed. Post exposure the sample was removed, and the next sample placed in the same location.

## 7.3 Methods

### 7.3.1 LBZA synthesis

All LBZA nanomaterial was synthesised and centrifuge cleaned using the method outlined in chapter 4.2.2.1 using  $[\text{OH}^-]/[\text{Zn}^{2+}]$  ratios of 1.5 and microwave time of 20 seconds.



### 7.3.2 Investigating the optical properties of LBZA

4 synthesis runs of LBZA were performed, and after the final centrifuge step the powders were dried at 50 °C for 2 days under a rough vacuum estimated between 0.1 and 0.3 bar. Post drying, external reflectance UV-VIS spectra and XRD diffractograms were recorded for the powders prior to and post annealing at 150 °C for 1 hour. External reflectance UV-VIS spectra were recorded using a Cary 100 spectrophotometer (Agilent Technologies LDA UK Limited, Cheshire, UK) between 200 nm and 800 nm, with a 1 nm step size. A tungsten halogen visible source with quartz window was used for wavelengths above 350 nm and a deuterium arc ultraviolet source for wavelengths below 350 nm. The powders were loaded into a spring-loaded powder cell and all spectra referenced to a Spectralon (Labsphere) diffuse reflectance standard. Tauc plots of the reflectance spectra were created by first calculating the Kubelka-Munk remission function  $F(R_{\infty})$  [321]:

$$F(R_{\infty}) = \frac{(1 - R_{\infty})^2}{2R_{\infty}}$$

Equation 7.1

Where  $R_{\infty}$ :

$$R_{\infty} = \frac{\text{Reflectivity}_{\text{sample}}}{\text{Reflectivity}_{\text{standard}}}$$

Equation 7.2

Is the reflectance of the sample with infinite thickness, assuming negligible sample holder reflectivity. Tauc plots were then produced by plotting  $(F(R_{\infty}) * \text{photon energy})^2$  vs photon energy, and the optical bandgap measured by plotting a line of best fit through the point of steepest gradient and extrapolating to the intercept with the photon energy axis [321].

The crystalline phase of each sample was recorded by x-ray diffraction using the same Discover D8 (Bruker) diffractometer with Cu  $\alpha$  source set up as used in chapter 5.2.2.2 . Diffractograms were recorded for  $2\theta$  between 2.5 ° and 60 ° in 0.019627 ° increments. To characterise the effect of ZnO impurities produced during the synthesis of the LBZA as observed in chapter 4.2 and Chapter 5, the reflectance of the samples at 328 nm were plotted

against normalised phase area and trendlines fit to the data. Normal phase areas (NPA) were calculated as:

$$NPA = \frac{X}{Peak\ area_{LBZA(001)} + Peak\ area_{ZnO(101)} + Peak\ area_{BLBZA(001)}}$$

Equation 7.3

Where X is the peak area of either LBZA (001), ZnO (101) or the so called BLBZA (001) phase.

### 7.3.3 Investigation of the effects of dehydration on the intense pulsed light conversion of LBZA to ZnO

#### 7.3.3.1 Sample preparation and intense pulsed light (IPL) annealing conditions

Post centrifuge cleaning the LBZA was solvent exchanged with a blend of 50% ethanol/ 50 % water by volume. 2 sections of silicon wafers were cleaned by ultrasonic cleaning with acetone, IPA and DI water for 30 minutes each and blow dried with dry N<sub>2</sub>. LBZA films were then tapecast/ doctor bladed onto the wafers using 30 µm Kapton adhesive tape as a height guide and left to air dry at ~20 °C. The resulting film thickness viewed under SEM varied locally with an estimated upper bound of 600 nm. One wafer was then annealed at 150 °C for 10 minutes in an oven, which has been shown via TGA by Moezzi *et al.* <sup>[131]</sup> to be long enough to dehydrate the material into 4 ZnO + ZnAc<sub>2</sub>. The two wafers were then scribed and split into 1 cm x 1 cm pieces. The sample set dehydrated at 150 °C are designated as '150 °C', and the sample set without dehydration step 'RT' in the following text. Highly doped silicon wafers were chosen as the substrate material as it has well characterised x-ray diffraction peaks, high electrical conductivity to prevent charging during SEM analysis, and an indirect bandgap that would produce no interfering emissions during photoluminescent characterisation.

Both sample sets were then exposed to intense pulsed light treatment using a Pulseforge 1200 photonic curing system (Novacentrix, Austin, Texas, US.) The system was set up using the same conditions used to anneal hydrothermally grown ZnO nanowires to a high

crystalline quality by Assaifan *et al.* <sup>[76]</sup>. Samples were held at 20 mm away from the lensing unit and exposed to three 2.2 ms micropulses each, separated by a 0.15 ms delay in air. Lamp voltages were set to 270 V, 290 V, 310 V, 330 V and 350 V. Calibration with the packaged bolometer produced estimates for radiant exposures of 3.92, 4.77, 5.72, 6.77 and 7.93 J/cm<sup>2</sup> respectively.

### **7.3.3.2 Sample characterisation**

#### **7.3.3.2.1 X-ray diffraction analysis**

X-ray crystallography was used to perform analysis of the phases present post exposure using the same Discover D8 (Bruker) diffractometer with Cu  $\alpha$  source set-up as in 7.3.2 and chapter 5.2.2.2 . Diffractograms were recorded for  $2\theta$  between 1.5 ° and 60 ° with increments of 0.0197 °. Diffractograms of the samples dehydrated at 150 °C showed weak broad peaks superimposed onto the tail of the Si(111) peak. To characterise the material an additional set of scans were performed with the same diffractometer set-up but at a 3 ° offset. As the silicon is a single crystal the offset led to a significant reduction in Si(111) peak intensity and increased resolution of the ZnO peaks. Offset diffractograms were recorded for  $2\theta$  between 26 ° and 55° with increments of 0.019627°. Gaussian-Lorentzian pseudo Voigt peaks were fit to the ZnO envelope and the c axis domain size approximated using Scherrer's equation from the (002) reflection FWHM.

#### **7.3.3.2.2 X-ray photoelectron spectroscopy (XPS) and Ultraviolet photoelectron spectroscopy (UPS)**

Surface chemistry of the sample was monitored using the same Axis Supra XPS (Kratos Analytics Ltd.) set-up as described in chapter 6.4.1.2 . For each sample region scans for the Na 1s, Si 2p, C 1s, O 1s and Zn 2p were recorded. Region scans were performed at a pass energy of 40 eV and a step size of 0.1 eV. The inbuilt charge neutraliser system was used to reduce sample charging. Spectra were fit in casaXPS using the GL(30) lineshape for samples without differential charging and GL(30)T(X) for samples with minor differential charging, where T(X) value controls the peak asymmetry characteristic of differential charging. To create a model of the acetate C1s envelop a control LBZA thick film on silicon sample was

made and scanned using the same settings. The dehydrated samples were then very mildly etched to remove surface contamination using a beam of argon clusters, singly ionized and accelerated at 5 kV. Each sample was 5 kV Ar2000+ etched for 5 minutes over a 3 mm x 3 mm area. Immediately after, the regions were re-scanned and the ultraviolet photon electron spectra measured using a Helium I source (photon energy 21.2 eV). For the UPS measurements a pass energy of 5 eV and step size 0.05 eV was used. From the UPS spectra sample work function and the valance band position was measured for each sample.

### ***7.3.3.2.3 Scanning electron microscopy (SEM)***

Grain structure of the dehydrated and IPL treated samples was recorded using a S4800 Type II field emission gun SEM (Hitachi High Technologies, Minato-ku, Tokyo, Japan.) Micrographs were recorded at maximum magnification (x800 k recorded) at 30 kV acceleration using a 30  $\mu\text{m}$  aperture, condenser lens set at 16, an extractor current of 1  $\mu\text{A}$ , and a resolution of 2560 x 1920 pixels. Images were filtered in imageJ using a FFT filter to dampen features 3 pixels or fewer, corresponding to 0.192 nm or smaller, and then local enhanced contrast adjusted. For each sample 150 particles were measured, mean, standard deviation and 95% bootstrapped confidence intervals of the mean (20,000 iterations) calculated and histograms of the distribution plotted.

### ***7.3.3.2.4 Photoluminescence spectroscopy***

Photoluminescence spectra were recorded, using an in-house built spectrometer, to measure the bandgap of the ZnO produced by IPL and to get a qualitative measure of defect concentration. Excitation was provided by a 325 nm Melles Griot He-Cd continuous wave laser, bandpass filtered to remove harmonics, and transmitted to the sample by a 600  $\mu\text{m}$  diameter fibre optic cable held at 45  $^\circ$  to the sample surface. The emitted light was collected perpendicular to the surface to remove off specular reflections by an additional 600  $\mu\text{m}$  fibre optic cable and then filtered with a low pass filter cutting wavelengths 350 nm or lower to completely remove any reflected laser light. A pre-calibrated ocean optics wavelength dispersive detector (1 nm resolution) was used to measure spectra between 350 nm and 850 nm. 3 spectra for each sample was recorded and the mean and standard deviation of the exciton peak maximum position and the UV ( $E_{\text{photon}} > 3.1 \text{ eV}$ )/ visible ( $E_{\text{photon}} \leq 3.1 \text{ eV}$ ) ratio measured. The ratio was used to gain a qualitative measure of visibly emitted defect states

within the bandgap compared to the UV exciton transition across the band gap. Spectra for a commercial hydrothermally grown single crystal ZnO wafer, unexposed LBZA with and without 150 °C treatment, and sensor 3 from the flexographically printed sensors in chapter 6.5.3 recorded and used for comparison.

## 7.4 Results

### 7.4.1 Investigation of the optical properties of LBZA pre and post dehydration

Prior to photonic annealing it was important to investigate the optical properties of the material for suitability. Figure 7.1 A) shows the diffuse reflectance spectra for centrifuge cleaned and vacuum dried LBZA and a ZnAc<sub>2</sub> reference. For the LBZA spectra an absorption threshold with onset of approximately 430 nm can be seen that is not present in the ZnAc<sub>2</sub> reference. The mean bandgap for the absorption threshold as measured from the Tauc plots in Figure 7.1 B) was 3.24 eV with a standard deviation 0.02 eV. Figure 7.1 C) shows XRD diffractograms for the powders in A). As was typically seen in the diffractograms within the investigations of LBZA growth in chapter 4.2 and Chapter 5, reflections from LBZA, as well as BLBZA and ZnO side products can be seen. From the plot of reflectance as a function of normalised XRD phase areas in Figure 7.1 D) it is clear that the reflection is proportional to the negative of the ZnO content i.e. the ZnO side product is the main absorber. The ZnAc<sub>2</sub> reference shows an absorption threshold at approximately 250 nm, a similar absorption threshold can be seen in the LBZA spectra (~220 nm) and likely relates to the acetate molecule. The absorption is significantly lower than the ZnO absorption and restricted to significantly higher energies. The lack of any noticeable absorption features at longer wavelengths relating to LBZA corresponds well with nickel and cobalt analogues that only show crystal field splitting transitions<sup>[75]</sup>. As the transitions correspond to d→d state transitions<sup>[155]</sup> the lack of any transitions within the [Zn<sup>2+</sup>] cations which has a full d-band is to be expected<sup>[155]</sup>.

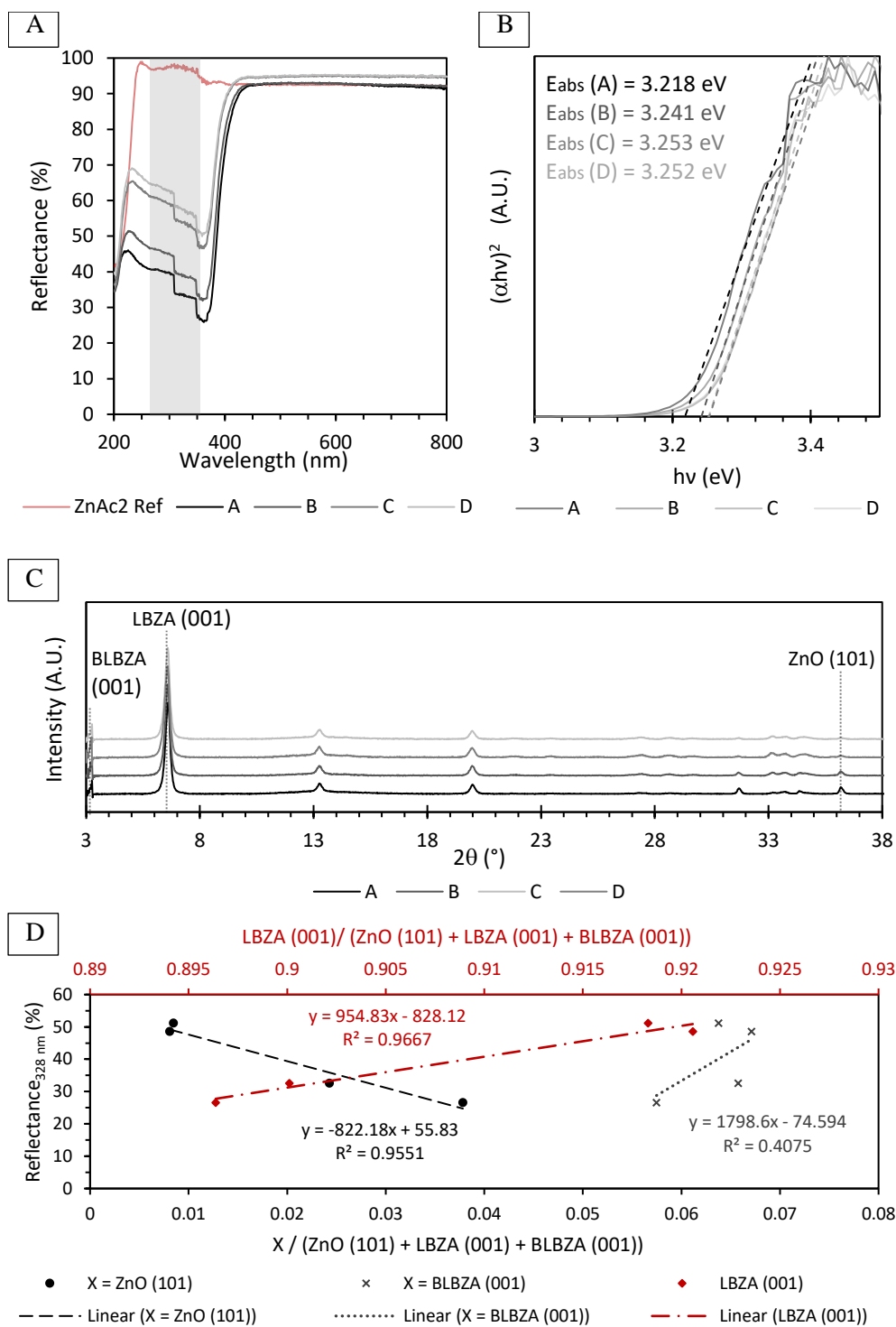


Figure 7.1: A) Diffuse reflectance (%) as a function of wavelength for centrifuge cleaned and vacuum dried (50 °C, 0.1-0.3 bar estimated, 48 hours) LBZA and ZnAc<sub>2</sub> reference powders. Note that the shaded area corresponds to artefacts arising from the lamp switching from visible to UV source. B) Tauc plots of the diffuse reflectance figures in A) with lines of best fits at the steepest gradient. The intercept of the line of best fits provide the optical bandgap included in the annotation for each powder. C) XRD diffractograms (Intensity as a function of 2θ) for each individual powder with annotation showing BLBZA (001), LBZA (001) and ZnO (101) reflections. D) Plots of reflectance at 328 nm vs normalised area ratios for each of the listed diffraction peaks in C. Linear lines of best fit clearly show that the reflectance is proportional to LBZA content and proportional to the negative ZnO content (i.e. optical absorption is due to ZnO.)

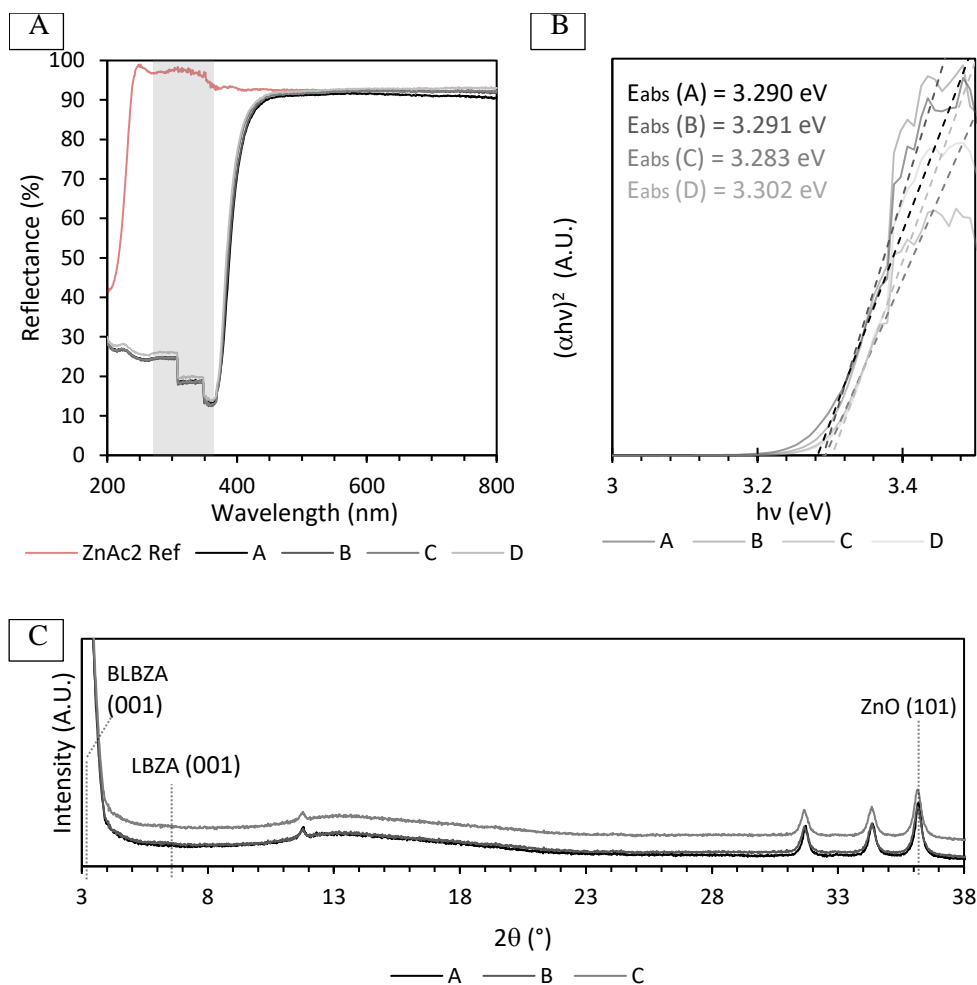


Figure 7.2: A) Diffuse reflectance (%) as a function of wavelength for centrifuge cleaned and vacuum dried (50 °C, 0.1-0.3 bar estimated, 48 hours) LBZA powder treated at 150 °C for 1 hour. Note that the shaded area corresponds to artefacts arising from the lamp switching from visible to UV source. B) Tauc plots of the diffuse reflectance figures in A) with lines of best fits at the steepest gradient. The intercept of the line of best fits provide the optical bandgap included in the annotation for each powder. C) XRD diffractograms (Intensity as a function of  $2\theta$ ) for each individual powder with annotation showing ZnO (101) reflections and positions of BLBZA (001), LBZA (001) which are absent.

Figure 7.2 A) shows the diffuse reflection spectra for the LBZA powders in Figure 7.1 post thermal treatment at 150 °C for 1 hour. Like in the untreated samples a large absorption threshold can be seen, with the Tauc plots (Figure 7.2 B) showing a mean Bandgap of 3.29 eV and a standard deviation of 0.01 eV, consistent with ZnO. The strength of absorption is consistent between samples, with the acetate related absorption significantly weaker in comparison. As the acetate content is expected to be unchanged <sup>[131][400]</sup> this indicates a very large increase in absorption strength. From the XRD diffractograms in Figure 7.2 C) the LBZA crystal structure has completely broken down and the ZnO intensity increased, accounting for the increase in absorption seen in the diffuse reflection spectra. The low absorption in LBZA, limited to short wavelengths, means LBZA would only be able to absorb a very limited amount of electromagnetic energy and would likely be too weak for

successful intense pulsed light-based calcination. In contrast, the ZnO in the dehydrated LBZA would be expected to absorb a significantly greater quantity of the exposure energy over a broader bandwidth. It would also lower the pulse energy required by completing the first endothermic step in the conversion process <sup>[131]</sup>. This would increase the likelihood for successful calcination.

#### **7.4.2 Intense pulsed light calcination of LBZA – the effect of dehydration**

Figure 7.3 show XRD diffractogram of intense pulse light exposed LBZA without (A and C) and with (B, D and E) a 150 °C dehydration step. Reflections corresponding to the LBZA (001), (002) and (003) are present in A). This shows that for radiant exposures up to 7.93 J/cm<sup>2</sup> IPL treatment on its own is not sufficient to calcine and convert LBZA to ZnO, as predicted within section 7.4.1 . As expected from diffractograms of dehydrated but non-IPL treated samples (Figure 7.2), the samples post dehydration have no reflections attributed to LBZA. In both sample sets weak reflections corresponding to the ZnO (002) reflection can be seen. The FWHM of the samples without dehydration is similar to that of the reaction side products. In contrast, the (002) reflection is significantly broader than either the IPL treated but undehydrated or dehydrated but non-IPL treated samples. The broad reflections suggest the granular texturing/ primary crystal domains in the dehydrated and IPL treated samples are significantly smaller. The change in ZnO line shape, as compared to both IPL exposed samples without dehydration, and that of the dehydrated but unexposed LBZA shows that calcination is successful; with the combination of thin layer, and the reflection being spread over a large 2θ range, resulting in the weak observed intensity. will be further supported and confirmed in the subsequent XPS and photoluminescence analysis.

Offset XRD diffractograms with a longer integration time, shown in Figure 7.3 E), show that the broad reflection is primarily composed of a broad (002) component with a weaker (101) component which shows the ZnO is primarily c-axis orientated. The c-axis ZnO reflection, which is produced by alternating Zn and O layers, suggests that the c-axis layered hydroxide structure which is generally composed of alternating layers of Zn and 2(OH) (with intercalated acetate, see Chapter 5 for a more extensive treatment on the structure of LBZA) is retained. As c-axis orientated ZnO surfaces are expected to be part of the cause of the sensitivity to hydrogen seen in Chapter 4, the material shows promise for use in hydrogen gas sensors.



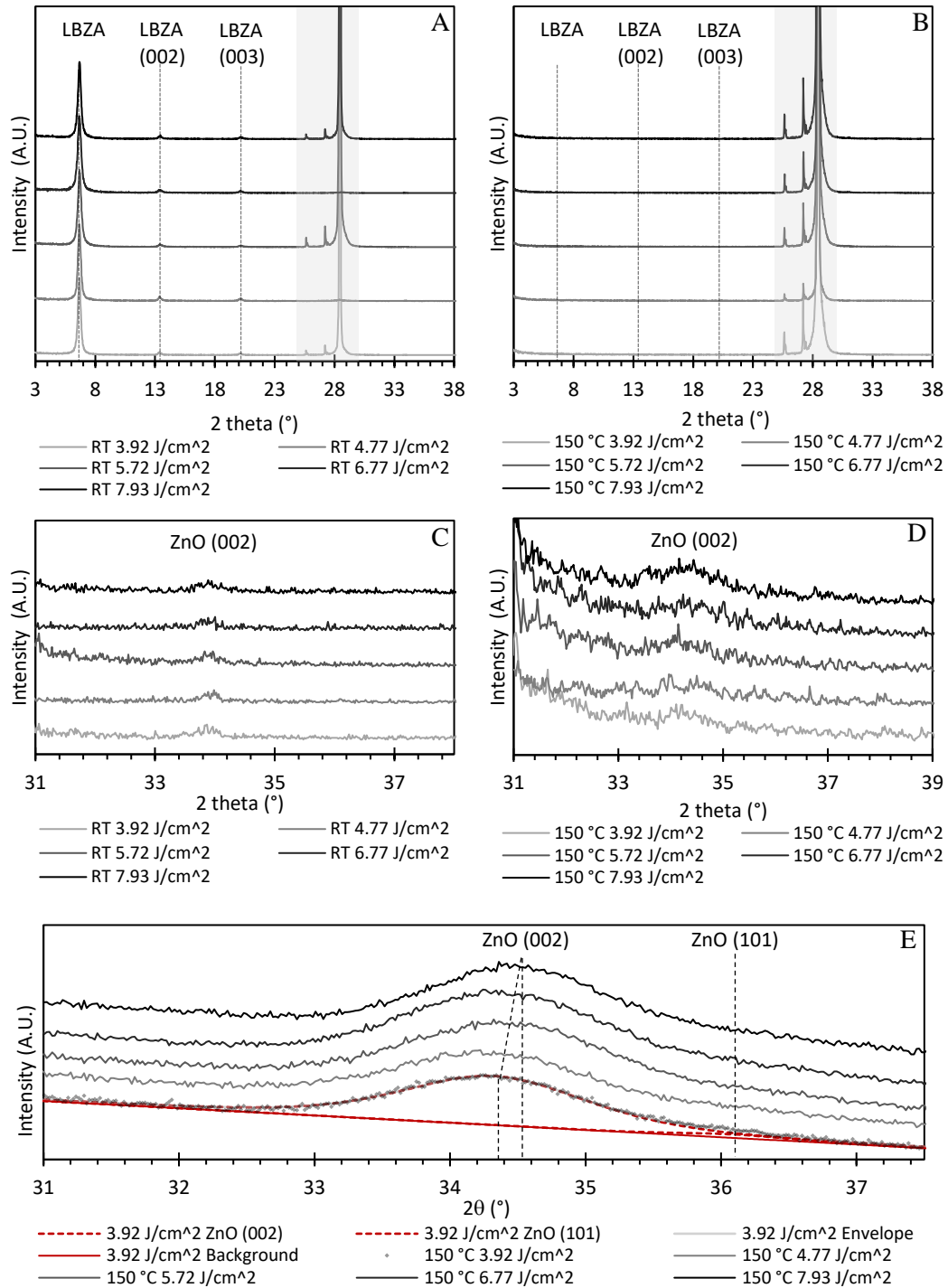


Figure 7.3: XRD diffractograms of tape cast LBZA on Si, dried at room temperature, with (B, D and E) and without (A and C) 150 °C dehydration step and exposed to intense pulse light treatment at radiant exposures of 3.92, 4.77, 5.72, 6.77 and 7.93 J/cm<sup>2</sup>. A) and B) show wide angle diffractogram, showing the presence of LBZA in exposed samples without dehydration (A). Note the reflections within the grey area correspond to the silicon substrate. C) and D) show the same diffractograms magnified with 2θ between 31 ° and 38 ° showing the ZnO reflection region. Both sample sets show ZnO (002) reflections though the reflections in D are significantly broader. The low intensity is a result of the combination of thin film and in D) the wider FWHM of the peak i.e. the intensity is spread out over a larger 2θ range. E) Longer exposure diffractograms of the dehydrated samples recorded at a 3° offset to the diffractometer normal showing the broad ZnO peak to be comprised of a strong (002) and weak (101) ZnO reflections.

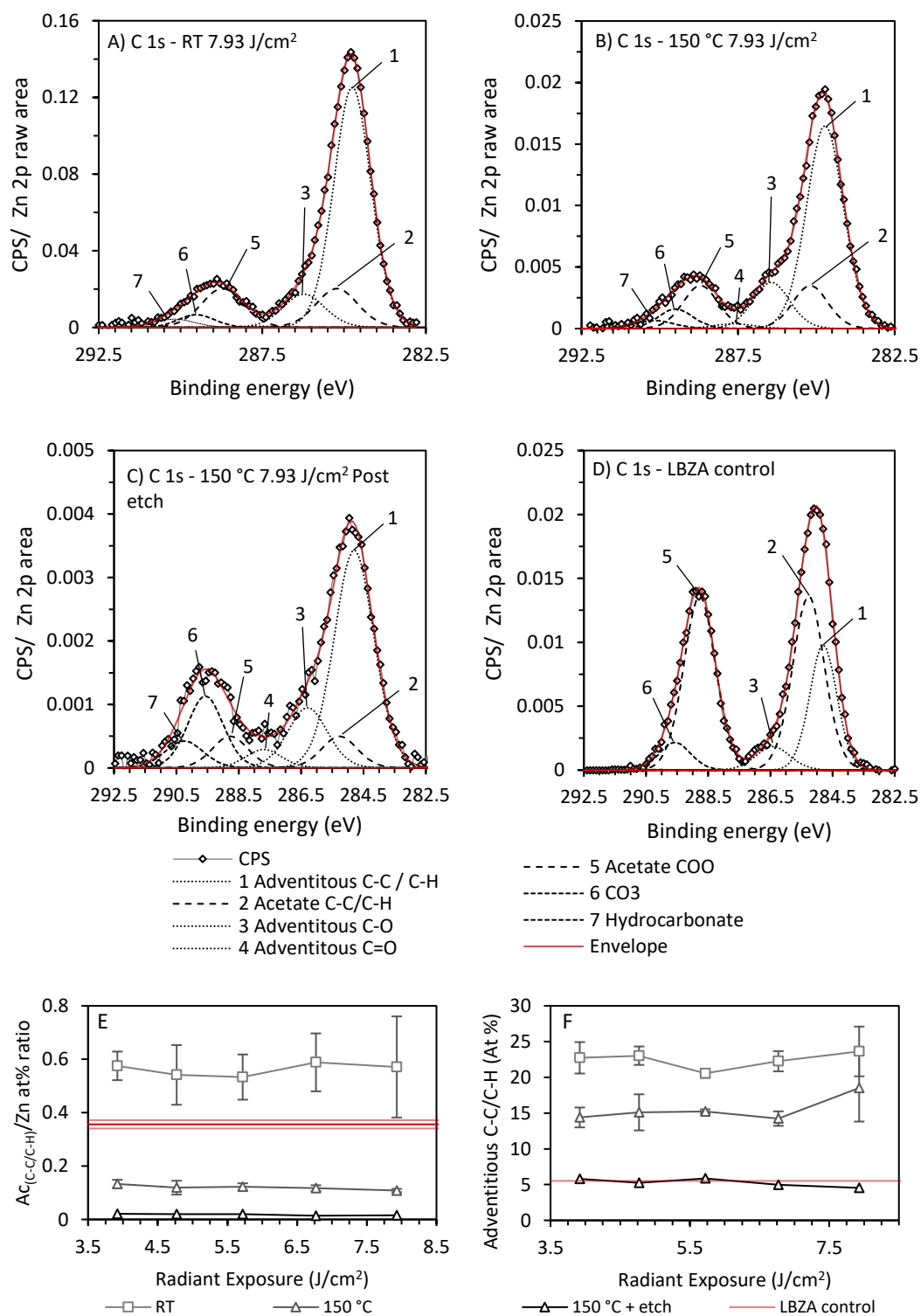


Figure 7.4: A) - D) XPS C 1s spectra showing C 1s intensity divided by the raw Zn 2p area as a function of binding energy for the IPL treated tapecast LBZA on Si, exposed to 7.93 J/cm<sup>2</sup> pulse A) without and B) with 150 °C dehydration step, C) the sample in B post Argon 2000+ cluster etch and D) a dropcast LBZA reference control sample. Peaks are annotated with all numbers corresponding to the functional groups in the figure legend. As the number of Zn atoms is expected to be relatively unchanged by normalising to the Zn area the difference in acetate content can be qualitatively seen. E) Plots of mean quantified atomic ratio of the acetate methyl atom divided by the zinc atomic % as a function of radiant exposure for the IPL treated samples with and without 150 °C step and 150 °C samples post 5 minute 5 keV Ar 2000+ etch. Error Bars: standard deviation, n=3. Dark red line mean acetate content in the drop cast LBZA control sample, with the standard deviation represented by the light red lines. F) Plot of mean adventitious aliphatic hydrocarbon (at %) as a function of radiant exposure for the sample set in E. Error bars: standard deviation, n=3.

Figure 7.4 shows XPS C 1s spectra of the 7.93 J/cm<sup>2</sup> exposed IPL treated tapecast LBZA samples without (A) and with (B) 150 °C dehydration step, the dehydrated sample post 5 minute 5 keV Ar 2000+ cluster etch (C), and a drop cast LBZA control sample. The spectra have been normalised by dividing the raw intensity by the Zn 2p raw area for comparison as the Zn content is not expected to change significantly. The spectra show 3 notable features the first being the presence of aliphatic (284.8 eV), ether/ hydroxyl (286.4eV) and carbonyl (287.7 eV) groups attributable to adventitious carbon. The second the presence of 2 peaks representative of the acetate methyl (285.3 eV) and carboxylate groups (288.8 eV), where the acetate aliphatic group is shifted relative to the adventitious aliphatic group due to inductive oxidation effects from the carboxylate group [305]. The final feature are two peaks at 289.6 eV and 290.3 eV which are most likely carbonate (CO<sub>3</sub><sup>2-</sup> reference energies: 289.3-290.1 eV [538]) and hydrocarbonate (HCO<sub>3</sub><sup>-</sup> reference energies: 289.9-290.2 eV [538]) groups respectively. Layered hydroxides are well known to preferentially absorb carbonate [164][539] and as such may be included from dissolved carbonate species during the synthesis procedure, potentially within the so called BLBZA phase.

Table 7.1 - Table 7.3 show the full quantification of recorded XPS spectra for the samples. Included within the table is a ratio of acetate to zinc to indicate the calcination progress which is plotted in Figure 7.4 as a function of radiant exposure. Compared to the control sample the IPL exposed sample without dehydration (series RT) shows an increase in acetate/zinc ratio, almost doubling. In contrast the sample with dehydration step shows a reduction in the ratio to approximately a third of the control sample. To try and ascertain whether remaining acetate was present as an overlayer or dispersed within the sample a gentle 5-minute argon cluster etch using 5 keV acceleration with singly ionized clusters of 2000 argon atoms. The settings were chosen as they typically do very little damage as is indicated by plots of atomic % for the aliphatic adventitious carbon peak shown in Figure 7.4 F), where scans performed immediately after etching show ~5 at.% of the hydrocarbon peak remains. Post etching a mean acetate ratio of 0.018 was observed, approximately 5 % of the control sample ratio indicating the acetate likely resides within an overlayer. Combined TGA, XRD and IR investigations of the thermal decomposition of LBZA by Moezzi *et al.* [131] showed that ZnAc<sub>2</sub> sublimates at temperatures exceeding 240 °C, and as such the presence of an overlayer of acetate can be explained by deposition of the ZnAc<sub>2</sub> vapour. As samples from each dataset were exposed to IPL treatment at the same lamp voltage directly after each other, the deposition of ZnAc<sub>2</sub> vapour may potentially explain the increased acetate content within the RT series as compared to the control sample.

Chapter 7 - Investigation of intense pulsed light (IPL) photonic annealing conditions for the conversion of LBZA to ZnO

Without dehydration (RT)	Mean At.%					Standard Deviation At.%				
	Radiant Exposure (J/cm <sup>2</sup> )					Radiant Exposure (J/cm <sup>2</sup> )				
Element	3.92	4.77	5.72	6.77	7.93	3.92	4.77	5.72	6.77	7.93
Zn 2p	5.18	8.07	9.17	8.16	7.49	1.94	1.14	2.17	2.45	2.86
O 1s	35.37	39.61	39.41	40.34	38.14	1.13	4.20	1.92	1.17	4.27
Adventitious C-C/C-H	22.74	23.03	20.56	22.25	23.62	2.20	1.29	0.63	1.41	3.48
Acetate methyl	2.92	4.32	4.82	4.30	3.91	0.85	0.88	0.44	1.25	0.21
Adventitious C-O	3.43	2.90	3.36	2.89	2.60	1.07	0.76	0.92	0.80	0.91
Adventitious C=O	0.08	0.02	0.04	0.01	0.19	0.11	0.02	0.04	0.01	0.12
Acetate COO-	2.92	4.32	4.82	4.30	3.91	0.85	0.88	0.44	1.25	0.21
Carbonate	1.32	1.27	1.44	1.32	1.61	0.20	0.78	0.58	0.31	1.32
Hydrocarbonate	0.36	1.4	1.45	1.79	0.94	0.06	0.26	0.06	0.47	0.14
Total C 1s	33.77	37.27	36.50	36.86	36.79	1.56	0.92	0.89	0.22	1.73
Silicon	14.03	6.73	7.93	6.04	9.73	1.41	5.94	2.49	2.34	4.67
Silicon oxides	10.42	7.40	5.88	7.30	6.55	3.38	1.47	2.26	3.85	0.63
Si Total	24.45	14.13	13.82	13.34	16.27	1.97	5.22	4.64	2.99	5.28
C <sub>Acetate-methyl</sub> /Zn	0.575	0.541	0.543	0.535	0.571	0.054	0.112	0.101	0.102	0.189

Table 7.1: Table of XPS quantification results for the tapecast LBZA samples exposed to IPL treatment without the 150 °dehydration step, showing mean and standard deviation of the concentration of elements and their functional groups in atomic %, n=3. Additionally, the ratio of acetate methyl group divided by Zinc is presented as a figure of merit for calcination.

With dehydration (150 °C)	Mean At.%					Standard Deviation At.%				
	Radiant Exposure (J/cm <sup>2</sup> )					Radiant Exposure (J/cm <sup>2</sup> )				
Element	3.92	4.77	5.72	6.77	7.93	3.92	4.77	5.72	6.77	7.93
Zn 2p	20.81	21.66	21.55	24.71	17.83	1.79	2.25	1.46	2.84	7.22
O 1s	41.90	42.49	43.60	43.99	45.60	0.13	1.60	0.04	0.25	1.63
Adventitious C-C/C-H	14.39	15.11	15.24	14.23	18.52	1.39	2.53	0.28	1.01	4.70
Acetate methyl	2.83	2.61	2.62	2.86	1.90	0.29	0.80	0.12	0.08	0.67
Adventitious C-O	3.20	2.73	2.90	2.40	3.19	0.24	0.20	0.41	0.24	0.18
Adventitious C=O	0.55	0.27	0.39	0.49	0.22	0.23	0.32	0.25	0.20	0.19
Acetate COO-	2.83	2.61	2.62	2.86	1.90	0.29	0.80	0.12	0.08	0.67
Carbonate	0.81	1.27	1.35	1.28	1.37	0.15	0.56	0.39	0.13	0.22
Hydrocarbonate	0.32	0.03	0.17	0.09	0.25	0.10	0.06	0.15	0.12	0.28
Total C 1s	24.93	24.64	25.30	24.23	27.35	1.84	1.43	0.50	0.88	3.39
Silicon	6.70	4.36	3.88	2.93	0.72	2.58	3.19	0.33	1.44	0.16
Silicon oxides	5.66	6.85	5.67	4.13	8.50	1.00	2.74	0.87	1.29	4.88
Si Total	12.36	11.21	9.55	7.07	9.22	3.58	0.99	1.19	2.39	4.96
C <sub>Acetate-methyl</sub> /Zn	0.136	0.119	0.122	0.117	0.108	0.003	0.026	0.013	0.011	0.006

Table 7.2: Table of XPS quantification results for the tapecast LBZA samples exposed to IPL treatment with the 150 °dehydration step, showing mean and standard deviation of the concentration of elements and their functional groups in atomic %, n=3. Additionally, the ratio of acetate methyl group divided by Zinc is presented as a figure of merit for calcination.

Element	With dehydration (150 °C) + Ar 2000+ etch (At.%)					LBZA control (At.%)	
	Radiant exposure (J/cm <sup>2</sup> )					Mean	Standard deviation
	3.92	4.77	5.72	6.77	7.93		
Zn 2p	32.84	35.19	35.23	40.91	40.29	24.83	0.62
O 1s	43.78	43.43	45.47	47.04	48.34	48.38	0.29
Adventitious C-C/C-H	5.8	5.26	5.86	4.97	4.54	5.52	0.04
Acetate methyl	0.69	0.68	0.69	0.56	0.65	8.84	0.17
Adventitious C-O	1.65	1.2	1.63	1.25	1.24	1.39	0.06
Adventitious C=O	0.21	0.29	0.28	0.07	0.33	0.00	0.00
Acetate COO-	0.69	0.68	0.69	0.56	0.65	8.84	0.17
Carbonate	1.17	1.18	1.32	1.49	1.34	1.46	0.05
Hydrocarbonate	0.6	0.65	0.41	0.47	0.56	0.01	0.02
Total C 1s	10.81	9.95	10.88	9.38	9.31	26.05	0.30
Silicon	7.11	6.69	4.49	1.37	0.67	0.28	0.20
Silicon oxides	5.47	4.73	3.91	1.29	1.37	0.48	0.42
Si Total	12.58	11.42	8.4	2.66	2.04	0.76	0.54
C <sub>Acetate-methyl</sub> /Zn	0.021	0.020	0.020	0.014	0.016	0.356	0.016

Table 7.3: Table of XPS quantification results for the tapecast LBZA samples exposed to IPL treatment with the 150 °C dehydration step and 5 minute 5 keV Ar 2000+ etch (Left), and dropcast LBZA control sample. For the IPL exposed samples n=1, for the LBZA control samples n=3 and mean and standard deviation reported. For each sample concentration of elements and their functional groups in atomic % are shown. Additionally, the ratio of acetate methyl group divided by Zinc is presented as a figure of merit for calcination.

Further testing would be required for confirmation and if proven to be the case deposition could likely be inhibited with continuous purging with air.

Figure 7.5 shows SEM micrographs of the tapecast LBZA with a 150 °C dehydration step, post IPL treatment at radiant exposures of A) 3.92 J/cm<sup>2</sup>, B) 4.77 J/cm<sup>2</sup>, C) 5.72 J/cm<sup>2</sup>, D) 6.77 J/cm<sup>2</sup> and E) 7.93 J/cm<sup>2</sup>. Figure 7.6 shows histograms of measured particle diameters taken from the micrographs (n=150) with the mean, 95 % confidence interval in the mean and standard deviation of the sampled datasets shown in Table 7.4 as well as Scherrer equation derived domain sizes extracted from the diffractograms in Figure 7.3 E). The micrographs and histograms show that the ZnO films are made up of nanoparticles smaller than 10 nm which is in general agreement with the XRD results, with the difference in size likely due to the uncertainty in diffractogram background shape used for the peak fitting procedure. Increasing pulse energy results in larger particle sizes with mean diameters of 3.54, 3.68, 3.85, 3.96 and 4.03 nm for radiant exposures of 3.92, 4.77, 5.72, 6.77 and 7.93 J/cm<sup>2</sup> respectively.

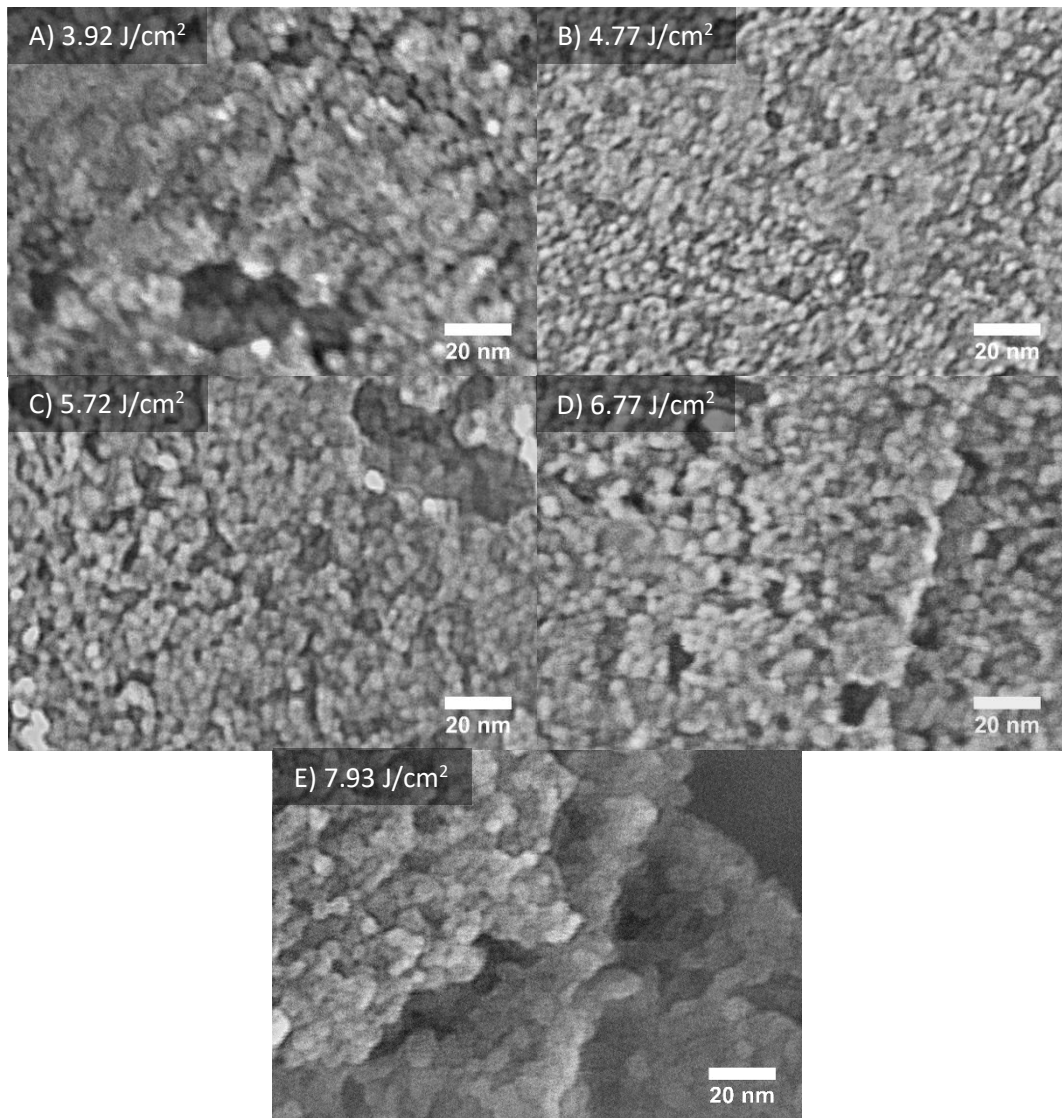


Figure 7.5: SEM Micrographs of the tapecast LBZA pre-treated with a 150 °C dehydration step and exposed to IPL with radiant exposures of A) 3.92 J/cm<sup>2</sup>, B) 4.77 J/cm<sup>2</sup>, C) 5.72 J/cm<sup>2</sup>, D) 6.77 J/cm<sup>2</sup> and E) 7.93 J/cm<sup>2</sup>. Scale bar 20 nm for all micrographs. Elongation/ stretching and discontinuous line artifacts are a result of charging and vibration, both a result of the ultra-high magnification (recording magnification x800k).

Assuming an Arrhenius like behaviour, plots of particle diameter as a function of 1/ Radiant exposure appears to follow the relationship:

$$\text{Particle diameter (nm)} = 4.604 * e^{-\frac{1.039}{\text{radiant exposure}}}$$

Equation 7.4

Although the trendline has a high R<sup>2</sup> value of 0.994, the majority of the confidence intervals overlap and a larger sample size would be needed to confirm and refine any relationship.

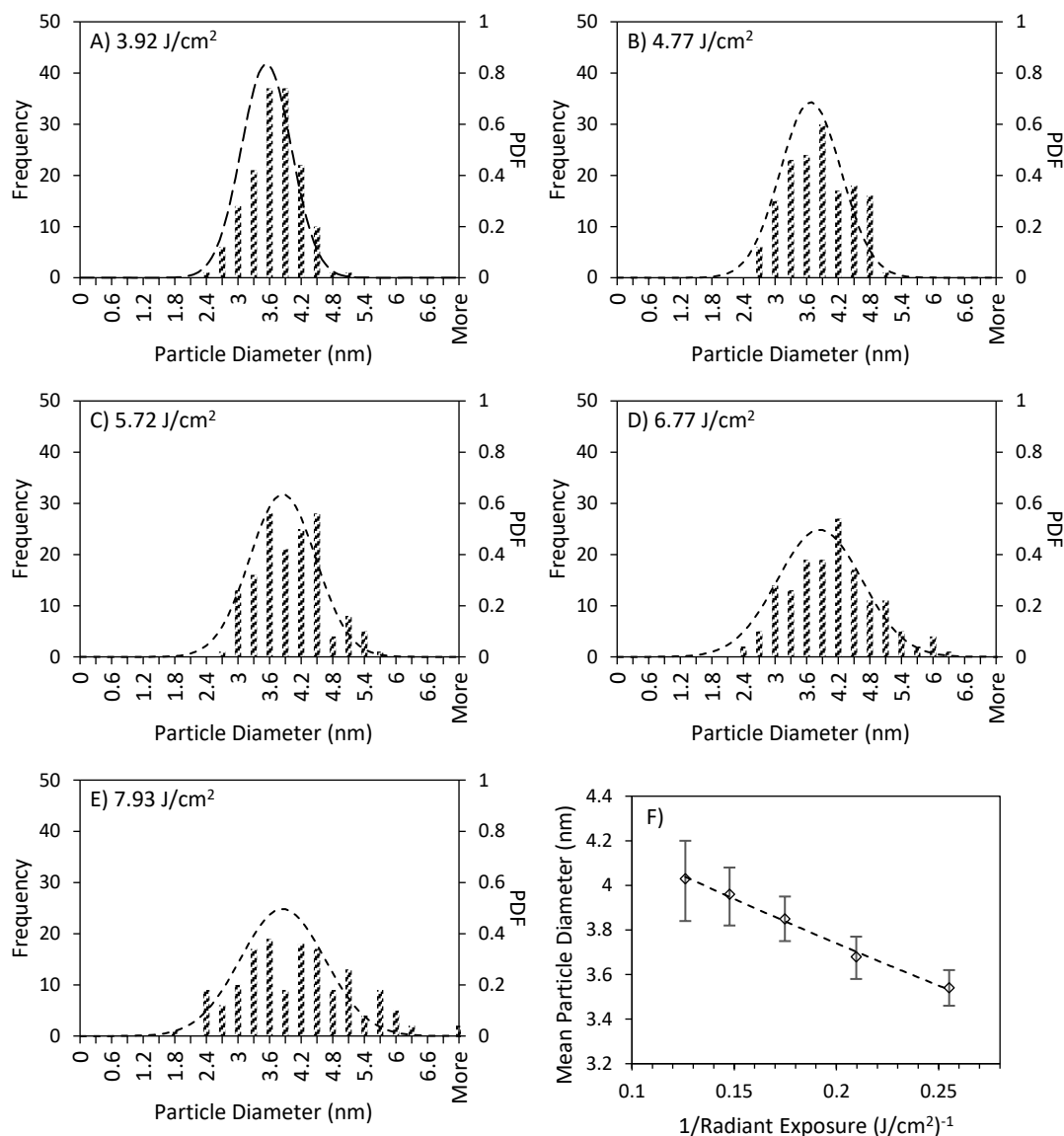


Figure 7.6: Histogram of observed particle diameters taken from the SEM Micrographs of the tapecast LBZA pre-treated with a 150 °C dehydration step and exposed to IPL with radiant exposures of A) 3.92 J/cm<sup>2</sup>, B) 4.77 J/cm<sup>2</sup>, C) 5.72 J/cm<sup>2</sup>, D) 6.77 J/cm<sup>2</sup> and E) 7.93 J/cm<sup>2</sup> within Figure 7.5. Overlay of a normal distribution with equivalent mean and standard deviation showing the majority of the observations follow normal distribution with minor amounts of skew for A and B. n=150. F) Plot of mean particle diameter as a function of 1/radiant exposure for the measured populations in A) – E). Trendline: Particle diameter (nm) =  $4.604 * e^{-1.039/\text{radiant exposure}}$ ,  $R^2 = 0.994$ . Error bars bootstrap 95 % confidence interval of the mean

In addition to the increase in mean size, there is an increased population spread with standard deviation increasing from 0.48-1.12 nm for 3.92-7.93 J/cm<sup>2</sup>. The mean particle sizes are on the same order of magnitude as the ~ 5nm LBZA primary particles observed by Li, Zhang and Wang [70], suggesting very limited sintering occurs within the particulates. This likely indicates the majority of the absorbed exposure energy is consumed, decomposing the organic constituents, limiting the energy converted to heat and thus limiting diffusion rates.

Radiant Exposure (J/cm <sup>2</sup> )	Mean (nm)	Standard Deviation (nm)	Boot strap 95% CI (of the Mean) (nm)	Scherrer domain size (nm)
3.92	3.54	0.48	3.46 -3.62	4.85
4.77	3.68	0.58	3.58 -3.77	4.76
5.72	3.85	0.63	3.75 -3.95	4.77
6.77	3.95	0.80	3.82-4.08	5.63
7.93	4.03	1.12	3.84-4.20	6.16

Table 7.4: Table of mean, standard deviation and the 95 % bootstrapped confidence interval in the mean ( $n=150$ , 20,000 iterations) for the datasets of measured particle diameters shown in Figure 7.6

The measured mean grain sizes are smaller than that of the HMTA derived ZnO sensor in chapter 4.1.3 which had a mean of 7.8 nm and a standard deviation of 1.3 nm. As the small grain size was suspected to be one of the main factors in the high hydrogen sensitivities, the particle sizes obtained by IPL should be ideal for use within hydrogen sensors.

Figure 7.7 shows photoluminescence (PL) spectra for the tapecast LBZA post IPL exposure for samples without (A) and with (B) 150 °C pre-treatment. In line with the XRD and XPS results no PL emission is seen for samples without the dehydration step, as expected by the lack of absorption at or below the source energy as shown in the diffuse reflectance UV-VIS results (Figure 7.1). In contrast all dehydrated samples show a strong UV emission band (photon energies > 3.1 eV), representative of the excitonic structure of the material, and a weak visible light band (photon energies < 3.1 eV). The visible band, also known as the deep level emission, arises from transitions between states within the bandgap of the material and is generally attributed to optically active defect and surface trap states.

Compared to the commercial hydrothermally grown (001) ZnO single crystal and the the 150 °C sample without IPL, presented in Figure 7.7 C), the exciton structure of the 150 °C samples post IPL treatment is broad and blue shifted, appearing to extend beyond the 3.54 eV (350 nm) cut off filter. Figure 7.7 shows plots of the mean measured exciton position as a function of the mean SEM measured particle radius.

The observed blue shift compared to the 3.31 eV exciton seen in the single crystal is relatively in line with shifts in the excitonic emission structure in ZnO quantum dots measured by Lin *et al.* [540]. For nanoparticles with radii of 1.75 nm and 2.09 nm they observed exciton emission centred at 3.428 eV and 3.408 eV, with absorption spectra showing an optical bandgap of 3.661 eV and 3.583 eV. In comparison the values observed here for radii of 1.77 nm and 2.01 nm produced exciton shifts of 3.444 eV and 3.415 eV.



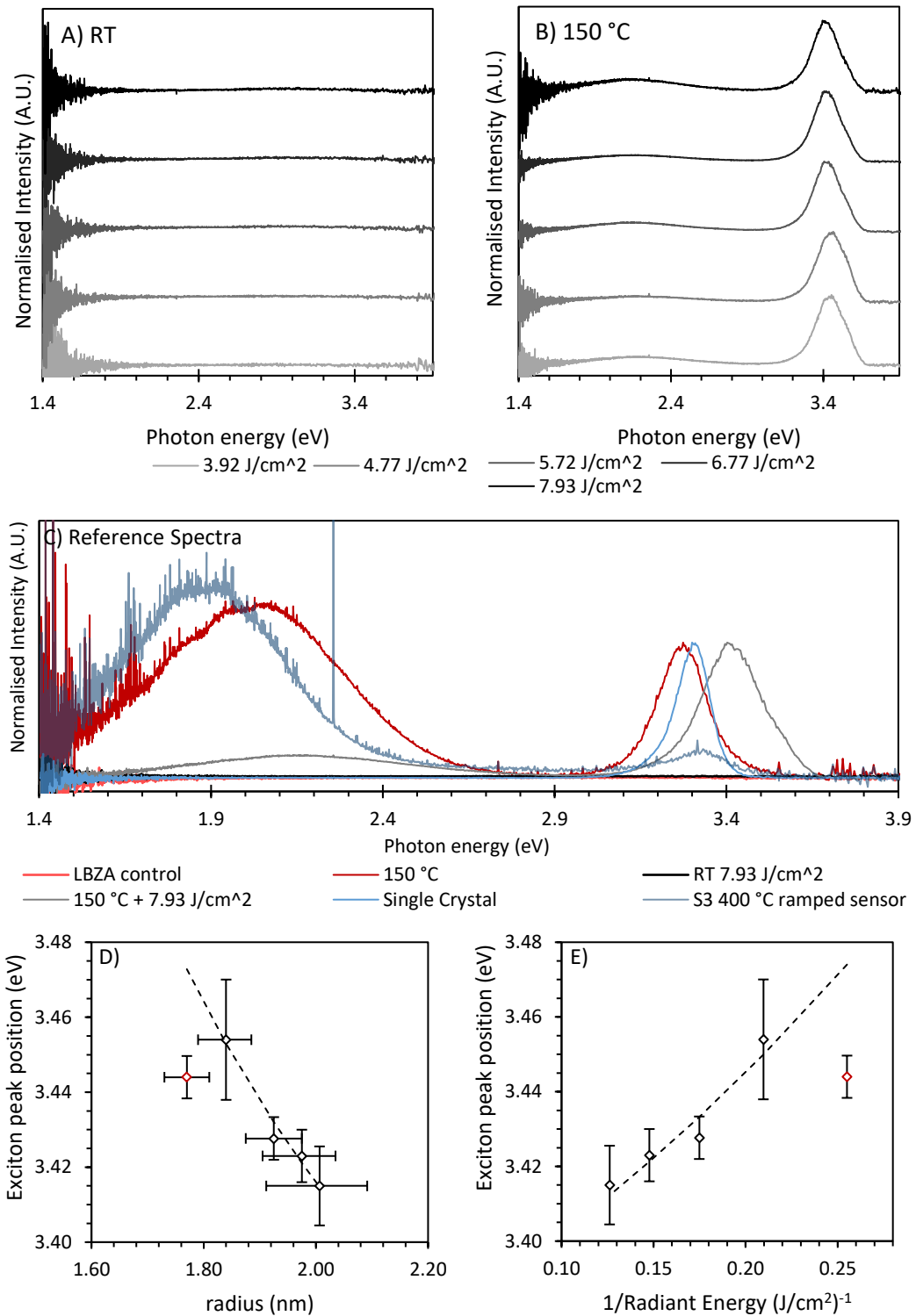


Figure 7.7: A-C) Plots of photoluminescence emission intensity as a function of photon energy (eV) for samples the IPL exposed tapecast LBZA without (A) and with (B) the 150 °C dehydration step. C) contains a comparison of the 7.93 J/cm<sup>2</sup> exposed samples with unexposed samples with (150 °C) and without (LBZA control) the 150 °C dehydration steps as well as a commercial hydrothermally grown ZnO single crystal and sensor 3 from chapter 6.5.3 . D) Plot of of UV band exciton peak as a function of mean SEM measured particle radius. Trendline (excluding 3.92 J/cm<sup>2</sup> sample in red): Exciton peak position (eV) = 1.171 (1/radius (nm))<sup>2</sup> - 0.3734\*(1/radius(nm)) + 3.31, R<sup>2</sup> = 0.973. Error bars, standard deviation of peak position, n = 3, 95% bootstrapped confidence interval (n = 150, iterations = 20,000.) E) Plot of UV band exciton peak position as a function of 1/Radiant Energy. Trendline, R<sup>2</sup> (excluding 3.92 J/cm<sup>2</sup> sample in red) = 0.934

They attributed the blue shift to quantum confinement, with their absorption spectra in strong agreement with calculations of transition energies predicted using strong confinement theory. As such the blue shift here can be attributed to quantum confinement effects. Strong confinement theory approximates the minimum transition energies as <sup>[540][541][542]</sup>:

$$E[eV] = E_{bandgap} + \frac{\hbar^2 \pi^2}{2er^2} \left( \frac{1}{m_e^*} + \frac{1}{m_h^*} \right) - \frac{1.8e}{4\pi\epsilon\epsilon_0 r}$$

Equation 7.5

Where  $\hbar$  is the reduced Planck constant,  $e$  is the charge of an electron,  $\epsilon$  and  $\epsilon_0$  are the relative permittivity and permittivity of free space respectively, and  $m_e^*$  and  $m_h^*$  are the effective mass of electron and holes in ZnO respectively. Where the second term term represents the electron and hole kinetic energies and the last term the charge screen Coulomb interaction.

Using reported values of  $m_e^*$  and  $m_h^*$  for ZnO of  $0.24m_0$  <sup>[540]</sup>,  $0.45m_0$  <sup>[540]</sup> respectively (where  $m_0$  is the electron rest mass), and the measured single crystal peak emission energy of 3.31 eV produces:

- For the lowest reported value of  $\epsilon_{ZnO-Quantum\ Dot} = 3.7$  <sup>[540]</sup>:

$$E[eV] = 3.31 + 1.162 * 10^{-18} \frac{1}{r^2} - 0.701 * 10^{-9} \frac{1}{r}$$

Equation 7.6

- And for the bulk reported value of  $\epsilon_{ZnO-bulk} = 7.9$  <sup>[540]</sup>:

$$E[eV] = 3.31 + 1.162 * 10^{-18} \frac{1}{r^2} - 0.328 * 10^{-9} \frac{1}{r}$$

Equation 7.7

Fitting a polynomial equation trendline to plots of exciton peak position as a function of nanoparticle radius produces the relation:

$$E[eV] = E_{bandgap} + 1.171 * 10^{-18} \frac{1}{r^2} - 0.373 * 10^{-9} \frac{1}{r}$$

Equation 7.8

Where r is the radius in meters.

It should be noted that areas of the 3.92 J/cm<sup>2</sup> sample were unstable under electron beam exposure, coalescing during SEM image capture. The anomolous peak energies for the sample in the PL therefore has the potential to be a result of laser exposure which produced continous radiant exitance on the order of 0.1 W/cm<sup>2</sup>. As such the sample has been excluded from all fitting procedures. The trendline is in close agreement with the data excluding the 3.92 J/cm<sup>2</sup> sample with an R<sup>2</sup> value of 0.973, with the coefficients functionally similar to the predicted values for  $\epsilon_{ZnO-Quantum\ Dot}$  and almost equal for  $\epsilon_{ZnO-bulk}$ . Figure 7.7 E) shows plots of exciton peak energy as a function of 1/Radiant exposure, where the trendline was produced by inserting the radii predicted by Equation 7.4 into Equation 7.8. The trendline shows strong agreement with measured data with an R<sup>2</sup> value (excluding the 3.92 J/cm<sup>2</sup> sample) of 0.934. Inserting the smallest and largest observed particle radii from the 290 V 4.77 J/cm<sup>2</sup> sample of 1.2 nm and 2.44 nm into Equation 7.8 predicts emission energies of 3.77 eV and 3.35 eV respectively. As such a significant proportion of the UV emission envelope breadth can likely be attributed to the breadth of the nanoparticle radius distribution. Additional sources of peak breadth and fine structure is expected to be related to stoke shifts, in particular emission from acceptor bound excitons (0.1 – 0.2 eV lower than the unbound exciton) and optical phonon shifted acceptor bound exciton (0.176-0.276 eV lower.)

In addition to the blue shift, Figure 7.7 C) also shows a signifcant reduction in the deep level emission compared to non IPL treated ZnO produced by IPL. Measurements of exciton band area / deep level emission area from all IPL treated samples (with 150 °C dehydration step) produced a mean ratio of 1.06 and a standard deviation of 0.32. No trend was seen between sample sets with the standard deviation of individual samples overlapping. In comparison spectra from the dehydrated sample without IPL and the spectra from Sensor 3 presented in chapter 6.5.3 (annealed via ramping up to 420 °C and holding for 5 minutes) had ratios of 0.08 and 0.02 respectively. In the original work by Assaifan *et al.* [31] that the pulse

configurations were based on, exciton/ deep level emission area ratios of 0.006 and 0.82 were observed pre and post IPL treated ZnO nanowires respectively. EIS modelling of the nanowires conductivity showed an 82.8 % reduction in resistance and was attributed to the reduction of defect states as implied by the reduction in deep level emission. The reduction in defect states would remove electron trapping and scattering sites thereby increasing the mean free path of electrons and therefore sample conductivity. As such it is reasonable to suggest that the large increase in the exciton/ defect emission ratios observed here predicts a similar increase in conductivity vs traditional thermally annealed LBZA.

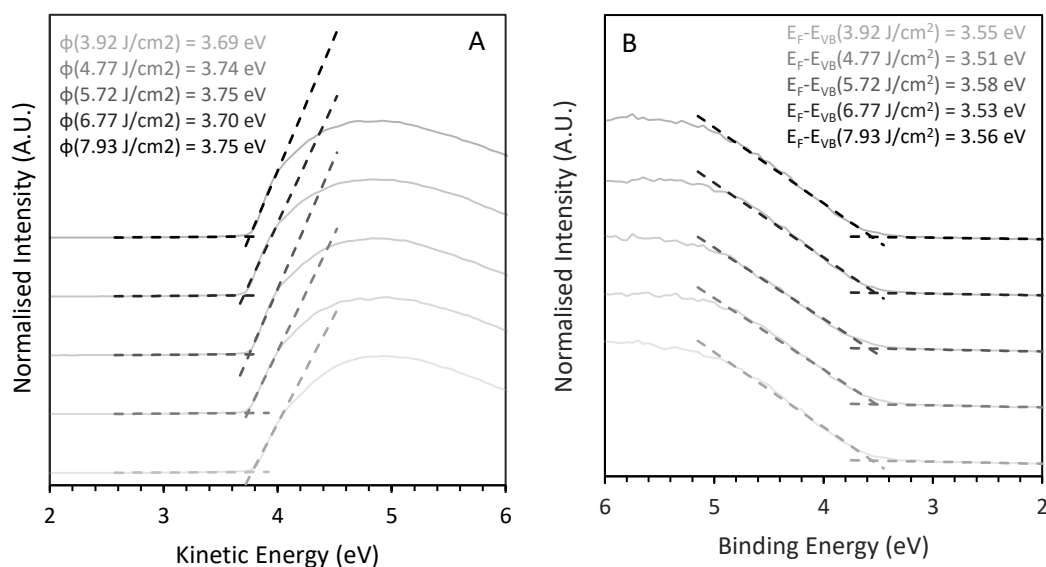


Figure 7.8: He I line (21.2 eV photon) ultraviolet photoelectron spectroscopy (UPS) secondary electron cut-off (A) and valance band scans (B) for the tapecast IPL treated LBZA with 150 °C dehydration step post 5 keV Ar2000+ etch. Annotations in A) show the workfunction ( $\phi$ ) for each sample, measured by fitting linear lines of best fits to the slope of the background and secondary electron cut off, and finding the intercept. Annotations in B) show valance band edge ( $E_F - E_{VB}$ ) measurements for each sample, measured by fitting linear lines of best fits to the slope of the background and valance band onset, and finding the intercept.

Figure 7.8 shows UPS secondary electron cut off (A) and valance band edge (B) scans for the tapecast IPL treated LBZA with 150 °C dehydration sample, measured post 5 minute of 5 keV Ar2000+ cluster etch directly after the XPS measurements were complete. Measurements of work function from the secondary electron cut off show mean values of  $\phi=3.73$  eV with a standard deviation of 0.03 eV, whilst measurements of the valance band edge show mean values of  $E_F - E_{VB} = 3.55$  eV with a standard deviation of 0.03 eV. No easily fittable, physically justified trend was observed suggesting the effect of varying pulse energy was small. Larger sample size would be needed to see if any meaningful underlying relationship is present. Combining the work function and valance band position relative to

the fermi level results in a mean ionization potential of  $IP=7.27$  eV, with a standard deviation of 0.05 eV. Coppa, Davis and Nemanich <sup>[202]</sup> reported electron affinities for ZnO (00 $\bar{1}$ ), one of the two potential terminating surfaces for the c-axis orientated grain structure, of  $\chi=4.1$  eV. Combining  $\chi$  with the 3.31 eV single crystal PL exciton emission, presented here, and the bulk exciton energy of 0.06 eV produces an IP value of 7.47 eV. This suggests the valance band maxima at the surface have shifted to approximately 0.2 eV higher energies.

## 7.5 Discussion

Based on the combination of:

- observed ZnO phases in the XRD, reduction in acetate/ Zn ratio and presence of photoluminescent emission for the samples dehydrated prior to IPL treatment
- the presence of LBZA observed via XRD and a lack of reduction in acetate/Zn ratio or photoluminescent emission versus the control sample

Dehydration is a requirement for successful calcination via IPL, in agreement with the UV-VIS observations, producing ZnO quantum dots (QDs). The QDs have high crystalline quality, producing significantly reduced defect associated visible PL emission as compared to ZnO derived from traditional thermally furnace treated LBZA presented here, and by Tarat *et al.* <sup>[67]</sup> and Barnett *et al.* <sup>[543][544]</sup>. The defect associated emission is also significantly reduced compared to QDs produced by:

- sol-gel/ wet chemical routes <sup>[541][545][546][547][548][549][550][551]</sup>
- DC reactive magnetron in argon/ oxygen environments <sup>[552]</sup>

As well as:

- Simonkoellite ( $Zn_5(OH)_8Cl_2 \cdot 2H_2O$ ) and hydrozincite ( $Zn_4(OH)_6CO_3 \cdot H_2O$ ) derived ZnO platelet structures annealed up to 700 °C <sup>[149]</sup>, and from 300 °C <sup>[553]</sup> up to 700 °C <sup>[554]</sup> respectively
- Microemulsion synthesised ZnO nanorods <sup>[555]</sup>
- Nanowires produced by:

- Vapour deposition CVD with substrate temperatures and/ or post annealing at temperatures up to 600 °C [97][556]
- Hydrothermal methods using a seed layer with ( $T= 130\text{ °C}$ ) [156] and without ( $T\leq 85\text{ °C}$ ) [557] [558] an autoclave
- calcination of crucible contained Zinc acetate at 300 °C. [559]
- ZnO thin films produced via magnetron sputtering and annealed at 300 °C [560], 450 °C [561] and 500 °C [562]
- Commercial 99.99 % purity ZnO purchased from Sigma Aldrich annealed at temperatures up to 1000 °C [563]

The synthesis of ZnO with lower defect associated emission typically requires more expensive synthesis techniques such as atomic layer deposition [564], or conditions that would limit its use with cheap substrate materials such as:

- Hydrozincite derived ZnO annealed at 600 °C in H<sub>2</sub> [554]
- Electrospun zinc acetate- polyvinyl acetate derived polycrystalline ZnO wires calcined at 600 °C [565]
- Pulsed laser deposition with the substrates held at temperatures greater than 450 °C [86][112]
- Magnetron sputtered ZnO thin film annealed greater than 600 °C [566]

At present time the reason for the large reduction in defect associated emission with only very limited sintering is unknown, however it is likely related in part to the energy differences between the processes. Reports of migration barriers for zinc interstitials of 0.57 eV [80][567], zinc vacancies of 1.4 eV [80], and for oxygen interstitials of 1.4 eV [80] are lower than the activation energy for densification in ZnO of 2.08 eV [568], which is also on the order of the neutral oxygen vacancy migration barrier of 2 eV [567]. Combined with the very small radii (< 2.01 nm) limiting diffusion distances required to anneal out, the defects should be removed faster than the ZnO in separate grains can diffuse together.

Figure 7.9 shows plots of measured valance band, fermi-level and exciton peak emission energies as well as the theoretical conduction band position (predicted by inserting the mean measured quantum dot radii into Equation 7.6 and Equation 7.7) as a function of radiant exposure for the 150 °C dehydrated LBZA.

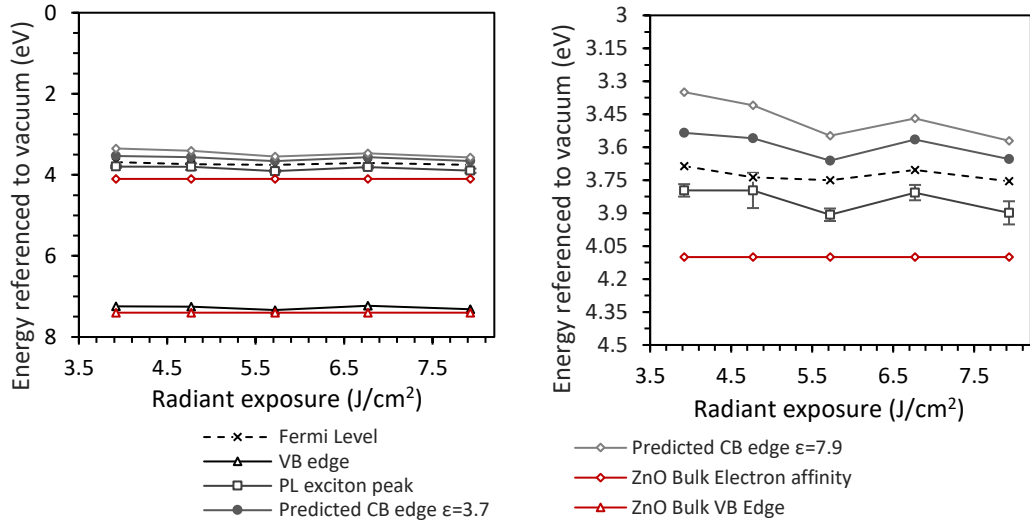


Figure 7.9: Plot of band positions (referenced to vacuum) as a function of radiant exposure for the 150 °C dehydrated LBZA samples with measured values of valance band edge/ ionization potential (UPS), fermi-level (UPS), exciton peak emission (PL) and theoretical valance band position  $\epsilon = 3.7$  (Equation 7.6) and  $\epsilon = 7.9$  (Equation 7.7) using the mean measured values of QD radii. For comparison literature value of bulk ZnO conduction band position/ electron affinity<sup>[202]</sup> and bulk ZnO valance band edge/ ionization potential (electron affinity + single crystal exciton peak + exciton binding energy (60 meV<sup>[80]</sup>)) have been added.

As can be seen in the plots the material is predicted to be highly n-type with predicted values for  $E_{CB}-E_F$  for radiant exposures of 3.92, 4.77, 5.72, 6.77 and 7.93 J/cm² between:

- 0.337, 0.328, 0.2030, 0.234 and 0.184 eV for  $\epsilon_{ZnO-bulk} = 7.9$ .
- 0.151, 0.177, 0.090, 0.139 and 0.100 eV for  $\epsilon_{ZnO-Quantum\ Dot} = 3.7$

The values are significantly lower than the 0.42-0.44 eV estimated by Jones from observed experimental parameters of traditional thermally treated, LBZA derived ZnO<sup>[77]</sup>. For a non-degenerate semiconductor the concentration of electrons in the bulk of the material ( $n_b$ ) in the absence of trap states is given by<sup>[77]</sup>:

$$n_b = N_D e^{-\frac{E_C - E_f}{k_B T}}$$

Equation 7.9

Where  $N_D$  is the number of donor dopant states (atoms or defects),  $k_B$  is the Boltzmann constant and  $T$  is temperature in Kelvin. Inserting the mean value of IPL exposed samples of  $E_{CB}-E_F$  of 0.257 eV ( $\epsilon_{ZnO-bulk} = 7.9$ ) and 0.131 eV ( $\epsilon_{ZnO-Quantum\ Dot} = 3.7$ ), and the 0.42 eV observed by Jones into  $\exp(-(E_C - E_f)/k_B T)$  produces values 634 and 27.1

times, and 91614 and 345 time greater than Jones's values for  $T=293.15$  K (20 °C) and  $T=573.15$  K (300 °C) respectively.

Combining the:

- expected increase in donor ionization due to the reduction in  $E_{CB}-E_F$
- with a reduction in trap states and the reduction in scattering centres (increasing the time between collisions and hence electron mobility<sup>[77]</sup>) as shown by the reduction in defect associated emission

The conductivity of the material, neglecting surface scattering, would be expected to increase significantly compared to the HMTA derived sensor in chapter 4.1.3 , which subsequently should increase signal to noise ratio and allow for cheaper and easier measurement electronic circuits.

To account for the effects of the treatment on gas sensor sensitivity it is important to first work out whether the device is in a flatband condition. For a small cylindrical compact grain with length approximately equal to its radius, the difference in conduction band energy between the centre of the grain and the grain surface is given by <sup>[192]</sup>:

$$\Delta E \text{ (eV)} = \frac{q^2 n_b R^2}{4\epsilon\epsilon_0}$$

Equation 7.10

Where R is the radius of the grain. Inserting values of  $n_b$  given by Equation 7.9 for  $N_D$  of  $10^{22} \text{ m}^{-3}$  and  $10^{25} \text{ m}^{-3}$  at 573.15 K (300 °C), and values for  $\epsilon=7.9$  and R of  $2.01 \cdot 10^{-9} \text{ m}$  (the mean value for  $7.93 \text{ J/cm}^2$ ) produces values of 0.126  $\mu\text{eV}$  and 0.127 meV, and for  $\epsilon=3.7$  1.61  $\mu\text{eV}$  and 1.61 meV. The values are significantly lower than  $k_B T$  which is 49.4 meV at 573.15 K (300 °C). The grain structure is therefore expected to be in the flatband condition, where the concentration of electrons in the material  $n_s$  (which includes perturbations due to adsorbed surface species) is constant throughout the material (formally  $\frac{dn(x)}{dx} \approx 0$ ) <sup>[192]</sup>.

As both the IPL treated materials are, and the HMTA derived sensor in chapter 4.1.3 was in the flatband condition (estimated  $\Delta E_{HMTA}=4.67 \text{ meV}$  using the values of  $E_{CB}-E_F$  presented by Jones), and are both c-axis orientated, the sensitivity of any IPL derived compact thin film should at least be equal to the HMTA derived sensor. However according to theories



governing catalysis, as provided in Chorkendorff and Niemantsverdriets 'Concepts of modern catalysts and kinetics' [204], the energy barrier for adsorption reduces as the electron energy of the highest occupied states within the catalyst shifts closer to the vacuum energy. This is due to the adsorbate antibonding orbital, which forms the bonds with the catalyst surface, of most adsorbates being close in energy to the vacuum level. As a result, the increased kinetic energy due to quantum confinement would be expected to increase the reaction rate of O<sub>2</sub> adsorption and thereby increase device sensitivity.

In chapter 4.1.3 the concentration of under-coordinated surface sites, derived from the high curvature resulting from the small radius (mean = 3.6 nm) of the nanogranular ZnO structure, was expected to partially account for the high sensitivities. The increase in curvature for the IPL treated sample, would result in an increased concentration of under-coordinated surface sites. In turn this should lead to an increase in device sensitivity.

This will need to be confirmed experimentally once the gas sensor testing rig is upgraded to reliably test the printed sensors, however the effect of IPL treatment on LBZA shows great potential for the use in gas sensors, printed or otherwise.

The compact nature of the material, in combination with high surface area, controllable band alignment and the expected high conductivity, whilst being printable (i.e. high throughput) also provides great opportunities for other uses. Examples include:

- Cheap UV sensors [515][557][109] for monitoring potential UV exposure from solar or hazardous work environmental sources. The ability to tune the bandgap provides minor flexibility in absorption threshold, whilst the significant reduction in recombination centres would lead to increased sensitivity and conductivity.
- Bio sensors such as the flexographically printed ZnO non-faradaic sensors by Assaifan *et al.* [31] for virus detection.

Though arguably the most interesting potential use is within printed perovskite photovoltaics (PV). In printed PV devices a compact 50-100 nm n-type semiconducting electron extraction/ hole blocking layer is used to extract electrons from the photon absorbing perovskite layer, increasing device efficiencies [536][569]. The traditional material of choice, anatase TiO<sub>2</sub>, has a bulk mobility of 1 cm<sup>2</sup>V<sup>-1</sup>s<sup>-1</sup> [536] which is significantly lower the bulk mobility for ZnO of 200 cm<sup>2</sup>V<sup>-1</sup>s<sup>-1</sup> [536]. The fact that band positions referenced to vacuum between the two materials are practically equivalent means that swapping materials should lead to a significant increase in device efficiencies. However, the surface defects in ZnO degrade the methylammonium cation in methyl ammonium lead iodide perovskites limiting long-term stability [536]. The ability to flexographically print thin compact layers of LBZA,

that when treated with IPL produces highly n-type ZnO with exceptionally low defects (as indicated by the PL emission) is almost uniquely ideal for the hole blocking layer.

## 7.6 Conclusion

Dehydration at 150 °C has been shown to be a key requirement for the successful calcination of LBZA via intense pulsed light treatment. Diffuse reflectance UV-VIS spectroscopy results have shown that LBZA does not absorb light within the bandwidth of exposure of the Pulseforge 1200 used. Dehydration of the layer into 4 zinc oxide + zinc acetate was then shown to photosensitise the layer. This was then shown experimentally to be a key requirement for the successful calcination, as confirmed by chemical (XPS), crystalline (XRD) and optical (photoluminescent) investigations. The resulting ZnO was shown to produce quantum dots with mean measured radii between 1.77 and 2.01 nm for radiant exposures between 3.92 J/cm<sup>2</sup> and 7.93 J/cm<sup>2</sup>. The radius was shown to follow a predictable Arrhenius like relationship with respect to radiant exposure. The quantum dots were shown to have high crystalline quality, with low optically active defects and an exciton to defect area ratio significantly lower than thermally treated LBZA and most reported values for nanoscale ZnO. The exciton emission was shown to be shifted in line with confinement effects and an empirical relationship linking the measured radii and peak emission energy produced. Combining the Arrhenius like relationship of radius vs radiant exposure with the confinement-based emission relationship led to a predictable relation between radiant exposure and exciton peak emission. The relationship was found to be in strong agreement with the measured values providing a useful predictive tool.

The experimentally measured properties were then compared theoretically to the HMTA derived sensor presented in Chapter 4, and to the material properties of HMTA derived ZnO sensors as measured by Jones <sup>[77]</sup>. The comparison suggests that the IPL treated material is ideal for gas sensing purposes and is an exciting avenue for future research in printed gas sensor development, and in other fields such as printed photovoltaics.

## Chapter 8 - Conclusion

---

In the preceding chapters, investigations into the synthesis, flexographic printing, processing of LBZA and the gas sensing properties of LBZA derived nanogranular ZnO were presented. Throughout the analysis of the presented results, recommendations were made towards the suitability of the processes towards the long-term goals of the production of a cheap, flexographic printed carbohydrate malabsorption breath sensor.

Initially in chapter 4.1, an inhouse modification of the HMTA derived, microwave assisted growth of LBZA of Tarat *et al.* <sup>[67]</sup> was investigated. The synthesis method was shown to produce high purity nanosheet morphology LBZA, with a mean length of 3.87  $\mu\text{m}$  (standard deviation = 2.29  $\mu\text{m}$ ) and Scherrer equation height estimate of 46.6 nm. Using the synthesised LBZA, a dropcast gas sensor was produced using a commercial alumina substrate. Calcination at 350 °C produced a compact ZnO layer with mean grain size 7.8 nm and a standard deviation of 1.3 nm; and a baseline resistance in dry air of 4 to 8 M $\Omega$  in the temperature range of 234 to 328 °C. Testing the gas sensing properties showed the sensor to be highly sensitive to H<sub>2</sub> producing a response of 7.27 to exposure of 200 ppm at a 328 °C. The sensor also showed a weak but appreciable response to 200 ppm of CO of 1.25 and CH<sub>4</sub> of 1.13 at the same temperature. The H<sub>2</sub> sensitivity is highly competitive with those presented in literature, and generally only less sensitive to composite surface decorated and doped sensors. The sensitivity was attributed to 3 main factors:

- The small grain size of mean 7.8 nm and standard deviation 1.3 nm. The small grain size was expected to result in a flatband condition; as a result, the resistance of each entire grain is dependent on the adsorbed species, as opposed to just the regions localised to the surface where band bending is present. Additionally, the high degree of curvature was expected to produce a high concentration of reactive under-coordinated surface sites.
- The preferred c-axis orientation producing a density of (001) ZnO surface, which has been shown to have increased reactivity compared to other facets
- The thin nature of the film. As the film is compact, the gas molecules will have a short diffusion length. The thin nature of the film limits the amount of unreactive material, and hence a constant resistance in parallel with the active surface resistance.

A brief summary of an investigation into surface decoration of LBZA with Au nanoparticles was then presented. The results showed that the production methods for producing

composites were easy to integrate with LBZA by simply mixing a suspension of LBZA with the catalytic material, waiting for deposition/ aggregation to complete, and centrifuging to purify the composite material.

Comparisons with current guidelines for carbohydrate malabsorption H<sub>2</sub> breath testing<sup>[49]</sup>, predicted H<sub>2</sub> responses for at the threshold for a positive test (20 ppm) of 1.34 and borderline positive (10 ppm) of 1.16. The predicted response to CO at the mean concentration post cigarette smoke inhalation<sup>[45]</sup> (20 ppm) was 1.03, and at the 95 % upper coincidence level (54.6 ppm), 1.09. For the mean case, and assuming additive responses, this would be predicted to produce a false positive of the next level (i.e. negative to borderline, borderline to positive) at approximately 2 ppm H<sub>2</sub> below each threshold. As current guidelines<sup>[49]</sup> suggest that testing be postponed if the patient has recently inhaled cigarette smoke, this was considered to have no effect on testing. The responses for CH<sub>4</sub> predicted negligible interference. Combined with the resistance easily measurable with cheap, off the shelf electronic components, this showed LBZA derived nanogranular ZnO to be ideal for the H<sub>2</sub> sensing element without modification.

Testing the mass yield per synthesis of the HMTA derived LBZA synthesis showed a mean of 37.2 mg. Using the mean yield, Scherrer equation predicted height, and a predicted flexographic ink concentration of 66.6 mg.mL<sup>-1</sup> led to an estimated 4.45 synthesis and cleaning runs to produce a 2.5 mL volume of ink, enough for a single print and subsequent viscosity test. The yield was determined to be too low for development of the flexographic printing ink that would be required for the long-term goals of the project. To overcome the issue the synthesis method was modified, using sodium hydroxide as the base.

A short trial of the modified method using 20 seconds of microwave exposure at 800 W was conducted. From x-ray diffractograms the material was shown to produce high purity LBZA; with the highest [OH<sup>-</sup>]/[Zn<sup>2+</sup>] ratio before reflections from ZnO impurities became measurable determined to be 1.5. The measurements also showed reflections determined to arise from the so called bilayered basic zinc acetate (BLBZA) crystalline structure. SEM and AFM measurements showed a mean length of 6.95 μm (standard deviation 2.42 μm), and mean height of 14.8 nm (standard deviation 7.5 nm) respectively. The length of the particles was below the 24 μm upper size limit for a 24 mL.m<sup>-2</sup> anilox and therefore compatible with the flexographic printing process. A mean mass yield of 1237 mg (standard deviation 61 mg; containing 10.0 mMol of [Zn<sup>2+</sup>]) from 2.508 g ZnAc<sub>2</sub> (11.4 mMol of [Zn<sup>2+</sup>]) was obtained. Using the measured AFM height; an initial ink LBZA mass concentration of 20.9 mg.mL<sup>-1</sup> was calculated. Using the same 2.5 mL ink volume as for the HMTA method, only 4.22 % of the mass of a single synthesis run would be required. This represents a significant

improvement and was ideal for the subsequent use in the development of a proof of concept printed sensor, and ideal for scaling up to both pilot and industrial scale in-line with final project goals.

The work was then split into two directions, performed simultaneously, to tackle the next two main requirements for the project development. The first, presented in Chapter 5, was the further development of the sodium hydroxide-based, microwave assisted LBZA growth. The chapter consisted of two separate experiments, performed with the aim of increasing phase purity and controlling the morphology and polydispersity of the synthesised particles.

The first experiment looked at the combined effect of  $[\text{OH}^-]/[\text{Zn}^{2+}]$  ratio and microwave exposure time. X-ray diffraction analysis showed the presence of LBZA, ZnO and so called BLBZA phase for all reaction conditions with  $[\text{OH}^-]/[\text{Zn}^{2+}] < 2$ ; with a maximum LBZA yield shown to occur at  $[\text{OH}^-]/[\text{Zn}^{2+}] = 1.6$ . From further phase analysis it was shown that LBZA has the lowest barrier for formation, whilst so called BLBZA and ZnO were the thermodynamically favoured products; with the impurity concentration increasing with microwave exposure, and an exposure time of 30 seconds producing the minimum observed LBZA phase area ratio of 0.93. Diffractograms of the reaction supernatant showed the additional reflections present in BLBZA, without any reflections from LBZA associated planes. This showed that the additional reflections, which, according to the literature were proofs of a single bilayered crystal structure <sup>[68][74][450][71]</sup>, producing both LBZA and BLBZA reflections; were in fact produced from a separate second crystalline phase.

Analysing the morphology showed that unexposed samples ( $T=294$  K) produced LBZA with nanobelt morphology. Maximum length was observed between a  $[\text{OH}^-]/[\text{Zn}^{2+}]$  ratio of 0.8 and 1.44; with a maximum recorded mean of  $39.1 \mu\text{m}$  (95% CI:  $33.8 \mu\text{m} - 44.7 \mu\text{m}$ ) for a ratio of 1.2. The maximum recorded aspect ratio was at  $[\text{OH}^-]/[\text{Zn}^{2+}]$  ratios between 1.4 and 1.47; with a maximum recorded mean of 51.1. Increasing the  $[\text{OH}^-]/[\text{Zn}^{2+}]$  ratios further led to a rapid decrease in length and aspect ratio, tending towards the nanosheet/nanoplatelet morphology; where a ratio of 1.6 had a mean length of  $16.5 \mu\text{m}$  (95% CI:  $14.3 \mu\text{m} - 18.8 \mu\text{m}$ ) and aspect ratio of 8.4 (95 % CI: 7.3-9.6). A similar trend with  $[\text{OH}^-]/[\text{Zn}^{2+}]$  ratio was seen in the samples that were microwaves exposed, though to a lesser extent. However, the increase in temperature led to a dramatic reduction in length and aspect ratio; with the maximum mean length after 30 seconds of exposure ( $T_{\text{peak}}=351$  K) of  $8.5 \mu\text{m}$  (95 % CI:  $7.3 \mu\text{m} - 9.7 \mu\text{m}$ ), and mean aspect ratio of 8.1 (95 % CI: 7.2 – 9.2) at a  $[\text{OH}^-]/[\text{Zn}^{2+}]$  ratio of 1.2.

In addition to the alteration in length and aspect ratio seen with the increasing  $[\text{OH}^-]/[\text{Zn}^{2+}]$  ratio and microwave exposure (i.e. temperature), a reduction in polydispersity was observed; with the standard deviation in length and aspect ratio without microwave exposure of:

- Length: 28.1  $\mu\text{m}$  (95 % CI: 21.1  $\mu\text{m}$  – 35.5  $\mu\text{m}$ ). Aspect ratio: 42.2 (95 % CI: 29.7 – 55.2); at a  $[\text{OH}^-]/[\text{Zn}^{2+}]$  ratio of 1.4
- Length: 11.7 (95 % CI: 10.1  $\mu\text{m}$  – 13.4  $\mu\text{m}$ ). Aspect ratio: 5.8 (95 % 4.9 – 6.6); at a  $[\text{OH}^-]/[\text{Zn}^{2+}]$  ratio of 1.6

And after 30 seconds exposure ( $T_{\text{peak}}=351 \text{ K}$ ):

- Length: 4.2  $\mu\text{m}$  (95 % CI: 3.2  $\mu\text{m}$  – 5.2  $\mu\text{m}$ ). Aspect ratio: 3.4 (95 % CI: 2.4 – 4.6); at a  $[\text{OH}^-]/[\text{Zn}^{2+}]$  ratio of 1.4
- Length: 2.3  $\mu\text{m}$  (95 % CI: 1.8  $\mu\text{m}$  – 2.8  $\mu\text{m}$ ). Aspect ratio: 2.3 (95 % 1.8 – 2.7); at a  $[\text{OH}^-]/[\text{Zn}^{2+}]$  ratio of 1.6

The high degree of polydispersity was attributed to the formation of a slurry, producing a large diffusion barrier and a reduction in mixing efficiency. This resulted in an extended period for nucleation to occur over; and as a result, a large standard deviation in growth times, with particles nucleating later producing shorter particles than those nucleated at a shorter time.

To understand the driving forces for the observed length and aspect ratio trends, the unit cell of the LBZA basal layer was examined for asymmetries. Alternating layers of  $[\text{Zn}^{2+}]$  and  $2[\text{OH}^-]$  ions were observed in the  $[1\bar{1}0]$  direction, indicative of a dipole. Planes  $90^\circ$  to the  $[1\bar{1}0]$  direction i.e. in the  $[110]$  direction were of mixed species and expected to lack any dipole moment. The distance between  $(1\bar{1}0)$  planes was equal to that of the  $(100)$  planes that has previously been shown in literature through diffraction experiments to align with the preferred direction of growth. Point charge calculations of the surface charge ruled out non thermal interactions of microwave exposure on the growth. From:

- The enhancement in growth rate using the predicted Stern layer potential from the point charge calculations, and kinetics for crystal growth at charged surfaces <sup>[172]</sup>
- Calculations of the concentration of complexed species

Primary particle growth was ruled out as the mechanism for the high lateral aspect ratios and the final nanobelt and nanosheet morphologies. The following observations heavily suggests that the aspect ratio and preferred  $[1\bar{1}0]$  direction growth for LBZA is a result of dipole driven oriented attachment:

- the  $[1\bar{1}0]$  direction of the dipole
- the aggregation of 58 nm particles at the tips of the longest direction in SEM micrographs
- the observations in literature of  $\sim 10$  nm LBZA primary particles with a preferred (100) orientation <sup>[70]</sup>
- an estimated difference in energy barriers between growth in length and width of  $2.7 k_B T$  (at 294 K) approximately equal to the  $3 k_B T$  for dipole driven oriented attachment for ZnO <sup>[179]</sup>.

The second experiment looked at the combined effects of addition rates and mixing methods, on nucleation conditions and phase purity. The experiments showed that if the mixing efficiency, and hence the transport rate of reactants relative to the nucleation rate, is too low; then the localised reactant concentration is highly inhomogeneous. The inhomogeneity, results in the particles nucleating in regions of high ionic strength; aggregating and forming the slurry. Simultaneously, localised regions of high  $[\text{OH}^-]/[\text{Zn}^{2+}]$  ratio lead to the nucleation of  $\text{Zn}(\text{OH})_2$  crystals; whilst low regions of  $[\text{OH}^-]/[\text{Zn}^{2+}]$  ratio subsequently lead to the nucleation of the so called BLBZA phase. Increasing the ratio of transport rate to nucleation rate leads to an increase in purity. When the transport ratio is high enough, such as with the simultaneous addition rate with high shear rate stirring method; the formation of impurities is prevented.

During the synthesis a precursor phase was observed, producing the largest phase areas in the diffractograms. With an increase in stir time a reduction in precursor phase area and an increase in LBZA phase area was seen. The observation was in line with the only other recorded observations of the phase <sup>[75][400]</sup>; where the phase was produced during TGA experiments and shown to slowly convert to LBZA with exposure to atmospheric moisture.

The results represent the most in-depth investigation into the synthesis conditions of LBZA synthesised in water reported to date. It is the first to observe the presence of a precursor phase during the synthesis; the first to show that the impurities arise from the ratio of transport rate to nucleation rate; and the first to predict a dipole structure, and theorise that the observed LBZA morphologies is a result of dipole assisted oriented attachment.

The final two chapters, Chapter 6 and Chapter 7, show the production of a proof of concept flexographic printed LBZA derived ZnO gas sensor; and the effect of intense pulsed light treatment conditions on the calcination requirements for LBZA, and the resulting quality of ZnO produced by the treatment.

Initial print tests of the PFI 722 Ag flexographic ink, used to print the interdigitated electrode (IDE) structure for the sensors, showed defects due to rapid drying and poor wetting of the Kapton HN substrate. To increase wetting, O<sub>2</sub> plasma; wet chemical hydrolysis in a 75 % ethanol/ 25 % ethanol blend; and a combination of 10 seconds O<sub>2</sub> plasma and 10 s of the wet chemical hydrolysis treatments were trialled. Contact angle analysis of PFI -722 showed the contact angle for the O<sub>2</sub> plasma treated surface was practically unchanged; with the contact angle for unmodified surface of 45.9 ° and 43.6 ° after 10 s of exposure. The wet chemical, and combined O<sub>2</sub> plasma and wet chemical treatment produced the lowest contact angles of 27.5 ° and 25.7 ° respectively. T-tests between the two showed the distance to be statistically insignificant with a p-value of 0.22. XPS analysis showed the difference in contact angle between surface treatments to likely arise from an increase in amide concentration after hydrolysis treatment. The acidity of the ink could protonate the amide groups resulting in a surface charge. The surface charge would produce a large increase in surface energy and as a result, increased wetting. Based on a combination of lowest PFI-722 contact angle, and a reduction in surface contamination as measured by XPS, the combined O<sub>2</sub> plasma and wet chemical treatment was used for all subsequent print tests. A glycerol-based binder-less LBZA ink was subsequently developed. The developed ink had a LBZA mass concentration of 46.6 mg.mL<sup>-1</sup>, and a solvent blend consisting of 30 %v/v glycerol, 30 %v/v propylene glycol and 40 %v/v n-butanol. The ink was shown to form a thixotropic shear thinning gel, with a viscosity post mixing of 9.88 Pa.s at 0.1 s<sup>-1</sup> and 67.7 mPa.s at 4261 s<sup>-1</sup>. The ink had a mean surface tension of 26.1 mN/m (standard deviation of 0.2 mN/m), and fully wet the combined O<sub>2</sub> plasma and hydrolysis treated substrate. Print tests showed an optimised print and anilox forces of 150 N, for a solid block print performed at 1.5 m.s<sup>-1</sup>.

Proof of concept gas sensors were then produced using PFI-722 ink printed on the combined O<sub>2</sub> plasma and hydrolysis treatment at a humidity of 90 %. They were then dried at 150 °C for 10 minutes, the LBZA ink was printed and dried at 150 °C; and finally the sensors were ramped to and calcined at 420 °C for 5 minutes in air and aged at 246 °C for 2 days. The increased humidity during the PFI-722 print inhibited drying defects and led to a reproducible electrode separation between sensors; with a total mean separation of 104.2 µm and a standard deviation 10.5 µm. The broad standard deviation was attributed to the regular



periodic variance in print plate line widths that stemmed from the plate manufacturing process and spanned 39  $\mu\text{m}$ . EDS maps showed coverage of the LBZA derived ZnO to be generally uniform, with minor deviations in coverage due to viscous fingering and changes in height between printed IDE and substrate.

The sensors produced large H<sub>2</sub> responses, with a maximum response to 200 ppm H<sub>2</sub> of 60.2 at a temperature of 300 °C. The H<sub>2</sub> response was 8.28 times greater than the maximum observed response to 200 ppm H<sub>2</sub> for the HMTA derived sensor. The sensors also showed peak responses for CO and CH<sub>4</sub> at temperatures between 240 °C and 250 °C, and 240 °C and 285 °C respectively. No such peak response was observed for the HMTA derived sensor, and the sensors also had a significantly increased baseline resistance between of 0.7 G $\Omega$  and 17.2 G $\Omega$ . Comparison of double Schottky barrier + Fermi level to conduction band energies, estimated from IV curves measured in dry air (0.9 – 1.2 eV), 200 ppm CH<sub>4</sub> (0.85-1.16 eV), CO (0.88 – 1.19 eV) and H<sub>2</sub> (0.57 – 0.88 eV) at 302 °C, against predicted values by Jones (0.61-0.70 eV) <sup>[77]</sup>, suggested the response to be extrinsic to the LBZA material. The following observations suggests that the increased sensitivity to H<sub>2</sub> and baseline resistance was a result of transferred Ag from the contact material, likely during the LBZA overprint procedure:

- the estimated barrier heights
- the peak response temperature for CH<sub>4</sub>
- the measurement of 2 separate particle populations with differing contrast in SEM micrographs

Whilst further work would be needed to rectify the issue, the printing process appears promising for the long term aims of the project. The proof of concept sensors results represent the second reported flexographic gas sensors, regardless of material, and the first to measure gasses other than oxygen.

In addition to the production of the glycerol-based ink, a secondary ink using PVP was trialled where the required mass load for LBZA was originally derived experimentally. The trial showed that the most uniform printing at low print pressures (50 N) occurred at viscosities on the order of 309 mPa.s. and confirmed the results of Baker *et al.* <sup>[4]</sup> of a threshold for successful printing of 20 mPa.s. The study showed an empirical  $\ln(\text{Viscosity (Pa.s)}/\text{nominal width (m)})$  relationship for printed line width and print gain perpendicular to the direction of print, for nominal line width/ anilox cell width ratios greater than 0.492. The observations are contrary to those by Deganello *et al.* <sup>[268]</sup> for ratios below 0.492 that showed an increase in print gain with nominal width. The results provide a useful tool for both electrical and graphical industries using flexographic printing, where deviation

from expected print widths and poor print fidelity may result from using the wrong relationship at a particular ratio.

Finally, Chapter 7 investigated the effects of intense pulsed light on the sodium-hydroxide microwave synthesised LBZA as an alternative calcination process. Initially, diffuse reflectivity was measured for LBZA with and without 150 °C dehydration; with the dehydration step converting LBZA to  $4 \text{ ZnO} + \text{ZnAc}_2$ . The results showed LBZA to be optically inactive, requiring dehydration to become an optical absorber. The lack of optical absorbance within the bandwidth of the pulseforge 1200 used was predicted to inhibit calcination of LBZA without dehydration. XRD, XPS and PL analysis confirmed the predictions for radiant exposures between  $3.92 \text{ J/cm}^2$  and  $7.93 \text{ J/cm}^2$ , producing highly crystalline ZnO QDs with mean radii between 1.77 nm and 2.02 nm respectively. The size was shown to be predictable following a simple Arrhenius like relationship. Photoluminescence analysis showed the quantum dots to have a lower defect region to exciton region emission ratio than reported for the majority of nanoscale ZnO in literature, showing its high crystalline quality. The PL spectra also showed the exciton emission to be blue shifted, the magnitude of the shift was in accordance with quantum confinement theory and predictable with respect to the particle radius, and therefore radiant exposure. Using the quantum confinement predicted electronic band gap and ultraviolet photoelectron spectroscopy predicted a conduction band – Fermi level energy separation between 0.131 eV and 0.257 eV; significantly lower than measured by Jones for HMTA derived ZnO of 0.42 eV. The material was therefore expected to be highly n-type, which when combined with the low defect density would be expected to increase the conductivity significantly. Due to the high curvature and flatband condition resulting from the small particle radii, and XRD measured (001) orientation, the particles are expected to be a highly sensitive for gas sensing. When the expected sensitivity is considered with the expected increase in conductivity, IPL treated dehydrated LBZA appears to be a promising sensing material for integration into the carbohydrate malabsorption breath analyser.

The ZnO produced by IPL is also expected to be a promising material for use in other electronic devices such as UV sensors, biosensors and most excitingly as a hole blocking layer in printed perovskite photovoltaics; where the high predicted conductivity and low concentration of defects would be expected to increase the efficiency over  $\text{TiO}_2$  blocking layers and increase device lifetime over traditional nanoparticle ZnO blocking layers.

To conclude, a strong foundation for future development of flexographically printed, LBZA derived, nanogranular ZnO, carbohydrate malabsorption sensors has been set. In doing so, a new, comprehensive theory for the formation mechanism of LBZA in aqueous media was

developed. Furthermore, the printed layers, especially with the introduction of intense pulse light treatment show promise for use in a wide variety of printed electronic devices.

## Chapter 9 - Future Work

---

The results presented leave a promising future for further experimental investigations; both in terms of the underlying science with respect to LBZA synthesis, and for the long-term development towards the final goals of producing a cheap carbohydrate malabsorption sensor.

At the current experimental understanding of LBZA synthesis; a ratio of 1.58-1.60, with a high shear stirring rate, and a method of introducing the reactants at a molar addition rate ratio of 1.58-1.6  $[\text{OH}^-]:1[\text{Zn}^{2+}]$ , has been recommended for future work. However, microwave exposure is currently advised against. This is due to an increase in polydispersity observed when the higher mass transport rate methods were used, in contrast to the reduction in polydispersity observed with the lower mass transport rate methods. This was theorised to be due to thermal gradients during the cooling step. The first potential work is the investigation of the effects of thermal gradients on polydispersity. Additionally, whilst the gravity controlled simultaneous addition method was shown to be able to decrease polydispersity and inhibit impurity formation when combined with a high shear technique, there is sufficient room for improvement. Replacing the simplistic low-cost centrifuge tube gravity fed system with a flow rate controllable pump, such as a syringe pump, would produce increased consistency and allow for the effects of feed rate to be better studied. The yield of LBZA produced by the synthesis method is likely large enough that short production runs of the sensors could be produced in standard laboratory conditions. If, however, the material is adopted in other uses e.g. scaled up printed photovoltaics, then the production method would likely need adapting. High shear methods such as in-line continuous flow microreactors would be recommended. Centrifuge cleaning at such scales would be one of the limiting methods for the synthesis, and as such other cleaning methods such as crossflow filtration would need to be investigated.

In terms of the underlying scientific understanding, observations of synthesis by in-situ TEM would allow for direct proof of the dipole assisted oriented attachment mechanism proposed within this work. Application of the mechanism to other anions, solvents and synthesis conditions might allow for a unified reaction method underlying the synthesis of all layered zinc hydroxides that share the same basal layer structure. In Chapter 5, layered basic zinc carbonate was used as an example <sup>[130][138]</sup> where primary particles with preferred orientation viewed under TEM resulted in nanobelt morphologies, however multiple nanobelts appeared to originate from a common nucleation source. As such, applying solubilities of zinc carbonate species to nucleation theories, may result in an explanation for the common

nucleation point, with dipole driven oriented attachment explaining the transformation to the final morphology.

Prior to further work relating to the printing process, a long-term strategy regarding the substrate material, and therefore the type of flexographic printing configuration is required. In Chapter 6, the defects arising from the rapid drying of water based PFI-722 ink restricted the printing of Ag electrode to a roll-to-roll lab scale flexographic printer with an ink reservoir, and for the printer to be encased in a 90 % humidity environment. The printer requirements for the Ag ink therefore limited the substrate material to Kapton and equivalent polyimides, and completely ruled out the use of brittle substrates such as alumina. When the high cost of Ag inks is considered; choice of printer, substrate and electrode deposition method are a long-term strategic requirement. In addition, different print plate suppliers, and/or in-house plate manufacturing methods, should be investigated to reduce the nominal line width variations; allowing for smaller electrode separation distances, and a smaller device footprint.

The transfer arising during the overprinting step of LBZA on pre-printed Ag electrodes led to a significant deviation from the gas sensing results for the HMTA derived sensor. A suggested method to counteract the problem was to swap the printing order of LBZA and Ag inks. As the Ag ink is restricted to a limited area during the printing step, the material transferred would generally be restricted to within the electrode boundary; the lack of material transferred outside of the boundary should stop any alteration of the sensing properties of the ZnO layer. Due to the exponentially higher conductivity of Ag than ZnO, the presence of ZnO would not be expected to significantly affect the conductivity of the electrode. The increased sensitivity to H<sub>2</sub> due to the transferred Ag nanoparticles does however present a promising surface decoration catalyst for the H<sub>2</sub> sensing element in a carbohydrate malabsorption sensor. Investigating the surface decoration with controlled Ag mass loading is worth investigating towards the long term aims of the project. As a small portion of people suffering from carbohydrate malabsorption produce CH<sub>4</sub> instead of H<sub>2</sub> [50][349][47], a CH<sub>4</sub> sensor will be required. As such either surface decoration with other catalysts, doping or a secondary sensing material will be required.

The surface decoration with catalyst, potentially integrated into a multi-sensing element electronic nose, also opens the possibility for use in gas sensors with other purposes, such as:

- CO monitoring to prevent carbon monoxide poisoning in residences and industry [41]
- Environmental monitoring of pollution levels [38]
- Gas concentration monitoring in manufacturing processes

- Monitoring of other poisonous gases and indoor pollutants hazardous to human health <sup>[354][570]</sup>
- Detection of explosives and nerve agents <sup>[571]</sup>
- Breath analysis of other diseases and conditions, such as cancer detection <sup>[43]</sup>; abnormal protein metabolism due to impaired kidney function, leading to toxic blood ammonia concentrations <sup>[43]</sup>, inflammatory conditions such as asthma <sup>[43]</sup>, chronic obstructive pulmonary disease <sup>[43]</sup>, cystic fibrosis <sup>[43]</sup>, bronchiectasis <sup>[43]</sup>, and obstructive sleep monitoring <sup>[43]</sup>; and CO monitoring to assess and aid quitting smoking <sup>[45]</sup>
- Quality control for manufactured goods (e.g. leak detection) and food spoilage <sup>[39]</sup>

IPL treatment of dehydrated LBZA was shown to produce ZnO with significantly improved optical and electrical properties. The successful application of IPL to printed LBZA films is a requirement to unlock its full potential, both for gas sensing and for other purposes such as in printed photovoltaics. As such, the pre-treatment required for printed films, and any potential ink alterations to allow for successful requirements is the logical next step towards integration of the treatment into such devices.

So far gas sensing experiments have been limited to dry air only. As breath contains a significant water content, the effect of humidity on sensitivity and selectivity will need to be quantified. The automated sensor testing rig will need to be adapted with a bubbler. In addition, breath contains a large quantity of other volatile compounds that will need to be tested for interference. The testing rig was designed with this in mind, and two expansion ports are available each with their own isolation valves, built into the rig. Further development towards the long-term goals will need to investigate filter materials to adapt to the interference that would arise from humidity and cross sensitivity to volatile compounds. Potential filter materials include packed bed activated alumina sorption filters <sup>[43]</sup>, and tuned microporous zeolite filters <sup>[43]</sup>.

## Chapter 10 – Appendix A1. Additional SEM micrographs for chapter 5

---

### 10.1 SEM Images for the $[\text{OH}^-]/[\text{Zn}^{2+}]$ microwave time growth experiment

#### 10.1.1 Aggregated 0 s unexposed LBZA

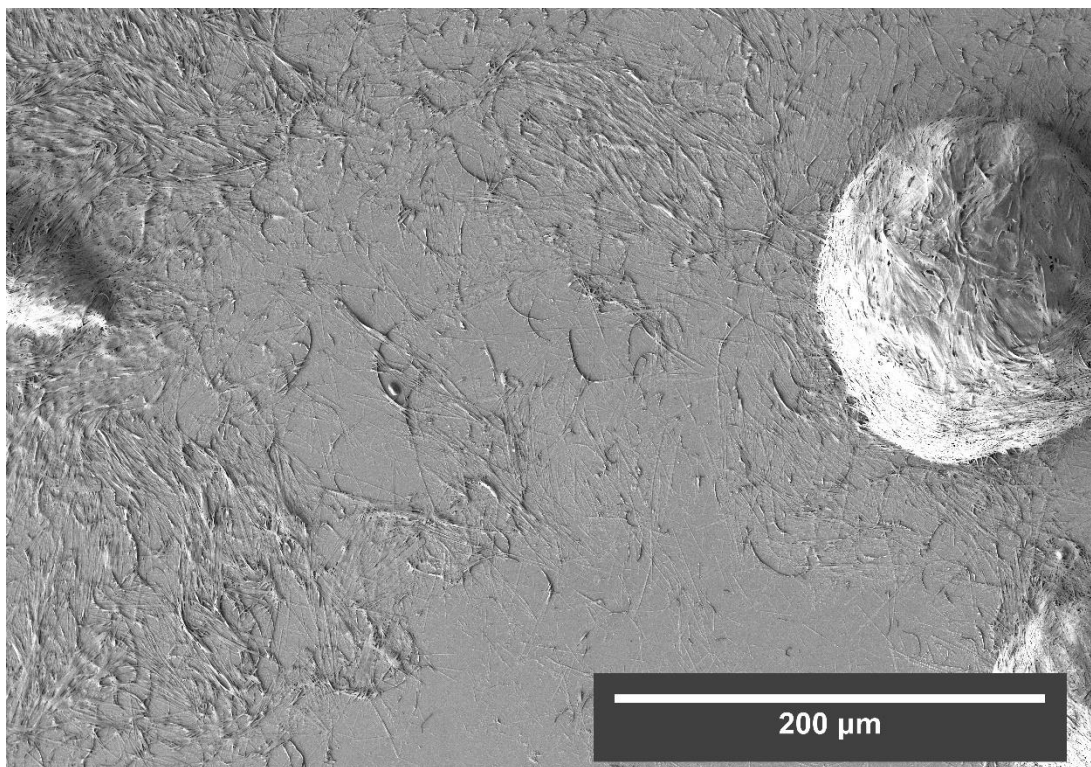


*Figure 10.1: SEM micrograph of LBZA synthesised without microwave exposure ( $\sim 294$  K) using  $[\text{OH}^-]/[\text{Zn}^{2+}]$  1.44:1 showing large scale aggregation and entanglement, likely arising from the high aspect ratio (51.1) and length (mean:  $35.2 \mu\text{m}$ , standard deviation:  $18.9 \mu\text{m}$ .) Scale bar:  $200 \mu\text{m}$ .*

**10.1.2 0 s Microwave exposure i.e. unexposed. (T = 294 K)**

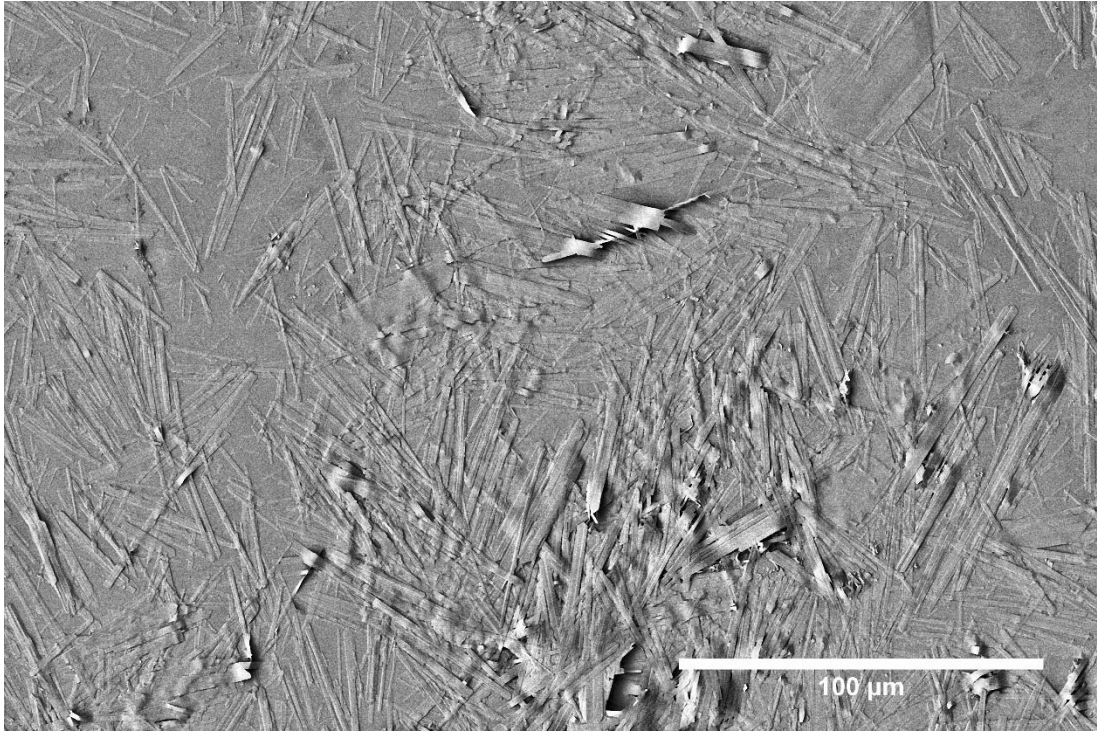


*Figure 10.2: SEM micrograph of LBZA synthesised without microwave exposure (~ 294 K) using  $[OH^-]/[Zn^{2+}]$  0.4:1. Full details of analysis is provided in chapter 5.3.1.2.1 . Scale bar: 100  $\mu$ m.*



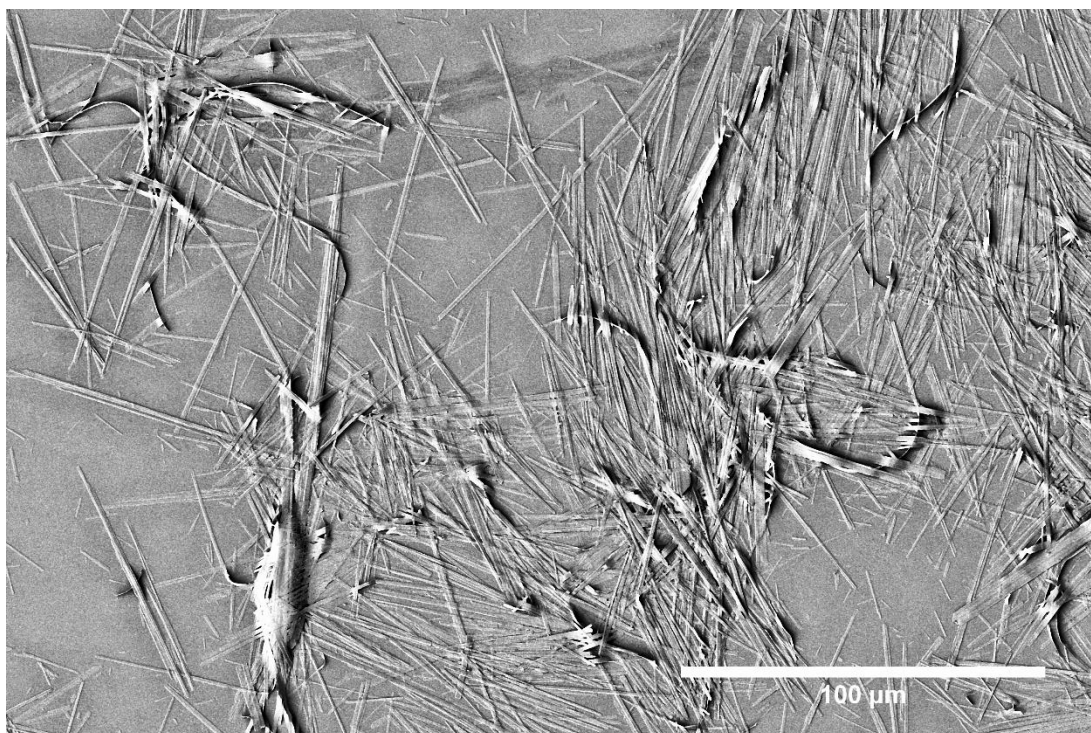


Figure 10.3: SEM micrograph of LBZA synthesised without microwave exposure ( $\sim 294$  K) using  $[\text{OH}^-]/[\text{Zn}^{2+}]$  0.8:1. Full details of analysis is provided in chapter 5.3.1.2.1 . Scale bar: 100  $\mu\text{m}$ . Note: The amplified electron shadow is an artifact of the local contrast enhancement performed in imageJ to make the particles distinguishable from the silicon substrate.

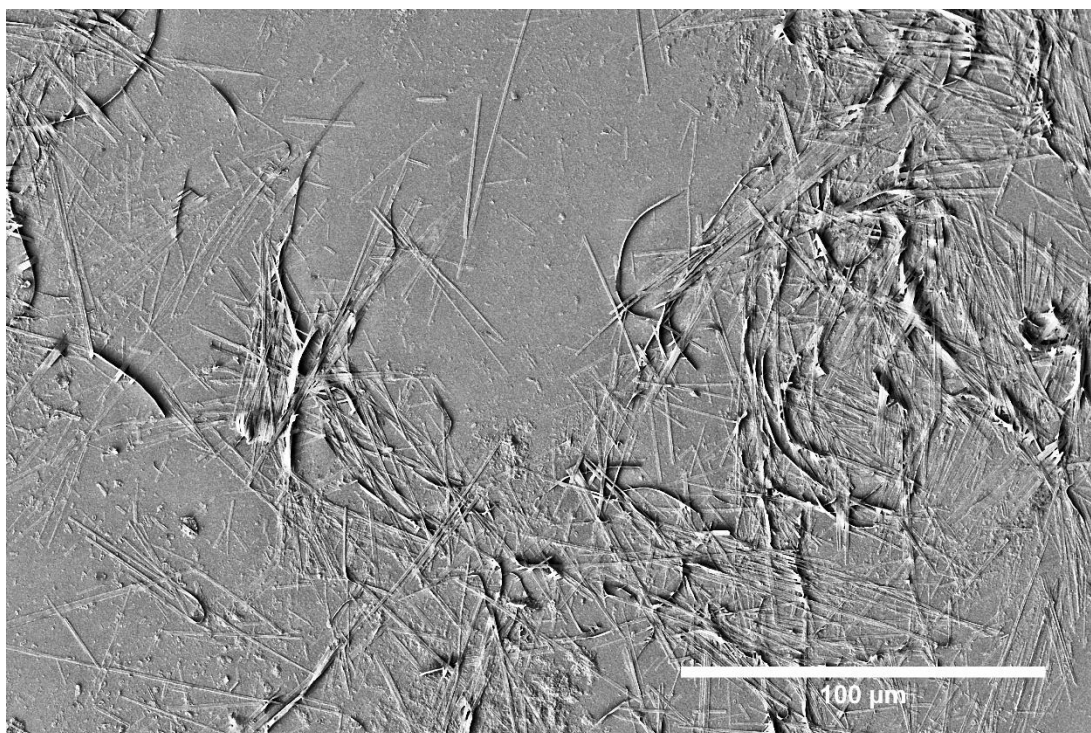


Figure 10.4: SEM micrograph of LBZA synthesised without microwave exposure ( $\sim 294$  K) using  $[\text{OH}^-]/[\text{Zn}^{2+}]$  1.2:1. Full details of analysis is provided in chapter 5.3.1.2.1 . Scale bar: 100  $\mu\text{m}$ . Note: The amplified electron shadow is an artifact of the local contrast enhancement performed in imageJ to make the particles distinguishable from the silicon substrate.

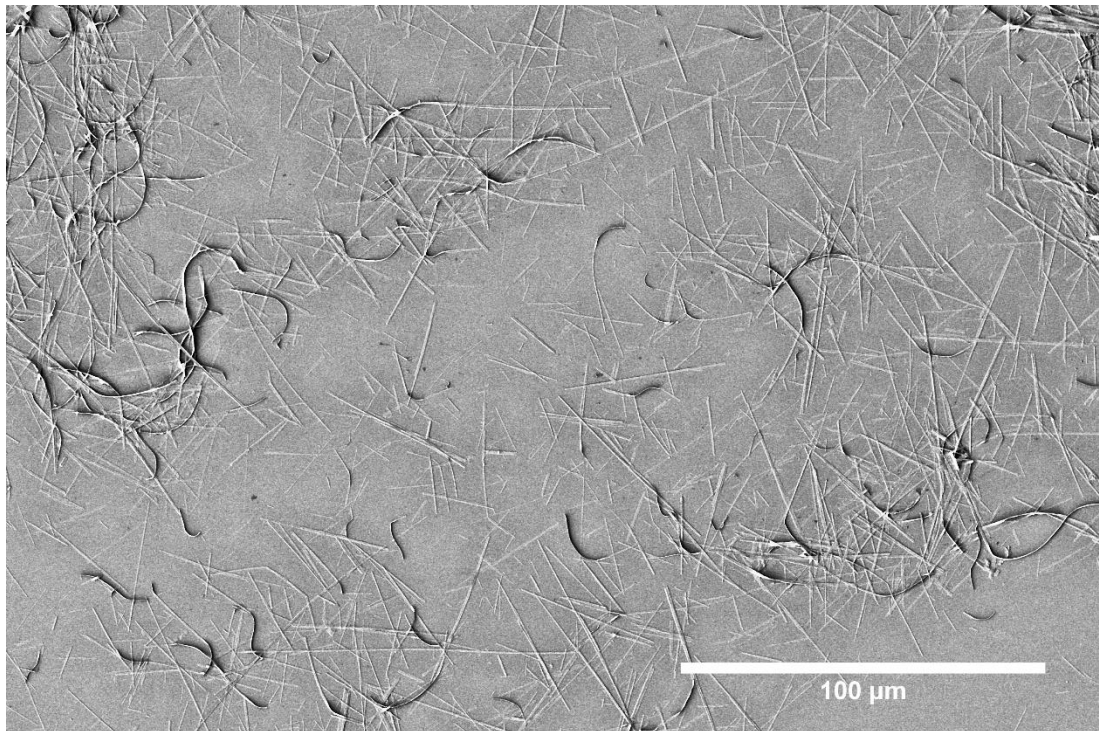


Figure 10.5: SEM micrograph of LBZA synthesised without microwave exposure ( $\sim 294$  K) using  $[\text{OH}^-]/[\text{Zn}^{2+}]$  1.4:1. Full details of analysis is provided in chapter 5.3.1.2.1 . Scale bar: 100  $\mu\text{m}$ . Note: The amplified electron shadow is an artifact of the local contrast enhancement performed in imageJ to make the particles distinguishable from the silicon substrate.

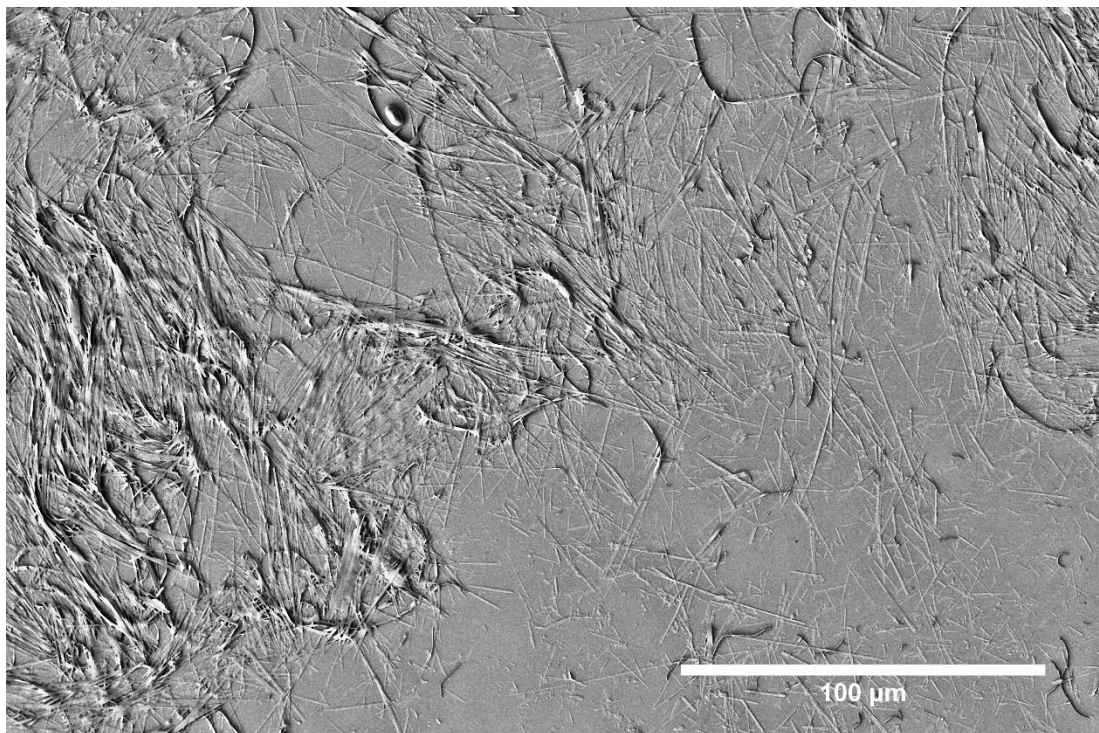
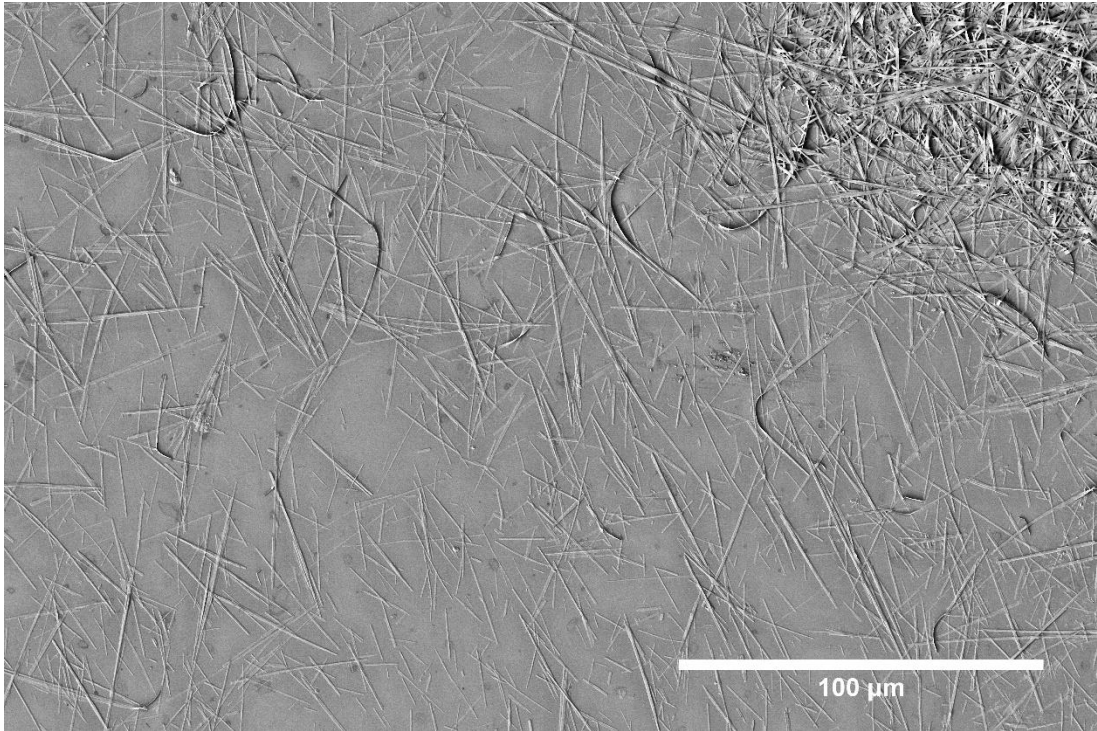
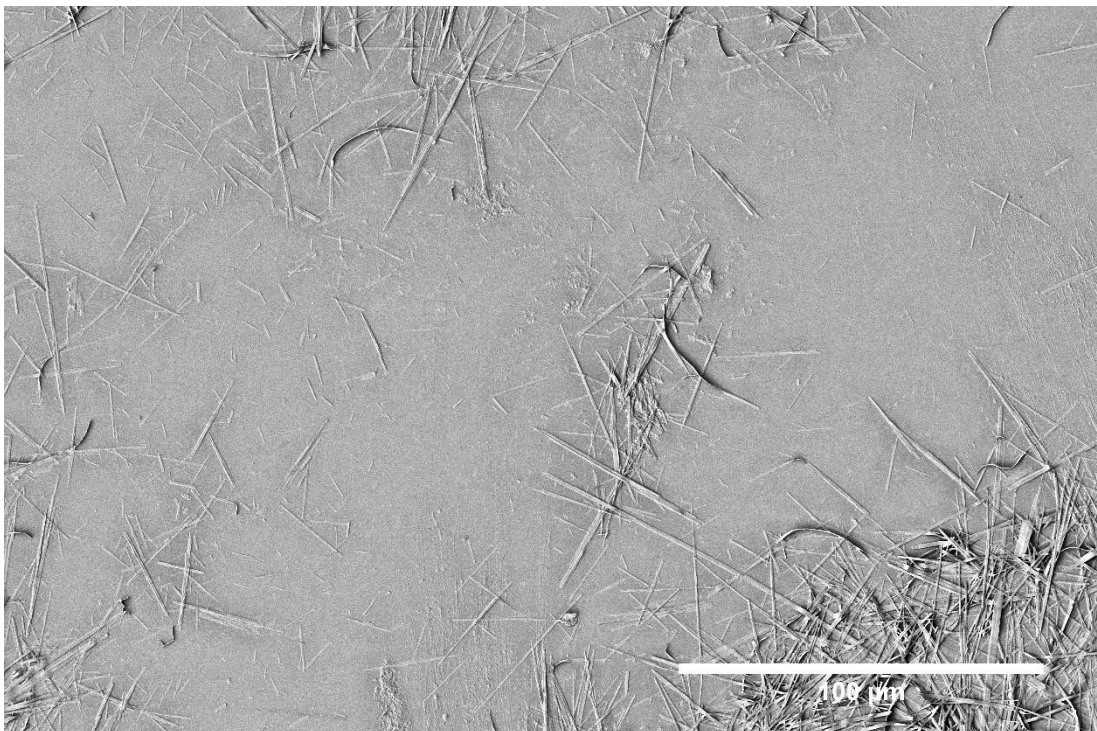


Figure 10.6: SEM micrograph of LBZA synthesised without microwave exposure ( $\sim 294$  K) using  $[\text{OH}^-]/[\text{Zn}^{2+}]$  1.44:1. Full details of analysis is provided in chapter 5.3.1.2.1 . Scale bar: 100  $\mu\text{m}$ . Note: The amplified electron shadow is an artifact of the local contrast enhancement performed in imageJ to make the particles distinguishable from the silicon substrate.



*Figure 10.7: SEM micrograph of LBZA synthesised without microwave exposure (~ 294 K) using  $[OH^-]/[Zn^{2+}]$  1.48:1. Full details of analysis is provided in chapter 5.3.1.2.1 . Scale bar: 100  $\mu m$ . Note: The amplified electron shadow is an artifact of the local contrast enhancement performed in imageJ to make the particles distinguishable from the silicon substrate.*



*Figure 10.8: SEM micrograph of LBZA synthesised without microwave exposure (~ 294 K) using  $[OH^-]/[Zn^{2+}]$  1.52:1. Full details of analysis is provided in chapter 5.3.1.2.1 . Scale bar: 100  $\mu m$ . Note: The amplified electron shadow is an artifact of the local contrast enhancement performed in imageJ to make the particles distinguishable from the silicon substrate.*

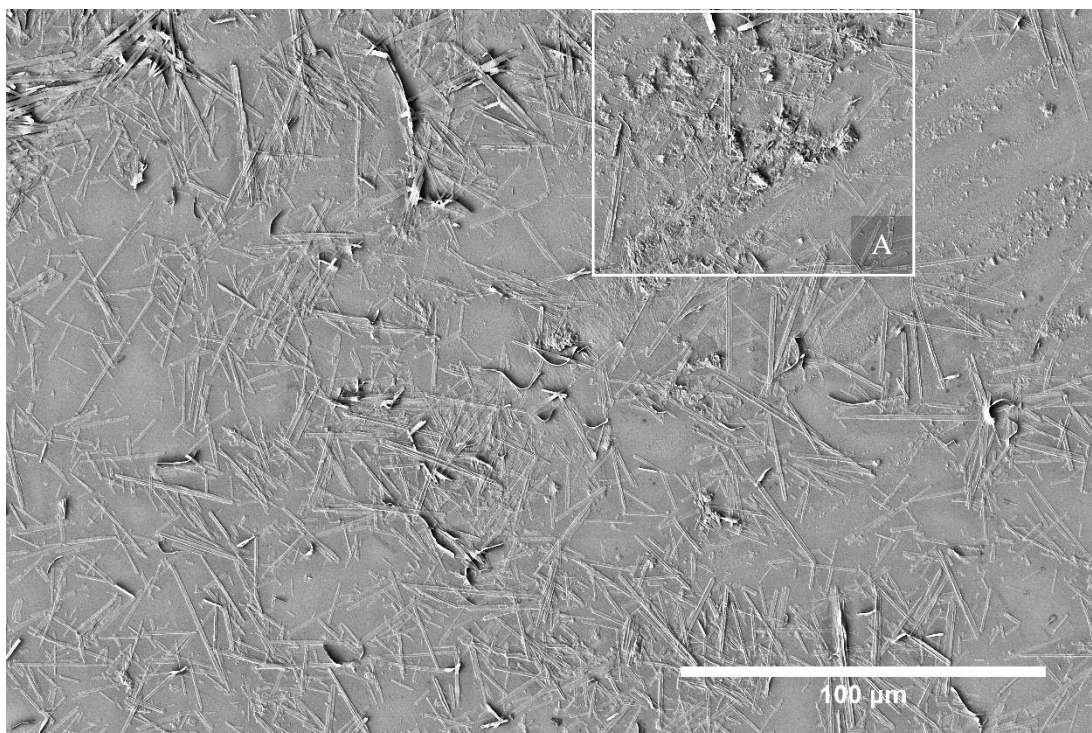


Figure 10.9: SEM micrograph of LBZA synthesised without microwave exposure ( $\sim 294$  K) using  $[\text{OH}^-]/[\text{Zn}^{2+}]$  1.56:1. Full details of analysis is provided in chapter 5.3.1.2.1 . Scale bar:  $100 \mu\text{m}$ . The small particles in the top right-hand corner are LBZA. Feature A is an area where larger LBZA particulates are forming from the smaller particles. Note: The amplified electron shadow is an artifact of the local contrast enhancement performed in imageJ to make the particles distinguishable from the silicon substrate.

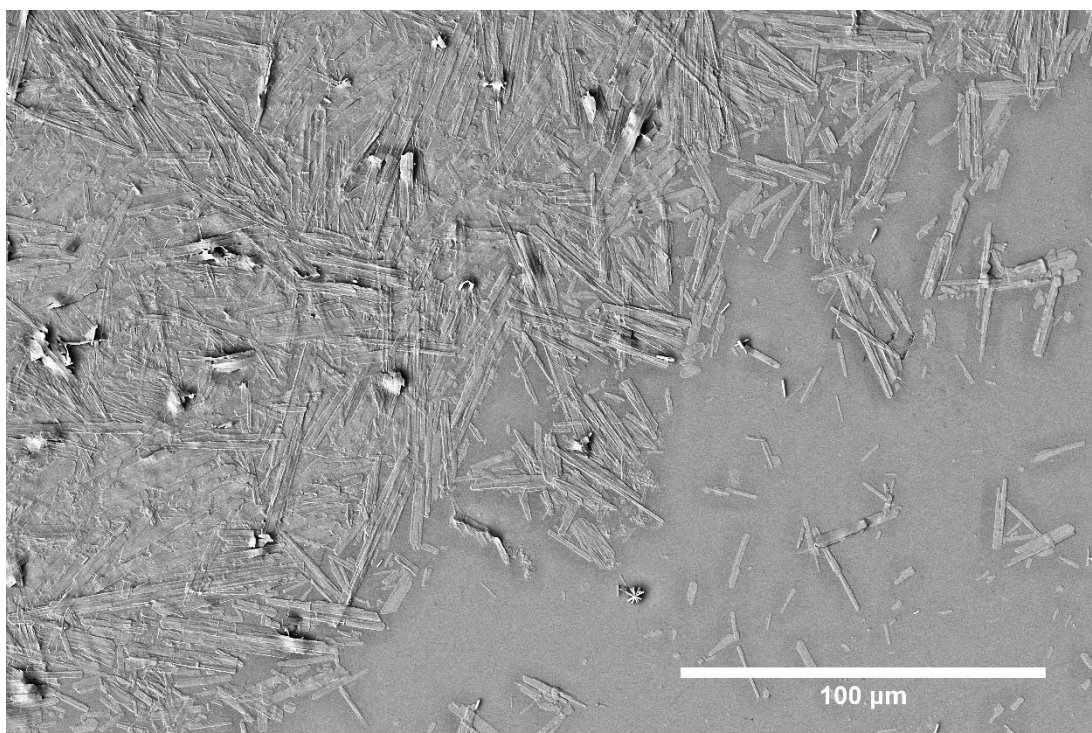
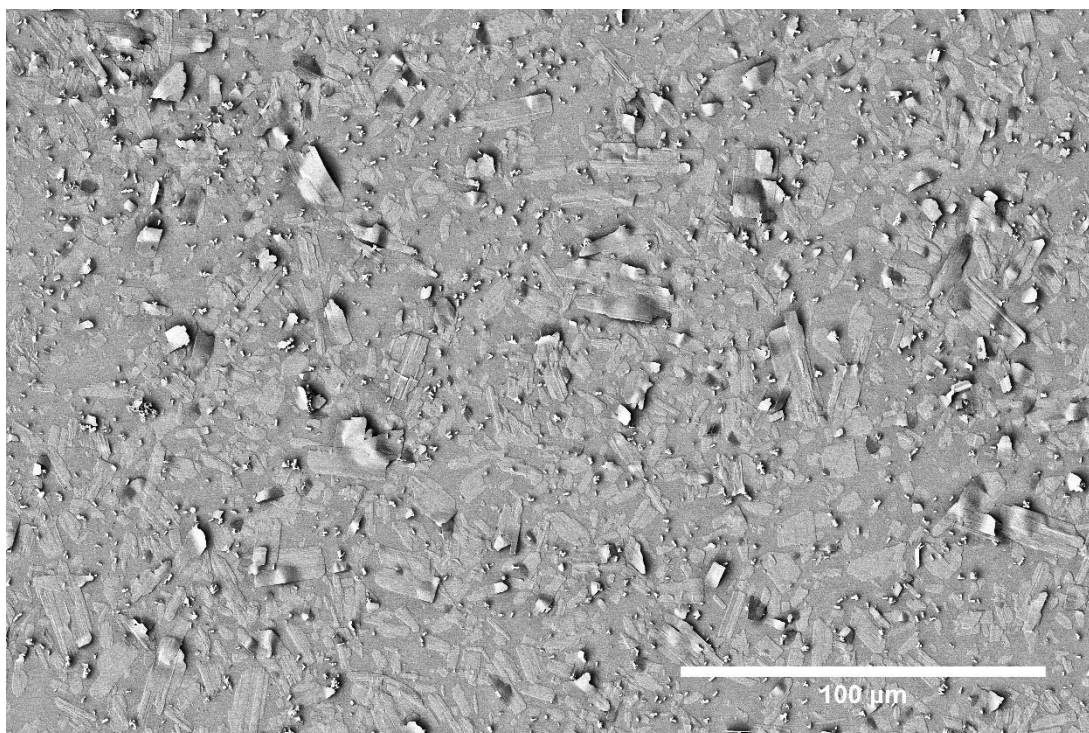
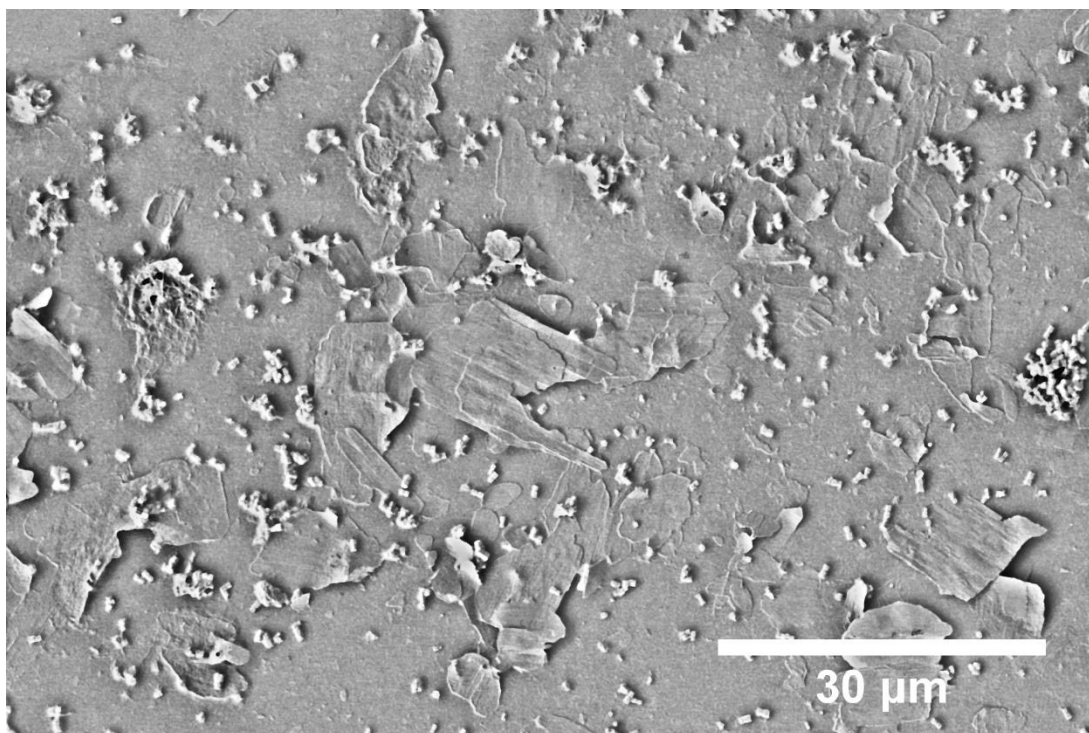


Figure 10.10: SEM micrograph of LBZA synthesised without microwave exposure ( $\sim 294$  K) using  $[\text{OH}^-]/[\text{Zn}^{2+}]$  1.6:1. Full details of analysis is provided in chapter 5.3.1.2.1 . Scale bar:  $100 \mu\text{m}$ . Note: The amplified electron shadow is an artifact of the local contrast enhancement performed in imageJ to make the particles distinguishable from the silicon substrate.



*Figure 10.11: SEM micrograph of LBZA synthesised without microwave exposure (~ 294 K) using  $[OH^-]/[Zn^{2+}]$  1.64:1. Full details of analysis is provided in chapter 5.3.1.2.1 . Small high contrast white particles are ZnO impurities. Scale bar: 100  $\mu m$ . Note: The amplified electron shadow is an artifact of the local contrast enhancement performed in imageJ to make the particles distinguishable from the silicon substrate.*



*Figure 10.12: SEM micrograph of LBZA synthesised without microwave exposure (~ 294 K) using  $[OH^-]/[Zn^{2+}]$  1.68:1. Full details of analysis is provided in chapter 5.3.1.2.1 . Smaller white particles are ZnO impurities. Scale bar: 30  $\mu m$ . Note: The amplified electron shadow is an artifact of the local contrast enhancement performed in imageJ to make the particles distinguishable from the silicon substrate.*

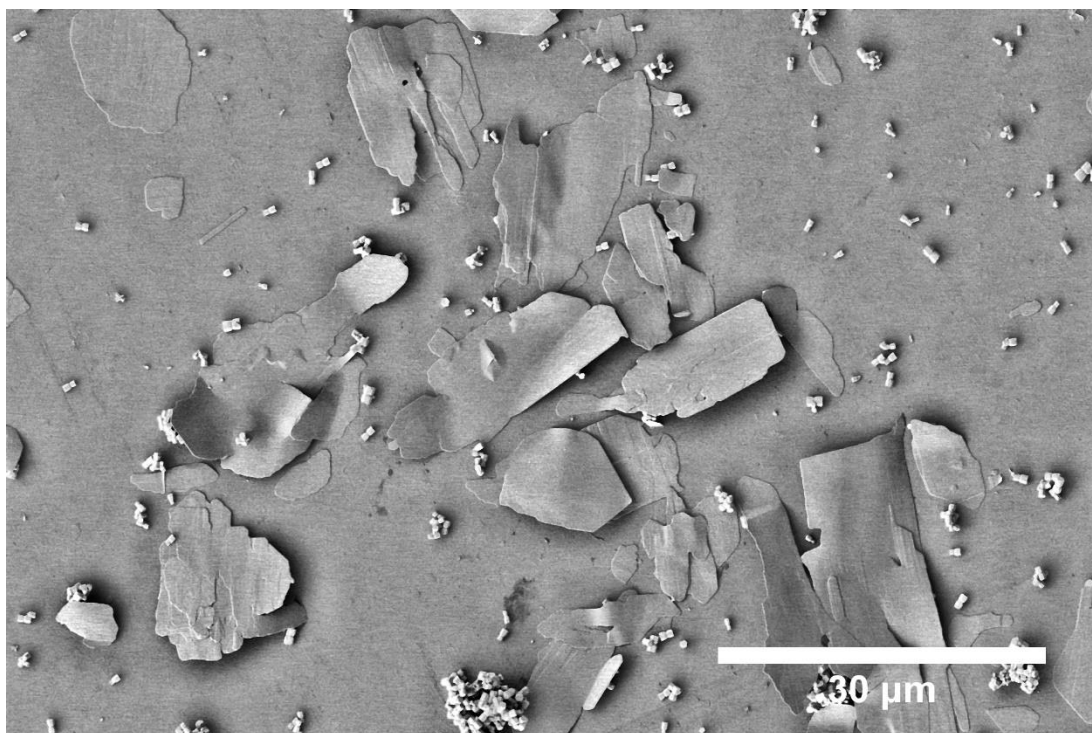


Figure 10.13: SEM micrograph of LBZA synthesised without microwave exposure ( $\sim 294$  K) using  $[\text{OH}^-]/[\text{Zn}^{2+}]$  1.72:1. Full details of analysis is provided in chapter 5.3.1.2.1 . Smaller white particles are ZnO impurities. Scale bar: 30  $\mu\text{m}$ . Note: The amplified electron shadow is an artifact of the local contrast enhancement performed in imageJ to make the particles distinguishable from the silicon substrate.

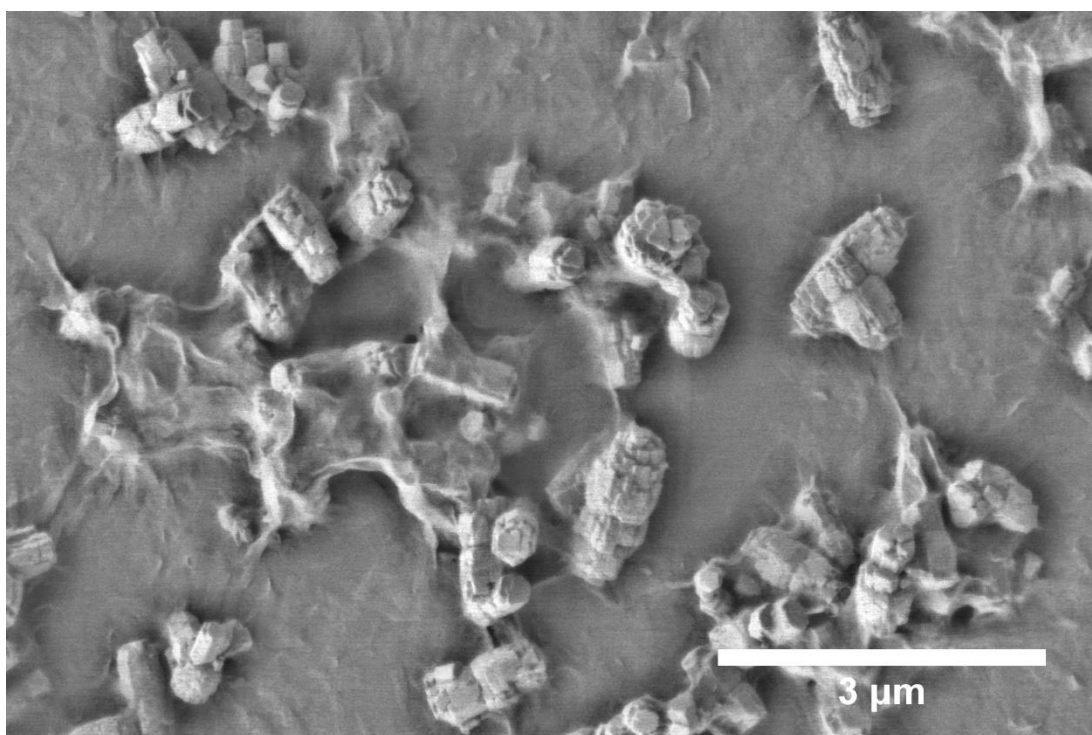


Figure 10.14: SEM micrograph of primarily ZnO impurities synthesised without microwave exposure ( $\sim 294$  K) using  $[\text{OH}^-]/[\text{Zn}^{2+}]$  1.76:1. Full details of analysis is provided in chapter 5.3.1.2.1 . The film coating is likely the so called BLBZA particles (rectangular particles) seen in the background. Scale bar: 3  $\mu\text{m}$ . Note: The amplified electron shadow is an artifact of the local contrast enhancement performed in imageJ to make the particles distinguishable from the silicon substrate.

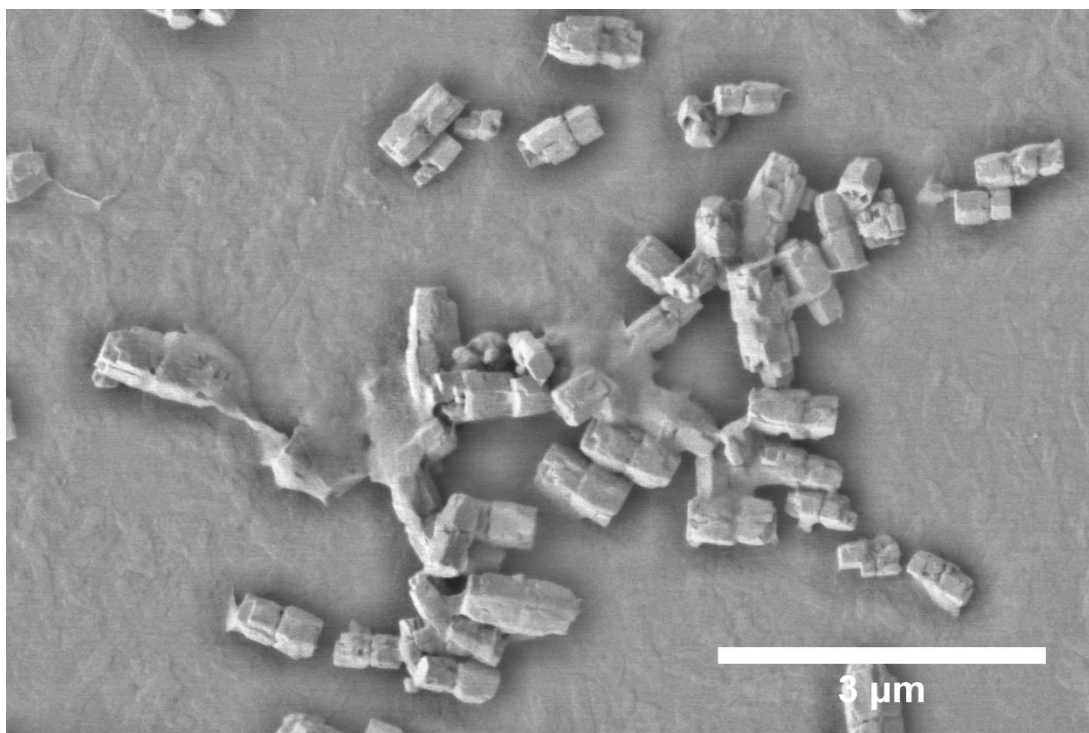


Figure 10.15: SEM micrograph of primarily ZnO impurities synthesised without microwave exposure ( $\sim 294$  K) using  $[\text{OH}^-]/[\text{Zn}^{2+}]$  1.80:1. Full details of analysis is provided in chapter 5.3.1.2.1. The film coating is likely the so called BLBZA particles (rectangular particles) seen in the background. Scale bar:  $3 \mu\text{m}$ . Note: The amplified electron shadow is an artifact of the local contrast enhancement performed in imageJ to make the particles distinguishable from the silicon substrate.

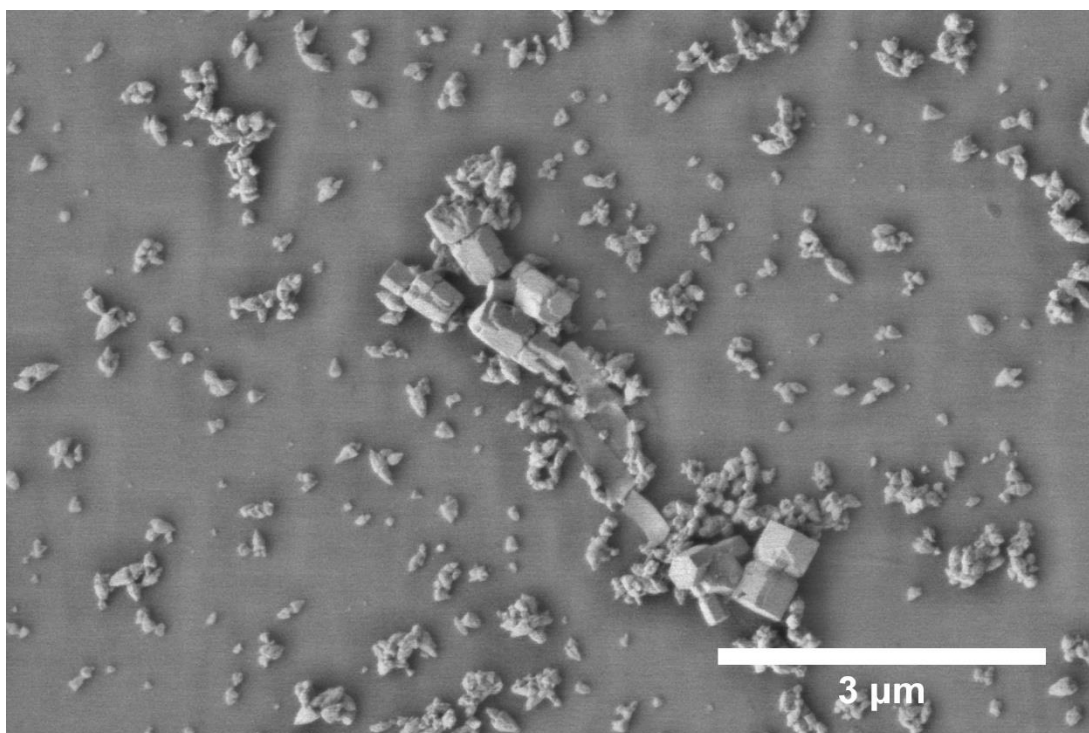
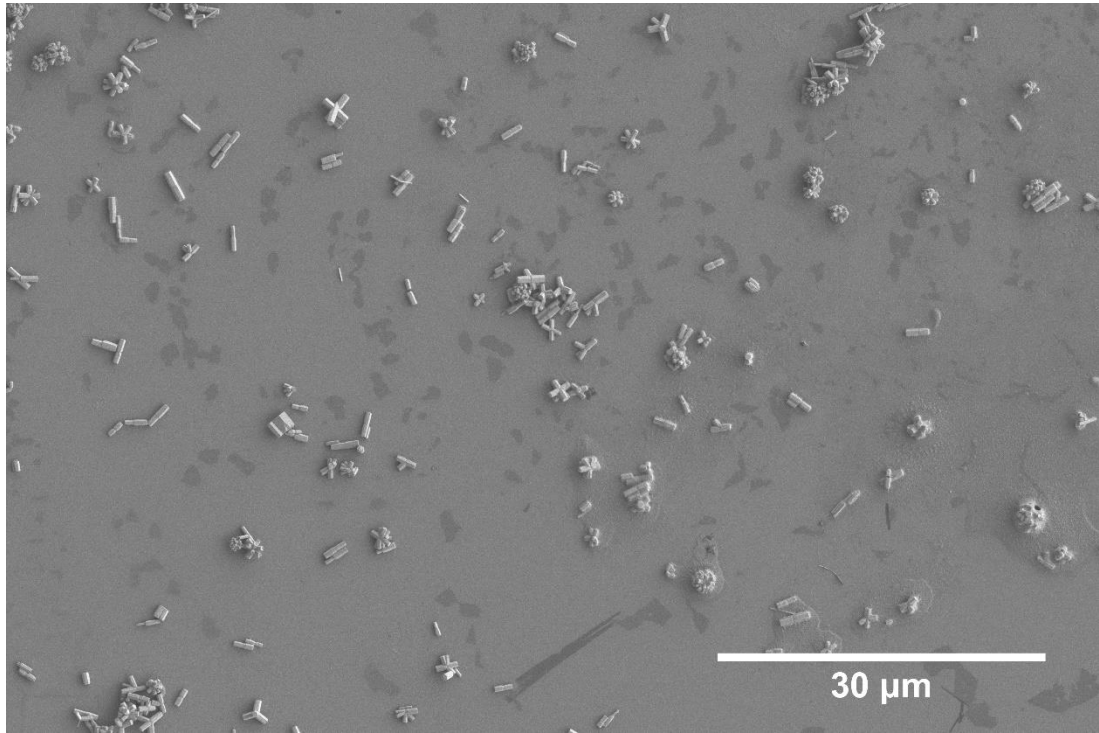


Figure 10.16: SEM micrograph of primarily ZnO impurities synthesised without microwave exposure ( $\sim 294$  K) using  $[\text{OH}^-]/[\text{Zn}^{2+}]$  1.76:1. Full details of analysis is provided in chapter 5.3.1.2.1. The film coating is likely the so called BLBZA particles (rectangular particles) seen in the background. Scale bar:  $3 \mu\text{m}$ . Note: The amplified electron shadow is an artifact of the local contrast enhancement performed in imageJ to make the particles distinguishable from the silicon substrate.

**10.1.3 10 s Microwave exposure i.e. unexposed. ( $T_{peak} = 309\text{ K}$ )**



*Figure 10.17: SEM micrograph of primarily ZnO impurities (high contrast particles) synthesised with 10 seconds of microwave exposure ( $T_{peak} = 309\text{ K}$ ) using  $[OH^-]/[Zn^{2+}]$  0.4:1. Full details of analysis is provided in chapter 5.3.1.2.1 . The darker particles are likely one of the LBZA phases seen in chapter 5.3.2 . Scale bar: 30  $\mu\text{m}$ .*



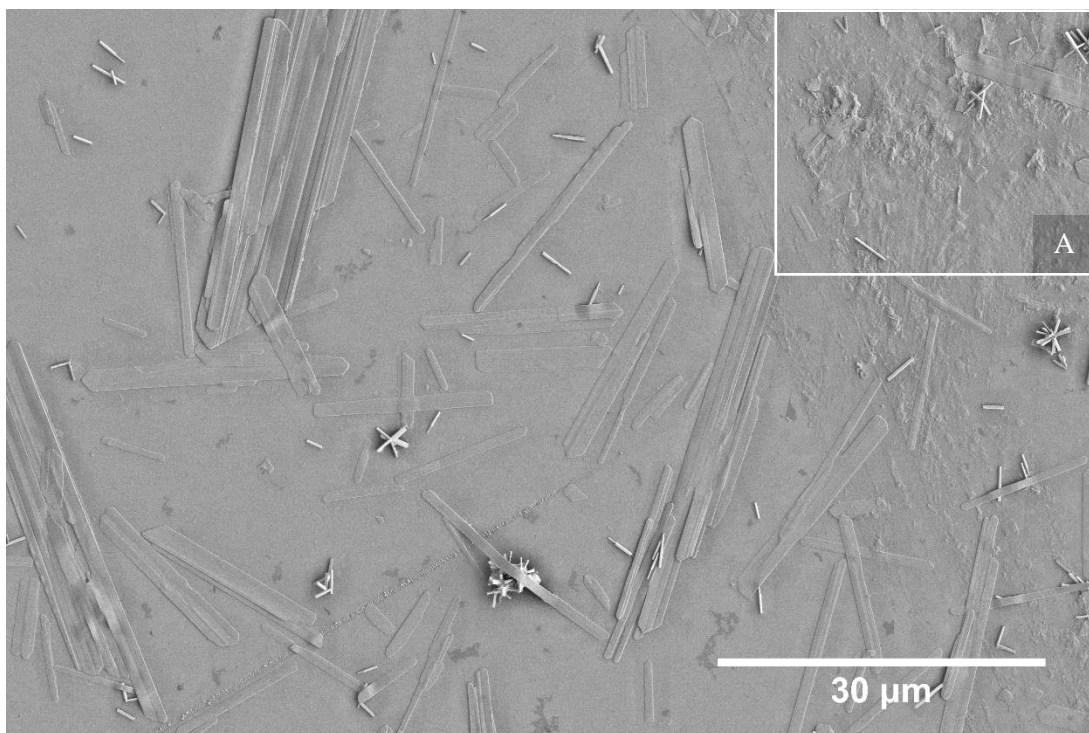


Figure 10.18: SEM micrograph of primarily LBZA (low contrast rectangular particles with pointed tips), and ZnO impurities (high contrast particles) synthesised with 10 seconds of microwave exposure ( $T_{peak}= 309\text{ K}$ ) using  $[OH^-]/[Zn^{2+}]$  0.8:1. Full details of analysis is provided in chapter 5.3.1.2.1 . The darker particles are likely one of the LBZA phases seen in chapter 5.3.2 . The small particles in the top right-hand corner are LBZA. Feature A is an area where larger LBZA particulates are forming from the smaller particles. Scale bar: 30  $\mu\text{m}$ . Note: The amplified electron shadow is an artifact of the local contrast enhancement performed in imageJ to make the particles distinguishable from the silicon substrate.

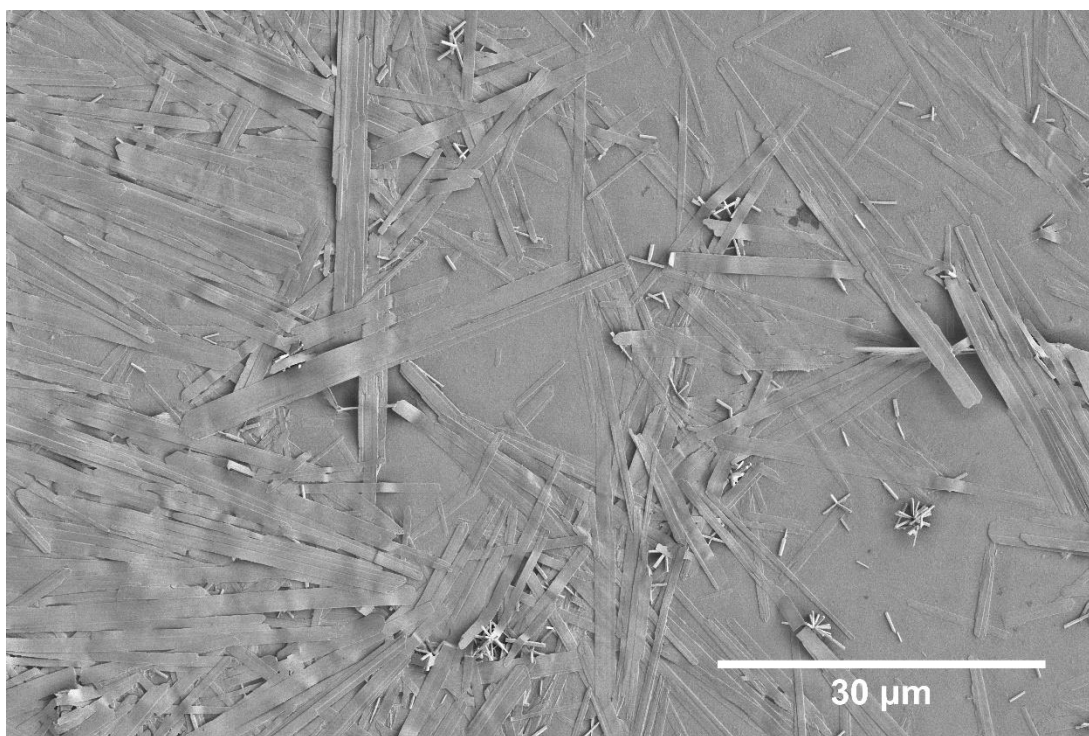


Figure 10.19: SEM micrograph of primarily LBZA (low contrast rectangular particles), and ZnO impurities (high contrast particles) synthesised with 10 seconds of microwave exposure ( $T_{peak}= 309\text{ K}$ ) using  $[OH^-]/[Zn^{2+}]$  1.2:1. Full details of analysis is provided in chapter 5.3.1.2.1 . Scale bar: 30  $\mu\text{m}$ .

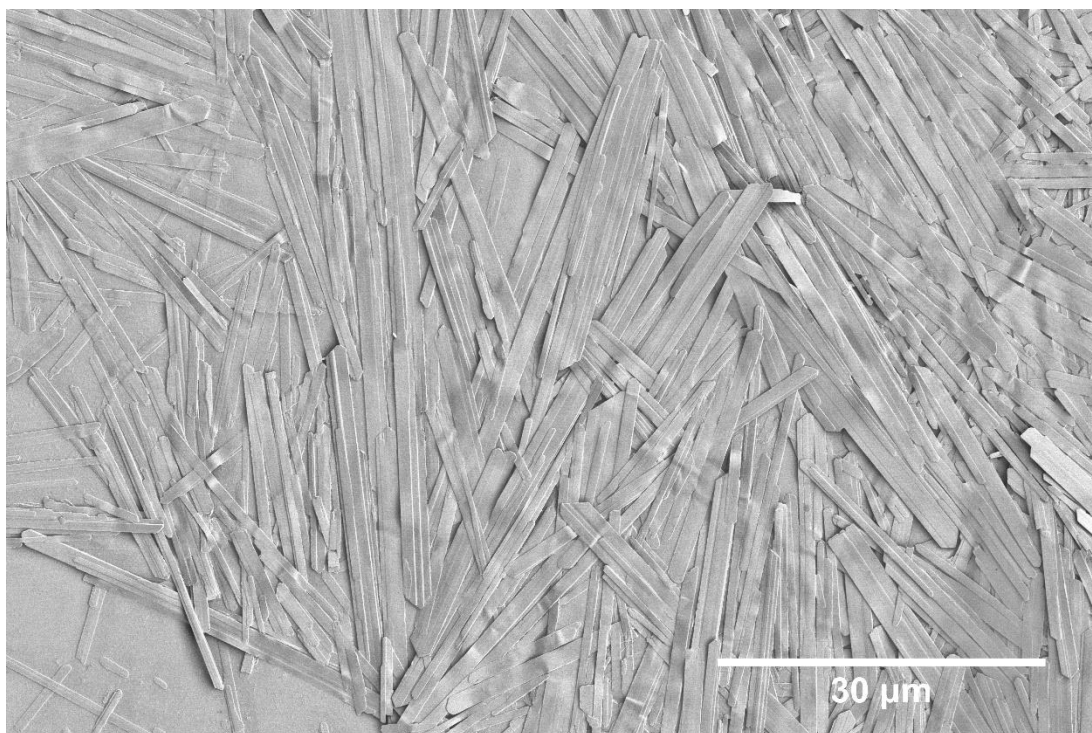


Figure 10.20: SEM micrograph of LBZA particulates (low contrast rectangular particles) synthesised with 10 seconds of microwave exposure ( $T_{peak} = 309$  K) using  $[OH^-]/[Zn^{2+}]$  1.4:1. Full details of analysis is provided in chapter 5.3.1.2.1 . Scale bar: 30  $\mu$ m.

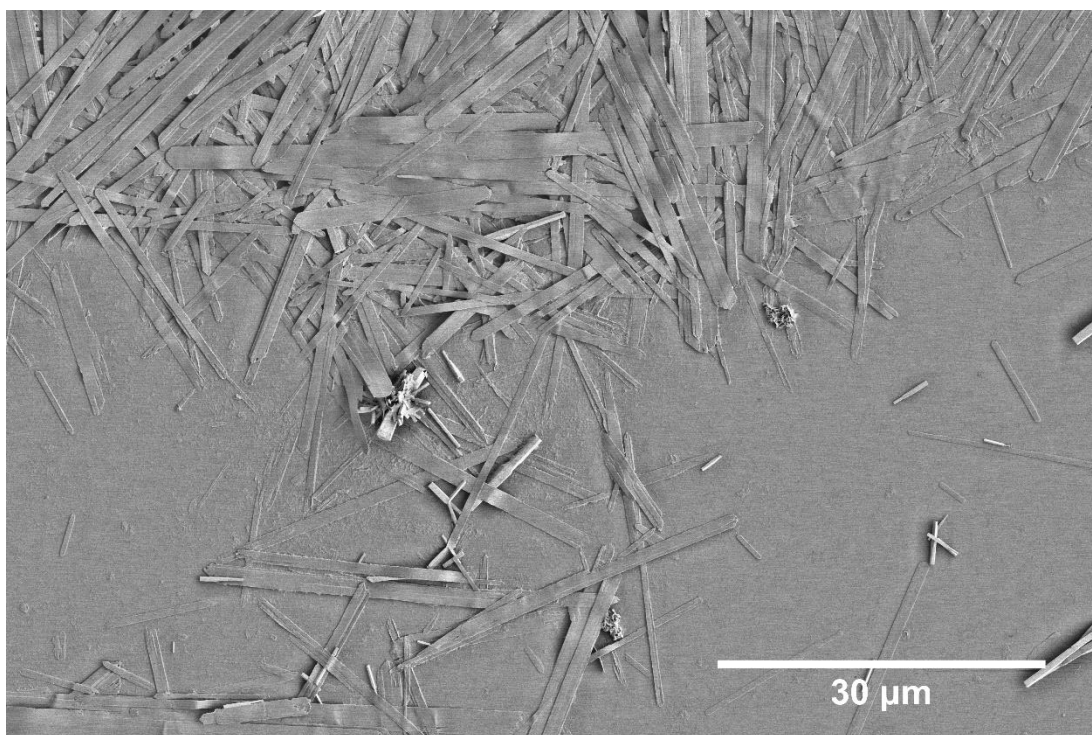


Figure 10.21: SEM micrograph of primarily LBZA (low contrast rectangular particles) and ZnO impurities (high contrast particles) synthesised with 10 seconds of microwave exposure ( $T_{peak} = 309$  K) using  $[OH^-]/[Zn^{2+}]$  1.44:1. Full details of analysis is provided in chapter 5.3.1.2.1 . Scale bar: 30  $\mu$ m. Note: The amplified electron shadow is an artifact of the local contrast enhancement performed in imageJ to make the particles distinguishable from the silicon substrate.

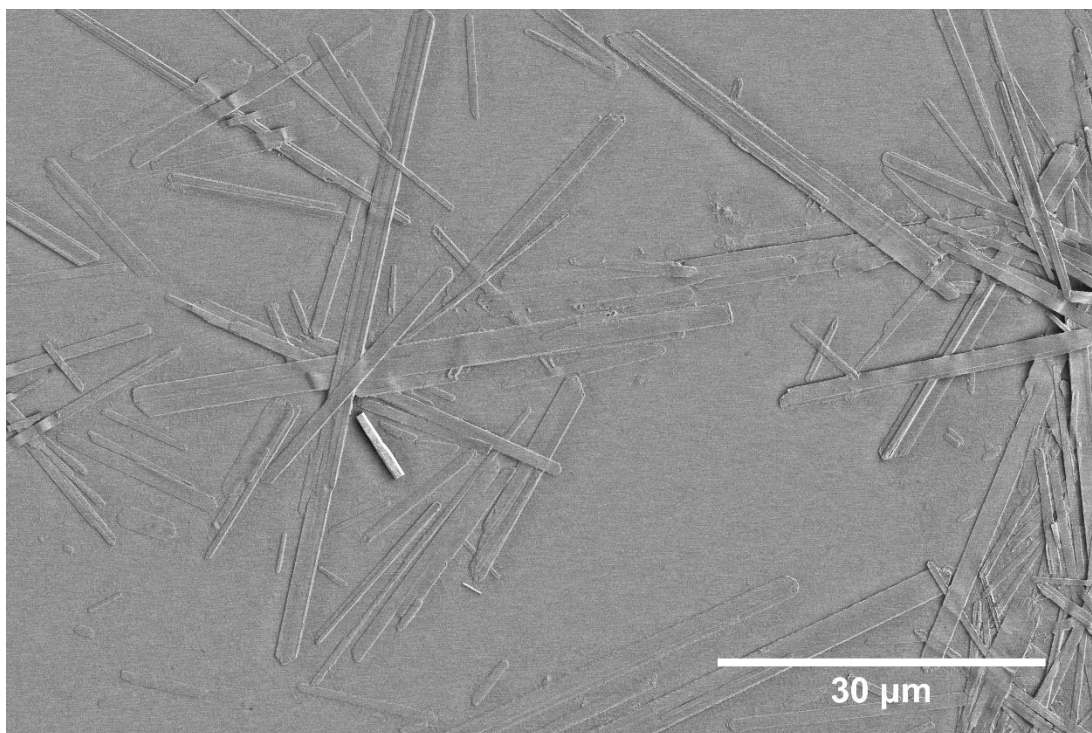


Figure 10.22: SEM micrograph of primarily LBZA (low contrast rectangular particles), and ZnO impurities (high contrast particle) synthesised with 10 seconds of microwave exposure ( $T_{peak}= 309\text{ K}$ ) using  $[OH^-]/[Zn^{2+}]$  1.48:1. Full details of analysis is provided in chapter 5.3.1.2.1 . Scale bar: 30  $\mu\text{m}$ . Note: The amplified electron shadow is an artifact of the local contrast enhancement performed in imageJ to make the particles distinguishable from the silicon substrate.

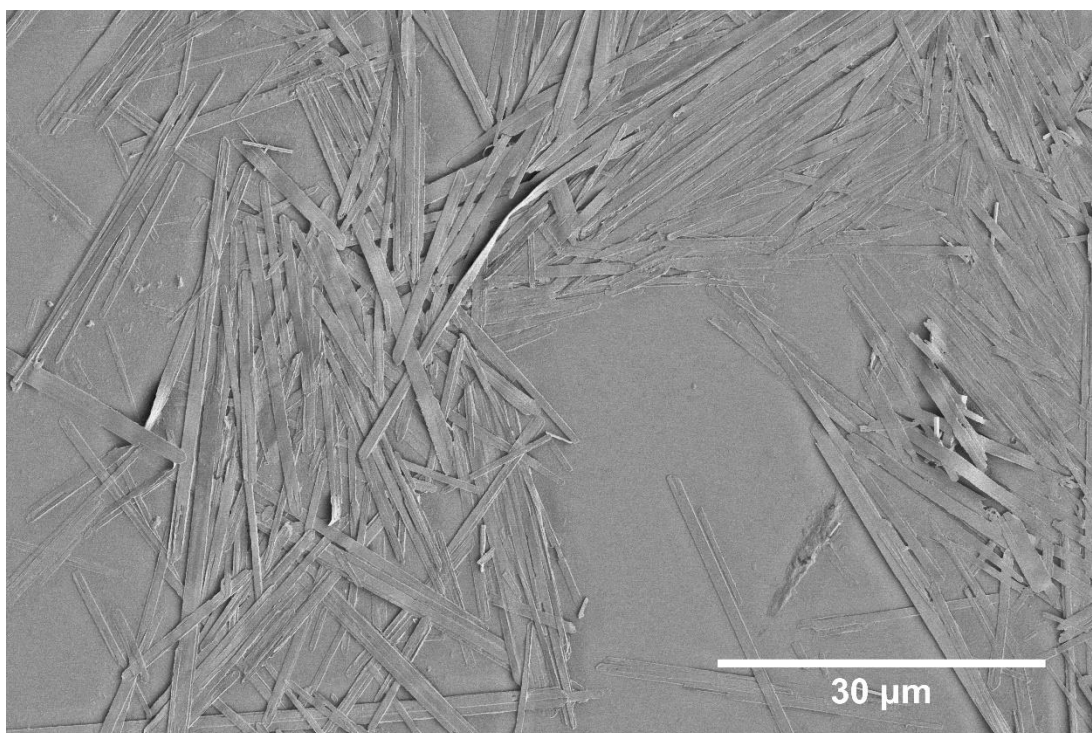


Figure 10.23: SEM micrograph of primarily LBZA (low contrast rectangular particles), and ZnO impurities (high contrast particles) synthesised with 10 seconds of microwave exposure ( $T_{peak}= 309\text{ K}$ ) using  $[OH^-]/[Zn^{2+}]$  1.52:1. Full details of analysis is provided in chapter 5.3.1.2.1 . Scale bar: 30  $\mu\text{m}$ . Note: The amplified electron shadow is an artifact of the local contrast enhancement performed in imageJ to make the particles distinguishable from the silicon substrate.

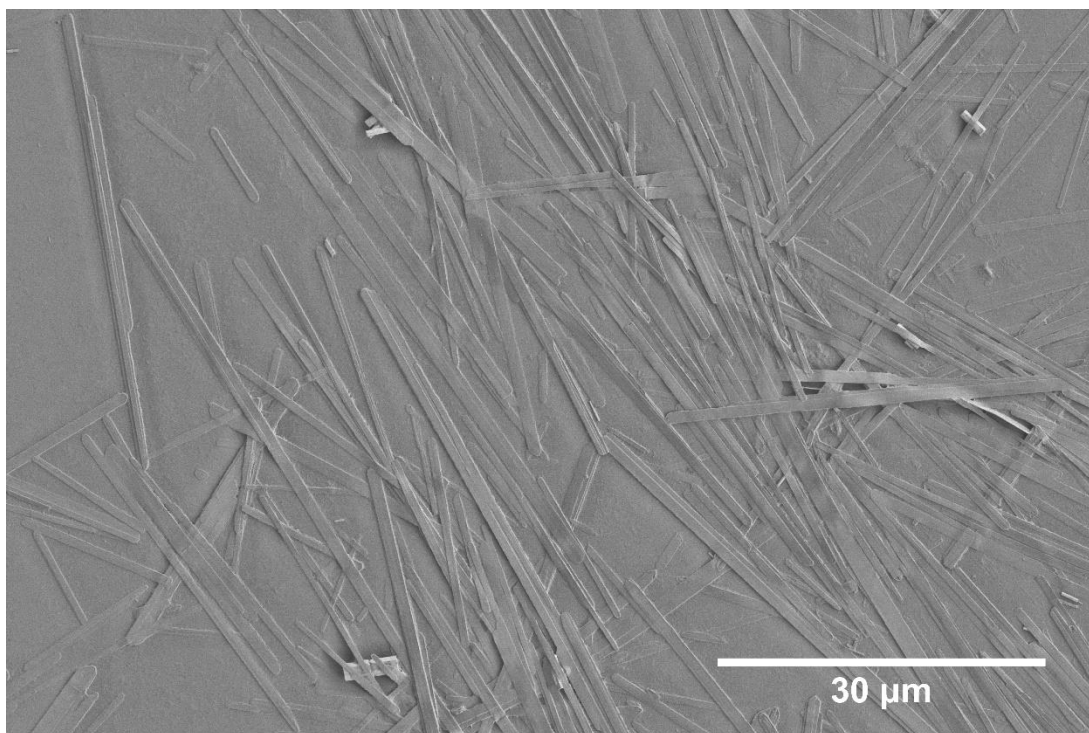


Figure 10.24: SEM micrograph of primarily LBZA (low contrast rectangular particles), and ZnO impurities (high contrast particle) synthesised with 10 seconds of microwave exposure ( $T_{peak}= 309\text{ K}$ ) using  $[OH^-]/[Zn^{2+}]$  1.56:1. Full details of analysis is provided in chapter 5.3.1.2.1 . Scale bar: 30 μm. Note: The amplified electron shadow is an artifact of the local contrast enhancement performed in imageJ to make the particles distinguishable from the silicon substrate.

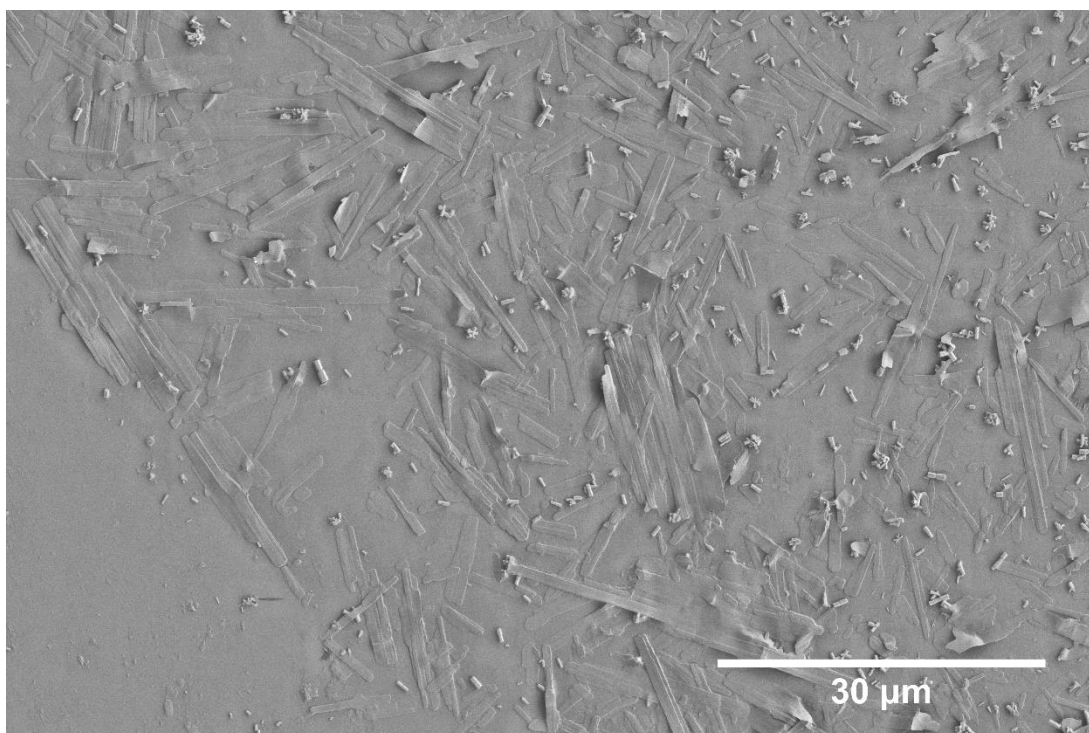


Figure 10.25: SEM micrograph of primarily LBZA (low contrast rectangular particles), and ZnO impurities (high contrast particle) synthesised with 10 seconds of microwave exposure ( $T_{peak}= 309\text{ K}$ ) using  $[OH^-]/[Zn^{2+}]$  1.60:1. Full details of analysis is provided in chapter 5.3.1.2.1 . Scale bar: 30 μm. Note: The amplified electron shadow is an artifact of the local contrast enhancement performed in imageJ to make the particles distinguishable from the silicon substrate.

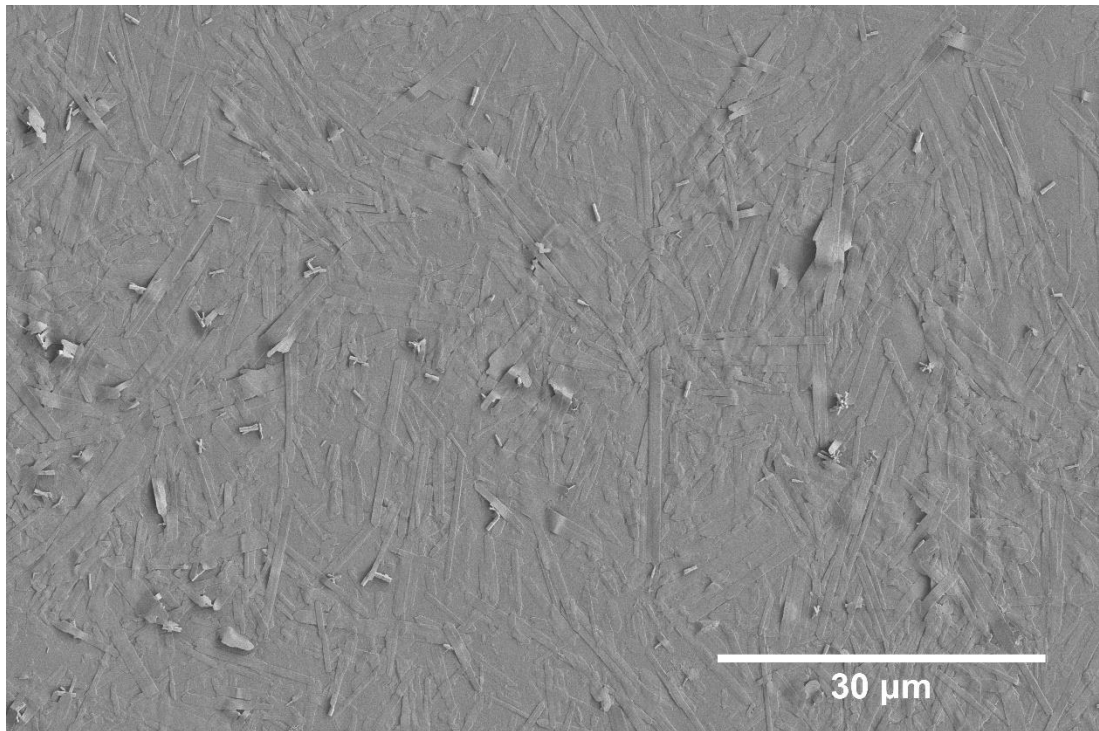


Figure 10.26: SEM micrograph of primarily LBZA (low contrast rectangular particles), and ZnO impurities (high contrast particle) synthesised with 10 seconds of microwave exposure ( $T_{peak} = 309\text{ K}$ ) using  $[OH^-]/[Zn^{2+}]$  1.64:1. Full details of analysis is provided in chapter 5.3.1.2.1 . Scale bar: 30  $\mu\text{m}$ .

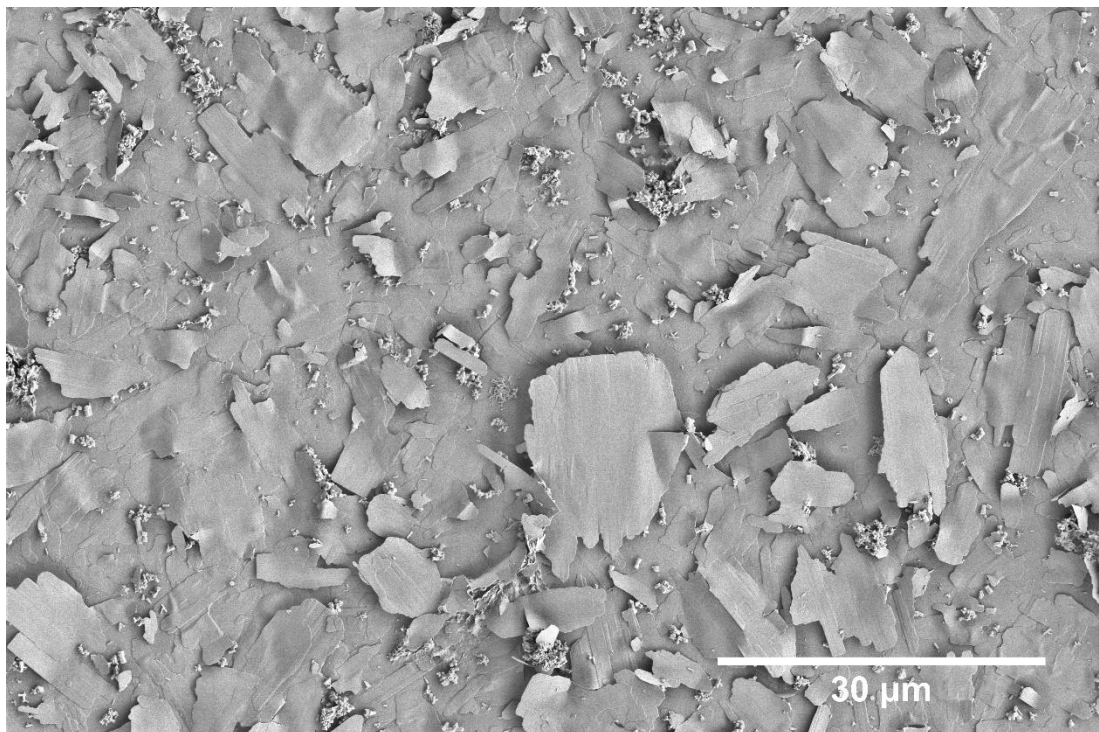


Figure 10.27: SEM micrograph of primarily LBZA (low contrast rectangular particles), and ZnO impurities (high contrast particle) synthesised with 10 seconds of microwave exposure ( $T_{peak} = 309\text{ K}$ ) using  $[OH^-]/[Zn^{2+}]$  1.68:1. Full details of analysis is provided in chapter 5.3.1.2.1 . Scale bar: 30  $\mu\text{m}$ . Note: The amplified electron shadow is an artifact of the local contrast enhancement performed in imageJ to make the particles distinguishable from the silicon substrate.

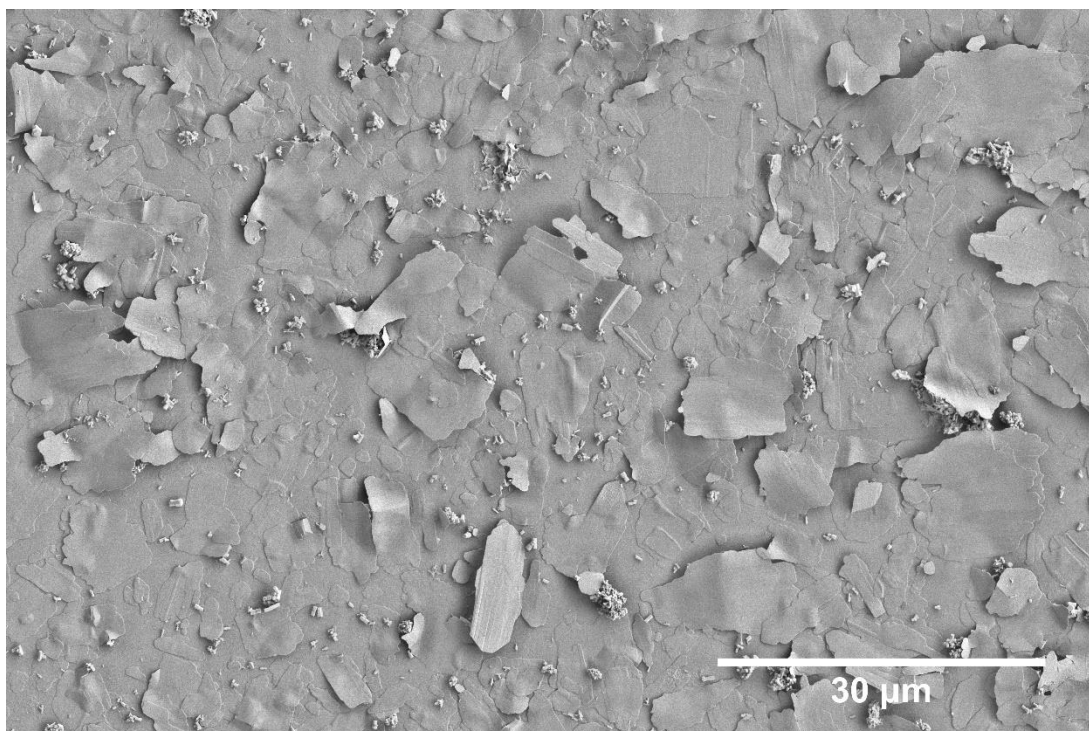


Figure 10.28: SEM micrograph of primarily LBZA (low contrast rectangular particles), and ZnO impurities (high contrast particle) synthesised with 10 seconds of microwave exposure ( $T_{peak} = 309$  K) using  $[OH^-]/[Zn^{2+}]$  1.72:1. Full details of analysis is provided in chapter 5.3.1.2.1 . Scale bar: 30  $\mu$ m. Note: The amplified electron shadow is an artifact of the local contrast enhancement performed in imageJ to make the particles distinguishable from the silicon substrate.

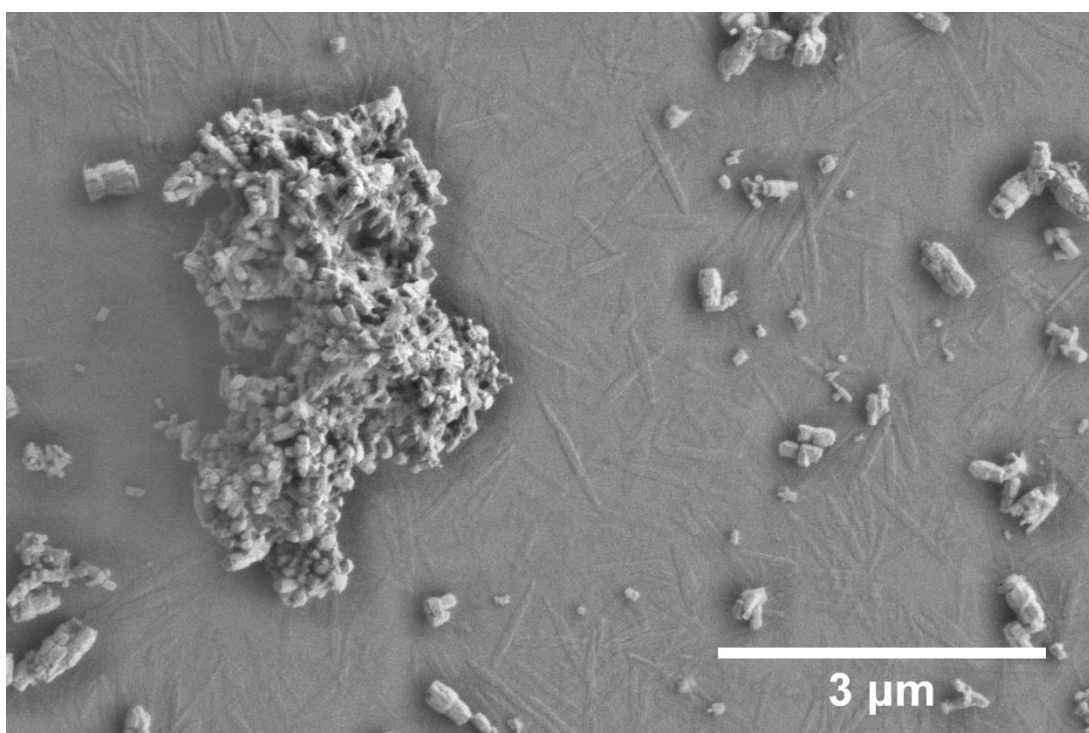


Figure 10.29: SEM micrograph of primarily ZnO impurities synthesised without microwave exposure ( $T_{peak} = 309$  K) using  $[OH^-]/[Zn^{2+}]$  1.76:1. Full details of analysis is provided in chapter 5.3.1.2.1 . The rectangular particles seen in the background are the so called BLBZA particles. Scale bar: 3  $\mu$ m. Note: The amplified electron shadow is an artifact of the local contrast enhancement performed in imageJ to make the particles distinguishable from the silicon substrate.

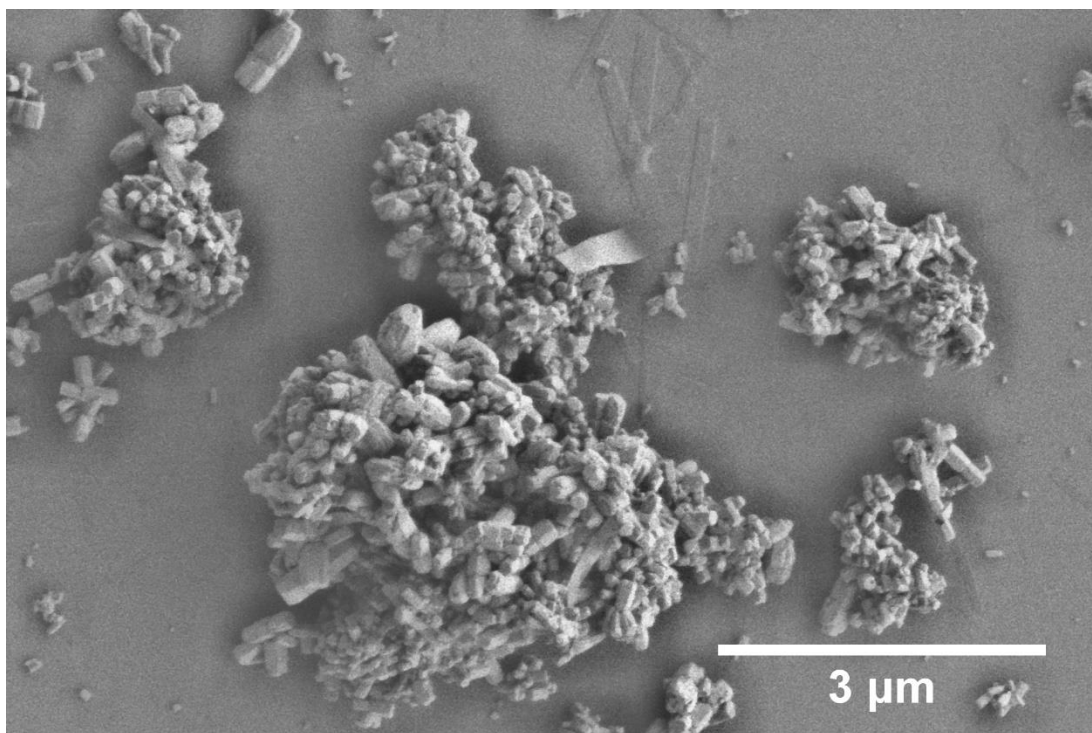


Figure 10.30: SEM micrograph of primarily ZnO impurities synthesised without microwave exposure ( $T_{peak} = 309$  K) using  $[OH^-]/[Zn^{2+}]$  1.80:1. Full details of analysis is provided in chapter 5.3.1.2.1 . The rectangular particles seen in the background are the so called BLBZA particles. Scale bar: 3 µm. Note: The amplified electron shadow is an artifact of the local contrast enhancement performed in imageJ to make the particles distinguishable from the silicon substrate.

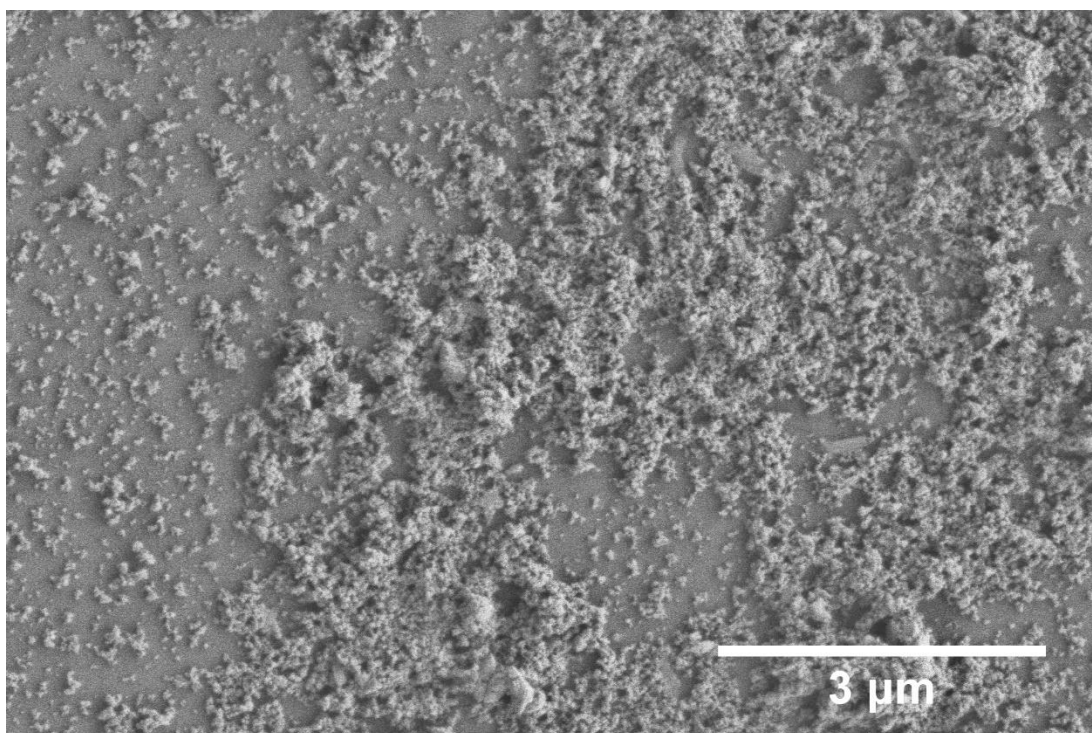
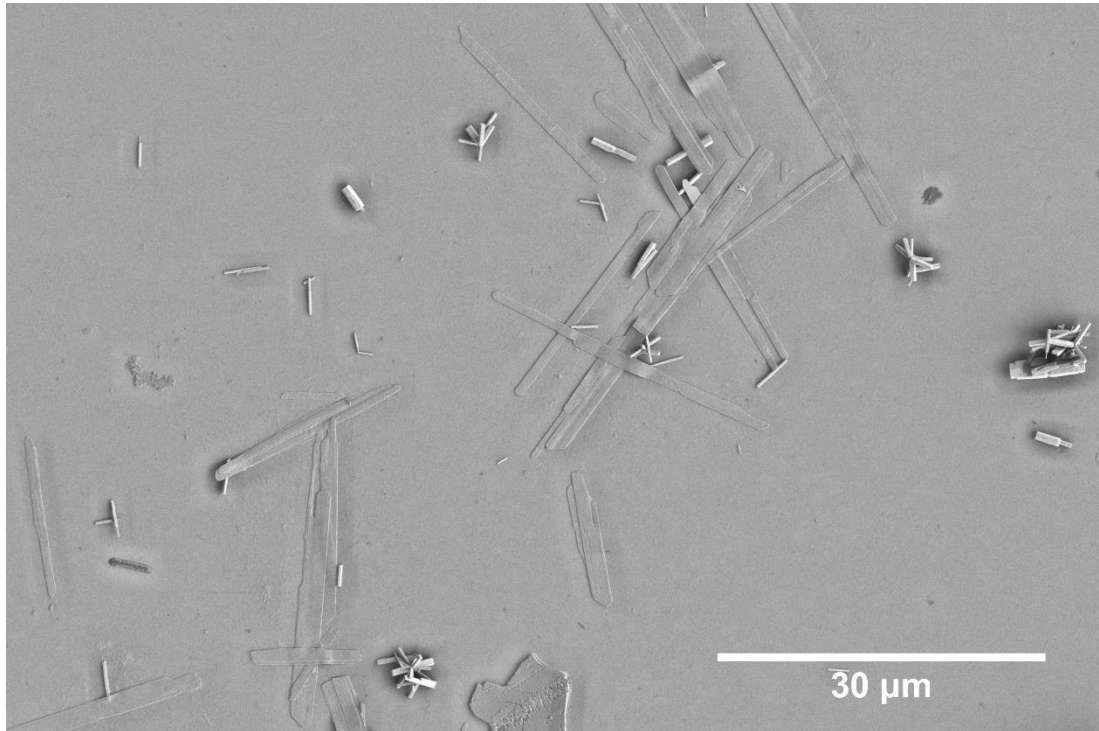


Figure 10.31: SEM micrograph of primarily ZnO impurities synthesised without microwave exposure ( $T_{peak} = 309$  K) using  $[OH^-]/[Zn^{2+}]$  1.76:1. Full details of analysis is provided in chapter 5.3.1.2.1 . Scale bar: 3 µm. Note: The amplified electron shadow is an artifact of the local contrast enhancement performed in imageJ to make the particles distinguishable from the silicon substrate.

**10.1.4 20 s Microwave exposure i.e. unexposed. ( $T_{\text{peak}} = 327 \text{ K}$ )**



*Figure 10.32: SEM micrograph of primarily LBZA (low contrast rectangular particles), and ZnO impurities (high contrast particles) synthesised with 20 seconds of microwave exposure ( $T_{\text{peak}} = 327 \text{ K}$ ) using  $[\text{OH}^-]/[\text{Zn}^{2+}]$  0.4:1. Full details of analysis is provided in chapter 5.3.1.2.1 . The darker particles are likely one of the LBZA phases seen in chapter 5.3.2 . Scale bar: 30  $\mu\text{m}$ . Note: The amplified electron shadow is an artifact of the local contrast enhancement performed in imageJ to make the particles distinguishable from the silicon substrate.*



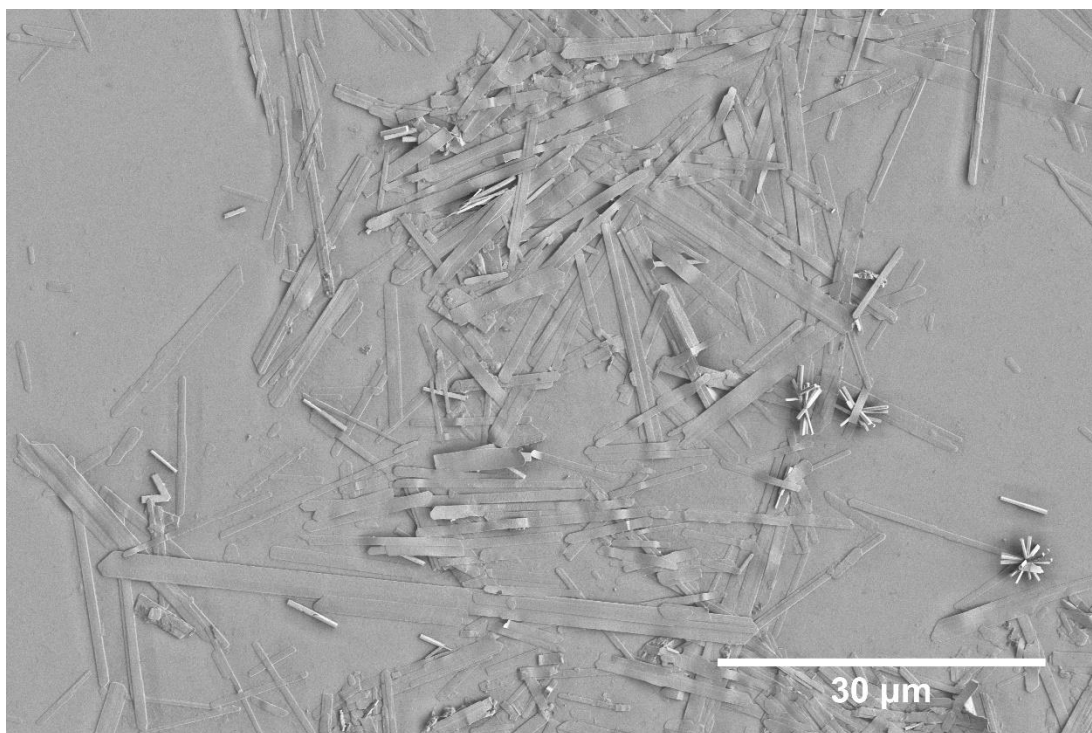


Figure 10.33: SEM micrograph of primarily LBZA (low contrast rectangular particles), and ZnO impurities (high contrast particles) synthesised with 20 seconds of microwave exposure ( $T_{peak}= 327\text{ K}$ ) using  $[OH^-]/[Zn^{2+}]$  0.8:1. Full details of analysis is provided in chapter 5.3.1.2.1 . Scale bar: 30  $\mu\text{m}$ . Note: The amplified electron shadow is an artifact of the local contrast enhancement performed in imageJ to make the particles distinguishable from the silicon substrate.

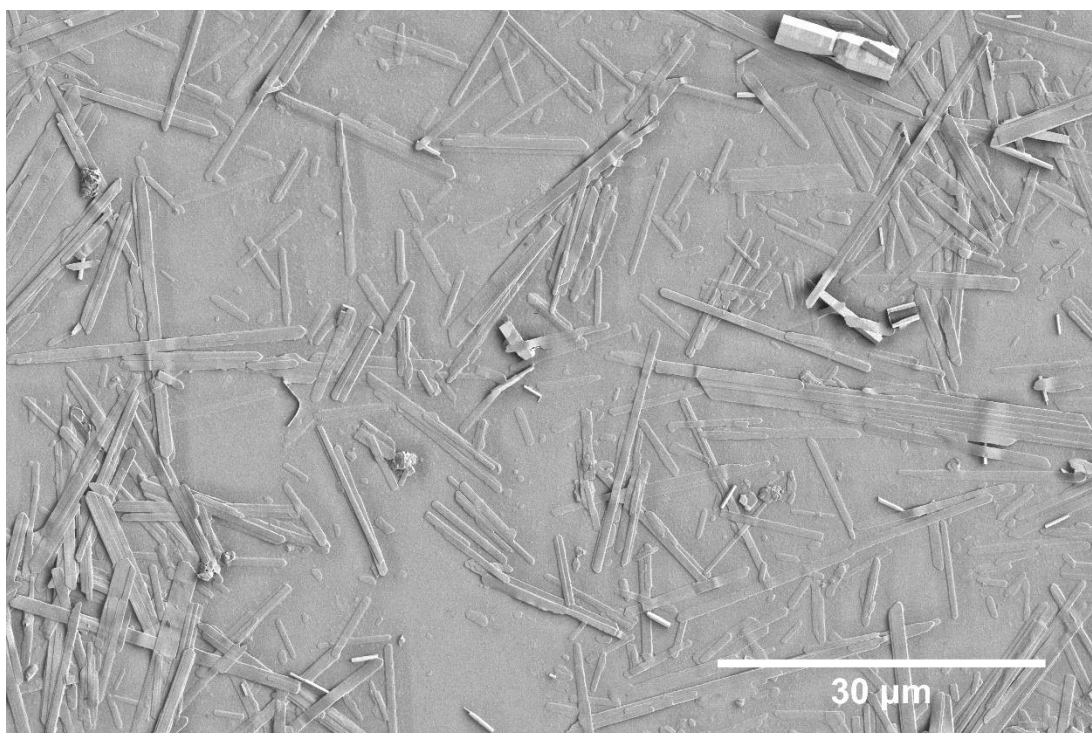


Figure 10.34: SEM micrograph of primarily LBZA (low contrast rectangular particles), and ZnO impurities (high contrast particles) synthesised with 20 seconds of microwave exposure ( $T_{peak}= 327\text{ K}$ ) using  $[OH^-]/[Zn^{2+}]$  1.2:1. Full details of analysis is provided in chapter 5.3.1.2.1 . Scale bar: 30  $\mu\text{m}$ . Note: The amplified electron shadow is an artifact of the local contrast enhancement performed in imageJ to make the particles distinguishable from the silicon substrate.

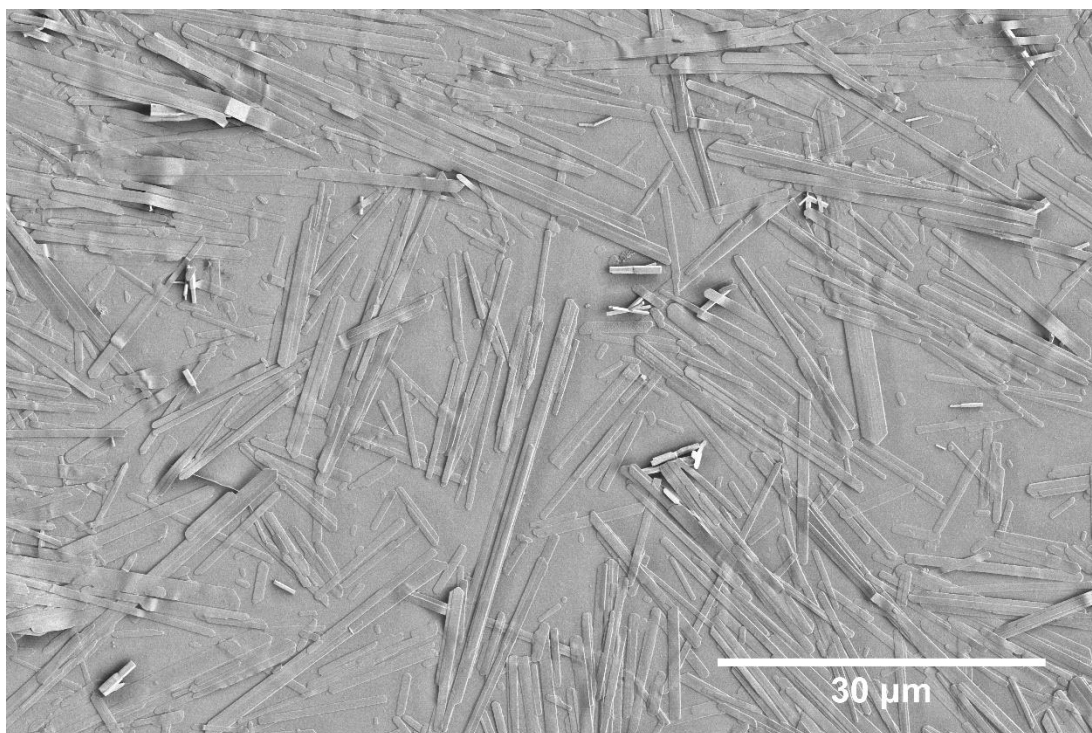


Figure 10.35: SEM micrograph of primarily LBZA (low contrast rectangular particles), and ZnO impurities (high contrast particles) synthesised with 20 seconds of microwave exposure ( $T_{peak}= 327\text{ K}$ ) using  $[OH^-]/[Zn^{2+}]$  1.4:1. Full details of analysis is provided in chapter 5.3.1.2.1 . Scale bar: 30  $\mu\text{m}$ .

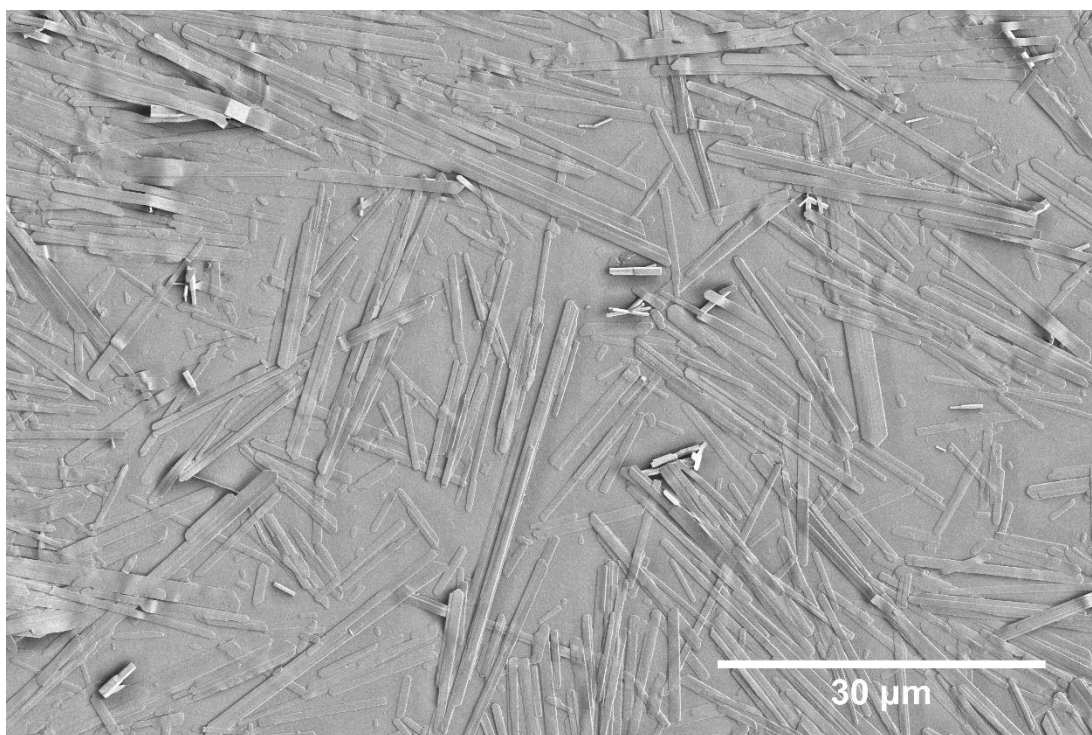


Figure 10.36: SEM micrograph of primarily LBZA (low contrast rectangular particles), and ZnO impurities (high contrast particles) synthesised with 20 seconds of microwave exposure ( $T_{peak}= 327\text{ K}$ ) using  $[OH^-]/[Zn^{2+}]$  1.44:1. Full details of analysis is provided in chapter 5.3.1.2.1 . Scale bar: 30  $\mu\text{m}$ .

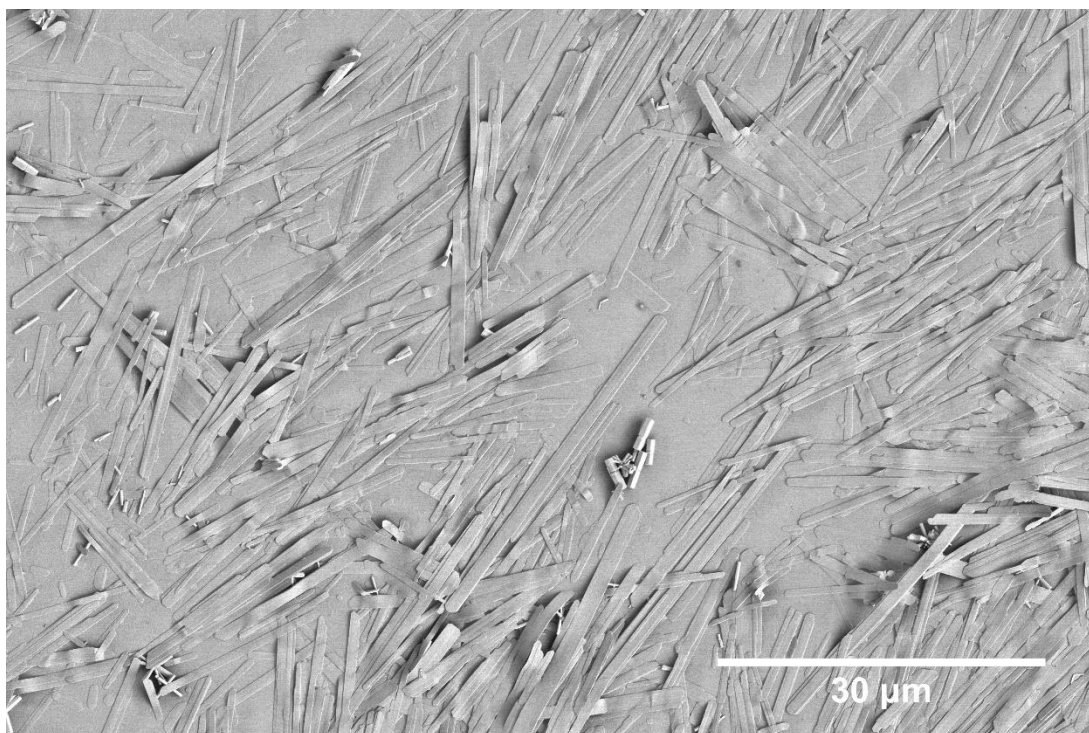


Figure 10.37: SEM micrograph of primarily LBZA (low contrast rectangular particles), and ZnO impurities (high contrast particles) synthesised with 20 seconds of microwave exposure ( $T_{peak}= 327$  K) using  $[OH^-]/[Zn^{2+}]$  1.48:1. Full details of analysis is provided in chapter 5.3.1.2.1 . Scale bar: 30  $\mu$ m. Note: The amplified electron shadow is an artifact of the local contrast enhancement performed in imageJ to make the particles distinguishable from the silicon substrate.

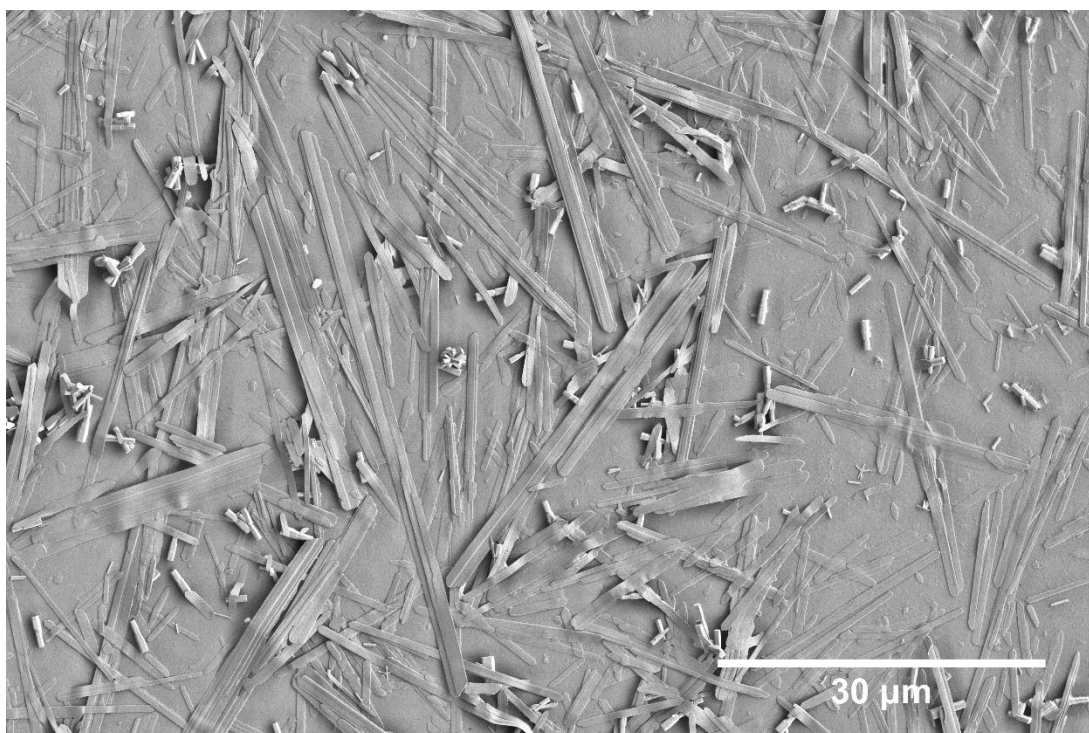


Figure 10.38: SEM micrograph of primarily LBZA (low contrast rectangular particles), and ZnO impurities (high contrast particles) synthesised with 20 seconds of microwave exposure ( $T_{peak}= 327$  K) using  $[OH^-]/[Zn^{2+}]$  1.52:1. Full details of analysis is provided in chapter 5.3.1.2.1 . Scale bar: 30  $\mu$ m. Note: The amplified electron shadow is an artifact of the local contrast enhancement performed in imageJ to make the particles distinguishable from the silicon substrate.

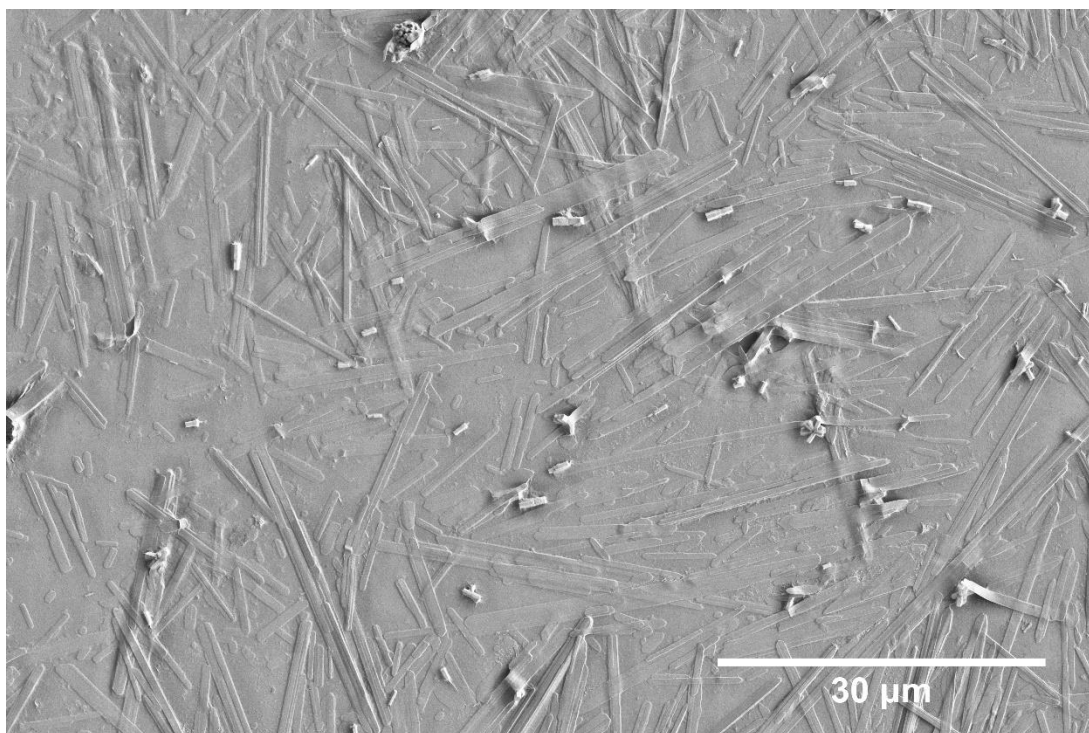


Figure 10.39: SEM micrograph of primarily LBZA (low contrast rectangular particles), and ZnO impurities (high contrast particles) synthesised with 20 seconds of microwave exposure ( $T_{peak}= 327\text{ K}$ ) using  $[OH^-]/[Zn^{2+}]$  1.56:1. Full details of analysis is provided in chapter 5.3.1.2.1 . Scale bar: 30  $\mu\text{m}$ . Note: The amplified electron shadow is an artifact of the local contrast enhancement performed in imageJ to make the particles distinguishable from the silicon substrate.

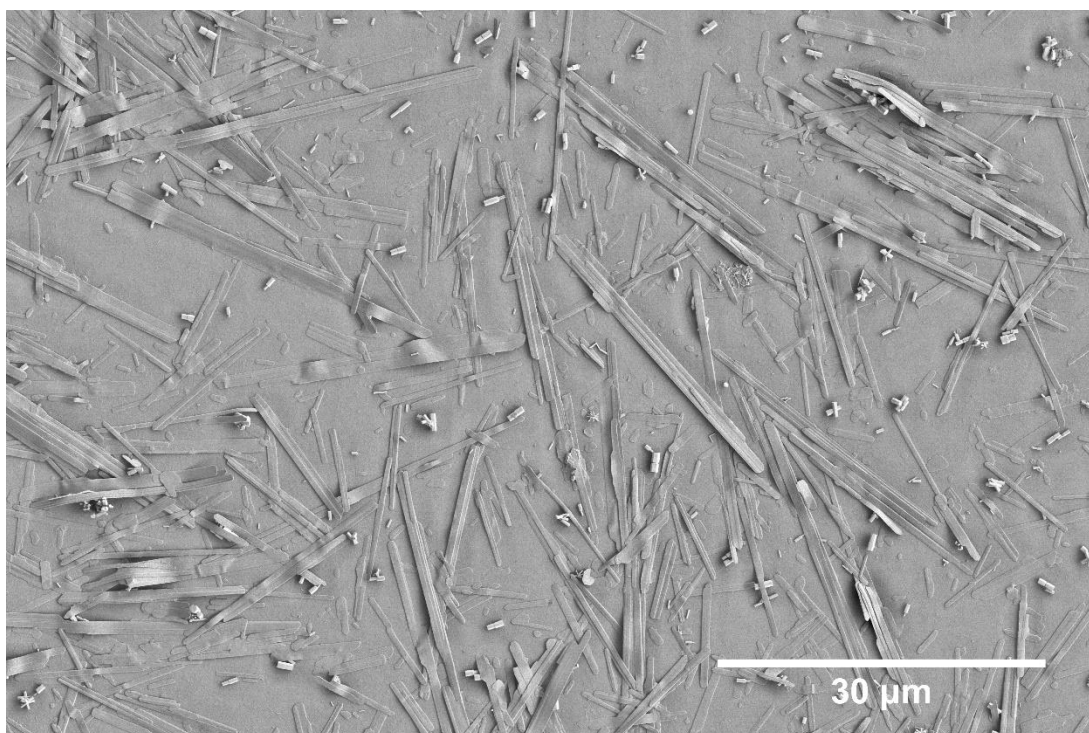


Figure 10.40: SEM micrograph of primarily LBZA (low contrast rectangular particles), and ZnO impurities (high contrast particles) synthesised with 20 seconds of microwave exposure ( $T_{peak}= 327\text{ K}$ ) using  $[OH^-]/[Zn^{2+}]$  1.6:1. Full details of analysis is provided in chapter 5.3.1.2.1 . Scale bar: 30  $\mu\text{m}$ . Note: The amplified electron shadow is an artifact of the local contrast enhancement performed in imageJ to make the particles distinguishable from the silicon substrate.

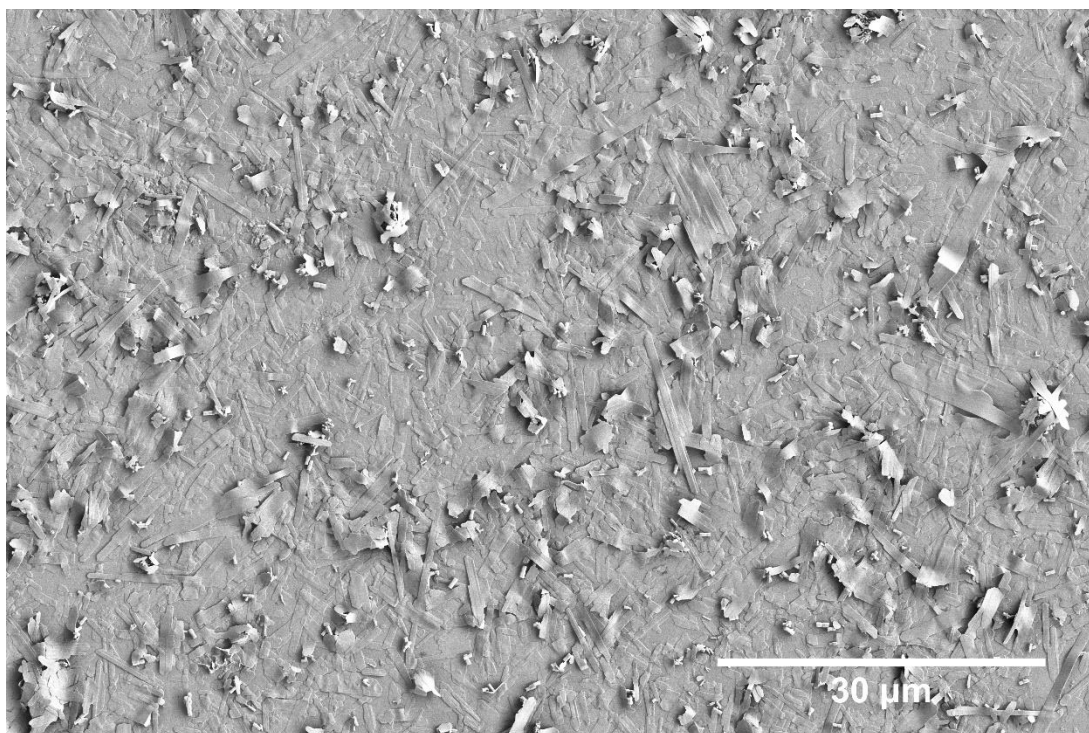


Figure 10.41: SEM micrograph of primarily LBZA (low contrast rectangular particles), and ZnO impurities (high contrast particles) synthesised with 20 seconds of microwave exposure ( $T_{peak}= 327\text{ K}$ ) using  $[OH^-]/[Zn^{2+}]$  1.64:1. Full details of analysis is provided in chapter 5.3.1.2.1 . Scale bar: 30  $\mu\text{m}$ . Note: The amplified electron shadow is an artifact of the local contrast enhancement performed in imageJ to make the particles distinguishable from the silicon substrate.

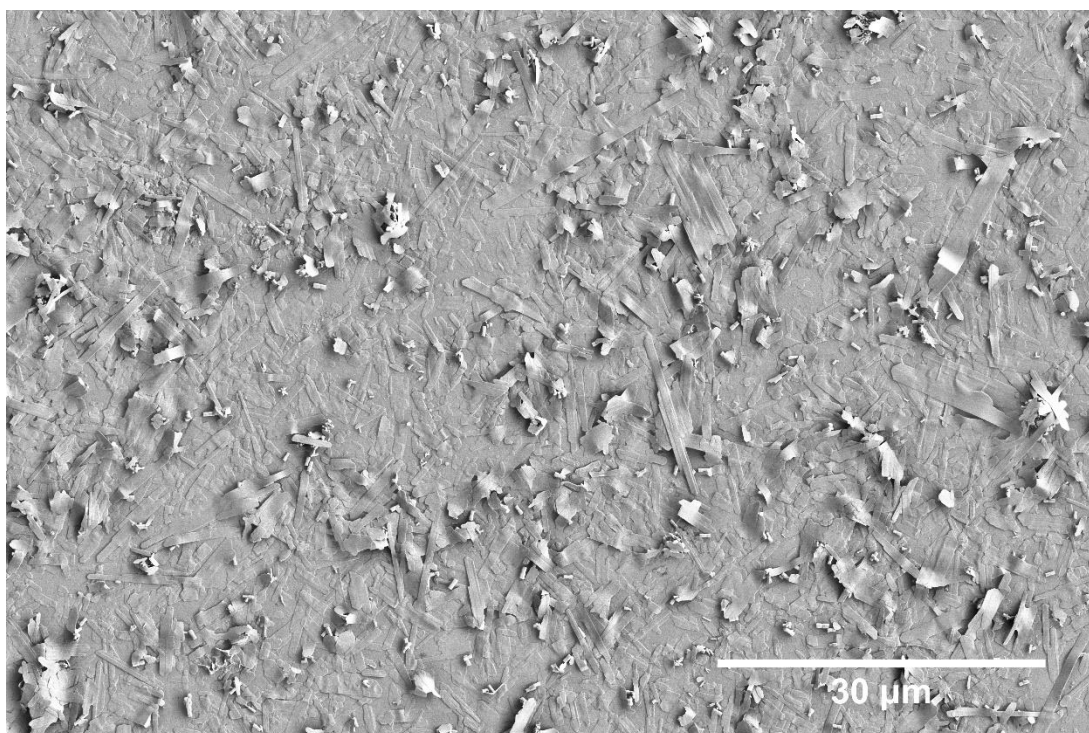


Figure 10.42: SEM micrograph of primarily LBZA (low contrast rectangular particles), and ZnO impurities (high contrast particles) synthesised with 20 seconds of microwave exposure ( $T_{peak}= 327\text{ K}$ ) using  $[OH^-]/[Zn^{2+}]$  1.68:1. Full details of analysis is provided in chapter 5.3.1.2.1 . Scale bar: 30  $\mu\text{m}$ . Note: The amplified electron shadow is an artifact of the local contrast enhancement performed in imageJ to make the particles distinguishable from the silicon substrate.

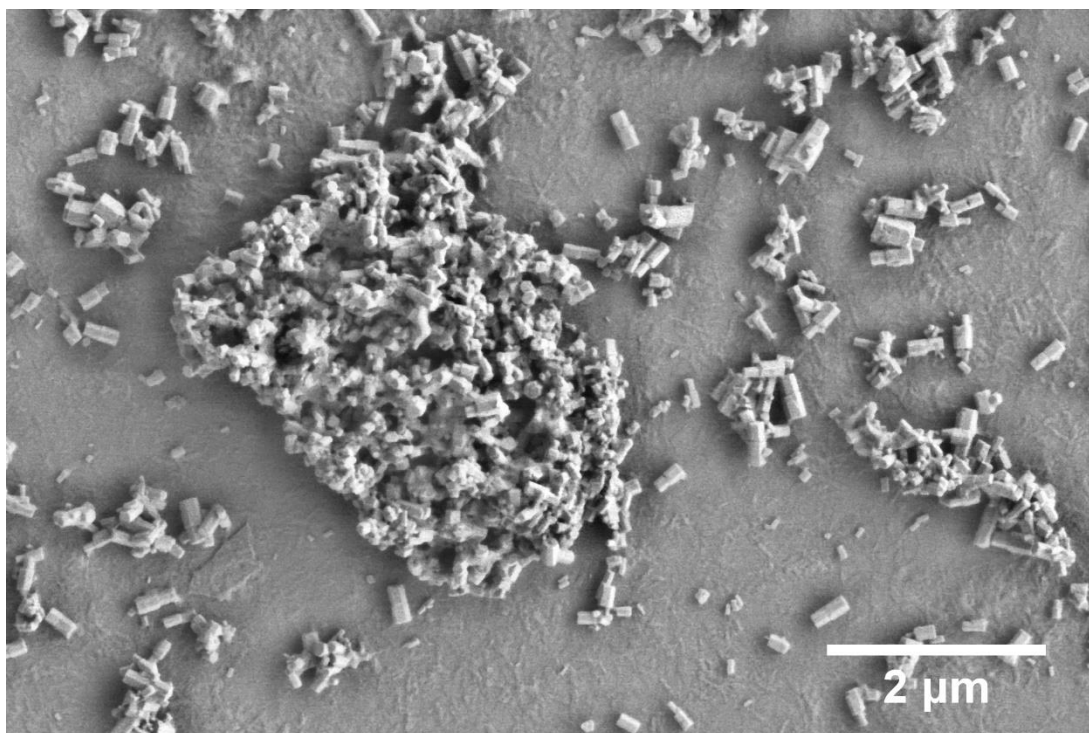


Figure 10.43: SEM micrograph of primarily ZnO impurities (high contrast particles) with the so called BLBZA (low contrast rectangular particles), synthesised with 20 seconds of microwave exposure ( $T_{peak}= 327$  K) using  $[OH^-]/[Zn^{2+}]$  1.72:1. Full details of analysis is provided in chapter 5.3.1.2.1 . Scale bar: 2  $\mu$ m. Note: The amplified electron shadow is an artifact of the local contrast enhancement performed in imageJ to make the particles distinguishable from the silicon substrate.

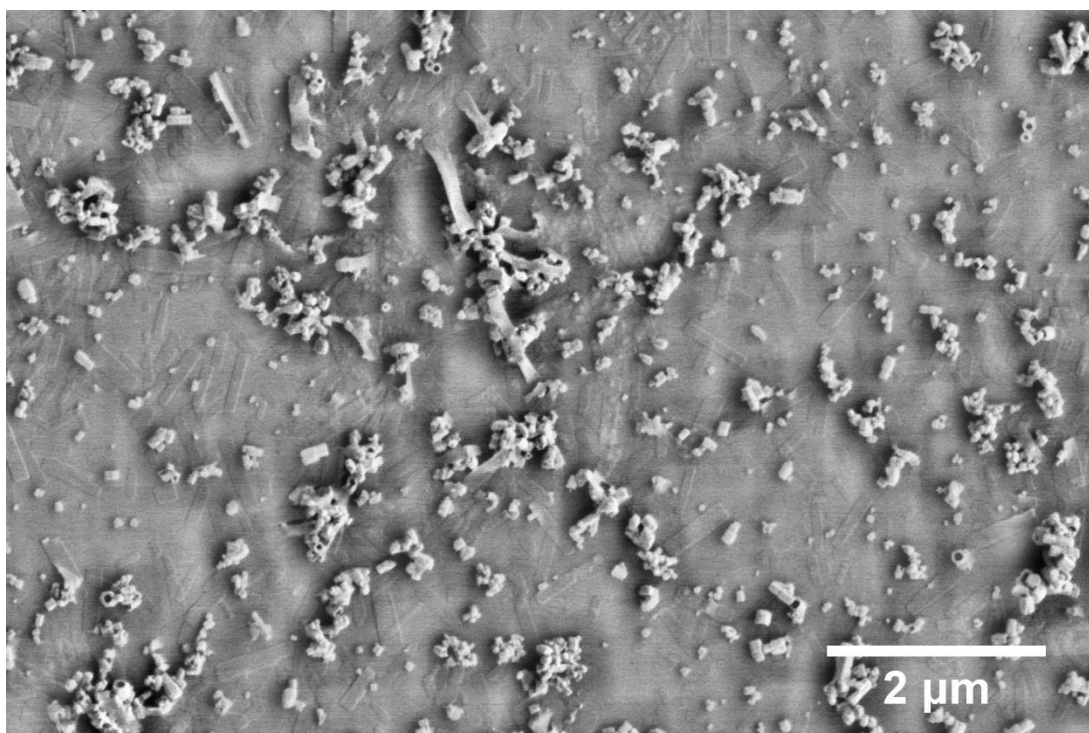


Figure 10.44: SEM micrograph of primarily ZnO impurities (high contrast particles) with the so called BLBZA (low contrast rectangular particles), synthesised with 20 seconds of microwave exposure ( $T_{peak}= 327$  K) using  $[OH^-]/[Zn^{2+}]$  1.76:1. Full details of analysis is provided in chapter 5.3.1.2.1 . Scale bar: 2  $\mu$ m. Note: The amplified electron shadow is an artifact of the local contrast enhancement performed in imageJ to make the particles distinguishable from the silicon substrate.

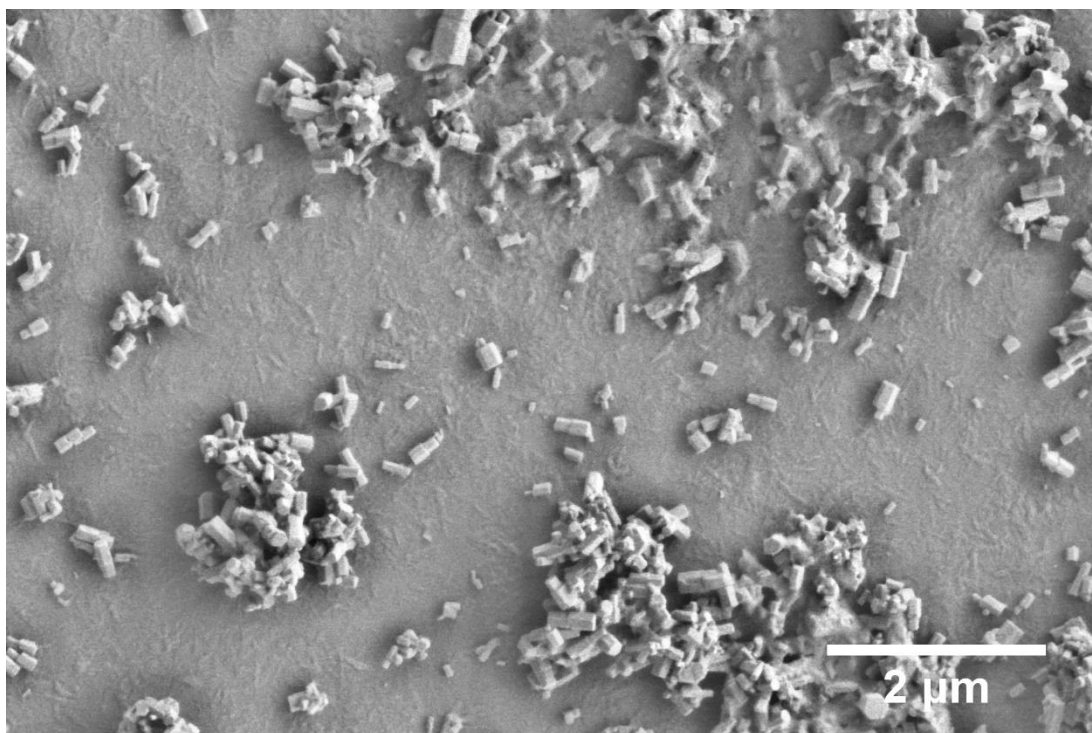


Figure 10.45: SEM micrograph of primarily ZnO impurities (high contrast particles) with the so called BLBZA (low contrast rectangular particles), synthesised with 20 seconds of microwave exposure ( $T_{peak}= 327\text{ K}$ ) using  $[OH^-]/[Zn^{2+}]$  1.80:1. Full details of analysis is provided in chapter 5.3.1.2.1 . Scale bar: 2  $\mu\text{m}$ . Note: The amplified electron shadow is an artifact of the local contrast enhancement performed in imageJ to make the particles distinguishable from the silicon substrate.

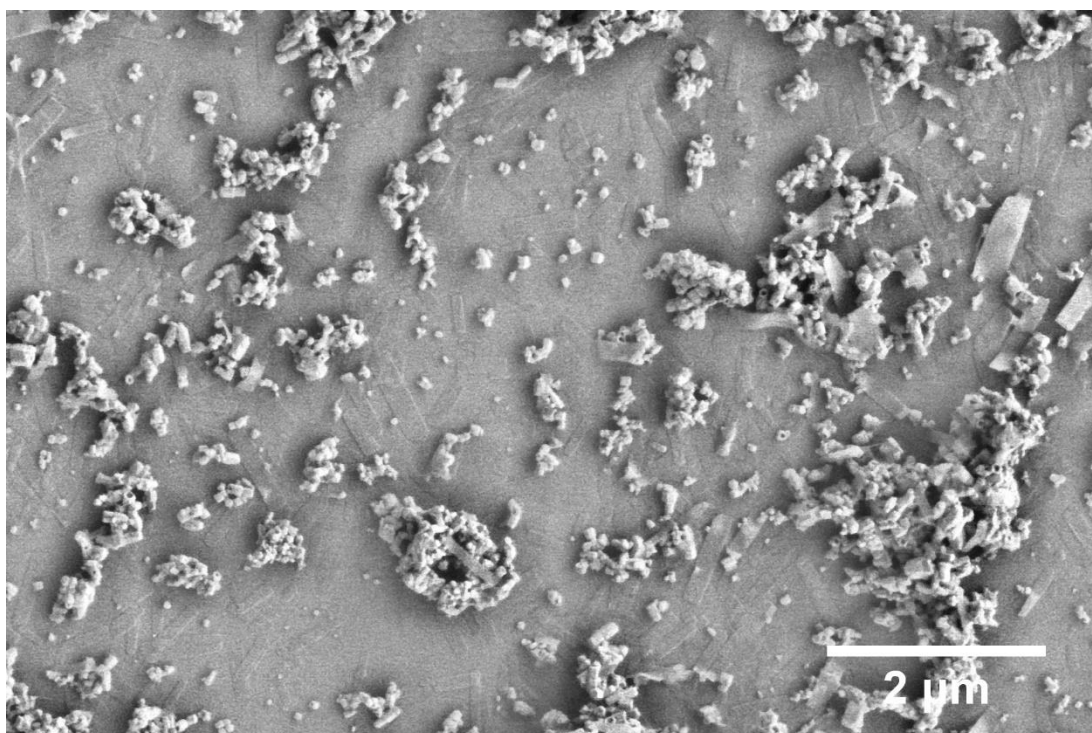
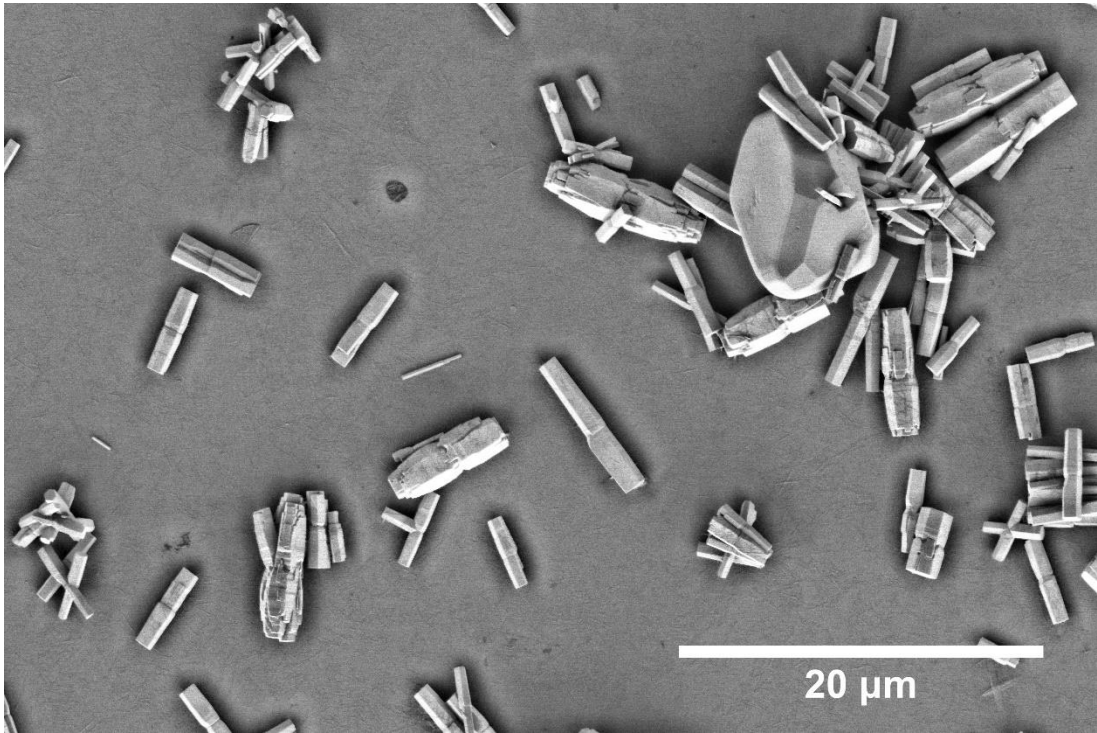


Figure 10.46: SEM micrograph of primarily ZnO impurities (high contrast particles) with the so called BLBZA (low contrast rectangular particles), synthesised with 20 seconds of microwave exposure ( $T_{peak}= 327\text{ K}$ ) using  $[OH^-]/[Zn^{2+}]$  2.00:1. Full details of analysis is provided in chapter 5.3.1.2.1 . Scale bar: 2  $\mu\text{m}$ . Note: The amplified electron shadow is an artifact of the local contrast enhancement performed in imageJ to make the particles distinguishable from the silicon substrate.

**10.1.5 30 s Microwave exposure i.e. unexposed. ( $T_{peak} = 351$  K)**



*Figure 10.47: SEM micrograph of primarily ZnO impurities (high contrast particles) with the so called BLBZA (faint low contrast rectangular particle in the background), synthesised with 30 seconds of microwave exposure ( $T_{peak} = 351$  K) using  $[OH^-]/[Zn^{2+}]$  1.4:1. Full details of analysis is provided in chapter 5.3.1.2.1 . Scale bar: 20  $\mu$ m. Note: The amplified electron shadow is an artifact of the local contrast enhancement performed in imageJ to make the particles distinguishable from the silicon substrate.*



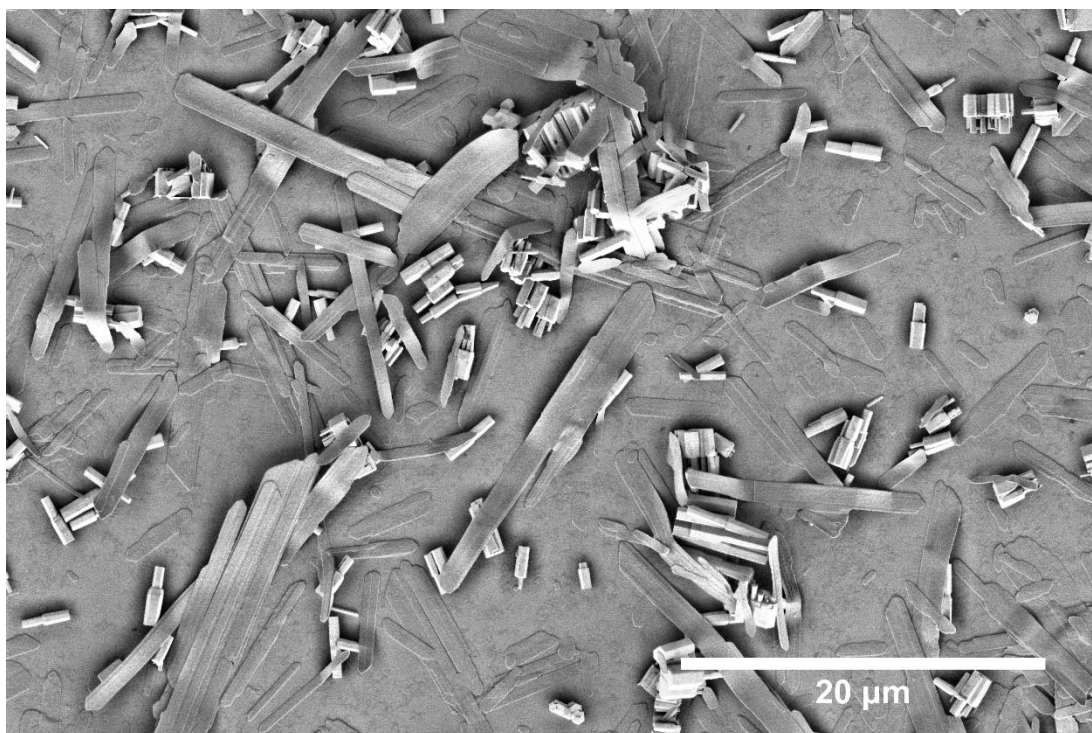


Figure 10.48: SEM micrograph of primarily LBZA (low contrast rectangular particles), and ZnO impurities (high contrast particles) synthesised with 30 seconds of microwave exposure ( $T_{peak} = 351$  K) using  $[OH^-]/[Zn^{2+}]$  0.8:1. Full details of analysis is provided in chapter 5.3.1.2.1 . Scale bar: 20  $\mu m$ . Note: The amplified electron shadow is an artifact of the local contrast enhancement performed in imageJ to make the particles distinguishable from the silicon substrate.

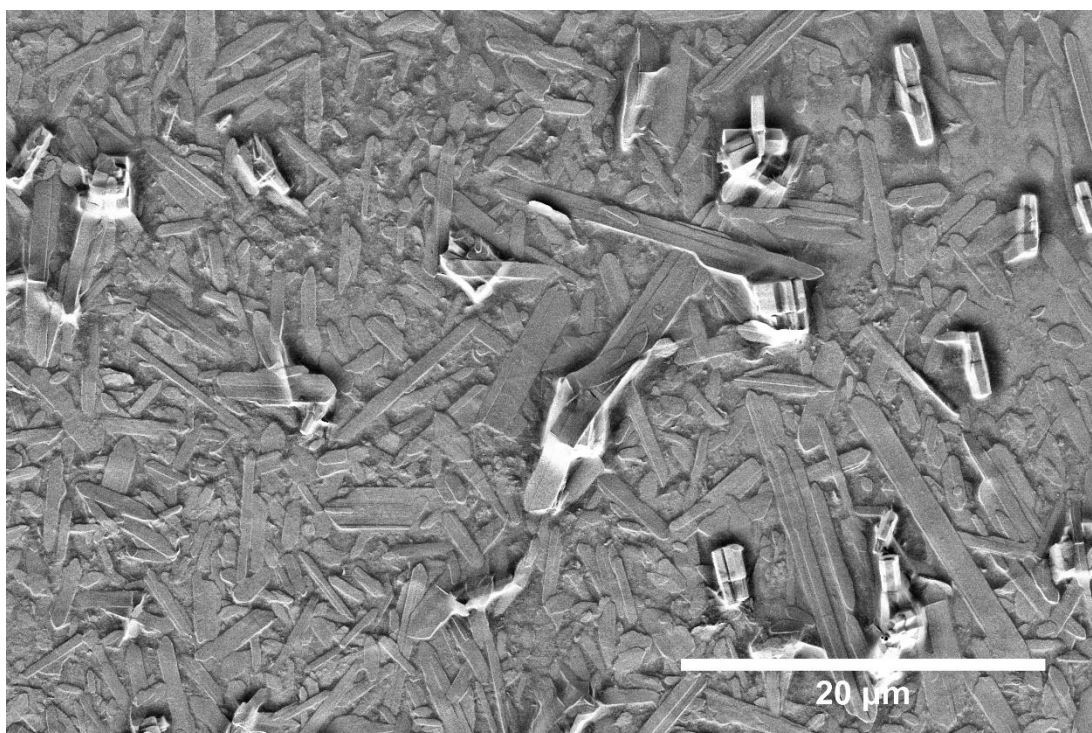


Figure 10.49: SEM micrograph of primarily LBZA (low contrast rectangular particles), and ZnO impurities (high contrast particles) synthesised with 30 seconds of microwave exposure ( $T_{peak} = 351$  K) using  $[OH^-]/[Zn^{2+}]$  1.2:1. Full details of analysis is provided in chapter 5.3.1.2.1 . Scale bar: 20  $\mu m$ . Note: The amplified electron shadow is an artifact of the local contrast enhancement performed in imageJ to make the particles distinguishable from the silicon substrate.

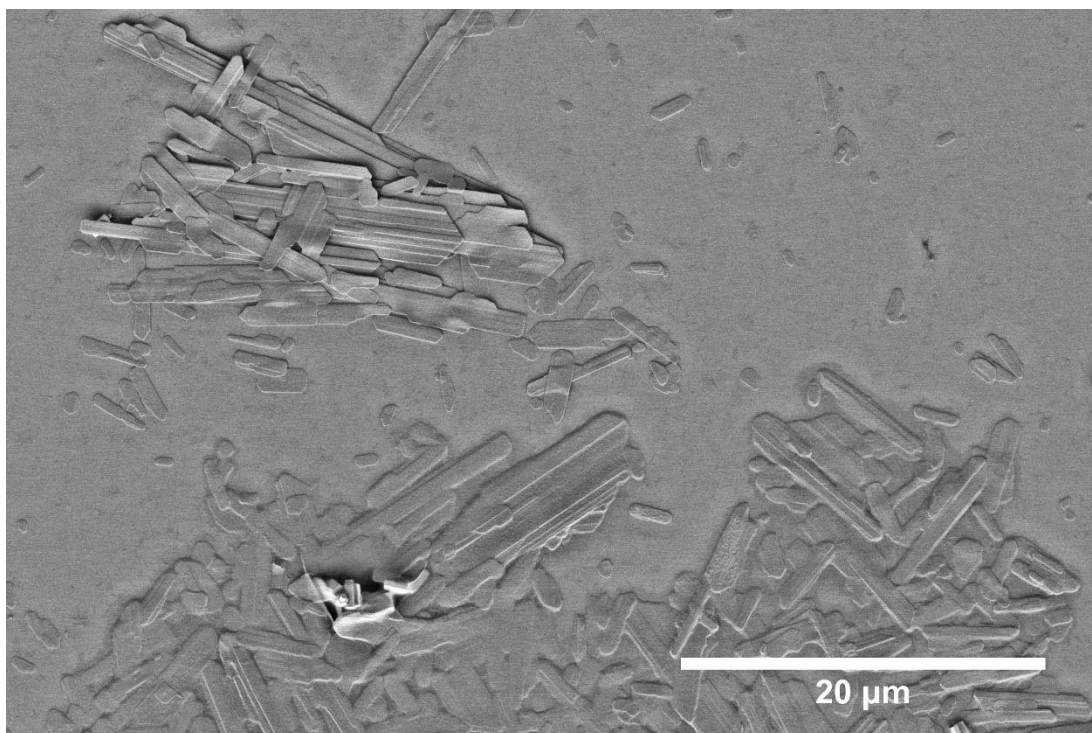


Figure 10.50: SEM micrograph of primarily LBZA (low contrast rectangular particles), and ZnO impurities (high contrast particles) synthesised with 30 seconds of microwave exposure ( $T_{peak}= 351$  K) using  $[OH^-]/[Zn^{2+}]$  1.4:1. Full details of analysis is provided in chapter 5.3.1.2.1 . Scale bar: 20  $\mu$ m. Note: The amplified electron shadow is an artifact of the local contrast enhancement performed in imageJ to make the particles distinguishable from the silicon substrate.

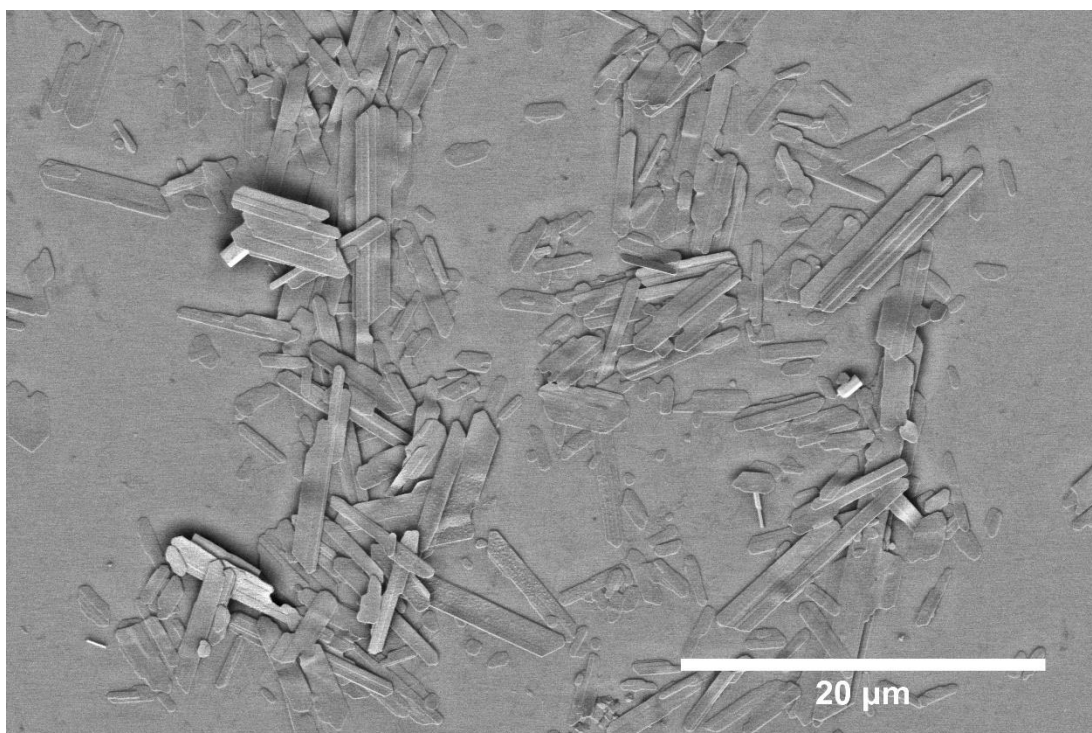


Figure 10.51: SEM micrograph of primarily LBZA (low contrast rectangular particles), and ZnO impurities (high contrast particles) synthesised with 30 seconds of microwave exposure ( $T_{peak}= 351$  K) using  $[OH^-]/[Zn^{2+}]$  1.44:1. Full details of analysis is provided in chapter 5.3.1.2.1 . Scale bar: 20  $\mu$ m. Note: The amplified electron shadow is an artifact of the local contrast enhancement performed in imageJ to make the particles distinguishable from the silicon substrate.

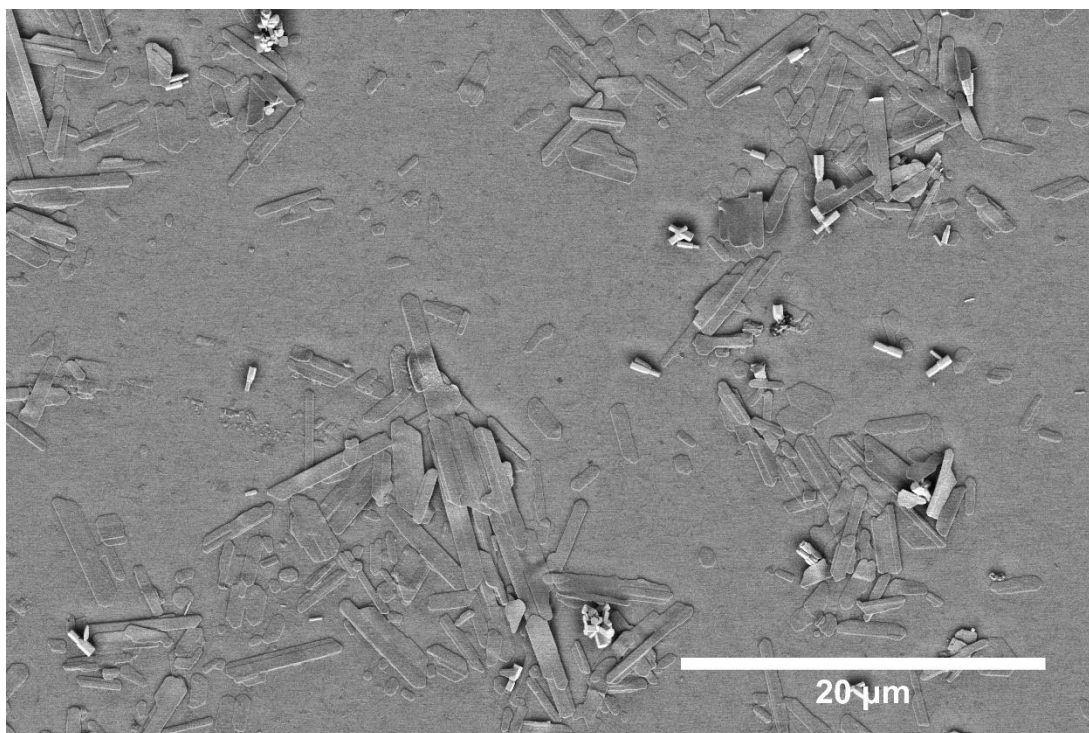


Figure 10.52: SEM micrograph of primarily LBZA (low contrast rectangular particles), and ZnO impurities (high contrast particles) synthesised with 30 seconds of microwave exposure ( $T_{peak} = 351$  K) using  $[OH^-]/[Zn^{2+}]$  1.48:1. Full details of analysis is provided in chapter 5.3.1.2.1 . Scale bar: 20  $\mu$ m. Note: The amplified electron shadow is an artifact of the local contrast enhancement performed in imageJ to make the particles distinguishable from the silicon substrate.

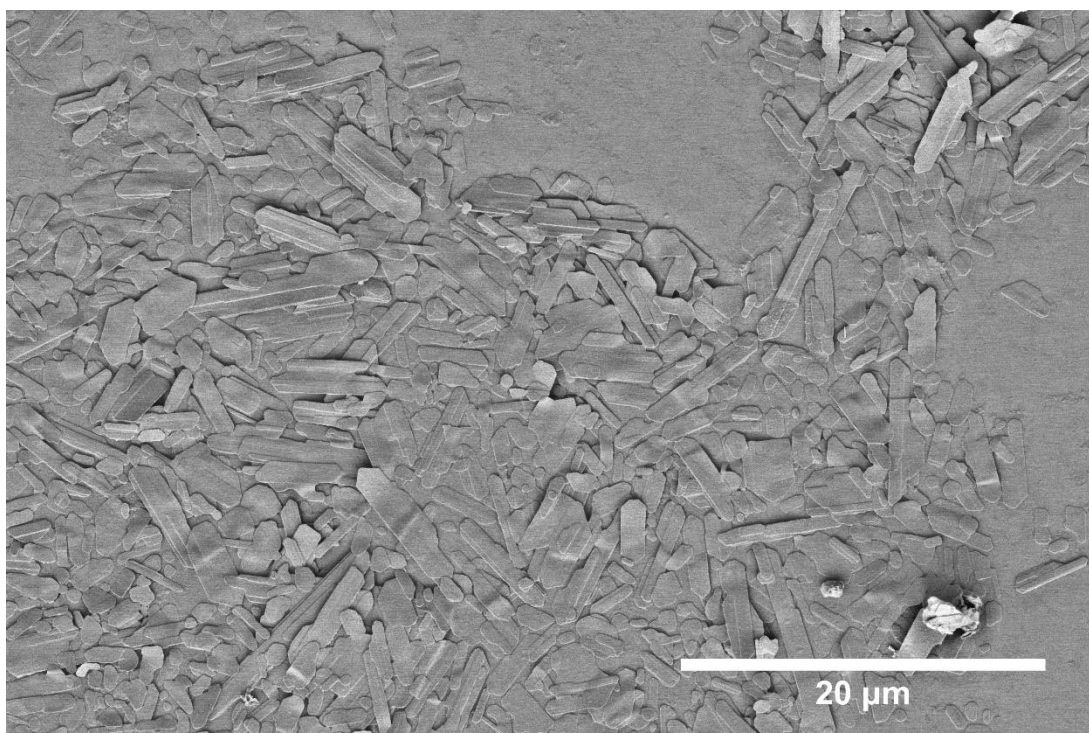


Figure 10.53: SEM micrograph of primarily LBZA (low contrast rectangular particles) synthesised with 30 seconds of microwave exposure ( $T_{peak} = 351$  K) using  $[OH^-]/[Zn^{2+}]$  1.52:1. Full details of analysis is provided in chapter 5.3.1.2.1 . Scale bar: 20  $\mu$ m.

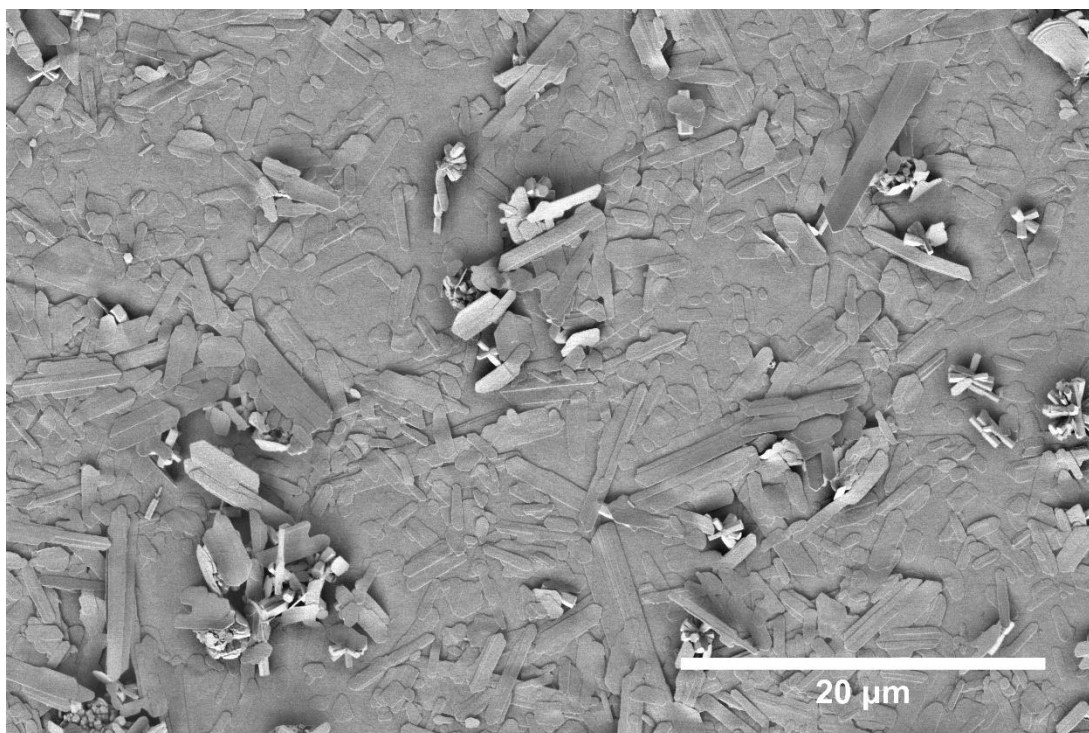


Figure 10.54: SEM micrograph of primarily LBZA (low contrast rectangular particles), and ZnO impurities (high contrast particles) synthesised with 30 seconds of microwave exposure ( $T_{peak} = 351$  K) using  $[OH^-]/[Zn^{2+}]$  1.56:1. Full details of analysis is provided in chapter 5.3.1.2.1 . Scale bar: 20 μm. Note: The amplified electron shadow is an artifact of the local contrast enhancement performed in imageJ to make the particles distinguishable from the silicon substrate.

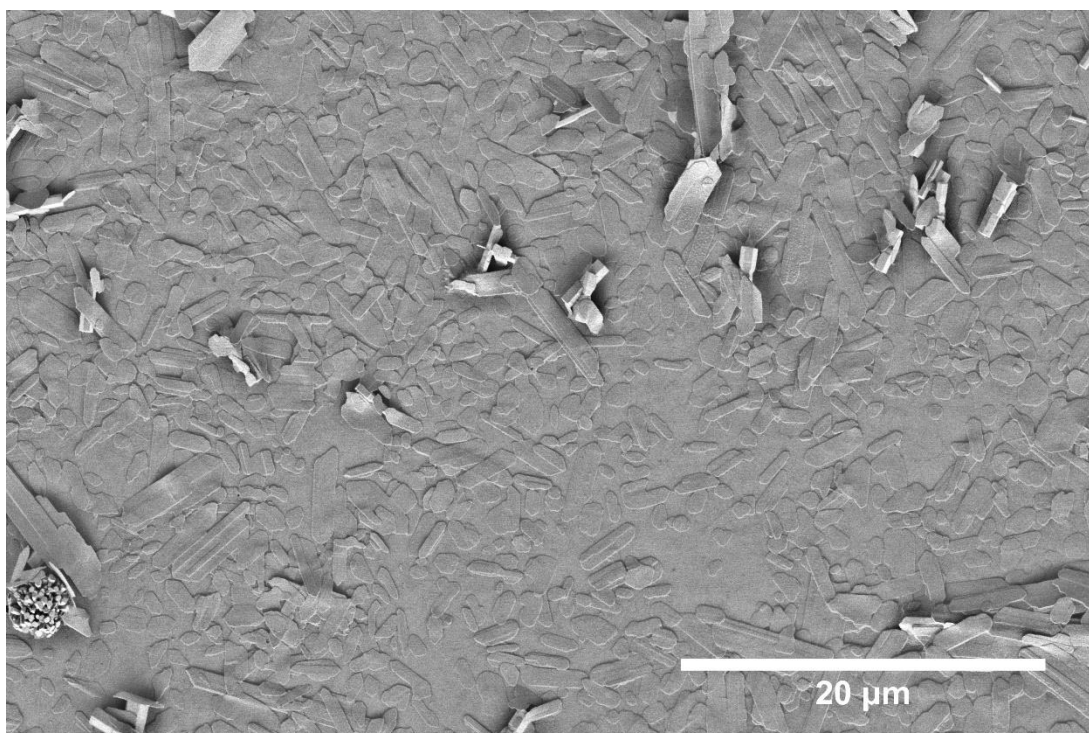


Figure 10.55: SEM micrograph of primarily LBZA (low contrast rectangular particles), and ZnO impurities (high contrast particles) synthesised with 30 seconds of microwave exposure ( $T_{peak} = 351$  K) using  $[OH^-]/[Zn^{2+}]$  1.60:1. Full details of analysis is provided in chapter 5.3.1.2.1 . Scale bar: 20 μm. Note: The amplified electron shadow is an artifact of the local contrast enhancement performed in imageJ to make the particles distinguishable from the silicon substrate.

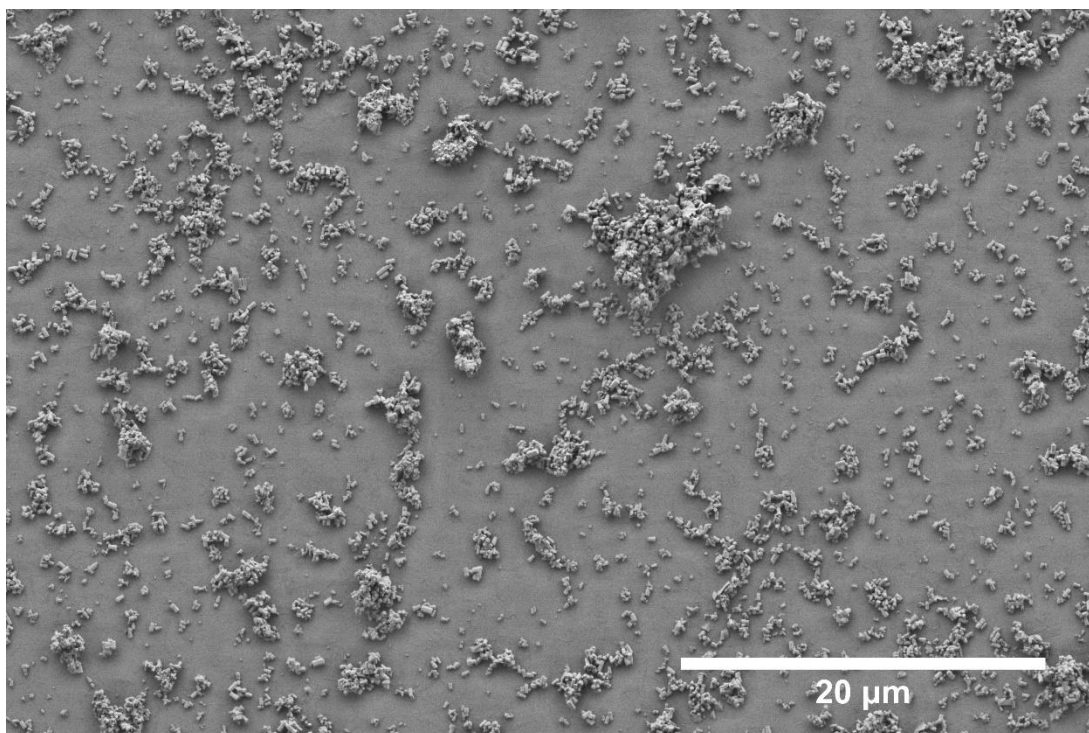


Figure 10.56: SEM micrograph of ZnO impurities (high contrast particles) synthesised with 30 seconds of microwave exposure ( $T_{peak} = 351$  K) using  $[OH^-]/[Zn^{2+}]$  1.64:1. Full details of analysis is provided in chapter 5.3.1.2.1 . Scale bar: 20  $\mu$ m. Note: The amplified electron shadow is an artifact of the local contrast enhancement performed in imageJ to make the particles distinguishable from the silicon substrate.

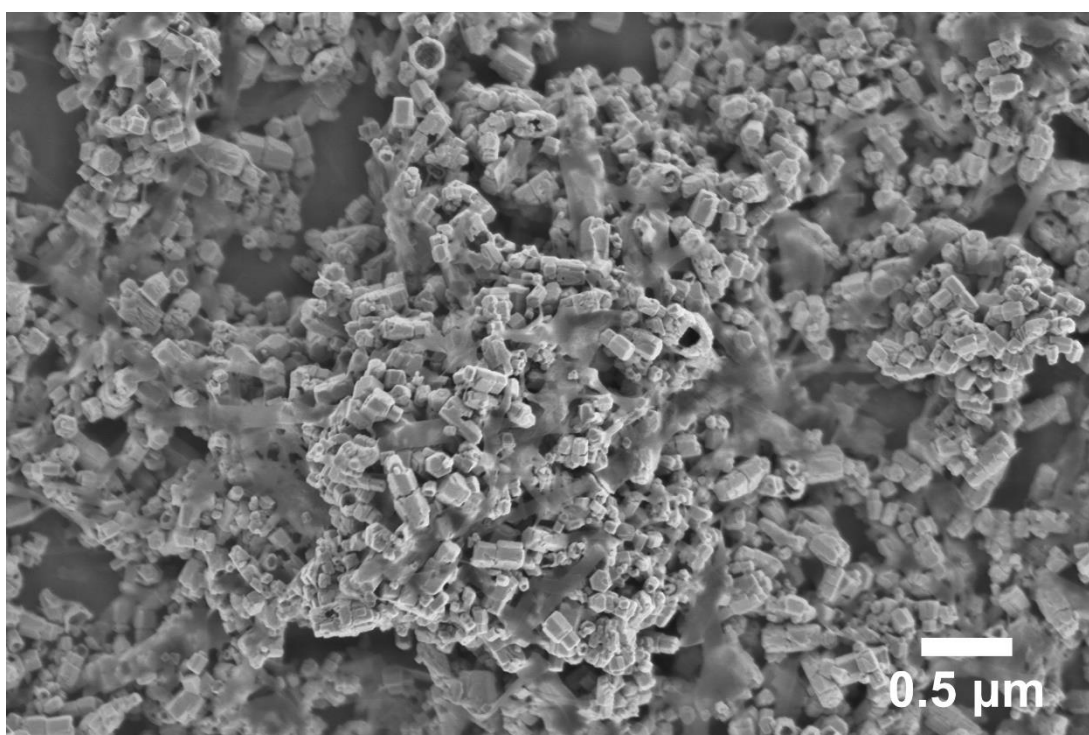


Figure 10.57: SEM micrograph of primarily ZnO impurities (high contrast particles) and the so called BLBZA (low contrast rectangular particles), synthesised with 30 seconds of microwave exposure ( $T_{peak} = 351$  K) using  $[OH^-]/[Zn^{2+}]$  1.68:1. Full details of analysis is provided in chapter 5.3.1.2.1 . Scale bar: 0.5  $\mu$ m. Note: The amplified electron shadow is an artifact of the local contrast enhancement performed in imageJ to make the particles distinguishable from the silicon substrate.

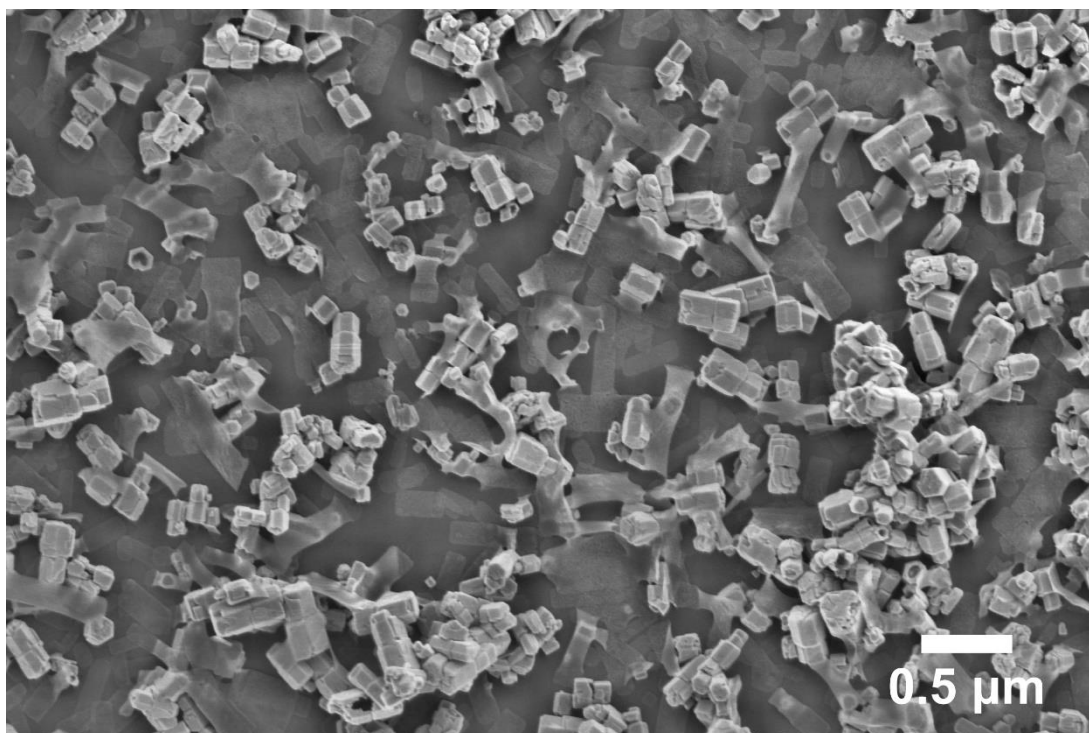


Figure 10.58: SEM micrograph of primarily ZnO impurities (high contrast particles) and the so called BLBZA (low contrast rectangular particles), synthesised with 30 seconds of microwave exposure ( $T_{peak} = 351$  K) using  $[OH^-]/[Zn^{2+}]$  1.72:1. Full details of analysis is provided in chapter 5.3.1.2.1 . Scale bar: 0.5  $\mu$ m. Note: The amplified electron shadow is an artifact of the local contrast enhancement performed in imageJ to make the particles distinguishable from the silicon substrate.

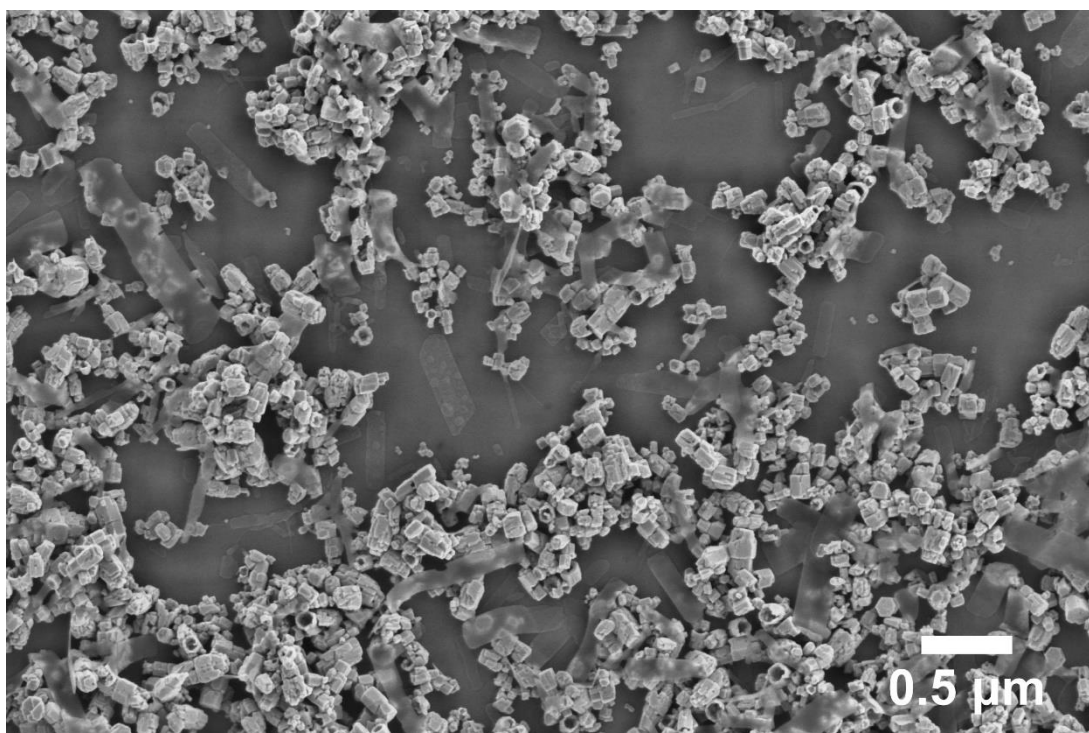


Figure 10.59: SEM micrograph of primarily ZnO impurities (high contrast particles) and the so called BLBZA (low contrast rectangular particles), synthesised with 30 seconds of microwave exposure ( $T_{peak} = 351$  K) using  $[OH^-]/[Zn^{2+}]$  1.76:1. Full details of analysis is provided in chapter 5.3.1.2.1 . Scale bar: 0.5  $\mu$ m. Note: The amplified electron shadow is an artifact of the local contrast enhancement performed in imageJ to make the particles distinguishable from the silicon substrate.

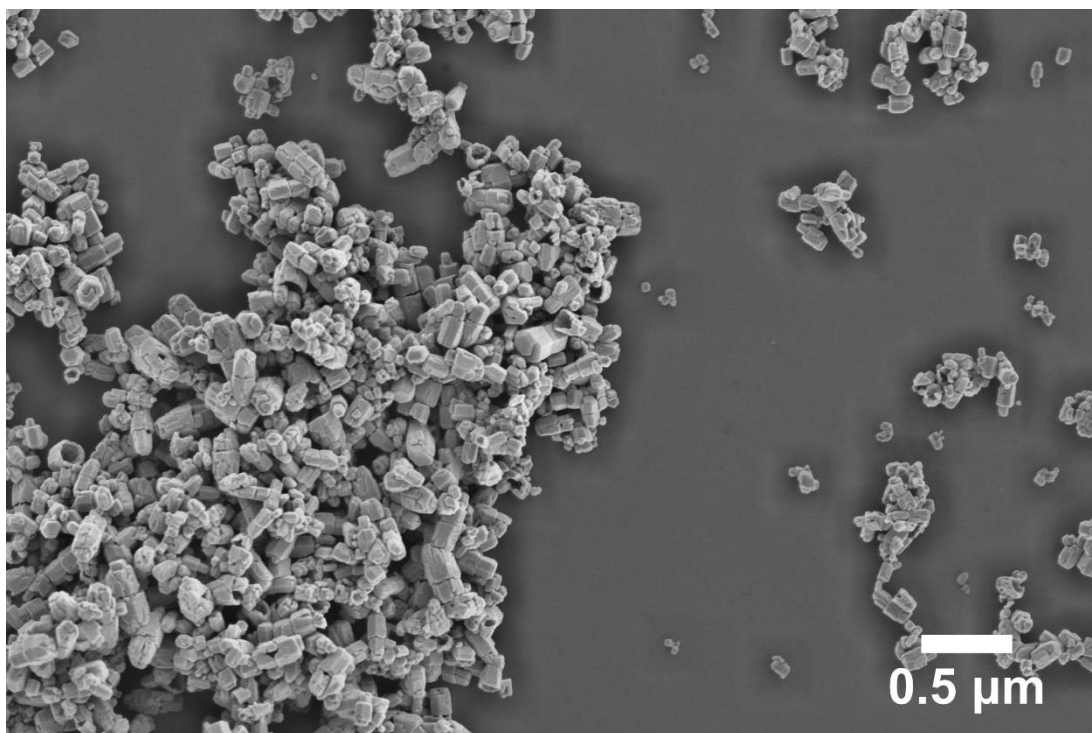


Figure 10.60: SEM micrograph of ZnO impurities (high contrast particles, synthesised with 30 seconds of microwave exposure ( $T_{peak}= 351$  K) using  $[OH]/[Zn^{2+}]$  1.8:1. Full details of analysis is provided in chapter 5.3.1.2.1 . Scale bar: 0.5  $\mu$ m. Note: The amplified electron shadow is an artifact of the local contrast enhancement performed in imageJ to make the particles distinguishable from the silicon substrate.

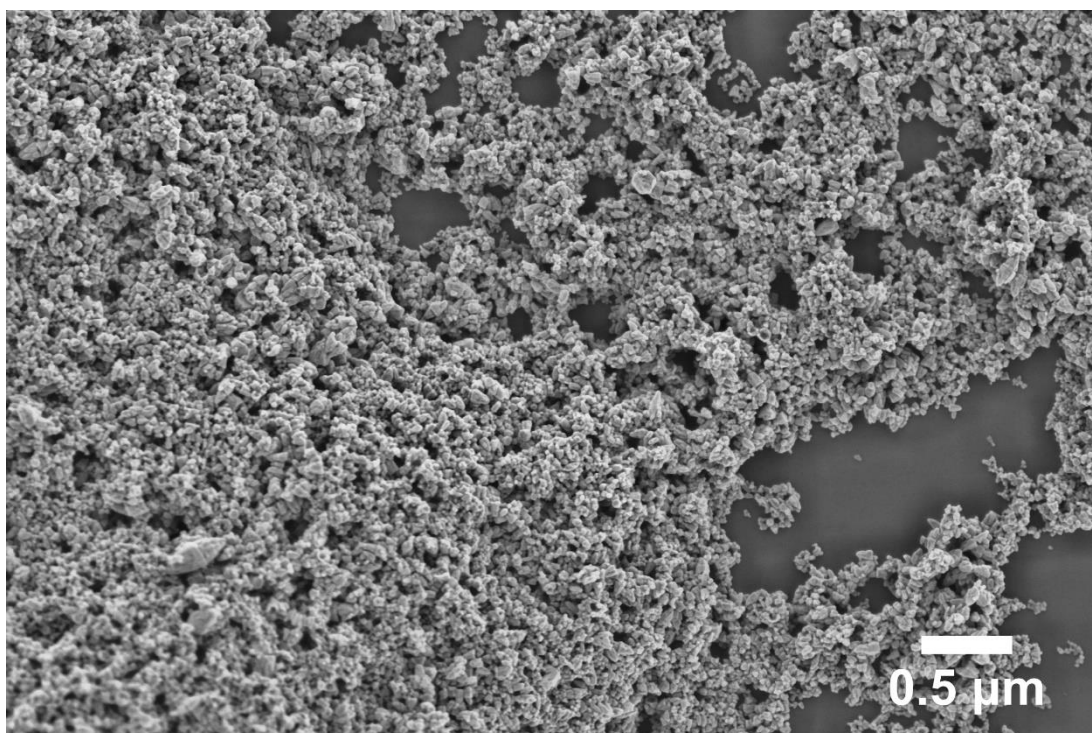


Figure 10.61: SEM micrograph of ZnO impurities (high contrast particles, synthesised with 30 seconds of microwave exposure ( $T_{peak}= 351$  K) using  $[OH]/[Zn^{2+}]$  2.0:1. Full details of analysis is provided chapter 5.3.1.2.1 . Scale bar: 0.5  $\mu$ m.

## Chapter 11 – Appendix A2. Simplified point charge surface potential calculation and calculation of the electrostatic/ electrochemical contribution to primary particle growth rate.

---

In this section; details for the calculations for the surface potential under neutral conditions of the LBZA (110) and (1 $\bar{1}$ 0) surfaces, and its effect on the electrostatic/ electrochemical  $\exp(-Z_{\pm}F\Delta\phi/2RT)$  factor <sup>[172]</sup> on primary particulate LBZA growth as shown in chapter 5.3.1.2.2.2 are described and results reported.

### 11.1 Method and geometry

To assess the potential of the surface structure present under neutral conditions for the surface of the basal layer of LBZA in the [110] and [1 $\bar{1}$ 0] directions, and its effect on Crundwells electrostatic/ electrochemical modification to the Erryng rate equation; a simple point charge 2D representation of the surface was modelled. Visual representation of the (110) surface is presented in Figure 11.3, the [Zn<sup>2+</sup>] terminated with [OH<sup>-</sup>] overlayer (1 $\bar{1}$ 0) surface in Figure 11.1 and the [OH<sup>-</sup>] terminated with [Zn<sup>2+</sup>] overlayer (1 $\bar{1}$ 0) surface in Figure 11.2). Using the model the Stern layer potential  $\phi_{Total}(x,y,z)$  and the Nernstian (electrostatic) factor  $\exp(-Z_{\pm}F\Delta\phi/2RT)$  <sup>[172]</sup> calculated along the width of the surface. The model assumed a polarised dielectric such that the opposing potential of the internal bonds cancel within the crystal <sup>[161]</sup>, and that the opposing oppositely charged surface is sufficiently far away so that it can be neglected (i.e. separation on the order of 100\*  $d_{Stern\ layer}$ ) . For each surface modelled, calculations were performed for a surface comprised of a single layer with thickness of  $c = 1.475\text{ nm}$  <sup>[75]</sup>, and 7 layers with thickness of  $7c = 10.325\text{ nm}$ , where  $c$  represents the vertical unit cell vector length for LBZA. The potential was calculated using Equation 11.1 <sup>[161]</sup>:

$$\phi_{Total}(x,y,z) = \sum \phi_n = \sum \frac{Q_n}{4\pi\epsilon_0\epsilon_{Stern}R_n} \text{ (Volts)}$$

Equation 11.1



Appendix A2. Simplified point charge surface potential calculation and calculation of the electrostatic/ electrochemical contribution to primary particle growth rate.

Where:

- $\phi_{Total}(x, y, z)$  is the total potential felt at the modelled Stern layer distance  $d_{Stern\ layer}$ , where positions: x represents the lateral distance along the surface, where the zero taken as the left hand corner; y is the direction of the approaching ion; and z the height out of the surface plane (i.e. the c-axis).<sup>[75]</sup>
- $Q_n$  is equal to the number of dangling bonds multiplied by the ion charge for the species represented by the point charges and equals:
  - o + e for Zinc cations and -1/3e for the hydroxide anions in the hydroxide terminated surface with zinc overlayer
  - o +1/3e for Zinc and -1/3e for hydroxide in the hydroxide terminated surface with zinc overlayer
  - o +2/3e for Zinc and -2/3e for combined hydroxides in the [110] surface.
- $\epsilon_0$  is the permittivity of free space and is equal to  $8.854188 \cdot 10^{-12}$  F/m.  $\epsilon_{Stern}$  is the relative permittivity within the stern layer and is usually between 20 – 60 for metal oxides<sup>[174]</sup> due to the polarisation induced by the high electric field across the stern layer<sup>[172]</sup>. A value of 39.2 i.e. half that of bulk water as has been previously used to successfully model the experimentally measured stern layer structure for mica-aqueous electrolyte by Bourg *et al.*<sup>[572]</sup> was used. Mica shares a similar clay like structure as LBZA and so the values should be similar in magnitude.
- $R_n$  is the distance between point charge n and the test charge (representing the depositing ion) and is given by:

$$R_n = \sqrt{(d_{Stern\ layer} + y_n)^2 + (x_n - x_0)^2 + (z_n - z_0)^2}$$

Equation 11.2

Where:  $x_n$ ,  $y_n$  and  $z_n$  represents the position of ion<sub>n</sub> at the surface, and  $x_0$  and  $z_0$  represents the position of the test charge in the Stern layer.

$d_{Stern\ layer}$  is the stern layer thickness which has historically been be approximated to be equal to the hydrated ionic radius of adsorbed ions<sup>[404]</sup>, with values for  $Zn(H_2O)_6^{2+} = 0.219$  nm<sup>[405]</sup>,  $OH(H_2O)_3^- = 0.3$  nm<sup>[406]</sup> and  $Na(H_2O)_4^+ = 0.36$  nm<sup>[573]</sup>. The hydration radius for  $Ac_{(aq)}^-$  is more complicated as it contains multiple hydration spheres, each between 0.17 nm

and 0.353 nm<sup>[574]</sup>.  $d_{\text{Stern layer}}$  was taken as 0.25 nm to simplify the calculations and is between the hydrated  $[\text{Zn}^{2+}]$  and  $[\text{OH}^-]$  species radii.

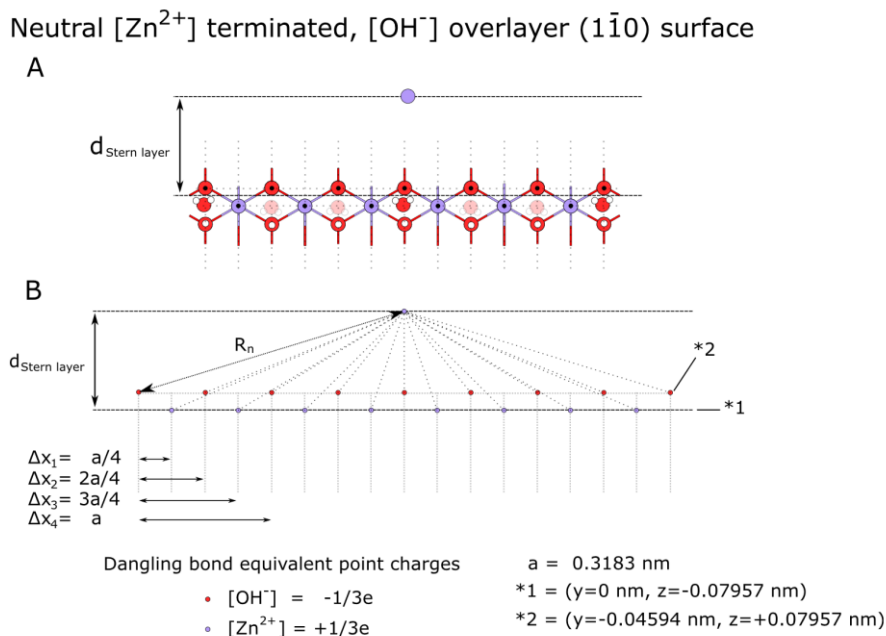


Figure 11.1: Graphical representation of the neutral ( $1\bar{1}0$ )  $[\text{Zn}^{2+}]$  terminated surface with  $[\text{OH}^-]$  overlayer. A) Ball and stick model of the equivalent surface. B) Point charge representation of the surface where the charges are equal to the undercoordinated charge in dangling bonds ( $-1/3e$  for  $[\text{OH}^-]$  and  $+1/3e$  for  $[\text{Zn}^{2+}]$ ). The repeat distance is equivalent to the unit cell vector  $a = 0.3183 \text{ nm}$ . All  $[\text{OH}^-]$  lie on a single plane, and all  $[\text{Zn}^{2+}]$  ions on a single separate plane. The zero in the  $z$  direction was taken as half the separation distance in the  $z$  direction between the  $[\text{OH}^-]$  and  $[\text{Zn}^{2+}]$  planes. Note that purple represent  $[\text{Zn}^{2+}]$ , red (with and without white circles)  $[\text{OH}^-]$ , and the green and white  $[\text{Ac}^-]$ . The lone point charge on the dashed line represents the test charge, which traces out the approach of an ion over the Stern layer. Dotted lines with  $R_n$  notation represents the separation between  $\text{ion}_n$  in the surface and the test charge.

The  $[\text{Zn}^{2+}]$  cations have an octahedral co-ordination; and  $[\text{OH}^-]$  anions trigonal pyramidal co-ordination, forming a tetrahedron with the  $[\text{OH}^-]$  anion at its apex. As such, assuming regular geometry, the angle between bonds on the  $[\text{Zn}^{2+}]$  cation in the basal layer plane are  $60^\circ$ , and on the  $[\text{OH}^-]$  anion  $120^\circ$ . The  $[\text{Zn}^{2+}]$  cations lie within the plane of the basal layer, whilst the  $[\text{OH}^-]$  anions have bond angles of  $60^\circ$  between the basal plane and the  $z$  axis (which oriented to be parallel to the unit cell vector direction  $c$ ). The  $a$  vector contains 2  $[\text{Zn}^{2+}]$  and 2 $[\text{OH}^-]$  ions, and assuming regular geometry have a lateral separation of  $a/4 = 0.079575$ .

Combining the bond angles and a vector length the  $[\text{Zn}^{2+}]$ - $[\text{OH}^-]$  bond length is given by:

$$d_{\text{Zn-OH}} = \frac{a}{4} \cos 30^\circ \cos 60^\circ = \frac{0.3183}{4} \cos 30^\circ \cos 60^\circ = 0.18377 \text{ nm}$$

Equation 11.3

Neutral  $[\text{OH}^-]$  terminated,  $[\text{Zn}^{2+}]$  overlayer ( $1\bar{1}0$ ) surface

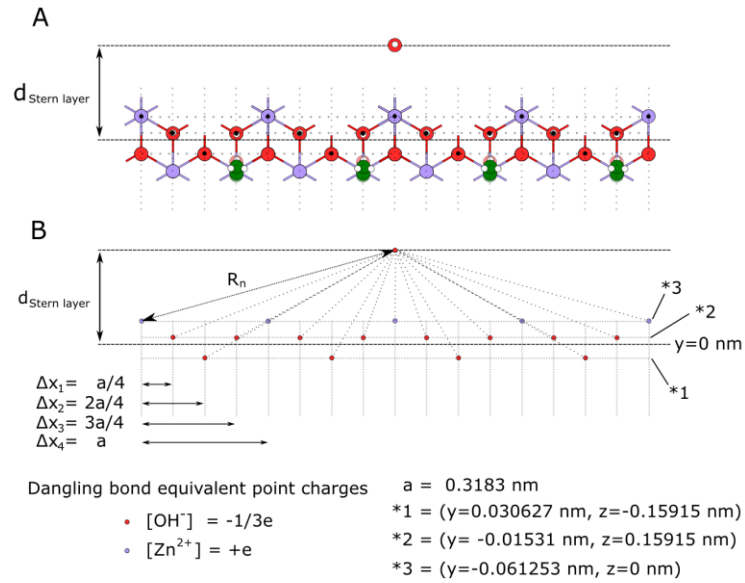


Figure 11.2: Graphical representation of the neutral ( $1\bar{1}0$ )  $[\text{OH}^-]$  terminated surface with  $[\text{Zn}^{2+}]$  overlayer. A) Ball and stick model of the equivalent surface. B) Point charge representation of the surface where the charges are equal to the undercoordinated charge in dangling bonds ( $-1/3e$  for  $[\text{OH}^-]$  and  $+e$  for  $[\text{Zn}^{2+}]$ ). The repeat distance is equivalent to the unit cell vector  $a = 0.3183 \text{ nm}$ .  $[\text{OH}^-]$  lie on two separate planes \*1 and \*2, and all  $[\text{Zn}^{2+}]$  ions on a single separate plane \*3. The zero in the  $z$  direction was taken as the  $[\text{Zn}^{2+}]$  plane. Note that purple represent  $[\text{Zn}^{2+}]$ , red (with and without white circles)  $[\text{OH}^-]$ , and the green and white  $[\text{Ac}^-]$ . The lone point charge on the dashed line represents the test charge, which traces out the approach of an ion over the Stern layer. Dotted lines with  $R_n$  notation represents the separation between  $\text{ion}_n$  in the surface and the test charge.

The  $[\text{OH}^-]$  anions are arranged in an alternating  $\pm z_{\text{OH}}$  pattern in the  $[1\bar{1}0]$  direction, where:

$$z_{\text{OH}} = d_{\text{Zn-OH}} \sin 60^\circ = 0.15915 \text{ nm}$$

Equation 11.4

In the ( $1\bar{1}0$ ) surfaces the  $[\text{Zn}^{2+}]$  cations and  $[\text{OH}^-]$  anions have lateral separations (i.e. in the  $x$  axis) of  $a/4$ .

Appendix A2. Simplified point charge surface potential calculation and calculation of the electrostatic/ electrochemical contribution to primary particle growth rate.

In the y direction (parallel with  $d_{\text{Stern layer}}$ ) there are two  $[\text{Zn}^{2+}] - [\text{OH}^-]$  separation distances, defined by the bond angle formed between the  $[\text{Zn}^{2+}]$  and  $[\text{OH}^-]$  ions, relative to the x axis.

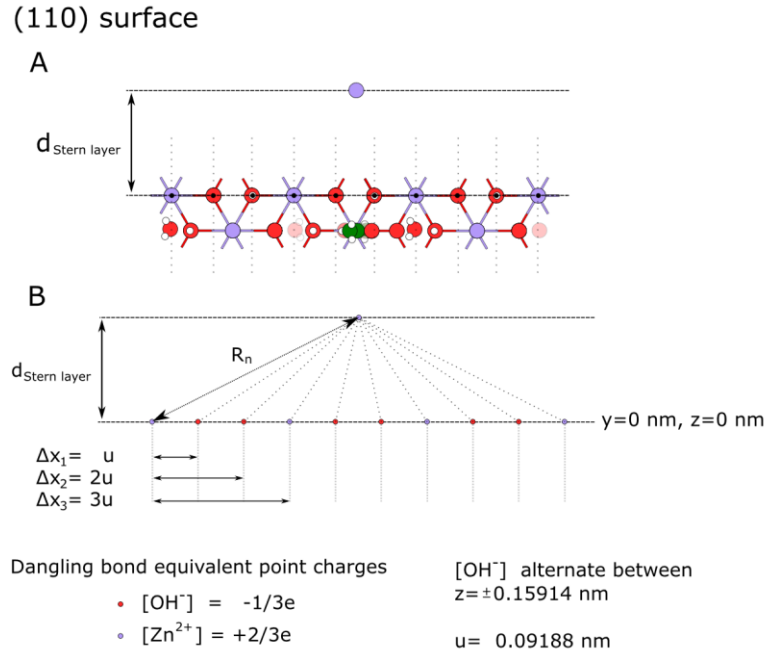


Figure 11.3: Graphical representation of the neutral (110) surface. A) Ball and stick model of the equivalent surface. B) Point charge representation of the surface where the charges are equal to the undercoordinated charge in dangling bonds ( $-1/3e$  for  $[\text{OH}^-]$  and  $+2/3e$  for  $[\text{Zn}^{2+}]$ ). The lateral repeat distance ( $\Delta x_3$ ) is equivalent to  $3u = 0.27564 \text{ nm}$ . The zero in the z direction was taken as the plane that all  $[\text{Zn}^{2+}]$  ions lie in, alternating  $[\text{OH}^-]$  ions have z values of  $\pm 0.15914 \text{ nm}$ . Note that purple represent  $[\text{Zn}^{2+}]$ , red (with and without white circles)  $[\text{OH}^-]$ , and the green and white  $[\text{Ac}^-]$ . The lone point charge on the dashed line represents the test charge, which traces out the approach of an ion over the Stern layer. Dotted lines with  $R_n$  notation represents the separation between  $\text{ion}_n$  in the surface and the test charge.

For the  $[\text{OH}^-]$  overlayer surface there is only a single y separation distance, formed with a  $30^\circ$  angle relative to the x-axis and given by:

$$y = \frac{a}{4} \tan 30^\circ = \frac{0.3183}{4} \tan 30^\circ = 0.0459 \text{ nm}$$

Equation 11.5

Appendix A2. Simplified point charge surface potential calculation and calculation of the electrostatic/ electrochemical contribution to primary particle growth rate.

This distance is shared by one of the planes that the  $[\text{OH}^-]$  anions lie in for the  $[\text{Zn}^{2+}]$  overlayer surface and contains two  $[\text{OH}^-]$  anions. The other anion is bonded  $90^\circ$  to the x-axis (i.e. in the y plane) and has a y separation of:

$$y = d_{\text{Zn-OH}} \cos 60^\circ = 0.091885 \text{ nm}$$

Equation 11.6

For the (110) neutral plane, all ions lie on the same plane in the y direction. As all ions lie in along a constant y plane, the lateral separation along the x-axis between ions is defined as:

$$\Delta x = d_{\text{Zn-OH}} \cos 60^\circ = 0.091885 \text{ nm}$$

Equation 11.7

As the x-axis is aligned with  $[\bar{1}\bar{1}0]$  direction the  $[\text{OH}^-]$  anions alternate between  $\pm z_{\text{OH}}$ . The zero in the z axis was taken as the average z-distance between all ions, whilst the zero in the y direction was defined as the average position of ions in the surface termination layer. For the  $(\bar{1}\bar{1}0)$  surface with  $[\text{Zn}^{2+}]$  overlayer this results in y positions for plane:

- \*1 that contains a single  $[\text{OH}^-]$  anion per unit cell,  $y=0.030627 \text{ nm}$
- \*2 that contains 2  $[\text{OH}^-]$  anions per unit cell,  $y=-0.01531 \text{ nm}$
- \*3 that contains 1  $[\text{Zn}^{2+}]$  per unit cell,  $y=-0.061253 \text{ nm}$ .

For each potential calculated the factor  $\exp(-Z_{\pm}F\Delta\phi/2RT)$  was calculated for both hydroxide and zinc cations approaching the surface. The temperatures used for analysing the electrostatic factor correspond to the temperatures measured immediately after microwave exposure and were 294 K, 309 K, 327 K and 351 K for 0, 10, 20 and 30 second exposures respectively.

## 11.2 Results and Discussion

### 11.2.1 Single layer geometry calculations

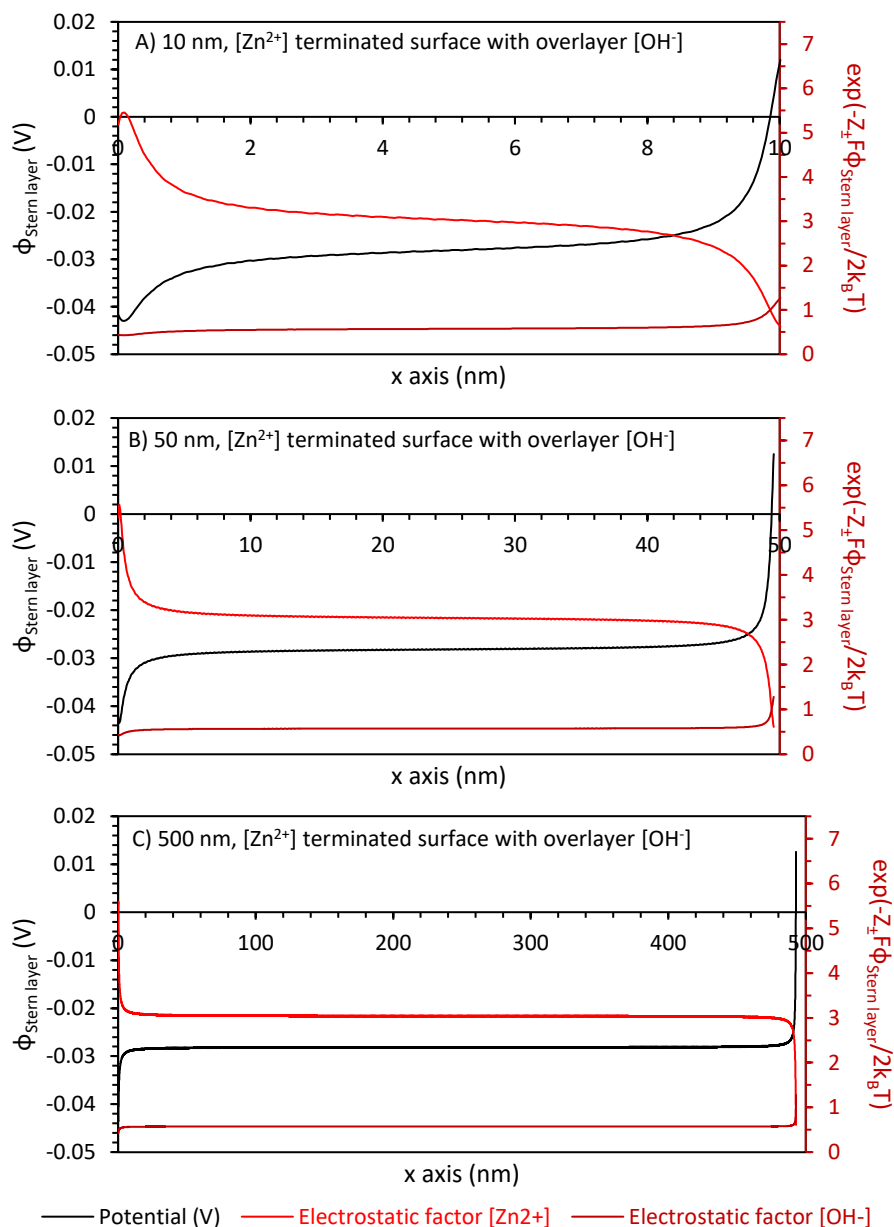


Figure 11.4: Plots of Stern layer potential  $\phi_{\text{Stern layer}}$  and the electrostatic factor  $\exp(-Z_{\pm}F\phi_{\text{Stern layer}}/2k_B T)$  for  $[\text{Zn}^{2+}]$  cations and  $[\text{OH}^-]$  anions at  $T=294$  K, with a Stern layer distance of  $0.25$  nm, for the  $[\text{Zn}^{2+}]$  terminated surface with an overlayer of  $[\text{OH}^-]$  anions. The surfaces, with geometry presented in Figure 11.1, have widths of A)  $\sim 10$  nm, B)  $\sim 50$  nm and C)  $\sim 500$  nm. Assuming a cubic particle, the  $10$  nm surface will be on the order of the dipole surface charge approximation, and the magnitude of the potential will therefore represent the upper boundary. The ion at  $x=0$  nm is an  $[\text{OH}^-]$  anion. The surface comprised of a single layer in the  $z$  direction.

Appendix A2. Simplified point charge surface potential calculation and calculation of the electrostatic/ electrochemical contribution to primary particle growth rate.

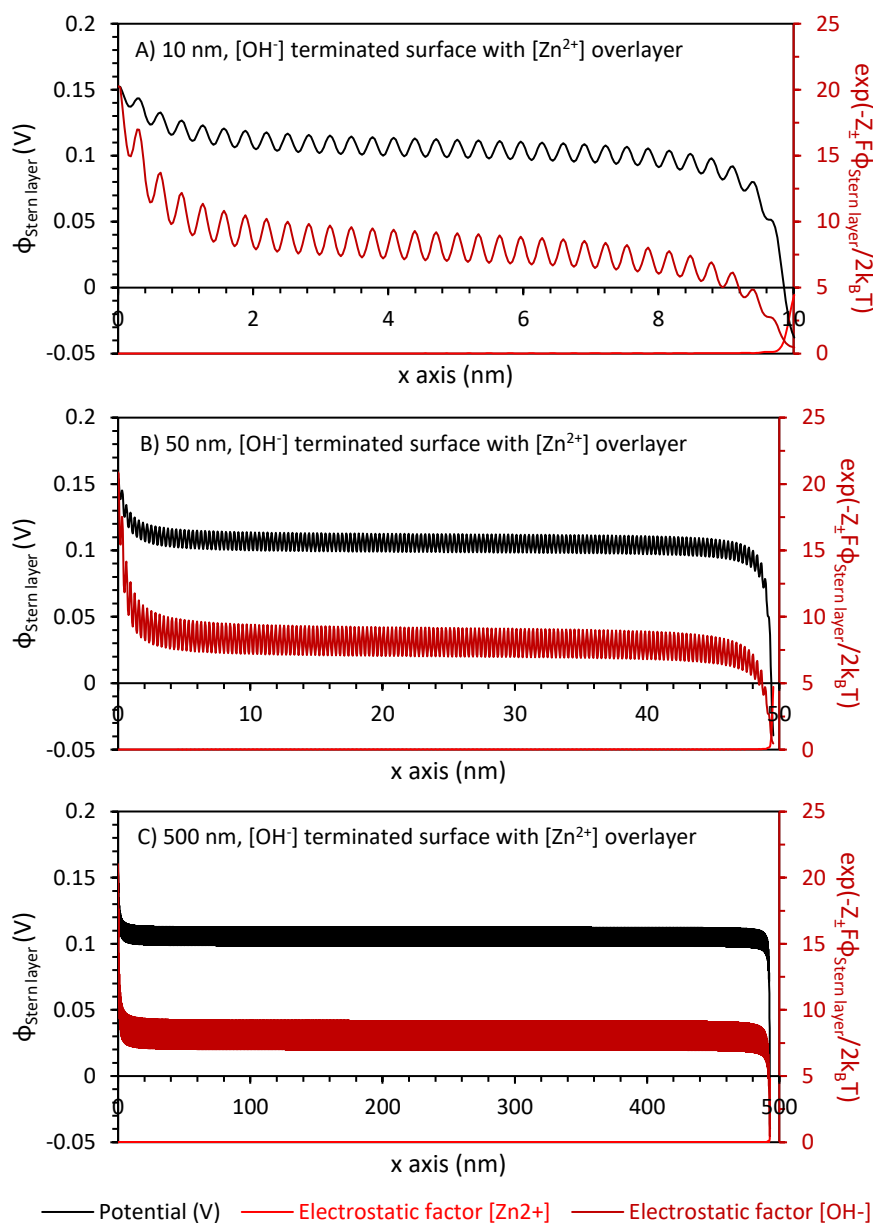


Figure 11.5: Plots of Stern layer potential  $\phi_{\text{Stern layer}}$  and the electrostatic factor  $\exp(-Z_i F \phi_{\text{Stern layer}} / 2k_B T)$  for  $[\text{Zn}^{2+}]$  cations and  $[\text{OH}^-]$  anions at  $T=294$  K, with a Stern layer distance of 0.25 nm, for the  $[\text{OH}^-]$  terminated surface with an overlayer of  $[\text{Zn}^{2+}]$  anions. The surfaces, with geometry presented in Figure 11.2, have widths of A)  $\sim 10$  nm, B)  $\sim 50$  nm and C)  $\sim 500$  nm. Assuming a cubic particle, the 10 nm surface will be on the order of the dipole surface charge approximation, and the magnitude of the potential will therefore represent the upper boundary. The ion at  $x=0$  nm is a  $[\text{Zn}^{2+}]$  cation. The surface comprised of a single layer in the  $z$  direction.

Figure 11.4 shows plots of the calculated Stern layer potential  $\phi_{\text{Stern layer}}$  and the corresponding electrostatic factor as a function of lateral position for the  $[\text{Zn}^{2+}]$  terminated surface with an overlayer of  $[\text{OH}^-]$  anions. From the plots of potential there is a weak nonzero potential, with a mean magnitude on the order of  $-27.4$  mV to  $-28.2$  mV. Interestingly, superimposed onto the mean potential is a lateral dipole that exists, due to the idealised geometry i.e. terminating  $[\text{OH}^-]$  anion at  $x=0$  and terminating  $[\text{Zn}^{2+}]$  cation at the

Appendix A2. Simplified point charge surface potential calculation and calculation of the electrostatic/ electrochemical contribution to primary particle growth rate.

maximum  $x$  positions. Whilst a localised potential would be expected at the corners, due to the disruption of the neutral surface, it is not clear whether the perfect geometrical order within the calculations would be present in the physical experiments, and likely overestimates the peak in potential.

The dipole results with a small region converting from a negative potential to a positive potential at the maximum  $x$  axis value. The potential profile is generally smooth, with a weak variation in potential visible in the 10 nm surface (Figure 11.4 A) corresponding to the  $[\text{OH}^-]$ - $[\text{Zn}^{2+}]$  repeat distance of  $a/2$ . Based on the mean potential, the plots of the electrostatic factor show that the reaction rate for  $[\text{OH}^-]$  anions will be reduced to 0.57-0.58 of its Erryng reaction rate value; whereas the reaction rate for  $[\text{Zn}^{2+}]$  cations will be increased by a factor of 2.95-3.04 at 294 K. Peak electrostatic factors for  $[\text{OH}^-]$  anions are 1.25-1.28 and  $[\text{Zn}^{2+}]$  cations 5.18-5.3. Reactions at the corner are more favourable than at the centre, but not significantly so; when surface area is taken into account, growth would be expected to start at any point along the width of the surface.

Figure 11.5 shows plots of the calculated Stern layer potential  $\phi_{\text{Stern layer}}$  and the corresponding electrostatic factor as a function of lateral position for the  $[\text{OH}^-]$  terminated surface with an overlayer of  $[\text{Zn}^{2+}]$  cations. The magnitude of the potential is significantly greater than for the  $[\text{OH}^-]$  overlayer surface, with mean potentials of +102.0 mV to +105.3 mV. Again, a lateral dipole is seen; however, unlike the  $[\text{OH}^-]$  overlayer surface a large oscillation in potential of 10-13 mV can be seen. The increased magnitude in potential and magnitude of the oscillation results from two conditions.

The first is the magnitude of the charge on the  $[\text{Zn}^{2+}]$  cation of  $+1e$  compared to the  $[\text{OH}^-]$  anion of  $-1/3e$  leading to the increase magnitude. The second arises from the separation of charges, in the  $[\text{OH}^-]$  overlayer surface the cations and anions had a lateral separation of  $a/4$ ; in the  $[\text{Zn}^{2+}]$  overlayer surface however, they have a separation between individual point charges of  $a/4$ , but a cation and anion centre separation of  $a/2$ , leading to the increased oscillations. Based on the mean potential, the plots of the electrostatic factor show that the reaction rate for  $[\text{Zn}^{2+}]$  cations will be reduced to 0.016-0.018 of its Erryng reaction rate value; whereas the reaction rate for  $[\text{OH}^-]$  anions will be increased by a factor of 7.48-7.99 at 294 K. Peak electrostatic factors for  $[\text{OH}^-]$  anions are 20.27-21.02 and  $[\text{Zn}^{2+}]$  cations 4.5-4.78. Reactions at the corner are more favourable than at the centre; depending on the width of the, growth of the next layer (within the basal layer i.e. in the  $[1\bar{1}0]$  direction) will potentially favour initiation at the corners.



Appendix A2. Simplified point charge surface potential calculation and calculation of the electrostatic/ electrochemical contribution to primary particle growth rate.

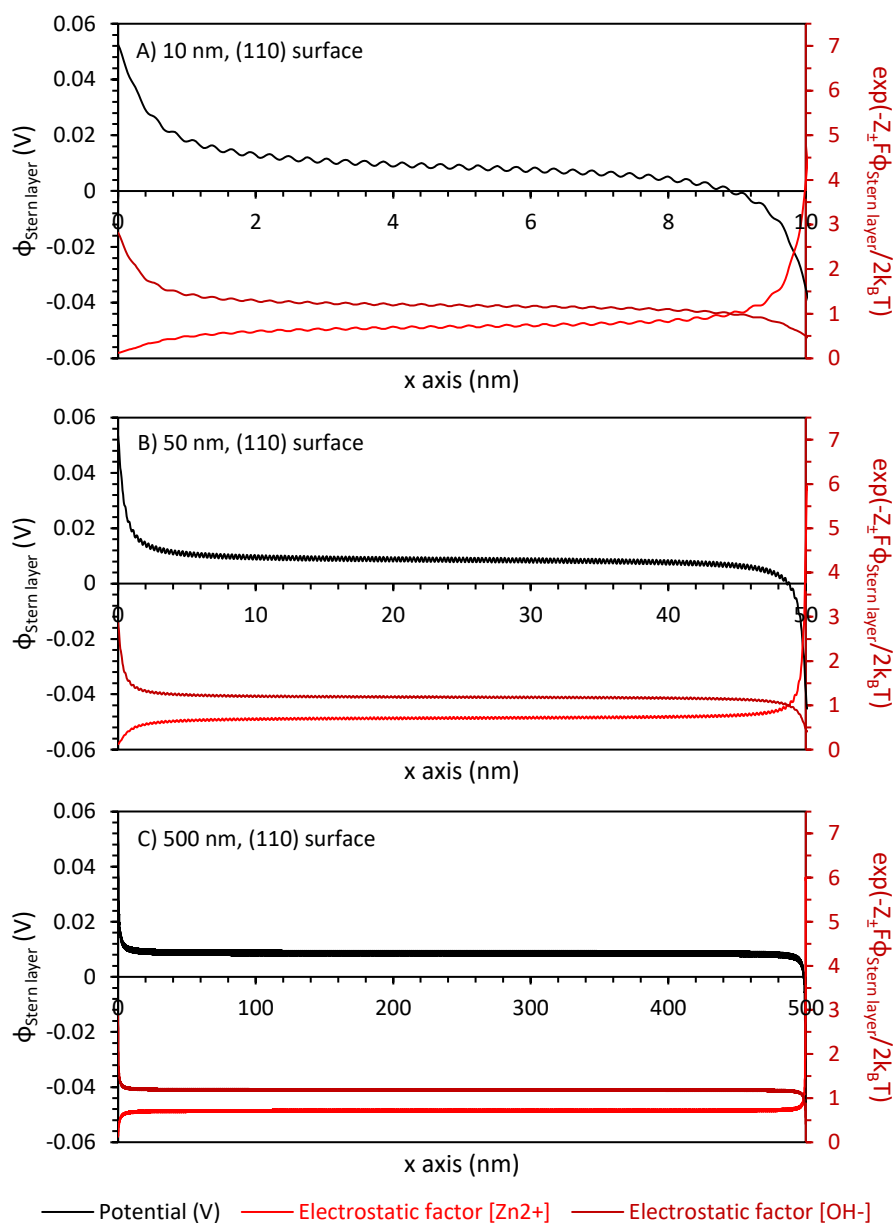


Figure 11.6: Plots of Stern layer potential  $\phi_{\text{Stern layer}}$  and the electrostatic factor  $\exp(-Z_i F \phi_{\text{Stern layer}} / 2k_B T)$  for  $[\text{Zn}^{2+}]$  cations and  $[\text{OH}^-]$  anions at  $T=294$  K, with a Stern layer distance of 0.25 nm, for the neutral (110) surface. The surfaces, with geometry presented in Figure 11.3, have widths of A)  $\sim 10$  nm, B)  $\sim 50$  nm and C)  $\sim 500$  nm. Assuming a cubic particle, the 10 nm surface will be on the order of the dipole surface charge approximation, and the magnitude of the potential will therefore represent the upper boundary. The ion at  $x=0$  nm is a  $[\text{Zn}^{2+}]$  cation. The surface comprised of a single layer in the  $z$  direction.

Figure 11.6 shows plots of the calculated Stern layer potential  $\phi_{\text{Stern layer}}$  and the corresponding electrostatic factor as a function of lateral position for the neutral (110) surface. The mean magnitude of the potentials are between +7.9 mV and +8.6 mV, with  $|\phi_{\text{Stern layer}}|$  approximately 0.078 to 0.081 the magnitude for the  $[\text{Zn}^{2+}]$  overlayer surface and 0.289 to 0.304 that of the  $[\text{OH}^-]$  overlayer surface. The net positive charge likely results from

the concentration of charge on the  $[\text{Zn}^{2+}]$  of  $+2/3e$  vs the  $-1/3e$  per  $[\text{OH}^-]$  anion, combined with the  $z$  displacement of the  $[\text{OH}^-]$  anions relative to the basal layer.

Like the other surfaces, a lateral dipole is seen, with the concentrated charge resulting in an increased spike in the positive potential at the edges of  $+52.5$  mV to  $+53.7$  mV; compared to the  $[\text{OH}^-]$  overlayer that had  $+12.0$  mV to  $+12.6$  mV. The spikes in negative potential between both surfaces are similar; with the (110) surface producing values of  $-43.9$  mV to  $-45.1$  mV, and the  $[\text{OH}^-]$  overlayer  $-41.6$  mV to  $-42.3$  mV. The similarity in negative values therefore arises from the shared co-ordination number of the hydroxide anions.

Again, a superimposed oscillation in potential is present, with peak to peak values of  $\sim 1.2$  mV to  $\sim 1.4$  mV. The oscillation is again expected to arise from the separation of charges, where the separation between individual point charges of  $0.09188$  nm, and between cation and anion centre of  $0.13782$  nm.

Based on the mean potential, the plots of the electrostatic factor show that the reaction rate for  $[\text{Zn}^{2+}]$  cations will be reduced to  $0.713$ - $0.732$  of its Erryng reaction rate value; whereas the reaction rate for  $[\text{OH}^-]$  anions will be increased by a factor of  $1.169$ - $1.184$  at  $294$  K. Peak electrostatic factors for  $[\text{OH}^-]$  anions are  $2.82$ - $2.88$  and  $[\text{Zn}^{2+}]$  cations  $5.67$ - $5.93$ . Reactions at the corner are more favourable than at the centre; depending on the width of the particle, growth of the next layer (within the basal layer i.e. in the  $[110]$  direction) will potentially favour initiation at the corners for the  $10$  nm samples.

### 11.2.2 7-layer geometry calculations

Figure 11.7, Figure 11.8, and Figure 11.9 shows plots of the calculated Stern layer potential  $\phi_{\text{Stern layer}}$  and the corresponding electrostatic factor as a function of lateral position of the;  $[\text{Zn}^{2+}]$  terminated  $(1\bar{1}0)$  surface with  $[\text{OH}^-]$  overlayer,  $[\text{OH}^-]$  terminated  $(1\bar{1}0)$  surface with  $[\text{Zn}^{2+}]$  overlayer, and neutral (110) surface respectively. Increasing the number of basal layers has only a minor effect on the mean potential, with the  $[\text{Zn}^{2+}]$  overlayer surface changing by  $\leq 0.5\%$ ,  $[\text{OH}^-]$  overlayer surface changing  $\leq 7.1\%$  and (110) surface  $\leq 11\%$ . The increased changes for the  $[\text{OH}^-]$  overlayer and (110) surfaces, as compared to the  $[\text{Zn}^{2+}]$  overlayer surface layer like results from the lower starting potential, and reduced cation – anion centre separation distances. The change in mean potential predominantly arises from the edges, a comparison of the edge potentials for the single layer and 7 layer geometries is shown in

Table 11.1. As the edge potentials arise from the idealised order imposed by the geometries used, it is not clear whether they will exist in the physical systems. If they do then growth would have a higher chance at initiation at the edges for all cases as compared to the single layer calculations.

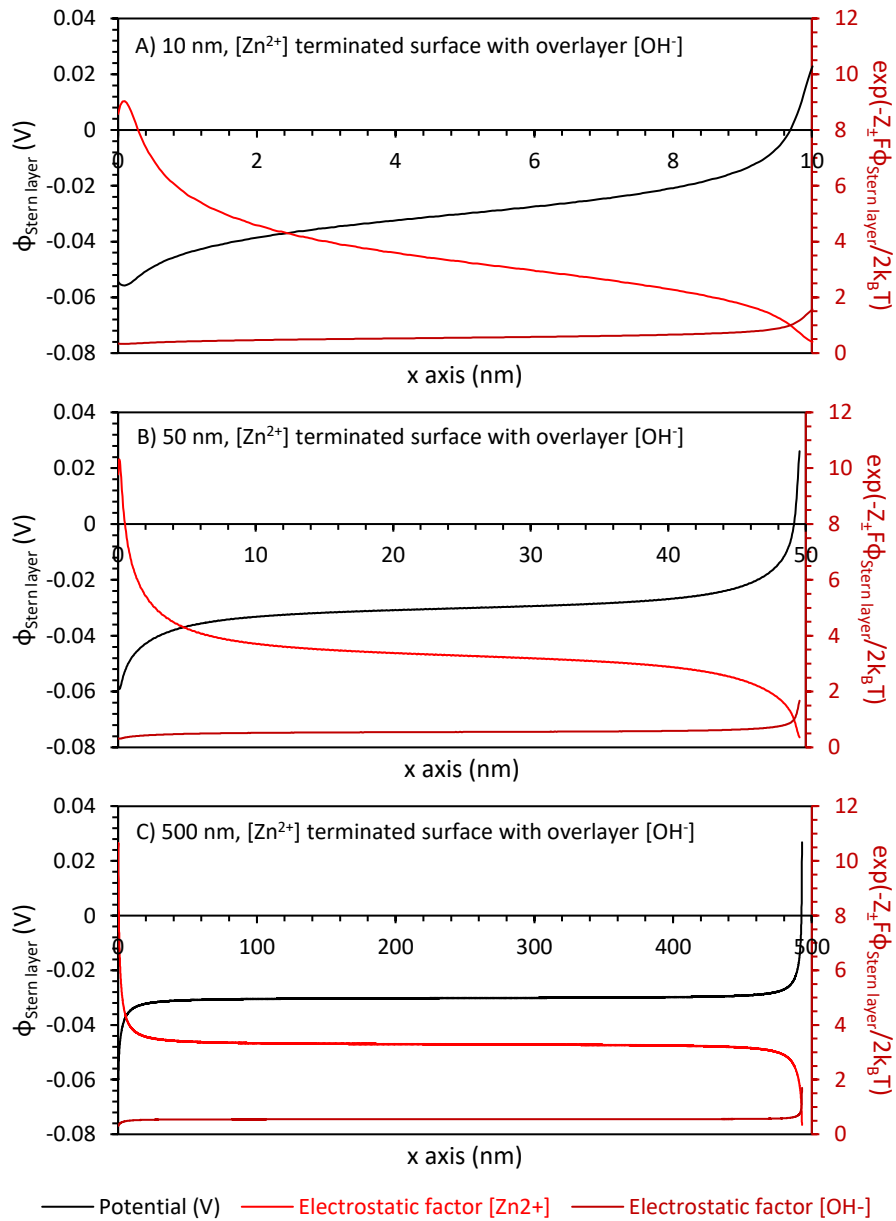


Figure 11.7: Plots of Stern layer potential  $\phi_{\text{Stern layer}}$  and the electrostatic factor  $\exp(-Z_i F \phi_{\text{Stern layer}} / 2k_B T)$  for  $[\text{Zn}^{2+}]$  cations and  $[\text{OH}^-]$  anions at  $T=294$  K, with a Stern layer distance of 0.25 nm, for the  $[\text{Zn}^{2+}]$  terminated surface with an overlayer of  $[\text{OH}^-]$  anions. The surfaces, with geometry presented in Figure 11.1, have widths of A)  $\sim 10$  nm, B)  $\sim 50$  nm and C)  $\sim 500$  nm. Assuming a cubic particle, the 10 nm surface will be on the order of the dipole surface charge approximation, and the magnitude of the potential will therefore represent the upper boundary. The ion at  $x=0$  nm is an  $[\text{OH}^-]$  anion. The surface comprised of 7 layers in the  $z$  direction.

Appendix A2. Simplified point charge surface potential calculation and calculation of the electrostatic/ electrochemical contribution to primary particle growth rate.

The minor effect on mean potential is likely limited to the Stern layer potential, due to the length scales between ion separation and stern layer distance. As test charge-surface separation distance increases relative to the ion separation potential (i.e. when all values of  $R_n$  tend to a single value), the more the number of layers would be expected to increase the mean.

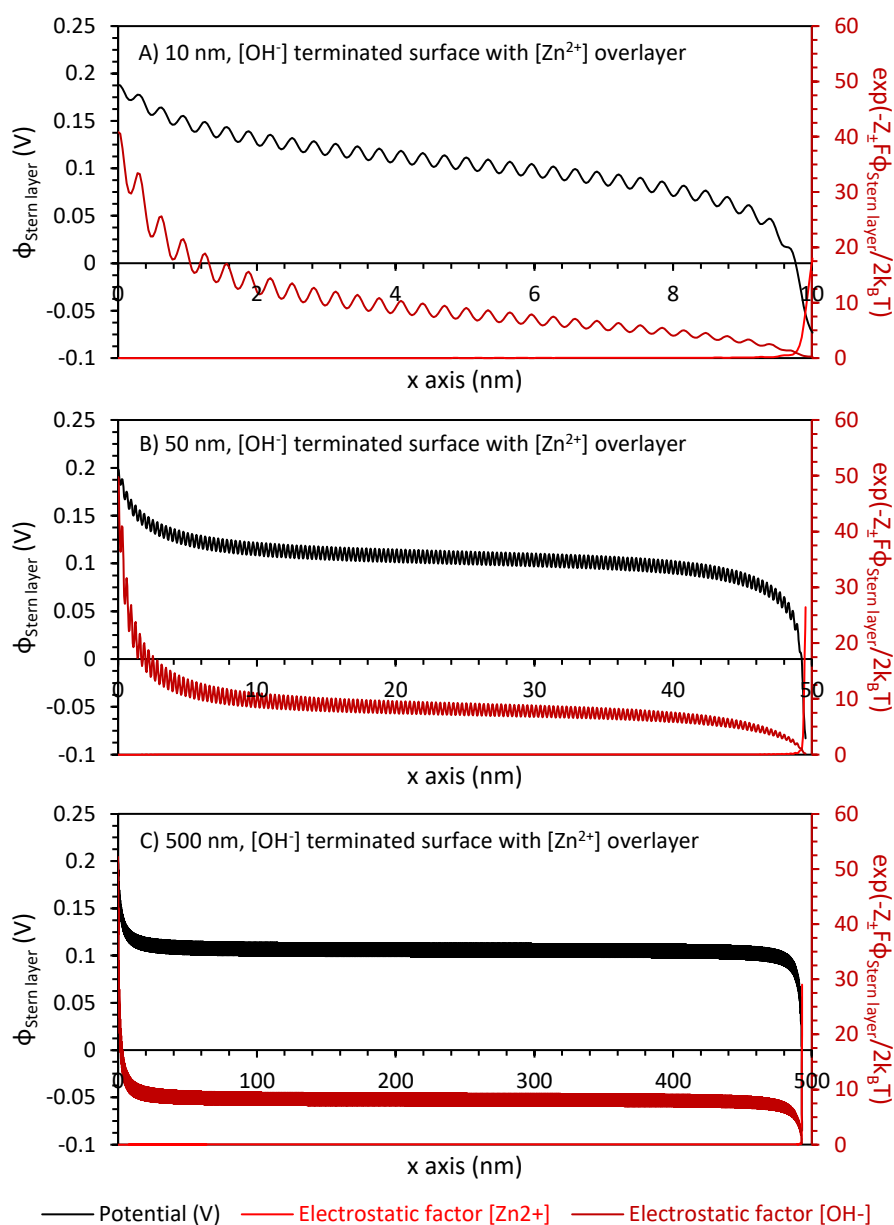


Figure 11.8: Plots of Stern layer potential  $\phi_{\text{Stern layer}}$  and the electrostatic factor  $\exp(-Z_{\pm}F\phi_{\text{Stern layer}}/2k_B T)$  for  $[\text{Zn}^{2+}]$  cations and  $[\text{OH}^-]$  anions at  $T=294$  K, with a Stern layer distance of  $0.25$  nm, for the  $[\text{OH}^-]$  terminated surface with an overlayer of  $[\text{Zn}^{2+}]$  anions. The surfaces, with geometry presented in Figure 11.2, have widths of A)  $\sim 10$  nm, B)  $\sim 50$  nm and C)  $\sim 500$  nm. Assuming a cubic particle, the  $10$  nm surface will be on the order of the dipole surface charge approximation, and the magnitude of the potential will therefore represent the upper boundary. The ion at  $x=0$  nm is a  $[\text{Zn}^{2+}]$  cation. The surface comprised of 7 layers in the  $z$  direction.

Appendix A2. Simplified point charge surface potential calculation and calculation of the electrostatic/ electrochemical contribution to primary particle growth rate.

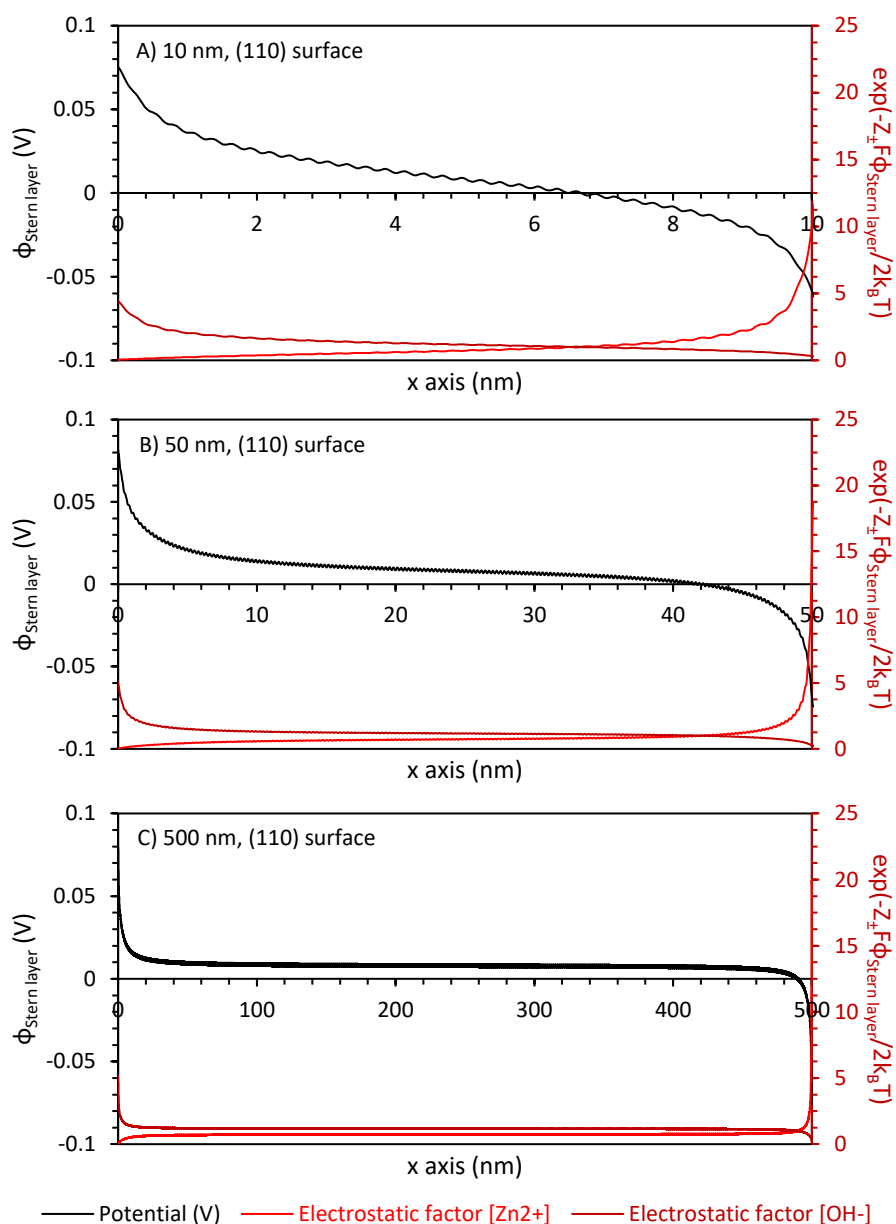


Figure 11.9: Plots of Stern layer potential  $\phi_{\text{Stern layer}}$  and the electrostatic factor  $\exp(-Z_i F \phi_{\text{Stern layer}} / 2 k_B T)$  for  $[\text{Zn}^{2+}]$  cations and  $[\text{OH}^-]$  anions at  $T=294$  K, with a Stern layer distance of 0.25 nm, for the neutral (110) surface. The surfaces, with geometry presented in Figure 11.3, have widths of A)  $\sim 10$  nm, B)  $\sim 50$  nm and C)  $\sim 500$  nm. Assuming a cubic particle, the 10 nm surface will be on the order of the dipole surface charge approximation, and the magnitude of the potential will therefore represent the upper boundary. The ion at  $x=0$  nm is a  $[\text{Zn}^{2+}]$  cation. The surface comprised of 7 layers in the  $z$  direction.

Appendix A2. Simplified point charge surface potential calculation and calculation of the electrostatic/ electrochemical contribution to primary particle growth rate.

Number of layers (50 nm wide surface)	$\phi_{\text{Stern Layer}}$ (mV)					
	[Zn <sup>2+</sup> ] terminated, [OH <sup>-</sup> ] overlayer (1 $\bar{1}$ 0) surface		[OH <sup>-</sup> ] terminated, [Zn <sup>2+</sup> ] overlayer (1 $\bar{1}$ 0) surface		(110) surface	
	X <sub>0</sub>	X <sub>Max</sub>	X <sub>0</sub>	X <sub>Max</sub>	X <sub>0</sub>	X <sub>Max</sub>
1	-42.1	11.2	154.0	-38.6	53.4	-44.9
7	-58.0	26.1	198.0	-83.0	81.8	-73.9

Table 11.1: Table of Stern layer potentials for the 50 nm wide surfaces with a single basal layer, and 7 basal layers as measured at the edges of each surface.

### 11.2.3 The effect of temperature on the electrostatic factor

Ion	$\exp(-Z_{\pm}F\phi_{\text{Stern layer}}/2k_{\text{B}}T)$ - 1 Layer			$\exp(-Z_{\pm}F\phi_{\text{Stern layer}}/2k_{\text{B}}T)$ - 7 Layers		
	(1 $\bar{1}$ 0) surfaces		(110) surface	(1 $\bar{1}$ 0) surfaces		(110) surface
	[OH <sup>-</sup> ] Overlayer	[Zn <sup>2+</sup> ] Overlayer		[OH <sup>-</sup> ] Overlayer	[Zn <sup>2+</sup> ] Overlayer	
T = 294 K						
[Zn <sup>2+</sup> ]	3.02	0.02	0.72	3.26	0.02	0.74
[OH <sup>-</sup> ]	0.58	7.89	1.18	0.55	7.92	1.16
Mean max factor ratio	5.75			5.88		
T = 351 K						
[Zn <sup>2+</sup> ]	2.52	0.03	0.76	2.69	0.03	0.77
[OH <sup>-</sup> ]	0.63	5.64	1.15	0.61	5.66	1.14
Mean max factor ratio	4.28			4.37		

Table 11.2: Table of electrostatic factor  $\exp(-Z_{\pm}F\phi_{\text{Stern layer}}/2k_{\text{B}}T)$  for the mean Stern layer potential for all surfaces modelled for both [Zn<sup>2+</sup>] cations and [OH<sup>-</sup>] anions. Mean max factor corresponds to the ratio of the mean maximum value per surface divided by the mean value for the (110) surface i.e. for a single layer at 294 K,  $\left(\frac{3.02+7.89}{2}\right)/\left(\frac{0.72+1.18}{2}\right)$

Table 11.2 shows the electrostatic factor for [Zn<sup>2+</sup>] and [OH<sup>-</sup>] ions for all surfaces modelled at room temperature T= 294K, and the peak temperature measured after 30 seconds of microwave exposure T = 351 K. Increasing temperature has a minor effect on the ions approaching the surface that have the same sign as the ions in the overlayer (i.e. anions for anion overlayer), with the factor increasing slightly.

Increasing temperature as expected decreases the factor significantly for ions of the opposite charge; with a maximum reduction to 71 % of the initial factor. Using the assumptions that:

Appendix A2. Simplified point charge surface potential calculation and calculation of the electrostatic/ electrochemical contribution to primary particle growth rate.

- desorption is negligible
- the reaction rate is limited by the time taken when the surface charge is neutralised
- That all other factors in the Erryng reaction rate are equal for all surfaces
- The reaction rate for the  $(1\bar{1}0)$  surfaces is dependent on only the largest factor for each face, and the final  $(1\bar{1}0)$  surface is the mean of the maximum factor for  $[\text{OH}^-]$  overlayer and  $[\text{Zn}^{2+}]$  overlayers surfaces i.e. dependant on the  $[\text{Zn}^{2+}]$  rate for the  $[\text{OH}^-]$  overlayer surface.
- The reaction rate for the  $(110)$  surface is dependent on the mean of the factor for both  $[\text{Zn}^{2+}]$  and  $[\text{OH}^-]$  ions due to their maximum difference of 0.46.

Then the aspect ratio can be approximated as the ratio of mean factors for  $(1\bar{1}0)$  surfaces and  $(110)$  surface. The maximum ratio calculated at 294 K from the mean Stern layer potentials was 5.75. Using the maximum calculated edged potentials instead produced a ratio of 2.22, lower than the ratio for the maximum ratio. The maximum ratio calculated was significantly lower than the maximum aspect ratio measured of 51.1 for an  $[\text{OH}^-]/[\text{Zn}^{2+}]$  ratio of 1.44 observed in chapter 5.3.1.2.2.1 . Increasing the temperature from 294 K to 351 K is expected to reduce the aspect ratio to 74.3 % of its initial value. The reduction is significantly lower than that physically measured, where the aspect ratio reduced from 51.1 to 5.71 i.e. to 11.17 % of its initial value.

### 11.3 Conclusion

The Stern layer potential of 10, 50 and 500 nm wide particles was calculated from first principles using a simplified point charge model, for the charge neutral  $(1\bar{1}0)$  and  $(110)$  surface equivalents of the stern layer. The presence of a dipole in the  $[1\bar{1}0]$  direction was confirmed by the increased magnitude of the mean potentials present of 104.7 mV and -28.0 mV for  $[\text{OH}^-]$  terminated surfaces ( $[\text{Zn}^{2+}]$  overlayer) and  $[\text{Zn}^{2+}]$  terminated surfaces ( $[\text{OH}^-]$  overlayer) respectively, compared to the mean potential of 8.4 mV in the  $[110]$  direction. Using assumptions to simplify the reaction rates, the aspect ratio calculated from the mean potential was 11.27 % that observed for the physical reaction. In chapter 5.3.1.2.2.2 , through observations made in literature, and calculation of the difference in energy barriers for growth in the  $[1\bar{1}0]$  and  $[110]$  directions; the aspect ratio is argued to arise from the effects of the dipole on secondary growth processes i.e. dipole driven oriented attachment.

# Chapter 12 - Appendix B1. Automated gas sensor testing rig

In Chapter 6.3.2 a brief overview of the new automated gas sensor testing rig was presented. Within this appendix a detailed description is provided for prosperity. The automated testing rig as shown in Figure 6.4 (and described directly below,) represents a major expansion and improvement in testing capability and reliability, it also contains the possibility for future expansion in line with the long term aims of the project.

## 12.1 Schematic

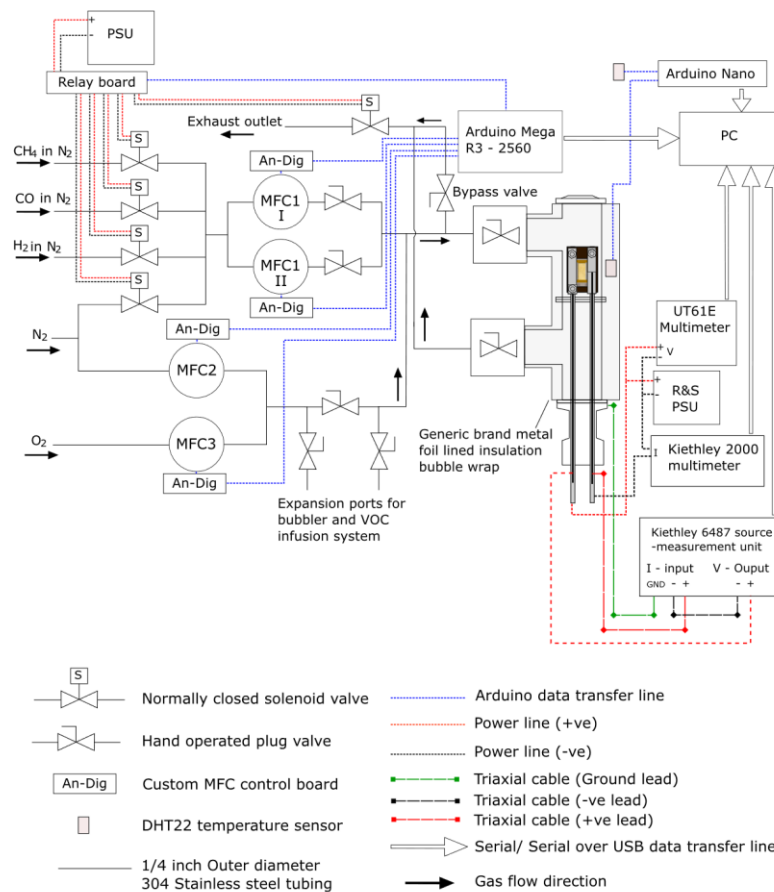


Figure 12.1: Annotated schematic of the automated gas sensor testing rig used within these investigations. The GFC 17 (Aalborg) mass flow controllers and DN25KF T-pieces (Lewvac) with internal diameter of approximately 20 mm used for the manual gas sensor testing rig presented in Chapter 4.1.2. were reused for the automated rig. Mass flow controller flow ranges: MFC1 I (Test gas line): 0–100 mL.min<sup>-1</sup>, MFC1 II (Test gas line): 0–10 mL.min<sup>-1</sup>, MFC2 (N<sub>2</sub> balance line): 0–1000 mL.min<sup>-1</sup> and MFC3 (O<sub>2</sub> line): 0–200 mL.min<sup>-1</sup>. GFC 17 MFC accuracy 1% of total flow range <sup>[489]</sup>.



## 12.2 Gas system

The same dual 20 mm diameter DN25KF T-piece (LewVac components Ltd, Sussex, UK) chamber and DN25KF 4 pin K-type thermocouple feedthrough (LewVac components Ltd, Sussex, UK) presented in chapter 4.1.1.5.2 was used in the manual sensor testing rig. The GFC-17 (Aalborg instruments and controls Inc., New York, US) mass flow controllers used in chapter 4.1.1.5.2 were reconfigured to be controlled via voltage signals using the inbuilt jumpers. An additional 10 mL.min<sup>-1</sup> GFC 17 MFC controller (MFC1 II - originally used as a secondary MFC by Jones for lower concentrations of test gas <sup>[77]</sup>) was added in parallel to the test gas MFC (MFC1 I) to allow for lower test gas concentrations to be tested accurately. ¼ inch hand operated plug valves (Swagelok, Bristol, England, UK) were added to isolate the MFC not in use during any individual test. 3 separate test gas inlet lines were installed into the system prior to the test gas MFCs, each gas was individually isolatable through SCG256A404VMS normally closed solenoid valves (ASCO Numatics, Emerson. United States). The test chamber and all gas flow controlling components were connected with ¼ inch outer diameter unpassivated 304 stainless steel tubing (Swagelok, Bristol, England, UK,) and ¼ inch 304 stainless steel t-piece and elbow connectors with compression fittings (Swagelok, Bristol, England, UK.) Room for future capability expansion was included through two t-pieces with hand operated plug valves for inclusion of a bubbler and/ or secondary VOC infusion system. The investigations used in this chapter use the same gasses as in chapter 4.1.3 i.e. 1000 ppm H<sub>2</sub> in N<sub>2</sub>, 1000 ppm CH<sub>4</sub> in N<sub>2</sub>, 1000 ppm CO in N<sub>2</sub> and 99.999 % purity O<sub>2</sub> (all supplied by BOC speciality products division, Surrey, UK) and 99.998 % purity oxygen free nitrogen (BOC industrial gasses division, Surrey, UK.)

## 12.3 Electronic systems

The solenoid valves and mass flow controllers were controlled via an Arduino Mega R3-2560 (Arduino LLC, Massachusetts, US) prototyping board communicating with a custom in house LabVIEW program (LabVIEW - National Instruments, Austin, Texas, US). The gas flow controller measurement readouts were converted from an analogue voltage output to a digital signal using the 10-bit ADC on the Arduino Mega whilst the gas flow was set using a 12 bit- MCP4921-E/P DAC (Microchip technologies, Arizona, US) on a custom in house PCB. The mass flow measurement readout precision was 0.0977 % of the total flow range of each individual MFC, the set point signal precision was 0.0244 % of the total flow

range of each individual MFC. In principle using the 1000 ppm test gasses and a combined gas flow of  $400 \text{ mL}\cdot\text{min}^{-1}$  an approximately 24.4(3) ppb step size can be obtained. The MFC accuracy of 1% will likely provide the fundamental limit of the test concentration, using the 1% accuracy for each MFC (using MFC1 II for its lower mass flow) and the 1000 ppm test gasses produces a minimum accuracy between 0 and 0.243 ppm at the 1% flow rate of MFC1 II. Solenoid valves were powered using a generic brand commercial relay board driven with by a 72-8690A laboratory testing PSU (Tenma). Room temperature and external chamber temperature were monitored using a DHT22 temperature sensor (Aosong Electronics co. Ltd. China) in communication with the LabVIEW program via an Arduino nano (Arduino LLC, Massachusetts, US). The testing chamber and external chamber temperature sensor was subsequently wrapped in a generic brand metal foil lined bubble wrap insulation tape to improve temperature stability. The external chamber sensor was used to monitor when the chamber temperature reached equilibrium.

### **12.4 Measurement System**

To improve the sensing resistance range, precision and accuracy, sensing layer resistance measurements were performed using a Keithley 6487 source measurement unit (Keithley Instruments LLC, Ohio, US). The 6487 was connected to and controlled by the LabVIEW program via a serial over USB connection. The 6487 had test current ranges between 20 mA and 2 nA at decade intervals. The maximum precision of the 6486 was approximately 0.01 pA though accuracy was mainly limited by test set up. Routine measurements of down to 0.58 nA ( $17.2 \text{ G}\Omega$  at 10 V) could be performed with the application of a digital low pass filter post measurement. Power to the heater track was applied by a manual controlled HMC8042 PSU (Rohde & Schwarz, Munich, Germany.) A Keithley 2000 multimeter (Keithley Instruments LLC, Ohio, US) was used to monitor heater track current and a UT61E Multimeter (UNI-T, Unit trend Co. Ltd. China) to monitor the voltage across the feedthrough electrodes. Both the 2000 and UT61E were connected to the LabVIEW program via serial over USB to provide real time monitoring of the heater track resistance. From the heater track resistance sensor surface temperature was estimated using a pre-determined calibration curve. A similar calibration procedure was performed as in chapter 4.1.1.5.3 , using a thermocouple to measure surface temperature over a set time period whilst heater track current and voltage was recorded. The calibration procedure however was performed within the test chamber under  $400 \text{ mL}\cdot\text{min}^{-1}$   $\text{N}_2$  flow to simulate test conditions and improve temperature calibration accuracy. In addition, the applied voltage and current were measured

simultaneously to provide an instantaneous resistance, allowing for standard deviation of the measurement to be calculated directly as opposed to being measured separately for the manual sensor testing rig. Due to the limited number of feedthroughs pins the chamber seal was broken to perform the calibration procedure. The seal was broken at the feedthrough flange between the sensor and the chamber gas outlet, with the gap approximated at 1-2 mm. The sensor testing rig was moved to a new location with temperature variations approximately 2 °C over a 24-hour period to further reduce uncertainties in temperature. A combination of new location, thermal insulation and improved power supply stability reduced estimated gas sensor temperature variations to no more than 4 °C over a typical 24-hour period. In comparison the manual sensor testing rig had a (weather derived,) room temperature dependent sensor temperature variations of up to 4 °C within the space of an hour. By reducing the MFC pressure to the bare minimum under continuous transition testing cycles using the solenoid valves, mass flow transients were successfully reduced from  $\pm 20 \text{ mL}\cdot\text{min}^{-1}$  to no more than  $\pm 3 \text{ mL}\cdot\text{min}^{-1}$ .

### 12.5 Custom LabVIEW test program

All instrumentation was in communication with the PC via serial connections, measurement data was recorded by the LabVIEW program in the .CSV file format. The number of data points recorded by the LabVIEW program were expanded from the 900-point limitation of the measurement program package provided with the Keithly 2000 (used for the manual operating system,) to a size limited purely by hard drive capability (1 TB). The increased data storage allows for longer and more complicated tests while measuring the sensing response with finer timing precision and accuracy. Routine sampling rates were on the order of 1 sample per second. Prior to testing the following static variables could be controlled:

- Power line cycle integration factor
- Heater track calibration factor Keithley 2000 and 6487 current limits
- Save file location

The following variables could be defined prior to and at any point during the test:

- Time per step
- Individual MFC gas flow set points
- Individual test gas and system outlet solenoid valve states
- Keithley 6487 voltage applied to the sensing layer

## Appendix B1. Automated gas sensor testing rig

- Current (and hence for the 6487 resistance) test range of the Keithley 2000 and 6487 multimeters
- Number of steps, number of program cycles. In addition, the program step could be skipped at any point during the test.

Test variables recorded by the program included:

- Date and time as well as elapsed time since the start of the test
- Program setup/ step index
- Individual MFC mass flow readouts
- Individual relay states
- Keithley 6487 current range, applied voltage and measured resistance
- UT61E (heater track) voltage range and measured voltage
- Keithley 2000 current range and measured (heater track) current
- Estimated sensor surface temperature and inputted temperature calibration factor
- DHT22 room and external chamber temperatures.

### **12.6 Heater track – surface temperature calibration procedure**

For both the manual and automated gas sensor testing rigs the surface temperature was predicted from the heater track resistance on the rear side of the commercial alumina substrate using a calibration factor. In Chapter 4 the calibration procedure was performed prior to deposition of the LBZA material.

The calibration procedure used for the manual sensor testing rig was introduced by Jones <sup>[77]</sup>. The procedure consisted of mounting the substrate to the feedthrough, which was then held in a clamp stand, exposed to the external (room) atmosphere. A pre-set voltage was applied and left until the surface temperature on the sensor substrate, measured using a K type thermocouple, came to equilibrium. The voltage across the heater track was then recorded over fifteen minutes using the Keithley 2000 (1 sample per second) whilst simultaneously measuring the surface temperature (1 sample every 10 seconds.) Once completed the same test was performed but measuring the heater track current instead of the voltage. The two tests were repeated in 2.5 V increments until a surface temperature exceeding 350 °C was measured. At each point the mean and standard deviation of the voltage, current and combined temperature recordings was calculated. From the mean voltage and current measurements, the mean resistance was calculated using Ohms law. The surface temperature was plot as a function of resistance and a trendline fit to produce the calibration factor.

## Appendix B1. Automated gas sensor testing rig

For the automated system a similar procedure was used, however the voltage and current were recorded simultaneously using the UT61E and Keithley 2000 multimeters, providing an instantaneous resistance measurement (1 sample per second). The same testing procedure was then performed over 10-minute periods. Initially testing was performed external to the testing rig, as in the manual testing rig, however for the final sensor (S3) presented within Chapter 6 the test was performed within the rig under  $400 \text{ mL}\cdot\text{min}^{-1}$  of  $\text{N}_2$  flow to better simulate the sensor testing conditions.

## Chapter 13      Appendix B2. Flexographic printing of LBZA nanomaterial using binder-based inks

---

### 13.1 Introduction

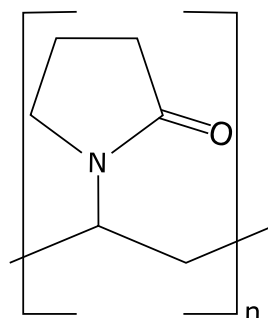


Figure 13.1: Skeleton diagram of PVP (Polyvinylpyrrolidone) used as binder and viscosity adjuster for the binder based LBZA flexographic inks.

In Chapter 6, flexographically printed nanogranular ZnO gas sensors using the particles synthesised in Chapter 4 were developed using a binderless all short-chained alcohol-based ink. The experiments within that chapter were guided by the development of a polyvinylpyrrolidone (PVP) binder-based ink. PVP (shown in Figure 13.1) had been shown to produce high quality thin films of metal oxide nanoparticles in simple alcohols which are compatible with the Digital Rave flexographic printing plates (McDermid Inc. Atlanta, Georgia, US) <sup>[496]</sup>. As such the material was chosen as a binder/ viscosity adjuster to increase viscosity and help aid against ink settling. The ink ultimately had a binder burnout temperature of 450 °C <sup>[575][576]</sup>, greater than the 350 °C <sup>[577][578]</sup> indicated within the literature that the material choice was made from. This ultimately led to the substrate within the test device failing. As certain parameters and observations of the binder-less print, specifically the loading of the ink were derived from the investigations of the PVP based ink, the results are presented below.

## 13.2 Methods

### 13.2.1 PVP Binder based LBZA ink development

#### 13.2.1.1 LBZA nanomaterial synthesis

All LBZA nanomaterial was synthesised, centrifuge cleaned and transferred into IPA as outlined in chapter 6.4.2.1 , producing a LBZA IPA blend with an LBZA mass loading of 49.48 mg.mL<sup>-1</sup>. All inks were produced using the IPA LBZA blend, and LBZA mass was measured out volumetrically using the estimated concentration and micropipettes.

#### 13.2.1.2 Initial LBZA ink loading/ concentration estimation

Due to the compact nature of the LBZA derived sheets annealed at 350 °C observed in chapter 4.1.3.1 , a thin layer of approximately 1 sheet in thickness was assumed to provide the best response (see chapter 4.1.3.2 for a discussion on the response of the sensor from which the decision here is derived). Sensing layer thickness of the drop cast sensor in chapter 4.1.3 was typically between 1 and 4 sheets thick. The drop-cast film however had large areas of the substrate uncovered, it was therefore assumed that the increased distribution of a printed layer would work to counter any resistance gains. The density of the LBZA phase has yet to be reported within literature, therefore with limited confidence in the ability to prevent and/ or remove voids and gas pockets in dried LBZA pellets with available equipment, (a requirement for an accurate density measurement,) initial ink mass loading was estimated theoretically. Starting from the initial estimate the required ink loading would then be optimised empirically.

Initial calculations were based on volumes of printed ink deposited per square metre and LBZA height estimated from AFM measurements presented in Chapter 4.2.3.2 ( $\mu = 14.8$  nm,  $\sigma = 7.5$  nm.) Anilox capacity is stated in volume per square metre, ink loading can therefore be estimated by calculating the mass of the material covering 1 square metre and then dividing that by the volume of the fluid film transferred by the anilox. To estimate mass, first a 1 square metre area of zinc oxide equal to the mean measured height of the LBZA phase was assumed. Using ZnO with a known density (5.606 gcm<sup>-3</sup>) a mass estimate can be produced for the final post calcination film thickness. The mass of LBZA for a 1 metre

square area layer can then be calculated by calculating the number of moles of Zinc in the theoretical ZnO layer and multiplying by the LBZA molecular weight normalised to a single zinc ion (i.e. the molecular weight of LBZA/ 5.) From the estimated LBZA 1 m<sup>2</sup> layer mass the volume concentration of the ink can be calculated. Based on these assumptions the following calculations were performed:

Mass of a 1 square metre layer of zinc oxide with mean height of 14.8 nm:

$$\begin{aligned} \text{Mass}_{\text{ZnO}(1\text{m}^2)}(g) &= \text{Height}(m) * \text{area}(m^2) * \text{density}_{\text{ZnO}}(gm^{-3}) \\ &= 14.8 * 10^{-9} * 1 * 5.606 * 100^3 = 82.969 * 10^{-3} g \end{aligned}$$

Equation 13.1

From this the moles of Zinc (equivalent to the moles of zinc oxide) was calculated:

$$\text{Moles of Zinc} = \frac{\text{Mass}}{\text{Molar Mass}_{\text{ZnO}}} = \frac{82.969 * 10^{-3}}{81.38} = 1.02 * 10^{-3} \text{ moles}$$

Equation 13.2

And the mass of LBZA calculated:

$$\begin{aligned} \text{Mass (LBZA)} &= \text{Moles}_{\text{Zinc}} * \text{Molar Mass}_{\text{LBZA-Zinc normalised}} \\ 1.02 * 10^{-3} * 123.414 &= 0.125(8) g \end{aligned}$$

Equation 13.3

Assuming the ink splits evenly between rollers, i.e. between anilox roller and print plate and between print plate and substrate, then the concentration must be doubled for each transfer event. Then by dividing by the total volume of ink provided by the anilox calculates the estimated concentration required:

$$\begin{aligned} \text{Concentration}_{\text{LBZA}} &= \\ &= \frac{\text{Mass (LBZA)}}{\text{anilox to plate transfer} * \text{plate to substrate transfer} * \text{Volume of ink per m}^2} \\ &= \frac{0.12588}{0.5 * 0.5 * 24} = 20.9 \text{ mg/ml} \end{aligned}$$

Equation 13.4



### **13.2.1.3 Ink mixing**

For all PVP based inks, first a solvent blend of 40 % mass Di(Propylene glycol) methyl ether/ 60 % mass IPA was mixed (DPGME 99% purity - Acros organics, Fisher Scientific, Leicestershire , UK) (IPA 99.5 % purity - Fisher Scientific, Leicestershire , UK). DPGME was chosen to arrest the rapid drying and subsequent clogging of the anilox in inks with IPA as the lone solvent and has a surface tension of  $28.8 \text{ mNm}^{-1}$  [579], boiling point of  $190 \text{ }^\circ\text{C}$  [579] and a vapour pressure of  $37.1 \text{ Pa}$  at  $20 \text{ }^\circ\text{C}$  [579]. PVP was added to the solvent blend to produce the desired blend concentration. Volumes of the IPA/ LBZA blend containing the desired LBZA mass was measured out using a 1 mL Eppendorf micropipette, centrifuged and excess IPA removed. For the theoretical  $20.9 \text{ mg.mL}^{-1}$  loading calculated in section 13.2.1.2 , 2.956 mL of the IPA/ LBZA blend was measured per test ink. Finally, inks were made by adding the PVP/solvent blends up to an approximately 7 mL total volume and mixing. Mixing was performed by varying between manually dispersing with a stirring rod and ultrasonic treatment until no visual aggregation was present and the LBZA was uniformly dispersed. Concentrations of the components of the test ink, estimated from mass measurements performed at each step and the estimated mass concentration of the IPA/ sheet blend, were recorded for all inks. Final concentrations include the estimated mass of IPA within the centrifuge pellet, estimation was based on the difference in LBZA mass (estimated from the volumetric measurement of the IPA/LBZA blend,) and the measured pellet mass. The desired PVP blend and LBZA mass concentrations and measured concentrations can be found within the details for each experiment.

### **13.2.1.4 Ink Characterisation**

#### **13.2.1.4.1 Interfacial tension (IFT) measurements**

Interfacial (surface) tension measurements of the inks were measured using the pendant drop method. Tests were performed using a FTÅ-1000B goniometer (First Ten Ångstrom, California, US) and analysed using the as packaged FTÅ-32 software (First Ten Ångstrom, California, US.) For each test a droplet of ink, typically 3- 4  $\mu\text{L}$  in volume, was formed at the end of a 22 gauge, 0.7mm external diameter flat tip needle attached to a 1 mL syringe (Becton, Dickinson and Company, New Jersey, US.) mounted within the goniometer. For each ink 5 measurements were performed, and the mean and standard deviation calculated.

To assess the density of the ink for the mass calculations performed by the analysis program, 5 sets of 1 mL ink were extracted, the mass recorded using a 4 decimal point analytical mass balance with accuracy of  $\pm 0.5$  mg and mean and standard deviation calculated.

#### ***13.2.1.4.2 Dynamic viscosity measurements***

To assess the dynamic viscosity of all inks, viscosity was recorded using a Bohlin Gemini HR nano rheometer (Malvern Panalytical, Worcester, UK). Measurements were performed in the cone and plate geometry using a 20 mm diameter cone with  $2^\circ$  radius. All tests were performed at 20 °C with a solvent trap to reduce the loss of volatile ink components. The table of shears method was used to measure the steady state dynamic viscosity, For the PVP loading experiment inks (inks A – F) dynamic viscosity was recorded at shear rates of 0.1 to 1000  $\text{s}^{-1}$  with 20 intervals separated by values of 0.158 on a  $\log_{10}$  scale. For the LBZA mass loading inks experiment (inks I – M) dynamic viscosities were measured at shear rates of 1 to 6781  $\text{s}^{-1}$  with 24 intervals separated by values of 0.1667 on a  $\log_{10}$  scale. For all inks 3 measurements were performed with the mean and standard deviation calculated.

#### ***13.2.1.5 Ink print tests***

##### ***13.2.1.5.1 General methodology (consistent parameters)***

All print tests were performed using the F1 flexographic printability tester (IGT testing systems, Amsterdam, Netherlands,) using a 24 mL.m<sup>-2</sup> anilox at approximately 20 °C. In line with the silver electrode print speeds, all print tests were performed at 1.5 m.s<sup>-1</sup> to simulate on-press conditions for sequential silver/ LBZA print. For each print a single revolution pre-coat was used for the inking step. General alignment and printing procedures are described in the printer overview in chapter 6.3.1.1 .

All print tests were performed on 25  $\mu\text{m}$  thick Kapton HN wet chemical and plasma surface treated substrates (see chapter 6.4.1 for treatment details) with a cross sectional area of 50 mm x 50 mm. Thinner substrates than for the silver prints were used with the F1 for the LBZA ink test prints. The change was performed to save on costs and was justified by the F1 using forces rather than engagement distances to control impression pressure; as such the change in thickness was not expected to affect the print quality in a significant manner. For

each print test 5 prints were performed, the first two prints of each test were used to allow for the printer to stabilise and were not used for analysis. Directly after each print the substrate was immediately transferred from the substrate to a hotplate set at 150 °C to remove residual solvent.

### 13.2.1.5.2 PVP binder mass loading – effect of viscosity experiment

For the ink viscosity/ PVP binder mass loading experiment inks were made with solvent blend mixtures of 5, 10, 15, 20, 25 and 30 % weight 55 kDa Mw PVP (Sigma-Aldrich, Dorset, UK) and desired LBZA concentration of 20.9 mg.mL<sup>-1</sup>. The estimated ink parameters based on the recorded masses are shown in

Table 13.1.

Ink	Solvent/ PVP Blend Parameter	Estimated ink parameters based on mass measurements			
	Blend PVP Conc. (%w/w)	Ink PVP Conc. (% w/w)	IPA Conc. (% w/w)	DPGME Conc. (% w/w)	LBZA Conc. (%w/w)
A	5	4.3	61.5	31.8	2.5
B	10	8.6	59.2	30.0	2.6
C	15	12.9	56.5	28.5	2.4
D	20	17.4	53.6	27.1	2.4
E	25	21.8	51.0	25.4	2.3
F	30	26.2	48.4	23.8	2.3

Table 13.1: Estimated blends weight by weight percentage concentrations. Concentrations are estimated based on measurements performed at each step and known mass concentrations of the solvent blends. Blend PVP concentration represents the concentration within the DPGME/ IPA/PVP solvent blend and the Ink PVP concentration represents the final ink PVP concentration estimate.

For the print tests anilox and print forces were set at 50 N. The forces were set as to limit over-impression and ink squeeze out. The digital design of the print plate used is shown in Figure 13.2, along with micrographs of the 5 smallest lines and squares. The digital test design had 9 squares and 8 lines:

- the squares had digital widths of 0.080, 0.127, 0.250, 0.500, 1, 2, 3, 4 and 5 mm. Measurements showed the squares to have widths of N/A (0.08 failed), 0.079 (partial failure), 0.219, 0.459, 0.926, 1.883, 2.795, 3.754 and 4.719 mm respectively
- the lines had digital lengths of 15 mm with and widths of 0.08, 0.117, 0.235, 0.470, 0.938, 1.875, 3.750 and 7.5 mm. Measurements showed the lines to have physical widths of 0.062, 0.114, 0.220, 0.434, 0.900, 1.75, 3.50, 6.99 mm. Line edges had

observed variations of up 0.039 mm in width, (greater than half the smallest line width.)

The 0.08 mm square was below the minimum dot diameter for the Digital Rave photopolymer plate of 0.127 mm <sup>[580]</sup> and failure to produce a flat top surface for the 0.08 mm square was expected, the design was added to see the effect of the process on features below the minimum dot size. For squares with widths of the minimum dot size, partial reproduction of the top surface occurred, for all higher widths the square morphology was reproduced.

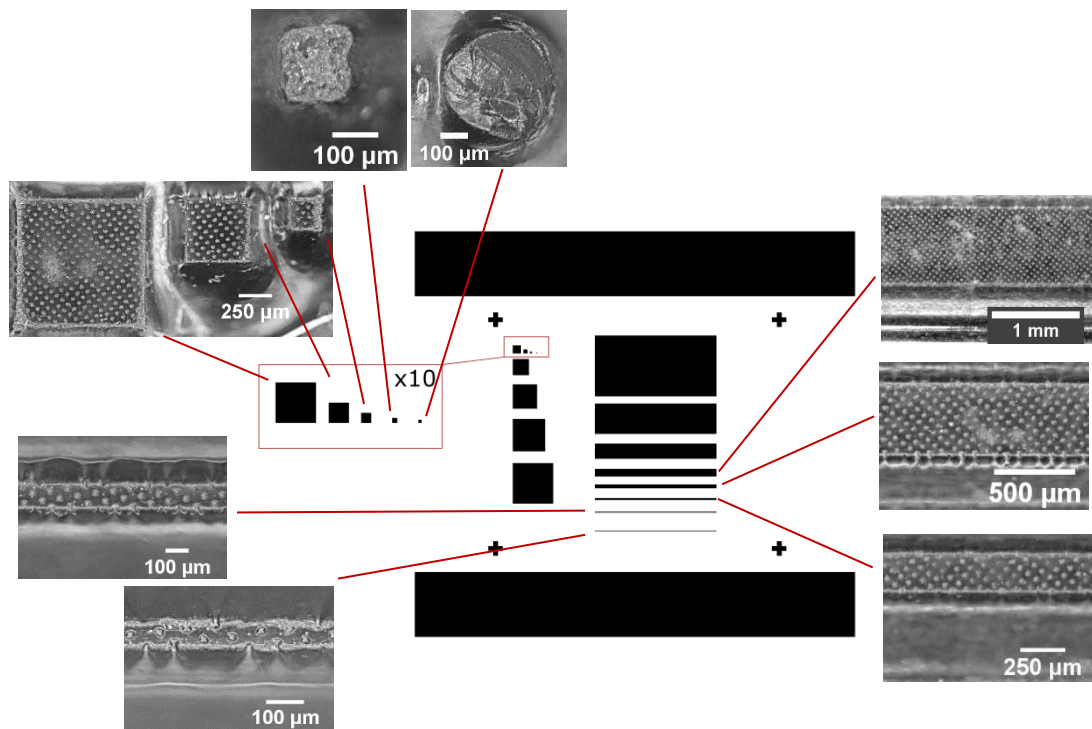


Figure 13.2: Custom print plate design used for the PVP based LBZA ink viscosity experiment with micrographs of the 5 smallest lines and squares. Note that the lines are parallel to the direction of print and that the plate was mounted such that the lines printed prior to the squares. Reproduction of the smallest square failed to produce a flat top surface producing a rounded surface lower than the other print features. The dot pattern present are depressions in the surface, likely caused by lower curing intensities, the pattern is likely a reproduction of the digital step size of the HD Lux laser ablation system used in the manufacturing of the plate to open areas within the applied LUX laminated mask to define the areas for curing <sup>[580]</sup>.

For the higher width values (> 1 mm) the side walls of the features were broader and had a shallower gradient. It is worth noting that the characterisation was performed post use and the observed partial failure for the 0.127 mm square may be a result of damage incurred

during printing. The change in height, as compared to the focal distance of the microscope, possibly accounts for the partial discrepancy in width between plate and digital design. A secondary possible error might be a difference in the industrial definition and measurement of the top surface, as such a simple top down measurement using a microscope might not produce equivalent values as the industrial standard method.

Printed film morphology was recorded using a DSLR with macrolens (Nikon, Tokyo, Japan) and compared visually. Additional micrographs were recorded using a VHX-1000 microscope with variable x20 – x200 lens (Keyence UK, Milton Keynes, UK). Print plate morphology was recorded using the VHX-1000 for comparison with the print features. Film morphology and LBZA dispersion was further assessed using backscatter electron microscopy. Backscatter electron micrographs were recorded using a Hitachi S4800 Type II FEG-SEM with annular YAG backscatter detector (Hitachi High Technologies, Minato-ku, Tokyo, Japan) at an acceleration voltage of 25 kV. Prior to imaging, the samples were coated with 5 nm chromium using a Quorum 150ET sputter coater (Quorum Technologies Ltd., Sussex UK). Sputtering was performed to mitigate sample charging and to increase contrast for recording the images.

#### ***13.2.1.5.3 Force optimisation experiments***

Due to the limitations in alignment capability of the F1 (up to ~2 mm, approximately 20 % of the length of the IDE) a solid block print plate was used for all further LBZA test prints. The decision was made such that the optimized values could be used to print initial test sensors with no variation in coverage due to misalignment. The larger area introduced pinhole defects which were assumed to be due to a reduction in print pressure, a result of the increased area and constant F1 print force.) Test prints to optimise the print force settings were performed using ink E (25% wt PVP/ IPA-DPGME solvent blend) which produced the most uniform prints in the viscosity tests. Anilox force was set to 50 N and prints were performed at print forces of 30, 40, 50, 60 and 80 N. A final set of prints was performed with both anilox and print forces set to 80 N. Print film morphology was recorded using the Keyence VHX-1000 optical microscope. From the recorded micrographs pin hole density was compared qualitatively by visual inspection.

**13.2.1.5.4 LBZA mass loading – effect on coverage experiment**

For the inks IPA/LBZA blend volumes of 2.956 mL, 3.695 mL, 4.434 mL, 5.173 mL, 5.912 mL and 6.651 mL, representing LBZA ink mass loadings of 20.90 mg.mL<sup>-1</sup>, 26.13 mg.mL<sup>-1</sup>, 31.35 mg.mL<sup>-1</sup>, 36.58 mg.mL<sup>-1</sup>, 41.80 mg.mL<sup>-1</sup> and 47.03 mg.mL<sup>-1</sup>, respectively, were measured out and used. The 25 %w/w PVP solvent blend was used for the inks. The final estimated ink component concentrations are shown within Table 13.2.

For all prints performed both anilox and print forces were set to 80 N. For each loading a 6<sup>th</sup> print was performed on a 50 mm x 50 mm area section cut out from the Ag electrode prints (presented in chapter 6.5.1.2 ) to test the effect of loading on gas sensing response. Each electrode sample contained 9 printed IDE.

Ink	Desired Sheet conc. (mg.mL <sup>-1</sup> )	Estimated ink parameters based on mass measurements				
		Sheet loading (mg.mL <sup>-1</sup> )	PVP Conc. (mg.mL <sup>-1</sup> )	IPA conc. (mg.mL <sup>-1</sup> )	DPGME Conc. (mg.mL <sup>-1</sup> )	PVP mass/wet mass
I	20.90	22.3	184	484	220	0.206
J	26.13	28.6	174	510	208	0.195
K	31.35	34.8	168	544	202	0.184
L	36.58	39.6	156	555	188	0.174
M	41.80	46.6	143	579	171	0.160
N	47.03	51.4	134	595	160	0.150

Table 13.2: Estimated loadings based on measured masses at each stage of addition and estimated nanosheet concentration within the IPA/LBZA blend. Wet mass consists of the combined mass of PVP, IPA and DPGME.

Printed LBZA coverage was assessed using backscatter electron micrographs recorded using an EVO LS25 SEM with LaB<sub>6</sub> source (Zeiss, Oberkochen, Germany). Electron acceleration voltage was set to 15 kV, probe current to 1.2 nA, field of view 285.8 μm x 214.4 μm and micrograph resolution to 3072 x 2304 pixels. For each LBZA concentration/ mass loading 1 micrograph from a randomly selected area was recorded from the 3<sup>rd</sup>, 4<sup>th</sup> and 5<sup>th</sup> prints. The micrographs contrast and brightness were adjusted, thresholded and converted to a binary level bitmap using ImageJ (National Institute of Health, US.) Values of 1 represented the presence of LBZA within the bitmap whilst values of 0 represented PVP with a lack of LBZA and/ or the substrate. Each bitmap was split into 307 x 230 pixel sections and coverage assessed by counting the number of pixels with a value of 1 and dividing by the total number of pixels. The mean and standard deviation of all sections per loading was calculated and plotted in Excel. 95% confidence intervals for the mean coverages were calculated using the bootstrap method in MATLAB.

### **13.2.1.6 Printed PVP LBZA ink calcination**

#### **13.2.1.6.1 Calcination time and temperature experiment**

Initial attempts at calcining the PVP layer at 350 °C (based on the observations by Yu *et.al.* [577] and Rioux *et.al.* [578]) in air failed to remove the PVP layer, revisiting literature revealed the decomposition temperature of PVP to be 450 °C. To assess the temperature and time conditions required to burn out the PVP binder 1 cm x 1cm pieces of printed and dried films using the 46.6 mg.mL<sup>-1</sup> loading ink were calcined in air at temperatures of 450, 460, 470, 480, 490 and 500 °C in a tube furnace (Carbolite, Derbyshire, UK). For each temperature calcination with times of 1,2,3,4 and 5 minutes were performed. Temperatures were monitored in situ using an RS PRO k type thermocouple rated to 1200 °C. Binder burn out and surface cleanliness for each sample was assessed using a Kratos axis supra XPS (as outlined for in section 6.4.1.1.2 ). For each condition 5 survey spectra were recorded with pass energies of 160 eV and a step size of 0.5 eV. Carbon, nitrogen, oxygen, zinc, phosphorous, silicon, calcium and sodium atomic concentrations were measured in CasaXPS. To account for pinholes within the printed film carbon and oxygen were corrected by subtracting the atomic concentrations of each element contained in Calcium hydrogen phosphate, calcium carbonate, and organic silicon (assumed to be polydimethylsiloxane) as estimated from the calcium, phosphorous and silicon concentrations. The data was then renormalized excluding calcium, phosphorous and silicon. The presence of calcium hydrogen phosphate (used as a slip/ release agent during manufacturing) in Kapton HN is well documented [581][466], calcium carbonate has also been observed in Kapton HN [466]. Organic silicon was assumed to be contamination introduced at an unknown point, most likely during the manufacturing and/ or packaging of the substrate. The oxygen concentration was then corrected by subtracting the Zn concentration (assumed to be contained within pure ZnO). From the corrected data, ratios of nitrogen to oxygen and carbon to oxygen were calculated and compared to the measured ratio in the combined wet chemical and plasma surface treated substrates (O/C = 0.394, N/O = 0.246) and pure Kapton (O/C = 0.227, N/O = 0.400). Comparison with pure Kapton was made as the amide and carboxylic acid groups in polyamic acid is known to cure into polyimide groups at temperatures exceeding 230 °C [491]. For all concentrations and ratios, the mean of each calcination condition and standard deviation were calculated.

Based on the results, 10-minute calcinations at 450 °C and 460 °C were performed. High resolution XPS measurements (Pass energy 20, step size 0.1 eV) and analysis was then

performed and compared on the Zn 2p, O 1s, C 1s for both conditions and for an uncalcined control.

## 13.3 Results

### 13.3.1 LBZA ink development - Ink 1) – PVP binder based

An initial set of PVP based LBZA NS inks was tested using purely IPA as solvent which resulted in the ink drying on the print press. To counteract the rapidity of drying 40 % of the solvent by mass was exchanged with Di(propylene glycol) methyl ether (DPGME) (boiling point 190 °C, surface tension 28.8 mN/m) for which all the following tests were performed with.

#### 13.3.1.1 Viscosity Optimization – Effect of PVP mass loading

Prior to printing the interfacial tension (IFT) of all inks was tested to check compatibility with the substrate. The mean IFT of each ink, regardless of PVP loading, was between 23 and 24 mN/m with the maximum standard deviation of any ink at 0.5 mN/m. The values showed that addition of PVP with mass loadings between 4.3 % and 26.2 % had minimal effect of surface tension. Performing Sessile drop test using the 4.3 % PVP loading ink onto the modified Kapton HN substrate resulted in complete wetting and was considered ideal for printing.

Figure 13.3 and Figure 13.4 shows photographs and backscatter electron micrographs respectively of flexographically printed samples, produced using the LBZA PVP based inks with mass loadings: A) 4.3 %, B) 8.6 %, C) 12.9 %, D) 17.4 %, E) 21.8 % and F) 26.2 %. In the photographs (Figure 13.3) Ink A (4.3 % PVP) shows ink extending out on the trailing edge (right hand side) of each print feature. A similar phenomenon was seen by Beynon when printing dots using low viscosity inks, with the ink building up behind the doctor blade and resulted in dot bridging <sup>[267]</sup>.



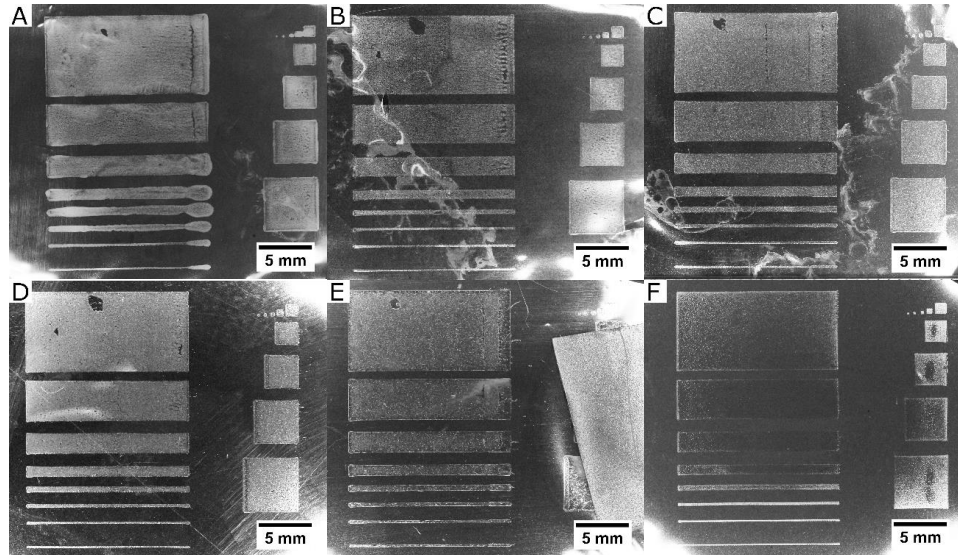


Figure 13.3: Photographs of the flexographic print tests samples using the LBZA PVP based inks with PVP mass loadings of A) 4.3 %, B) 8.6 %, C) 12.9 %, D) 17.4 %, E) 21.8 % and F) 26.2 %. All print tests were performed on the combined wet chemical and plasma treated Kapton HN substrates, using the F1 printability tester (IGT.) Both print force and anilox force set at 50 N and print speed was set to  $1.5 \text{ m.s}^{-1}$ . Print direction left to right, photograph taken from the 5<sup>th</sup> print of each sample set. Note that the significant glare in the images from sample B and C is an artefact arising from substrates adhering to each other during the wet chemical treatment. The artefact affects the reverse (non-printed) side only and is not expected to affect the results in any significant manner. Note the electrical tape in E was required to stabilize the substrate during chromium coating, an uncoated photograph is presented in appendix 14.5 for comparison and transparency.

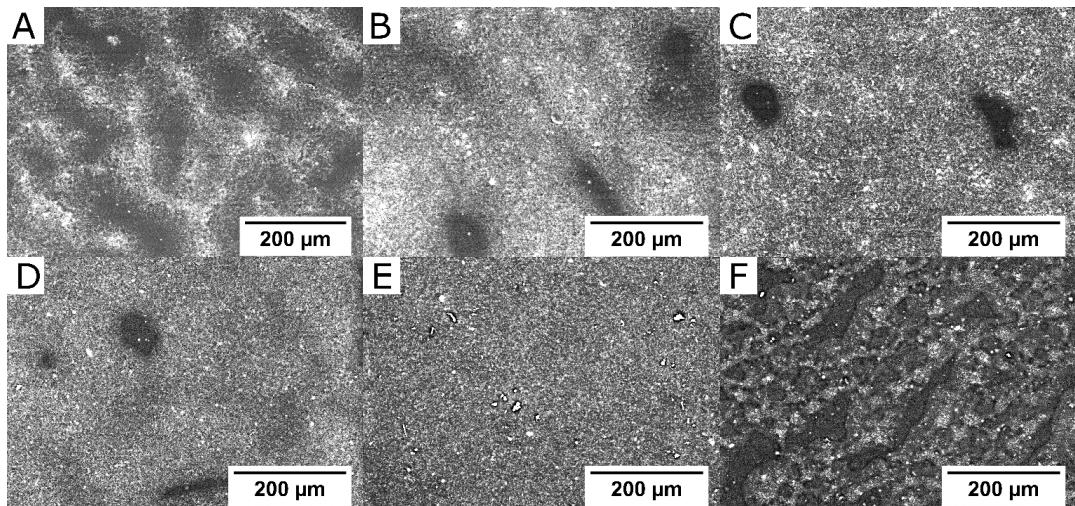


Figure 13.4: Backscattered electron micrographs of the flexographic print tests samples using the LBZA PVP based inks with PVP mass loadings of A) 4.3 %, B) 8.6 %, C) 12.9 %, D) 17.4 %, E) 21.8 % and F) 26.2 %. All print tests were performed on the combined wet chemical and plasma treated Kapton HN substrates, using the F1 printability tester (IGT.) Both print force and anilox force set at 50 N and print speed was set to  $1.5 \text{ m.s}^{-1}$ . Micrographs taken in the centre of the thickest line (top of each photograph) from each sample.

Increasing the PVP content and viscosity eliminates the effect and results in a defined trailing edge. For inks with a PVP content lower than 21.8 % the prints presented with pinholing. The defects can be seen most clearly within the backscattered electron micrographs (Figure 13.4 B – D) and decrease with increasing PVP loading. Simultaneously an increase in edge and corner definition can be seen. Increasing the PVP content to 21.8 % mass removes the presence of pinholing and produces the most uniform printed film. Further increasing PVP content to 26.2 % mass resulted in the sharpest edge definition however the centre of each print showed low uniformity and coverage. The low uniformity was primarily assigned to the ink drying on the print press, with the ink becoming increasingly tacky, and with increasing amounts of filamentation visually observed during separation of the plate from the substrate with each subsequent print. The decreased initial solvent content produced a significant increased solid content during the print runs and resulted in increased ink adhesion, cohesion and poor ink transfer. As was stated within Chapter 6 the large effect of ink drying is a consequence of the open-air ink storage and the time taken between exchanging substrates and is not expected to occur on larger, industrial print presses.

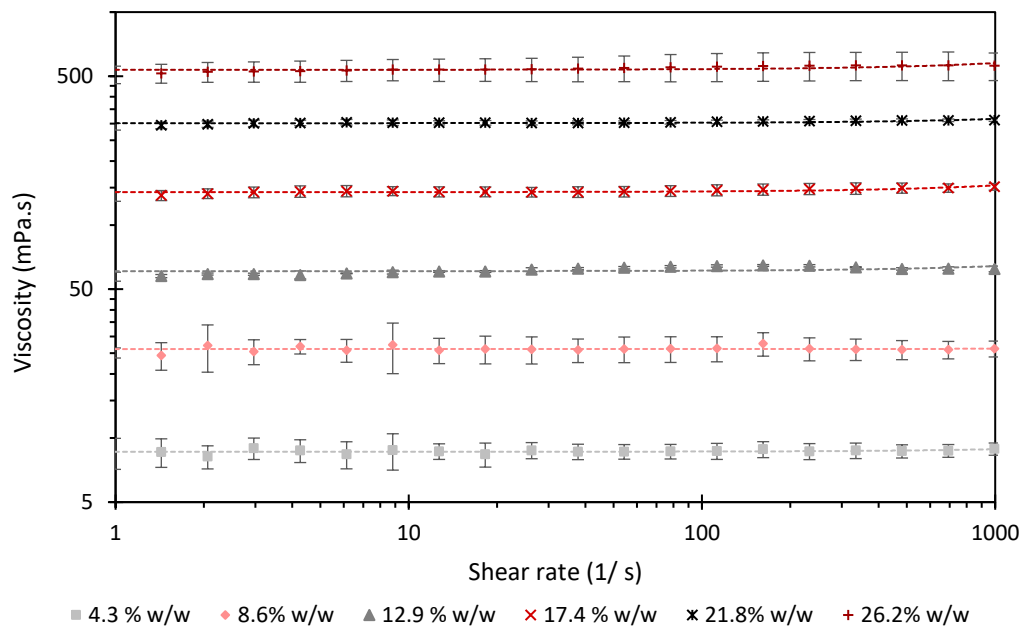


Figure 13.5: Log-log dynamic viscosity profiles as a function of shear rate of the flexographic LBZA PVP based test inks with PVP mass loadings of A) 4.3 %, B) 8.6 %, C) 12.9 %, D) 17.4 %, E) 21.8 % and F) 26.2 %. Trendlines – linear fit. Note that the 26.2 % mass PVP ink required an additional ring of ink to saturate the solvent trap to counter-act a drift in viscosity as a result of solvent evaporation.

Figure 13.5 shows dynamic viscosity profiles of each of the trialed PVP based inks as a function of shear rate. All inks show near Newtonian behaviour, with their rheology

dominated by the mass loading of the polymer. The viscosity at  $1000 \text{ s}^{-1}$  appears to conform to a cubic polynomial of the form:

$$\text{Viscosity (Pa.s)} = 4.41 * 10^{-5}x^3 - 4.72 * 10^{-4}x^2 + 3.37 * 10^{-3}x + 0.0024$$

Equation 13.5

Where  $x$  is the mass loading as a percentage, ( $R^2 = 0.9999$ ). The Newtonian behavior would be generally expected considering the relatively low molecular weight of the PVP used (55 kDa  $\sim$  495 monomers) [582][583], and low mass loadings of both PVP [582] and LBZA particulates ( $\leq 2.6$  % mass) [434]. The low mass loadings and low molecular weight would have limited interactions, leading to a reduced ability for the ink to form any significant internal structure. The inks with 4.3 % PVP have a mean viscosity at  $1000 \text{ s}^{-1}$  of 8.7 mPa.s, which is below the minimum required for successful printing to occur, as stated by Baker *et al.* [4], and corroborates well with observations here.

For ink F evaporation of 25 %, 50 %, 75 % and 100 % of the initial IPA content (48.4 %) would be expected to increase the viscosity from 559 mPa.s to 848, 1365, 2776 and 4630 mPa.s, respectively. Experiments on gravure cell filling by Cen, Kitsomboonloha and Subramanian [253] showed that inks with high capillary number (Ca), approaching 1, led to an increasing quantity of air entrapment within the cells. For Ca values greater than 1 cells were completely filled with air [253]. As capillary number is proportional to viscosity, the significantly increased viscosity would be expected to entrap air in the anilox cells and therefore reduce ink transfer to the print plate. The cubic dependence of mass loading on viscosity, coupled with the volatility of IPA, can therefore explain the majority of the changing printing properties observed for the 26.2 % PVP ink, as well as the added requirement of saturating the solvent trap with added ink whilst testing the viscosity.

Figure 13.6 shows optical micrographs of the printed fine line features for the tested inks, with Figure 13.7 A and B showing measured print width and print gain (printed line width - print plate line feature width) as a function of viscosity for the fine line features. As typically seen for flexographic printing [269][268][17] the printed line width, for a nominal width below  $434 \mu\text{m}$ , is significantly greater than the nominal on print plate line width. This results from ink squeeze and plate deformation [268]. The print measurements show an initial decrease in printed widths when the viscosity is increased from 8.7 mPa.s (4.3 % PVP) to 26.4 mPa.s (8.6 % PVP). Further increasing viscosity to 63.4 (12.9 % PVP), 148.5 (17.4 % PVP) and 308.7 mPa.s (21.8 % PVP) leads to an increase in printed line width and print gain. Beynon

[267] observed an increase in ink transfer with increasing viscosity, the increasing width here is likely then, at least partially, a result of an increase in ink transfer with viscosity.

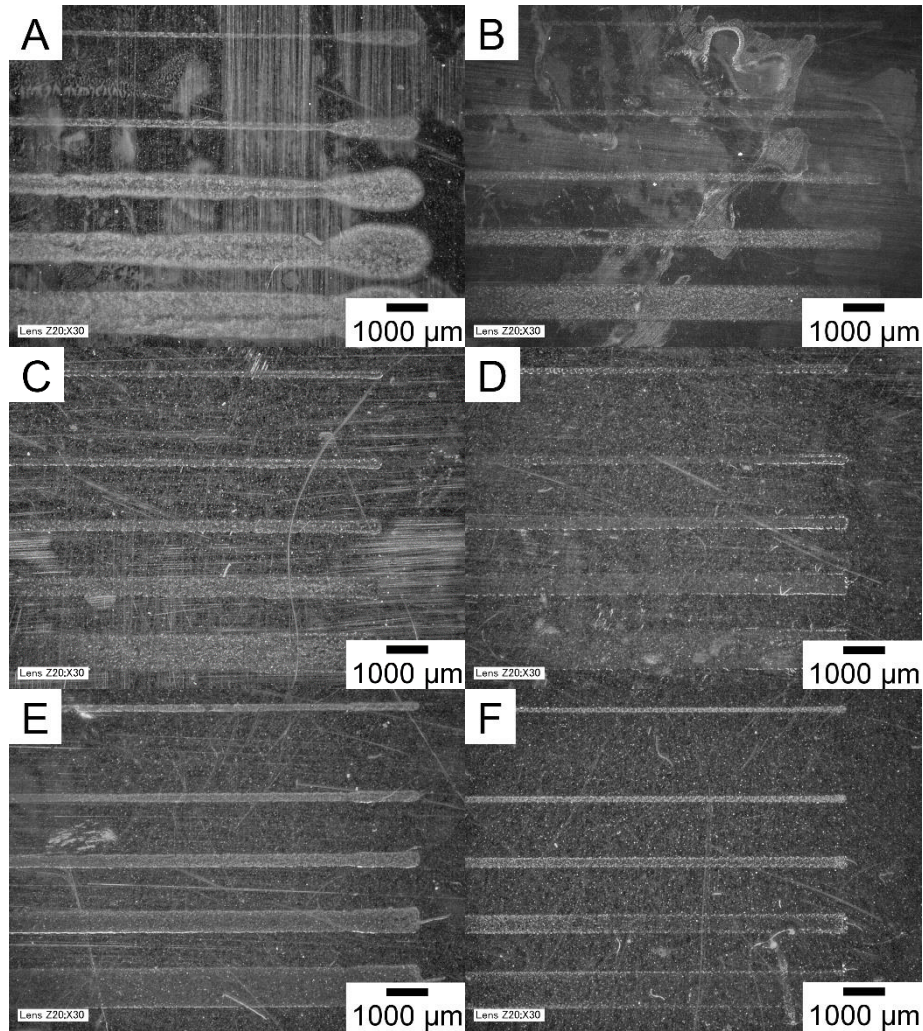


Figure 13.6: Optical micrographs of the flexographic print tests samples using the LBZA PVP based inks with PVP mass loadings of A) 4.3 %, B) 8.6 %, C) 12.9 %, D) 17.4 %, E) 21.8 % and F) 26.2 %. Scale bar – 1000 µm. Note that the significant glare in the images from sample A and B is an artefact arising from substrates adhering to each other during the wet chemical treatment. The artefact affects the reverse (non-printed) side only and is not expected to affect the results in any significant manner.

The increased ink transfer can also account for the decrease in pinholing with increasing PVP content. Increasing the PVP content further leads to a decrease in line width, likely due to the limited ink transfer due to air entrapment.

For all viscosities greater than 8.7 mPa.s, the mean lines widths show an increase in print gain with a reduction in print plate line width. Interestingly the trend is opposite to the relation observed by Deganello *et al.* who observed that print gain increases with nominal width [268]. In their studies nominal line widths between 20 µm and 50 µm were used with

nominal width/ Anilox cell width ratios of between 0.295 and 0.492. In contrast nominal width/ Anilox cell width ratios of 0.496 to 7.2 were used here. This generally suggests that at lower ratio values the lines on the print plate dip into the cell, providing a larger area for ink to transfer from in a manner analogous to dot dipping [264][245].

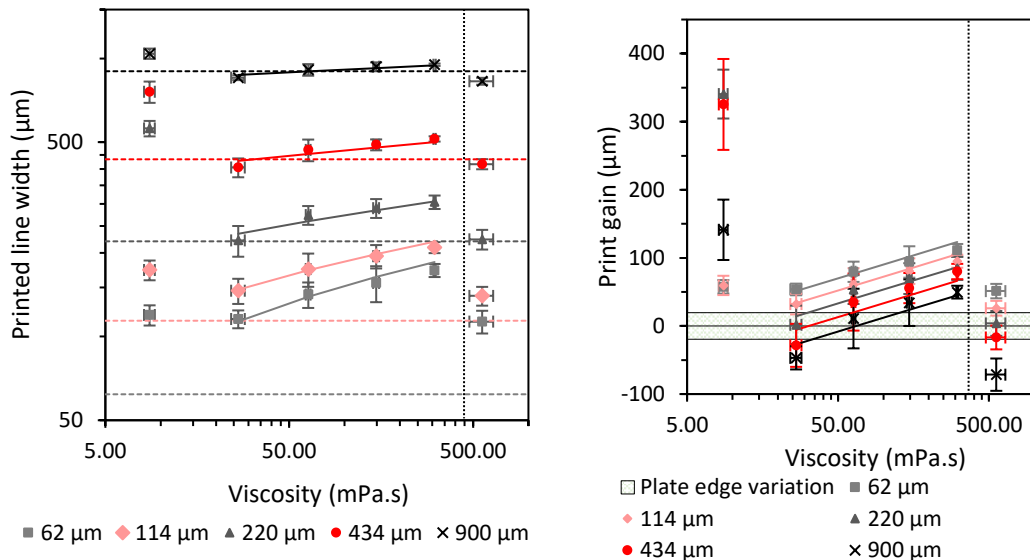


Figure 13.7: A) Log-log plot of mean printed line width as a function of mean viscosity at  $1000 \text{ s}^{-1}$  for the printed lines shown in Figure 13.6. Note that the dashed lines show the mean nominal widths measured directly from the print plate and had an edge max-min variation range of approximately  $39 \text{ }\mu\text{m}$ . B) Plot of print gain (printed line width – width of feature on print plate) as a function of viscosity. For values of viscosity higher than the dotted line viscosity deviates from the measured value due to on press drying effects. The green shaded area is equivalent to the variation range in line width measured on the print plate. The variation is periodic and related to the digital/ direct write manufacturing method used by the manufacturers. Error bars for both figures is equal to 1 standard deviation of  $x$  – viscosity,  $y$  – print line width. From each image 60 samples were taken for each line. Trend lines:  $\text{Print width (m)} = \text{nominal width (m)} + 29.28 \cdot 10^{-6} \cdot \ln(\text{viscosity (Pa.s)} / \text{nominal width (m)}) - 125.9 \cdot 10^{-6}$ ;  $R^2 = 0.999$ .  $\text{Print gain (m)} = \text{Print width (m)} - \text{nominal width (m)}$ ;  $R^2 = 0.927$ .

At larger ratios, the print width is more dependent on the volume of ink transferred and at the lowest viscosities produces a negative print gain as seen here. As a result, all printed track widths for  $62 \text{ }\mu\text{m}$  and  $114 \text{ }\mu\text{m}$  (ratios of 0.50 and 0.91 respectively) are lower than the  $225 \text{ }\mu\text{m}$  print width observed by Degenallo *et al.* [268] for a nominal line width of  $50 \text{ }\mu\text{m}$  using a  $24.22 \text{ mL}\cdot\text{m}^{-2}$  anilox volume (ratio of 0.35.)

Regression analysis performed on all nominal widths with viscosity greater than 20 mPa.s (the cut off quoted by Baker *et al.*) but excluding the 26.2 % PVP, where anilox inking is expected to be deficient, produced the following relationships:

*Print width (m) =*

$$\text{nominal width (m)} + 29.28 * 10^{-6} * \ln\left(\frac{\text{Viscosity (Pa.s)}}{\text{nominal width (m)}}\right) - 129.5 * 10^{-6}$$

*Equation 13.6*

$$\text{Print gain (m)} = 29.28 * 10^{-6} * \ln\left(\frac{\text{Viscosity (Pa.s)}}{\text{nominal width (m)}}\right) - 129.5 * 10^{-6}$$

*Equation 13.7*

The R<sup>2</sup> values for Print width and print gain are 0.999 and 0.927 respectively. ln(Viscosity/nominal width) p-value = 1.5\*10<sup>-11</sup>, and intercept p-value = 5.2\*10<sup>-9</sup>. All p-values are below the 0.05 threshold used for significance.

The relationships between viscosity, nominal width and print gain has relevance for IDE design. For electrodes printed parallel to the direction of print, with a fixed-on plate gap/spacing, there appears to be an inherent minimum nominal and print widths that can be used for any particular ink. As this observation is the opposite to that of Deganello *et al.* a study of viscosity, nominal width and plate hardness with nominal width/ cell width ratios spanning the combined ranges would be required to provide a unified relation. The presence of an underlying unified relation is supported by measurements of dot gain vs tonal coverage by Mai *et al.* [245] that showed a peak dot gain at tonal values between 40 % and 50 %, with a sharp drop off in dot gain at higher tonal values.

Based on the print uniformity, inks with 308 mPa.s at 1000 s<sup>-1</sup> are recommended for ink development with the print forces, feature sizes and print speeds used here. Following the recommendation provided, ink E (21.8 % PVP) was chosen for all further PVP based ink experiments.

### 13.3.1.2 Print force optimization

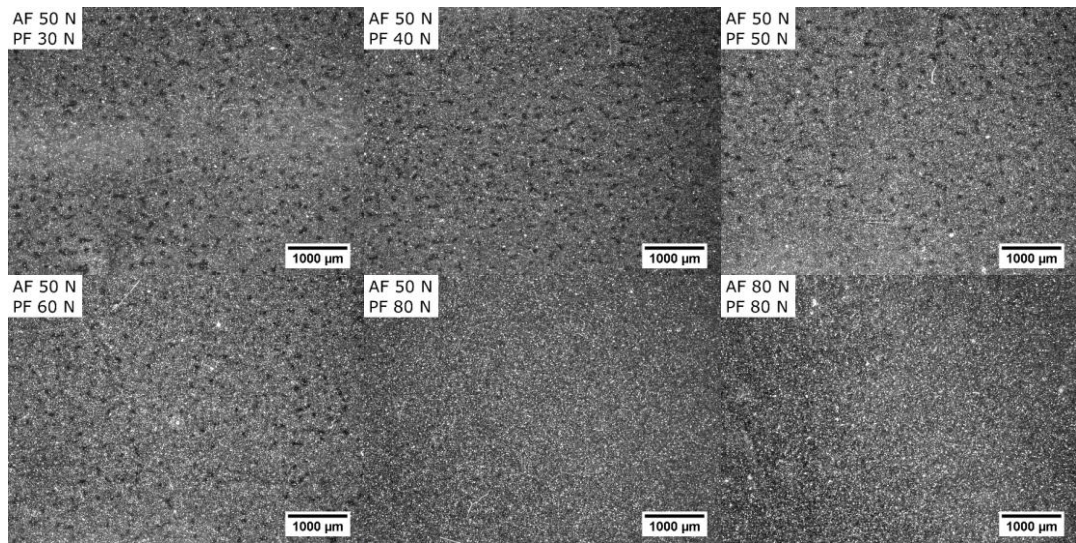


Figure 13.8: Representative micrographs of solid block prints at print forces of 30, 40, 50, 60 and 80 N using the 21.8 % PVP LBZA ink. All print tests were performed on the combined wet chemical and plasma treated Kapton HN substrates, using the F1 printability tester (IGT.) Print speed = 1.5 m.s<sup>-1</sup>, anilox force = 50 N (final sample anilox force = 80 N).

Figure 13.8 shows representative micrographs for solid block prints using the 21.8 % PVP LBZA ink at print forces of 30, 40, 50, 60 and 80 N. The micrographs show a decreasing degree of pin holing with increasing print force, with pin holing being eliminated at a print force of 80 N. Increasing the anilox force to 80 N produced little difference in uniformity of the micrographs, however a subtle increase in brightness under the same lighting conditions can be seen suggesting a thicker layer.

Based on the equivalent uniformity in the micrographs and the slightly increased reflection 80 N print and anilox forces were chosen.

### 13.3.1.3 LBZA mass loading – effect on coverage experiment

To maximize conductivity of any given sensing layer it is important to maximize particulate overlap and coverage to maximize the number of conductive paths present. Figure 13.9 shows representative backscatter electron micrographs for inks produced using the 21.8 % mass loading PVP solvent blend with LBZA mass loadings of 22.3, 28.6, 34.8, 39.6, 46.6 and 51.4 mg.mL<sup>-1</sup>. The micrographs show a steadily increasing coverage of LBZA particulates reaching a maximum at 46.6 mg.mL<sup>-1</sup>, followed by a decrease in coverage.

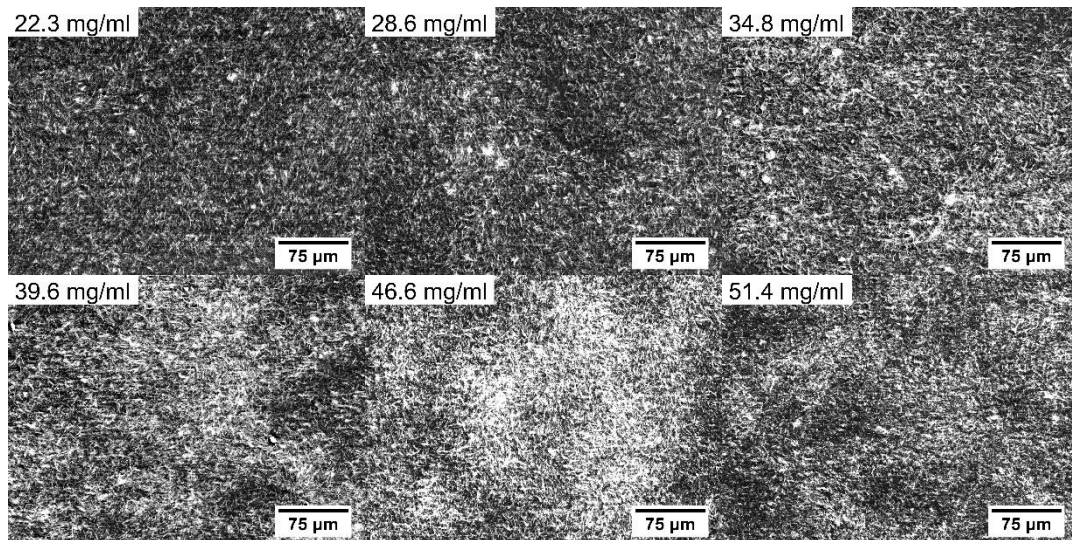


Figure 13.9: Representative backscattered electron micrographs of the flexographic print tests samples using the LBZA PVP based inks with PVP mass loading of 21.8 % and LBZA loadings of 22.3, 28.6, 34.8, 39.6, 46.6 and 51.4 mg.mL<sup>-1</sup>. All print tests were performed on the combined wet chemical and plasma treated Kapton HN substrates, using the F1 printability tester (IGT.) Both print force and anilox force set at 80 N and print speed was set to 1.5 m.s<sup>-1</sup>. Micrograph dimensions: 285.8 µm x 214.4 µm.

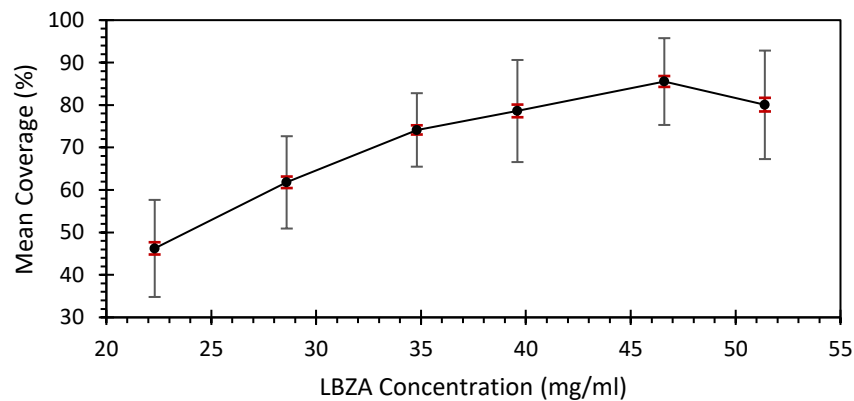


Figure 13.10: Calculated mean percentage coverage as a function of ink LBZA concentration. Black error bars = 1 standard deviation, red error bars = 95% confidence interval. Coverage calculated by converting the backscattered electron micrographs into a binary bitmap, dividing into 28.5 µm x 21.4 µm sections and calculating the mean and standard deviation of white pixels/ total pixels for 243 sections derived from 3 samples.

Figure 13.10 shows the calculated mean coverage as a function of mass loadings with standard deviation (black) and 95 % confidence intervals (red.) The standard deviations, varying between 8.65 % and 12.78 %, show that coverage has a generally broad distribution. At 46.6 mg.mL<sup>-1</sup> the coverage reaches a maximum of 85.4 % (95 % confidence interval: 84.2 % - 86.9 %,) the lack of overlap of confidence interval suggests that the maximum is statistically significant relative to the other measurements. The loading produces a standard deviation of 10.22 %, 1.57 % larger than the minimum value that occurs at 34.8 mg.mL<sup>-1</sup> which produces a coverage of 74.1 % (95 % confidence interval: 73.0 %, 75.2 %.)



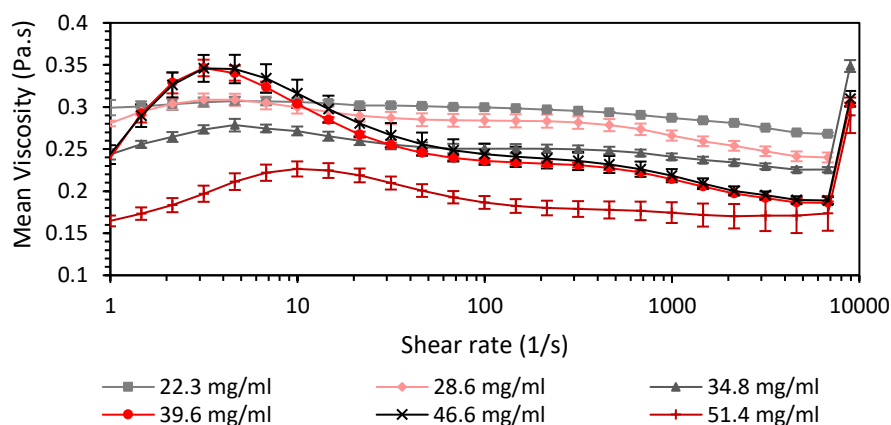


Figure 13.11: Mean viscosity measurements as a function of shear rate for the tested LBZA inks with LBZA mass loadings of 22.3, 28.6, 34.8, 39.6, 46.6 and 51.4 mg.mL<sup>-1</sup>. Error bars = 1 standard deviation, N=3.

Figure 13.11 shows the mean viscosity as a function of shear rate for each mass loading. The inks appear to show relatively significant non-Newtonian characteristics appearing to show at low shear rates shear thickening, followed by shear thinning behaviour. The local peak viscosity at low shear rates appears to increase and then broaden, spreading to higher shear rates with an increase of mass loading. At a shear rate of 8926 1/s the inks all appear to show shear thickening. Whilst the behaviour was reproducible it is not known currently if it is a physical property of the system or an artefact. The presence of a maximum coverage with increasing loading was originally attributed to the non-Newtonian nature of the inks which is known to be dependent on solid fraction <sup>[434]</sup>. Re-examining the data and comparing the measured ink constituent concentration, the maximum was assigned to a reduction in viscosity at higher shear rates. The reduction which appears continuous with increasing sheet loading correlates well to that seen with a reduction in PVP concentration. The ink with mass loading of 51.4 mg.mL<sup>-1</sup>, which had a viscosity of 175 mPa.s at 1000 s<sup>-1</sup>, had a PVP mass/ wet mass ratio of 0.15. This PVP ratio is on the same order as ink C with a ratio of 0.174 and a viscosity of 148 mPa.s. The lower viscosity as noted in 13.3.1.1 leads to lower ink transfer, the production of a maxima in coverage would then be a result of the decrease in ink transfer becoming more dominant in comparison to the increase in ink loading. The dilution was attributed to residual IPA solvent present in the centrifuged LBZA pellet measured and extracted from the master batch of LBZA sheets in IPA. For all future ink measurements and mixing an initial solvent exchange step with the final ink mixture was used to remove the dilution. The exchange step is recommended for all future ink manufacturing conditions derived from centrifuged samples.

#### 13.3.1.4 LBZA mass loading – PVP Calcination

During the initial coverage test prints a 6<sup>th</sup> print was performed on printed PFI-722 Ag IDE (produced in chapter 6.5.1.2 ) to ascertain the effect of loading on sensor resistance and sensitivity. Prior to the calcination of the test sensors, samples of the 46.6 mg.mL<sup>-1</sup> prints were annealed at 350 °C for varying times up to 24 hours, the degradation temperature as stated by Yu *et al.* [577] and Rioux *et al.* [578]. Unexpectedly all the samples resulted in a brown residue. Revisiting literature revealed that the brown residue forms from the degradation of C-H bonds and formation of C=C bonds, and the loss of the pyrrolidone between 300 °C and 350 °C [576]. Following the results of Kim *et al.* [584] and Loría-Bastarrachea *et al.* [575] that showed the final mass loss to be centred between 450 °C and 480 °C samples were annealed at temperatures between 440 °C and 500 °C.

Figure 13.12 shows low resolution survey scan XPS elemental quantification of A) zinc, B) nitrogen, C) oxygen and D) carbon results of the sample surfaces annealed at 440 °C, 450 °C, 460 °C, 470 °C, 480 °C, 490 °C and 500 °C, annealed for 0, 1, 2, 3, 4 and 5 minutes. Whilst the results show a large variance, likely a result of the incomplete LBZA sheet coverage seen in 13.3.1.3 , two separate degradation profiles can be seen. At temperatures below 460 °C there appears to be a slow increase in Zinc, nitrogen, oxygen and loss in carbon. From 460 °C the increase in Zinc and nitrogen and loss in carbon is significantly higher. Figure 13.12 E) and F) show the ratios at each time and temperature of oxygen/ carbon and nitrogen/ oxygen respectively. For both figures the oxygen content is corrected for the presence of ZnO by subtracting the oxygen present in zinc oxide. The results are separated into 3 main regions, regions where the values:

- are between that of PVP and Kapton
- vary between pure Kapton and the combined treated Kapton (which is expected to recure into almost pure Kapton)
- show an excess loss of nitrogen/ gain of oxygen.

The figures show that calcining at 440 °C as expected to not undergo complete PVP decomposition. All other temperatures at 5 minutes have oxygen/carbon ratios within the theoretically clean region. For the nitrogen/ oxygen ratios at 5 minutes, temperatures between 460 °C and 470 °C are within the theoretically clean range.

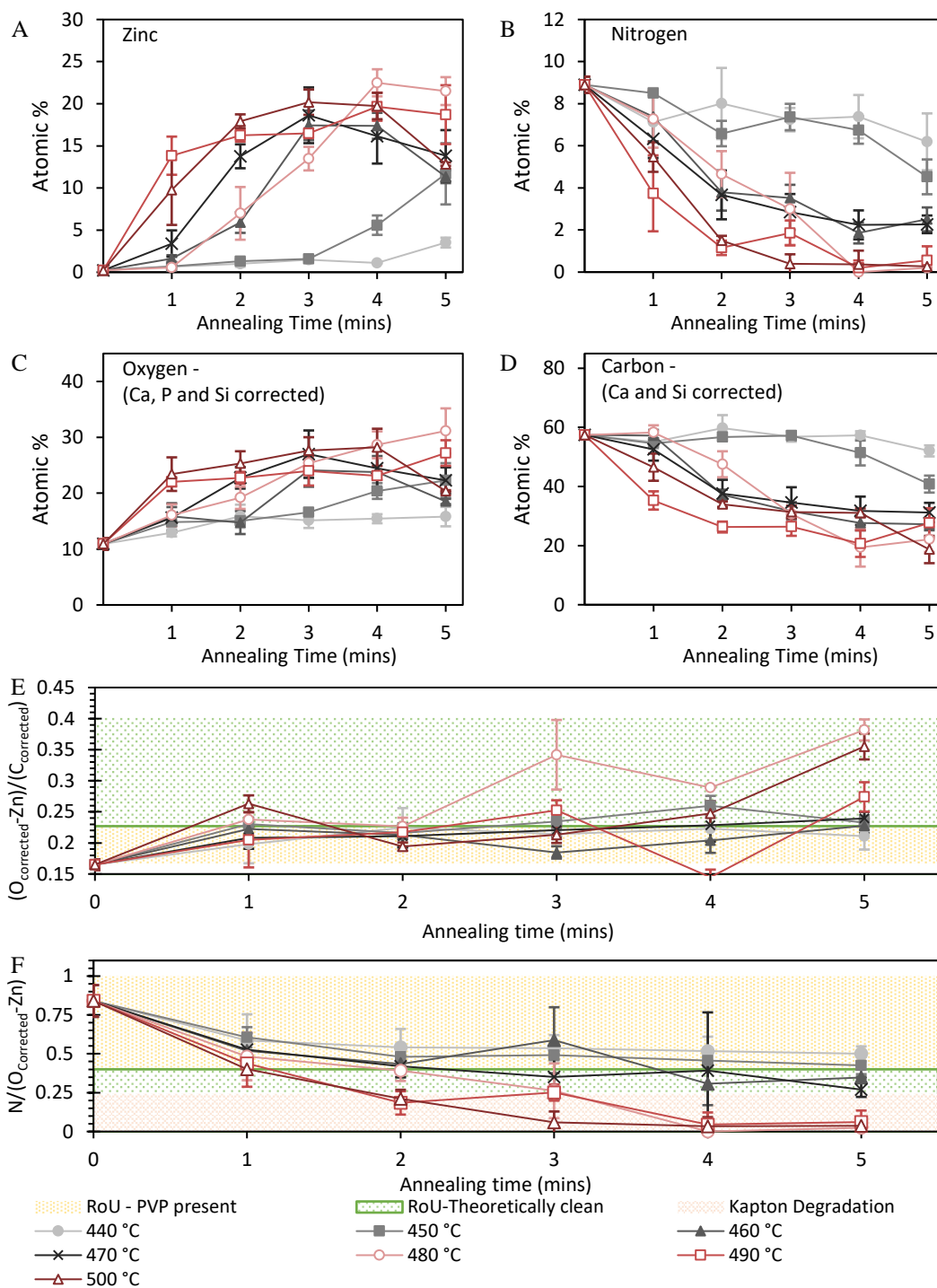


Figure 13.12: A)-D) Elemental quantification from XPS (low resolution) survey scans of the printed LBZA-PVP ink with LBZA loading of  $46.6 \text{ mg}\cdot\text{mL}^{-1}$  on the combined treated Kapton substrate, as a function of annealing time at temperatures of 440 °C, 450 °C, 460 °C, 470 °C, 480 °C, 490 °C and 500 °C. To correct for the presence of calcium phosphate dibasic<sup>[581]</sup> and calcium carbonate<sup>[466]</sup> (additives present in the substrate) and surface organic silicon the following corrections were used  $O_{\text{corrected}} = O - \text{Si} - 4 * \text{P} - 3 * (\text{Ca} - \text{P})$  and  $C_{\text{corrected}} = C - (\text{Ca} - \text{P}) - 2 * \text{Si}$ . E) and F) represent the ratio of organic oxygen to carbon (E:  $(O_{\text{corrected}} - \text{Zn}) / C_{\text{corrected}}$ ), and nitrogen to oxygen (F:  $\text{N} / (O_{\text{corrected}} - \text{Zn})$ ) present as a function of annealing time. The regions of uncertainty (RoU) represent two separate cases, the presence of PVP on the substrate (yellow), and the theoretically clean substrate without PVP (green). As the hydrolysis of the substrate is reversible, recurring into aromatic polyimide above 230 °C<sup>[491]</sup>, the theoretically clean range varies between the elemental ratios recorded for the as treated substrate ( $O/C = 0.403$ ,  $\text{N}/O = 0.243$ ) and the theoretical value for pure Kapton (solid green line,  $O/C = 0.227$ ,  $\text{N}/O = 0.400$ .) XPS survey scans presented in appendix 14.6. Error bars: 1 standard deviation,  $N = 5$ .

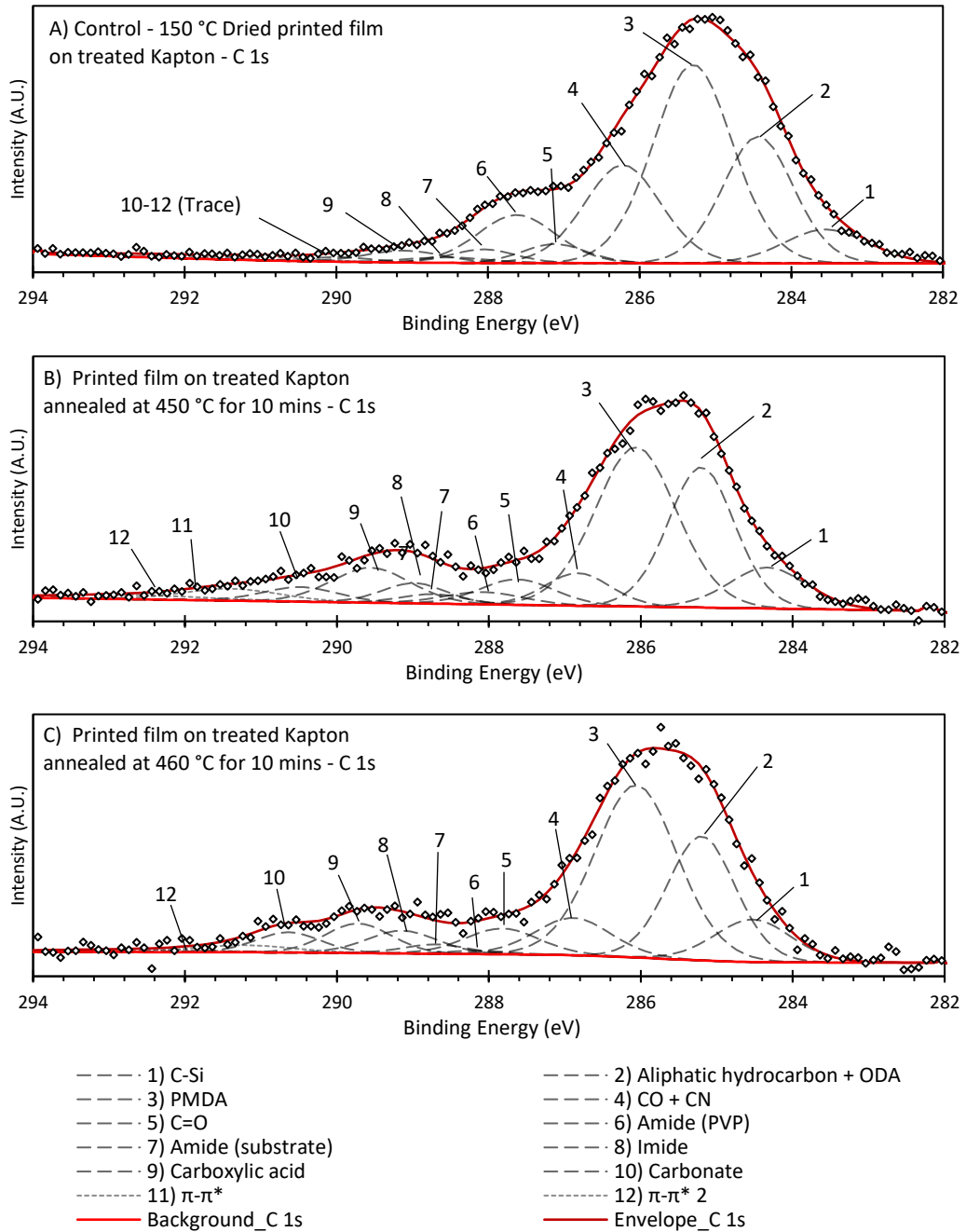


Figure 13.13: High resolution XPS C1 spectra for flexographic print tests samples using the LBZA PVP based inks with PVP mass loading of 21.8 % and LBZA loading of 46.6 mg.mL<sup>-1</sup> on the combined wet chemical and plasma treated Kapton HN substrates. Post printing samples treated by drying for 10 minutes at 150 °C (A - control) and then either 450 °C for 10 minutes (B) or 460 °C for 10 minutes (C).

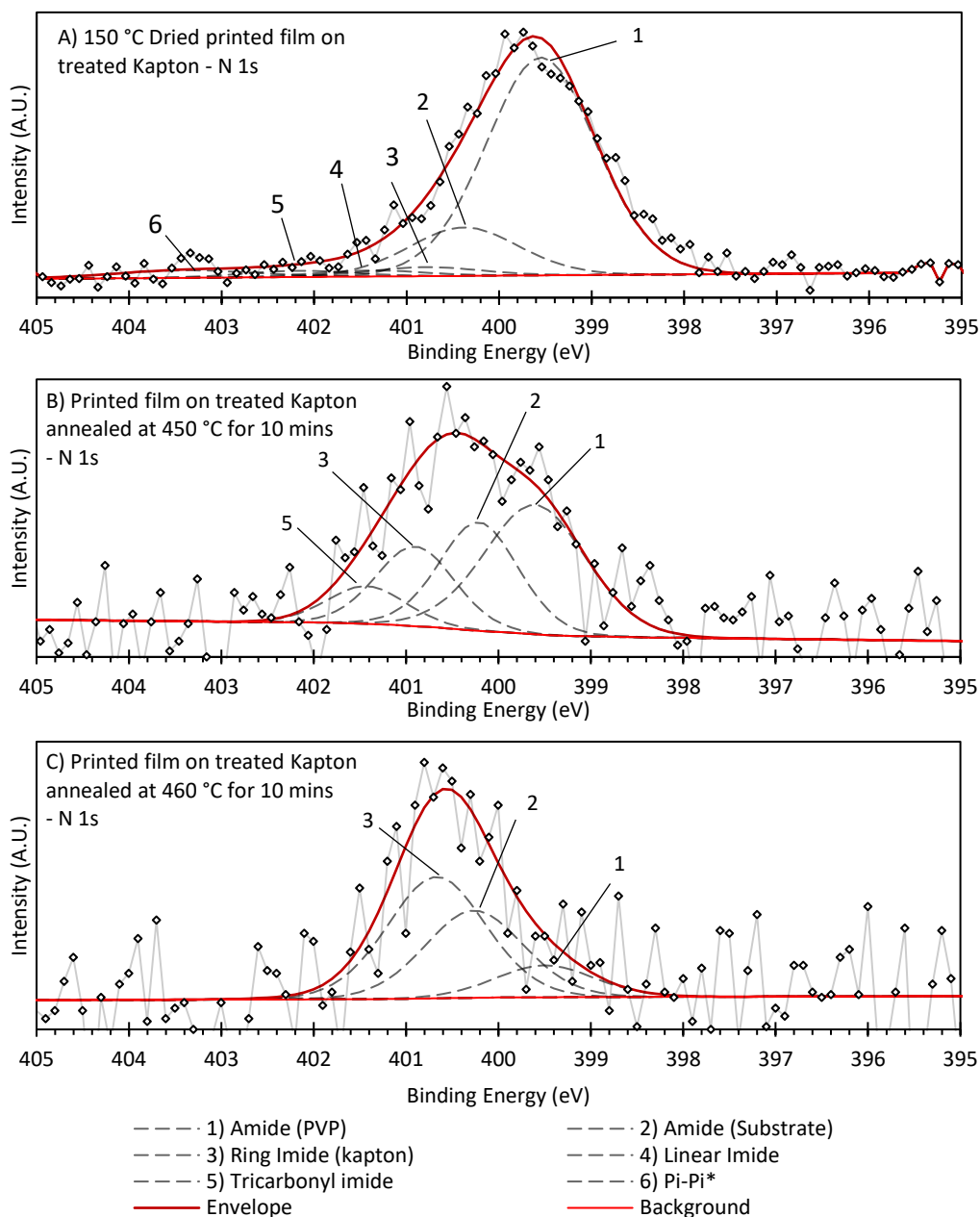


Figure 13.14: High resolution XPS N1 spectra for flexographic print tests samples using the LBZA PVP based inks with PVP mass loading of 21.8 % and LBZA loading of 46.6 mg.mL<sup>-1</sup> on the combined wet chemical and plasma treated Kapton HN substrates. Post printing samples treated by drying for 10 minutes at 150 °C (A - control) and then either 450 °C for 10 minutes (B) or 460 °C for 10 minutes (C).

Temperatures exceeding 470 °C are within the degradation region resulting from an excessive loss of nitrogen as seen in B). The mean value of 450 °C is within the PVP region of uncertainty however the standard deviation overlaps into the theoretically clean region. Based on the results, 2 final samples were annealed at 10 minutes at 450 °C and 460 °C. As Kapton starts to degrade with an expected mass loss in air at 10 minutes of 1.6 % and 3.9 %

at 450 °C and 500 °C, the temperatures were chosen as to minimize substrate degradation whilst trying to maximize decomposition of the PVP.

Element	Element Components	Concentration (Atomic %)		
		Control	450 °C	460 °C
Zn	Total Zinc 2p	0.34	17.84	27.09
O	Total Oxygen 1s	14.50	34.37	37.41
N	1) Amide (PVP)	6.47	1.02	0.17
	2) Amide (Substrate)	1.44	0.65	0.47
	3) Imide (aromatic ring)	0.27	0.48	0.66
	4) Imide (Linear)	0.18	0.23	0.00
	5) Tri-carbonyl Imide	0.19	0.00	0.01
	Total Nitrogen 1s	8.55	2.38	1.31
C	1) Organic Silicon	4.86	3.47	2.65
	2) Aliphatic hydrocarbon + unoxidized ODA	15.31	10.21	6.87
	3) PMDA	26.99	14.22	11.64
	4) C-O + C-N	12.87	2.33	2.32
	5) C=O	2.10	2.07	1.56
	6) Amide (PVP)	6.43	1.06	0.17
	7) Amide (Substrate)	2.69	0.66	0.49
	8) Imide	0.78	1.43	1.32
	9) Carboxylic Acid	1.57	3.01	1.60
	10) Carbonate + Tri-carbonyl Imide	0.50	1.20	1.07
Total Carbon 1s	72.91	39.66	29.69	
Si	Total Silicon 2p	3.69	3.47	2.43
Ca	Total Calcium 2p	0.00	2.26	2.05

Table 13.3: High resolution XPS quantification results (atomic %) for flexographic print tests samples using the LBZA PVP based inks with PVP mass loading of 21.8 % and LBZA loading of 46.6 mg.mL<sup>-1</sup> on the combined wet chemical and plasma treated Kapton HN substrates. Post printing samples treated by drying for 10 minutes at 150 °C (control) and then either 450 °C for 10 minutes or 460 °C for 10 minutes. Note that the numbers in the label for each functional group are the same as that for the spectra in Figure 13.13 and Figure 13.14.

High resolution XPS spectra for the two samples and an as dried control sample for the C 1s region, N 1s region and a table of quantified results are shown in Figure 13.13, Figure 13.14 and Table 13.3 respectively. The quantification results of the control samples have two main features:

- A large (6.47 at.%) N 1s peak centred at 399.6 eV assigned to PVP and a Zn content of only 0.34 at.%. This suggests that the LBZA is generally buried by at least 6 nm of PVP (calculated using the universal curves for polymers <sup>[305]</sup>, a kinetic energy of 464.8 eV (the measured energy of the Zn 2p 3/2,) and a density for PVP of 1200 kg/m<sup>3</sup> <sup>[585]</sup> and a sampling depth of 3 times the inelastic mean free path.)
- A relatively significant amount of pinholing present with ~24.3 % of N 1s content arising from the substrate. Annealing at 450 °C shows an increase in high binding

energy components in the C 1s spectra from the underlying substrate. Additionally a significant increase in zinc content is seen at 17.84 at.% with a drop in PVP amide to 1.02 at.%. Increasing the annealing temperature to 460 °C produces another significant increase in zinc content raising to 27.12 %, with the PVP amide dropping to 0.17 % and starting to enter within the noise floor of the spectra.

In addition to the continuing increase in zinc content and decrease in PVP amide, a decrease in aliphatic hydrocarbon and ODA content is seen. The sample annealed at 460 °C has an ODA/PMDA ratio of 0.59, approaching the 0.66 of the as treated substrate (seen Table 6.1 for details), it should be noted that the ODA/ aliphatic hydrocarbon content is approaching that of adventitious carbon, as such variations in background vacuum cleanliness can easily account for the majority of the difference seen between the ratios. The combination of results suggests that after annealing at 460 °C for 10 minutes, only trace residue of PVP remains, whilst at 450 °C a significant residue of PVP remains.

In addition to the cleanliness of the surface the results also indicate that re-curing of the substrate is incomplete at 460 °C, however the lack of linear imide suggests the samples at least partially revert to a pre-plasma state. The lack of tricarbonyl imide present within the N 1s spectra of any sample suggests the component to be unstable. The retained presence of amide and carboxylic acid is favourable for adhesion, presenting additional polar groups capable of interacting with printed overlayers.

### ***13.3.1.5 Thermal stability and test sensor failure***

Following on from the XPS results an initial sensor from each loading below 51.4 mg.mL<sup>-1</sup> was calcined at 460 °C for 10 minutes. Following the annealing the sensors were aged at 200 °C for 2 days. In between each step of the heat treatment process the resistance across the ‘backbone’ of the left electrode (between the two points shown in Figure 13.15) was measured.

Although all sensors survived the initial annealing step, after 2 days at 200 °C, 60 % of the electrodes had failed, losing all conductivity. Furthermore after an additional 2 days at 300 °C within the gas sensor testing chamber the 46.6 mg.mL<sup>-1</sup> sensor failed, undergoing pyrolysis and losing a significant portion of the Kapton substrate as shown in Figure 13.16.

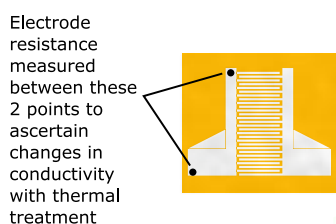


Figure 13.15: Schematic showing the points where the resistance of the IDE was measured across after each thermal treatment step.

Nanosheet Loading (mg/ml)	Electrode resistance ( $\Omega$ )		
	Dried at 150 °C - 10 minutes	460 °C - 10 minutes	200 °C - 2 days
22.3	18.2	8.2	Overflow (>20 M)
28.6	10.2	59.8	14
34.8	11.3	42.7	Overflow (>20 M)
39.6	12.3	77.4	Overflow (>20 M)
46.6	6.5	7.7	10

Table 13.4: Table of left electrode resistances for each sample after drying at 150 °C for 10 minutes, 460 °C for 10 minutes and finally aging 200 °C for 2 days.

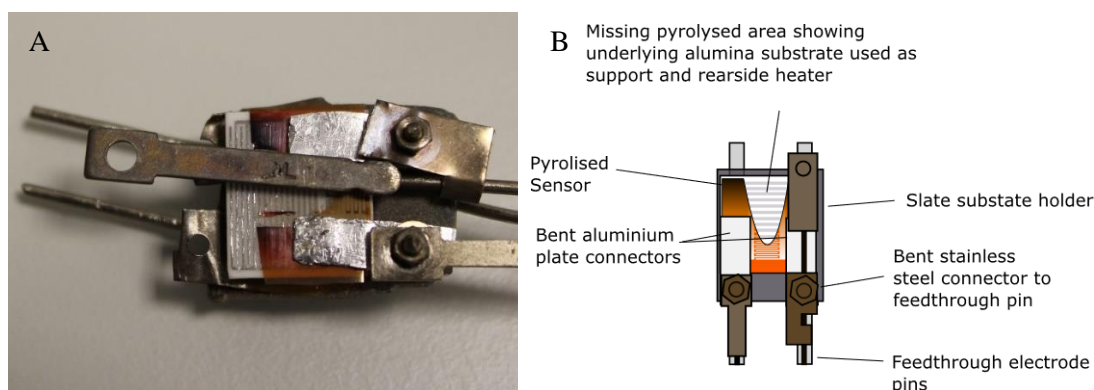


Figure 13.16: A) Photograph of failed 46.6 mg.mL<sup>-1</sup> LBZA ink printed sensor in the substrate holder after spending 2 days at 300 °C in the gas sensor testing chamber. Sensor calcined at 460 °C for 10 minutes and aged for 2 days at 200 °C prior to insertion into the chamber. B) Annotated schematic of the sensor, underlying commercial alumina substrate used as a rearside heater, slate substrate holder, aluminium plate connectors and feedthrough electrode pins. Primary failure mode is assigned to oxidation induced reduction ultimate elongation of the Kapton substrate.

From the datasheet <sup>[586]</sup> the substrate would be expected to lose little to no mass at 300 °C within the aging time, with an estimated upper bound of 3 % mass based on the manufacturer provided isothermal weight loss profiles.

As the physical properties of the substrate are linked to thermal oxidation, a first order approximation of the ultimate elongation (UE – the strain at failure as a percentage) can be gathered by fitting the change in UE (an energy barrier dependent process,) with time and temperature, to chemical kinetics equations.



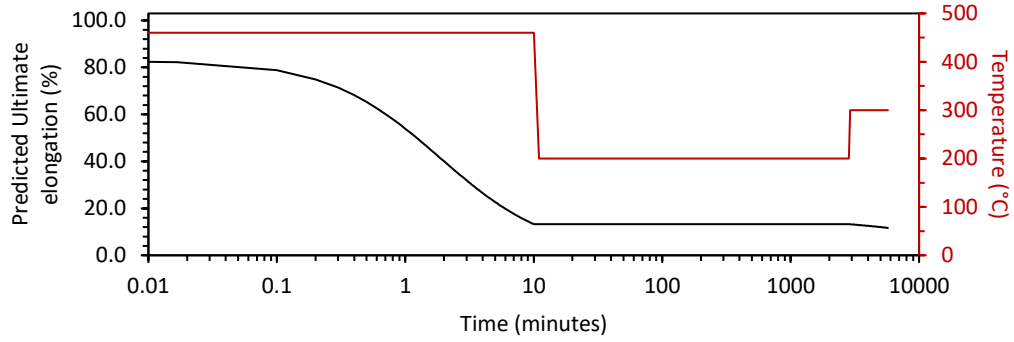


Figure 13.17: Predicted ultimate elongation (UE) as a function of time, following the temperature profile indicated in red. The function was based on a second order reaction:  $UE_{t+1} = UE_t - k\Delta t[UE_t]^2$ , where  $k = e^{\left(\frac{-19619}{T} + 22.193\right)}$  where  $T$  is temperature in Kelvin.  $k$  was calculated for the time for ultimate elongation to decrease from 70 % to 1 % at temperatures between 450 °C and 250 °C in 25 °C intervals as provided within the manufacturer datasheet [586][469].  $\ln(k)$  was then plotted as a function of  $1/T$  and a linear trendline fit to produce the relationship and had a  $R^2$  value of 0.998. The initial value of UE listed in the datasheet was 83 %. As the value of  $k$  was based on only 2 values of UE at each temperature the values should be taken as a first order approximation. 2<sup>nd</sup> order rate was chosen by measuring the time series of elongation retained at 325 °C in ImageJ, then plotting  $1/\text{elongation}$  retained against time produced a straight line, characteristic of 2<sup>nd</sup> order reaction rates [155].

By measuring the UE time series within the manufacturers data sheet [586] using imageJ and plotting  $1/UE$  as a function of time, a straight-line indicative of an equation equivalent to a 2<sup>nd</sup> order reaction [155] was produced. Using the times listed within the datasheet for UE to reduce from 70 % to 1% and the integrated 2<sup>nd</sup> order reaction rate equation (Equation 13.8), first order approximations for values of  $k$  between 250 °C and 450 °C were calculated.

$$\frac{1}{2t} \left( \frac{1}{UE_{Final}} - \frac{1}{UE_{Initial}} \right) = k$$

Equation 13.8

Where  $t$  is the time taken in seconds at a specific temperature for the change to occur and  $k$  is the rate constant.

Plotting  $\ln(k)$  vs  $1/T$  a relationship of  $k = e^{\left(\frac{-19619}{T} + 22.193\right)}$  ( $R^2=0.998$ ) was calculated, where  $T$  is absolute temperature in Kelvin. Using a finite difference approximation of the 2<sup>nd</sup> order rate equation  $UE_{t+1} = UE_t - k\Delta t[UE_t]^2$  and the temperature profile of the thermal treatment, approximate values of UE as a function of time (plotted in Figure 13.17) were calculated. The plot shows that the UE drops significantly post calcination with a predicted drop from the initial 83 % quoted in the data sheet to approximately 13 %, after which a total change of less than 2 % is predicted. Whilst only a first order approximation the plots show

a dramatic change in UE, and as such thermal stability, at the required temperature to remove PVP. In contrast a 10 minute 350 °C anneal as was originally planned would be expected to drop the UE by 3.6 %. The failure was therefore primarily assigned to the reduction in ultimate elongation during the 460 °C annealing step required to remove the PVP. The loss of material being restricted to between the aluminium electrodes likely indicates the contacts to be the stress risers that caused the final failure to occur.

Based on the results a conclusion was reached that PVP in combination with Kapton is unsuitable for further development. As the substrates needed to be flexible to print the PFI-722 Ag NP ink (a result of the need to use the RK FlexiProof 100) and budgetary restrictions limiting replacement of the silver ink, it was decided that a replacement of PVP with a lower temperature binder was required. It is worth noting prior to the planning of future work and development, the long-term strategy over the temperature of operation and substrate would be needed to be made. Alumina, whilst more expensive would not be subject to the same thermal restrictions as Kapton. If alumina was chosen, a solvent based silver nanoparticle ink compatible with the IGT F1 would likely need to be chosen as well for small scale development. Additionally, the contacts and substrate holder were redesigned with a polyimide mask added, as discussed in chapter 6.3.2.1.1 , to reduce the concentration of applied stresses.

### **13.3.2 LBZA ink development - Ink 2 - Polyethylene glycol binder (A brief overview)**

A 35 kDa polyethylene glycol (PEG) ink, which depolymerises in a single step starting at 250 °C <sup>[587]</sup>, was developed. As higher molecular weight PEG is insoluble in alcohols and other plate compatible solvents at room temperature <sup>[588]</sup>, water containing solvent blends were required. For the 150 - 180 mg.mL<sup>-1</sup> PEG content, which produced viscosities on a similar order to that of the 15 % – 25 % PVP solutions (determined using the qualitative vortex height measurement described in chapter 6.4.2.2 ,) water contents of 10 – 20 % volume were needed. The water content led to poor wetting and subsequently printing results, even with increased anilox forces of 125 N and print forces of 150 N ( micrograph of the best print produced during the trial is shown in Figure 13.18.)

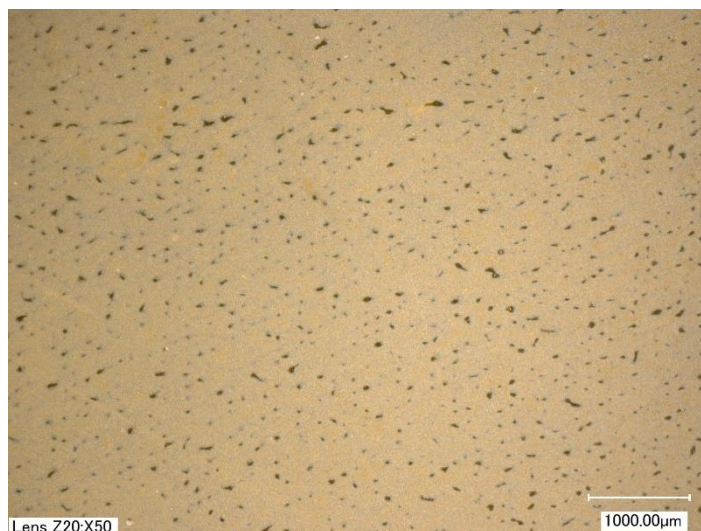


*Figure 13.18: Micrograph of the best print produced during the PEG trial. Ink constituents (% mass): PEG - 15.4 %, Glycerol - 27.4 %, water - 11.2 %, LBZA - 4.44 %, N-butanol - 41.6 %. Printed using the IGT F1 using the 24 mL.m<sup>2</sup> anilox. Print speed: 1.5 m.s<sup>-1</sup>, Anilox force: 125 N, Print force 150 N. The high concentration of pinholes was mainly attributed to poor wetting.*

During experiments to minimize the water content by solvent replacement, it was noted that the addition of glycerol led to successful suspension of the LBZA particulates. The suspension of LBZA in the presence of glycerol was also successful without the addition of PEG leading to the possibility of a binder-less ink. Based on the observations, an all alcohol solvent blend, consisting of 30 % glycerol, 30 % propylene glycol, 40 % n-butanol, and a LBZA mass loading of 46.6 mg.mL<sup>-1</sup>, was designed as detailed within chapter 6.4.2 .

## 13.4 Conclusion

PVP has been shown to be an ideal binder for the purpose of creating uniform printed films. For the investigations pertinent to the development of LBZA derived nanotextured ZnO gas sensors, a mass loading of 46.6 mg.mL<sup>-1</sup> was shown to produce the highest substrate coverage. Ultimately however, the 450 °C calcination temperature required to burnout PVP as a binder has been shown to be incompatible with flexible and cheap substrate materials. In the case of Kapton, it would appear based on information within the data sheet that the main failure mechanism is due to a significant reduction in ultimate elongation.

For the broader flexographic printed device field, a viscosity of approximately 309 mPa.s has been shown to be produce the most uniform prints when forces (50 N) and rapid print speeds (1.5 m.s<sup>-1</sup>) are used. A lower viscosity limit between 8.7 mPa.s and 26.4 mPa.s has

been shown for acceptable printability, in support of observations of Baker *et al.* [4]. An empirical  $\ln(\text{viscosity/nominal width relation})$  has been observed for nominal line width/anilox cell width ratios greater than 0.492. The observations appear to be the first reported within ratio ranges of 0.496-7.2 providing a useful predictive tool for future electronic device development. At lower viscosities than 309 mPa.s, and for greater areas (and therefore lower pressures) than the initial test prints, increased forces were required to reach the same level of print uniformity. Open air testing using the lab-scale printability flexographic printers has been shown to be significantly affected by the rapidity of drying. Whilst this is expected to be less of an issue at industrial scales, care is required with development at the lab scale and with any future scale up to larger presses.

## **Chapter 14 - Appendix B3. Miscellaneous Data**

---

### **14.1 Introduction**

This appendix is dedicated to miscellaneous data that either isn't used in the final sensor or would take up unnecessary length within Chapter 6 and Chapter 13, complicating the ability to communicate the necessary information. The information presented covers: Print plate designs (section 14.2 ), Aqueous hydrolysis of Kapton HN, conversion to polyamic acid (section 14.3 ), 0.375 M 75 % ethanol/ 25 % water wet chemical hydrolysis treated Kapton HN survey scans (section 14.4 ), Photo of uncoated 21.8 % weight PVP LBZA ink flexographic test print (section 14.5 ), XPS survey scans of the printed PVP based LBZA ink undergone calcination (section 14.6 ) and Measurements of important surface kinetic properties (section 14.7 ).

### **14.2 Print plate designs**

The digital design of the print plate features used within chapter 6.5.1.2 and chapter 6.5.3.1 for the interdigitated electrodes are displayed on the following two pages at x0.925 scale in Figure 14.1 and Figure 14.2 respectively.

### **14.3 Aqueous hydrolysis of Kapton HN, conversion to polyamic acid**

#### **14.3.1 Methods**

The aqueous hydrolysis treatment of 25  $\mu\text{m}$  Kapton HN polyimide film, presented below, followed the methods presented within chapter 6.4.1.2 . The only variations in method were for the hydrolysis step, water was used as reactant solvent and NaOH concentrations of 0.1 M, 0.5 M and 2 M were used. For each sample, 5 equilibrium deionized water contact angles were recorded, and the mean and standard deviation calculated. Surface roughness of a control (untreated) sample and the 50 second 2 M NaOH treated sample was measured using AFM. The AFM scans were performed using a NanoWizard® II NanoScience (JPK Instruments, Bruker, Berlin, Germany) in intermittent contact mode.

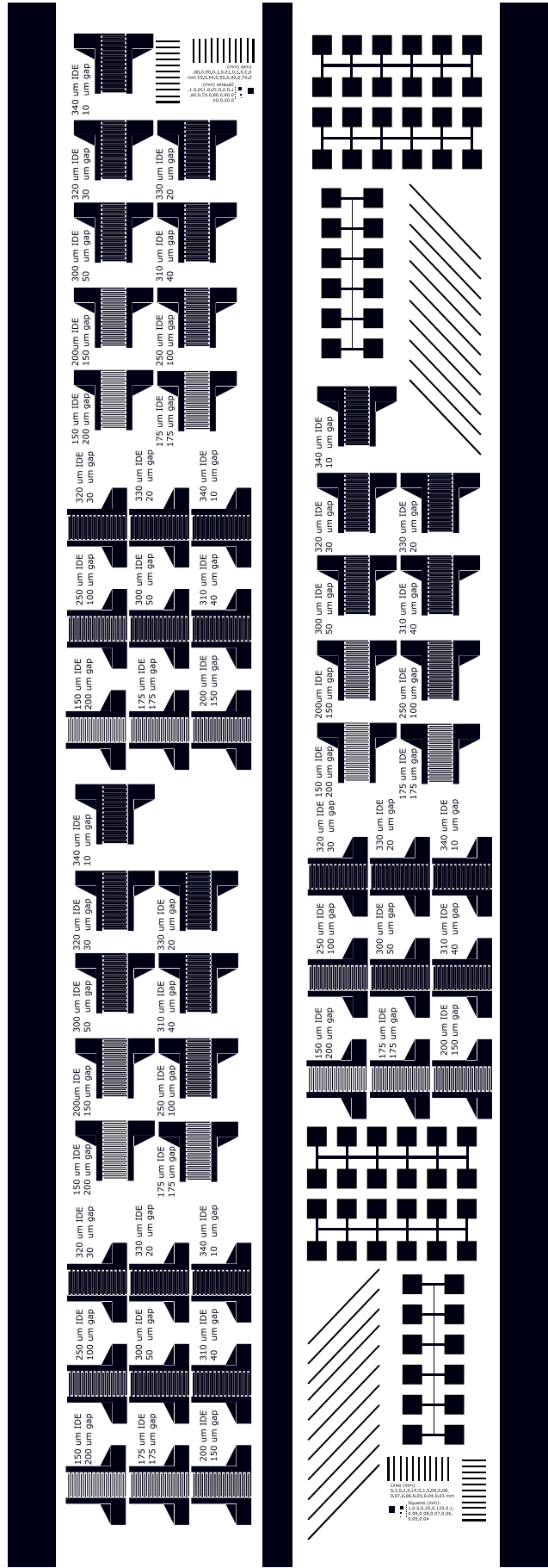


Figure 14.1: Interdigitated electrode test print used with the RK flexiproof 100 and the PFI 722 Ag NP ink. Scale x0.925.

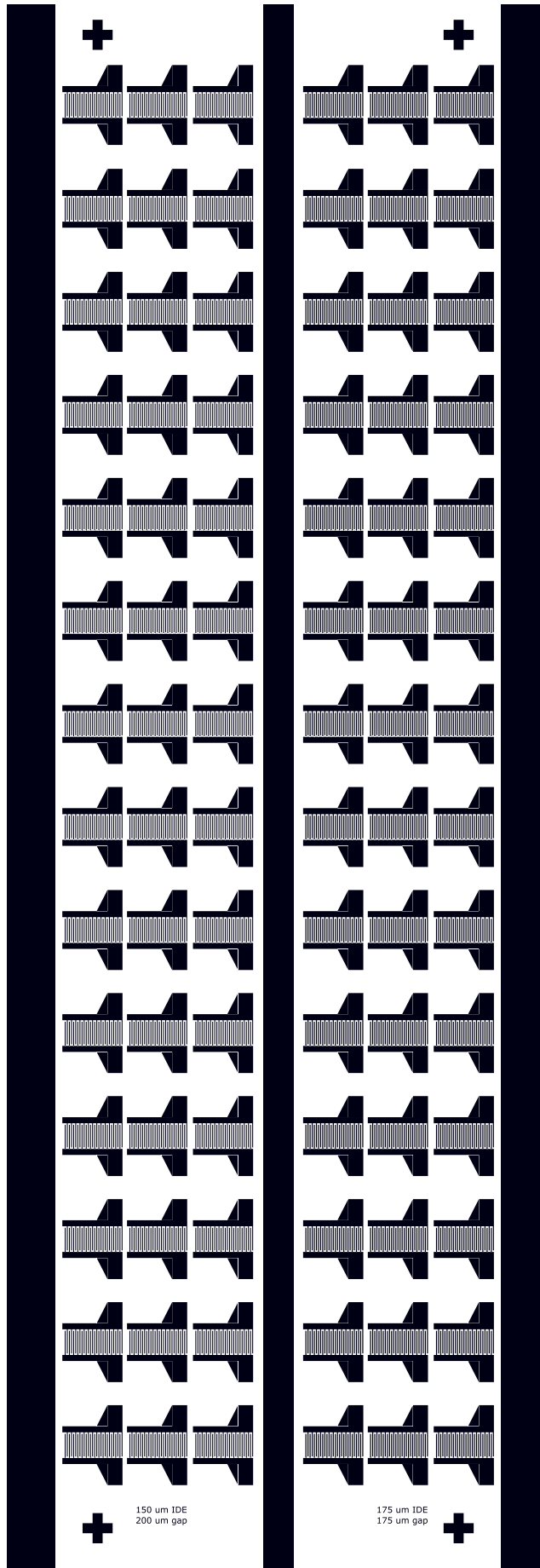


Figure 14.2: Interdigitated electrode test print used for the proof of concept sensors in Chapter 6 and the PFI 722 Ag NP ink. Scale x0.925.

### 14.3.2 Aqueous hydrolysis of Kapton HN Results

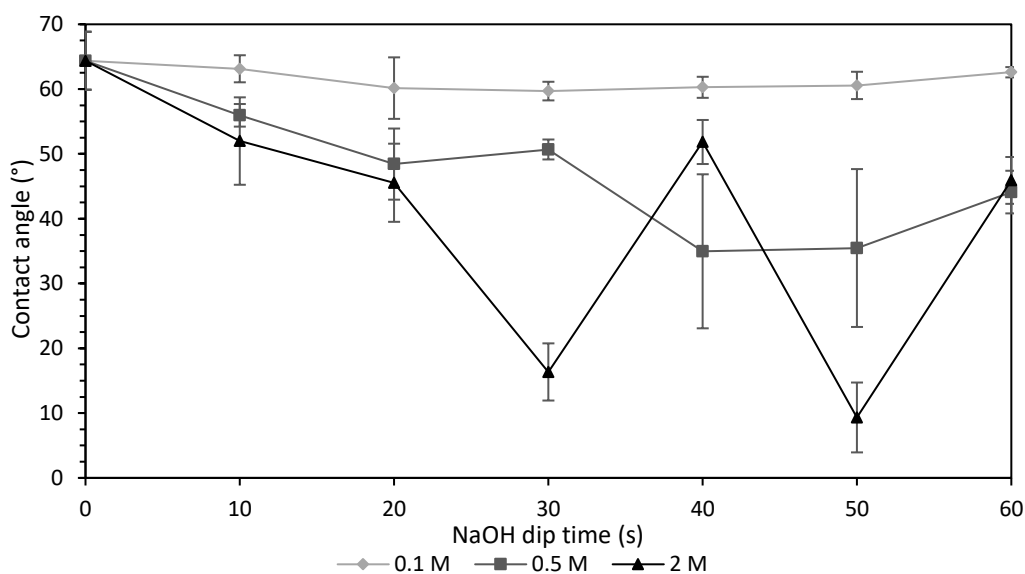


Figure 14.3: Plot of mean deionized water equilibrium contact angle as a function of sodium hydroxide treatment time for NaOH concentrations of 0.1 M, 0.5 M and 2 M. Error bars represent the standard deviation in contact angle,  $n=5$ .

Figure 14.3 shows the equilibrium water contact angles as a function of treatment time. The values within 0.1 M NaOH show no significant change, with all changes within the standard deviation of control sample. Treatments with 0.5 M and 2 M show a decrease in mean contact angle with NaOH treatment time. However, the contact angle showed large variations withing the mean values and had large standard deviations.

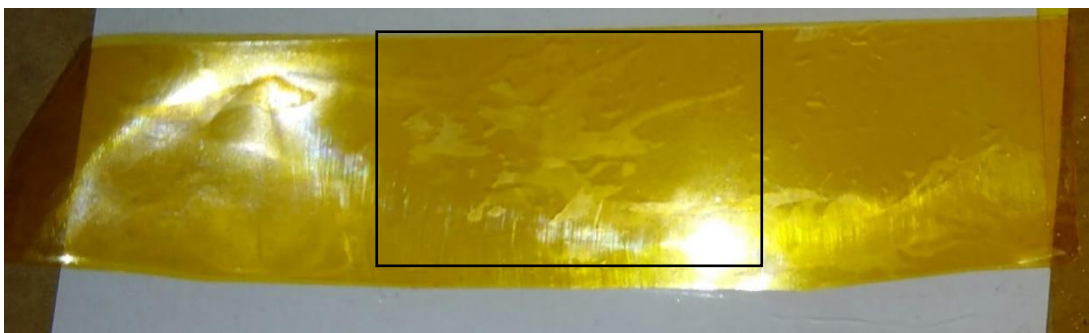


Figure 14.4: Photograph of the as treated Kapton substrates showing contrast variations in the centre of the image (encased within the black box) attributed to dissolution during the hydrolysis step. Hydrolysis step condition 2M NaOH, 50 seconds.



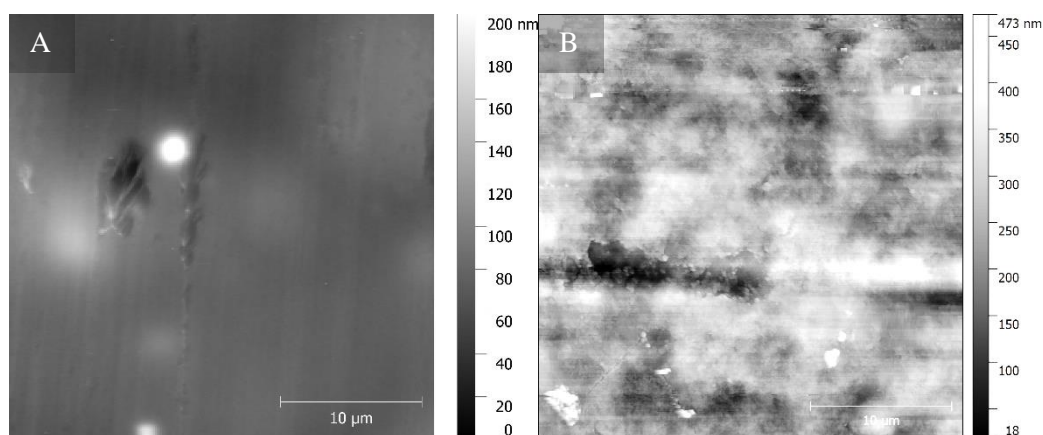


Figure 14.5: A)  $30\ \mu\text{m} \times 30\ \mu\text{m}$  AFM scan of control untreated solvent cleaned Kapton HN sample.  $R_a = 9.9\ \text{nm}$   $R_{RMS} = 14.0\ \text{nm}$ . B)  $30\ \mu\text{m} \times 30\ \mu\text{m}$  AFM scan of the 50 second aqueous 2M NaOH hydrolysis treated sample, taken from the highlighted area in Figure 14.4.  $R_a = 48.4\ \text{nm}$   $R_{RMS} = 64.2\ \text{nm}$

During the treatment a colourless liquid could be seen diffusing from the substrate, and after completion of the treatment, the samples showing the largest shifts in the mean contact angle contained areas of noticeable lighter contrast as can be seen in Figure 14.4.

Figure 14.5 shows AFM scans of an untreated control sample A) and the 2 M NaOH treated sample with a 50 second treatment step. Compared to the control sample a significant increase in roughness can be seen, with  $R_{RMS}$  values of 14.0 nm for the control and 64.2 nm for the treated sample. The increase is significantly greater than that observed for Kapton H (PMDA-ODA without slip additives) by Lee et al. <sup>[500]</sup> where the control sample had an  $R_{RMS}$  of 1.4 nm and a 5 M KOH treated sample had a  $R_{RMS}$  of 6.3 nm. The increased roughness, along with variability within the water contact angle, and large decrease in 30 s and 50 s 2 M NaOH treated sample observed here, was assigned to either dissolution, or dissolution followed by deposition of the dissolved material.

### 14.4 0.375 M 75 % ethanol/ 25 % water wet chemical hydrolysis treated Kapton HN survey scans

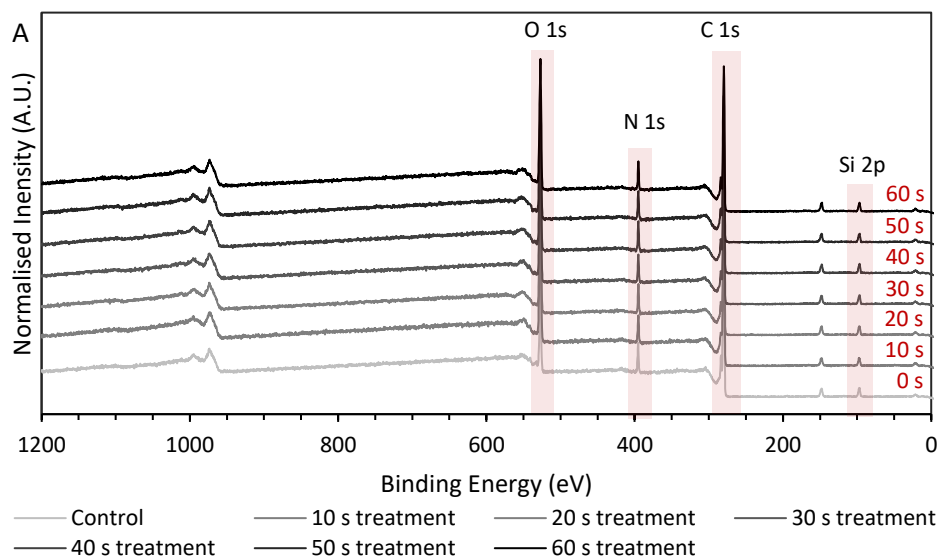


Figure 14.6: XPS survey scan plot of normalised intensity as a function of binding energy for the 0.375 M NaOH 75 % ethanol/ 25 % water wet chemical hydrolysis treated Kapton HN films. Highlighted and annotated are the photoelectron peaks from each element present used for quantification.

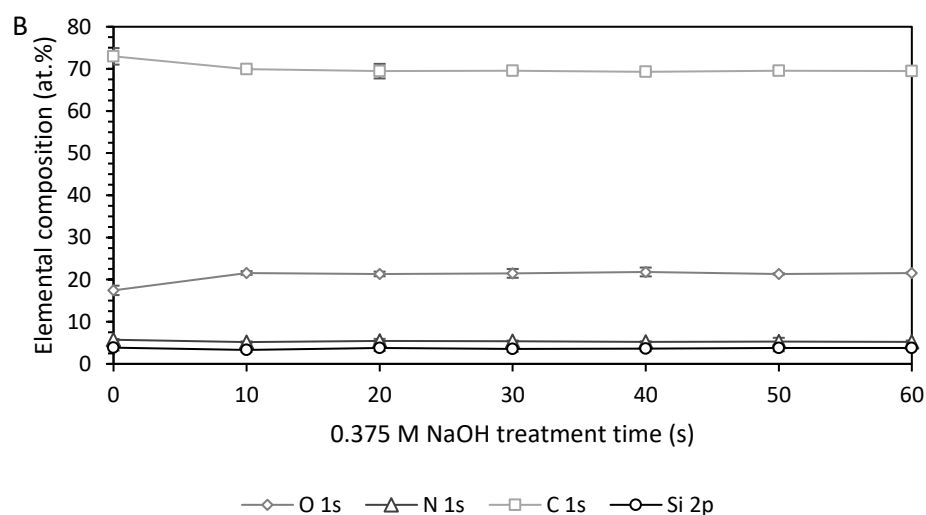


Figure 14.7: Plot of XPS survey scan mean quantified elemental concentration (at.%) as a function of treatment time for the wet chemical hydrolysis treated samples in 75 % ethanol/25 % ethanol. Error bars: 3\*standard deviation.

### 14.5 Photo of uncoated 21.8 % weight PVP LBZA ink flexographic test print

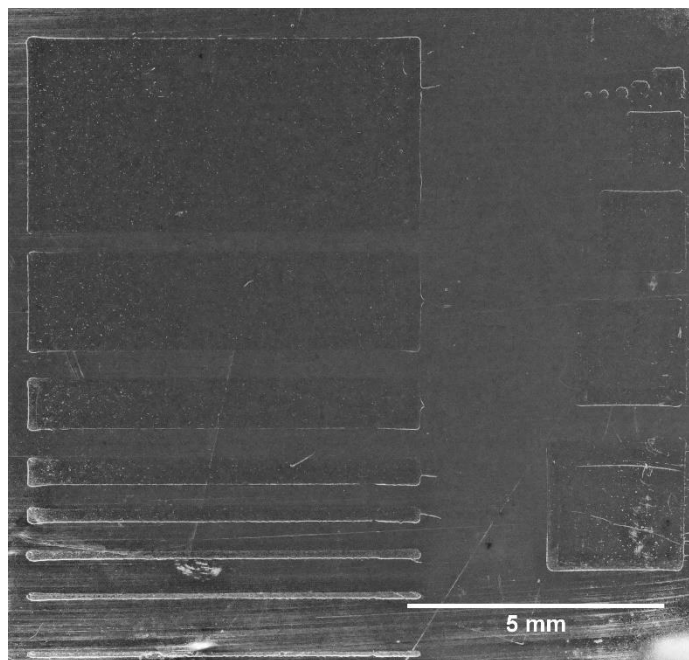
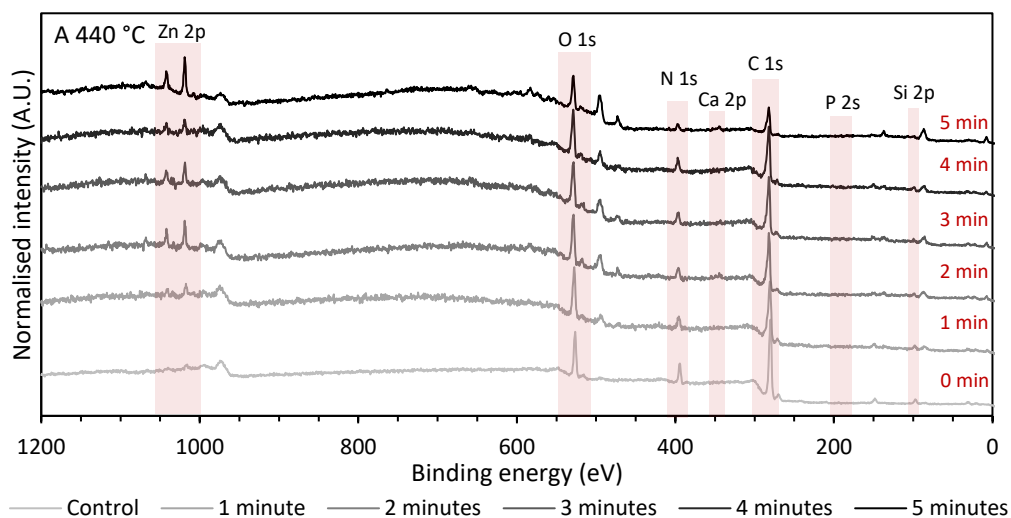
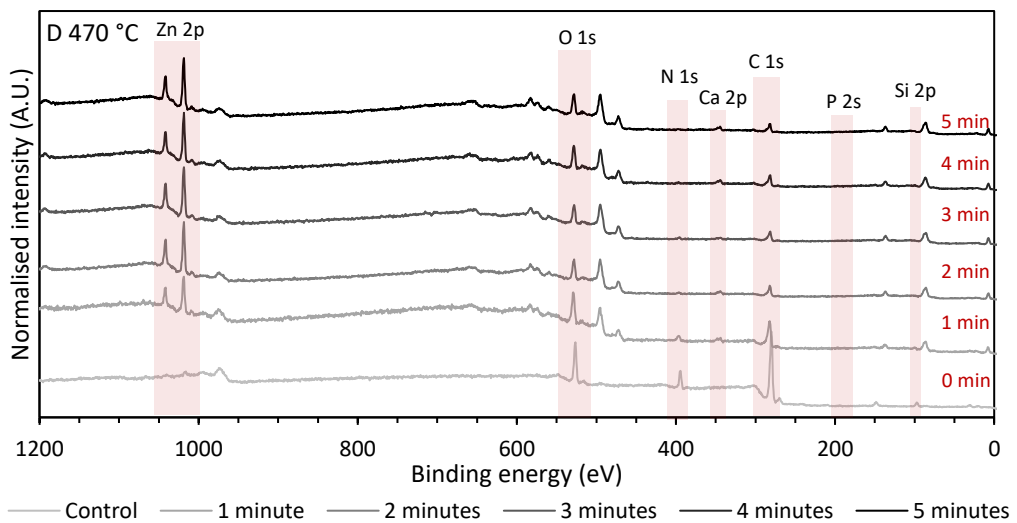
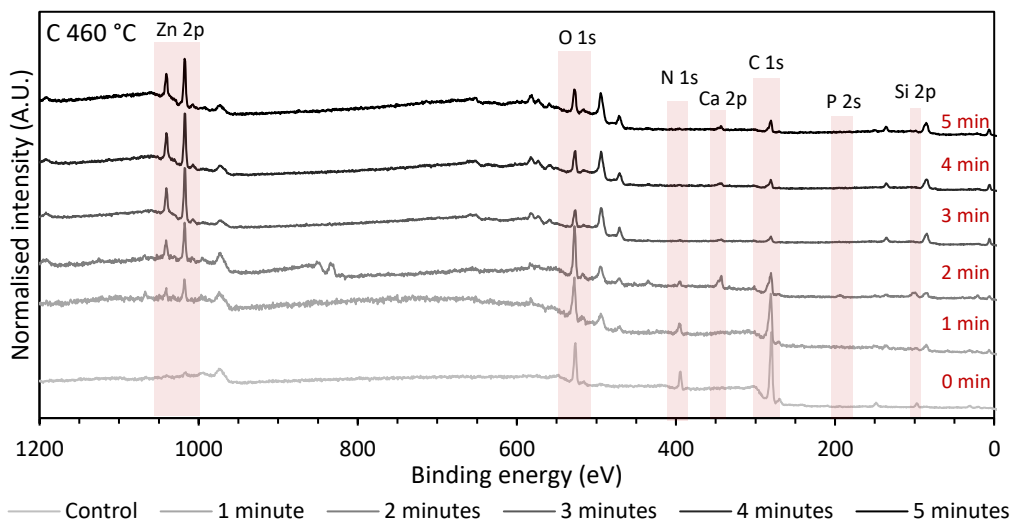
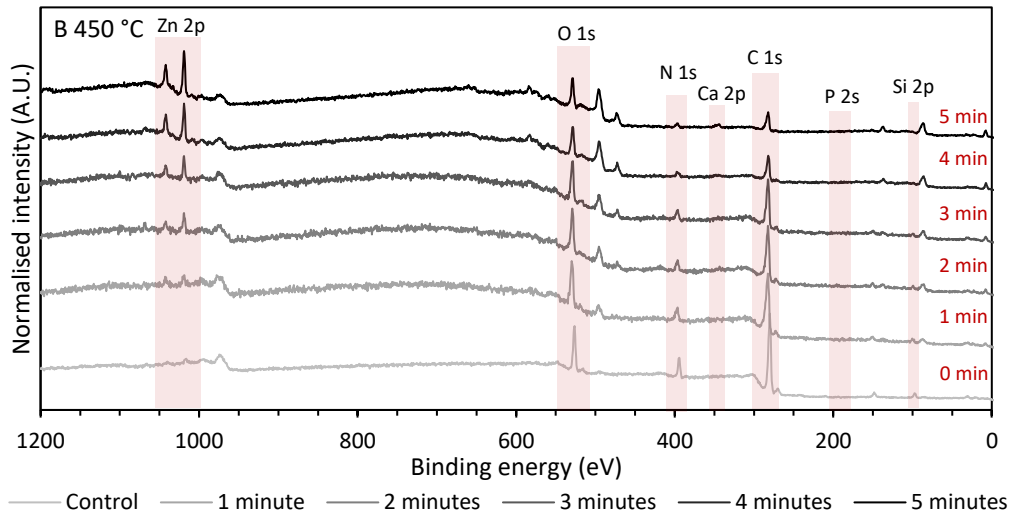


Figure 14.8: Photo of uncoated 21.8 % weight PVP LBZA ink test print presented within appendix 13.3.1.1 . Print force = Anilox force = 50 N, print speed = 1.5 m.s<sup>-1</sup>, LBZA loading 20.9 mg.mL<sup>-1</sup>

### 14.6 XPS survey scans of the printed PVP based LBZA ink undergone calcination



Appendix B3. Miscellaneous Data



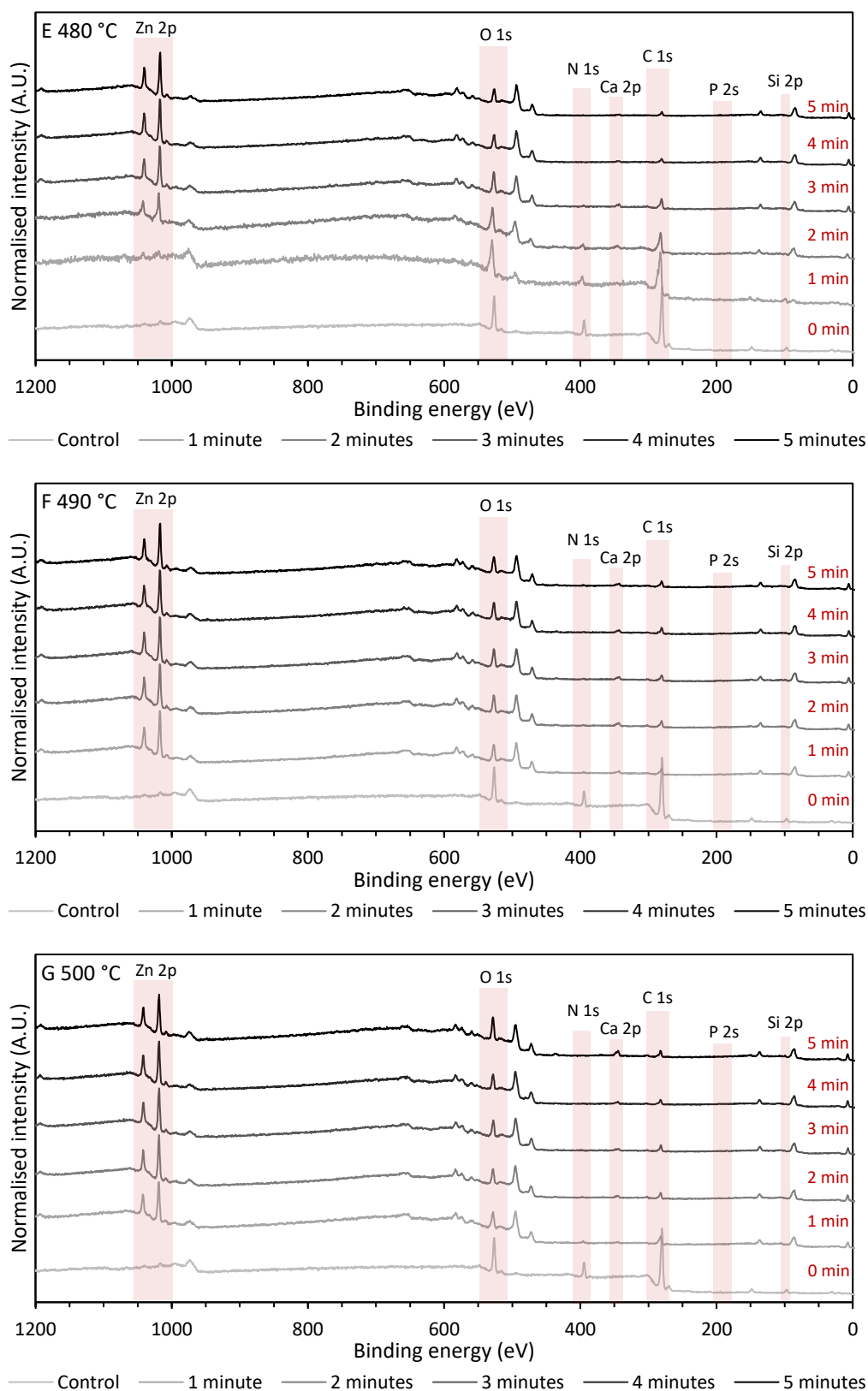


Figure 14.9: Representative XPS survey scans of the printed LBZA films calcined within a tube furnace for 1, 2, 3, 4 and 5 minutes at temperatures of A) 440 °C, B) 450 °C, C) 460 °C, D) 470 °C, 480 °C, 490 °C and 500 °C. Highlighted and annotated peaks represent the photoelectron lines used within the quantification presented within appendix 13.3.1.4 . Sample: ink dry contents; 143 mg.mL<sup>-1</sup> PVP, 46.6 mg.mL<sup>-1</sup> LBZA. Substrate: Combined hydrolysis and O<sub>2</sub> plasma treated Kapton HN.

## 14.7 Measurements of important surface kinetic properties

In the following section measurements of  $\alpha$  and  $\theta_o^2$  for LBZA derived ZnO from the work performed by Jones <sup>[77]</sup> have been extracted and the data replot and trendlines fit.  $\alpha$  and  $\theta_o^2$  are important material parameters used to describe the effect of surface kinetic present at the surface of a gas sensor on resistance as defined by:

$$R = R_0 e^{\alpha \theta_o^2}$$

*Equation 14.1*

$\theta_o$  represents the fraction of negatively ionized oxygen or other species, present at the sensor surface and is defined as:

$$\theta_o = \frac{n_{surf}}{n_{sites}}$$

*Equation 14.2*

Where  $n_{surf}$  is the total number of occupied sites by  $[O]^-$  and species such as  $[CO_2]^-$ , and  $n_{sites}$  is the total number of surface sites.

$\alpha$  is a material function that acts as the proportionality factor that relates  $\theta_o$  to the barrier energy for electron transport (i.e. conduction). The function is produced by the consolidation of terms presented within Equation 14.3:

$$\alpha = \frac{q^3 n_{sites}^2}{2 \epsilon \epsilon_0 k_B T q_{dep} N_{dep}}$$

*Equation 14.3*

Where  $q$  is the charge of the electron,  $\epsilon_0$  is the permittivity of free space,  $\epsilon$  is the relative permittivity,  $q_{dep}$  is the charge of an ion present in the depletion region and  $N_{dep}$  the concentration of cations in the depletion region formed by the donation of electrons to adsorbates.

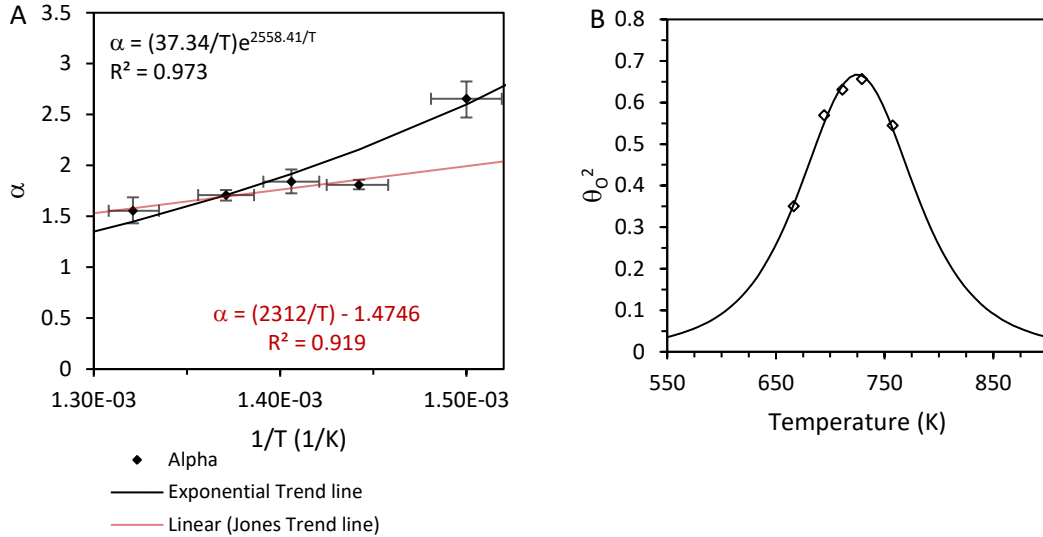


Figure 14.10: Plot of  $\alpha$  as a function of temperature as measured using image J from the work by Jones [589]. The linear trend line was presented within the work by Jones, whilst the exponential fit was applied here assuming that permittivity and/or  $N_{dep}$  may have thermally activated components following Boltzmann statistics. Note the error barriers had no labels and are assumed to be standard deviation based on the lack of other methods for calculating error or confidence in the results. B) Plot of  $\theta_0^2$  as a function of temperature. Trendline:  $\theta_0^2 = \left( \frac{1}{0.00013342*T^2 - 0.19343*T + 71.332} \right)^2$ ,  $R^2=0.989$ . Note that the trendline follows the form expected for occupied sites from the Langmuir isotherm.

Figure 14.10 shows plots of  $\alpha$  and  $\theta_0^2$  reproduced from Jones work [77] using imageJ to extract the values plotted. Figure 14.10 A) was reproduced from fig 5.19 [77], the red trendline shows the linear trendline by Jones assuming all non T factors in Equation 14.3 are temperature invariant. The trendline shows increasing deviations at lower temperatures indicating the temperature invariant assumptions were violated. As  $N_{dep}$  is a product of thermally activated processes it was assumed that Boltzmann like statistics would provide a better approximation of the data. This was shown to be the case with the black trendline in Figure 14.10 A) (showing the function shown in Equation 14.4) with an  $R^2$  value of 0.973, more accurately representing the data.

$$\alpha = \frac{37.34}{T e^{\frac{2558.41}{T}}}$$

Equation 14.4

Figure 14.10 B) shows plots of  $\theta_0^2$  as a function of absolute temperature. The values of  $\theta_0^2$  were extracted from plots of  $\ln(R(CO_{off}))$  as a function of  $\theta_0(CO_{off})^2$  (fig 5.6 [77]). The values of  $\theta_0^2$  were taken from values of  $P_{O_2}/P_{Tot}$  of 0.2 for each temperature series. The

resulting trendline (Equation 14.5) is in close agreement with the measured data ( $R^2=0.989$ ), and follows a rough approximation of form the fraction of occupied sites the Langmuir Isotherm<sup>[204]</sup> would predict.

$$\theta_o^2 = \left( \frac{1}{0.00013342 * T^2 - 0.19343 * T + 71.332} \right)^2$$

*Equation 14.5*

However, as the function is highly non-linear the data should only be taken as a first order approximation for values outside the sampled data points, i.e. at 575.15 K (302 °C) where the IV measurements within chapter 6 are performed. The values at 575.15 K predict a value of  $\alpha=5.55$  and  $\theta_o^2 = 0.056$ , which produces a maximum sensitivity of 1.34 assuming interactions occur entirely via their interactions with oxygen adsorbates (i.e.  $R_o e^{\alpha \theta_o^2} / R_o e^{\alpha * 0}$ ). The value is greater than the response for 200 ppm CO of 1.07 for the HMTA derived sensor but within the same order of magnitude. As such, whilst the results may not necessarily be accurate, are physically sensible and serve as a sensible upper limit for the energy barriers introduced by oxygen adsorption and the responses derived from their reactions.



## Chapter 15 Bibliography

---

- [1] S. M. Lindsay, *Introduction to Nanoscience*, 1st ed. Oxford University Press, 2010.
- [2] V. Subramanian, J. B. Chang, A. de la F. Vornbrock, *et al.*, “Printed electronics for low-cost electronic systems: Technology status and application development,” *ESSDERC 2008 - 38th Eur. Solid-State Device Res. Conf.*, pp. 17–24, 2008.
- [3] Bcc Research, “Global Printed Electronics Market to See 13.6% Growth Through 2022.” [Online]. Available: <https://www.bccresearch.com/pressroom/ift/global-printed-electronics-market-to-see-136-growth-through-2022>. [Accessed: 02-May-2018].
- [4] J. Baker, D. Deganello, D. T. Gethin, and T. M. Watson, “Flexographic printing of graphene nanoplatelet ink to replace platinum as counter electrode catalyst in flexible dye sensitised solar cell,” *Mater. Res. Innov.*, vol. 18, no. 2, pp. 86–90, 2014.
- [5] S. Khan, L. Lorenzelli, and R. S. Dahiya, “Technologies for printing sensors and electronics over large flexible substrates: A review,” *IEEE Sens. J.*, vol. 15, no. 6, pp. 3164–3185, 2015.
- [6] W. Zhang and S. Y. Chou, “Fabrication of 60-nm transistors on 4-in. wafer using nanoimprint at all lithography levels,” *Appl. Phys. Lett.*, vol. 83, no. 8, pp. 1632–1634, 2003.
- [7] G. Grau, J. Cen, H. Kang, R. Kitsomboonloha, W. J. Scheideler, and V. Subramanian, “Gravure-printed electronics: Recent progress in tooling development, understanding of printing physics, and realization of printed devices,” *Flex. Print. Electron.*, vol. 1, no. 2, 2016.
- [8] T. M. Liou, C. Y. Chan, and K. C. Shih, “Effects of actuating waveform, ink property, and nozzle size on piezoelectrically driven inkjet droplets,” *Microfluid. Nanofluidics*, vol. 8, no. 5, pp. 575–586, 2010.
- [9] A. Khan, K. Rahman, D. S. Kim, and K. H. Choi, “Direct printing of copper conductive micro-tracks by multi-nozzle electrohydrodynamic inkjet printing process,” *J. Mater. Process. Technol.*, vol. 212, no. 3, pp. 700–706, 2012.
- [10] “SEFAR - Description of mesh opening.” [Online]. Available: <https://www.sefar.com/en/607/Description-of-mesh-opening.htm?Article=6566821&ArticleReturn=606&UniqueName=meshOpening>.

## Bibliography

[Accessed: 19-Jul-2021].

- [11] “Aluminum Screen with 38 White Mesh - 20x24in | by ScreenPrinting.com.” [Online]. Available: <https://www.screenprinting.com/collections/screen-printing-screens-and-frames/products/aluminum-screen-20x24-38-white-mesh>. [Accessed: 19-Jul-2021].
- [12] K. Inukai, Y. Takahashi, K. Ri, and W. Shin, “Rheological analysis of ceramic pastes with ethyl cellulose for screen-printing,” *Ceram. Int.*, vol. 41, no. 4, pp. 5959–5966, 2015.
- [13] X. Huang, T. Leng, X. Zhang, *et al.*, “Binder-free highly conductive graphene laminate for low cost printed radio frequency applications,” *Appl. Phys. Lett.*, vol. 106, no. 20, 2015.
- [14] Y. Jin, G. Xu, X. Li, *et al.*, “Fast cathodic reduction electrodeposition of a binder-free cobalt-doped Ni-MOF film for directly sensing of levofloxacin,” *J. Alloys Compd.*, vol. 851, p. 156823, 2021.
- [15] Y. A. Aggour, “Thermal decomposition behaviour of ethyl cellulose grafted copolymers in homogeneous media,” *J. Mater. Sci.*, vol. 35, no. 7, pp. 1623–1627, 2000.
- [16] M. S. Yusof, “Printing Fine Solid Lines in Flexographic Printing Process Swansea University - Prifysgol Abertawe,” Swansea University, 2011.
- [17] J. S. Lloyd, C. M. Fung, D. Deganello, *et al.*, “Flexographic printing-assisted fabrication of ZnO nanowire devices,” *Nanotechnology*, vol. 24, no. 19, 2013.
- [18] L. Schmidt-Mende and J. L. MacManus-Driscoll, “ZnO - nanostructures, defects, and devices,” *Mater. Today*, vol. 10, no. 5, pp. 40–48, 2007.
- [19] M. A. Carpenter, S. Mathur, and A. Kolmakov, *Metal Oxide Nanomaterials for Chemical Sensors*. New York, NY: Springer New York, 2013.
- [20] S. T. Meyers, J. T. Anderson, C. M. Hung, J. Thompson, J. F. Wager, and D. A. Keszler, “Aqueous inorganic inks for low-temperature fabrication of ZnO TFTs,” *J. Am. Chem. Soc.*, vol. 130, no. 51, pp. 17603–17609, 2008.
- [21] Y. Y. Noh, X. Cheng, H. Siringhaus, J. I. Sohn, M. E. Welland, and D. J. Kang, “Ink-jet printed ZnO nanowire field effect transistors,” *Appl. Phys. Lett.*, vol. 91, no. 4, 2007.
- [22] K. H. Choi, M. Mustafa, K. Rahman, B. K. Jeong, and Y. H. Doh, “Cost-effective

## Bibliography

- fabrication of memristive devices with ZnO thin film using printed electronics technologies,” *Appl. Phys. A Mater. Sci. Process.*, vol. 106, no. 1, pp. 165–170, 2012.
- [23] N. M. Muhammad, N. Duraisamy, K. Rahman, H. W. Dang, J. Jo, and K. H. Choi, “Fabrication of printed memory device having zinc-oxide active nano-layer and investigation of resistive switching,” *Curr. Appl. Phys.*, vol. 13, no. 1, pp. 90–96, 2013.
- [24] G. S. Pekar, A. F. Singa, O. F. Kolomys, *et al.*, “Materials Science in Semiconductor Processing Magnetic and optical properties of printed ZnO: Co polycrystalline layers,” vol. 135, no. July, pp. 1–10, 2021.
- [25] J. G. Sánchez, V. S. Balderrama, S. I. Garduño, *et al.*, “Impact of inkjet printed ZnO electron transport layer on the characteristics of polymer solar cells,” *RSC Adv.*, vol. 8, no. 24, pp. 13094–13102, 2018.
- [26] D. Corzo, E. Bihar, E. B. Alexandre, D. Rosas-Villalva, and D. Baran, “Ink Engineering of Transport Layers for 9.5% Efficient All-Printed Semitransparent Nonfullerene Solar Cells,” *Adv. Funct. Mater.*, vol. 31, no. 7, pp. 1–10, 2021.
- [27] Y. Wu, T. Tamaki, T. Volotinen, L. Belova, and K. V. Rao, “Enhanced photoresponse of inkjet-printed ZnO thin films capped with CdS nanoparticles,” *J. Phys. Chem. Lett.*, vol. 1, no. 1, pp. 89–92, 2010.
- [28] C. García Núñez, F. Liu, W. T. Navaraj, A. Christou, D. Shakthivel, and R. Dahiya, “Heterogeneous integration of contact-printed semiconductor nanowires for high-performance devices on large areas,” *Microsystems Nanoeng.*, vol. 4, no. 1, 2018.
- [29] G. Dubourg, M. Radovic, and B. Vasic, “Laser-tunable printed zno nanoparticles for paper-based uv sensors with reduced humidity interference,” *Nanomaterials*, vol. 11, no. 1, pp. 1–11, 2021.
- [30] M. Choi, G. Murillo, S. Hwang, *et al.*, “Mechanical and electrical characterization of PVDF-ZnO hybrid structure for application to nanogenerator,” *Nano Energy*, vol. 33, no. December 2016, pp. 462–468, 2017.
- [31] A. K. Assaifan, J. S. Lloyd, S. Samavat, D. Deganello, R. J. Stanton, and K. S. Teng, “Nanotextured Surface on Flexographic Printed ZnO Thin Films for Low-Cost Non-Faradaic Biosensors,” *ACS Appl. Mater. Interfaces*, vol. 8, no. 49, pp. 33802–33810, 2016.
- [32] C. M. Fung, J. S. Lloyd, S. Samavat, D. Deganello, and K. S. Teng, “Facile

## Bibliography

- fabrication of electrochemical ZnO nanowire glucose biosensor using roll to roll printing technique,” *Sensors Actuators, B Chem.*, vol. 247, pp. 807–813, 2017.
- [33] C. Bax, R. Bernasconi, F. Massironi, *et al.*, “Inkjet Printed ZnO Sensors for Early Prostate Cancer Detection by Means of Urine Odor Analysis,” *J. Electrochem. Soc.*, vol. 168, no. 4, p. 047513, 2021.
- [34] N. J. Dayan, S. . Sainkar, R. . Karekar, and R. . Aiyer, “Formulation and characterization of ZnO:Sb thick-film gas sensors,” *Thin Solid Films*, vol. 325, no. 1–2, pp. 254–258, 1998.
- [35] M. S. Wagh, G. H. Jain, D. R. Patil, S. A. Patil, and L. A. Patil, “Modified zinc oxide thick film resistors as NH<sub>3</sub> gas sensor,” *Sensors Actuators, B Chem.*, vol. 115, no. 1, pp. 128–133, 2006.
- [36] M. Peng, D. Lv, D. Xiong, W. Shen, W. Song, and R. Tan, “Facile Preparation of a ZnO/SnO<sub>2</sub>-Based Gas Sensor Array by Inkjet Printing for Gas Analysis with BPNN,” *J. Electron. Mater.*, vol. 48, no. 4, pp. 2373–2381, 2019.
- [37] K. Suematsu, K. Watanabe, A. Tou, Y. Sun, and K. Shimanoe, “Ultrasensitive Toluene-Gas Sensor: Nanosized Gold Loaded on Zinc Oxide Nanoparticles,” *Anal. Chem.*, vol. 90, no. 3, pp. 1959–1966, 2018.
- [38] A. Oprea, J. Courbat, D. Briand, N. Bârsan, U. Weimar, and N. F. De Rooij, “Environmental monitoring with a multisensor platform on polyimide foil,” *Sensors Actuators, B Chem.*, vol. 171–172, pp. 190–197, 2012.
- [39] T. R. Pavase, H. Lin, Q. ul ain Shaikh, *et al.*, “Recent advances of conjugated polymer (CP) nanocomposite-based chemical sensors and their applications in food spoilage detection: A comprehensive review,” *Sensors Actuators, B Chem.*, vol. 273, no. June, pp. 1113–1138, 2018.
- [40] J. R. Stetter and J. Li, “Amperometric gas sensors - A review,” *Chem. Rev.*, vol. 108, no. 2, pp. 352–366, 2008.
- [41] W.H.O., “Environmental Health Criteria 213: Carbon Monoxide (second edition),” 1977.
- [42] “[?]Alcotest 3820 Personal Digital Breathalyzer - AlcoDigital.” [Online]. Available: [https://www.breathalyzer.co.uk/product/3820/?gclid=Cj0KCQjwxdSHBhCdARIsAG6zhlU3GDMaCTPj2ncq57NnvdhPV16cVdYaH0DZUlaup75VHI\\_HtoaRN4aAhGDEALw\\_wcB](https://www.breathalyzer.co.uk/product/3820/?gclid=Cj0KCQjwxdSHBhCdARIsAG6zhlU3GDMaCTPj2ncq57NnvdhPV16cVdYaH0DZUlaup75VHI_HtoaRN4aAhGDEALw_wcB). [Accessed: 19-Jul-2021].

## Bibliography

- [43] A. T. Güntner, S. Abegg, K. Königstein, P. A. Gerber, A. Schmidt-Trucksäss, and S. E. Pratsinis, “Breath sensors for health monitoring,” *ACS Sensors*, vol. 4, no. 2, pp. 268–280, 2019.
- [44] S. Rao, M. Schmulson, M. Valdovinos, S. Zakko, M. Pimentel, and C. Frisp, “Hydrogen and Methane-Based Breath Testing in Gastrointestinal Disorders : The North American Consensus,” *Nat. Publ. Gr.*, no. August 2016, pp. 1–10, 2017.
- [45] A. Sandberg, C. M. Sköld, J. Grunewald, A. Eklund, and Å. M. Wheelock, “Assessing Recent Smoking Status by Measuring Exhaled Carbon Monoxide Levels,” *PLoS One*, vol. 6, no. 12, p. e28864, Dec. 2011.
- [46] S. Das and M. Pal, “Review—Non-Invasive Monitoring of Human Health by Exhaled Breath Analysis: A Comprehensive Review,” *J. Electrochem. Soc.*, vol. 167, no. 3, p. 037562, Feb. 2020.
- [47] B. P. J. De Lacy Costello, M. Ledochowski, and N. M. Ratcliffe, “The importance of methane breath testing: A review,” *J. Breath Res.*, vol. 7, no. 2, 2013.
- [48] R. J. Saad and W. D. Chey, “Breath Tests for Gastrointestinal Disease: The Real Deal or Just a Lot of Hot Air?,” *Gastroenterology*, vol. 133, no. 6, pp. 1763–1766, 2007.
- [49] A. Eisenmann, A. Amann, M. Said, B. Datta, and M. Ledochowski, “Implementation and interpretation of hydrogen breath tests,” *J. Breath Res.*, vol. 2, no. 4, 2008.
- [50] G. Losurdo, G. Leandro, E. Ierardi, *et al.*, “Breath tests for the non-invasive diagnosis of small intestinal bacterial overgrowth: A systematic review with meta-analysis,” *Journal of Neurogastroenterology and Motility*, vol. 26, no. 1. pp. 16–28, 30-Jan-2020.
- [51] B. S. Limited, “GastroCH4ECK® Gastrolyzer® Data sheet.” Bedford® Scientific Limited, 2020.
- [52] “GASTROGENIUS Hydrogen & Methane Breath Monitor | Laborie.” [Online]. Available: <https://www.laborie.com/health-care-professionals/products/gastroenterology/gastrogenius>. [Accessed: 19-Jul-2021].
- [53] “H2 Check - MD Diagnostics Ltd - The Breath Test Experts.” [Online]. Available: <https://www.mdd.org.uk/products/h2-check/>. [Accessed: 19-Jul-2021].
- [54] “QuinTron Breath Testing: Instrumentation.” [Online]. Available: <https://www.breathtests.com/instrumentation>. [Accessed: 19-Jul-2021].
- [55] P. T. Gaffney, R. L. Buttenshaw, and M. J. Thomas, “Faster assay of H<sub>2</sub> in breath by

## Bibliography

- dedicated instruments compared with conventional gas chromatography,” *Clin. Chem.*, vol. 32, no. 9, pp. 1784–1788, 1986.
- [56] X. Liu, S. Cheng, H. Liu, S. Hu, D. Zhang, and H. Ning, “A survey on gas sensing technology,” *Sensors (Switzerland)*, vol. 12, no. 7, pp. 9635–9665, 2012.
- [57] G. Anderson and D. Hadden, *The Gas Monitoring Handbook*. Avocet Press Inc., 1999.
- [58] G. Korotcenkov, “Metal oxides for solid-state gas sensors: What determines our choice?,” vol. 139, pp. 1–23, 2007.
- [59] D. Briand, S. Colin, J. Courbat, S. Raible, J. Kappler, and N. F. de Rooij, “Integration of MOX gas sensors on polyimide hotplates,” *Sensors Actuators, B Chem.*, vol. 130, no. 1, pp. 430–435, 2008.
- [60] L. D’Arsié, V. Alijani, S. T. S. Brunelli, *et al.*, “Improved recovery time and sensitivity to H<sub>2</sub> and NH<sub>3</sub> at room temperature with SnO<sub>x</sub> vertical nanopillars on ITO,” *Sci. Rep.*, vol. 8, no. 1, pp. 1–9, 2018.
- [61] S. Khan and D. Briand, “All-printed low-power metal oxide gas sensors on polymeric substrates,” *Flex. Print. Electron.*, vol. 4, no. 1, 2019.
- [62] H. T. Wang, B. S. Kang, F. Ren, *et al.*, “Hydrogen-selective sensing at room temperature with ZnO nanorods,” *Appl. Phys. Lett.*, vol. 86, no. 24, pp. 1–3, 2005.
- [63] Y. S. Kim, S. C. Ha, K. Kim, *et al.*, “Room-temperature semiconductor gas sensor based on nonstoichiometric tungsten oxide nanorod film,” *Appl. Phys. Lett.*, vol. 86, no. 21, pp. 1–3, 2005.
- [64] P. C. Chen, F. N. Ishikawa, H. K. Chang, K. Ryu, and C. Zhou, “A nanoelectronic nose: A hybrid nanowire/carbon nanotube sensor array with integrated micromachined hotplates for sensitive gas discrimination,” *Nanotechnology*, vol. 20, no. 12, 2009.
- [65] K. Arshak, E. Moore, G. M. Lyons, J. Harris, and S. Clifford, “A review of gas sensors employed in electronic nose applications,” *Sens. Rev.*, vol. 24, no. 2, pp. 181–198, 2004.
- [66] K. Arshak, E. Moore, G. M. Lyons, J. Harris, and S. Clifford, “A review of gas sensors employed in electronic nose applications,” *Sensor Review*, vol. 24, no. 2, pp. 181–198, 2004.
- [67] A. Tarat, C. J. Nettle, D. T. J. Bryant, *et al.*, “Microwave-assisted synthesis of

## Bibliography

- layered basic zinc acetate nanosheets and their thermal decomposition into nanocrystalline ZnO,” *Nanoscale Res. Lett.*, vol. 9, no. 1, pp. 1–8, 2014.
- [68] Y. Wang, Y. Li, Z. Zhou, X. Zu, and Y. Deng, “Evolution of the zinc compound nanostructures in zinc acetate single-source solution,” *J. Nanoparticle Res.*, vol. 13, no. 10, pp. 5193–5202, 2011.
- [69] A. Tarat, R. Majithia, R. A. Brown, M. W. Penny, K. E. Meissner, and T. G. G. Maffei, “Synthesis of nanocrystalline ZnO nanobelts via pyrolytic decomposition of zinc acetate nanobelts and their gas sensing behavior,” *Surf. Sci.*, vol. 606, no. 7–8, pp. 715–721, 2012.
- [70] H. Li, Y. Zhang, and J. Wang, “ZnO nanosheets derived from surfactant-directed process: Growth mechanism, and application in dye-sensitized solar cells,” *J. Am. Ceram. Soc.*, vol. 95, no. 4, pp. 1241–1246, 2012.
- [71] Q. Cui, K. Yu, N. Zhang, and Z. Zhu, “Porous ZnO nanobelts evolved from layered basic zinc acetate nanobelts,” *Appl. Surf. Sci.*, vol. 254, no. 11, pp. 3517–3521, Mar. 2008.
- [72] J. Xu, Q. Pan, Y. Shun, and Z. Tian, “Grain size control and gas sensing properties of ZnO gas sensor,” *Sensors and Actuators, B: Chemical*, vol. 66, no. 1, pp. 277–279, 2000.
- [73] H. Morioka, H. Tagaya, J. -I. Kadokawa, and K. Chiba, “Studies on layered basic zinc acetate,” *J. Mater. Sci. Lett.*, vol. 18, no. 12, pp. 995–998, 1999.
- [74] R. Q. Song, A. W. Xu, B. Deng, Q. Li, and G. Y. Chen, “From layered basic zinc acetate nanobelts to hierarchical zinc oxide nanostructures and porous zinc oxide nanobelts,” *Adv. Funct. Mater.*, vol. 17, no. 2, pp. 296–306, 2007.
- [75] L. Poul, N. Jouini, and F. Fievet, “Layered hydroxide metal acetates (metal = zinc, cobalt, and nickel): Elaboration via hydrolysis in polyol medium and comparative study,” *Chem. Mater.*, vol. 12, no. 10, pp. 3123–3132, 2000.
- [76] A. K. Assaifan, N. A. Alshehri, A. R. Lewis, *et al.*, “Effect of intense pulsed light on hydrothermally grown ZnO nanowires,” *Mater. Lett.*, vol. 271, p. 127797, 2020.
- [77] D. R. (Swansea U. Jones, “Characterisation of the surface reactions and gas sensing properties of zinc oxide nanosheets,” Swansea University, 2015.
- [78] C. H. Park, S. B. Zhang, and S. H. Wei, “Origin of p-type doping difficulty in ZnO: The impurity perspective,” *Phys. Rev. B - Condens. Matter Mater. Phys.*, vol. 66, no.

- 7, pp. 1–3, 2002.
- [79] A. Kolodziejczak-Radzimska and T. Jesionowski, “Zinc oxide-from synthesis to application: A review,” *Materials (Basel)*, vol. 7, no. 4, pp. 2833–2881, 2014.
- [80] A. Janotti and C. G. Van De Walle, “Fundamentals of zinc oxide as a semiconductor,” *Reports Prog. Phys.*, vol. 72, no. 12, 2009.
- [81] M. D. McCluskey and S. J. Jokela, “Defects in ZnO,” *J. Appl. Phys.*, vol. 106, no. 7, pp. 0–13, 2009.
- [82] D. M. Hofmann, D. Pfisterer, J. Sann, *et al.*, “Properties of the oxygen vacancy in ZnO,” *Appl. Phys. A Mater. Sci. Process.*, vol. 88, no. 1, pp. 147–151, 2007.
- [83] A. Boonchun and W. R. L. Lambrecht, “Electronic structure of defects and doping in ZnO: Oxygen vacancy and nitrogen doping,” *Phys. Status Solidi Basic Res.*, vol. 250, no. 10, pp. 2091–2101, 2013.
- [84] N. P. Herring, L. S. Panchakarla, and M. S. El-Shall, “P-Type nitrogen-Doped ZnO nanostructures with controlled shape and doping level by facile microwave synthesis,” *Langmuir*, vol. 30, no. 8, pp. 2230–2240, 2014.
- [85] X. Nie, B. Zhang, J. Wang, L. Shi, Z. Di, and Q. Guo, “Room-temperature ferromagnetism in p-type nitrogen-doped ZnO films,” *Mater. Lett.*, vol. 161, pp. 355–359, 2015.
- [86] B. Panigrahy and D. Bahadur, “P-type Phosphorus doped ZnO nanostructures: An electrical, optical, and magnetic properties study,” *RSC Adv.*, vol. 2, no. 15, pp. 6222–6227, 2012.
- [87] B. Yao, Y. P. Xie, C. X. Cong, *et al.*, “Mechanism of p-type conductivity for phosphorus-doped ZnO thin film,” *J. Phys. D. Appl. Phys.*, vol. 42, no. 1, 2009.
- [88] S. D. Baek, P. Biswas, J. W. Kim, Y. C. Kim, T. Il Lee, and J. M. Myoung, “Low-Temperature Facile Synthesis of Sb-Doped p-Type ZnO Nanodisks and Its Application in Homo Junction Light-Emitting Diode,” *ACS Appl. Mater. Interfaces*, vol. 8, no. 20, pp. 13018–13026, 2016.
- [89] C. Yuen, S. F. Yu, E. S. P. Leong, *et al.*, “Room temperature deposition of p -type arsenic doped ZnO polycrystalline films by laser-assist filtered cathodic vacuum arc technique,” *J. Appl. Phys.*, vol. 101, no. 9, 2007.
- [90] G. Braunstein, A. Muraviev, H. Saxena, N. Dhere, V. Richter, and R. Kalish, “P type doping of zinc oxide by arsenic ion implantation,” *Appl. Phys. Lett.*, vol. 87, no. 19,



- pp. 1–3, 2005.
- [91] C. Park, S. Kim, and S. Lim, “Synthesis of arsenic-doped p-type ZnO films by addition of As<sub>2</sub>O<sub>3</sub> to the ZnO spin coating solution,” *Solid State Commun.*, vol. 167, pp. 18–22, 2013.
- [92] I. S. Kim, E. K. Jeong, D. Y. Kim, M. Kumar, and S. Y. Choi, “Investigation of p-type behavior in Ag-doped ZnO thin films by E-beam evaporation,” *Appl. Surf. Sci.*, vol. 255, no. 7, pp. 4011–4014, 2009.
- [93] Y. J. Zeng, Z. Z. Ye, J. G. Lu, *et al.*, “Identification of acceptor states in Li-doped p-type ZnO thin films,” *Appl. Phys. Lett.*, vol. 89, no. 4, pp. 87–90, 2006.
- [94] Y. J. Zeng, Z. Z. Ye, W. Z. Xu, *et al.*, “Realization of p-type ZnO films via monodoping of Li acceptor,” *J. Cryst. Growth*, vol. 283, no. 1–2, pp. 180–184, 2005.
- [95] S. S. Lin, J. G. Lu, Z. Z. Ye, *et al.*, “p-type behavior in Na-doped ZnO films and ZnO homojunction light-emitting diodes,” *Solid State Commun.*, vol. 148, no. 1–2, pp. 25–28, 2008.
- [96] S. S. Lin, H. P. He, Y. F. Lu, and Z. Z. Ye, “Mechanism of Na-doped p-type ZnO films: Suppressing Na interstitials by codoping with H and Na of appropriate concentrations,” *J. Appl. Phys.*, vol. 106, no. 9, 2009.
- [97] W. Liu, F. Xiu, K. Sun, *et al.*, “Na-Doped p-Type ZnO Microwires,” *J. Am. Chem. Soc.*, vol. 132, no. 8, pp. 2498–2499, 2010.
- [98] R. Kumar, O. Al-Dossary, G. Kumar, and A. Umar, “Zinc oxide nanostructures for NO<sub>2</sub> gas-sensor applications: A review,” *Nano-Micro Lett.*, vol. 7, no. 2, pp. 1–24, 2014.
- [99] A. Wei, L. Pan, and W. Huang, “Recent progress in the ZnO nanostructure-based sensors,” *Mater. Sci. Eng. B Solid-State Mater. Adv. Technol.*, vol. 176, no. 18, pp. 1409–1421, 2011.
- [100] L. Zhu and W. Zeng, “Room-temperature gas sensing of ZnO-based gas sensor: A review,” *Sensors Actuators, A Phys.*, vol. 267, pp. 242–261, 2017.
- [101] V. S. Bhati, M. Hojamberdiev, and M. Kumar, “Enhanced sensing performance of ZnO nanostructures-based gas sensors: A review,” *Energy Reports*, vol. 6, pp. 46–62, 2020.
- [102] C. N. Wang, Y. L. Li, F. L. Gong, Y. H. Zhang, S. M. Fang, and H. L. Zhang, “Advances in Doped ZnO Nanostructures for Gas Sensor,” *Chem. Rec.*, vol. 20, no.

- 12, pp. 1553–1567, 2020.
- [103] C. B. Ong, L. Y. Ng, and A. W. Mohammad, “A review of ZnO nanoparticles as solar photocatalysts: Synthesis, mechanisms and applications,” *Renew. Sustain. Energy Rev.*, vol. 81, no. August 2017, pp. 536–551, 2018.
- [104] S. B. A. Hamid, S. J. Teh, and C. W. Lai, “Photocatalytic water oxidation on ZnO: A review,” *Catalysts*, vol. 7, no. 3, 2017.
- [105] T. J. Hall, J. S. J. Hargreaves, G. J. Hutchings, R. W. Joyner, and S. H. Taylor, “Catalytic synthesis of methanol and formaldehyde by partial oxidation of methane,” *Fuel Process. Technol.*, vol. 42, no. 2–3, pp. 151–178, 1995.
- [106] S. H. Taylor, J. S. J. Hargreaves, G. J. Hutchings, R. W. Joyner, and C. W. Lembacher, “The Partial Oxidation of Methane to Methanol: An Approach to Catalyst Design,” *Catal. Today*, vol. 42, no. 3, pp. 217–224, 1998.
- [107] Z. K. Tang, G. K. L. Wong, P. Yu, *et al.*, “Room-temperature ultraviolet laser emission from self-assembled ZnO microcrystallite thin films,” *Appl. Phys. Lett.*, vol. 72, no. 25, pp. 3270–3272, 1998.
- [108] V. T. Tran, Y. Wei, H. Yang, Z. Zhan, and H. Du, “All-inkjet-printed flexible ZnO micro photodetector for a wearable UV monitoring device,” *Nanotechnology*, vol. 28, no. 9, 2017.
- [109] M. Gong, Q. Liu, B. Cook, *et al.*, “All-Printable ZnO Quantum Dots/Graphene van der Waals Heterostructures for Ultrasensitive Detection of Ultraviolet Light,” *ACS Nano*, vol. 11, no. 4, pp. 4114–4123, 2017.
- [110] S. Goktas and A. Goktas, “A comparative study on recent progress in efficient ZnO based nanocomposite and heterojunction photocatalysts: A review,” *J. Alloys Compd.*, vol. 863, 2021.
- [111] E. Hosono, S. Fujihara, T. Kimura, and H. Imai, “Non-basic solution routes to prepare ZnO nanoparticles,” *J. Sol-Gel Sci. Technol.*, vol. 29, no. 2, pp. 71–79, 2004.
- [112] L. Wang, X. Zhang, S. Zhao, G. Zhou, Y. Zhou, and J. Qi, “Synthesis of well-aligned ZnO nanowires by simple physical vapor deposition on c -oriented ZnO thin films without catalysts or additives,” *Appl. Phys. Lett.*, vol. 86, no. 2, pp. 10–13, 2005.
- [113] T. Sahoo, M. Kim, J. H. Baek, *et al.*, “Synthesis and characterization of porous ZnO nanoparticles by hydrothermal treatment of as pure aqueous precursor,” *Mater. Res. Bull.*, vol. 46, no. 4, pp. 525–530, 2011.

## Bibliography

- [114] F. Meng, S. A. Morin, A. Forticaux, and S. Jin, "Screw dislocation driven growth of nanomaterials," *Acc. Chem. Res.*, vol. 46, no. 7, pp. 1616–1626, 2013.
- [115] D. Yan, J. Cen, W. Zhang, A. Orlov, and M. Liu, "Hydrothermal growth of ZnO nanowire arrays: fine tuning by precursor supersaturation," *CrystEngComm*, vol. 19, no. 3, pp. 584–591, 2017.
- [116] S. P. Garcia and S. Semancik, "Controlling the morphology of zinc oxide nanorods crystallized from aqueous solutions: The effect of crystal growth modifiers on aspect ratio," *Chem. Mater.*, vol. 19, no. 16, pp. 4016–4022, 2007.
- [117] R. C. Hoffmann, M. Trapp, E. Erdem, *et al.*, "Synthesis and Assembly of Zinc Oxide Microcrystals by a Low-Temperature Dissolution–Reprecipitation Process: Lessons Learned About Twin Formation in Heterogeneous Reactions," *Chem. - A Eur. J.*, vol. 26, no. 42, pp. 9319–9329, 2020.
- [118] C. Chevalier-César, M. Capochichi-Gnambodoe, and Y. Leprince-Wang, "Growth mechanism studies of ZnO nanowire arrays via hydrothermal method," *Appl. Phys. A*, vol. 115, no. 3, pp. 953–960, 2014.
- [119] S. A. Morin, M. J. Bierman, J. Tong, and S. Jin, "Mechanism and Kinetics of Spontaneous Nanotube Growth Driven by Screw Dislocations," *Science (80-. )*, vol. 328, no. 5977, pp. 476–480, Apr. 2010.
- [120] S. Yamabi and H. Imai, "Growth conditions for wurtzite zinc oxide films in aqueous solutions," *J. Mater. Chem.*, vol. 12, no. 12, pp. 3773–3778, 2002.
- [121] X. Wen, W. Wu, Y. Ding, and Z. L. Wang, "Seedless synthesis of patterned ZnO nanowire arrays on metal thin films (Au, Ag, Cu, Sn) and their application for flexible electromechanical sensing," *J. Mater. Chem.*, vol. 22, no. 19, pp. 9469–9476, 2012.
- [122] C. H. Ku, H. H. Yang, G. R. Chen, and J. J. Wu, "Wet-chemical route to ZnO nanowire-layered basic zinc acetate/ZnO nanoparticle composite film," *Cryst. Growth Des.*, vol. 8, no. 1, pp. 283–290, 2008.
- [123] M. Navaneethan, J. Archana, M. Arivanandhan, and Y. Hayakawa, "Functional properties of amine-passivated ZnO nanostructures and dye-sensitized solar cell characteristics," *Chem. Eng. J.*, vol. 213, pp. 70–77, 2012.
- [124] T. Marimuthu, N. Anandhan, and R. Thangamuthu, "Electrochemical synthesis of one-dimensional ZnO nanostructures on ZnO seed layer for DSSC applications,"

- Appl. Surf. Sci.*, vol. 428, pp. 385–394, 2018.
- [125] K. M. McPeak, T. P. Le, N. G. Britton, Z. S. Nickolov, Y. A. Elabd, and J. B. Baxter, “Chemical bath deposition of ZnO nanowires at near-neutral pH conditions without hexamethylenetetramine (HMTA): Understanding the role of HMTA in ZnO nanowire growth,” *Langmuir*, vol. 27, no. 7, pp. 3672–3677, 2011.
- [126] S. Cho, S.-H. Jung, and K.-H. Lee, “Morphology-Controlled Growth of ZnO Nanostructures Using Microwave Irradiation: from Basic to Complex Structures,” *J. Phys. Chem. C*, vol. 112, no. 33, pp. 12769–12776, 2008.
- [127] J. B. Miller, H. J. Hsieh, B. H. Howard, and E. Broitman, “Microstructural evolution of sol-gel derived ZnO thin films,” *Thin Solid Films*, vol. 518, no. 23, pp. 6792–6798, 2010.
- [128] Y. Natsume and H. Sakata, “Zinc oxide films prepared by sol-gel spin-coating,” *Thin Solid Films*, vol. 372, no. 1, pp. 30–36, 2000.
- [129] X. Liu, J. Zhang, L. Wang, *et al.*, “3D hierarchically porous ZnO structures and their functionalization by Au nanoparticles for gas sensors,” *J. Mater. Chem.*, vol. 21, no. 2, pp. 349–356, 2011.
- [130] X. L. Cheng, Z. Rong, X. F. Zhang, *et al.*, “In situ assembled ZnO flower sensors based on porous nanofibers for rapid ethanol sensing,” *Sensors Actuators, B Chem.*, vol. 188, pp. 425–432, 2013.
- [131] A. Moezzi, A. McDonagh, A. Dowd, and M. Cortie, “Zinc hydroxyacetate and its transformation to nanocrystalline zinc oxide,” *Inorg. Chem.*, vol. 52, no. 1, pp. 95–102, 2013.
- [132] G. G. C. Arizaga, K. G. Satyanarayana, and F. Wypych, “Layered hydroxide salts: Synthesis, properties and potential applications,” *Solid State Ionics*, vol. 178, no. 15–18, pp. 1143–1162, 2007.
- [133] T. Shinagawa, M. Watanabe, T. Mori, J. I. Tani, M. Chigane, and M. Izaki, “Oriented Transformation from Layered Zinc Hydroxides to Nanoporous ZnO: A Comparative Study of Different Anion Types,” *Inorg. Chem.*, vol. 57, no. 21, pp. 13137–13149, 2018.
- [134] E. Hosono, S. Fujihara, T. Kimura, and H. Imai, “Growth of layered basic zinc acetate in methanolic solutions and its pyrolytic transformation into porous zinc oxide films,” *J. Colloid Interface Sci.*, vol. 272, no. 2, pp. 391–398, 2004.

- [135] G. Patrinoiu, J. M. Calderón-Moreno, D. C. Culita, R. Birjega, R. Ene, and O. Carp, “Eco-friendly synthetic route for layered zinc compound and its conversion to ZnO with photocatalytic properties,” *Solid State Sci.*, vol. 23, pp. 58–64, 2013.
- [136] D. Hacıu and Ö. Birer, “Sonochemical zinc oxide and layered hydroxy zinc acetate synthesis in fenton-like reactions,” *Ultrason. Sonochem.*, vol. 35, pp. 326–332, 2017.
- [137] N. A. Jose, H. C. Zeng, and A. A. Lapkin, “Hydrodynamic assembly of two-dimensional layered double hydroxide nanostructures,” *Nat. Commun.*, vol. 9, no. 1, pp. 1–12, 2018.
- [138] J. Li, H. Fan, and X. Jia, “Multilayered ZnO Nanosheets with 3D Porous Architectures Synthesis and Gas Sensing Application,” *ACS J. Physical Chem. C*, vol. 114, no. 35, pp. 14684–14691, 2010.
- [139] X. Pang, L. Chen, Y. Liu, M. Chi, Z. Li, and J. Plank, “Growth behavior of water dispersed MgAl layered double hydroxide nanosheets,” *RSC Adv.*, vol. 7, no. 25, pp. 14989–14997, 2017.
- [140] N. D. Burrows, C. R. H. Hale, and R. L. Penn, “Effect of ionic strength on the kinetics of crystal growth by oriented aggregation,” *Cryst. Growth Des.*, vol. 12, no. 10, pp. 4787–4797, 2012.
- [141] W. Lv, W. He, X. Wang, *et al.*, “Understanding the oriented-attachment growth of nanocrystals from an energy point of view: A review,” *Nanoscale*, vol. 6, no. 5, pp. 2531–2547, 2014.
- [142] A. Forticaux, L. Dang, H. Liang, and S. Jin, “Controlled synthesis of layered double hydroxide nanoplates driven by screw dislocations,” *Nano Lett.*, vol. 15, no. 5, pp. 3403–3409, 2015.
- [143] W. K. Burton, N. Cabrera, and F. C. Frank, “The growth of crystals and the equilibrium structure of their surfaces,” *Philos. Trans. R. Soc. London. Ser. A, Math. Phys. Sci.*, vol. 243, no. 866, pp. 299–358, Jun. 1951.
- [144] S. Khamlich, A. Bello, M. Fabiane, B. D. Ngom, and N. Manyala, “Hydrothermal synthesis of simonkolleite microplatelets on nickel foam-graphene for electrochemical supercapacitors,” *J. Solid State Electrochem.*, vol. 17, no. 11, pp. 2879–2886, 2013.
- [145] J. Sithole, B. D. Ngom, S. Khamlich, *et al.*, “Simonkolleite nano-platelets: Synthesis and temperature effect on hydrogen gas sensing properties,” *Appl. Surf. Sci.*, vol. 258,

- no. 20, pp. 7839–7843, 2012.
- [146] S. Cousy, N. Gorodylova, L. Svoboda, and J. of synthesis conditions over simonkolleite/ZnO precipitation Zelenka, “Influence of synthesis conditions over simonkolleite/ZnO precipitation,” *Chem. Pap.*, vol. 71, no. 12, pp. 2325–2334, 2017.
- [147] S. Khamlich, T. Mokrani, M. S. Dhlamini, B. M. Mothudi, and M. Maaza, “Microwave-assisted synthesis of simonkolleite nanoplatelets on nickel foam-graphene with enhanced surface area for high-performance supercapacitors,” *J. Colloid Interface Sci.*, vol. 461, pp. 154–161, 2016.
- [148] M. Pal, S. Bera, and S. Jana, “Sol–gel based simonkolleite nanopetals with SnO<sub>2</sub> nanoparticles in graphite-like amorphous carbon as an efficient and reusable photocatalyst,” *RSC Adv.*, vol. 5, no. 92, pp. 75062–75074, 2015.
- [149] Y. Li, Y. Zou, and Y. Hou, “Synthesis and characterization of simonkolleite nanodisks and their conversion into ZnO nanostructures,” *Cryst. Res. Technol.*, vol. 46, no. 3, pp. 305–308, 2011.
- [150] J. D. Yoo, P. Volovitch, A. Abdel Aal, C. Allely, and K. Ogle, “The effect of an artificially synthesized simonkolleite layer on the corrosion of electrogalvanized steel,” *Corros. Sci.*, vol. 70, pp. 1–10, 2013.
- [151] S. A. Morin, A. Forticaux, M. J. Bierman, and S. Jin, “Screw dislocation-driven growth of two-dimensional nanoplates,” *Nano Lett.*, vol. 11, no. 10, pp. 4449–4455, 2011.
- [152] B. Song, X. Cui, Y. Xie, S. Cheng, Y. Shao, and Y. Sun, “Controllable Growth of Monodisperse Multilayered Three-Dimensional Simonkolleite and Its Supercapacitor Activity,” *Cryst. Growth Des.*, vol. 17, no. 6, pp. 3548–3555, 2017.
- [153] C. Hawthorne and E. Sokolova, “SIMONKOLLEITE, Zn<sub>5</sub>(OH)<sub>8</sub>Cl<sub>2</sub>(H<sub>2</sub>O), A DECORATED INTERRUPTED-SHEET STRUCTURE OF THE FORM [M<sub>2</sub>]4,” *Can. Mineral.*, vol. 51, no. 1, pp. 192–192, Feb. 2013.
- [154] G. Alagona, C. Ghio, and P. Kollman, “Monte Carlo Simulation Studies of the Solvation of Ions. 1. Acetate Anion and Methylammonium Cation,” *J. Am. Chem. Soc.*, vol. 108, no. 2, pp. 185–191, 1986.
- [155] G. P. Andrew Burrows, John Holman, Andrew Parsons, Gwen Pilling, *Chemistry3 introducing inorganic, organic and physical chemistry*, 2nd ed. Oxford University Press, 2013.

## Bibliography

- [156] S. H. Hu, Y. C. Chen, C. C. Hwang, C. H. Peng, and D. C. Gong, "Development of a wet chemical method for the synthesis of arrayed ZnO nanorods," *J. Alloys Compd.*, vol. 500, no. 2, pp. L17–L21, 2010.
- [157] J. Macan, M. Ivanko, I. Bukovčan, I. Grčić, and A. Gajović, "Stable hierarchical ZnO structures for photocatalytic degradation of 2,5-dihydroxybenzoic acid," *Mater. Sci. Semicond. Process.*, vol. 97, no. March, pp. 48–55, 2019.
- [158] G. Capellini, M. De Seta, P. Zaumseil, G. Kozłowski, and T. Schroeder, "High temperature x ray diffraction measurements on Ge/Si(001) heterostructures: A study on the residual tensile strain," *J. Appl. Phys.*, vol. 111, no. 7, 2012.
- [159] V. L. Ene, D. Dinescu, I. Zai, *et al.*, "Study of Edge and Screw Dislocation Density in GaN/Al<sub>2</sub>O<sub>3</sub> Heterostructure," *Materials (Basel)*, vol. 12, no. 24, p. 4205, Dec. 2019.
- [160] T. Nakamura, R. Nagahata, S. Suemitsu, and K. Takeuchi, "In-situ measurement of microwave absorption properties at 2 . 45 GHz for the polycondensation of lactic acid," *Polymer (Guildf)*, vol. 51, no. 2, pp. 329–333, 2010.
- [161] K. Fleisch, *Electromagnetics with applications.*, 5th ed. McGraw-Hill, 2017.
- [162] B. Yang, X. Cao, H. Lang, S. Wang, and C. Sun, "Study on hydrogen bonding network in aqueous methanol solution by Raman spectroscopy," *Spectrochim. Acta - Part A Mol. Biomol. Spectrosc.*, vol. 225, p. 117488, 2020.
- [163] S. A. Morin and S. Jin, "Screw dislocation-driven epitaxial solution growth of ZnO nanowires seeded by dislocations in GaN substrates," *Nano Lett.*, vol. 10, no. 9, pp. 3459–3463, 2010.
- [164] N. Choy, Jin-Ho Intra- and inter-layer structures of layered hydroxy double salts, Y.-M. Kwon, K.-S. Han, S.-W. Song, and S. H. Chang, "Intra- and inter-layer structures of layered hydroxy double salts, Ni<sub>1-x</sub>Zn<sub>2x</sub>(OH)<sub>2</sub>(CH<sub>3</sub>CO<sub>2</sub>)<sub>2x</sub>·nH<sub>2</sub>O," *Mater. Lett.*, vol. 34, no. 3–6, pp. 356–363, 1998.
- [165] J. Demel, J. Pleštil, P. Bezdička, P. Janda, M. Klementová, and K. Lang, "Layered zinc hydroxide salts: Delamination, preferred orientation of hydroxide lamellae, and formation of ZnO nanodiscs," *J. Colloid Interface Sci.*, vol. 360, no. 2, pp. 532–539, 2011.
- [166] M. M. J. van Rijt, B. M. Oosterlaken, R. R. M. Joosten, *et al.*, "Counter-ion influence on the mechanism of HMTA-mediated ZnO formation," *CrystEngComm*, vol. 22, no.

- 35, pp. 5854–5861, 2020.
- [167] A. Tarat, R. Majithia, R. A. Brown, M. W. Penny, K. E. Meissner, and T. G. G. Maffei, “Synthesis of nanocrystalline ZnO nanobelts via pyrolytic decomposition of zinc acetate nanobelts and their gas sensing behavior,” *Surf. Sci.*, vol. 606, no. 7–8, pp. 715–721, 2012.
- [168] Y. Liu, H. Geng, X. Qin, *et al.*, “Oriented Attachment Revisited: Does a Chemical Reaction Occur?,” *Matter*, vol. 1, no. 3, pp. 690–704, 2019.
- [169] V. K. Lamer and R. H. Dinegar, “Theory, Production and Mechanism of Formation of Monodispersed Hydrosols,” *J. Am. Chem. Soc.*, vol. 72, no. 11, pp. 4847–4854, 1950.
- [170] Y. Wang, J. He, C. Liu, W. H. Chong, and H. Chen, “Thermodynamics versus kinetics in Nanosynthesis,” *Angew. Chemie - Int. Ed.*, vol. 54, no. 7, pp. 2022–2051, 2015.
- [171] Z. A. Peng and X. Peng, “Nearly monodisperse and shape-controlled CdSe nanocrystals via alternative routes: Nucleation and growth,” *J. Am. Chem. Soc.*, vol. 124, no. 13, pp. 3343–3353, 2002.
- [172] F. K. Crundwell, “Concerning the Influence of Surface Charge on the Rate of Growth of Surfaces during Crystallization,” *Cryst. Growth Des.*, vol. 16, no. 10, pp. 5877–5886, Oct. 2016.
- [173] F. K. Crundwell, “A novel mechanism for the rate of growth during the crystallisation of salts and the precipitation of minerals,” *Hydrometallurgy*, vol. 166, pp. 62–72, 2016.
- [174] S. Parez, M. Předota, and M. Machesky, “Dielectric properties of water at rutile and graphite surfaces: Effect of molecular structure,” *J. Phys. Chem. C*, vol. 118, no. 9, pp. 4818–4834, 2014.
- [175] F. K. Crundwell, “On the Mechanism of the Dissolution of Quartz and Silica in Aqueous Solutions,” *ACS Omega*, vol. 2, no. 3, pp. 1116–1127, 2017.
- [176] F. K. Crundwell, “The mechanism of dissolution of minerals in acidic and alkaline solutions: Part v surface charge and zeta potential,” *Hydrometallurgy*, vol. 161, pp. 174–184, 2016.
- [177] S. Sharma, N. Soleimanioun, R. Kaur, M. Rani, and S. K. Tripathi, “Comparative study of the effect of Mg, Zn and Ag dopants on properties of titanium dioxide as



## Bibliography

- mesoporous ETL for photovoltaic application,” *Mater. Chem. Phys.*, vol. 257, no. June 2020, p. 123730, 2021.
- [178] C. Misbah, F. Renard, J. P. Gratier, and K. Kassner, “Dynamics of a dissolution front for solids under stress,” *Geophys. Res. Lett.*, vol. 31, no. 6, pp. 1–5, 2004.
- [179] L. Liu, E. Nakouzi, M. L. Sushko, *et al.*, “Connecting energetics to dynamics in particle growth by oriented attachment using real-time observations,” *Nat. Commun.*, vol. 11, no. 1, pp. 1–11, 2020.
- [180] L. M. Anovitz, X. Zhang, J. Soltis, *et al.*, “Effects of Ionic Strength, Salt, and pH on Aggregation of Boehmite Nanocrystals: Tumbler Small-Angle Neutron and X-ray Scattering and Imaging Analysis,” *Langmuir*, vol. 34, no. 51, pp. 15839–15853, 2018.
- [181] M. Alimohammadi and K. A. Fichthorn, “Molecular Dynamics Simulation of the Aggregation of Titanium Dioxide Nanocrystals: Preferential Alignment,” *Nano Lett.*, vol. 9, no. 12, pp. 4198–4203, Dec. 2009.
- [182] D. Li, M. H. Nielsen, J. R. I. Lee, C. Frandsen, J. F. Banfield, and J. J. De Yoreo, “Direction-Specific Interactions Control Crystal Growth by Oriented Attachment,” *Science (80-. )*, vol. 336, no. 6084, pp. 1014–1018, May 2012.
- [183] H. G. Liao, L. Cui, S. Whitlam, and H. Zheng, “Real-time imaging of Pt3Fe nanorod growth in solution,” *Science (80-. )*, vol. 336, no. 6084, pp. 1011–1014, 2012.
- [184] Z. Zhang, M. Lu, H. Xu, and W.-S. Chin, “Shape-Controlled Synthesis of Zinc Oxide: A Simple Method for the Preparation of Metal Oxide Nanocrystals in Non-aqueous Medium,” *Chem. - A Eur. J.*, vol. 13, no. 2, pp. 632–638, 2007.
- [185] E. J. H. Lee, C. Ribeiro, E. Longo, and E. R. Leite, “Oriented attachment: An effective mechanism in the formation of anisotropic nanocrystals,” *J. Phys. Chem. B*, vol. 109, no. 44, pp. 20842–20846, 2005.
- [186] E. Gongadze, U. van Rienen, V. Kralj-Iglič, and A. Iglič, “Spatial variation of permittivity of an electrolyte solution in contact with a charged metal surface: a mini review,” *Comput. Methods Biomech. Biomed. Engin.*, vol. 16, no. 5, pp. 463–480, 2013.
- [187] C. Noguera, “Polar oxide surfaces,” *J. Phys. Condens. Matter*, vol. 12, no. 31, 2000.
- [188] R. D. Gunning, C. O’Sullivan, and K. M. Ryan, “A multi-rate kinetic model for

## Bibliography

- spontaneous oriented attachment of CdS nanorods,” *Phys. Chem. Chem. Phys.*, vol. 12, no. 39, pp. 12430–12435, 2010.
- [189] W. H. Brattain and J. Bardeen, “Surface Properties of Germanium,” *Bell System Technical Journal*, vol. 32, no. 1, pp. 1–41, 1953.
- [190] T. Seiyama, A. Kato, K. Fujiishi, and M. Nagatani, “A New Detector for Gaseous Components Using Semiconductive Thin Films,” *Anal. Chem.*, vol. 34, no. 11, pp. 1502–1503, 1962.
- [191] A. Gurlo, “Interplay between O<sub>2</sub> and SnO<sub>2</sub>: Oxygen ionosorption and spectroscopic evidence for adsorbed oxygen,” *ChemPhysChem*, vol. 7, no. 10, pp. 2041–2052, 2006.
- [192] N. Barsan and U. Weimar, “Conduction model of metal oxide gas sensors,” *J. Electroceramics*, vol. 7, no. 3, pp. 143–167, 2001.
- [193] N. Yamazoe and K. Shimano, “Theory of power laws for semiconductor gas sensors,” *Sensors Actuators, B Chem.*, vol. 128, no. 2, pp. 566–573, 2008.
- [194] P. Bhattacharyya, P. K. Basu, B. Mondal, and H. Saha, “A low power MEMS gas sensor based on nanocrystalline ZnO thin films for sensing methane,” *Microelectron. Reliab.*, vol. 48, no. 11–12, pp. 1772–1779, 2008.
- [195] S. T. Shishiyanu, T. S. Shishiyanu, and O. I. Lupan, “Sensing characteristics of tin-doped ZnO thin films as NO<sub>2</sub> gas sensor,” *Sensors Actuators, B Chem.*, vol. 107, no. 1 SPEC. ISS., pp. 379–386, 2005.
- [196] T. T. Trinh, N. H. Tu, H. H. Le, *et al.*, “Improving the ethanol sensing of ZnO nanoparticle thin films - The correlation between the grain size and the sensing mechanism,” *Sensors Actuators, B Chem.*, vol. 152, no. 1, pp. 73–81, 2011.
- [197] S. Seal and S. Shukla, “Nanocrystalline SnO gas sensors in view of surface reactions and modifications,” *Jom*, vol. 54, no. 9, pp. 35–38, 2002.
- [198] N. Yamazoe, “New approaches for improving semiconductor gas sensors,” *Sensors Actuators B Chem.*, vol. 5, no. 1–4, pp. 7–19, Aug. 1991.
- [199] M. H. Seo, M. Yuasa, T. Kida, J. S. Huh, K. Shimano, and N. Yamazoe, “Gas sensing characteristics and porosity control of nanostructured films composed of TiO<sub>2</sub> nanotubes,” *Sensors Actuators, B Chem.*, vol. 137, no. 2, pp. 513–520, 2009.
- [200] K. Darcovich, F. F. Garcia, C. A. Jeffrey, J. J. Tunney, and M. L. Post, “Coupled microstructural and transport effects in n-type sensor response modeling for thin

- layers,” *Sensors Actuators, A Phys.*, vol. 147, no. 2, pp. 378–386, 2008.
- [201] S. Kim, B. S. Kang, F. Ren, *et al.*, “Sensitivity of Pt/ZnO Schottky diode characteristics to hydrogen,” *Appl. Phys. Lett.*, vol. 84, no. 10, pp. 1698–1700, 2004.
- [202] B. J. Coppa, R. F. Davis, and R. J. Nemanich, “Gold Schottky contacts on oxygen plasma-treated, n-type ZnO(0001),” *Appl. Phys. Lett.*, vol. 82, no. 3, pp. 400–402, 2003.
- [203] C. Wang, L. Yin, L. Zhang, D. Xiang, and R. Gao, “Metal oxide gas sensors: Sensitivity and influencing factors,” *Sensors*, vol. 10, no. 3, pp. 2088–2106, 2010.
- [204] I. Chorkendorff and J. . Niemantsverdriet, *Concepts of Modern Catalysis and Kinetics*. WILEY-VCH Verlag GmbH & Co. KGaA, 2003.
- [205] B. P. Luther, S. D. Wolter, and S. E. Mohny, “High temperature Pt Schottky diode gas sensors on n-type GaN,” *Sensors Actuators, B Chem.*, vol. 56, no. 1, pp. 164–168, 1999.
- [206] J. Schalwig, G. Müller, U. Karrer, *et al.*, “Hydrogen response mechanism of Pt-GaN Schottky diodes,” *Appl. Phys. Lett.*, vol. 80, no. 7, pp. 1222–1224, 2002.
- [207] P. Bhattacharyya, G. P. Mishra, and S. K. Sarkar, “The effect of surface modification and catalytic metal contact on methane sensing performance of nano-ZnO-Si heterojunction sensor,” *Microelectron. Reliab.*, vol. 51, no. 12, pp. 2185–2194, 2011.
- [208] D. R. Miller, S. A. Akbar, and P. A. Morris, “Nanoscale metal oxide-based heterojunctions for gas sensing: A review,” *Sensors Actuators, B Chem.*, vol. 204, pp. 250–272, 2014.
- [209] J. Chen, K. Wang, and W. Zhou, “Vertically Aligned ZnO Nanorod Arrays Coated with SnO<sub>2</sub> / Noble Metal Nanoparticles for Highly Sensitive and Selective Gas Detection,” vol. 10, no. 5, pp. 968–974, 2011.
- [210] T. R. Rashid, D. T. Phan, and G. S. Chung, “A flexible hydrogen sensor based on Pd nanoparticles decorated ZnO nanorods grown on polyimide tape,” *Sensors Actuators, B Chem.*, vol. 185, pp. 777–784, 2013.
- [211] H. T. Wang, B. S. Kang, F. Ren, *et al.*, “Detection of hydrogen at room temperature with catalyst-coated multiple ZnO nanorods,” *Appl. Phys. A Mater. Sci. Process.*, vol. 81, no. 6, pp. 1117–1119, 2005.
- [212] A. S. M. Iftekhar Uddin, D. T. Phan, and G. S. Chung, “Low temperature acetylene gas sensor based on Ag nanoparticles-loaded ZnO-reduced graphene oxide hybrid,”

- Sensors Actuators, B Chem.*, vol. 207, no. Part A, pp. 362–369, 2015.
- [213] E. Wongrat, N. Hongstith, D. Wongratanaphisan, A. Gardchareon, and S. Choopun, “Control of depletion layer width via amount of AuNPs for sensor response enhancement in ZnO nanostructure sensor,” *Sensors Actuators, B Chem.*, vol. 171–172, pp. 230–237, 2012.
- [214] J. Kukkola, M. Mohl, A.-R. Leino, *et al.*, “Inkjet-printed gas sensors: metal decorated WO<sub>3</sub> nanoparticles and their gas sensing properties,” *J. Mater. Chem.*, vol. 22, no. 34, p. 17878, 2012.
- [215] I. Jiménez, M. A. Centeno, R. Scotti, *et al.*, “NH<sub>3</sub> interaction with chromium-doped WO<sub>3</sub> nanocrystalline powders for gas sensing applications,” *J. Mater. Chem.*, vol. 14, no. 15, pp. 2412–2420, 2004.
- [216] F. Meng, T. Qi, J. Zhang, *et al.*, “MoS<sub>2</sub>-templated porous hollow MoO<sub>3</sub> microspheres for highly selective ammonia sensing via a Lewis acid-base interaction,” *IEEE Trans. Ind. Electron.*, vol. 0046, no. c, 2021.
- [217] S. Leonardi, “Two-Dimensional Zinc Oxide Nanostructures for Gas Sensor Applications,” *Chemosensors*, vol. 5, no. 2, p. 17, 2017.
- [218] Y. V. Kaneti, Z. Zhang, J. Yue, *et al.*, “Crystal plane-dependent gas-sensing properties of zinc oxide nanostructures: Experimental and theoretical studies,” *Phys. Chem. Chem. Phys.*, vol. 16, no. 23, pp. 11471–11480, 2014.
- [219] Y. Al-Hadeethi, A. Umar, S. H. Al-Heniti, *et al.*, “2D Sn-doped ZnO ultrathin nanosheet networks for enhanced acetone gas sensing application,” *Ceram. Int.*, vol. 43, no. 2, pp. 2418–2423, 2017.
- [220] Y. V. Kaneti, X. Zhang, M. Liu, *et al.*, “Experimental and theoretical studies of gold nanoparticle decorated zinc oxide nanoflakes with exposed {1 0 1<sup>-</sup> 0} facets for butylamine sensing,” *Sensors Actuators, B Chem.*, vol. 230, pp. 581–591, 2016.
- [221] J. Xu, Z. Xue, N. Qin, Z. Cheng, and Q. Xiang, “The crystal facet-dependent gas sensing properties of ZnO nanosheets: Experimental and computational study,” *Sensors Actuators, B Chem.*, vol. 242, pp. 148–157, 2017.
- [222] L. Zhang, J. Zhao, H. Lu, *et al.*, “Facile synthesis and ultrahigh ethanol response of hierarchically porous ZnO nanosheets,” *Sensors Actuators, B Chem.*, vol. 161, no. 1, pp. 209–215, 2012.
- [223] Y. Xiao, L. Lu, A. Zhang, *et al.*, “Highly enhanced acetone sensing performances of

- porous and single crystalline ZnO nanosheets: High percentage of exposed (100) facets working together with surface modification with pd nanoparticles,” *ACS Appl. Mater. Interfaces*, vol. 4, no. 8, pp. 3797–3804, 2012.
- [224] C. Gu, H. Huang, J. Huang, *et al.*, “Chlorobenzene sensor based on Pt-decorated porous single-crystalline ZnO nanosheets,” *Sensors Actuators, A Phys.*, vol. 252, pp. 96–103, 2016.
- [225] Z. Jing and J. Zhan, “Fabrication and gas-sensing properties of porous ZnO nanoplates,” *Adv. Mater.*, vol. 20, no. 23, pp. 4547–4551, 2008.
- [226] J. Chang, M. Z. Ahmad, W. Wlodarski, and E. R. Waclawik, “Self-assembled 3D ZnO porous structures with exposed reactive {0001} facets and their enhanced gas sensitivity,” *Sensors (Switzerland)*, vol. 13, no. 7, pp. 8445–8460, 2013.
- [227] A. Vena, E. Perret, S. Tedjini, *et al.*, “Design of chipless RFID tags printed on paper by flexography,” *IEEE Trans. Antennas Propag.*, vol. 61, no. 12, pp. 5868–5877, 2013.
- [228] D. Maddipatla, B. B. Narakathu, S. G. R. Avuthu, *et al.*, “A novel flexographic printed strain gauge on paper platform,” *2015 IEEE SENSORS - Proc.*, pp. 8–11, 2015.
- [229] A. C. Hübler, G. C. Schmidt, H. Kempa, K. Reuter, M. Hamsch, and M. Bellmann, “Three-dimensional integrated circuit using printed electronics,” *Org. Electron. physics, Mater. Appl.*, vol. 12, no. 3, pp. 419–423, 2011.
- [230] F. C. Krebs, J. Fyenbo, and M. Jørgensen, “Product integration of compact roll-to-roll processed polymer solar cell modules: methods and manufacture using flexographic printing, slot-die coating and rotary screen printing,” *J. Mater. Chem.*, vol. 20, no. 41, p. 8994, 2010.
- [231] M. Hösel, R. R. Søndergaard, M. Jørgensen, and F. C. Krebs, “Fast Inline Roll-to-Roll Printing for Indium-Tin-Oxide-Free Polymer Solar Cells Using Automatic Registration,” *Energy Technol.*, vol. 1, no. 1, pp. 102–107, 2013.
- [232] M. Frey, F. Clement, S. Dilfer, D. Erath, and D. Biro, “Front-side metalization by means of flexographic printing,” *Energy Procedia*, vol. 8, no. April, pp. 581–586, 2011.
- [233] Y. Li, L. Mao, Y. Gao, *et al.*, “ITO-free photovoltaic cell utilizing a high-resolution silver grid current collecting layer,” *Sol. Energy Mater. Sol. Cells*, vol. 113, pp. 85–

- 89, 2013.
- [234] H. Kempa, M. Hambsch, K. Reuter, *et al.*, “Complementary ring oscillator exclusively prepared by means of gravure and flexographic printing,” *IEEE Trans. Electron Devices*, vol. 58, no. 8, pp. 2765–2769, 2011.
- [235] S. Dilfer, R. C. Hoffmann, and E. Dörsam, “Characteristics of flexographic printed indium-zinc-oxide thin films as an active semiconductor layer in thin film field-effect transistors,” *Appl. Surf. Sci.*, vol. 320, pp. 634–642, 2014.
- [236] G. L. Mar, P. Y. Timbrell, and R. N. Lamb, “Factors Influencing the Chemical Vapor Deposition of Oriented ZnO Films Using Zinc Acetate,” *Chem. Mater.*, vol. 7, no. 10, pp. 1890–1896, 1995.
- [237] J. D. Berry, M. J. Neeson, R. R. Dagastine, D. Y. C. Chan, and R. F. Tabor, “Measurement of surface and interfacial tension using pendant drop tensiometry,” *J. Colloid Interface Sci.*, vol. 454, pp. 226–237, 2015.
- [238] E. Y. Bormashenko, *Wetting of Real Surfaces*. DE GRUYTER, 2013.
- [239] Accudyne, “Viscosity, Surface Tension, Specific Density and Molecular Weight of Selected Liquids (sort by surface tension descending).” [Online]. Available: [https://www.accudynetest.com/visc\\_table.html?sortby=sort\\_surface\\_tension\\_DESC](https://www.accudynetest.com/visc_table.html?sortby=sort_surface_tension_DESC). [Accessed: 01-Jun-2018].
- [240] L. K. Filippov, “Dynamic surface tension of aqueous surfactant solutions. 2. diffusion-kinetic-convective controlled adsorption,” *Journal of Colloid And Interface Science*, vol. 164, no. 2, pp. 471–482, 1994.
- [241] W. Chen, Q. Kuang, Q. Wang, and Z. Xie, “Engineering a high energy surface of anatase TiO<sub>2</sub> crystals towards enhanced performance for energy conversion and environmental applications,” *RSC Adv.*, vol. 5, no. 26, pp. 20396–20409, 2015.
- [242] S. Khandavalli and J. P. Rothstein, “Ink transfer of non-Newtonian fluids from an idealized gravure cell: The effect of shear and extensional deformation,” *J. Nonnewton. Fluid Mech.*, vol. 243, pp. 16–26, 2017.
- [243] L. Leger and J. F. Joanny, “Liquid spreading,” *Reports Prog. Phys.*, vol. 55, no. 4, pp. 431–486, Apr. 1992.
- [244] C. Redon, F. Brochard-Wyart, and F. Rondelez, “Dynamics of dewetting,” *Phys. Rev. Lett.*, vol. 66, no. 6, pp. 715–718, 1991.
- [245] R. Mai, A. Pekarovicova, P. D. Fleming, S. Savarmand, and O. V. Chandorkar, “Ink

## Bibliography

- rheology and press performance of water-based flexographic inks,” *Flexo*, vol. 32, no. 10, pp. 48–53, 2007.
- [246] Y. Nakayama, R. Boucher, and K. Izawa, *Introduction to Fluid Mechanics*, vol. 19, no. 4. Elsevier Science & Technology, 1998.
- [247] M. A. Mulla, H. N. Yow, H. Zhang, O. J. Cayre, and S. Biggs, “Colloid Particles in Ink Formulations,” *Fundam. Inkjet Print.*, pp. 141–168, 2015.
- [248] D. W. Litchfield, D. G. Baird, D. W. Litchfield, and D. G. Baird, “The Rheology of High Aspect Ratio Nano- Particle Filled Liquids,” *Rheol. Rev.*, no. November, pp. 1–60, 2006.
- [249] R. Faddoul, N. Reverdy-bruas, and A. Blayo, “Formulation and screen printing of water based conductive flake silver pastes onto green ceramic tapes for electronic applications,” vol. 177, pp. 1053–1066, 2012.
- [250] M. L. Morgan, A. Holder, D. J. Curtis, and D. Deganello, “Formulation, characterisation and flexographic printing of novel Boger fluids to assess the effects of ink elasticity on print uniformity,” *Rheol. Acta*, vol. 57, no. 2, pp. 105–112, 2018.
- [251] B. Havlínová, V. Cicák, V. Brezová, and L. Hornáková, “Water-reducible flexographic printing inks-rheological behaviour and interaction with paper substrates,” *J. Mater. Sci.*, vol. 34, no. 9, pp. 2081–2088, 1999.
- [252] S. M. Olhero and J. M. F. Ferreira, “Influence of particle size distribution on rheology and particle packing of silica-based suspensions,” *Powder Technol.*, vol. 139, no. 1, pp. 69–75, 2004.
- [253] J. Cen, R. Kitsomboonloha, and V. Subramanian, “Cell filling in gravure printing for printed electronics,” *Langmuir*, vol. 30, no. 45, pp. 13716–13726, 2014.
- [254] G. Hu, J. Kang, L. W. T. Ng, *et al.*, “Functional inks and printing of two-dimensional materials,” *Chem. Soc. Rev.*, vol. 47, no. 9, pp. 3265–3300, 2018.
- [255] C. Cano-Raya, Z. Z. Denchev, S. F. Cruz, and J. C. Viana, “Chemistry of solid metal-based inks and pastes for printed electronics – A review,” *Appl. Mater. Today*, vol. 15, pp. 416–430, 2019.
- [256] M. Bruening, J. Libman, A. Shanzer, E. Moons, D. Yaron-Marcovich, and D. Cahen, “Polar Ligand Adsorption Controls Semiconductor Surface Potentials,” *J. Am. Chem. Soc.*, vol. 116, no. 7, pp. 2972–2977, 1994.
- [257] A. Vilan, A. Shanzer, and D. Cahen, “Molecular control over Au/GaAs diodes,”

## Bibliography

- Nature*, vol. 404, no. 6774, pp. 166–168, 2000.
- [258] R. Cohen, N. Zenou, D. Cahen, and S. Yitzchaik, “Molecular electronic tuning of Si surfaces,” *Chem. Phys. Lett.*, vol. 279, no. 5–6, pp. 270–274, 1997.
- [259] D. Gal, E. Sonea, R. Cohen, *et al.*, “Engineering the interface energetics of solar cells by grafting molecular properties onto semiconductors,” *Proc. Indian Acad. Sci. Chem. Sci.*, vol. 109, no. 6, pp. 487–496, 1997.
- [260] R. Schwalm, *UV Coatings: Basics, Recent Developments and New Applications*. Emerald Group Publishing Limited, 2008.
- [261] Z. Zołek-Tryznowska, J. Izdebska, and M. Tryznowski, “Branched polyglycerols as performance additives for water-based flexographic printing inks,” *Prog. Org. Coatings*, vol. 78, pp. 334–339, 2015.
- [262] J. Cherry, “Ink Release Characteristics of Anilox Rolls,” *Welsh Cent. Print. Coat.*, vol. PhD, no. March, 2007.
- [263] RK, “FlexiProof 100 technical specifications - RK PrintCoat Instruments Ltd.” [Online]. Available: <https://www.rkprint.com/wp-content/uploads/2018/02/New-FLEXI-100-02.17.pdf>. [Accessed: 10-Jan-2021].
- [264] S. Hamblyn, “The Role of the Plate in the Ink Transfer Process in Flexographic Printing,” Swansea University, 2004.
- [265] R. Kitsomboonloha, S. J. S. Morris, X. Rong, and V. Subramanian, “Femtoliter-scale patterning by high-speed, highly scaled inverse gravure printing,” *Langmuir*, vol. 28, no. 48, pp. 16711–16723, 2012.
- [266] A. v. Chadov and E. D. Yakhnin, “Investigation of the transfer of a liquid from one solid surface to another. I. Slow transfer. Method of approximate calculation,” *Kolloidn.*, vol. 41, pp. 700–703, 1979.
- [267] D. G. Beynon, “Plate to Substrate Ink Transfer in the Flexographic Printing Process,” no. September, 2007.
- [268] D. Deganello, J. A. Cherry, D. T. Gethin, and T. C. Claypole, “Impact of metered ink volume on reel-to-reel flexographic printed conductive networks for enhanced thin film conductivity,” *Thin Solid Films*, vol. 520, no. 6, pp. 2233–2237, 2012.
- [269] D. Deganello, J. A. Cherry, D. T. Gethin, and T. C. Claypole, “Patterning of micro-scale conductive networks using reel-to-reel flexographic printing,” *Thin Solid Films*, vol. 518, no. 21, pp. 6113–6116, 2010.



- [270] D. C. Bould, T. C. Claypole, and M. F. J. Bohan, "An Investigation into Quality Improvements in Flexographic Printing," *Proc. Instn Mech. Engrs*, vol. 218, pp. 1499–1511, 2004.
- [271] D. C. Bould, S. M. Hamblyn, D. T. Gethin, and T. C. Claypole, "Effect of impression pressure and anilox specification on solid and halftone densityg," *Proc. Inst. Mech. Eng. Part B J. Eng. Manuf.*, vol. 225, no. 5, pp. 699–709, 2011.
- [272] A. A. Darhuber, S. M. Troian, and S. Wagner, "Physical mechanisms governing pattern fidelity in microscale offset printing," *J. Appl. Phys.*, vol. 90, no. 7, pp. 3602–3609, 2001.
- [273] K. Reuter, H. Kempa, N. Brandt, M. Bartzsch, and A. C. Huebler, "Influence of process parameters on the electrical properties of offset printed conductive polymer layers," *Prog. Org. Coatings*, vol. 58, no. 4, pp. 312–315, 2007.
- [274] S. E. Orchard, "On surface levelling in viscous liquids and gels," *Applied Scientific Research, Section A*, vol. 11, no. 4–6, pp. 451–464, 1963.
- [275] R. D. Deegan, O. Bakajin, T. F. Dupont, G. Huber, S. R. Nagel, and T. A. Witten, "Capillary flow as the cause of ring stains from dried liquid drops," *Nature*, vol. 389, no. 6653, pp. 827–829, 1997.
- [276] D. Soltman and V. Subramanian, "Inkjet-printed line morphologies and temperature control of the coffee ring effect," *Langmuir*, vol. 24, no. 5, pp. 2224–2231, 2008.
- [277] I. Scheideler, WJ., J. Jang, M. A. U. Karim, R. Kitsomboonloha, A. Zeumault, and V. Subramanian, "Gravure-Printed Sol-Gels on Flexible Glass: A Scalable Route to Additively Patterned Transparent Conductors," *ACS Appl. Mater. Interfaces*, vol. 7, no. 23, pp. 12679–12687, 2015.
- [278] J. A. Lim, W. H. Lee, H. S. Lee, J. H. Lee, Y. D. Park, and K. Cho, "Self-organization of ink-jet-printed triisopropylsilylethynyl pentacene via evaporation-induced flows in a drying droplet," *Adv. Funct. Mater.*, vol. 18, no. 2, pp. 229–234, 2008.
- [279] Z. Ding, R. Xing, Q. Fu, D. Ma, and Y. Han, "Patterning of pinhole free small molecular organic light-emitting films by ink-jet printing," *Org. Electron. physics, Mater. Appl.*, vol. 12, no. 4, pp. 703–709, 2011.
- [280] B. J. De Gans and U. S. Schubert, "Inkjet printing of well-defined polymer dots and arrays," *Langmuir*, vol. 20, no. 18, pp. 7789–7793, 2004.

- [281] T. Druffel, R. Dharmadasa, B. W. Lavery, and K. Ankireddy, “Intense pulsed light processing for photovoltaic manufacturing,” *Sol. Energy Mater. Sol. Cells*, vol. 174, no. September 2017, pp. 359–369, 2018.
- [282] M. Hösel and F. C. Krebs, “Large-scale roll-to-roll photonic sintering of flexo printed silver nanoparticle electrodes,” *J. Mater. Chem.*, vol. 22, no. 31, p. 15683, 2012.
- [283] D. J. Lee, S. H. Park, S. Jang, H. S. Kim, J. H. Oh, and Y. W. Song, “Pulsed light sintering characteristics of inkjet-printed nanosilver films on a polymer substrate,” *J. Micromechanics Microengineering*, vol. 21, no. 12, 2011.
- [284] J. Niittynen, R. Abbel, M. Mäntysalo, J. Perelaer, U. S. Schubert, and D. Lupo, “Alternative sintering methods compared to conventional thermal sintering for inkjet printed silver nanoparticle ink,” *Thin Solid Films*, vol. 556, pp. 452–459, 2014.
- [285] J. S. Kang, J. Ryu, H. S. Kim, and H. T. Hahn, “Sintering of inkjet-printed silver nanoparticles at room temperature using intense pulsed light,” *J. Electron. Mater.*, vol. 40, no. 11, pp. 2268–2277, 2011.
- [286] H. S. Kim, S. R. Dhage, D. E. Shim, and H. T. Hahn, “Intense pulsed light sintering of copper nanoink for printed electronics,” *Appl. Phys. A Mater. Sci. Process.*, vol. 97, no. 4, pp. 791–798, 2009.
- [287] B. Y. Wang, T. H. Yoo, Y. W. Song, D. S. Lim, and Y. J. Oh, “Cu ion ink for a flexible substrate and highly conductive patterning by intensive pulsed light sintering,” *ACS Appl. Mater. Interfaces*, vol. 5, no. 10, pp. 4113–4119, 2013.
- [288] K. Ankireddy, A. H. Ghahremani, B. Martin, G. Gupta, and T. Druffel, “Rapid thermal annealing of  $\text{CH}_3\text{NH}_3\text{PbI}_3$  perovskite thin films by intense pulsed light with aid of diiodomethane additive,” *J. Mater. Chem. A*, no. 150 C, pp. 9378–9383, 2018.
- [289] B. W. Lavery, S. Kumari, H. Konermann, G. L. Draper, J. Spurgeon, and T. Druffel, “Intense Pulsed Light Sintering of  $\text{CH}_3\text{NH}_3\text{PbI}_3$  Solar Cells,” *ACS Appl. Mater. Interfaces*, vol. 8, no. 13, pp. 8419–8426, 2016.
- [290] J. H. Lee, Y. M. Lee, S. J. Lim, D. K. Choi, and J. W. Yu, “Intense pulsed light annealed buffer layers for organic photovoltaics,” *Sol. Energy Mater. Sol. Cells*, vol. 143, pp. 517–521, 2015.
- [291] E. B. Secor, B. Y. Ahn, T. Z. Gao, J. A. Lewis, and M. C. Hersam, “Rapid and Versatile Photonic Annealing of Graphene Inks for Flexible Printed Electronics,”

- Adv. Mater.*, vol. 27, no. 42, pp. 6683–6688, 2015.
- [292] E. B. Secor, T. Z. Gao, M. H. Dos Santos, S. G. Wallace, K. W. Putz, and M. C. Hersam, “Combustion-Assisted Photonic Annealing of Printable Graphene Inks via Exothermic Binders,” *ACS Appl. Mater. Interfaces*, vol. 9, no. 35, pp. 29418–29423, 2017.
- [293] L. Pei and Y.-F. Li, “Rapid and efficient intense pulsed light reduction of graphene oxide inks for flexible printed electronics,” *RSC Adv.*, vol. 7, no. 81, pp. 51711–51720, 2017.
- [294] A. Van Dijken, E. A. Meulen Kamp, D. Vanmaekelbergh, and A. Meijerink, “The Kinetics of the Radiative and Nonradiative Processes in Nanocrystalline ZnO Particles upon Photoexcitation,” *J. Phys. Chem. B*, vol. 104, no. 8, pp. 1715–1723, 2000.
- [295] G. Montambaux, “Generalized Stefan–Boltzmann Law,” *Found. Phys.*, vol. 48, no. 4, pp. 395–410, 2018.
- [296] S. Wünscher, R. Abbel, J. Perelaer, and U. S. Schubert, “Progress of alternative sintering approaches of inkjet-printed metal inks and their application for manufacturing of flexible electronic devices,” *J. Mater. Chem. C*, vol. 2, no. 48, pp. 10232–10261, 2014.
- [297] W. Zhou, R. Apkarian, Z. L. Wang, and D. Joy, “Fundamentals of scanning electron microscopy (SEM),” *Scanning Microsc. Nanotechnol. Tech. Appl.*, pp. 1–40, 2007.
- [298] Y. Sakai, T. Yamada, T. Suzuki, and T. Ichinokawa, “Contrast mechanisms of secondary electron images in scanning electron and ion microscopy,” *Appl. Surf. Sci.*, vol. 144–145, pp. 96–100, 1999.
- [299] J. Piňos, Mikmeková, and L. Frank, “About the information depth of backscattered electron imaging,” *J. Microsc.*, vol. 266, no. 3, pp. 335–342, 2017.
- [300] L. M. Gignac, M. Kawasaki, S. H. Boettcher, and O. C. Wells, “Imaging and analysis of subsurface Cu interconnects by detecting backscattered electrons in the scanning electron microscope,” *J. Appl. Phys.*, vol. 97, no. 11, 2005.
- [301] J. Tamayo and R. García, “Deformation, contact time, and phase contrast in tapping mode scanning force microscopy,” *Langmuir*, vol. 12, no. 18, pp. 4430–4435, 1996.
- [302] R. Knoll, K. Magerle, and G. Krausch, “Tapping Mode atomic force microscopy on polymers: Where is the true sample surface?,” *Macromolecules*, vol. 34, no. 12, pp.

- 4159–4165, 2001.
- [303] D. E. Newbury and N. W. M. Ritchie, “Is scanning electron microscopy/energy dispersive X-ray spectrometry (SEM/EDS) quantitative?,” *Scanning*, vol. 35, no. 3, pp. 141–168, 2013.
- [304] N. Brodusch, K. Zaghib, and R. Gauvin, “Improvement of the energy resolution of energy dispersive spectrometers (EDS) using Richardson–Lucy deconvolution,” *Ultramicroscopy*, vol. 209, no. July 2019, p. 112886, 2020.
- [305] D. Briggs, *Surface Analysis of Polymers by XPS and Static SIMS*. Cambridge University Press, 1998.
- [306] M. C. Biesinger, L. W. M. Lau, A. R. Gerson, and R. S. C. Smart, “Resolving surface chemical states in XPS analysis of first row transition metals, oxides and hydroxides: Sc, Ti, V, Cu and Zn,” *Appl. Surf. Sci.*, vol. 257, no. 3, pp. 887–898, 2010.
- [307] D. R. Jones, V. Gomez, J. C. Bear, *et al.*, “Active removal of waste dye pollutants using Ta<sub>3</sub>N<sub>5</sub>/W<sub>18</sub>O<sub>49</sub> nanocomposite fibres,” *Sci. Rep.*, vol. 7, no. 1, pp. 1–16, 2017.
- [308] C. J. Barnett, J. Navarro-Torres, J. D. McGettrick, T. G. G. Maffei, and A. R. Barron, “Inducing upwards band bending by surface stripping ZnO nanowires with argon bombardment,” *Nanotechnology*, vol. 31, no. 50, 2020.
- [309] J. Zhang, L. Cong, H. Wan, and T. Wang, “Green-emission and n-type conductivity of ZnO:Zn films obtained using vapor deposition method,” *Appl. Surf. Sci.*, vol. 255, no. 6, pp. 3530–3533, 2009.
- [310] S. Y. Lee, Y. W. Song, and K. A. Jeon, “Synthesis and analysis of resistance-controlled Ga-doped ZnO nanowires,” *J. Cryst. Growth*, vol. 310, no. 20, pp. 4477–4480, 2008.
- [311] H. Khan, A. S. Yerramilli, A. D’Oliveira, T. L. Alford, D. C. Boffito, and G. S. Patience, “Experimental methods in chemical engineering: X-ray diffraction spectroscopy—XRD,” *Can. J. Chem. Eng.*, vol. 98, no. 6, pp. 1255–1266, 2020.
- [312] D. Kriegner, Z. Matěj, R. Kužel, and V. Holý, “Powder diffraction in bragg-brentano geometry with straight linear detectors,” *J. Appl. Crystallogr.*, vol. 48, no. 2005, pp. 613–618, 2015.
- [313] L. Zevin and K. U. Leuven, “Impact of clay particle orientation on quantitative clay diffractometry,” 1990.

## Bibliography

- [314] H. Vanderstraeten, D. Neerinck, K. Temst, Y. Bruynseraede, E. E. Fullerton, and I. K. Schuller, "Low-angle X-ray diffraction of multilayered structures," *J. Appl. Crystallogr.*, vol. 24, no. 5, pp. 571–575, Oct. 1991.
- [315] J. M. Westra, V. Vavruňková, P. Šutta, R. A. C. M. M. Van Swaaij, and M. Zeman, "Formation of thin-film crystalline silicon on glass observed by in-situ XRD," *Energy Procedia*, vol. 2, no. 1, pp. 235–241, 2010.
- [316] B. Akbari, M. Pirhadi Tavandashti and M. Zandrahimi, "Particle Size Characterization of Nanoparticles - A Practical Approach," *Cell. Mol. Neurobiol.*, vol. 8, no. 2, pp. 48–56, Apr. 2011.
- [317] S. C. Wallwork, "Introduction to the Calculation of Structure Factors," *Int. Union Crystallogr.*, p. 12, 1980.
- [318] L. B. Mccusker, R. B. Von Dreele, D. E. Cox, D. Louër, and P. Scardi, "Rietveld refinement guidelines," *J. Appl. Crystallogr.*, vol. 32, no. 1, pp. 36–50, 1999.
- [319] H. Lips, "The Study of Metals and Alloys by X-ray Powder Diffraction Methods," *Teach. Pam. Commision Crystallogr. Teach.*, no. i, pp. 1–30, 1981.
- [320] T. H. Gfroerer, "Photoluminescence in Analysis of Surfaces and Interfaces," *Encycl. Anal. Chem.*, no. February, 2006.
- [321] P. R. Jubu, F. K. Yam, V. M. Igba, and K. P. Beh, "Tauc-plot scale and extrapolation effect on bandgap estimation from UV–vis–NIR data – A case study of  $\beta$ -Ga<sub>2</sub>O<sub>3</sub>," *J. Solid State Chem.*, vol. 290, no. May, p. 121576, 2020.
- [322] G. Attard and C. Barnes, *Oxford Chemistry Primers - Surfaces*. Oxford University Press, 1998.
- [323] C. Y. Chen, J. R. D. Retamal, I. W. Wu, *et al.*, "Probing surface band bending of surface-engineered metal oxide nanowires," *ACS Nano*, vol. 6, no. 11, pp. 9366–9372, 2012.
- [324] *Axis Supra - UPS User Manual*. Kratos Analytic Ltd., 2017.
- [325] R. P. Woodward, "Surface Tension Measurements Using the Drop Shape Method," *First Ten Angstroms Inc Tech. Inf.*, pp. 1–6, 2008.
- [326] A. T. Morita, D. J. Carastan, and N. R. Demarquette, "Influence of drop volume on surface tension evaluated using the pendant drop method," *Colloid Polym. Sci.*, vol. 280, no. 9, pp. 857–864, 2002.

## Bibliography

- [327] R. Woodward, "Contact angle measurements using the drop shape method," *First Ten Angstroms Inc., Portsmouth, VA*, vol. 66, no. Lvl, pp. 1–8, 1999.
- [328] R. L. Powell, "Rotational Viscometry," in *Rheological Measurement*, Dordrecht: Springer Netherlands, 1993, pp. 247–296.
- [329] "Bohlin Gemini & CVO Rheometer user manual - Malvern Instruments," 2919.
- [330] D. C. -. Cheng, "Thixotropy," *Int. J. Cosmet. Sci.*, vol. 9, no. 4, pp. 151–191, 1987.
- [331] K. F. Riley, M. . Hobson, and S. J. Bence, *Mathematical Methods for Physics and Engineering*, 3rd ed. Cambridge University Press, 2006.
- [332] T. Matsuyama, "An application of bootstrap method for analysis of particle size distribution," *Adv. Powder Technol.*, vol. 29, no. 6, pp. 1404–1408, 2018.
- [333] "Bootstrap sampling - MATLAB bootstrp - MathWorks United Kingdom." [Online]. Available: <https://uk.mathworks.com/help/stats/bootstrp.html>. [Accessed: 26-Dec-2020].
- [334] T.-C. Hu and R. L. Taylor, "On the strong law for arrays and for the bootstrap mean and variance," *Int. J. Math. Math. Sci.*, vol. 20, no. 2, pp. 375–382, 1997.
- [335] "Use the Analysis ToolPak to perform complex data analysis - Office Support." [Online]. Available: <https://support.microsoft.com/en-us/office/use-the-analysis-toolpak-to-perform-complex-data-analysis-6c67ccf0-f4a9-487c-8dec-bdb5a2cefab6>. [Accessed: 21-Jul-2021].
- [336] M. R. Spiegel and L. J. Stephens, *Schaum's Outline of Statistics*, 5th ed. McGraw-Hill.
- [337] J. H. Hallaq, "Adjustment for bias in discriminant analysis," *Journal of the Academy of Marketing Science*, vol. 3, no. 2. pp. 172–181, 1975.
- [338] A. Krężel and W. Maret, "The biological inorganic chemistry of zinc ions," *Arch. Biochem. Biophys.*, vol. 611, pp. 3–19, 2016.
- [339] R. S. Kolat and J. E. Powell, "Acetate Complexes of the Rare Earth and Several Transition Metal Ions," *Inorg. Chem.*, vol. 1, no. 2, pp. 293–296, 1962.
- [340] L. Robles and R. Priefer, "Lactose intolerance: What your breath can tell you," *Diagnostics*, vol. 10, no. 6. p. 412, 17-Jun-2020.
- [341] M. Amieva-Balmori, E. Coss-Adame, N. S. Rao, B. M. Dávalos-Pantoja, and S. S. C. Rao, "Diagnostic Utility of Carbohydrate Breath Tests for SIBO, Fructose, and

## Bibliography

- Lactose Intolerance,” *Dig. Dis. Sci.*, vol. 65, no. 5, pp. 1405–1413, 2020.
- [342] L. F. J. Piper, A. R. H. Preston, A. Fedorov, S. W. Cho, A. Demasi, and K. E. Smith, “Direct evidence of metallicity at ZnO (000  $\Gamma$ ) - (1 $\times$ 1) surfaces from angle-resolved photoemission spectroscopy,” *Phys. Rev. B - Condens. Matter Mater. Phys.*, vol. 81, no. 23, pp. 1–5, 2010.
- [343] K. Ozawa and K. Mase, “Angle-resolved photoelectron spectroscopy study of hydrogen adsorption on ZnO( $\overline{100}$ ),” *Phys. status solidi*, vol. 207, no. 2, pp. 277–281, Feb. 2010.
- [344] T. Li, M. Wang, X. Liu, M. Jin, and F. Huang, “Hydrogen Impurities in ZnO: Shallow Donors in ZnO Semiconductors and Active Sites for Hydrogenation of Carbon Species,” *J. Phys. Chem. Lett.*, vol. 11, no. 7, pp. 2402–2407, 2020.
- [345] S. N. Das, J. P. Kar, J. H. Choi, T. Lee, K. J. Moon, and J. M. Myoung, “Fabrication and characterization of ZnO single nanowire-based hydrogen sensor,” *J. Phys. Chem. C*, vol. 114, no. 3, pp. 1689–1693, 2010.
- [346] O. Lupan, G. Chai, and L. Chow, “Fabrication of ZnO nanorod-based hydrogen gas nanosensor,” *Microelectronics Journal*, vol. 38, no. 12, pp. 1211–1216, 2007.
- [347] N. M. Vuong, D. Kim, and H. Kim, “Surface gas sensing kinetics of a WO<sub>3</sub> nanowire sensor: Part 2 - Reducing gases,” *Sensors and Actuators, B: Chemical*, vol. 224, pp. 425–433, 2016.
- [348] S. Suresh, K. M. B. Urs, A. T. Vasudevan, S. Sriram, and V. B. Kamble, “Analysis of Unusual and Instantaneous Overshoot of Response Transients in Gas Sensors,” *Phys. Status Solidi - Rapid Res. Lett.*, vol. 13, no. 6, pp. 1–7, 2019.
- [349] D. Enko, E. Rezanka, R. Stolba, and G. Halwachs-baumann, “Lactose Malabsorption Testing in Daily Clinical Practice: A Critical Retrospective Analysis and Comparison of the Hydrogen / Methane Breath Test and Genetic Test ( C / T – 13910 Polymorphism ) Results,” vol. 2014, 2014.
- [350] A. Materna, C. Wermelinger, and J. Schuler, “Alimentary Pharmacology and Therapeutics Fructose and lactose intolerance and malabsorption testing: the relationship with symptoms in functional gastrointestinal disorders,” pp. 1074–1083, 2013.
- [351] A. Erdogan, S. S. C. Rao, D. Gulley, C. Jacobs, and Y. Y. Lee, “Small intestinal bacterial overgrowth: duodenal aspiration vs glucose breath test,” pp. 481–489,

2015.

- [352] P. Vernia, M. Di Camillo, V. Marinaro, and R. Caprilli, "Effect of predominant methanogenic flora on the outcome of lactose breath test in irritable bowel syndrome patients," *Eur. J. Clin. Nutr.*, vol. 57, no. 9, pp. 1116–1119, 2003.
- [353] S. Hazardous and H. Regulations, "EH40 / 2005 Workplace exposure limits limits for use with the Control of Substances," vol. 2002, 2020.
- [354] W. H.O. Working Group Bonn 3-6 November 2009, *WHO guidelines for indoor air quality: Selected pollutants*. World Health Organisation - Regional office for Europe, 2010.
- [355] L. Hamilton, *Breath tests and gastroenterology*, 2nd ed. QuinTron Instrument Company, 1998.
- [356] N. Barsan, M. Schweizer-Berberich, and W. Göpel†, "Fundamental and practical aspects in the design of nanoscaled SnO<sub>2</sub> gas sensors: a status report," *Fresenius J. Anal. Chem.*, vol. 365, no. 4, pp. 287–304, 1999.
- [357] Y. Shen, T. Yamazaki, Z. Liu, D. Meng, and T. Kikuta, "Hydrogen sensors made of undoped and Pt-doped SnO<sub>2</sub> nanowires," *Journal of Alloys and Compounds*, vol. 488, no. 1. 2009.
- [358] J. Gong, J. Sun, and Q. Chen, "Micromachined sol-gel carbon nanotube/SnO<sub>2</sub> nanocomposite hydrogen sensor," *Sensors Actuators, B Chem.*, vol. 130, no. 2, pp. 829–835, Mar. 2008.
- [359] L. MARTIN, "Electrochemical hydrogen sensor for safety monitoring," *Solid State Ionics*, vol. 175, no. 1–4, pp. 527–530, Nov. 2004.
- [360] S. K. Hazra and S. Basu, "Hydrogen sensitivity of ZnO p–n homojunctions," *Sensors Actuators B Chem.*, vol. 117, no. 1, pp. 177–182, Sep. 2006.
- [361] D. Barreca, D. Bekermann, E. Comini, *et al.*, "1D ZnO nano-assemblies by Plasma-CVD as chemical sensors for flammable and toxic gases," *Sensors Actuators B Chem.*, vol. 149, no. 1, pp. 1–7, Aug. 2010.
- [362] N. H. Al-Hardan, M. J. Abdullah, and A. A. Aziz, "Sensing mechanism of hydrogen gas sensor based on RF-sputtered ZnO thin films," *Int. J. Hydrogen Energy*, vol. 35, no. 9, pp. 4428–4434, 2010.
- [363] Y. Liu, C. Gao, X. Pan, *et al.*, "Synthesis and H<sub>2</sub> sensing properties of aligned ZnO nanotubes," *Appl. Surf. Sci.*, vol. 257, no. 6, pp. 2264–2268, Jan. 2011.



## Bibliography

- [364] A. Qurashi, N. Tabet, M. Faiz, and T. Yamzaki, "Ultra-fast microwave synthesis of ZnO nanowires and their dynamic response toward hydrogen gas," *Nanoscale Res. Lett.*, vol. 4, no. 8, pp. 948–954, 2009.
- [365] D. G. Rickerby, M. C. Horrillo, J. P. Santos, and P. Serrini, "Microstructural characterization of nanograin tin oxide gas sensors," *Nanostructured Materials*, vol. 9, no. 1–8, pp. 43–52, 1997.
- [366] C. Li, Z. Du, H. Yu, and T. Wang, "Low-temperature sensing and high sensitivity of ZnO nanoneedles due to small size effect," *Thin Solid Films*, vol. 517, no. 20, pp. 5931–5934, Aug. 2009.
- [367] S. G. Ansari, P. Boroojerdian, S. R. Sainkar, R. N. Karekar, R. C. Aiyer, and S. K. Kulkarni, "Grain size effects on H<sub>2</sub> gas sensitivity of thick film resistor using SnO<sub>2</sub> nanoparticles," *Thin Solid Films*, vol. 295, no. 1–2, pp. 271–276, 1997.
- [368] B. Chwierothe, B. R. Patton, and Y. Wang, "Conduction and Gas–Surface Reaction Modeling in Metal Oxide Gas Sensors," *J. Electroceramics*, vol. 6, no. 1, pp. 27–41, 2001.
- [369] R. Khan, H. W. Ra, J. T. Kim, W. S. Jang, D. Sharma, and Y. H. Im, "Nanofunction effects in multiple ZnO nanowire gas sensor," *Sensors and Actuators, B: Chemical*, vol. 150, no. 1, pp. 389–393, 2010.
- [370] S. Mubeen, T. Zhang, B. Yoo, M. A. Deshusses, and N. V. Myung, "Palladium nanoparticles decorated single-walled carbon nanotube hydrogen sensor," *J. Phys. Chem. C*, vol. 111, no. 17, pp. 6321–6327, 2007.
- [371] H. J. Cho, V. T. Chen, S. Qiao, W. T. Koo, R. M. Penner, and I. D. Kim, "Pt-Functionalized PdO Nanowires for Room Temperature Hydrogen Gas Sensors," *ACS Sensors*, vol. 3, no. 10, pp. 2152–2158, 2018.
- [372] C. Lee and W. C. Liu, "A high-performance Pd nanoparticle (NP)/WO<sub>3</sub> thin-film-based hydrogen sensor," *IEEE Electron Device Lett.*, vol. 40, no. 7, pp. 1194–1197, Jul. 2019.
- [373] B. Y. Ke and W. C. Liu, "Enhancement of Hydrogen Sensing Performance of a Pd Nanoparticle/Pd Film/GaOx/GaN-Based Metal-Oxide- Semiconductor Diode," *IEEE Trans. Electron Devices*, vol. 65, no. 10, pp. 4577–4584, Oct. 2018.
- [374] J. Moon, H. P. Hedman, M. Kemell, A. Tuominen, and R. Punkkinen, "Hydrogen sensor of Pd-decorated tubular TiO<sub>2</sub> layer prepared by anodization with patterned

- electrodes on SiO<sub>2</sub>/Si substrate,” *Sensors Actuators, B Chem.*, vol. 222, pp. 190–197, 2016.
- [375] Z. Zhang, C. Yin, L. Yang, J. Jiang, and Y. Guo, “Optimizing the gas sensing characteristics of Co-doped SnO<sub>2</sub> thin film based hydrogen sensor,” *J. Alloys Compd.*, vol. 785, pp. 819–825, 2019.
- [376] Z. Li, S. Yan, Z. Wu, *et al.*, “Hydrogen gas sensor based on mesoporous In<sub>2</sub>O<sub>3</sub> with fast response/recovery and ppb level detection limit,” *Int. J. Hydrogen Energy*, vol. 43, no. 50, pp. 22746–22755, Dec. 2018.
- [377] L. Chen, X. He, Y. Liang, Y. Sun, Z. Zhao, and J. Hu, “Synthesis and gas sensing properties of palladium-doped indium oxide microstructures for enhanced hydrogen detection,” *Journal of Materials Science: Materials in Electronics*, vol. 27, no. 11, pp. 11331–11338, 2016.
- [378] C. Rama Krishna, S. Y. Oh, and Y. T. Yu, “Enhanced H<sub>2</sub> gas sensing properties of Au@In<sub>2</sub>O<sub>3</sub> core-shell hybrid metal-semiconductor heteronanostructures,” *CrystEngComm*, vol. 18, no. 20, pp. 3655–3666, 2016.
- [379] O. Lupan, V. Postica, N. Wolff, *et al.*, “Low-Temperature Solution Synthesis of Au-Modified ZnO Nanowires for Highly Efficient Hydrogen Nanosensors,” *ACS Appl. Mater. Interfaces*, vol. 11, no. 35, pp. 32115–32126, Sep. 2019.
- [380] Q. Xiang, G. F. Meng, H. B. Zhao, *et al.*, “Au nanoparticle modified WO<sub>3</sub> nanorods with their enhanced properties for photocatalysis and gas sensing,” *Journal of Physical Chemistry C*, vol. 114, no. 5, pp. 2049–2055, 2010.
- [381] S. Vallejos, P. Umek, T. Stoycheva, *et al.*, “Single-step deposition of au- and pt-nanoparticle-functionalized tungsten oxide nanoneedles synthesized via aerosol-assisted CVD, and used for fabrication of selective gas microsensor arrays,” *Adv. Funct. Mater.*, vol. 23, no. 10, pp. 1313–1322, 2013.
- [382] C. Zhang, A. Boudiba, C. Navio, *et al.*, “Highly sensitive hydrogen sensors based on co-sputtered platinum-activated tungsten oxide films,” *Int. J. Hydrogen Energy*, vol. 36, no. 1, pp. 1107–1114, 2011.
- [383] N. Van Toan, N. Viet Chien, N. Van Duy, *et al.*, “Fabrication of highly sensitive and selective H<sub>2</sub> gas sensor based on SnO<sub>2</sub> thin film sensitized with micro-sized Pd islands,” *J. Hazard. Mater.*, vol. 301, pp. 433–442, 2016.
- [384] F. Fan, J. Zhang, J. Li, *et al.*, “Hydrogen sensing properties of Pt-Au bimetallic

## Bibliography

- nanoparticles loaded on ZnO nanorods,” *Sensors Actuators, B Chem.*, vol. 241, pp. 895–903, 2017.
- [385] A. R. Lewis, J. Náhlík, D. R. Jones, and T. G. G. Maffei, “Highly Sensitive Hydrogen Gas Sensors Based on Gold Nanoparticle Decorated Zinc Oxide Nanosheets,” *Procedia Eng.*, vol. 168, no. 1792, pp. 321–324, 2016.
- [386] C. Machingauta, “Synthesis, Characterization and Application of Two-Dimensional Layered Metal Hydroxides for Environmental Remediation Purposes,” 2013.
- [387] J. Chung, J. Lee, J. K. Kim, *et al.*, “An analytical method to characterize the crystal structure of layered double hydroxides: synthesis, characterization, and electrochemical studies of zinc-based LDH nanoplates,” *J. Mater. Chem. A*, vol. 8, no. 17, pp. 8692–8699, 2020.
- [388] Institute for Health and Consumer Protection. Joint Research European Commission, “Sodium Hydroxide - Summary Risk Assessment Report,” 2008.
- [389] J. Demel, P. Kubát, I. Jirka, P. Kovář, M. Pospíšil, and K. Lang, “Inorganic–Organic Hybrid Materials: Layered Zinc Hydroxide Salts with Intercalated Porphyrin Sensitizers,” *J. Phys. Chem. C*, vol. 114, no. 39, pp. 16321–16328, Oct. 2010.
- [390] S. P. Newman and W. Jones, “Comparative Study of Some Layered Hydroxide Salts Containing Exchangeable Interlayer Anions,” *J. Solid State Chem.*, vol. 148, no. 1, pp. 26–40, 1999.
- [391] C. Jaubertie, M. J. Holgado, M. S. San Román, and V. Rives, “Structural Characterization and Delamination of Lactate-Intercalated Zn,Al-Layered Double Hydroxides,” *Chem. Mater.*, vol. 18, no. 13, pp. 3114–3121, Jun. 2006.
- [392] X. Peng, J. Wickham, and A. P. Alivisatos, “Kinetics of II-VI and III-V Colloidal Semiconductor Nanocrystal Growth: ‘Focusing’ of Size Distributions,” *J. Am. Chem. Soc.*, vol. 120, no. 21, pp. 5343–5344, Jun. 1998.
- [393] R. A. Reichle, K. G. McCurdy, and L. G. Hepler, “Zinc Hydroxide: Solubility Product and Hydroxy-complex Stability Constants from 12.5–75 °C,” *Can. J. Chem.*, vol. 53, no. 24, pp. 3841–3845, 1975.
- [394] D. Kashchiev and G. M. van Rosmalen, “Review: Nucleation in solutions revisited,” *Cryst. Res. Technol.*, vol. 38, no. 78, pp. 555–574, 2003.
- [395] D. Liu, D. Weng, and J. Wang, “Collection of nanoparticles at the air-liquid interface by surface tension gradients,” *Colloids Interface Sci. Commun.*, vol. 33, no. August,

- p. 100205, 2019.
- [396] P. G. Koutsoukos, A. N. Kofina, and D. G. Kanellopoulou, "Solubility of salts in water: Key issue for crystal growth and dissolution processes," *Pure Appl. Chem.*, vol. 79, no. 5, pp. 825–850, 2007.
- [397] D. J. Bursleson and R. L. Penn, "Two-step growth of goethite from ferrihydrite," *Langmuir*, vol. 22, no. 1, pp. 402–409, 2006.
- [398] G. Kumar and A. K. Sharma, "On processing strategy to minimize defects while drilling borosilicate glass with microwave energy," *Int. J. Adv. Manuf. Technol.*, vol. 108, no. 11–12, pp. 3517–3536, 2020.
- [399] Z. Jingwei, Z. Pengli, L. Zhiwei, C. Jianmin, W. Zhishen, and Z. Zhijun, "Fabrication of polycrystalline tubular ZnO via a modified ultrasonically assisted two-step polyol process and characterization of the nanotubes," *Nanotechnology*, vol. 19, no. 16, 2008.
- [400] T. Biswick, W. Jones, A. Pacuła, E. Serwicka, and J. Podobinski, "Evidence for the formation of anhydrous zinc acetate and acetic anhydride during the thermal degradation of zinc hydroxy acetate,  $Zn_5(OH)_8(CH_3CO_2)_2 \cdot 4H_2O$  to ZnO," *Solid State Sci.*, vol. 11, no. 2, pp. 330–335, 2009.
- [401] S. García-García, S. Wold, and M. Jonsson, "Effects of temperature on the stability of colloidal montmorillonite particles at different pH and ionic strength," *Appl. Clay Sci.*, vol. 43, no. 1, pp. 21–26, 2009.
- [402] T. J. Jacobsson and T. Edvinsson, "Absorption and fluorescence spectroscopy of growing ZnO quantum dots: Size and band gap correlation and evidence of mobile trap states," *Inorg. Chem.*, vol. 50, no. 19, pp. 9578–9586, 2011.
- [403] X. Chen, X. Song, W. Qiao, *et al.*, "Solvent-directed and anion-modulated self-assemblies of nanoparticles: a case of ZnO," *CrystEngComm*, vol. 18, no. 47, pp. 9139–9151, 2016.
- [404] H. Wang, J. Varghese, and L. Pilon, "Simulation of electric double layer capacitors with mesoporous electrodes: Effects of morphology and electrolyte permittivity," *Electrochim. Acta*, vol. 56, no. 17, pp. 6189–6197, 2011.
- [405] E. Cauët, S. Bogatko, J. H. Weare, J. L. Fulton, G. K. Schenter, and E. J. Bylaska, "Structure and dynamics of the hydration shells of the  $Zn^{2+}$  ion from ab initio molecular dynamics and combined ab initio and classical molecular dynamics

- simulations,” *J. Chem. Phys.*, vol. 132, no. 19, 2010.
- [406] J. A. Vega, C. Chartier, and W. E. Mustain, “Effect of hydroxide and carbonate alkaline media on anion exchange membranes,” *J. Power Sources*, vol. 195, no. 21, pp. 7176–7180, 2010.
- [407] T. Santos, L. Costa, and M. Valente, “3D electromagnetic field simulation in microwave ovens: a tool to control thermal runaway,” *Proc. COMSOL Conf. 2010 Paris*, pp. 3–7, 2010.
- [408] A. González, A. Ramos, N. G. Green, A. Castellanos, and H. Morgan, “Fluid flow induced by nonuniform ac electric fields in electrolytes on microelectrodes. II. A linear double-layer analysis,” *Phys. Rev. E - Stat. Physics, Plasmas, Fluids, Relat. Interdiscip. Top.*, vol. 61, no. 4, pp. 4019–4028, 2000.
- [409] O. C. Wilson, T. Olorunyolemi, A. Jaworski, *et al.*, “Surface and interfacial properties of polymer-intercalated layered double hydroxide nanocomposites,” *Appl. Clay Sci.*, vol. 15, no. 1–2, pp. 265–279, 1999.
- [410] P. Woolston and J. S. van Duijneveldt, “Isotropic-nematic phase transition in aqueous sepiolite suspensions,” *J. Colloid Interface Sci.*, vol. 437, no. September, pp. 65–70, 2015.
- [411] R. Lee Penn, K. Tanaka, and J. Erbs, “Size dependent kinetics of oriented aggregation,” *J. Cryst. Growth*, vol. 309, no. 1, pp. 97–102, 2007.
- [412] K. A. Jackson, *Kinetic Processes*. Wiley, 2004.
- [413] R. Sathiyarayanan, M. Alimohammadi, Y. Zhou, and K. A. Fichthorn, “Role of solvent in the shape-controlled synthesis of anisotropic colloidal nanostructures,” *J. Phys. Chem. C*, vol. 115, no. 39, pp. 18983–18990, 2011.
- [414] M. J. Clifford and S. M. Cox, “Smart baffle placement for chaotic mixing,” *Nonlinear Dyn.*, vol. 43, no. 1–2, pp. 117–126, 2006.
- [415] Y. Sano and H. Cusui, “Effects of paddle dimensions and baffle conditions on the interrelations among discharge flow rate, mixing power and mixing time in mixing vessels,” *J. Chem. Eng. Japan*, vol. 20, no. 4, pp. 399–404, 1987.
- [416] A. Moezzi, M. Cortie, C. A. Dowd, and A. Mcdonagh, “Supporting Information .,” pp. 1–11.
- [417] V. Mote, Y. Purushotham, and B. Dole, “Williamson-Hall analysis in estimation of lattice strain in nanometer-sized ZnO particles,” *J. Theor. Appl. Phys.*, vol. 6, no. 1,

- pp. 2–9, 2012.
- [418] F. Demoisson, R. Piolet, and F. Bernard, “Hydrothermal synthesis of ZnO crystals from Zn(OH)<sub>2</sub> metastable phases at room to supercritical conditions,” *Cryst. Growth Des.*, vol. 14, no. 11, pp. 5388–5396, 2014.
- [419] P. Bindu and S. Thomas, “Estimation of lattice strain in ZnO nanoparticles: X-ray peak profile analysis,” *J. Theor. Appl. Phys.*, vol. 8, no. 4, pp. 123–134, 2014.
- [420] J. S. I. Kwon, M. Nayhouse, G. Orkoulas, and P. D. Christofides, “Enhancing the crystal production rate and reducing polydispersity in continuous protein crystallization,” *Ind. Eng. Chem. Res.*, vol. 53, no. 40, pp. 15538–15548, 2014.
- [421] P. F. Liu and Y. F. Zhang, “Nucleation and Structure of Supersaturated Sodium Zincate Solution,” *Ind. Eng. Chem. Res.*, vol. 58, no. 47, pp. 21187–21193, 2019.
- [422] R. A. Reichle, K. G. McCurdy, and L. G. Hepler, “Zinc Hydroxide: Solubility Product and Hydroxy-complex Stability Constants from 12.5–75 °C,” *Can. J. Chem.*, vol. 53, no. 24, pp. 3841–3845, 1975.
- [423] L. Hiltunen, M. Leskelä, M. Mäkelä, L. Niinistö, and L. Niinistö, “Crystal Structure of mu<sub>4</sub>-Oxo-hexakis(mu-acetato)tetrazinc and Thermal Studies of its Precursor, Zinc Acetate Dihydrate,” *Acta Chem. Scand.*, vol. 41a, pp. 548–555, 1987.
- [424] T. Biswick, W. Jones, A. Pacuła, E. Serwicka, and J. Podobinski, “The role of anhydrous zinc nitrate in the thermal decomposition of the zinc hydroxy nitrates Zn<sub>5</sub>(OH)<sub>8</sub>(NO<sub>3</sub>)<sub>2</sub>·2H<sub>2</sub>O and ZnOHNO<sub>3</sub>·H<sub>2</sub>O,” *J. Solid State Chem.*, vol. 180, no. 4, pp. 1171–1179, 2007.
- [425] T. Threlfall, “Structural and Thermodynamic Explanations of Ostwald’s Rule,” *Org. Process Res. Dev.*, vol. 7, no. 6, pp. 1017–1027, 2003.
- [426] R. A. Van Santen, “The Ostwald step rule,” *J. Phys. Chem.*, vol. 88, no. 24, pp. 5768–5769, 1984.
- [427] L. N. Hutfluss and P. V. Radovanovic, “Controlling the mechanism of phase transformation of colloidal In<sub>2</sub>O<sub>3</sub> nanocrystals,” *J. Am. Chem. Soc.*, vol. 137, no. 3, pp. 1101–1108, 2015.
- [428] B. Xie, T. J. Halter, B. M. Borah, and G. H. Nancollas, “Tracking amorphous precursor formation and transformation during induction stages of nucleation,” *Cryst. Growth Des.*, vol. 14, no. 4, pp. 1659–1665, 2014.
- [429] M. He, Y. Wang, and E. Forssberg, “Slurry rheology in wet ultrafine grinding of

- industrial minerals: A review,” *Powder Technol.*, vol. 147, no. 1–3, pp. 94–112, 2004.
- [430] J. F. Boyle, I. Manas-Zloczower, and D. L. Feke, “Hydrodynamic analysis of the mechanisms of agglomerate dispersion,” *Powder Technol.*, vol. 153, no. 2, pp. 127–133, 2005.
- [431] S. I. A. Shah, L. W. Kostiuk, and S. M. Kresta, “The effects of mixing, reaction rates, and stoichiometry on yield for mixing sensitive reactions - Part I: Model development,” *Int. J. Chem. Eng.*, vol. 2012, 2012.
- [432] N. Barsan, D. Koziej, and U. Weimar, “Metal oxide-based gas sensor research: How to?,” *Sensors Actuators, B Chem.*, vol. 121, no. 1, pp. 18–35, 2007.
- [433] M. A. Han, H. J. Kim, H. C. Lee, J. S. Park, and H. N. Lee, “Effects of porosity and particle size on the gas sensing properties of SnO<sub>2</sub> films,” *Appl. Surf. Sci.*, vol. 481, no. March, pp. 133–137, 2019.
- [434] P. F. Luckham and M. A. Ukeje, “Effect of particle size distribution on the rheology of dispersed systems,” *J. Colloid Interface Sci.*, vol. 220, no. 2, pp. 347–356, 1999.
- [435] O. B. Adeyinka, S. Samiei, Z. Xu, and J. H. Masliyah, “Effect of particle size on the rheology of athabasca clay suspensions,” *Can. J. Chem. Eng.*, vol. 87, no. 3, pp. 422–434, 2009.
- [436] Sun Chemicals, “Flexographic | Ink Troubleshooting App.” [Online]. Available: <http://inktsa.sunchemical.com/flexographic/>. [Accessed: 31-Jul-2018].
- [437] Sun Chemical, “Troubleshooting Guide Flexographic Inks.” Sun Chemical.
- [438] E. Bohlin, M. Lestelius, and C. Johansson, “Flexographic ink-coating interactions - Effects of porous structure variations of coated paperboard,” *Nord. Pulp Pap. Res. J.*, vol. 28, no. 4, pp. 573–581, 2013.
- [439] M. Rivallin, M. Benmami, A. Kanaev, and A. Gaunand, “Sol-gel reactor with rapid micromixing modelling and measurements of titanium oxide nano-particle growth,” *Chem. Eng. Res. Des.*, vol. 83, no. 1 A, pp. 67–74, 2005.
- [440] K. He, W. Han, and K. L. Yeung, “Preparation and performance of catalytic MOFs in microreactor,” *J. Taiwan Inst. Chem. Eng.*, vol. 98, pp. 85–93, 2019.
- [441] B. Zhao, Y. Ren, D. Gao, L. Xu, and Y. Zhang, “Heat transfer methodology of microreactor based on Bandelet finite element method,” *Int. J. Heat Mass Transf.*, vol. 132, pp. 715–722, 2019.

- [442] J. R. Burns and C. Ramshaw, "Development of a microreactor for chemical production," *Chem. Eng. Res. Des.*, vol. 77, no. 3, pp. 206–211, 1999.
- [443] Y. Chen, S. Wang, F. Pan, and J. Zhang, "A numerical study on electrical percolation of polymer-matrix composites with hybrid fillers of carbon nanotubes and carbon black," *J. Nanomater.*, vol. 2014, 2014.
- [444] X. Ni, C. Hui, N. Su, W. Jiang, and F. Liu, "Monte Carlo simulations of electrical percolation in multicomponent thin films with nanofillers," *Nanotechnology*, vol. 29, no. 7, 2018.
- [445] L. Yue, G. Pircheraghi, S. A. Monemian, and I. Manas-Zloczower, "Epoxy composites with carbon nanotubes and graphene nanoplatelets - Dispersion and synergy effects," *Carbon N. Y.*, vol. 78, pp. 268–278, 2014.
- [446] M. Niederberger, "Multiscale Nanoparticle Assembly: From Particulate Precise Manufacturing to Colloidal Processing," *Adv. Funct. Mater.*, vol. 27, no. 47, pp. 1–18, 2017.
- [447] S. Barwich, J. Medeiros de Araújo, A. Rafferty, C. Gomes da Rocha, M. S. Ferreira, and J. N. Coleman, "On the relationship between morphology and conductivity in nanosheet networks," *Carbon N. Y.*, vol. 171, pp. 306–319, 2021.
- [448] D. Choi, S. Lee, S. Kim, *et al.*, "Dependence of adhesion and friction on porosity in porous anodic alumina films," *Scr. Mater.*, vol. 58, no. 10, pp. 870–873, 2008.
- [449] M. C. Li, Q. Wu, K. Song, S. Lee, Y. Qing, and Y. Wu, "Cellulose Nanoparticles: Structure-Morphology-Rheology Relationships," *ACS Sustain. Chem. Eng.*, vol. 3, no. 5, pp. 821–832, 2015.
- [450] F. Ye, Y. Peng, C. Guang-Yi, B. Deng, and X. An-Wu, "Facile solution synthesis and characterization of ZnO mesocrystals and ultralong nanowires from layered basic zinc salt precursor," *J. Phys. Chem. C*, vol. 113, no. 24, pp. 10407–10415, 2009.
- [451] H. Bönemann and K. S. Nagabhushana, "Chapter 2: Metal Nanoclusters: Synthesis and Strategies for their Size Control," in *Metal Nanoclusters in Catalysis and Materials Science – The Issue of Size Control*, 1st ed., no. November 2007, B. Corain, G. Schmid, and N. Toshima, Eds. Elsevier B.V., 2008.
- [452] N. E. Chayen, "Methods for separating nucleation and growth in protein crystallisation," *Prog. Biophys. Mol. Biol.*, vol. 88, no. 3, pp. 329–337, 2005.
- [453] A. Janssen, Y. Shi, and Y. Xia, "Separating Growth from Nucleation for Facile



- Control over the Size and Shape of Palladium Nanocrystals,” *Chem. - A Eur. J.*, vol. 26, no. 61, pp. 13890–13895, 2020.
- [454] S. D. Carnevale, J. Yang, P. J. Phillips, M. J. Mills, and R. C. Myers, “Three-dimensional GaN/AlN nanowire heterostructures by separating nucleation and growth processes,” *Nano Lett.*, vol. 11, no. 2, pp. 866–871, 2011.
- [455] D. Zhang, X. Liu, H. Wan, *et al.*, “Large-Scale Preparation, Chemical Exfoliation, and Structural Modification of Layered Zinc Hydroxide Nanocones: Transformation into Zinc Oxide Nanocones for Enhanced Photocatalytic Properties,” *ACS Sustain. Chem. Eng.*, vol. 5, no. 7, pp. 5869–5879, 2017.
- [456] J. He, J. Hu, X. Mo, *et al.*, “Novel photocatalyst nitrogen-doped simonkolleite  $Zn_5(OH)_8Cl_2 \cdot H_2O$  with vis-up-conversion photoluminescence and effective visible-light photocatalysis,” *Appl. Phys. A Mater. Sci. Process.*, vol. 125, no. 1, pp. 1–9, 2019.
- [457] H. Chen, L. Zhu, H. Liu, and W. Li, “ $Zn_5(OH)_8Cl_2 \cdot H_2O$ -based quantum dots-sensitized solar cells: A common corrosion product enhances the performance of photoelectrochemical cells,” *Electrochim. Acta*, vol. 105, pp. 289–298, 2013.
- [458] E. Hosono, S. Fujihara, I. Honma, and H. Zhou, “The fabrication of an upright-standing zinc oxide nanosheet for use in dye-sensitized solar cells,” *Adv. Mater.*, vol. 17, no. 17, pp. 2091–2094, 2005.
- [459] J. H. Yang, Y. S. Han, M. Park, T. Park, S. J. Hwang, and J. H. Choy, “New inorganic-based drug delivery system of indole-3-acetic acid-layered metal hydroxide nanohybrids with controlled release rate,” *Chem. Mater.*, vol. 19, no. 10, pp. 2679–2685, 2007.
- [460] J. Gong, Q. Chen, W. Fei, and S. Seal, “Micromachined nanocrystalline SnO<sub>2</sub> chemical gas sensors for electronic nose,” *Sensors Actuators, B Chem.*, vol. 102, no. 1, pp. 117–125, 2004.
- [461] M. Karimi, J. Saydi, M. Mahmoodi, *et al.*, “A comparative study on ethanol gas sensing properties of ZnO and Zn<sub>0.94</sub>Cd<sub>0.06</sub>O nanoparticles,” *J. Phys. Chem. Solids*, vol. 74, no. 10, pp. 1392–1398, 2013.
- [462] J. K. Srivastava, P. Pandey, V. N. Mishra, and R. Dwivedi, “Sensing mechanism of Pd-doped SnO<sub>2</sub> sensor for LPG detection,” *Solid State Sci.*, vol. 11, no. 9, pp. 1602–1605, 2009.

## Bibliography

- [463] I. D. Kim, A. Rothschild, B. H. Lee, D. Y. Kim, S. M. Jo, and H. L. Tuller, "Ultrasensitive chemiresistors based on electrospun TiO<sub>2</sub> nanofibers," *Nano Lett.*, vol. 6, no. 9, pp. 2009–2013, 2006.
- [464] A. Forleo, L. Francioso, S. Capone, P. Siciliano, P. Lommens, and Z. Hens, "Synthesis and gas sensing properties of ZnO quantum dots," *Sensors Actuators, B Chem.*, vol. 146, no. 1, pp. 111–115, 2010.
- [465] J. Courbat, D. Briand, L. Yue, S. Raible, and N. F. De Rooij, "Drop-coated metal-oxide gas sensor on polyimide foil with reduced power consumption for wireless applications," *Sensors Actuators, B Chem.*, vol. 161, no. 1, pp. 862–868, 2012.
- [466] Y. Fang, J. G. D. Hester, W. Su, J. H. Chow, S. K. Sitaraman, and M. M. Tentzeris, "A bio-enabled maximally mild layer-by-layer Kapton surface modification approach for the fabrication of all-inkjet-printed flexible electronic devices," *Nat. Publ. Gr.*, no. December, pp. 1–9, 2016.
- [467] K. Crowley, A. Morrin, A. Hernandez, *et al.*, "Talanta Fabrication of an ammonia gas sensor using inkjet-printed polyaniline nanoparticles," vol. 77, pp. 710–717, 2008.
- [468] M. Baucio, *ASM engineered materials reference book*, 2nd ed. ASM International, 1994.
- [469] DuPont, "DuPont Kapton HN Technical Data Sheet," vol. 5213, pp. 1–4, 2011.
- [470] "Alumina 135x25x0.5mm x 5 - PI-KEM." [Online]. Available: <https://www.pi-kem.co.uk/shop/product/alumina-135x25x05mm-x-5>. [Accessed: 08-Jan-2021].
- [471] "KAPTON FILM 304X200X0.025MM | Kapton HN Thermal Insulating Film, 304mm x 200mm x 0.025mm | RS Components." [Online]. Available: <https://uk.rs-online.com/web/p/plastic-film/5363946/>. [Accessed: 08-Jan-2021].
- [472] "KAPTON FILM 304X200X0.075MM | Kapton HN Thermal Insulating Film, 304mm x 200mm x 0.075mm | RS Components." [Online]. Available: <https://uk.rs-online.com/web/p/plastic-film/5363968/>. [Accessed: 08-Jan-2021].
- [473] Q. Simon, D. Barreca, A. Gasparotto, *et al.*, "Ag/ZnO nanomaterials as high performance sensors for flammable and toxic gases," *Nanotechnology*, vol. 23, no. 2, 2012.
- [474] O. Singh and R. C. Singh, "Enhancement in ethanol sensing response by surface activation of ZnO with SnO<sub>2</sub>," *Mater. Res. Bull.*, vol. 47, no. 3, pp. 557–561, 2012.
- [475] A. Katoch, S. W. Choi, H. W. Kim, and S. S. Kim, "Highly sensitive and selective

## Bibliography

- H<sub>2</sub> sensing by ZnO nanofibers and the underlying sensing mechanism,” *J. Hazard. Mater.*, vol. 286, pp. 229–235, 2015.
- [476] C. Liewhiran, A. R. Camenzind, A. Teleki, S. E. Pratsinis, and S. Phanichphant, “Doctor-bladed thick films of flame-made Pd/ZnO nanoparticles for ethanol sensing,” *Curr. Appl. Phys.*, vol. 8, no. 3–4, pp. 336–339, 2008.
- [477] D. Mardare, N. Iftimie, M. Crişan, *et al.*, “Electrical conduction mechanism and gas sensing properties of Pd-doped TiO<sub>2</sub> films,” *J. Non. Cryst. Solids*, vol. 357, no. 7, pp. 1774–1779, 2011.
- [478] P. Mitra and A. Mukhopadhyay, “ZnO thin film as methane sensor,” *Bull. Polish Acad. ...*, vol. 55, no. 3, pp. 281–285, 2007.
- [479] CreativeMaterials, “114-34 SOLVENT-RESISTANT Solvent-Resistant 150 Ohm / Square Ink - Creative materials.” [Online]. Available: [http://server.creativematerials.com/datasheets/DS\\_114\\_34.pdf](http://server.creativematerials.com/datasheets/DS_114_34.pdf). [Accessed: 09-Jan-2021].
- [480] CreativeMaterials, “124-50 Conductive Ink - Creative materials.” [Online]. Available: [http://server.creativematerials.com/datasheets/DS\\_124\\_50.pdf](http://server.creativematerials.com/datasheets/DS_124_50.pdf). [Accessed: 09-Jan-2021].
- [481] CreativeMaterials, “120-24 Electrically Conductive, Carbon Filled, Epoxy Ink - Creative materials.” [Online]. Available: [http://server.creativematerials.com/datasheets/DS\\_120\\_24.pdf](http://server.creativematerials.com/datasheets/DS_120_24.pdf). [Accessed: 09-Jan-2021].
- [482] CreativeMaterials, “118-41 SOLVENT-RESISTANT SOLVENT-RESISTANT ELECTRICALLY CONDUCTIVE INK - Creative materials.” [Online]. Available: [http://server.creativematerials.com/datasheets/DS\\_118\\_41.pdf](http://server.creativematerials.com/datasheets/DS_118_41.pdf). [Accessed: 09-Jan-2021].
- [483] CreativeMaterials, “110-19 Polyimide Electrically Conductive Adhesive - Creative materials.” [Online]. Available: [http://server.creativematerials.com/datasheets/DS\\_110\\_19.pdf](http://server.creativematerials.com/datasheets/DS_110_19.pdf). [Accessed: 09-Jan-2021].
- [484] B. Whittle, D. Greenhill, K. Adams, and J. Cocker, “A New Polymeric Carbon Undercoat for Improved Leakage Current Performance of Tantalum Capacitors,” Bristol, 2015.

## Bibliography

- [485] G. I. N. Waterhouse, G. A. Bowmaker, and J. B. Metson, "The thermal decomposition of silver (I, III) oxide: A combined XRD, FT-IR and Raman spectroscopic study," *Phys. Chem. Chem. Phys.*, vol. 3, no. 17, pp. 3838–3845, 2001.
- [486] A. F. Benton and L. C. Drake, "THE DISSOCIATION PRESSURE OF SILVER OXIDE BELOW 200°," *J. Am. Chem. Soc.*, vol. 54, no. 6, pp. 2186–2194, Jun. 1932.
- [487] Novacentrix, "Product User Guide PFI-722 Conductive Flexographic Ink Product Description."
- [488] IGT, "IGT F1 Printability testers Testers for flexo and gravure inks - IGT Testing Systems." [Online]. Available: <https://www.igt.nl/wp-content/uploads/IGT-F1-brochure-ENG.pdf>. [Accessed: 09-Jan-2021].
- [489] Aalborg, "OPERATING MANUAL - GFC MASS FLOW CONTROLLER."
- [490] "Cirlex: Kapton Performance Without Limitations." [Online]. Available: <http://www.cirlex.com/>. [Accessed: 09-Jun-2021].
- [491] K. W. Lee, S. P. Kowalczyk, and J. M. Shaw, "Surface Modification of Pmda-Oda Polyimide: Surface Structure-Adhesion Relationship," *Macromolecules*, vol. 23, no. 7, pp. 2097–2100, 1990.
- [492] K. Takamura, H. Fischer, and N. R. Morrow, "Physical properties of aqueous glycerol solutions," *J. Pet. Sci. Eng.*, vol. 98–99, pp. 50–60, 2012.
- [493] Accudyne-Test, "Viscosity, Surface Tension, Specific Density and Molecular Weight of Selected Liquids (sort by surface tension descending)." [Online]. Available: [https://www.accudynetest.com/visc\\_table.html?sortby=sort\\_surface\\_tension\\_DESC](https://www.accudynetest.com/visc_table.html?sortby=sort_surface_tension_DESC). [Accessed: 12-Jan-2021].
- [494] Sigma-Aldrich, "1,2 - Propanediol SDS -SIGMA-ALDRICH." [Online]. Available: <https://www.sigmaaldrich.com/MSDS/MSDS/PleaseWaitMSDSPage.do?language=&country=GB&brand=SIAL&productNumber=82280&PageToGoToURL=https://www.sigmaaldrich.com/catalog/product/sial/82280?lang=en&region=GB>. [Accessed: 12-Jan-2021].
- [495] Acros-Organics, "n-Butanol SDS - Acros Organics," 2020. [Online]. Available: <https://www.fishersci.co.uk/store/msds?partNumber=10376070&productDescription=2.5LT+1-Butanol%2C+99%25%2C+extra+pure&countryCode=GB&language=en>. [Accessed: 12-Jan-2021].
- [496] McDermid, "Digital Rave flexographic photopolymer plate technical bulletin -

## Bibliography

- McDermid, Inc.” [Online]. Available: <https://graphics.macdermid.com/application/files/3015/7012/4358/2019-Tech-Bulletin-Digital-RAVE.pdf>. [Accessed: 09-Jan-2021].
- [497] Sigma-Aldrich, “2-Propanol SDS-SIGMA-ALDRICH.” .
- [498] F. D. Egitto, L. J. Matienzo, K. J. Blackwell, and A. R. Knoll, “Oxygen plasma modification of polyimide webs: effect of ion bombardment on metal adhesion,” *J. Adhes. Sci. Technol.*, vol. 8, no. 4, pp. 411–433, Jan. 1994.
- [499] M. Lindner, N. Rodler, M. Jesdinszki, M. Schmid, and S. Sangerlaub, “Surface energy of corona treated PP, PE and PET films, its alteration as function of storage time and the effect of various corona dosages on their bond strength after lamination,” *J. Appl. Polym. Sci.*, vol. 135, no. 11, pp. 1–9, 2018.
- [500] H.-K. Lee, S. Son, H. Lee, and S. Koo, “Adhesion Enhancement of Electroplated Cu/Electroless Ni Composite Layer to (PMDA-ODA)-Type Polyimide Films,” *J. Adhes. Sci. Technol.*, vol. 22, no. 1, pp. 47–64, Jan. 2008.
- [501] J. Siegel, M. Polıvkova, M. Staszek, K. Kolarova, S. Rimpelova, and V. ˇSvorcık, “Nanostructured silver coatings on polyimide and their antibacterial response,” *Mater. Lett.*, vol. 145, pp. 87–90, 2015.
- [502] P. Sen Wang, T. N. Wittberg, and J. D. Wolf, “A characterization of Kapton polyimide by X-ray photoelectron spectroscopy and energy dispersive spectroscopy,” *J. Mater. Sci.*, vol. 23, no. 11, pp. 3987–3991, Nov. 1988.
- [503] N. Inagaki, S. Tasaka, and K. Hibi, “Improved adhesion between plasma-treated polyimide film and evaporated copper,” *J. Adhes. Sci. Technol.*, vol. 8, no. 4, pp. 395–410, 1994.
- [504] M. Ramiasa, J. Ralston, R. Fetzer, and R. Sedev, “The influence of topography on dynamic wetting,” *Adv. Colloid Interface Sci.*, vol. 206, pp. 275–293, 2014.
- [505] X. D. Huang, S. M. Bhangale, P. M. Moran, N. L. Yakovlev, and J. Pan, “Surface modification studies of Kapton® HN polyimide films,” *Polym. Int.*, vol. 52, no. 7, pp. 1064–1069, 2003.
- [506] G. Ducom, B. Laubie, A. Ohannessian, C. Chottier, P. Germain, and V. Chatain, “Hydrolysis of polydimethylsiloxane fluids in controlled aqueous solutions,” *Water Sci. Technol.*, vol. 68, no. 4, pp. 813–820, 2013.
- [507] R. Tadmor, “Line energy and the relation between advancing, receding, and Young

- contact angles,” *Langmuir*, vol. 20, no. 18, pp. 7659–7664, 2004.
- [508] E. Karásková and U. Mollin, “Calculation of Alkoxide and Hydroxide Ion Activity Ratios in the Water — Ethanol System,” *Chem. Pap.*, vol. 47, no. 4, pp. 156–159, 1993.
- [509] A. J. B. Milne, J. A. W. Elliott, and A. Amirfazli, “Contact angles of surfactant solutions on heterogeneous surfaces,” *Phys. Chem. Chem. Phys.*, vol. 17, no. 8, pp. 5574–5585, 2015.
- [510] E. Virga, E. Spruijt, W. M. De Vos, and P. M. Biesheuvel, “Wettability of Amphoteric Surfaces: The Effect of pH and Ionic Strength on Surface Ionization and Wetting,” *Langmuir*, vol. 34, no. 50, pp. 15174–15180, 2018.
- [511] H. Horiuchi, A. Nikolov, and D. T. Wasan, “Calculation of the surface potential and surface charge density by measurement of the three-phase contact angle,” *J. Colloid Interface Sci.*, vol. 385, no. 1, pp. 218–224, 2012.
- [512] V. V. Naik and S. Vasudevan, “Sol-gel transition in dispersions of layered double-hydroxide nanosheets,” *Langmuir*, vol. 27, no. 21, pp. 13276–13283, 2011.
- [513] Y. R. Ryu, T. S. Lee, J. H. Leem, and H. W. White, “Fabrication of homostructural ZnO p-n junctions and ohmic contacts to arsenic-doped p-type ZnO,” *Appl. Phys. Lett.*, vol. 83, no. 19, pp. 4032–4034, 2003.
- [514] L. J. Brillson and Y. Lu, “ZnO Schottky barriers and Ohmic contacts,” *J. Appl. Phys.*, vol. 109, no. 12, 2011.
- [515] Y. Li, A. Paulsen, I. Yamada, Y. Koide, and J. J. Delaunay, “Bascule nanobridges self-assembled with ZnO nanowires as double Schottky barrier UV switches,” *Nanotechnology*, vol. 21, no. 29, 2010.
- [516] D. Somvanshi and S. Jit, “Mean barrier height and richardson constant for Pd/ZnO Thin film-based Schottky Diodes grown on n-Si substrates by thermal evaporation method,” *IEEE Electron Device Lett.*, vol. 34, no. 10, pp. 1238–1240, 2013.
- [517] N. S. Parmar and K. G. Lynn, “Sodium doping in ZnO crystals,” *Appl. Phys. Lett.*, vol. 106, no. 2, pp. 8–11, 2015.
- [518] Z. Wu, Y. Li, L. Gao, S. Wang, and G. Fu, “Synthesis of Na-doped ZnO hollow spheres with improved photocatalytic activity for hydrogen production,” *Dalt. Trans.*, vol. 45, no. 27, pp. 11145–11149, 2016.
- [519] M. W. Allen, S. M. Durbin, and J. B. Metson, “Silver oxide Schottky contacts on n-

- type ZnO,” *Appl. Phys. Lett.*, vol. 91, no. 5, p. 053512, Jul. 2007.
- [520] T. Wang, Y. Liao, B. Luo, *et al.*, “Synthesis and Application of Ag<sub>2</sub>O Doped ZnO Based Sensor for Detecting CH<sub>4</sub> Gas,” *ICEMPE 2019 - 2nd Int. Conf. Electr. Mater. Power Equipment, Proc.*, pp. 139–142, 2019.
- [521] Z. Karami Horastani, S. M. Sayedi, M. H. Sheikhi, and E. Rahimi, “Effect of silver additive on electrical conductivity and methane sensitivity of SnO<sub>2</sub>,” *Mater. Sci. Semicond. Process.*, vol. 35, pp. 38–44, 2015.
- [522] “Nanosilver Powders | NovaCentrix.” [Online]. Available: <https://www.novacentrix.com/products/nanopowders/nanosilver>. [Accessed: 09-Jun-2021].
- [523] H. Abdullah, D. H. Kuo, Y. R. Kuo, F. A. Yu, and K. Bin Cheng, “Facile Synthesis and Recyclability of Thin Nylon Film-Supported n-Type ZnO/ p-Type Ag<sub>2</sub>O Nano Composite for Visible Light Photocatalytic Degradation of Organic Dye,” *J. Phys. Chem. C*, vol. 120, no. 13, pp. 7144–7154, 2016.
- [524] H. L. Yu, Q. X. Wu, J. Wang, *et al.*, “Simple fabrication of the Ag-Ag<sub>2</sub>O-TiO<sub>2</sub> photocatalyst thin films on polyester fabrics by magnetron sputtering and its photocatalytic activity,” *Appl. Surf. Sci.*, vol. 503, no. August 2019, 2020.
- [525] H. W. Kim, H. G. Na, D. S. Kwak, H. Y. Cho, and Y. J. Kwon, “Enhanced gas sensing characteristics of Ag<sub>2</sub>O-functionalized networked In<sub>2</sub>O<sub>3</sub> nanowires,” *Jpn. J. Appl. Phys.*, vol. 52, no. 10 PART2, pp. 1–7, 2013.
- [526] H. von Wenckstern, A. Lajn, A. Laufer, *et al.*, “Ag related defect state in ZnO thin films,” 2010, vol. 122, no. January 2010, pp. 122–123.
- [527] B. Du Ahn, H. S. Kang, J. H. Kim, G. H. Kim, H. W. Chang, and S. Y. Lee, “Synthesis and analysis of Ag-doped ZnO,” *J. Appl. Phys.*, vol. 100, no. 9, p. 093701, Nov. 2006.
- [528] V. Postica, A. Vahl, D. Santos-Carballal, *et al.*, “Tuning ZnO Sensors Reactivity toward Volatile Organic Compounds via Ag Doping and Nanoparticle Functionalization,” *ACS Appl. Mater. Interfaces*, vol. 11, no. 34, pp. 31452–31466, 2019.
- [529] A. V. Kolobov, A. Rogalev, F. Wilhelm, N. Jaouen, T. Shima, and J. Tominaga, “Thermal decomposition of a thin AgO<sub>x</sub> layer generating optical near-field,” *Appl. Phys. Lett.*, vol. 84, no. 10, pp. 1641–1643, 2004.

## Bibliography

- [530] Y. C. Her, Y. C. Lan, W. C. Hsu, and S. Y. Tsai, "The Characteristics of Reactively Sputtered AgOx Films Prepared at Different Oxygen Flow Ratios and Its Effect on Super-Resolution Near-Field Properties," *Japanese J. Appl. Physics, Part 1 Regul. Pap. Short Notes Rev. Pap.*, vol. 43, no. 1, pp. 267–272, 2004.
- [531] A. I. Boronin, S. V. Koscheev, O. V. Kalinkina, and G. M. Zhidomirov, "Oxygen states during thermal decomposition of Ag<sub>2</sub>O: XPS and UPS study," *React. Kinet. Catal. Lett.*, vol. 63, no. 2, pp. 291–296, Mar. 1998.
- [532] J. F. Weaver and G. B. Hoflund, "Surface Characterization Study of the Thermal Decomposition of AgO," *J. Phys. Chem.*, vol. 98, no. 34, pp. 8519–8524, Aug. 1994.
- [533] UBE industries Ltd., "Upilex-RN and S grade technical specifications," no. 0. .
- [534] "Efficient Ink Delivery: The Evolution of the Chambered Doctor Blade System - Flexographic Technical Association." [Online]. Available: <https://www.flexography.org/industry-news/efficient-ink-delivery-evolution-chambered-doctor-blade-system/>. [Accessed: 26-May-2021].
- [535] A. Lee, K. Sudau, K. H. Ahn, S. J. Lee, and N. Willenbacher, "Optimization of experimental parameters to suppress nozzle clogging in inkjet printing," *Ind. Eng. Chem. Res.*, vol. 51, no. 40, pp. 13195–13204, 2012.
- [536] K. Valadi, S. Gharibi, R. Taheri-Ledari, S. Akin, A. Maleki, and A. E. Shalan, "Metal oxide electron transport materials for perovskite solar cells: a review," *Environ. Chem. Lett.*, vol. 19, no. 3, pp. 2185–2207, 2021.
- [537] "Pulseforge® 1200 technical specifications| NovaCentrix." [Online]. Available: <https://www.novacentrix.com/products/pulseforge/1200>. [Accessed: 26-Sep-2018].
- [538] A. V Shchukarev and D. V Korolkov, "Central European Science Journals XPS Study of Group IA Carbonates," *Cent. Eur. J. Chem. CEJC*, vol. 2, no. 2, pp. 347–362, 2004.
- [539] E. S. Jang, J. H. Won, Y. W. Kim, Z. Cheng, and J. H. Choy, "Synthesis of porous and nonporous ZnO nanobelt, multipod, and hierarchical nanostructure from Zn-HDS," *J. Solid State Chem.*, vol. 183, no. 8, pp. 1835–1840, 2010.
- [540] K. F. Lin, H. M. Cheng, H. C. Hsu, L. J. Lin, and W. F. Hsieh, "Band gap variation of size-controlled ZnO quantum dots synthesized by sol-gel method," *Chem. Phys. Lett.*, vol. 409, no. 4–6, pp. 208–211, 2005.
- [541] L. Zhang, L. Yin, C. Wang, Y. Qi, and D. Xiang, "Origin of Visible



- Photoluminescence of ZnO Quantum Dots : Defect-Dependent and Size-Dependent,” *Society*, pp. 9651–9658, 2010.
- [542] M. K. Patra, M. Manoth, V. K. Singh, *et al.*, “Synthesis of stable dispersion of ZnO quantum dots in aqueous medium showing visible emission from bluish green to yellow,” *J. Lumin.*, vol. 129, no. 3, pp. 320–324, 2009.
- [543] C. J. Barnett, G. Jackson, D. R. Jones, *et al.*, “Investigation into the effects of surface stripping ZnO nanosheets,” *Nanotechnology*, vol. 29, no. 16, 2018.
- [544] C. J. Barnett, N. A. Smith, D. R. Jones, T. G. G. Maffei, and R. J. Cobley, “Effects of Vacuum Annealing on the Conduction Characteristics of ZnO Nanosheets,” *Nanoscale Res. Lett.*, vol. 10, no. 1, pp. 4–9, 2015.
- [545] J. Pan, J. Chen, Q. Huang, *et al.*, “Size Tunable ZnO Nanoparticles to Enhance Electron Injection in Solution Processed QLEDs,” *ACS Photonics*, vol. 3, no. 2, pp. 215–222, 2016.
- [546] X. Xu, C. Xu, J. Dai, J. Hu, F. Li, and S. Zhang, “Size dependence of defect-induced room temperature ferromagnetism in undoped ZnO nanoparticles,” *J. Phys. Chem. C*, vol. 116, no. 15, pp. 8813–8818, 2012.
- [547] A. Layek, P. C. Stanish, V. Chirmanov, and P. V. Radovanovic, “Hybrid ZnO-based nanoconjugate for efficient and sustainable white light generation,” *Chem. Mater.*, vol. 27, no. 3, pp. 1021–1030, 2015.
- [548] S. Wilken, J. Parisi, and H. Borchert, “Role of oxygen adsorption in nanocrystalline ZnO interfacial layers for polymer-fullerene bulk heterojunction solar cells,” *J. Phys. Chem. C*, vol. 118, no. 34, pp. 19672–19682, 2014.
- [549] R. Pérez-Cuapio, J. A. Alvarado, M. Pacio, *et al.*, “Enhanced green photoluminescence and dispersion of ZnO quantum dots shelled by a silica shell,” *J. Nanoparticle Res.*, vol. 22, no. 9, 2020.
- [550] X. Wang and J. Li, “Sol-gel fabrication of Ag-Coated ZnO quantum dots nanocomposites with excellent photocatalytic activity,” *Opt. Mater. (Amst.)*, vol. 118, no. May, p. 111235, 2021.
- [551] D. Haranath, S. Sahai, and P. Joshi, “Tuning of emission colors in zinc oxide quantum dots,” *Appl. Phys. Lett.*, vol. 92, no. 23, pp. 44–47, 2008.
- [552] A. A. Mosquera, D. Horwat, A. Rashkovskiy, *et al.*, “Exciton and core-level electron confinement effects in transparent ZnO thin films,” *Sci. Rep.*, vol. 3, pp. 1–7, 2013.

## Bibliography

- [553] Z. Jin, Y. X. Zhang, F. L. Meng, *et al.*, “Facile synthesis of porous single crystalline ZnO nanoplates and their application in photocatalytic reduction of Cr(VI) in the presence of phenol,” *J. Hazard. Mater.*, vol. 276, pp. 400–407, 2014.
- [554] N. Han, X. Wu, L. Chai, H. Liu, and Y. Chen, “Counterintuitive sensing mechanism of ZnO nanoparticle based gas sensors,” *Sensors Actuators, B Chem.*, vol. 150, no. 1, pp. 230–238, 2010.
- [555] S. K. Lim, S. H. Hwang, S. Kim, and H. Park, “Preparation of ZnO nanorods by microemulsion synthesis and their application as a CO gas sensor,” *Sensors Actuators, B Chem.*, vol. 160, no. 1, pp. 94–98, 2011.
- [556] G. Sberveglieri, C. Baratto, E. Comini, *et al.*, “Synthesis and characterization of semiconducting nanowires for gas sensing,” *Sensors Actuators, B Chem.*, vol. 121, no. 1, pp. 208–213, 2007.
- [557] D. K. Kwon, Y. Porte, K. Y. Ko, H. Kim, and J. M. Myoung, “High-Performance Flexible ZnO Nanorod UV/Gas Dual Sensors Using Ag Nanoparticle Templates,” *ACS Appl. Mater. Interfaces*, vol. 10, no. 37, pp. 31505–31514, 2018.
- [558] A. Hassanpour, S. Shen, and P. Bianucci, “Sodium-doped oriented zinc oxide nanorod arrays: Insights into their aqueous growth design, crystal structure, and optical properties,” *MRS Commun.*, vol. 8, no. 2, pp. 570–576, 2018.
- [559] C. C. Lin and Y. Y. Li, “Synthesis of ZnO nanowires by thermal decomposition of zinc acetate dihydrate,” *Mater. Chem. Phys.*, vol. 113, no. 1, pp. 334–337, 2009.
- [560] P. K. Kannan, R. Saraswathi, and J. B. B. Rayappan, “A highly sensitive humidity sensor based on DC reactive magnetron sputtered zinc oxide thin film,” *Sensors Actuators, A Phys.*, vol. 164, no. 1–2, pp. 8–14, 2010.
- [561] P. K. Kannan, R. Saraswathi, and J. B. B. Rayappan, “CO<sub>2</sub> gas sensing properties of DC reactive magnetron sputtered ZnO thin film,” *Ceram. Int.*, vol. 40, no. 8 PART B, pp. 13115–13122, 2014.
- [562] X. Wen, Y. He, C. Chen, *et al.*, “Magnetron sputtered ZnO buffer layer for Sb<sub>2</sub>Se<sub>3</sub> thin film solar cells,” *Sol. Energy Mater. Sol. Cells*, vol. 172, no. February, pp. 74–81, 2017.
- [563] N. Kondal and S. K. Tiwari, “Origin of polychromatic emission and defect distribution within annealed ZnO nanoparticles,” *Mater. Res. Bull.*, vol. 88, pp. 156–165, 2017.

## Bibliography

- [564] W. Park, S. F. Shaikh, J. W. Min, S. K. Lee, B. H. Lee, and M. M. Hussain, "Contact resistance reduction of ZnO thin film transistors (TFTs) with saw-shaped electrode," *Nanotechnology*, vol. 29, no. 32, 2018.
- [565] W. Y. Wu, J. M. Ting, and P. J. Huang, "Electrospun ZnO Nanowires as Gas Sensors for Ethanol Detection," *Nanoscale Res. Lett.*, vol. 4, no. 6, pp. 513–517, 2009.
- [566] W. Yang, J. Liu, Z. Guan, *et al.*, "Morphology, electrical and optical properties of magnetron sputtered porous ZnO thin films on Si(100) and Si(111) substrates," *Ceram. Int.*, vol. 46, no. 5, pp. 6605–6611, 2020.
- [567] M. D. McCluskey and S. J. Jokela, "Defects in ZnO," *J. Appl. Phys.*, vol. 106, no. 7, 2009.
- [568] J. Han, P. Q. Mantas, and A. M. R. Senos, "Densification and grain growth of Al-doped ZnO," *J. Mater. Res.*, vol. 16, no. 2, pp. 459–468, 2001.
- [569] W. Hadouchi, J. Rousset, D. Tondelier, B. Geffroy, and Y. Bonnassieux, "Zinc oxide as a hole blocking layer for perovskite solar cells deposited in atmospheric conditions," *RSC Adv.*, vol. 6, no. 72, pp. 67715–67723, 2016.
- [570] H. Li, S. Member, X. Mu, Y. Yang, A. J. Mason, and S. Member, "Low Power Multimode Electrochemical Gas Sensor Array System for Wearable Health and Safety Monitoring," vol. 14, no. 10, pp. 3391–3399, 2014.
- [571] P. C. Chen, G. Shen, and C. Zhou, "Chemical sensors and electronic noses based on 1-D metal oxide nanostructures," *IEEE Trans. Nanotechnol.*, vol. 7, no. 6, pp. 668–682, 2008.
- [572] I. C. Bourg, S. S. Lee, P. Fenter, and C. Tournassat, "Stern Layer Structure and Energetics at Mica-Water Interfaces," *J. Phys. Chem. C*, vol. 121, no. 17, pp. 9402–9412, 2017.
- [573] J. N. Israelachvili, "Interactions Involving Polar Molecules," in *Intermolecular and Surface Forces*, Elsevier, 2011, pp. 71–90.
- [574] M. V. Fedotova and S. E. Kruchinin, "Hydration of acetic acid and acetate ion in water studied by 1D-RISM theory," *J. Mol. Liq.*, vol. 164, no. 3, pp. 201–206, 2011.
- [575] M. I. Loría-Bastarrachea, W. Herrera-Kao, J. V. Cauich-Rodríguez, J. M. Cervantes-Uc, H. Vázquez-Torres, and A. Ávila-Ortega, "A TG/FTIR study on the thermal degradation of poly(vinyl pyrrolidone)," *J. Therm. Anal. Calorim.*, vol. 104, no. 2, pp. 737–742, 2011.

## Bibliography

- [576] V. M. Bogatyrev, N. V. Borisenko, and V. A. Pokrovskii, “Thermal degradation of polyvinylpyrrolidone on the surface of pyrogenic silica,” *Russ. J. Appl. Chem.*, vol. 74, no. 5, pp. 839–844, 2001.
- [577] D. Yu, C. Chen, S. Xie, *et al.*, “Mesoporous vanadium pentoxide nanofibers with significantly enhanced Li-ion storage properties by electrospinning,” *Energy Environ. Sci.*, vol. 4, no. 3, pp. 858–861, 2011.
- [578] R. M. Rioux, H. Song, M. Grass, *et al.*, “Monodisperse platinum nanoparticles of well-defined shape: synthesis, characterization, catalytic properties and future prospects,” *Top. Catal.*, vol. 39, no. 3–4, pp. 167–174, 2006.
- [579] “DOWANOL™ DPM Glycol Ether | Dow Inc.” [Online]. Available: <https://www.dow.com/en-us/pdp.dowanol-dpm-glycol-ether.22345z.html>. [Accessed: 11-Jan-2021].
- [580] “MacDermid Graphics Solutions | Digital RAVE Photopolymer Printing Plates.” [Online]. Available: <https://graphics.macdermid.com/products/photopolymer-plates/digital-sheet-photopolymer/standard-digital/digital-rave>. [Accessed: 11-Jan-2021].
- [581] M. K. Williams, A. E. S. Snla, M. A. Huelskamp, K. P. Armstrong, J. L. Brandon, and J. M. Lavoie, “Kapton HN Investigations U , S , DEPARTMENT OF ENERGY,” 1990.
- [582] J. S. R. Wheeler and S. G. Yeates, “Polymers in Inkjet Printing,” *Fundam. Inkjet Print.*, pp. 117–140, 2015.
- [583] A. K. Sankaran and J. P. Rothstein, “Effect of viscoelasticity on liquid transfer during gravure printing,” *J. Nonnewton. Fluid Mech.*, vol. 175–176, pp. 64–75, 2012.
- [584] S. Jeong Kim, S. Jun Park, I. Young Kim, Y. Hee Lee, and S. I. Kim, “Thermal characteristics of poly(vinyl alcohol) and poly(vinylpyrrolidone) IPNs,” *J. Appl. Polym. Sci.*, vol. 86, no. 8, pp. 1844–1847, 2002.
- [585] Sigma-Aldrich, “Polyvinylpyrrolidone powder, average Mw ~ 55,000 | 9003-39-8 | Sigma-Aldrich.” [Online]. Available: <https://www.sigmaaldrich.com/catalog/product/aldrich/856568?lang=en&region=GB>. [Accessed: 09-Jan-2021].
- [586] Dupont, “DuPont™ Kapton® Datasheet,” <http://www.dupont.com/content/dam/dupont/products-and-services/membranes-and->

## Bibliography

- films/polyimide-films/documents/DEC-Kapton-summary-of-properties.pdf*, vol. 50, pp. 1–7, 2012.
- [587] D. Zhang, M. Chen, S. Wu, Q. Liu, and J. Wan, “Preparation of expanded graphite/polyethylene glycol composite phase change material for thermoregulation of asphalt binder,” *Constr. Build. Mater.*, vol. 169, pp. 513–521, 2018.
- [588] D. L. Ho, B. Hammouda, S. R. Kline, and W. R. Chen, “Unusual phase behavior in mixtures of poly(ethylene oxide) and ethyl alcohol,” *J. Polym. Sci. Part B Polym. Phys.*, vol. 44, no. 3, pp. 557–564, 2006.
- [589] D. R. Jones, A. Tarat, and T. G. G. Maffei, “Gas Sensing Using Zinc Oxide Nanosheets,” p. 3, 2013.